A NOVEL DUAL-SPIN ACTUATION MECHANISM FOR SMALL CALIBRE, SPIN STABILISED, GUIDED PROJECTILES

JAMES J. NORRIS

A THESIS SUBMITTED FOR THE DEGREE OF
DOCTOR OF PHILOSOPHY
AT THE UNIVERSITY OF CRANFIELD

ACADEMIC YEAR 2017–2021

CRANFIELD UNIVERSITY

Cranfield Defence and Security

PhD.

Academic Year 2017 – 2021

James J. Norris

A novel dual-spin actuation mechanism for small calibre, spin stabilised, guided projectiles

Supervised by

A. Hameed and J. Economou

Abstract

SMALL calibre projectiles are spin-stabilised to increase ballistic stability, often at high frequencies. Due to hardware limitations, conventional actuators and methods are unable to provide satisfactory control at such high frequencies. With the reduced volume for control hardware and increased financial cost, incorporating traditional guidance methods into small-calibre projectiles is inherently difficult. This work presents a novel method of projectile control which addresses these issues and conducts a systems level analysis of the underlying actuation mechanism. The design is shown to be a viable alternative to traditional control methods.

Firstly, a 7 Degree-of-Freedom (DoF) dynamic model is created for dual-spin projectiles, including aerodynamic coefficients. The stability of dual-spin projectiles, governed by the gyroscopic and dynamic stability factors is given, discussed and unified across available literature. The model is implemented in a Matlab/Simulink simulation environment, which is in turn validated against a range of academic literature and experimental test data.

The novel design and fundamental operating principle are presented. The actuation mechanism (AM) is then mathematically formulated from both a velocity change (ΔV) and a lateral acceleration ($\tilde{a}$) perspective. A set of axioms are declared and verified using the 7-DoF model, showing that the inherently discrete system behaviour can be controlled continuously via these control variables, ΔV or $\tilde{a}$. Control state switching is simplified to be instantaneous, then expanded to be generically characterised by an arbitrarily complex mathematical function. A detailed investigation, parametric analysis and sensitivity study is undertaken to understand the system behaviour.

A Monte Carlo procedure is described, which is used to compare the correction capabilities of different guidance laws (GLs). A bespoke Zero-Effort-Miss (ZEM) based GL

is synthesised from the mathematical formulation of the AM, with innately more knowledge of the system behaviour, which allows superior error correction. This bespoke GL is discussed in detail, a parametric study is undertaken, and both the GL parameters and PID controller gains are optimised using a genetic algorithm. Artificial Intelligence (AI) Reinforcement learning methods are used to emulate a GL, as well as controlling the AM and operating as a GL, simultaneously.

The novel GLs are compared against a traditional proportional navigation GL in a nominal system and all GLs were able to control the AMs, reducing the miss distance to a satisfactory margin. The ZEM-based GL provided superior correction to the AI GL, which in turn provided superior correction over proportional navigation. Example CAD models are shown, and the stability analysis is conducted on the geometry. The CAD model is then used in CFD simulations to determine aerodynamic coefficients for use in the 7-DoF dynamic model. The novel control method was able to reduce the 95% dispersion diameter of a traditional ballistic 7.62mm projectile from 70mm to 33mm. Statistical data analysis showed there was no significant correlation or bias present in either the nominal or 7-DoF dispersion patterns.

This project is co-sponsored by BAE Systems and ESPRC (ref. 1700064). The contents of this thesis are covered by patent applications GB2011850.1, GB 2106035.5 and EP 20275128.5. Two papers are currently published (DOI: 10.1016/j.dt.2019.06.003, the second DOI is pending) and one is undergoing peer review.

Keywords - Guided, direct-fire, ballistic, dual-spin, small-calibre, projectile, actuation mechanism, artificial intelligence, reinforcement learning, DDPG, DQN, genetic algorithm, PID controller, CEP

Acknowledgements

AFTER four years and more than 700 pages of work, half of which didn't make the cut, I'm faced with writing the acknowledgements which are by far the most daunting task. There so many people to thank for their contributions to this project and I am not the one with the words to do it adequately. With that being said, I would like to thank:

Prof. Amer Hameed first and foremost, for going above and beyond what can be expected of a supervisor. My secondary supervisor Dr. John Economou; other faculty members at Cranfield, Marco Debiasi, Steve Champion and Dr Aimee Helliker for their tremendous help, support and guidance throughout this project and other academic endeavours. Project co-sponsor BAE, and their company supervisor Simon Parker for his assistance throughout.

My friends for the persiflage - Gareth Jones, Alex Shield, Alan Brangwyn, Alex Main and Mark Durham. My colleagues Jordan Hamilton and Ayden Clay, for the insightful, thought provoking conversations, and of course putting up with my incessant questions. It's been a genuine pleasure working with you both, truly the best rubber duck debuggers one could ask for.

My parents Linda and David, and my family, without whose constant love, support and encouragement, none of this would have been possible. Of course, thanks to new puppy Melee for all her assistance in the final few months! And finally my fiancée, Charlotte Newton. You've been a constant pillar of support throughout this. Thank you for your encouragement and belief from the start.

Thank you all for your contributions.

Contents

List of Figures

List of Tables

List of Algorithms

Nomenclature

The following are a list of the global terms, symbols, abbreviations and acronyms used throughout the manuscript. There may be instances where terms are reused and defined locally with different definitions, but this will be explicitly stated in the text, in close proximity to the new usage, and the redefinition will not clash with other related terms.

Greek

α	Angle of Attack
α_t	Combined angle of attack $\sqrt{\alpha^2+\beta^2}$
$\dot{\alpha}$	$\frac{d\alpha}{dt}$
β	Angle of side-slip
Γ	Flight envelope of q-LPV model
δ_i	Canard deflection angle in the i plane
ε	Integral normalised miss error
$\hat{\varepsilon}$	Monte Carlo batch averaged normalised integral error
ζ	Complex yaw, $\alpha + i\beta$
η	Genetic algorithm mutation chance
η_λ	Genetic algorithm mutation chance decay
θ	Pitch angle
λ_1, λ_n	Nutation damping exponent
λ_2, λ_p	Precession damping exponent
$\dot{\lambda}$	Line of Site rate of change
μ	Mean
ξ	Bespoke GL closing velocity damping coefficient

ρ	Medium density
ρ	Airframe trimming vector
τ	Period for one complete roll rotation with bias manoeuvre
$\tau_{F,A}$	Frictional torque at bearing
τ_M	Motor torque at the bearing
ϕ	Roll angle
ϕ_{ON}/ϕ_{OFF}	Roll angles for beginning and end of bias manoeuvre
ϕ_a	Size of bias manoeuvre
ϕ_B	Angle of bias manoeuvre mid point
ϕ_{ω_0}, ϕ_{ω_B}	The angle ϕ at which the spin rate ω reaches the equilibrium value of ω_0 and ω_B respectively
ψ	Yaw angle
$\vec{\Omega}$	Rotation vector of line of sight
$\omega_{0,B}$	Roll rate of control force in (Un)Biased state
ω	Roll rate ($\dot{\phi}$)

Latin

a	Acceleration
$\tilde{a}$	Latax from one bias manoeuvre, $[a_{\text{Mag}}, a_\phi]^{\text{T}}$
$\tilde{a}_{Max}$	Maximum latax available from one bias manoeuvre
a_{Mag}	Magnitude of bias manoeuvre latax
a_ϕ	Roll angle of latax from one bias manoeuvre
D	Reference diameter (calibre)
d	Radial miss distance in picture plane
d[_]	Infinitesimal change in [_]
F	Force
F_c	Lateral control force on projectile
G	Genetic algorithm generations
g	Gravitational constant (9.81m.s^{-2})

$\mathbf{H}$	Global generic controller
I_{ij}	moment of inertia of axis i about axis j (xx axial, yy transverse, zz also transverse for longitudinally symmetric bodies)
i	Imaginary unit $\sqrt{-1}$
$k_{ON/OFF}$	Decay and growth rates for chosen bias switching functions
$k_{P,I,D}$	Proportional, Integral, Differential Gains of PID controller
k_s	Static friction coefficient
k_v	Viscous friction coefficient
$\mathscr{M}$	Mach number, $\rho(h)/v_{\text{sound}}(h)$
M	Turning moment
m	Projectile mass
N	Proportional Navigation Constant
N_I	Total number of impacts
$\vec{p}$	Spin vector
$\vec{p}_{(A/F)}$	Spin vector (Of Aft/Forward section)
p_H	p-value under the assumption of probability H
$\bar{q}$	Dynamic pressure, $= \frac{1}{2}\rho V^2$
$\vec{r}_{(A/F)x}$	Distance from composite CoM to section CoM
$\vec{R}_{(A/F)x}$	Distance between section CoM and Magnus CoP
R	Longitudinal range to target
S	Reference area
S_d	Dynamic stability factor
S_g	Gyroscopic stability factor
S_c	Reference area of canards
S_d^{DS}	Dual-spin Dynamic stability factor
S_g^{DS}	Dual-spin Gyroscopic stability factor
T	Total flight time
T_{ON}, T_{OFF}	Time taken for activation/deactivation of bias manoeuvre to switch completely
t	Time
u	Velocity along longitudinal axis of the earth reference frame

V	Total projectile velocity
V_k	Bespoke GL linear regime closing velocity
V_{PT}	Bespoke GL closing velocity function
ΔV	Change in velocity from one bias manoeuvre
δV	Change in velocity from one bias manoeuvre
δV_{Max}	Maximum change in velocity from bias manoeuvre
v	Velocity along lateral axis of the earth reference frame
w	Velocity along normal axis of the earth reference frame
$\vec{x}$	Longitudinal axis of projectile
x_c	Distance of canard root chord from total CoM
x_{COM}	Distance from projectile base to CoM
x	Distance in longitudinal axis of the earth reference frame
y	Distance in lateral axis of the earth reference frame
z	Distance in normal axis of the earth reference frame

Aerodynamic Coefficients, Forces and Moments

C_A	Total Longitudinal
C_Y	Total Lateral
C_N	Total Normal
$C_{D_0}/C_{D_{\delta^2}}$	Zero yaw / yaw dependant drag term
C_D	Drag force
C_{l_P}	Spin damping moment
C_{l_δ}	Spin driving moment
C_{L_0}	Zero yaw lift
C_{L_α}	Lift (slope) force
$C_{N_{P\alpha}}$	Magnus force
$C_{M_{P\alpha}}$	Magnus moment
C_{N_α}	Normal force
C_{M_α}	Overturning (Pitching) moment

$C_{N_q} + C_{N_\alpha}$	Pitch Damping force
$C_{M_q} + C_{M_{\dot{\alpha}}}$	Pitch damping moment
C_{N_δ}	Normal force of canards
C_{M_δ}	Overturning (Pitching) moment caused by canards

F_D	Drag force
F_{D0}	Zero yaw drag force
F_L	Lift force
$F_{N_{P\alpha}}$	Magnus force
$F_{\mathscr{N}} = \mathscr{N}_q + \mathscr{N}_{\dot{\alpha}}$	Pitch damping force
M_{l_P}	Spin Damping moment
M_{l_δ}	Spin driving moment
$M_{M_{P\alpha}}$	Magnus moment
M_α	Overturning moment
$M_{\mathscr{N}} = M_q + M_{\dot{\alpha}}$	Pitch damping moment

Universal Subscripts

0	Initial condition
A	Aft section of dual-spin projectile
Dem	Demanded value from controller
e	Earth axis reference frame
F	Forward section of dual-spin projectile
T	Target parameter
t	Instantaneous value at time t
x	Longitudinal axis of the earth reference frame
y	Lateral axis of the earth reference frame
z	Normal axis of the earth reference frame

Universal Superscripts

B	Body axis
DS	Pertaining specifically to dual-spin projectiles
E	Earth axis
S	Value or measurement from a sensor
W	Wind axis
$*$	Multiplied by $\frac{\rho SD}{2m}$

Acronyms and Abbreviations

AI	Artificial Intelligence
AM	Actuation Mechanism
AoA	Angle of Attack
CAD	Computer Aided Design
CEP	Circular Error Probability
CFD	Computational Fluid Dynamics
CoM	Centre of Mass
CoP	Centre of Pressure
`DATCOM`	USAF Stability and Control Data Compendium
DDPG	Deep Deterministic Policy Gradient
DoF	Degree of freedom
DQN	Deep Q-Network
DRMS	Direct Root Mean Squared
DSC	Dual-spin projectile with active control surfaces
DSNC	Dual-spin projectile with no or passivated control surfaces
GA	Genetic algorithm
GL	Guidance Law
GSCP	Guided Small Calibre Projectiles
IMU	Inertial Measurement Unit

LATAX	Lateral acceleration
LoS	Line-of-sight
LPV	Linear parameter varying
LTI	Linear Time Invariant
LTV	Linear Time Varying
MCS	Monte Carlo Simulation
MEMS	Microelectromechanical Systems
NN	Neural Network
PDF	Probability density function
PID	Proportional Integral Derivative feedback
PN	Proportional Navigation
PZT	Piezoelectric
q-	quasi-
R95	Radius containing 95%
RL	Reinforcement Learning
SCGP	Small Calibre Guided Projectiles
SMC	Sliding Mode Control
SSC	Single-spin projectile with active control surfaces
SSNC	Single-spin projectile with no or passivated control surfaces
TRL	Technological Readiness Level
ZEM	Zero Effort Miss

Chapter 1

Introduction

LONG range weapons have been an integral part of warfare throughout human history. The ability to cause a desired effect on a target from range enables the user to keep distance from potential danger. Early weapon development was primarily focused on increasing the area of effect, which led to the introduction of artillery. Originally using tension energy system like catapults and trebuchets to simply fire larger calibre projectiles, artillery evolved quickly with the introduction of black powder to deliver these larger projectiles at higher speeds and longer ranges. Projectiles were adapted from being purely kinetic, into missiles and shells which carry payloads of secondary munitions or explosives to increase the area of effect. The up-scaling continued in World-War II, with the German V-2 rocket system introducing the concept of long-range ballistic missiles, and then intercontinental ballistic missiles (ICBMs).

With the advent of modern warfare, munition development has reversed direction and demanded a higher accuracy of the systems. Primarily, a higher munition accuracy means a larger probability of achieving a successful target effect on the first round; this results in a lower economic and logistical burden since less munitions are needed. In addition, large scale volume of fire tactics like artillery barrages, are a high a risk for collateral damage. While this was less of a problem throughout history, where battlefields were often well away from any civilisations, modern warfare is increasingly taking place in built up areas, with a high density of civilian populations and structures. Both factors led to the advent of guided weapons, which are now well established in modern arsenals.

Guided weapons encompass a family of ranged munitions which are adorned with some

kind of control mechanism, able to intentionally modify the trajectory. The weapons can be missiles or rockets, such as the aforementioned ICBMs, with consumable onboard fuel or resources to constantly impart thrust throughout flight; or they can be projectiles such as artillery shells, which are ballistic and have no onboard resources for thrust. Predominantly, guided weapons all use some combination of rearward mounted fins and forward mounted canards. Theses lifting surfaces can be passivated and stationary, which are traditionally used for ensuring munition stability, or they can be active which are used for physically imparting the control force. Much like the ailerons on aircraft wings, these controllable fins have an adjustable pitch angle, which changes the lift force they produce. The control and guidance architecture is built around this lift force. The control method is not restricted to using lifting surfaces, in fact many other novel methods have been investigated, rather lifting surfaces are a mainstay in commercial aviation and are thus very well understood and researched.

Early concepts of guided weapons tend to use proprietary munitions and launch platforms and this is true for most technological advancements. For guided weapons in modern militaries, swapping munition stocks for the latest advancements is a logistical and financially burden. As such, it is highly advantageous to develop guided munitions in a conventional and standardised form factor, so they can be interchanged with conventional unguided munitions as the situation requires. Some examples of this are Raytheon's 155mm M982 Excalibur [1], the US Army's 155mm M712 Copperhead [2], and Saab Bofors Dynamics' 120mm 'THOR' [3] (or STRIX). These projectiles all use fin stabilisation and contain the flight computer, guidance actuators and sensors on board. The former two use fin guidance as well, but the Bofors THOR uses 12 lateral thruster rockets to provide mid-course corrections. They are more expensive, guided versions of the standard 155mm artillery munition.

Projectiles are by definition, ballistic, there are no onboard resources for sustained thrust. To maintain stability throughout the flight they are spun during launch by rifling in the weapon barrels. Helical grooves are cut through the full length of the barrel to induce a spin as the projectile travels down the barrel. Generally speaking, a higher spin rate means a projectile is more stable and is more resistant to aerodynamic perturbation. At longer ranges however, projectiles can be spun *too* much resulting in 'super-stability', where the

projectile is less able to follow a natural trajectory which thereby results in it being more susceptible to perturbations (discussed in §3). Either way, spinning the projectile makes the trajectories more reliable and importantly, predictable.

One consistent theme across the majority of guided weapons is that they have a relatively low spin rate. High roll rates are detrimental to the stability of rockets and missiles, owing to the high coupling between degrees of freedom, comparatively low response frequency of the actuators and actuator mechanisms, and the general desire to conserve onboard resources by demanding as little effort from the actuators as possible. This naturally low spin rate, combined with the relatively large volumetric budget available, means that actually implementing the control hardware in missiles is comparatively simple; though this of course does not deduct from the complexities of the hardware and control theory which goes into these systems.

Smaller calibre weapons systems (<40mm) still mostly rely on volume of fire to achieve a desired effect on target: rotary cannons on aircraft, infantry light machine guns and anti-aircraft emplacements to name a few. One notable exception for small arms where accuracy is paramount, is for snipers. Infantry sniper weapons, or sniper rifles, have evolved to effectively deliver conventional ballistic ammunition out to distances of up to 5km, up to the range of accuracy permitted by the ammunition itself [4]. Sniper rifles can use widely available ammunition such as the 7.62x51mm, 7.62x54mmR or 12.7x99mm NATO, or they can use speciality ammunition such as 8.6×70mm Lapua Magnum; specifically designed for accuracy at long ranges. Modern sniper systems, the combination of the rifle, ammunition and trained operators are usually only range limited by the accuracy of the cartridge.

Robinson & Berefelt of the Swedish Defence Research Agency have produced a report detailing the implementation of guidance and control into spinning artillery projectiles [5]. The major conclusion of the report is that a significant factor hindering the development of guided, spinning projectiles is the implementation of actuators and servos with a response frequency comparable to the projectile rotation rate. As a result of this, stability of the projectile cannot currently be ensured by conventional actuators alone, it must be guaranteed by the gyroscopic stability factor: "*stability must be guaranteed by open loop characteristics of the system and not by synthesized closed loop properties*". It was high-

lighted that guidance subsystems must be substantially reduced in size, leading to a lack of redundancy in critical components.

Large calibres have more payload space and less extreme flight conditions, so are easier to guide in the first instance. Research and developments for large calibre projectiles focuses on optimising and miniaturising the existing guidance and control systems. Small calibre projectiles remain almost completely unguided, with research predominantly optimising the relation between the spin rate and projectile geometry, such as boat-tail angles and ogive contours. Medium calibres are currently the forefront of control and guidance innovation. They are small enough to still traditionally require spin imparted on them for accuracy but also large enough that advanced technologies, such as Micro-electromechanical systems (MEMS) can now begin to be installed. The emergence of guided small calibre projectiles hinges entirely on the success of miniaturisation and performance increases of existing technologies in medium calibres.

Innovations and concepts are emerging to fulfil this requirement for medium calibre projectiles. The projectile can be by de-spun in flight to a point where control and guidance hardware can operate. This is achieved in one of two ways: firstly, the projectile can be intentionally designed with a roll damping moment, which opposes the rifling of the barrel and reduces the roll rate of the projectile through flight. Secondly, the concept of a dual-spin projectile is proposed, with two separate rolling sections connected by a bearing. This allows the back section to spin freely and keep gyroscopic stability while the front section can be relatively de-spun to a point where the actuators are effective. Dual-spin projectiles are the most promising technology for driving development in the sector, primarily because of the design of conventional shells include a front mounted fuse.

Another consideration for guided weapon design is that large stockpiles of conventional unguided munitions already exist. As described above, instead of dismantling and wasting the munitions they can be upgraded using the dual-spin design, which is achieved by retrofitting the shells a course-correcting fuse (CCF). Unlike the above artillery shells, which have most of the projectile volume available for guidance hardware if needed, a CCF contains the control and guidance hardware within the size of a traditional mortar fuse. Examples of currently manufactured CCFs are Orbital ATK Armament Systems' M1156 Precision Guidance Kit (PGK) [6], BAE's Silver Bullet [7], the Israeli Top Gun

155mm [8, 9] and the Guidance Integrated Fuze (GIF) [10]. Figure 1.0.1 shows the scale of the PGK which was chosen by the US Army over the Silver bullet and adopted as the XM1156 [11]. A CCF is able to be used on most of the available 105-155mm artillery/mortar rounds available to date, provided the characteristics of the round (such as aerodynamic coefficients) can be uploaded to the guidance computer, so the trajectory can be calculated. The XM1156 is currently being fielded in the M982 Excalibur round [6].

FIGURE 1.0.1 Orbital ATK Armament Systems M1156 PGK [11]

All these examples above show the effort that are being made to adapt existing guidance methodologies to spinning projectiles, with the smallest calibre able to be guided being dictated by the dimensions of the control hardware. However, different projects have been undertaken which specifically focus on guiding small calibre projectiles. Since the research is on the cutting edge of defence engineering research, details of the projects remain scarce.

DARPA have developed the Extreme Accuracy Tasked Ordnance (EXACTO) program, which uses a proprietary gun platform and optic system to guide a .50cal (12.7mm) bullet [12]. There were no specifications of the design, but in 2015 a video was released (figure 1.0.2A) showing the performance of the round. EXACTO reportedly uses real time optical guidance from the scope to guide the projectile, as opposed to being a beam rider or homing system. Figure 1.0.2B shows the official illustration of EXACTO publication by DARPA.

There is no obvious external control system is visible on the projectile, suggesting the use of some internal mechanism of steering during flight. The purpose of the three concentric white rings around the circumference of the projectile is not addressed and there is no apparent indication of guidance and control systems which have been used.

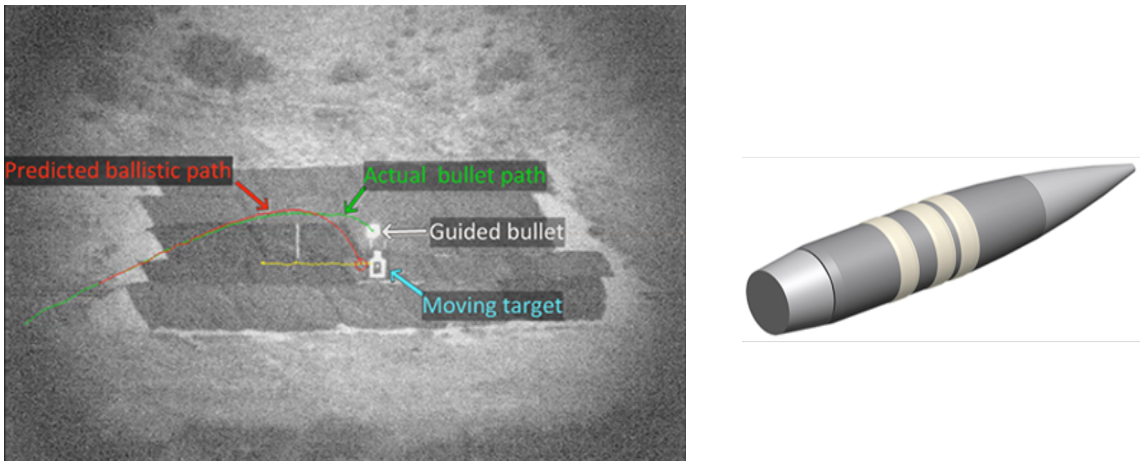

(A) Live fire demonstration [12] (B) Design depiction [13]

FIGURE 1.0.2 DARPA Extreme Accuracy Tasked Ordnance (EXACTO) projectile

A sabot is a structural device, used to keep a sub-calibre projectile centred in the barrel of a weapon system during expulsion. They are primarily used in tank systems, allowing the use of kinetic energy penetrator (KEP) ammunition from a large bore cannon designed for HE rounds. The spin rates used in the traditional HE rounds is very high and detrimental to the KEP munition. This necessitated the inclusion of a slip obturating ring or slip obturator. This is a layer of relatively soft material designed to deform under pressure, which ensures good contact with the rifling of the barrel. Importantly it prevents the rifling from imparting the full amount of rotational kinetic energy it would otherwise. This allows optimal performance of both sabot and non-sabot rounds with a rifled barrel. M. Minnicino [14] has developed a program which can model de-spun projectiles fired out of a gun tube with a progressive rifling twist. Its purpose is to test the performance of the materials used in the creation of novel band-slip designs.

Sandia National Laboratories have also demonstrated a .50cal guided bullet prototype [15]. The Sandia prototype, shown in figure 1.0.3B, uses homing guidance via on-board front mounted sensors to detect reflected laser light from a target. The Sandia design is fired from a proprietary smooth bore barrel, with a plastic sabot to provide an adequate seal.

There was no disclosure whether the projectile is encased within a loaded cartridge case and fired in a manner similar to traditional rounds. The form factor of the Sandia round is much longer than a traditional bullet. This long aft section has 4 control fins on the exterior which are controlled by electromagnetic actuators. There is no inertial measurement unit used in the prototype, which traditional guided projectiles use for tracking a position in space. Figure 1.0.3A shows a test firing, where a LED was attached to the back of the projectile to prove the electronics and guidance systems could survive the launch and flight. There is no mention as to whether the path was a pre-programmed or whether the projectile responded during flight. The tests also showed the projectile reached Mach 2.1 using commercially available gunpowder. Computer simulations estimate the projectile could correct 0.2m lateral distance over a range of 1km.

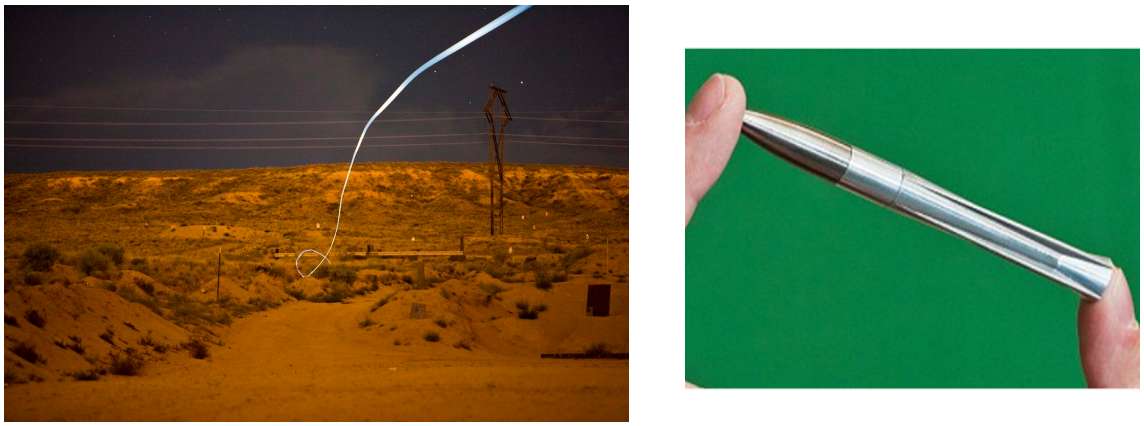

(A) Depiction of live fire demonstration [16] (B) Prototype design [15]

FIGURE 1.0.3 Sandia National Labs guided bullet prototype

In the following years, a very similar geometry has been investigated by Zhang *et al.* , from the Chinese College of Mechatronic Engineering, and Chongqing Jialing special equipment Co. [17]. The authors used a CAD model of the geometry to investigate the aerodynamic coefficients of the novel projectile design in an effort to analyse the flight properties. The work was primarily concerned with finding the optimal location for the centre of mass by comparing experimental results with live fire tests to analyse the variation of the static margin, or static stability. It was noted at the end of the manuscript that further work should investigate the control architecture of the projectile using a 6-DoF model. There was no mention of ‘control’ or ‘controlled flight’ in the manuscript, which would suggest that the prototype is a structural representation of further work.

(A) CAD model

(B) Prototype in cartridge without sabot

FIGURE 1.0.4 Finned smart bullet by Zhang *et al.* [17]

The American 'Smart Rounds' has shown a product in development called Smart Anti-Vehicle Aerial Guided Engagement (SAVAGE) [18], for use in counter UAV scenarios. The design is a 40mm rocket propelled projectile intended to be fired from either shoulder-fired launcher, or from a ground based 64-tube emplacement. The design features a parachute used to recover the fuselage, which should not suffer serious structural damage due to the usage as a counter-UAV missile. The projectile uses onboard sensors, but it is not mentioned whether this is for laser homing or image recognition. The projectile is guided by MEMS activated canards. Machine learning is described as being used for the control surface actuation and guidance. In addition, AI also supposedly enables swarm behaviour for multiple SAVAGE missiles, though neither implementation methodology for the AI are disclosed.

General Dynamics and BAE have introduced the Roll Controlled Guided Mortar (RCGM), use a proprietary control and guidance assembly mounted between the well-established L16A2 (US M252) mortar body and M734A1 fuse [19]. Figure 1.0.6 shows the projectile. The main body, in green, is the standard L16A2 mortar which is usually adorned with a fuse. On the far right side of the figure is the M734A1 fuse, a small golden

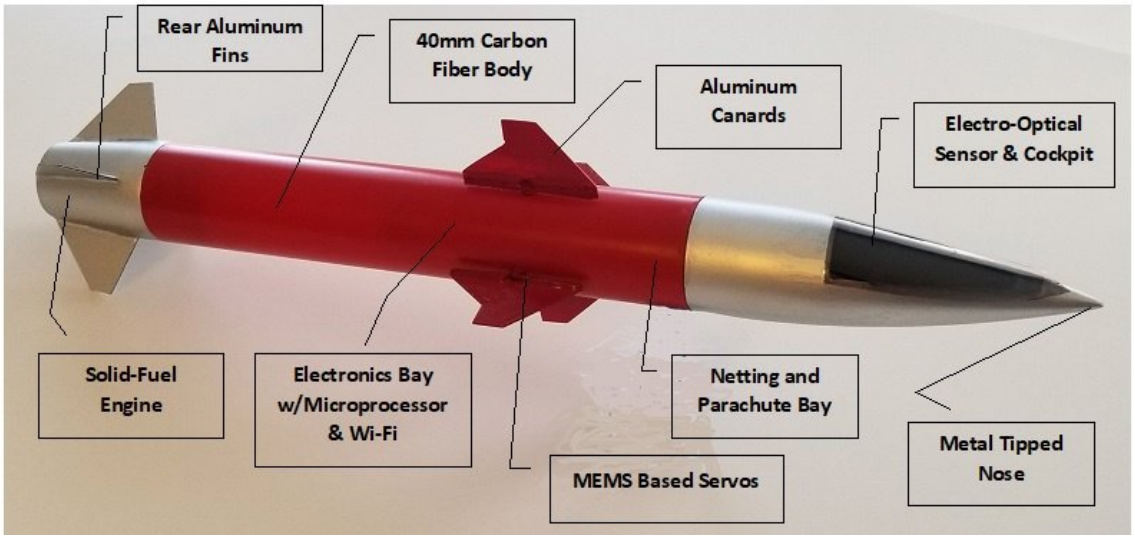

FIGURE 1.0.5 Smart Anti-Vehicle Aerial Guided Engagement (SAVAGE) from Smart Rounds [18]

end cap. Connecting the two is a long, silver cylindrical body with lateral fixed canards, which is the actual guidance assembly. The projectile operation is not strictly dual-spin in the sense of two discrete sections of a projectile, rather it operates with a spin-band type mechanism. General Dynamics have released a computer animation of the projectile operation, as well as the footage of the first instance of the projectile after launch. The tail, main body, fuse and main body of the guidance module all rotate in one direction. The canards are attached to a slipping ring, free to rotate around the guidance assembly which it does in the opposite direction to the main body. There is some kind of mechanism which can control the roll rate of the canard slip band with respect to the main body. At certain points, roll rate of the slip band is adjusted so its orientation remains stationary relative to the earth reference frame, which produces a control force. It is unclear what the spin rates and frequencies of the body and band are intended to be, but it is speculated that all roll rates are low, to enable the operation of the GPS tracking.

FIGURE 1.0.6 General Dynamics Roll Controlled Guided Mortar (RCGM) [19]

The STARSTREAK High Velocity Missile (HVM) is a close-range surface to air

missile (SAM), manufactured by Thales Air Defence Ltd. [20]. Details of the project and the missile are classified, but some details of the platform are available through public means, and examination of a prototype located at the Defence Academy of the United Kingdom in Shrivenham, England. The missile is comprised of a rocket motor with 3 independent submunitions, each carrying their own 0.9kg payload. During prelaunch, the operator tracks the target from the sight and can assign wind directions/conditions to improve performance. At launch, the rocket fires the first stage of the motor to clear the gun tube but stops the burn before it leaves the tube to protect the operator. When it is clear of the weapons platform and operator, around 4m, the second stage motor kicks in and accelerates the munition up to Mach 4 (the fastest in the world at the time of writing). Once the rocket has reach terminal speed it launches the 3 submunitions. The submunitions are beam riding tungsten alloy darts, 396mm long by 22mm in diameter, weighing around 0.9kg with approximately 0.45kg of that being an explosive payload. The darts feature a dual spin design. The forward section has two fixed canards, while the non-rotating aft section is adorned with 4 stabilising fins and the guidance electronics and optical sensor used for the beam riding functionality. The two forward mounted control fins impart a constant control force on the projectile. Control is enacted by means of a bi-directional motor rotating the front section to align the control force direction axis with the direction required by the guidance law.

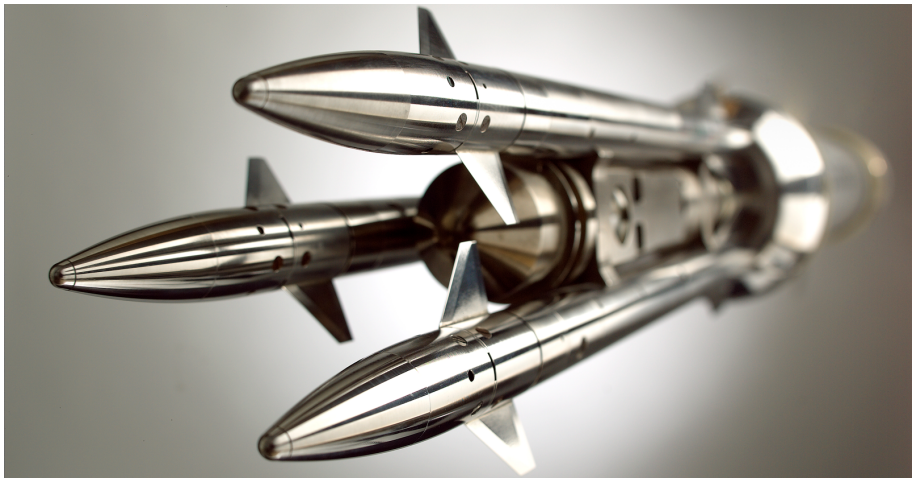

FIGURE 1.0.7 STARSTREAK dart submunitions mounted on main rocket body [21]

The development of dual-spin designs is driving the miniaturisation of the major missile sub-systems. Technology is being adapted from other fields of industry, such as

Microelectromechanical Systems (MEMS). Efforts are already being undertaken to make them more resilient, as a by-product of their use in aerospace [22]. Additionally, new technologies such as piezoelectric actuators, which are robust and have very high operational frequencies, are being implemented. Different designs of piezoelectric actuators, such bi-morph actuators [23, 24] and snap-through actuators [25], have been incorporated into projectile fins and control methodologies have been considered [26, 27]. Smaller designs usually equate to higher projectile speeds [28]. Both numerical and experimental investigations have been undertaken to show that conventional fin designs are able to produce significant deflections when subjected to supersonic speeds in excess of Mach 4, for example a 25mm projectile achieved a deflection of 1.4m at a range of 160m [29].

While fin controlled designs are being successfully implemented, research is still being undertaken to explore more unconventional methods of control. Project SCORPION, a collaboration between DARPA, U.S Army Research Labs (USARL) and the Georgia Institute of Technology, has investigated micro-adaptive flow control (MAFC) with respect to their potential effectiveness at controlling spin stabilised projectiles [30]. It utilised the Coandă effect interaction with the projectile boattail, as well as a high bandwidth piezoelectric actuator which distorts the boattail geometry. USARL have also suggested an alternative asymmetric, spin stabilised projectile with a singular 'paddle' [31]. 'Tail-spoilers' have been shown able to manoeuvre a 105mm projectile up to Mach 3 [32]. A range enhancement of 7% was achieved, with a controllable deflection of 1.5km at a range of 10km. Articulable noses, or ogives, have been investigated, achieving bandwidths of up to 200Hz in wind tunnels at Mach 3.3 [28]. In terms of other approaches, Microvanes have been investigated for flow control modification on a supersonic spinning projectile [33]. The vanes were found to inhibit flow separation on the surface of the projectile, resulting in the normal force coefficient and pitching moment stabilising, leading to greater projectile stability as a result of the reduced oscillations. In addition, there exist a plethora of patents [34, 35, 36, 37, 38] describing novel guidance methods such as air jets, gyroscopes and asymmetric ogives.

1.1 Design and operation

Guided projectiles are advantageous because of the significant increase in accuracy they bring. They reduce the number of rounds necessary to achieve the desired effect on target, which reduces logistical and financial burden as well as significantly reducing the likelihood of collateral damage in modern engagement scenarios. It is logistically beneficial for new guided projectiles to adhere to conventional form factors, so that the new projectiles can be interchanged with traditional munitions in existing weapon platforms; no proprietary launch systems are needed. The weapons systems used to launch small calibre projectiles are traditionally rifled, to impart the necessary spin on the projectile to ensure the necessary gyroscopic stability is maintained along the trajectory. This results in high projectile spin-rates and very turbulent launch conditions. Small calibre projectiles are mostly used in direct-fire scenarios, which means shorter flight times. Lifting surfaces, or fin guidance, are the most prevalent and well understood method of control. However, they are not conducive to use in spinning projectiles since the current response frequency of currently available robust actuation technologies is not significantly higher than the spin rate of the small calibre projectiles.

This project proposes a dual-spin projectile design to address the above discussion. Figure 1.1.1 shows the basic design layout with the key components. The projectile is dual-spin, with a front and aft section connected by a bearing. Attached to the bearing is a brake, which is able to lock and unlock the two sections on demand. Another option would be to connect the two sections with a motor; instead of having two discrete states, locked or unlocked, the motor allows more continuous control over the spin-rate discrepancy of the two sections. Either way, an electronic receiver will be attached to the braking mechanism, which is responsible for relaying the brake/no-brake command from an external source.

The design uses a non-actuating blunted ogive section as a method of control, to constantly impart lift onto the projectile. Figure 1.1.1 shows the entire bottom portion of the ogive as being blunted but in reality, the length, angle and area of blunting are all parameters which will be adjusted to provide the desired lift force. Any method of imparting lift could be used but a blunt edge is suggested to reduce complexity and increase robustness of the overall design. This is because there are no protruding geometries like

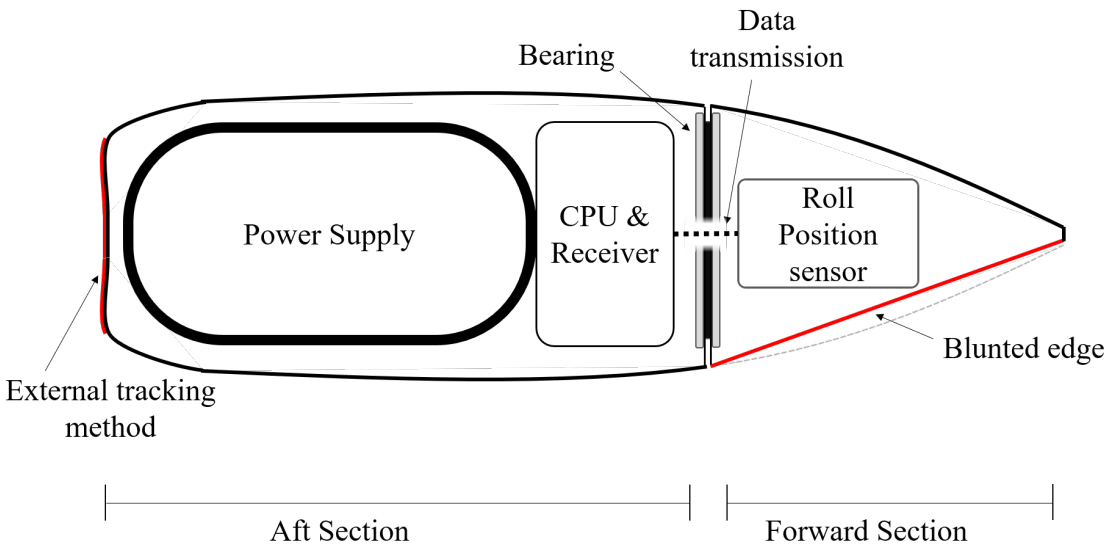

FIGURE 1.1.1 Block schematic of novel dual-spin projectile design

fins which could interfere with the barrel profile during launch. Blunting the ogive results in a mass asymmetry which will need to be accounted for in the control system and stability analysis.

When the projectile is fired from the gun system, the aft section will engage with the rifling and be spun to the normal operating spin speed of that weapons platform. The brake will be engaged during launch and thus the forward section will also accelerate to the same spin as the aft, as if it were one whole body. Since the aft section contains the high-density material necessary for ballistic stability, and also likely a power source, it will have much higher rotational energy and therefore a higher moment of inertia compared to the forward section. This high inertia is what keeps the forward section spinning when the brake is engaged.

When the brake disengages, the forward section will begin to de-spin slightly, due to the aerodynamic roll damping moment. The magnitude of the roll damping moment and thus the rate of de-spinning can be altered by the blunt face geometry but it will be a trade-off with drag, mass asymmetry and ballistic instability. After a transient period, the system will reach a new steady-state, where spin rate of the front section is lower than the aft section. It is non-zero due to friction in the bearing, but it will be lower than the aft spin rate. When the brake is re-engaged the forward section is accelerated by the aft section, which still has the relatively higher spin rate, back to the initial state the system

was in before the brake was first dis-engaged. It is assumed that the high inertia of the aft section will be able to reliably and repeatedly re-accelerate the front section with repeated engage/disengages. There will of course be decay of the whole system, but that can be taken into consideration. This is the procedure used to alter the spin rate of the forward section which is adorned with the lifting surface.

This projectile is designed to be a direct-fire beam rider, with some external observer capable of discerning its location in free space relative to the target. The controller then acts to keep the projectile on path to the target. Due to the small cross section of a bullet, the projectile can facilitate controller tracking by implementing a source of illumination on the aft face. This could be a reflective surface which passively reflects a tracking pulse (*e.g.* a laser) back towards the observer, or it could be an active tracker *e.g.* a diode emitting light in the IR spectrum.

Mechanism of enacting control

A traditional un-spun projectile will effectively travel along a straight trajectory, as shown in figure 1.1.2A. Lifting surfaces such as canards or fins can be incorporated onto a projectile producing a lift vector which results in the projectile moving laterally, shown in figure 1.1.2B. Spin-stabilised projectiles rotate about their longitudinal axis. If a spin-stabilised projectile is also adorned with surfaces producing a fixed lift vector, then the lift vector will rotate or oscillate with the projectile. This oscillatory lift force results in a helical trajectory, shown in figure 1.1.2C. The rate of projectile spin speed is proportional to the diameter of the helical trajectory, a quicker spin rate produces a tighter helix with a smaller diameter (figure 1.1.2D). If the spin rate of the lifting surface is changed, the diameter of the helix will change accordingly, as shown in figure 1.1.2E. Switching between different lifting surface spin speeds results in a switching of the helix sizes and it is this which will be the mechanism of control. When the brake is disengaged the front section spins slower and the helix is larger. When the brake is engaged, the forward section matches the aft and the helix is smaller.

Figure 1.1.3 shows the key parameters of the projectile and the method of control, as well as the YZ plane, also known as the ‘picture plane’. The picture plane aspect can be thought of as the perspective of an observer if they were behind the gun system during

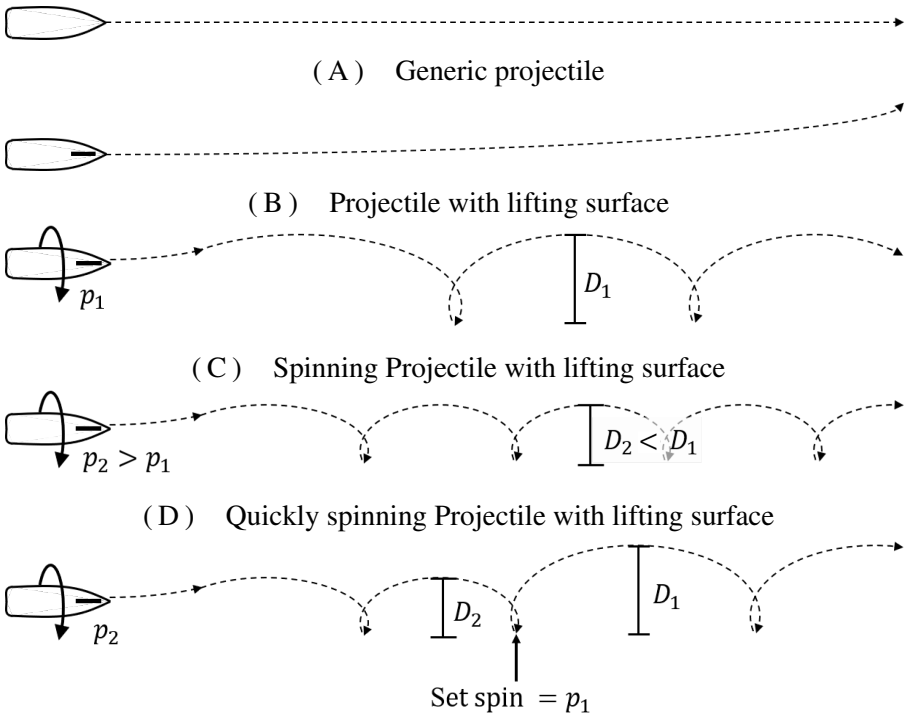

(E) Spin rate change during flight

FIGURE 1.1.2 Development of helical control method using a spinning lifting surface

launch, watching the projectile travel down its trajectory towards the target. This is an important perspective, as it is the view most operators or controllers have when using direct fire projectiles, in addition to which it is also the perspective from which the mathematical framework will describe the actuation mechanism, control and guidance of the projectile. The constant magnitude control force F_c, produced by the blunted ogive, rotates through a roll angle ϕ with roll rate ω. The roll rate would act towards one of two values, ω_0 or ω_B (where $\omega_B < \omega_0$) depending on whether the brake is locked or unlocked following the procedure previously described. The roll orientation $\phi \in [0, 2\pi]$ of F_c is with respect to the normal axis and wraps in the negative mathematical direction, since most conventional projectiles have a right hand twist. This follows the conventional ballistic axis and the coordinate system described in §3.1.

If the roll rate remains at either ω_0 or ω_B for one full revolution, the net force on the projectile will be zero, since it is a symmetrical distribution of F_c. However, a net force can be imparted on the projectile in one revolution by switching ω through certain roll angles. Figure 1.1.4 shows F_c rotating at the slower rate ω_B through the angle ϕ_1, then switching to rotate at the faster ω_0 through the angle ϕ_2. The novel control strategy

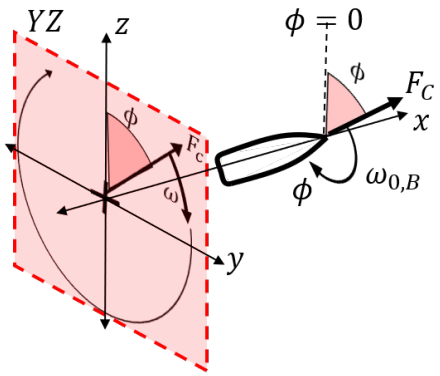

FIGURE 1.1.3 Earth axis perspective of picture plane and control force F_c rotating at rate ω through angle ϕ

proposed herein uses a fixed magnitude F_c rolling at speed ω_0. The roll rate is slowed to ω_B through favourable roll angles when F_c is aligned, to some degree, with the desired correction axis. It is then accelerated back to ω_0 through the remaining unfavourable roll angles. This results in a net impulse and thus acceleration in the direction indicated in the figure. This procedure of slowing F_c when sweeping through favourable roll angles is henceforth referred to as a 'bias'. All measurements and symbols henceforth are given in the 'picture plane' reference frame unless explicitly stated.

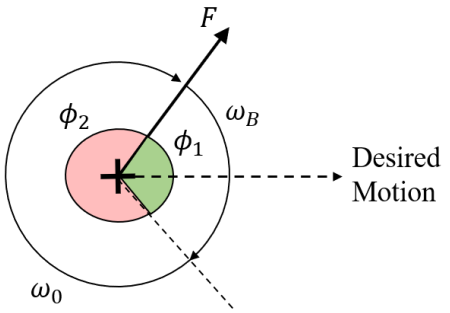

FIGURE 1.1.4 Force rotates through angle ϕ_1 at lower rate ω_B and rotates through angle ϕ_2 at higher rate ω_0

Objective novelty of control method, actuation mechanism and discussion

Most guided projectiles have fins which can roll the projectile and induce a control force, F_c, along a pitching axis. The conventional guidance strategy is to roll the projectile to align the controllable pitch axis with the desired direction, then increase F_c by actuating the control surfaces resulting in lateral movement. The novel guidance strategy proposed herein uses a *fixed* F_c rolling at speed ω_0. The roll rate is slowed to ω_B through favourable

roll angles when F_c is aligned with the desired correction axis, then accelerated back to ω_1 through the remaining unfavourable roll angles. There is no ability in this design for any part of the projectile to have zero roll rate in the earth frame, as utilised by the slip-band in ref. [19]. At the time of writing, there is currently no literature describing the design, control and guidance of such a projectile

The design is informed by a variety of different sources, of which many current projectiles designs are discussed in the literature review. Other resources pertaining to generic projectile research and development have also been used such as the WSTC0129 report by Thales, a catalogue investigating a wide variety of novel projectile morphologies [39]. It will be shown that a dual-spin design is a good compromise between complexity and robustness, which provides an satisfactory level of correction capability while still remaining feasible with modern technology. In addition, the mathematical tools used to investigate a dual-spin design can be readily simplified to describe traditional single-body projectile; the design, conduct and evaluation of the enclosed methodology can be used on other projectiles.

A faithful constraint of this prototype is that it should be operationally indistinguishable and functionally interchangeable with, conventional ammunition; meaning that no proprietary weapons systems, not modification to existing weapon systems will be necessary for its operation, beyond the attachment of the guidance hardware (such as laser designators *etc.*). Under this notion, the proposed idea offers the most promising design aspects from a sensical perspective.

A dominant principle for guided small calibre projectile design is to use fewer moving parts; this means there is less volume occupied, fewer subsystems which can fail and fewer components which must be physically hardened to operate in such an extreme environment. In reality there are many different methods by which a projectile can be controlled, ranging from traditional methods such as fins and pulse jets, to more unconventional approaches such as internal inertial/gyroscopic control or air-skin morphological changes. Using a fixed control surface means there a fewer moving parts; the bearing is the only moving part used in the design, it is simple and intrinsically robust.

Conceptually an ideal dual-spin design completely dissociates the most difficult aspect of small calibre projectile control, which is the high spin rate, from the control archi-

tecture itself. The aft section would be free to rotate at any speeds provided the front section can remain relatively stationary to control the projectile as necessary. However to completely eliminate the spin relies on large, power intensive components which are not conducive to small calibre designs. Spin mitigation technology such as a sabot is counter-intuitive, because the volumetric budget necessary for control hardware would be lost at a proportionately higher rate that advantages from the sabot would be gained.

There are notable issues with such a design which must be addressed. First and foremost is the power requirement. While delivering power to large scale missile and rockets is readily demonstrable, this control method is design for small calibre projectiles. This already reduces the available volume budget, but splitting the body in two for the dual-spin design reduces the budget further. While the power supply could also be split into two sections, any mechanism responsible for passing power between those two sections would itself, consume more volume than it is worth. The front section is designed to be small and have low mass, so adding any power system which are notoriously heavy would be counter intuitive. Logically the power source would be situated in the aft section and it may be possible to utilise kinetic energy harvesting during launch, since the flight time is relatively small.

The next large problem is the actuation frequency of the actuators. The problem is somewhat mitigated by having the actuation mechanism and effector contained within the projectile housing: *i.e.* the actuator is not moving an external fin which would be subject to aerodynamic forces, it is acting on a section of metal inside the projectile. The ideal candidate for the actuator would be a piezoelectric (PZT) material. PZT actuators have operational frequencies in the MHz range, as well as being as robust as traditional ceramic materials. The PZT material would function as a disc brake, with a continuous range of motion to press against the front section. This allows control over the torque acting against the front section rotation at a rate high enough for high fidelity control. Some PZT require very high voltages, over 1kV, to function. However, some newer PZT materials have can operate in the -20 to +120V range. This feeds back to the power issue, where the already volumetrically stretched power supply would now have high voltage demands as well. At the time of writing, the most promising identified technology to fulfil this roll are capacitors, which would able to meet the power requirements when future innovations

reduce the size. It is unlikely that supercapacitors would be needed due to the lower voltage capabilities, and the increased power capacity is wasted due to the relatively short flight times.

1.1.1 Project aims and objectives

The proposed design has been demonstrated to be volumetrically small and efficient. It is power efficient, using components that are robust and able to withstand the hostile launch conditions. The mechanism is deployable quick enough after launch to allow significant correction distances over the short flight time expected from a small calibre projectile. And lastly, the mechanism is capable of utilising an actuation frequency which is significant compared to the spin rate of the projectiles for high-fidelity control. Conceptually, the idea is robust. This project aims to answer the following:

Is the underlying operating principle of the novel actuation mechanism actually feasible as a method of controlling a projectile?

This will be achieved by addressing the following objectives, each with auxiliary sub-goals:

1. Objective 1: Can a mathematical framework be formulated which robustly describes the motion of the system as a response to the controller instructions?
    - Can the motion of the projectile be characterised in terms of a controllable parameter?
    - Can this parameter be expressed linearly in terms of a control variable?
2. Objective 2: Does a projectile geometry exist which can fulfil the requirements of the control mechanism?
    - Does the geometry provide sufficient aerodynamic and control characteristics at expected operational conditions?
    - Does the geometry fulfilling the above do so without detriment to stability along the ballistic trajectory, in the event no control authority is exerted.

Manuscript overview

The project will be laid out in the following manner. Firstly in chapter 2, a literature review will be conducted to discover the extent to which different technologies can be implemented in the project. The literature review will cover the following aspects: Ballistic

stability, dual-spin projectiles, aerodynamic coefficient modelling, guidance laws and AI implementation in projectiles. Stability criteria contains stability factors, which govern projectile stability [5]. It is pertinent to understand projectile stability and the associated factors to ensure any successful small-scale prototype is actually able to be physically guided. The dual-spin design allows conventional guidance methods to be used on a projectile with a very high spin rate and it has been used in many different guided projectiles including recently, STARSTREAK [20]. The concept works with and utilises the spin of the projectile instead of trying to mitigate it, which is beneficial since spin stabilisation is paramount to the design of almost all small calibre projectiles. If a dual-spin design is feasible at small-scales, this could permit a guided projectile design which can be fired from conventional weapon systems, without the need for a proprietary smooth-bore platform.

The necessary theory to describe the enclosed work is shown in Chapter 3. The earth and projectile axis reference frame are established, a description of the aerodynamic effects on a projectile in flight is given along with the associated aerodynamic coefficients. The equations of motion are then formulated and expressed in state-space representation in aero-ballistic coordinates (V, α, β). The equations are trimmed at a certain flight envelope to allow computational simulations with partial knowledge of aerodynamic coefficients. A Jacobian linearisation is used to reclassify the non-linear system as a quasi-Linear Parameter Varying (q-LPV) system for closed loop stability analysis and use in MATLAB/Simulink simulation environments.

The pitching and yawing motion of projectiles is discussed with the precessional and nutational modes of instability, with a description of how these modes lead to the gyroscopic and dynamic stability factors, S_g and S_D respectively. These factors govern the ballistic stability framework, which determine whether a projectile is innately stable without a control system. Here, the nomenclature is unified across multiple sources to allow a design utilising the enclosed methods to remain stable in the event of guidance module malfunctions, and thereby always result in a predictable trajectory. The evolution of these stability factors is surmised, which led to the publication of a review article [40] (Appendix C). Additionally, a novel procedure for using these stability factors at trim conditions along the whole flight envelope is illustrated in a conference paper (Appendix C).

Chapter 4 describes how the physical control mechanisms produce a variable numeric

value which can be demanded of the projectile by a guidance architecture to physically steer the projectile towards a target. Next, an in-depth analysis is conducted, showing how the actuation mechanism can be characterised from different perspectives. These actuation frameworks are responsible for illustrating how the motion can be viewed and used continuously, even though the behaviour of the control mechanism is, as will be shown, inherently discrete. Then, the nuances and intricacies of the velocity based and acceleration-based actuation mechanism models are shown, illustrating how they can both be best utilised to deliver an effective and robust control and guidance strategy.

Chapter 5 presents a series of guidance laws (GLs), which are responsible for intelligently deciding the controller effort necessary for the projectile to approach the target in a desirable way. To meaningfully compare the guidance laws against each other in a variety of situations, a test procedure is shown which uses Monte Carlo simulations. A large number of different simulations can then be averaged to provide a characteristic response, individual to a specific GL. Proportional Navigation (PN) is chosen to represent traditional GLs and its implementation is shown. A novel Zero Effort Miss (ZEM) based GL is then presented, which is a natural progression of describing the actuation mechanism in terms of velocity changes, akin to the 'delta-v' used in spacecraft flight dynamics. This novel guidance law is explored in-depth by conducting a parametric investigation, applying PID and Fuzzy logic controllers, and finally optimising the parameters using a Genetic Algorithm (GAs). Reinforcement Learning (RL) Artificial Intelligence (AI) is then discussed, presenting different approaches for implementing an RL agent into the control architecture. Firstly, the agent is given complete control of both the actuation mechanism and the guidance law to determine whether it is able to control the novel system as a whole. Then, the agents are modified and then tested to see if they are able to learn and control the actuation mechanism and guidance law respectively.

In chapter 6, the GLs from the preceding chapter are directly compared in a nominal control case using the Monte Carlo procedure, to determine their effectiveness at reducing the miss distance in the normal-horizontal plane. Two possible projectile designs are illustrated in CAD. Aspects of the geometry are presented and an explanation is given for where further work should be directed to optimise the design. CFD is used to determine aerodynamic coefficients for a projectile. The methodology is tested using a conventional

155mm projectile, coefficients of which are already available in existing literature and can thus be used to validate the procedure is producing viable results. Coefficients for the novel projectile design are then computed and used to conduct the ballistic stability analysis. The 7-DoF model in MATLAB/Simulink is used in conjunction with the aerodynamic coefficients computed from the CFD simulations and the control architecture from chapters 4 and 5, to produce some example trajectories. The trajectories are compared against the unmodified ballistic cases.

Finally, the conclusions of this project are shown in Chapter 7, with a list of possible future work. Appendix A contains a full list of explicit calculations which were considered too long to include in the main text, in addition to any simulation or experiment parameters lists. Appendix B contains a parametric investigation of projectile geometry using the ballistic modelling software PRODAS. It also shows how PRODAS can be used in conjunction with the enclosed stability analysis to evaluate the feasibility of a novel bullet design which uses tungsten, delivering the same ballistic flight properties as its conventional equivalent, while vacating an internal volume toward the ogive. Appendix C contains a list of academic publications which have resulted from this project.

Chapter 2

Literature Review

FROM the introductory discussions it has been shown that there is an apparent need to develop a new control mechanism for small calibre guided projectiles (SCGPs) to better enable the adaption of pre-existing technology. Without it, the wide scale development and adoption of SCGPs is rate limited by the volumetric constraints of technology already used in traditional guidance package subsystems. As such, this project does not focus on the miniaturisation of these subsystems, rather it will investigate the feasibility of a novel actuation mechanism which aims to facilitate the guidance of small calibre projectiles using pre-existing technology that would otherwise be unfeasible. The development of such a mechanism will also benefit larger calibre direct-fire projectiles (*eg.* BOFORS 40mm) by allowing the use of less complex or expensive technologies. This also offers the opportunity to refine and improve the mechanism in these larger projectiles.

In this chapter, relevant works pertaining to the project or associated theory are presented. Firstly, the most similar projectile prototypes and concepts are discussed, highlighting the key operational and design differences. It must be understood how to present and model a projectile and its operation, so that any ideas and designs can be sufficiently discussed. This includes mathematical modelling, linearisation procedures and implementation into software capable of computing and running dynamic simulations. Next, ballistics stability is investigated, which ensures there are no significant oscillations caused by the projectile, which would be a hindrance to the control and guidance architecture. Aerodynamic analysis is necessary to compute the associated aerodynamic coefficients, without having to conduct live-fire experiments. Relevant approaches and their results will

be investigated. Then the control and guidance itself will be reviewed, including a review of guidance laws which control the projectile approach to a target. Artificial intelligence and reinforcement learning will be evaluated for the most promising implementations. A summary will then be given highlighting the most important aspects and addressing how they affect the enclosed discussions.

An issue that has become evident during the literature review is the categorisation of the relevant works. In designing and testing projectiles, the subsystems are often heavily dependent on each other; *e.g.* a trajectory prediction is only as good as the aerodynamic coefficients used for the projectile. As such, many of the works cover and are relevant to many of the different sections and subsections. The works have been grouped to represent the primary focus of the manuscript, but some descriptions of particular works may include discussions which are relevant to other subsections.

2.1 Similar projectile designs

The design and operation of novel projectiles and projectile control mechanisms are unlikely to be found in academic publications; papers focus on specific methods or aspects of the design and control architecture. Patents however, focus on broader design and operational descriptions to fully capture and describe the enclosed invention. The most relevant projectile designs and control methods already in use today have been shown in the introduction, but a few patents exist which describe relevant material.

In 2007, General Dynamics patented a method of control for a dual-spin projectile [41]. The result of this patent is ultimately the Roll Controlled Guided Mortar (RCGM) [19] from figure 1.0.6. The patent describes a dual-spin projectile, where the front section is adorned with variable or fixed control surfaces, where control is enacted by changing the speeds of either section with relation to one another. The RCGM operates using a fixed control force being produced by a slip-band around the main body. Additional aero-surfaces on the slip-band generate a large spin-damping moment which de-spins the slip band sufficiently from the main body that it rotates in the opposite direction to the main body, in the earth reference frame. Because the control force rotates uniformly, there is no net lateral force produce by them in normal rotation.

When correction is required a brake will engage, increasing the torque between the two sections. The brake is applied just enough that the slip band then remains stationary with respect to a reference frame*, such that control force then points in the direction in which correction is required. Because the force is now relatively stationary, the projectile accelerates in the desired direction. When control is no longer required, the brake is released and the slip band begins rotating in the opposite direction to the main projectile again.

The primary difference between this description and the mechanism described in this project pertains to the rolling behaviour of the front section. In the proposed mechanism, the roll rate will never be 0Hz, or approaching 0Hz, with respect to the earth reference frame. In fact, the mechanism does not rely on the roll rate being reduced to a relatively low rate, or even being significantly different from the roll rate of the main body. It only relies on there being some spin disparity, and the correction force will accumulate over time to produce the desired correction. The proposed design specifically addresses the high spin rate of spin-stabilised projectiles through the use of a piezoelectric brake mechanism, as opposed to the magnetically actuated or magneto-rheological fluid brakes described in the patent. The piezoelectric brakes are simplistic, robust and are capable of delivering equivalent response times. It is true however that a larger spin disparity, and lowering the spin rate as much as possible will produce the most responsive and highest fidelity control architecture.

In 2009, Thales patented a similar control mechanism with a projectile design more similar to that which is presented here [37]. Figure 2.1.1 shows the design, including a dual-spin projectile design with a blunted face on the forward section. The forward section adorned with the blunt face provides a constant lift force which as already discussed, no significant deflection is produced in normal flight due to the roll symmetry. A motor is present connecting the two sections, which can adjust the roll angle of the forward section to any orientation with respect to the earth reference frame. Importantly the front section is described as being able to rotate in any direction, by any amount, with respect to the main body. In this sense while the appearance of the Thales patent embodiment is more

*the patent explicitly states that the "*reference frame*" is completely generic [41], however both the description of the operation mechanism and the demonstration video [42] imply that it is in fact the earth reference frame

similar to the design in this project, the operation and control is less similar.

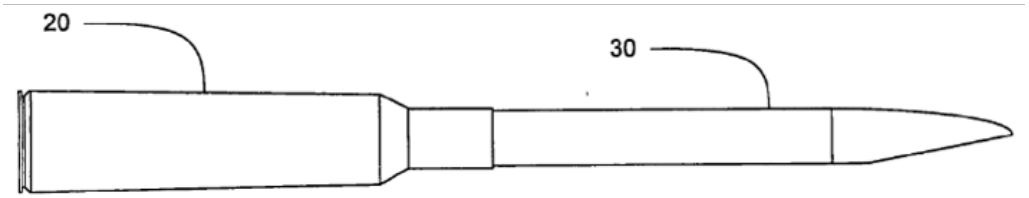

FIGURE 2.1.1 Illustration of patent design by Thales [37] with bullet (30) and case (20)

Another patent by Minnicino adds to the design of Thales by including a cover to the blunt edge [43], so that the projectile remains symmetric until correction is needed. At this point, control is enacted using the same method as the Thales design, using a motor to align the control force with the desired axis and leaving it stationary with respect to the earth frame. A patent by Jenkins *et al.* describes a projectile which functions in a similar manner to Thales [37] and Minnicino [43], however the control force is provided by an axially articulated nose as opposed to aerodynamic surfaces [44]. This design also changes the spin rate using an active DC motor instead of additional aerodynamic surfaces with a large roll damping moment. Other patents also show similar designs and operating principles [45], but non as similar as those discussed above.

The major differences between all of the above patents and the presented design is that the front sections are always able to assume any orientation required by the control system, and it can maintain this orientation indefinitely. In the presented design, the rotation direction of the front end remains fixed. The only controllable variable is the roll rate of the front section. In addition, the roll rate of the front section can remain sufficiently high with respect to the earth reference frame, provided there is a sufficient difference between the front and aft roll rates.

2.2 Ballistic stability and control of projectiles

Ballistic stability determines whether a projectile will remain on a predicable course over the trajectory. Oscillations are present throughout the flight of all projectiles in the form of precession and nutation, discussed in detail in §3.3. If projectiles are unstable then these oscillations begin to chaotically amplify until undue aerodynamic effects become

so great that the projectile will deviate off course. This unpredictability is unacceptable for projectiles and thus, guaranteeing ballistic stability for projectiles is of paramount importance. This section describes how ballistic stability is characterised by different sources and the work which has been undertaken to understand different aspects. The following review forms the basis publication, "A Review of Dual-Spin Projectile Stability" [40], which is included in the appendices. There has since been more literature released on the topic, which have been integrated into this section without particular note.

Lloyd & Brown investigated the dynamic stability of spinning projectiles subject to constant horizontal and vertical forces applied to the nose [46]. It was found that before the artillery shell reaches apogee, a right horizontal nose force tends to destabilize precession and stabilize nutation, and a lifting nose force tends to stabilize precession and destabilize nutation. The opposite occurs after the projectile has reached apogee, before terminal impact. Lloyd & Brown found that a 15 kg, 105-mm shell could experience no more than a 40N force applied to the nose before the motion of the projectile becomes dynamically unstable. This equates to a generic projectile limit of around $0.34g$ of lateral acceleration.

Cooper, Fresconi & Costello have investigated the flight stability of asymmetric projectiles with control mechanisms, by extending standard linear theory to account for the asymmetric mass [47]. The projectile model used in this work was the same as that considered in the text discussed earlier, [48], which investigated aerodynamic data using spark range firings. The resulting analytical model is validated using parameters for a mortar shell and is found to be in good agreement with the classical 6-DoF model. It was highlighted that there can be dynamic instability issues when the actuation frequency is close to one of the pitch/yaw modes. In addition, a spinning projectile with actuating canards will undergo a ‘coning motion’, or pitch/yaw precession, as a result of the normal control forces present.

Li *et al.* continued this work and proposed a novel method of deriving the instability boundaries as a function of control force magnitude [49]. The procedure is again demonstrated with a 15kg 105mm shell, with emphasis placed on the horizontal nose force (right positive). It was found that when the horizontal control force F_{yc} [N] lies in the unstable scope, the projectile is unstable. If F_{yc} is outside of this, in the stable scope, the projectile

will maintain stability. The unstable and stable scopes are defined by

$$\text{Stable Scope} \rightarrow F_{yc}[N] \in [-35.48, 58.33] \tag{2.1}$$

$$\text{Unstable Scope} \rightarrow F_{yc}[N] \in [-\text{inf}, -35.48] \cup [58.33, +\text{inf}] \tag{2.2}$$

Less scrutinous methods also exist and have evolved to give even rudimentary guidance to weapons designers. The 'Miller twist rule' is an imperial unit formula which can be used to calculate the optimal twist rate of a barrel as a function of bullet attributes and the gyroscopic stability factor (S_g) [50], thus it can also be used to determine S_g if the twist rate is known. Courtney *et al.* has shown empirically that the Miller rule can be modified for use with plastic tipped bullets with non-homogenous densities [51], as well as for open tip style bullets [52].

2.2.1 Dual-spin projectile stability

This subsection contains works which consider ballistic stability, specifically pertaining to dual-spin projectiles or some aspect of them. There is a notable contribution to projectile instability caused by the coupling of the front and aft sections. In addition, dual-spin instability equations simplify to single-spin projectile by nature of the equations.

Theodoulis & Wernert have modelled and conducted stability analysis on a spin-stabilised 155mmm projectile with a course correcting fuse [53]. The traditional 6-DoF model is expanded to 7-DoF, to include the roll of the front section, which is independent of the rear. Aerodynamic coefficients for the projectile are determined through wind tunnel experiments and CFD analysis. The equilibrium manifold and accelerations are then computed through an LPV model of the projectile and stability analysis is conducted by means of pole analysis. It was found that as the roll rate increases the stability increases, which agrees with the traditional results from gyroscopic stability. In addition, two of the poles possess a large oscillatory motion, which represents the precession and nutation present in the classic ballistic theory. These results indicate that stability analysis on an LPV model agrees with stability analysis form classic aero-ballistic theory, which is discussed in depth later.

In the same year, the authors also studied flight control of the same spin-stabilised

155mm projectile, with a CCF, by means of a trajectory autopilot [54]. The non-linear airframe dynamics are approximated using a Linear-Parameter-Varying (LPV) model, which can produce accurate predictions of the complex dynamics. An optimised linear-quadratic integrator is used for the controller, with gain scheduling implemented to cover the whole flight envelope. Traditional pole-based stability analysis is conducted on the linearised system to establish the stability of the system throughout the trajectory. This work is continued the following year by Spagni & Theodoulis, using a quasi-LPV model, and [55]. In both cases, it was found that the autopilot was able to provide a sufficient step response to control the projectile along the majority of the flight envelope.

Tipàn & Theodoulis *et al.* have continued the flight control work on spin-stabilised 155mm projectiles by evaluating a method of lateral dynamics control utilising non-linear dynamic inversion (NDI) [56]. Due to the high spin rate of the aft section traditionally considered in dual-spin projectiles, the lateral dynamics are highly coupled. Any resulting lateral autopilot must then deliver the required performance while guaranteeing projectile stability from the coupling. NDI methods are noted as potentially lacking robustness, which the manuscript addresses using a timescale separation scheme. In addition, the aerodynamic uncertainties are also large which can lead to large irregularities in the control and aerodynamic forces. The assumed aerodynamic coefficient uncertainties used in the simulations are listed in the paper, which are shown in table 2.1 The control scheme is tested for a nominal, where there are no uncertainties, and real-world situation. Once the NDI autopilot loop is implemented, a ZEM guidance law is used in both the nominal and real-world simulations, but there is no description of the ZEM methodology.

A more traditional control theory approach to stability analysis has been conducted by Theodoulis *et al.* [57], created a LPV model for a canard guided, single spin projectile. The aerodynamic information is encoded into certain state space matrices, the eigenvalues of which correspond to the precession and nutation frequencies of the projectile at any given instance. Additionally, root locus analysis of the system can identify stable operating regions, the parameters of which can be obtained and substituted into the stability criteria, depending on how the system is modelled. The French German Research Institute of Saint-Louis (ISL) have conducted a significant amount of research into the modelling and control of dual-spin projectiles [58, 59, 57, 60, 61, 62].

Airframe modification effects on control

Lahti *et al.* [63] designed a methodology to control the exterior ballistic properties of a spinning projectile by re-distributing the centre of mass around the inside of the bullet. The stability factors used in the paper follow McCoy [64], an appropriate usage since bullets are single-spin stabilised projectiles with no control method. The aerodynamic coefficients used in the analysis are calculated from a modified version of Slender Body Theory [65], where a correction term $\sqrt{M_v}$ is appended to account for flow compressibility. While it is stated the coefficients are not well estimated near the transonic boundary, they are assumed to be representative based on experimental data [66]. A bullet model was created with a large number of cells populating the interior, each may possess a specific density. A global optimisation algorithm was then used to find the mass distribution which can provide ballistic stability at the lowest velocity, by satisfying the stability factors. Since velocity decreases with projectile range, this method will find the mass distribution which enables the longest range (a training round with limited range was also investigated, but this review is mainly concerned with results from the long range specimen). Figure 2.2.1 shows the result from their paper.

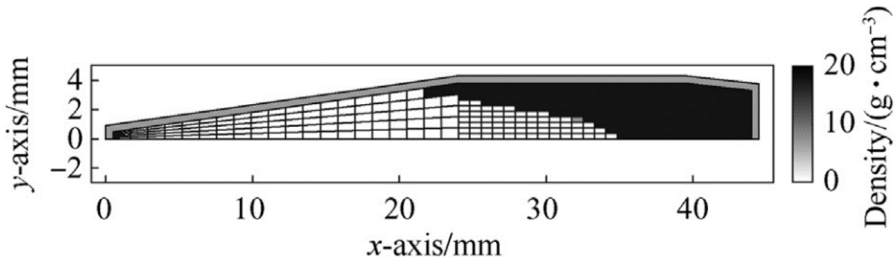

FIGURE 2.2.1 The optimal mass distribution of a long range bullet, from [63]

It is stated the Magnus effect is the main method by which the mass distribution affects stability, especially toward the aft of the projectile [64]. From figure 2.2.1, it is apparent the algorithm selected the largest available density to populate mostly the aft of the projectile, which has the effect of minimising the resulting Magnus moment. These results indicate that mounting control and guidance hardware in the forward section of a projectile is beneficial for projectile stability, since electronic components generally have a lower density than conventional materials such as lead.

Xu *et al.* [67] have modelled the stability factors for a missile under thrust, assuming

a flexible chassis. It was shown that thrust has a 'critical value' where dynamic stability is maximised; if thrust is higher or lower than the critical value, then dynamic instability is induced by elastic or rigid vibrational frequencies respectively. Additionally, structural stiffness is lowered as thrust increases, which leads to reduced static stability.

Chang *et al.* [68] have investigated the spin-rate of dual-spin projectiles as a function of canard properties, by characterising the ratio of aft to forward axial moment of inertia, I_x^A/I_x^F. The canards were modelled with zero deflection angle, so any contribution comes purely from the roll damping moment. For an initial spin rate of 420 rev/s (muzzle velocity 980 m/s with elevation angle of 45^o), the dual-spin configuration itself causes a spin-rate discrepancy of 25 rev/s between the aft and forward sections, while deploying the canards led to a difference of 250 rev/s. The spin attenuation of the aft section was greater for values of $I_x^A/I_x^F < 1$, while the spin attenuation of the forward section was greater for values of $I_x^A/I_x^F > 1$. For very large values of I_x^A/I_x^F, the aft section spin-rate was found to drastically reduce at first, then increase for a short period and finally attenuate as prior. Impact point drift was caused by any deviation from $I_x^A/I_x^F = 1$. The maximum angle of attack was found to increase drastically to 16^o for $I_x^A/I_x^F < 0.3$, but remain around 1.7^o for all $I_x^A/I_x^F > 0.3$. The ratio of inertial moments has significant effects on both spin rate and angle of attack and must therefore be considered carefully during the design of a dual-spin projectile.

Wang *et al.* [69] have conducted numerical simulations investigating the effect of yawing force frequency on the angular motion and ballistic characteristics of dual-spin projectiles. The precession and nutation rates (λ_p and λ_n) were calculated following traditional linear theory. It was found λ_p and λ_n for the system decrease over the projectile trajectory. As a result, the spin-rate of the aft or forward section could coincide with these intrinsic frequencies at certain intervals, which are dependent on the chosen projectile parameters. At resonance, there is an increase in angle of attack (approximately $0.2°$) and decrease in projectile range (approximately 0.4km decrease over 33.5km). A Monte Carlo simulation was then conducted, which showed a 10Hz control force applied to the projectile is capable of reducing projectile dispersion by a small amount.

Cooper *et al.* [70] have investigated the implications on flight stability caused by projectile asymmetry from the addition of canards. Linear projectile theory was extended

to account for radial mass asymmetries, which was shown to reduce back to standard theory when the asymmetry was zero. The dynamic stability of the projectile was found by root locus analysis of the system eigenvalues in state space, in the same way as Theodoulis *et al.* [59, 57, 62]. The canards were modelled with sinusoidal actuation, when the frequency of this driving wave is close to λ_p or λ_n, dynamic instability results; this is in agreement with the investigation of [69]. When the actuation moment of the canards was sufficiently large, it was shown to adversely affect the oscillatory motion of the projectile, leading to ballistic instability.

Canard modification and general control

Chang [71] has studied the dynamic response of a dual-spin, canard-stabilised projectile, when the coupling between canard control and gravity are considered. A new analytical solution was proposed to predict the maximum angle of attack induced by canard actuation, the yaw of repose due to canard control and the phase shift of the swerve response. It was found if the moment imparted on the projectile by the canards, or 'control moment', is large then it will more drastically alter the trajectory, but lead to airframe instability.

Wang *et al.* [72] investigated the effects of different control strategies on the flight stability criterion, assuming the only varying parameters are those associated with the rolling motion of the body. It was found that canards should be designed so the produced roll moment is as small as possible. During the period in which the roll angle is adjusted, it was found that control strategy has no impact on flight stability; it was suggested that the target spin rate of the forward section should be as low as possible for practical purposes. The behaviour of the motor torque was also characterised in terms of both trajectory and projectile parameters.

Ollerenshaw & Costello have investigated the swerve response of both fin and spin stabilised projectiles in response to control inputs [73]. It was found that the maximum swerve response for spin stabilised projectiles was found when the control is applied to the base of the projectile, while for fin stabilised the control force must be applied to the nose to elicit maximum swerve. In addition, fin-stabilized projectiles were found to respond in-phase to control-force inputs forward of the centre of pressure, whereas spin-stabilized projectiles were found to respond out of phase.

Cheng *et al.* proposed a guidance method for a 155mm projectile mounted with a fixed canard adorned CCF [74]. It is again noted in the manuscript high spin rates create a large coupling between the normal and lateral corrective forces. The procedure effectively calculates trajectories which terminate at the desired impact point, then produce the necessary control inputs to keep the projectile on the trajectory while minimising the orientations errors. This 'virtual target method' was able to reduce the Circular-error-probability[†] (CEP) from 90.75m to 69.3m, a reduction of around 20%. It was also noted that the corrective capabilities of the control force are biased due to the presence of gravity, *e.g.* corrections to the right are more difficult than those to the left.

Maley *et al.* developed an extended Kalman filter utilising magnetometers, which estimates the roll speeds and attitude of a spin-stabilised projectile with front mounted canards, a CCF and GPS [75]. The steady-state Kalman filter was found to perform as well and in some cases better, than the extended Kalman filter. The largest source of error in the algorithm was caused by a large-scale error from the magnetometer readings, while the next largest source of error was from incorrect wind readings used in the dynamic model. There is no mention as to which calibre projectile is used during the modelling, but the list of aerodynamic coefficients and associated error budgets used to simulate the projectile in the dynamic model were included. The included diagrams appear to depict a standard M107, 155mm projectile, but this is purely speculative. The conventional 6-DoF dynamic model was used in MATLAB/Simulink to create the projectile, which was in turn used to validate the observer.

In 2005 Ollerenshaw and Costello have investigated methods of control for direct fire projectiles with canards [76]. An impact point prediction control scheme is employed to reduce the miss distance from launch instabilities, which can lead to very large miss distances for short-range direct fire projectiles. The control inputs are decided based on which possible action state in a linearised model converges quickest to the desired trajectory. A parametric study is then conducted for various projectile and model parameters, using the conventional 6-DoF model, which shows the control methodology described is able to reduce the CEP from 34.6m in the ballistic case, to 6×10^{-3}m for the corrected case. The CEP for the guided trajectory shown here is substantially smaller than other

[†]Radius of a circle containing 50% of the impacts

articles stating a CEP reduction [74, 77, 78, 79], which came in subsequent years. This is primarily because this article considers a direct fire projectile, which has significantly less time to be subjected to aerodynamic disturbances and perturbations.

Liu *et al.* have incorporated the moment terms for a fixed canard dual-spin projectile into the stability equations of traditional pitching/yawing ballistic theory [80]. The 'swerve orientation' or pitching and yawing motion, can then be analysed without knowledge of the projectile attitude.

Tang *et al.* have investigated methods of controlling muzzle velocity and spin rate for projectiles fired from a novel rail-gun platform, by adjusting the voltages in the rail-gun platform itself [81]. It was also noted that velocity and spin rate would have to be balanced according to the gyroscopic stability factor. The stability factor quoted by Tang *et al.* was from [82], which appears to be a secondary source of the conventionally used textbooks such as McCoy [64] and [83]. The proposed methodology to induce a spin rate in the projectile is to generate an asymmetrical magnetic field. A prototype was constructed and voltages of 2kV were able to produce spin speeds of up to 1.4×10^5 rad.s^{-1} and muzzle velocities of up to 1600m.s^{-1}. Importantly, this reinforces the idea that the stability factors can be used as a primary design criterion by projectile designers.

2.3 Aerodynamic coefficients of projectiles

It is likely, since unconventional control methods and subsystems might be used in the creation of a guided small calibre projectile, that an unconventional aerodynamic surface will result. Thus, it is pertinent to investigate, at least superficially, the methods by which projectile geometries are investigated for aerodynamic effectiveness, or any relevant novel projectile geometries which have been considered by literature thus far. Discussed in more depth in §A.1, aerodynamic coefficients are effectively constants of proportionality, which represent the forces and effects a body will undergo in dynamic flight. There is no formula to derive or calculate them, rather they are empirically computed either from CFD analysis or real experiments. They are however functions of different flight aspects, such as angle of attack α and velocity V. These parameters can be varied for each experiment to derive a mapping of the coefficients over the whole flight envelope. Accurate computation

of these coefficients is vital for improving the accuracy of dynamic simulations, and the work necessary to compute them is very resource intensive. As such, coefficients for specific projectile designs and especially active service munitions are highly controlled. Coefficients and methodologies available in literature can only be used to verify a dynamic model is in good agreement with those experiments, to within the uncertainty provided by the coefficients and projectile trim data.

The aerodynamic characteristics of 105mm, 120mm and 155mm fin-stabilised projectiles have been investigated by experimental firings to understand the effect of canard control on manoeuvrability, roll rate, and dynamic stability [84]. All of the tested projectiles had super-calibre tail fins to induce roll and canards to enact guided control. A sensor suite was installed into all of the projectiles and they were fired from a mortar platform at a dedicated firing range. Aerodynamic coefficients for all projectiles over a small range of velocities were included in the paper. The 105mm projectile was found to have a very small dynamic instability (1-3 degree coning motion) while allowing a 30% increase in range due to the addition of canards. The 120mm projectile had very high static stability which adversely affected the ability to correct the trajectory, however this did guarantee a suitable dynamic stability for the airframe. The 155mm projectile was found to be stable at subsonic speeds but highly sensitive to angle-of-attack differences in the transonic region causing a coning motion of 10 degrees. It was suggested that careful canard design could mitigate the unwanted coning motion in the transonic region. All projectiles had a satisfactory roll rate for control purposes. The results of the experimental firing were found to be in good agreement with traditional 6-DoF models.

A similar analysis was conducted by Ren *et al.* [85] using a novel mortar shell geometry with a nose which can be deflected. The investigation methodology is largely the same as seen before, however the modification made to the projectile is significant and therefore the coefficients in this paper cannot be meaningfully compared to coefficients pertaining the original unmodified mortar. Ren *et al.* used a 'typical' 120mm mortar round and interchanging varying fixed nose structures, each having different angles of deflection. As one would expect, increasing the deflection angle causes the aerodynamic coefficients to be affected, primarily an increase in pitching moment. It was stated that the mortar would be able to be sufficiently controlled using the overturning moment of the deflected nose,

and simulations were used to compute trajectories using the coefficients generated from the CFD analysis.

Wind tunnel experimentation was used to investigate the aerodynamic performance of a standard 155mm M549 projectile and a variant of the round designed with less aerodynamic features, such as no ogive curvature [86]. The measurements were taken over a Mach range of 1.8 to 4 and an angle-of-attack range of -5 to +5 degrees. The modified round was found to have a lower drag and lower pitching moment derivative, both of which are desirable for increased ballistic stability. However, there was no discussion on the effect of reducing the projectile weight and shortening the distance between the CoM and CoP, both of which are detrimental to projectile stability.

The aerodynamic characteristics of a dual-spin 155mm projectile have been investigated using Navier-Stokes based CFD [87], utilising a spinning mesh. Canard shedding vortices affect the aft body aerodynamics, at a rate proportional to the forward spin rate. The spin rate of the aft section has a very large effect on the lateral body coefficient (C_Y), but minimal effect on the normal force coefficient (C_N). As Mach number increases, both the time averaged C_N and C_Y increase, while fluctuations within them decrease. An increasing angle of attack increases the magnitude of canard shedding vortices and their effect. Beyond a critical value, the cross-body flow will dominate in the detrimental effect on aft section aerodynamics, while the canard shedding vortices will have less of an effect.

Yin *et al.* have investigated the aerodynamics of a spinning projectile which experiences elastic deformation [88]. The Magnus force, Magnus moments, normal and lateral coefficients are investigated at varying time-steps for against both elastic deformation and angles of attack. The results of the analysis showed, amongst other things, that deformation frequency correlated to a high fluctuation amplitude of coefficients, as well as coupling of the normal and Magnus force coefficients. In addition, the effective angle of attack caused by body deformation lowers as Mach number increases. It was shown that aerodynamic coefficients increase with movement frequency, that an elastic deformation induces two aerodynamic components opposite and perpendicular to the deformation, and that the induced angle of attack from deformation decreases as Mach number increases.

Liang *et al.* [89] have proposed a methodology for optimising the aerodynamic parameters of control canards. A 3D model is created with chosen canard parameters, then

the aerodynamic coefficients for this are generated through the CFD program FLUENT and the efficiency is analysed by mapping how the normal force coefficient ($C_{N\alpha}$) changes with respect to canard deflection angle, over different angles of attack and Mach numbers. It would be interesting to see how this methodology could improve if used in conjunction with all the works listed above, where the canards' performance is quantified for each mechanism of affecting projectile stability, for varying control strategies, and having the optimum configuration selected based upon this. While this procedure is time consuming, it can be automated by an external code structure. In addition, this reaffirms the procedure of creating CAD models and deriving coefficients through CFD analysis.

Jiajan *et al.* have investigated the aerodynamic characteristics of a 155m M549 projectile [86]. The characteristics were measured over a speed range of Mach 1.8 - 4 and angles of attack from -5° to $+5^\circ$. This was calculated by creating a metal model of the projectile with a measuring sting inserted into the base, then placing the apparatus in a wind tunnel. A render of the projectile and sting assembly is shown in figure 2.3.1. The projectile model is constructed in two sections such that the ogive can be replaced to test different profiles. The projectile coefficients were only measured for a non-spinning projectile, providing the static aerodynamic coefficients: Drag-minus-base-drag C_{BD}, zero lift drag C_{D0}, Normal force derivative $C_{N\alpha}$ and pitching moment derivative $C_{M\alpha}$. The 'base-minus-base-drag' coefficient mentioned here accounts for the contribution of the sting to the measured drag force, which would not be present in an actual free-fire of the projectile. The results from these coefficients were then linked to the stability criterion which will be discussed later. The design tested in the manuscript was found to lower drag and pitching moment derivative coefficients, both contributing to enhanced range and stability.

Fresconi has also investigated the aerodynamic characteristics of an asymmetric, non-spinning projectile with canards, through live-fire experiments at a 'spark range' [48]. The spark range is an indoor ballistic range with shadowgraphs (similar to Schlieren photography) which are capable of capturing instantaneous images of the projectile and disturbed air currents. The experiment uses a proprietary 105mm projectile shown in figure 2.3.2. The traditional 6-DoF projectile model is used to identify which coefficients are being derived from the experiments: the pitch force coefficient derivative $C_{Z\alpha}$, yaw force coefficient derivative $C_{y\beta}$, yaw damping coefficient, C_{mq} and the yaw damping coefficient

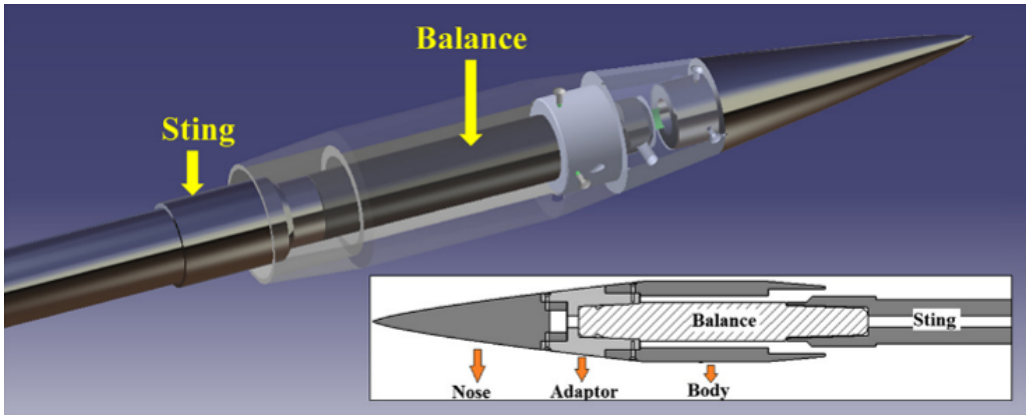

FIGURE 2.3.1 Apparatus for estimating aerodynamic coefficients [86]

C_{nr}. These coefficients and their error were measured against the predicted error, for 5 different projectile configurations which were achieved with masses to shift the centre of gravity to different locations in the nose. It was found that 5 test firings were needed to effectively derive the coefficients, but that the methodology was viable and a valid way of experimentally determining the projectile coefficients.

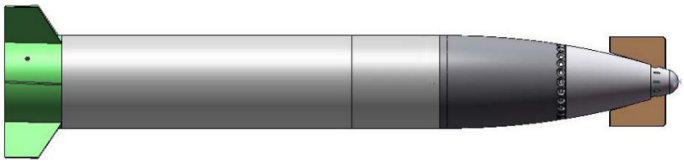

FIGURE 2.3.2 Depiction of custom 105mm projectile [48]

Hamel & Gagnon have conducted ANSYS-Fluent CFD analysis, as well as a Monte Carlo parametric study on a NATO 155mm artillery shell adorned with a CCF [90]. The CFD meshes ranged from 4.4×10^6 cells for the finest and 9.7×10^5 cells for the most coarse. Rotation of the projectile was simulated by applying a constant rotational velocity at the projectile wall. These coefficients are then used in a dynamic model, which is then run multiple times in a Monte Carlo simulation. The parameters which were varied were muzzle velocity, azimuth angle, elevation angle, crosswind, headwind and guidance lock delay. The guidance lock delay is an artificial delay induced to emulate the latency from sensor and actuator activation.

While it is stated that there is a control architecture implemented with associated gains, there is no mention of the actual method of control, PID *etc.* A figure in the paper only describes a generic ‘controller’ which takes expected, demanded, and measured pitch

and yaw rates, then outputs a saturated normal and lateral control force. The guidance law for generating the required pitch and yaw rates is also not shown. The projectile position is assumed to be known, though it is usually determined by GPS or Inertial Measurement System (IMU) measurements being fed through a Kalman filter. It was found that the CCF was able to lower the present normal and lateral disturbances as well as being able to reduce the muzzle velocity fluctuations. The CCF was noted as having a small, non-negligible, ability to correct lateral, perturbations caused by wind. It was unable to significantly correct the longitudinal perturbations. Importantly, it was found that the accuracy provided by the CCF was most profound for low gun elevations, with high muzzle velocities and low guidance lock delay.

Tipàn & Theodoulis *et al.* [56] have further investigated the stability of dual spin projectiles and have included a table showing the relative uncertainties that the authors would expect for various aerodynamic coefficients; shown in table 2.1. A non-linear autopilot was designed for a dual-spin projectile. A Zero-Effort-Miss based Guidance Law was used for the trajectory simulation, which in both nominal and uncertain cases, indicated the controller was able to provide satisfactory control. Importantly, the uncertainty associated with the aerodynamic coefficients was estimated to be very high by the authors. Due to the variation in simulation type and parameters in combination with the close control over distribution of the coefficients, this high uncertainty is likely to be an accurate representation of the current disparity.

Forces		Moments	
Coefficient	Uncertainty [%]	Coefficient	Uncertainty [%]
$C_{N\alpha}$	5	$C_{m\alpha}$	5
		$C_{np\alpha}$	30
$C_{Yp\alpha}$	30	C_{lp}	5
		C_{mq}	30
$C_{N\delta}$	20	$C_{l\delta}$	20
		$C_{m\delta}$	20

TABLE 2.1 Expected uncertainties for dual-spin 155mm coefficients used in ref. [56]

Wessam & Chen have also investigated the aerodynamic properties of the M107 shell using ANSYS Fluent [91, 92]. The listed projectile parameters and initial conditions are close to those used by [90]. The coefficients are then used with a point mass model to generate examples trajectories one can expect from the projectile. The point mass model

used is the traditional one as described by McCoy [93] for aero-ballistic analysis. A Monte Carlo simulation was run using 100 rounds, including uncertainty for all of the projectile parameters: mass, inertias and firing angles. Dispersion characteristics are investigated by analysing the drift and range of each round, and taking an average over all, as opposed to using CEP.

McCoy [64] is referenced by many authors in the field for the aerodynamic data it contains; showing drag coefficients measured for a 155mm M107 projectile found experimentally in a transonic range. It is one of the main texts in the field of ballistics, along with others by Carlucci & Jacobson [83] and the UK MoD [94].

Khalil *et al.* have conducted a parametric investigation of the projectile parameters, to determine their effect on the terminal dispersion of an M107 155mm projectile [95]. The mass, inertia and roll rate *etc.* were swept over a small range and a 6-DoF trajectory is run for various values within this range. The terminal impact points are recorded, and the error is plotted against the parameter variation. To run these simulations, the aerodynamic coefficients are of course needed, which were obtained in the manuscript using PRODAS on a CAD model of the projectile.

Figures 2.3.3A and 2.3.3B compare the coefficients shown by Hamel [90], Wessam [91, 92], Khalil *et al.* [95] and McCoy [64, 93]. Only the drag coefficient C_D is shared by all three sources, while pitching moment $C_{M\alpha}$ is shared only by the two academic journals. In both cases, the coefficients are of the same order of magnitude of the uncertainties predicted by Tipan [56] in table 2.1. Figure 2.3.3A shows the sudden increase in C_D at the transonic boundary, which is an expected characteristic of the regime change. All sources are in agreement with the gradual change in coefficient, but the coefficients shown by Hamel *et al.* seem to be more noisy than the other points, though this is only apparent for Mach numbers above Mach 1, where there are a few data points; the noise is likely therefore to be an artefact of sparse data. This discrepancy would indicate the disagreement for $C_{M\alpha}$ shown in fig. 2.3.3B is due to inaccurate or noisy data from ref. [90].

Ko *et al.* have, in a similar manner, investigated the aerodynamic properties of a less conventional 120mm projectile, using PRODAS and DATCOM CFD analysis [96]. The Mach range investigated was from 0.14 to 1.2, a slightly lower but more densely populated sweep than from Hamel [90]. The investigated coefficients are the zero C_{X0} and the quad-

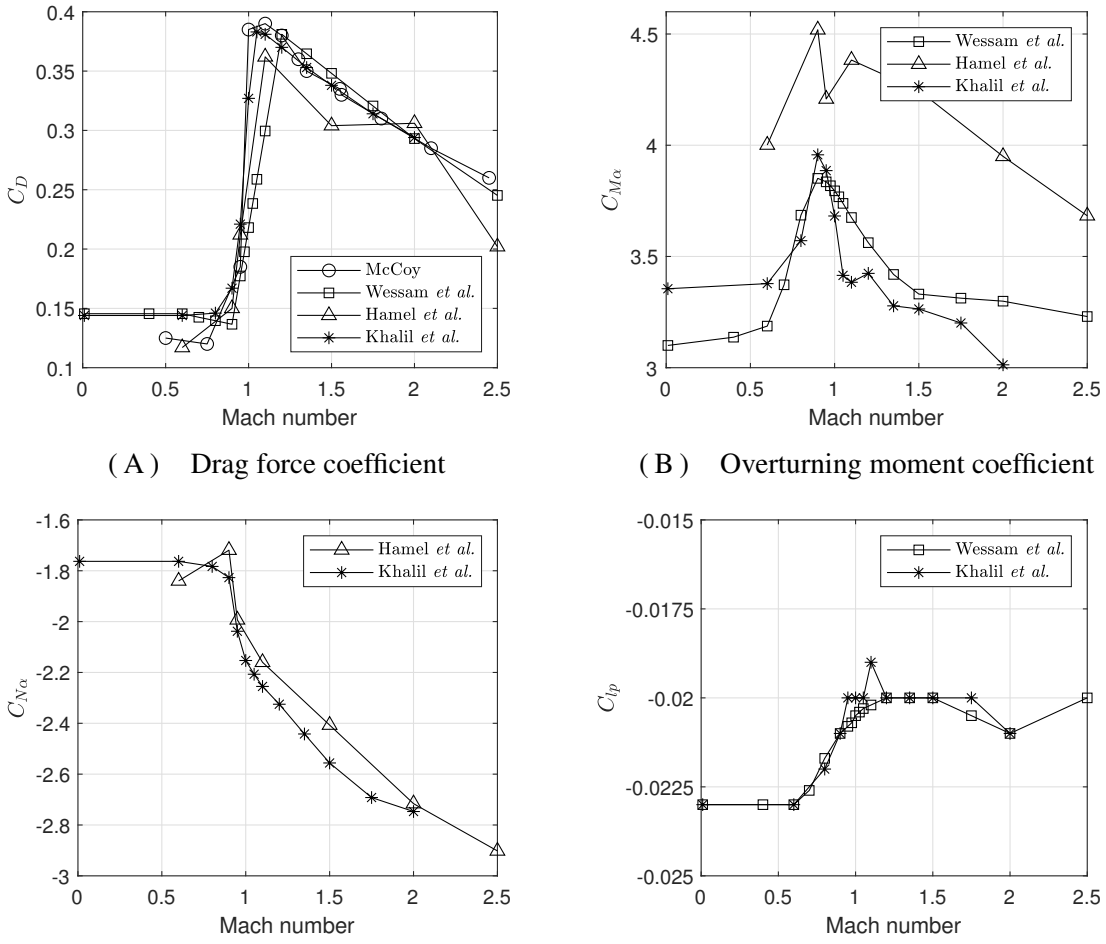

(A) Drag force coefficient

(B) Overturning moment coefficient

(C) Normal force coefficient

(D) Spin damping coefficient

FIGURE 2.3.3 Comparison of aerodynamic coefficients for M107 155mm projectile across different sources

ratic drag coefficient C_{X^20}, lift force coefficient derivative $C_{L\dot{\alpha}}$, Magnus force coefficient derivative $C_{Np\dot{\alpha}}$, overturning moment coefficient $C_{m\alpha}$ and spin-damping moment coefficient C_{lp}. The derivative coefficients were found by conducting a subsequent analysis of the projectile at an angle of attack of 2.5°. Importantly for both [90] and [96], the analysis was conducted for speeds across Mach 1, so any non-linear transonic behaviour can be observed. It was determined that the CFD modelling was able to predict and show the non-linear behaviour of the derivative coefficients just before the transonic region, however the semi empirical method PRODAS software, was unable to predict this behaviour and assumed the coefficients would be linear in the transonic region. Without using CFD analysis, Navier stokes equations can be used to approximate the aerodynamic coefficients of projectiles, as was demonstrated by Silton for a subsonic 0.50cal (12.7mm NATO) bullet

[97]; which was shown to be in good agreement with experimental data for a 0.50cal M33 bullet [98].

S. Silton used Navier-stokes based CFD analysis to investigate the stability of a 12.7×99mm NATO (or .50 cal Browning) bullet [97]. The coefficients investigated were C_D, C_{D0}, C_{lp}, C_{N_α},C_{m_α}, $C_{m_q}+C_{m_{\dot{\alpha}}}$, and $C_{n_{p\alpha}}$. They were investigated over a range of angles of attack and Mach speeds. These coefficients were then used in conjunction with the parameters for the bullet to investigate the fast and slow damping modes $\lambda_{F,S}$ respectively, which was discussed in §3.3. The paper gives a formula for these modes, which is derived from McCoy [64], as:

$$\lambda_{F,S} = \frac{\rho S}{4m}\left(2C_X - \frac{C_{N_\alpha}}{1\mp\tau} + (1\pm\tau)\left(\frac{C_{m_q}+C_{m_\alpha}}{2k_y^2} \pm C_{n_{p\alpha}}\frac{\tau}{k_x^2}\right)\right) \tag{2.3}$$

where τ is a substitution parameter given by

$$\tau = \left(1 - \frac{1}{S_g}\right)^{-\frac{1}{2}} \tag{2.4}$$

Here, S_g is the gyroscopic stability factor (§3.3.4) and all other terms and coefficients use the respective definitions listed in the nomenclature. The coefficients were used to find $\lambda_{F,S}$ for an angle of attack of 2° and 5°, but only the 2° is used here. This work reaffirms the fact that the stability factors are vital to the design process and that due attention should be paid to computing them as accurately as possible with bespoke aerodynamic coefficients if possible.

2.4 Guidance laws

A projectile is comprised of many subsystems, each of which has an associated controller and autopilot which is responsible for characterising the subsystem dynamics in such a way that it can deliver precisely what is required of it. All of these subsystems together are used to deliver a bodily motion of the projectile which will be demanded by the operator: *e.g.* a lateral acceleration or a change in velocity. A guidance Law (GL) is responsible for controlling these variables to dictate the approach behaviour of the projectile to the

target, based on engagement scenario characteristics such as range and closing velocity. Conventional control methods used in GLs include Proportional Navigation (PN), Proportional Derivative (PD) and Sliding Mode Control (SMC) [99]. The most commonly used GLs [100] include: Proportional Navigation (PN), Sliding-Mode-Control (SMC), Zero-effort-miss (ZEM) [101] adaptive non-linear guidance (ANG) *etc.*, though there were many more speciality and more niche GLs which can be considered. In many cases it is necessary to create a bespoke GL and it is common practice to neglect external forces (gravity *etc.*) when doing so [102, 103, 104, 105]. GLs are usually a stand-alone framework, independent from traditional system stability theory. However it has been shown that GLs can be combined with traditional system stability theory, for example by utilising both SMC and Lyapunov theory together whilst also considering impact time constraints [106].

2.4.1 Proportional Navigation (PN)

Proportional navigation (PN) is a GL used in a large number of homing missiles [99, 107]. The aim of the law is to demand a lateral acceleration (latax) of the projectile such that the velocity vector of the projectile rotates at the same rate and direction as the Line-of-Sight (LoS). The LoS is defined as a straight line from the projectile to the target, connecting the two. If the LoS doesn't change with the reduction of range then the two are on a collision course. The traditional PN equation is given by

$$\alpha = N\dot{\lambda}V \tag{2.5}$$

where α is the demanded latax of the projectile, N is the PN constant, $\dot{\lambda}$ is the rate of change of LoS and V is the closing velocity of the missile. In effect, the aim of the equation is to reach a situation where the velocity vector of the projectile rotates at a factor N faster than the LoS rate $\dot{\lambda}$. In conventional applications, the closing velocity is the magnitude of both the downrange velocity and the lateral velocity. In turn, the lateral velocity is the magnitude of both the normal and lateral velocities. As the distance between the projectile and target gets smaller on final approach, any movement of the two relative to each other causes a respectively large rotation of the line of sight. This is converted through the

equation as demanding a large lateral acceleration from the projectile to compensate for this. PN is primarily used in scenarios where the target dynamics are significant compared to the missile dynamics. There is little actuator demand from a PN GL initially to get the missile on course.

There are two primary classifications of PN navigation, categorised depending on the direction of the acceleration demand with respect to the chaser's velocity vector. 'True Proportional Navigation Guidance' (TPNG) demands an acceleration which is perpendicular to the missile-target LoS, which does not strictly include the missile velocity since $\diamond(V_m \cdot \lambda \neq 0)$ [‡]. 'Pure Proportional Navigation Guidance' (PPNG) gives the demanded acceleration perpendicular to the missile velocity vector. 'Augmented Proportional Navigation Guidance' (APNG) includes an additional acceleration term with the demand to account for any target acceleration which is known, but this can be a derivative itself of either TPNG or PPNG.

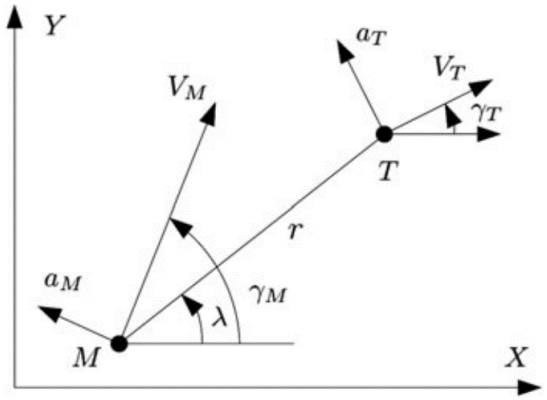

FIGURE 2.4.1 Traditional PN engagement scenario [108]

2.4.2 Sliding-Mode-Control (SMC)

Sliding-Mode-Control (SMC) is a non-linear, variable structure control method which applies a set control signal with specified value to a non-linear system in order to change the dynamics. SMC is sometimes referred to as Variable Structure Control (VSC). There are two phases of executing SMC, firstly the sliding (hyper)surface must be constructed and then the switching feedback gains must be constructed. Figure 2.4.2 shows an example

[‡]it is possible that V_m can be non-zero

of a systems' evolution under SMC. A single-input single-output (SISO) dynamic system

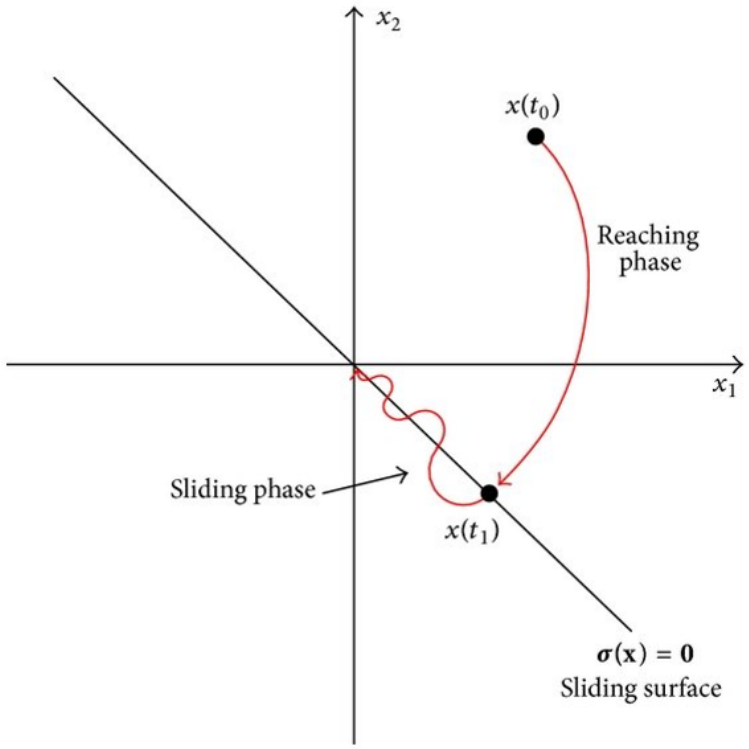

FIGURE 2.4.2 Example of sliding mode control [109]

which is linear in the input can be written as:

$$\dot{x}(t) = f(x(t)) + g(x(t)).u(t). \tag{2.6}$$

With state vectors $x(t) \in \Re^n$ and input vectors $u(t) \in \Re^m$ such that $n \geq m$, and the functions $f : \Re^n \to \Re^n$ and $g : \Re^m \to \Re^m$ such that both f and g are smooth functions. In which case, Σ can be defined as the regular $(n-1)$D submanifold in $\Re^n$:

$$\Sigma := \{x \in \Re^n \mid \sigma_i(x) = 0, i = 1,2,...,m\} \tag{2.7}$$

where $\sigma(x)_i : \Re^n \to \Re(i = 1,2,...,m)$ is a smooth function. We define $\sigma_i(x) = 0$ as the individual sliding (switching) surface. The sliding surface which is used for SMC is found by intersecting *m individual* sliding surfaces:

$$\Sigma := \bigcap_{i=1}^{m} \Sigma_i = \bigcap_{i=1}^{m} \{x \in \Re^n \mid \sigma_i(x) = 0\} \tag{2.8}$$

$$\therefore \Sigma := \{x \in \Re^n \mid \sigma(x) = 0\} \tag{2.9}$$

where $\sigma(x) = [\sigma_1(x), \sigma_2(x), ..., \sigma_m(x)]^T$. If the system states $x(t)$ are on the sliding surface Σ (*i.e.* $\sigma(x(t)) = 0$) then the behaviour of the states are referred to as being in the 'sliding mode'. If the sliding mode actually exists, then the state vector are forced to track along the sliding surface. The sliding mode control law entries $u_i(t)$ $(i = 1, 2, ..., m)$ are found from one the following values:

$$u_i(t) =: \begin{cases} u_i^+, & \text{if } \sigma_\text{i}(\text{x(t)}) > 0, \\ u_i^-, & \text{if } \sigma_\text{i}(\text{x(t)}) < 0, \end{cases} \tag{2.10}$$

The resulting system defined by both equations 2.6 and 2.10 is defined as a *variable structure system*. There is another condition called 'attractiveness', which states that the motion of the system in the near vicinity of the sliding surface tends towards the sliding surface. The conditions for this is $\sigma_i(x(t))\dot{\sigma}_i(x(t)) < 0$, if fulfilled then the sliding surface is a sliding mode. Raymong *et al.* have shown a variety of implementations of SMC [110] and there are a variety of other sources which give origins and applications of SMC [111, 112, 113, 114].

Sliding mode control has previously been implemented as the control method for air to air interception for a projectile and target, again reducing the control problem to 2 dimensions [115]. Yang *et al.* have used SMC in conjunction with other control methods to develop a robust controller for the formation flying of spacecraft [109]. A textbook by Wu *et al.* [116] gives a description of SMC as well as example applications to systems such as the inverted pendulum.

He *et al.* have created a SMC based composite GL for the missile-target interceptions, which operates without line-of-sight information as well as considering actuator lag [108]. While LoS rate information is critical for PN-like GLs, SMC is capable of operating without it. A sliding surface is constructed from actual and estimated system states. Classic stability analysis of the system shows that the LoS rate can be definitely stabilised locally around zero. The bounding is asymptotic around zero and the upper limit of the stabilisation was shown to reduce if the GL parameters were correctly chosen. Numerical

simulations were then used to validate the GL was delivering suitable performance.

A GL using SMC has been created to account for a missile with autopilot lag as well as actuator fault [117]. Geng *et al.* have developed an Adaptive back-stepping SMC terminal GL which accounts for accelerator saturation [118]. SMC based GLs have also been used to consider impact angle and trajectory time constraints [119], angle of attack constraints, damping factors [120]. Zeren [120] has also used Monte Carlo simulations to validate the robustness of the method. A modified guidance and control sliding mode controller was used to improve the chattering, miss-distance and finite time over conventional SMC and PN methods [121]. The validity of the PN-like LoS GL has been investigated for a three body (two aircraft, one missile) system where the launch platform is also moving [122]. A novel variation, called 'airbourne-CLoS' utilises two separate LoS rates with one gain to control the three body problem [123]. A terminal GL using PN has been created with manoeuvrability and terminal angle of attack constraints, such that there is no overloading of the control system in the terminal phase [124].

2.4.3 Zero-Effort-Miss (ZEM)

Zero-Effort-Miss (ZEM) GLs are especially useful for ballistic projectiles. They use a concept of zero-effort-miss distance Z, which is the distance between the projectile impact point and target if the projectile is left completely unguided in a free ballistic trajectory. ZEM GLs aim to produce an equation which relates the control variable, *e.g.* canard deflection angle, to the ZEM distance. This equation usually involves the system kinematics, and is used to achieve $Z = 0$ within the range of actions available to the controller. If the current trajectory of a projectile is already on course to intercept the target, then no controller input is required throughout the flight. At a time when the trajectory indicates the projectile will miss, $Z > 0$, the required control inputs to put the projectile back on a collision trajectory are calculated via the chosen equation/relation. This concept makes ZEM very attractive for this novel projectile design, and indeed ballistic projectiles in general, as actuator effort requires power which is the only consumable resource. In addition, this means that corrections can be made early enough, when the disturbances are still small, so that the GL always demands a controller response which it is feasible to deliver during the later stages, as is sometimes uncharacteristic of PN. This is especially

useful when actuator saturation is a primary focus of the GL.

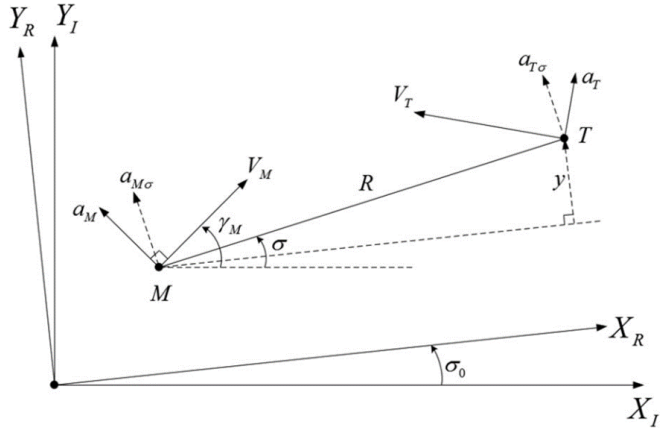

FIGURE 2.4.3 Reference frame of kinematic model used in ZEM GLs [125]

ZEM GLs traditionally use a kinematic model of the projectile/target system in addition to considering motion only in the longitudinal-normal plane [126, 127, 128, 101], which is shown in fig. 2.4.3. An advantage of modelling the GL using kinematics is that the full body dynamics of the target are often unknown. In the case of a direct fire projectile, it is unlikely that the target dynamic would be significant compared to those of the projectile, *i.e.* the movement of the target is likely to be small. Instead, the control capabilities are required for disturbance rejection, small drift corrections and minor target displacement along the trajectory. In the longitudinal-normal reference frame, henceforth refereed to as the 'range frame', the projectile and target have accelerations normal to their velocity vectors, a_P & a_M respectively and normal to the LoS vectors, $a_{P\sigma}$ & $a_{M\sigma}$ respectively. From the figure, and using the small angle scenario, the linearised kinematics of the system can be written as

$$\dot{y} = v \tag{2.11}$$

$$\dot{v} = a_{T\sigma} - a_{M\sigma} \tag{2.12}$$

From the definition of ZEM, which is the miss distance if the projectile remains in its current uncorrected ballistic trajectory, we can write the ZEM, or Z as

$$Z = y + vt_{go} + \frac{1}{2}a_{T\sigma}t_{go}^2 \tag{2.13}$$

where t_{go} is the remaining time until impact/collision/interception, which can be approximated using the closing velocity V_c and distance R using

$$t_{go} = \frac{R}{V_c}. \tag{2.14}$$

By combining equations 2.11 and 2.13, the time derivative of Z can be expressed as

$$\dot{Z} = -a_{M\sigma} t_{go} \tag{2.15}$$

$$\ddot{Z} = -a_{\dot{M}\sigma} t_{go} + a_{M\sigma} \tag{2.16}$$

For the projectile to intercept the target, Z should not depend on the time of interception. In essence, ZEM GLs specifically link the terminal or instantaneous miss distance to the actuator command or airframe control parameter, such as latax or velocity. This is especially useful in direct-fire projectiles where there is very little comparative 3D motion. Calise *et al.* have investigated a control and guidance methodology for a novel projectile incorporating synthetic jets, which interact with the flow to produce a control force [129]. The projectile is both spin-stabilised and direct fire. The GL uses trajectory shaping, whereby the trajectory of the projectile under no controller effort is derived with dynamic model equations, this is the ZEM. The miss distance and calculated required time to go is used to calculate the necessary latax throughout the remaining flight, which would result in the projectile hitting the target. The projectile actuator is modelled as increasing the control force over a given time. For $T_0 < t < T_1$ the jet is activated and for $T_1 < t < T_2$ the jet is deactivated, according to the equation:

$$F_{jet} = F_0 + \frac{(F_1 - F_0)(1 - e^{-at})}{1 - e^{-aT_1}} \tag{2.17}$$

Here the actuator control force has been arbitrarily mathematically modelled, to represent a real force loading situation. The control force demanded of the actuation mechanism is given by $F_c = m\sqrt{A_{yc}^2 + A_{zc}^2}$ where A_{yc} and A_{zc} are the lateral and normal accelerations respectively, both of which are functions of the ZEM distance in the respective planes. The roll direction the jet is activated along can be adjust by a use tunable parameter. Figure 2.4.4 shows the controller architecture considered in the paper, an adaptation of work pre-

viously published by the same lead author [130]. The target and projectile coordinates are fed into the GL, which is used to determine the control inputs u. Since the pulsing jets are activated once per revolution, the desired control effort is update once every 25 revolutions, since the spinning projectile is assumed to be spun sufficiently fast in comparison to the update rate of the GL that a polling rate of 25Hz is sufficient. It seems that in reality, this update rate is arbitrary and can be chosen to reflect the update frequencies of any system being considered. An adaptive neural network is also used in the control architecture,

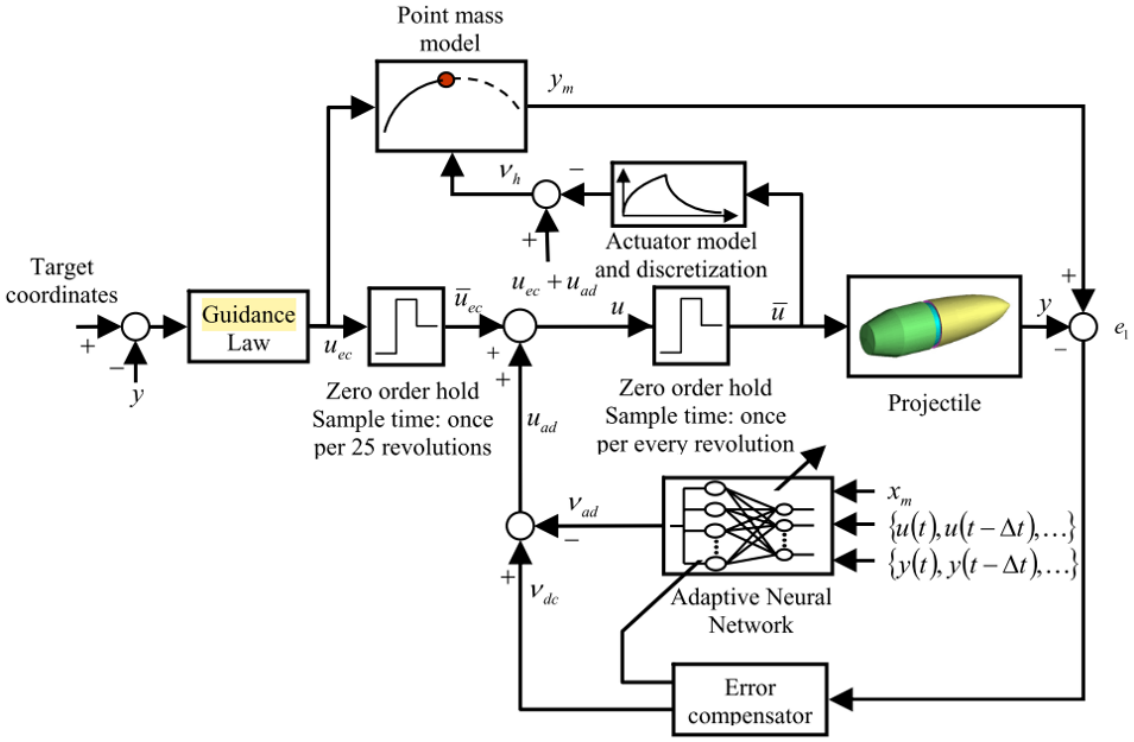

FIGURE 2.4.4 Adaptive controller used by Calise *et al.* [129]

to modify the control signal u demanded by the GL for distance errors which become present during the simulations. The low update rate means the neural network is polled less often, which reduces the computational intensity of the simulations. Primarily however, it is done to reduce feedback in the guidance loop, caused by projectile precession. The controller commands are then fed to both the projectile and the discretised actuator model. The actuator model is used to calculate what the control force will be, which is then in turn used to evaluate the dynamic model according to a point mass model, to be compared to the simulated measurements of the dynamic model, to finally determine the effectiveness of the control architecture and feed the error which needs correcting back

into the neural network to update future control commands. This feedback is made via an 'adaptive control term' v_{ap} which scales the control demand u.

It was found that the induced moment of the actuator amplified the attenuation of the control force and also, depending on the moment direction, increased the peak control force. The resulting peak force on the projectile was no more than 0.9N, this is found to be well within the desired limits described in [49]. We can assume this force is constant when evaluated 'from a distance' in the sense that it is produced by each revolution continuously. While the GL alone was sufficient to guide the projectile to the target in the cases presented, introducing the adaptive controller reduces the actuator effort by 30% throughout the flight, leading to a much more consistent control force profile throughout the flight. This is essential for reducing the actuator demand during the terminal phase, when the actuator may be saturated from the controller demanding a latax it is unable to deliver. Finally, the augmented controller was able to reduce the peak control force by 70%, which is desirable since the actual performance of the actuator was abstractly modelled.

Gao *et al.* have investigated the effect of impulse shapes on the correction capabilities of fin-stabilised, guided projectiles [131]. The projectile is adorned with numerous impulse thrusters, radially distributed about the circumference of the projectile body. The thrusters deliver a force on the projectile over time after their actuation, which is shown in fig. 2.4.5A. These single-use thrusters are capable of firing at predetermined points in the projectile roll rotation, shown in fig. 2.4.5B, to laterally impart a control force. Because the rotation of the projectile in question is low compared to the actuation time of the impulse thruster, the impulse is delivered in its entirety in addition to being symmetric about the deployment point. This cannot accurately depict the radial direction of impulse delivery in the event of an asymmetric impulse shape. A test projectile was manufactured and tested; with a correction capability of 598.3m at a range of 30km, using a total impulse of 600Ns. Simulations were in good agreement with the experimental tests, but neither the simulation procedure or the requisite coefficients are described at all.

Fresconi describes a novel trajectory shaping method for an indirect fire projectile, which reduces the burden on both the sensor and the actuator [78]. The intention is to use the procedure on 'control authority-limited' projectiles, where volumetric or cost requirements mean the projectile is unable to meet the demands of GLs. The comparisons

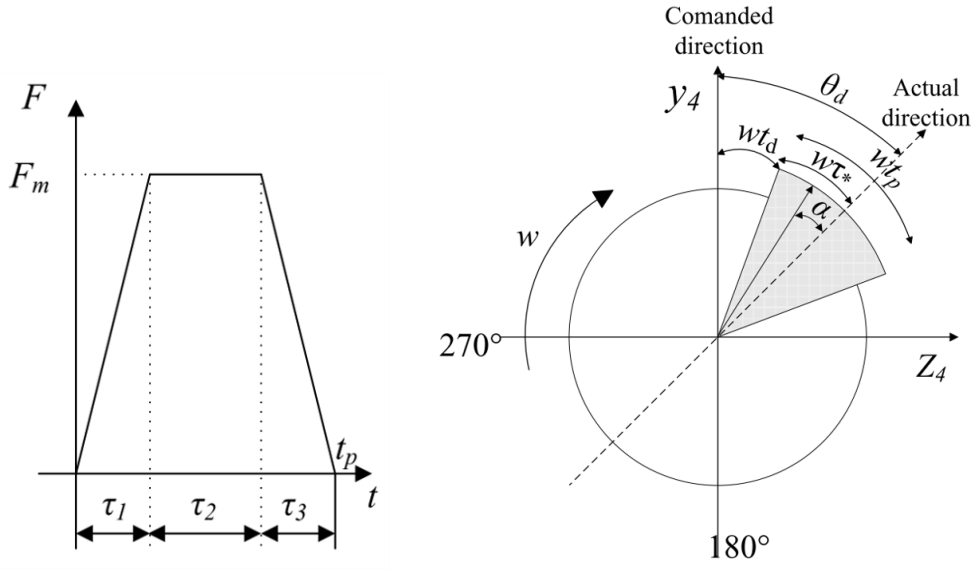

(A) Impulse shape (B) Radial trigger of impulse

FIGURE 2.4.5 Actuation mechanism of impulse thrusters considered by Gao *et al.* [131]

showed that PN GLs demanded a latax that the projectile being considered was always unable to deliver, while the impact point prediction method described was at all times, demanding a latax within the capabilities of the projectile. The procedure involved finding a relation between the canard correction angle and the miss distance. During the terminal phase of flight, the projectile is assumed to be travelling near vertically downwards, with negligible angle of attack, the only normal force present is the control force, which is assumed to act through the centre of mass. It is noted that assuming the inertial reference frame remains fixed to the airframe is ill-advised, but that by including controller feedback, any concerns raised by asserting this assumption are mitigated. The relation found is

$$\delta_c = K_P \frac{\pi I_{trans} e_\lambda \dot{\phi}^2}{4qSN^c_{N\alpha}(\delta_{CoP} - x_{CoG})} \tag{2.18}$$

This shows the relation between the proportional gain K_P, transverse inertia I_{trans}, angular error e_λ, angular rate $\dot{\phi}$ and demanded canard control angle δ_c. There is also the location of the canard centre of pressure δ_{CoP} and the total projectile CoM, x_{CoG}. There is no stability analysis of the system, but Monte Carlo simulations were used to analyse the performance of the control system subject to variations. The CEP was reduced from 200m in the ballistic case to under 1m for the guided case. The analysis was verified with live-fire experiments using a 155mm spin-stabilised projectile. This also confirms the conventional

6-DoF ballistic model was a good representation of the experimental tests conducted and that the inclusion of Monte Carlo simulations to test trajectory perturbations is also a viable approach. Fresconi continued this work the following year with L. Fairfax [132], detailing a position estimation procedure using low cost and therefore relatively inaccurate sensors and augmenting the information with known flight dynamics and GPS. Using an array or 10 Inertial Measurement Unit (IMU) sensors, the positional error was found to reduce by a factor of 10, but increasing the array size to 100 led to no further increase in positional measurement accuracy.

Common textbooks show that PN guidance can be derived from ZEM based laws, but this is predominantly only shown in a planar engagement scenario [103]. V. Lam has shown that 'True' Proportional Navigation (TPN) can be derived from ZEM [126]. Lam analysed the effectiveness of TPN, 'Pure' PN (PPN), 'Augmented' proportional navigation (APN) and an 'acceleration-compensated' zero-effort-miss (ACZEM) against various engagement scenarios. The performance of the GL is compared in terms of an 'acceleration index', given by the formula

$$a_I = \int_0^T ||a_c|| \mathrm{d}t \tag{2.19}$$

where a_c is the instantaneous acceleration demand from the GL. In this sense a_I is essentially the total acceleration demand from the GL over the whole flight of the projectile and as such. A higher a_I is generally regarded as worse, since it translates to a higher actuator effort. For constant accelerations where the acceleration is known perfectly, ACZEM performed the best, with the lowest miss distances and lowest a_I. The increase in performance is stated as being due to the early compensation for target movement. It was found that when the acceleration data was noisy then ACZEM would begin to perform worse because the projectile was incorrectly manoeuvring earlier to compensate for the incorrect acceleration measurement data. To compensate for this, an acceleration confidence factor was applied to the acceleration term which scaled from 0 for highly noisy data up to 1 for perfect data. This is a simplistic solution to the problem, which requires minimal alterations to the GL, while also allowing the possibility to be a function which itself can be optimised.

Lee *et al.* have shown a different approach for shaping ZEM trajectories, such as that considered in [129]. It is reinforced in the paper that it is difficult to guide projectiles with a modelled actuator saturation using PN guidance, without using gain scheduling or scaling. The proposed methodology is suggested as an alternative in such situations, where it is undesirable to enact large changes in the guidance constant in PN-like GLs. In essence, the proposed method adds a multiplicative weighting term to the ZEM distance to be corrected. The weighting function can itself have as many gains or parameters as the creator defines and optimises, but the functions itself adds another degree of freedom to control the shaping of traditional ZEM. A GL is then presented in the paper which takes the form of a PN GL with time varying controller gain. The desired ZEM is determined, the weighting function necessary to produce this ZEM is derived and then the control value is found. The application and performance of the GL is then tested on an arbitrary system as well as a real-world system. The hybrid system was found to outperform traditional PN for the considered scenarios.

ZEM and zero-effort-velocity control have been applied to a variety of other uses aside from the missile scenario, such as asteroid interception and landing problem, orbital transfer/raising [127] and as mid-course correction for exo-atmospheric ballistic missiles [128].

2.4.4 Novel and bespoke guidance laws

A polar GL has been investigated which controls a missile based on the polar radius and angle of the target from the missile [133]. However, the control force is assumed to be variable and the roll rate and direction is adjustable. The lateral distance error of the system was found significantly reduce over the duration of correction though there were small amplitude oscillations present which were noted to also reduce toward zero. A polar GL has been investigated which controls a missile based on the polar radius and angle of the target from the missile [133].

An Expanded 2D proportional derivative GL (E2DPDGL) has been created for a skid-to-turn command to line-of-sight anti-tank guided missile, which builds upon classical PD GLs (CPDGL), with the objective of eliminating a spiral trajectory which is an artefact of PD GLs [134]. The E2DPDGL law acts as a traditional PD GL when in close proximity to

the target, outside of this area the GL includes additional terms which are functions of the position vector derivatives. This approach was shown to successfully eliminate the spiral trajectory present in the picture plane. An Expanded 2D PD GL (E2DPDGL) was created for a skid-to-turn command to LoS anti-tank guided missile, which builds upon classic PD, with the objective of eliminating a spiral trajectory which is an artefact of PD GLs [134].

Pamadi & Ohlmeyer have investigated two less common GLs for controlling the flight angle of a spin-stabilised projectile [135]. These laws are the Generalized Explicit (GENEX) and the Forward Integration of Terminal States (FITS). GENEX, primarily designed for missiles with onboard propulsion, allows the designer to modify the extent of the trajectory shaping, while still aiming to minimise the resulting miss distance at impact. FITS is a predictive guidance method originally designed for ballistic projectiles. Unlike GENEX however, FITS does not conventionally include the trajectory angle. A method called Gravity Bias Scaling (GBS) is used to incorporate the trajectory angle considerations into the FITS law. The effectiveness of both methods is compared in a 6-DoF dynamic model. It was found that both laws provided a comparable performance, however when GPS information is removed (to emulate target jamming) GENEX performed significantly better than FITS/GBS, albeit at the expense of miss distance. This will be a consideration of the designer as to where trajectory following is more important than miss distance minimisation. In instances where trajectory angle is more important than miss distance, these GLs can be considered.

Gruenwald & Bryson use a relatively new adaptive control architecture, which in turn uses an expanded reference model, to a fin-guided projectile [136]. The aim of the paper is to address the limited actuator bandwidth that will likely be present in projectiles. Linear matrix inequalities are used to relate the available actuator bandwidths present in the actuator dynamics, to the system uncertainties and stabilities. While the approach was proven to be effective at characterising the aerodynamic uncertainties and actuator bandwidth, the approach appears convoluted; there are more suitable and bespoke solutions available to novel systems without necessitating such mathematical complexity.

Park *et al.* have introduced a new GL which aims to improve upon some of the shortcomings of proportional navigation, namely the high proportion of the flight in which the actuator is unnecessarily engaged [137]. The premise of the proposed method is

essentially a hybrid of trajectory shaping and ZEM laws, in that the ballistic flight is altered at certain points to reduce the miss distance. The law follows a similar form to PN, however the considered flight variable is the trajectory angle, the same which was considered in [135], as opposed to the line-of-sight rate. In addition to this, the impact point prediction uses a neural network as a non-linear function approximator, as opposed to the traditional 6-DoF or modified point mass models. The authors do use 6-DoF models to compare the predictions of the neural network approximators, as well as testing the performance of the novel GL method against traditional PN. In all conditions, wind and Magnus effects are neglected. The accuracy of the model is as expected, highly dependent on the accuracy of the model used to predict the ballistic path of the projectile. This guidance method would be more useful for projectiles which require minor accuracy improvements, such as cluster munitions, where there is less emphasis on single projectile maximum precision but a large group of them would benefit from having the CEP lowered even slightly. In addition, the relatively more mass produced but inexpensive projectile would take advantage from having less expensive computational hardware.

A CCF-equipped spin-stabilised projectile has been considered by Wang *et al.* for their implementation of a guidance and control design [79]. They used an effective hybrid strategy, combining both impact point prediction and perturbation theory. Monte Carlo simulations showed that the control strategy is viable for the considered CCF adorned projectile, which was capable of reducing the CEP from approximately 200m to almost 20m, nearly a 90% reduction. The authors mention that "*The five main types of guidance most considered in guided ammunition contexts are trajectory shaping, model predictive guidance, path following, impact point prediction control, and proportional navigation. When only small correction to a trajectory is possible, only the later four are applicable*". Model predictive guidance uses a high-fidelity dynamic model of the projectile and environment to determine the outcome of the controller action space, but these method are computationally intensive if a high degree of accuracy is required. Path following guidance compares the current path of the projectile against an *a priori* or online generated path, the error is used to generate the control action; however path following guidance only considers position, as opposed to velocity, which can cause compounding errors in some cases. The most popular subset of impact point prediction is trajectory integration, which suffers from

the same dependency on high-fidelity dynamic models as model predictive guidance. In addition, the gyroscopic stability of the projectile must be considered across the whole trajectory, making this method more suited to short range projectiles, where the time scale is short enough that there is no decay of the gyroscopic stability. Proportional navigation is the most common form of guidance method for many guided weapons, especially missiles, due to its simplicity and effectiveness. However, at the time of authoring the manuscript they noted that only projectiles using jet motors had incorporated PN control [129, 138].

It is very common for literature to consider the impact angle of a projectile when designing the GL since impact angle, especially with ballistic projectiles, have terminal effectiveness directly proportional to the angle of attack upon contact [139, 140]. Novel virtual target methods have been created for impact angle and burst height constraints [141]. Some guided projectiles carry explosive payloads, and the detonation direction is dependent on the angular orientation of the primary projectile. Wang *et al.* have considered impact angle constraint using a state-dependent Riccati equation (SDRE) approach [142]. A Riccati equation is, in essence, any ordinary differential equation where the unknown function is quadratic. Once the projectile engagement scenario is considered using a planar kinematic model, the system is reduced to states, which can then be solved using the SDRE approach. The resulting GL has a series of coefficients, which it is noted designers can change for any given projectile. However, the GL proposed is tested on an unrealistic kinematic model, thus the real-world performance is questionable, especially since this methodology uses conventionally abstract mathematics.

Impact angle control with field of view constraints has been considered in similar works by Sharma & Ratnoo [143], and Lee & Kim [144]. As with Wang *et al.* [142], the GLs are tested entirely on a kinematic model of the engagement scenario. A ‘capture region’ is defined, essentially being the effective region in which sufficient information and capability is available for the GL and projectile system to successfully reduce the miss distance. A closed form variation of direct-pure-pursuit (DPP) is used to derive what CR will provide the desired impact angle, as a function of the initial position and trajectory angle. When the missile FOV is small, the possible impact angles are also small and possibly discontinuous in the output space.

Classic PN has been augmented with a polynomial which describes the heading error

and the parameters of the polynomial are tuned with a 'big-bang big-crunch' (BBC) algorithm [145]. The algorithm searches for the optimum parameters by moving along a normal distribution with heuristic values. In testing, the GL is initialised with a high distance error and analysis is conducted with a latax constraint. The algorithm was compared to Pure PN and Differential Evolution PN, and was shown to be the most time and energy efficient of the three algorithms.

A few publications specifically pertain to the guidance of dual-spin projectiles. Iterative impact point prediction has been used to create a GL for a dual-spin projectile with control force imparted by fixed canards [146]. A modified form of projectile linear theory is used to predict where the projectile will land and make the necessary corrections to the control system. Proportional navigation has been used in the GL of a dual-spin mortar during the ascent and descent phase [147]. The results of the GL were validated with hardware-in-the-loop testing and Monte Carlo simulations. Intriguingly, there currently exists no literature which describes a GL for a missile with roll-direction, roll-rate, and control-force magnitude constraints.

2.5 Artificial intelligence and reinforcement learning in guidance systems

Within the field of artificial intelligence (AI), machine learning is concerned with the development of algorithms which a computer can use to complete a task optimally, without being given explicit instructions on how to complete said task. Reinforcement Learning (RL) is a specific type of machine learning where an agent autonomously derives an optimal policy to maximise the future cumulative reward of every possible action.

Figure 2.5.1 shows a diagram for the operation of a typical RL agent. The Agent uses a certain policy $\pi(s,a)$[§], to evaluate which action a it should take given the current state s of the system, in order to maximise its expected reward r. To determine what the optimum policy should be, it uses a reinforcement learning algorithm, to change the policy by comparing the actual to expected reward. Figure 2.5.2 shows a hierarchy of different

[§]Note that the policy is a function of the actions and states, hence $\pi(s,a)$. However the operation of the policy selects an action based on an observed state, consequently it is sometimes written as $\pi(a|s)$

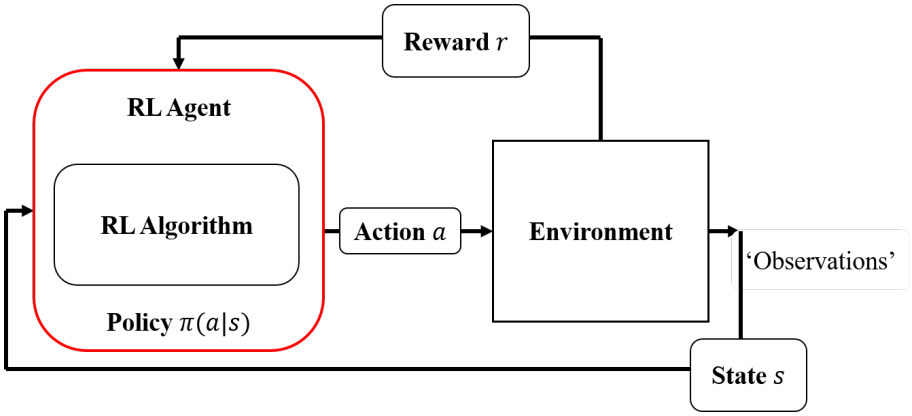

FIGURE 2.5.1 Diagram of a typical Reinforcement learning agent

RL algorithms.

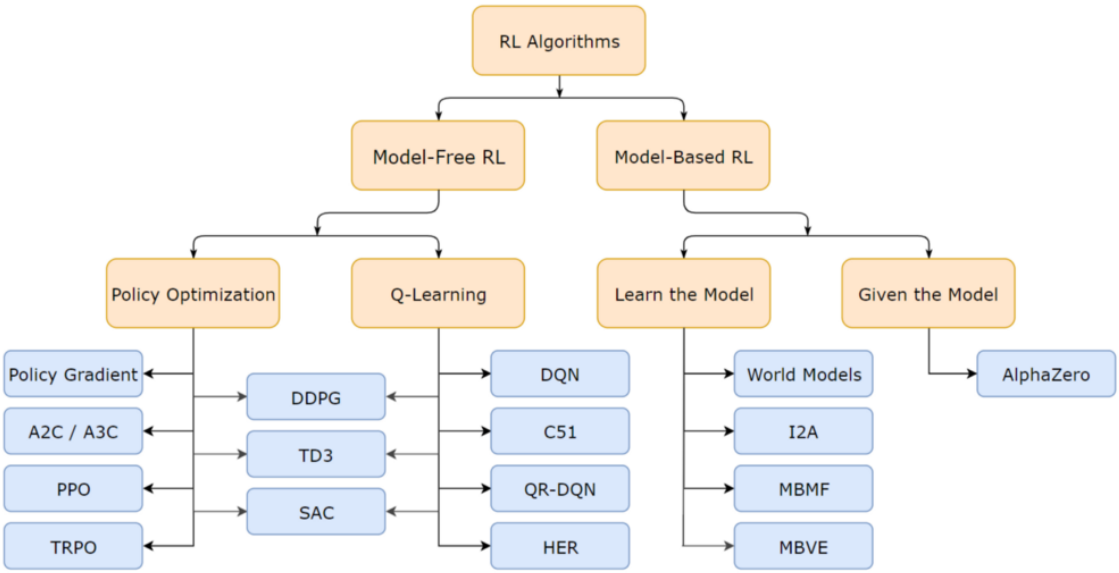

FIGURE 2.5.2 Hierarchy of RL algorithms [148]

The first branching in figure 2.5.2 shows whether the algorithm is 'model-based' or 'model-free'. In model-based RL, the agent will learn or be provided with a function which maps state transitions. Only a few situations exist where the known model is a perfect representation of the real system, since it will be the same system. One example is the renowned AlphaZero, an adaptation of the AlhpaGo, which has been designed to play the game of chess, shogi and Go [149]. In less than 24 hours of learning, "*Starting from random play, and given no domain knowledge except the game rules, AlphaZero achieved within 24 hours a superhuman level of play [...] and convincingly defeated a world-champion program in each case*". In the majority of cases, there is no ground truth

model available to the agent and a model will be used. In this case, the model used to represent the system will never perfectly reflect the real-world environment, there will always be some simplification or inaccuracy in the modelling process. Imperfect models and improperly chosen reward functions lead to an agent exploiting certain aspects or nuances of the training environment which will maximise the reward function, but in such a way that doesn't translate to the desired real-world performance. In some instances there is zero prior knowledge and the model itself must be learned in its entirety; this learning process is inherently difficult and can even be completely futile [148].

In model-free RL, no knowledge of the model is necessary for the algorithm to perform, the operation is entirely abstract. Q-learning and policy optimisation are both types of model-free reinforcement learning algorithms. Policy optimisation methods represent the policy in by a set of parameters θ, *i.e.* $\pi_\theta(s,a)$. The π_θ is then maximised against θ using either gradients ascent or some local maximisation. This allows one to optimise for any chosen set of θ, but this method is hindered if the end performance of the model cannot be quantified in terms of the chosen θ. In Q-learning, the agent uses a Q-value $Q(s,a)$ in addition to the policy. The Q-value of a given action represents the expected reward from all successive actions in the current state. The action with the highest $Q(s,a)$ indicates it leads to the highest cumulative reward. We define the Optimal Action-value function $Q^*(s,a)$, as a function that returns the highest average $Q(s,a)$ of every action given the current state. Q-learning methods learn an approximator function $Q_\theta(s,a)$ which is updated during training so the $Q(s,a)$ more accurately represent the reward and approach the optimal action function. This update process used the Bellman equation:

$$Q(s,a)_{\text{new}} = Q(s,a) + \alpha \left[r(s,a) + \gamma \max_{a'} \left[Q^*(s',a') \right] - Q(s,a) \right] \tag{2.20}$$

with learning rate α, reward $r(s,a)$, discount factor γ updated Q-value $Q(s,a)_{\text{new}}$. Table 2.2 contains a list of terminology for this section.

In relatively simple systems, there may be a computationally manageable amount of states and actions within the environment. A common approach for the Q-function is to use a lookup table, which maps every state-action pair to a Q-value, which is then updated with every iteration of the loop. If the system is significantly complicated, or the states

are continuous then a lookup table is no longer practical, and a new function must be used. Deep[¶] Q-Neural Network learning (DQN) is a variant of Q-learning which uses a neural network to approximate the Q-function for a given state-action pair [150]. The action space for DQN is binary, but can have any number of actions. Deep Q-learning agents have been demonstrated to perform at least as well, in some cases considerably better than humans in a variety of arcade style games [151]. There are also many other variants of Q-learning, such as Fuzzy Q-learning [152]. Other deep methods include Deep Deterministic Policy Gradient (DDPG), which has a continuous action space.

Another common structure in RL algorithms is the 'actor-critic' method. Here, the actor can be thought of as the traditional policy function $\pi(s,a)$, which determines the optimal action to maximise the expected reward given the current state. In general, the critic will in some way evaluate how well the actor is performing and will provide the actor with feedback to adjust its performance based on this; *i.e.* the critic will compute a value function, which assists the actor in learning the optimal policy. Q-learning is an example of this, where the Q-value is what encapsulates the actor performance information. The critic takes the current state and the action from the actor and uses these to compute an expected reward. It then compares the expected reward value to the actual reward once the action outputted from the actor has been fed to the environment. Actor-critic methods can be 'deep', whereby either one or both of the actor-critic pair can be a neural network. Common algorithms including actor-critic methods are A2C and the A3C used by Deepmind [153]. Figure 2.5.3 shows a DQN agent using an algorithm, in which neural networks are used for both the actor and critic. Using neural networks instead of traditional functions allows the agent to handle a very large domain.

A general problem with reinforcement learning is that an agent which is perfectly trained in the virtual environment will completely fail to perform when it is implemented into a real-world system. This is because even the most accurate model is still not accurate enough to portray the stochastic nature of the real-world. To combat this, a methodology is being used where the observations are intentionally perturbed during the training process to emulate real-world noise. The is done by means of an 'adversary', which introduces pertubations according to its own policy. It has been shown that under such circumstances,

[¶] 'Deep' in the title of any RL algorithm indicates the use of a neural network at some point

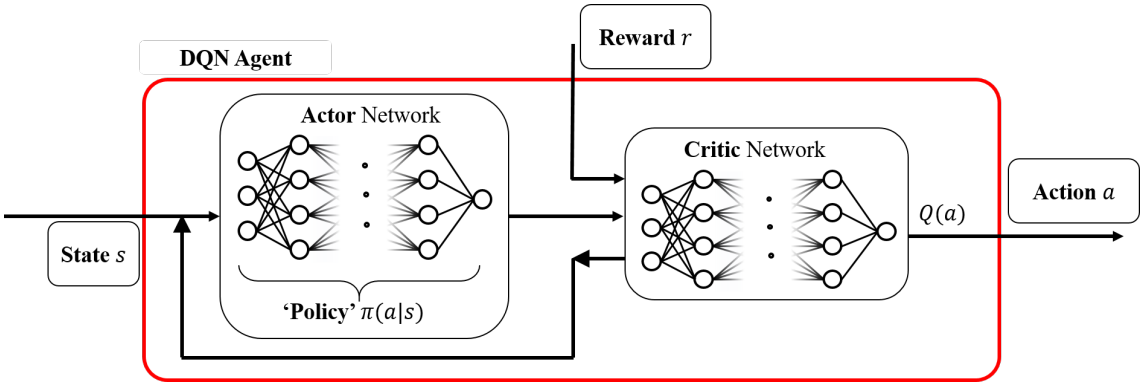

FIGURE 2.5.3 Diagram of a DQN agent using the actor-critic method

algorithms can be written which are able to successfully mitigate the impact perturbations have on the training procedure successfully [154, 155]. Pinto *et al.* investigated the effect of implementing an adversary which is also a deep learning agent, trained in tandem with the primary agent [156].

When machine learning is being used for control, it is advantageous to make the system it is controlling as simple as possible. A complex system requires a large neural network to be able to process the different system states and interpret the correlation between desirable actions and the specific parameter set which caused them. Also, the environment the agent is trained in should be as similar as possible to the environment it will operate in. For example, when using machine learning in image recognition [157], the images used in training samples are identical to what the agent will experience when implemented. By contrast, an agent can be trained using a computer simulated environment to control a walking robot, but this is vastly different to the real-world environment the agent will be implemented in [158].

2.5.1 Projectiles and guidance laws

Gaudet & Furfaro [159] used reinforcement learning to derive a homing-phase missile GL, to compare against traditional proportional navigation (PN) methods. PN methods are very accurate for ideal conditions, but system dynamics, noise and component delays cause deterioration. In some cases systems are so complex they are modelled stochastically, such as helicopter blades. The model used in the paper to train the AI agent is a statistical representation of the system, pulled from flight telemetry and wind tunnel data. This is

Term	Definition
Action ($a \in A$)	A parameter of the environment the agent can change in order to cause a desirable change. In Deep Q-learning the *agent* can be comprised of an *actor* and *critic* network.
Actor	A neural network responsible in place of the operational *policy*
Agent	The operator which takes an *action* to change the *state* of the *environment*
Critic	A neural network which evaluates the performance of the *actor* based on the new *reward* and is capable of adjusting the actor to optimise the new reward
Discount factor (γ)	A scalar factor between 0 and 1 sets the importance of immediate ($\gamma \to 0$) or long term reward ($\gamma \to 1$).
Environment	The external place where the system evolves
Learning Rate (α)	A parameter which determines the step size of each iteration when minimising a *loss function*
Loss function	A function which maps an event to a real number characterising the cost associated with that particular event
Observation	Parameters or measurements of the system which are taken from the environment and passed to the agent
Policy ($\pi(s\|a)$)	The decision-making function used by the *agent* which calculates the *action* that provides the maximum *reward*
Reward	A scalar value representing the desirability of a state
RL Algorithm	The method used by the *agent* to optimise the *policy* according to the received *reward*
Q-value ($Q(s,a)$)	The cumulative *reward* which would be expected if an *agent* in a *state s*, performed an *action a* and continued to operate under the current *policy* π
Reward Function	An equation which calculates the *reward* for a given *state*/*action* combination.
State ($s \in S$)	A particular combination of a given Observation and actions

TABLE 2.2 Terminology for Q-Learning environment

stated to be, in some case, more accurate than using a simplified mathematical model. This would be especially true when dynamic models are simplified to kinematic models. It was found in the results that the neural network used in the agent was overtrained, likely due to too many hidden layers being used (16 layers). The agent tested used weights and biases from the optimisation phase before the agent overtrained. It was noted that a preferable solution if time permitted was to penalise the agent via a regularization term, which sums the squares of the non-bias weight values. The result of the comparison showed that the RL agent was able to provide smaller miss distances in more complex engagement scenarios. In addition, it was found that the RL agent was employing different GLs at different points in space, instead of employing different controller gains for different points in space.

Gaudet *et al.* [160] have used proximal policy optimisation to construct a novel GL relying only on observations of LoS angle and its rate of change. A 6-DoF kinematic model was used and the agent was able to control the actuators of the missile. The agent was unable to exceed the performance of the state-of-the-art conventional method (zero-effort-miss policy), after 140,000 episodes of training, but the agent was robust enough to perform when subjected to novel scenarios outside the scope of the training data. At the time, a GL was unable to be formulated relying solely on the angle and angle rate as this agent was.

Liang *et al.* [161] have developed a novel impact-angle GL under partial actuator failure, using a model-based deep RL agent. A neural network is used as a predictive model for the guidance dynamics, which is then fed into a model predictive path integral (MPPI) control framework. MMPI methods falter when there is a discrepancy between the training and real environments, to counteract this an online neural network learning method is used to adapt to the changing model dynamics. A kinematic model is used in the training, two hidden layers of 200 neurons were used in the neural network. There was no mention of the number of episodes required to train the agent. The resulting agent was shown to have better performance than the traditional MPPI method, due to the ability to adapt to environment perturbations on the fly.

Yan *et al.* [162] have used RL and transfer learning as a way of designing projectiles. Shared- Layer Deep-Deterministic-Policy-Gradient is used to generate dimensions of a generic projectile frame with the intent to maximise the lift/drag ratio (R_{LD}) while keeping

the centre of pressure constant. Both DDPG and SL- DDPG RL techniques were compared against NSGA-II, NCGA and MOPSO, which are optimization algorithms commonly used in aerospace design. It was found that both DDPG and SL-DDPG methods converged quickly to the terminal R_{LD}, taking only around 50 episodes. While NSGA-II, NCGA and MOPSO were still increasing when the training was terminated at 100 episodes. DDPG provided the least accurate R_{LD} of 3.35, while NSGA-II, NCGA and MOPSO all terminated at approximately 3.47. SL-DDPG was the best algorithm, achieving a terminal value of 3.53.

A Recurrent Convolutional Neural Network has been used in an Augmented PN GL to switch the navigational constant online during the flight of the projectile [163]. It was found that a combination of recurrence and convolution provided better results than either method independently. In addition, positional error of the pursuer as well as a delay of the evader's acceleration was considered.

2.5.2 Path planning

Zhao *et al.* [164] have implemented a Deep Q-Network (DQN) agent as a path planning method for a UAV. The environment is set to be a 2D plane with obstacles included which the UAV must avoid. A neural network is implemented to reduce the time it takes for the agent to learn in a continuous action space, as opposed to separating the environment into discrete sections. There are no permissible actions for the agent listed, but from the data provided the agent is allowed to move in any direction at any time; though it is likely the bearing of movement is also discrete to reduce the action space. Zheng *et al.* [165] have also used a DQN agent to implement path planning for a UAV. Similar to Zhao *et al.* [164], the agent is free to move in any direction within the 2D planar environment. However, the scope of work by Zheng focusses on the integration of radar data, which is outside the scope of this project.

Zhang *et al.* [166] have used DQN to assist in manoeuvrer planning for air to air UAV combat. The UAV is placed in a kinematic 3D environment and the states are the air coordinates, rotation angles and air speed. The permissible actions of the agent are to slightly turn left, right, up and down, accelerate, decelerate and maintain speed. The reward function is designed to keep the UAV at a sufficient altitude to prevent stalling, keeping a

close distance to the aircraft, and finally attaining a high relative velocity between the two aircraft. This may be good for initial testing but as will be explained in §5.3.1, this will lead to the agent flying straight past the target instead of holding on course. It is reported that the agent is generating acceptable flight paths after only 200 episodes of training, which is very quick considering one would expect a DQN agent to require more than 10^5 or even 10^6 episodes to train [149, 150, 154, 151, 158]

Gaudet *et al.* [167] have used a policy gradient learning to train an agent to control a craft during powered descent and landing for planetary excursion missions. A dynamic 6-DoF model is used and the agent is responsible for controlling the thrust of 4 engines placed on the bottom of the craft. The agent is rewarded for minimising the terminal position, velocity, attitude and rotational velocity errors, and minimising control effort. The observations are the velocity error and rotational velocity, time-to-go, estimated attitude and altitude. A maximum reward was reached after approximately 75,000 episodes. The trained agent was validated with a Monte Carlo simulation, where it proved robust against noise and parameter variation while being able to "*pinpoint accuracy and a soft landing with minimal deviation from an ideal landing attitude and rotational velocity, with large divert distance capability*".

Wang *et al.* have used DQN in an effort to control an aircraft during the descent for landing [168]. In essence, a 2D grid is used to describe the aircraft movement. The effective objective is to move around the grid from a randomised initial location to a runway of fixed location. The aircraft is fixed to move in a straight line at constant speed, being able to turn left or right permitted the turning circle is at a constant radius. The agent was able to produce satisfactory guidance for the kinematic model after around 1200 episodes.

Sung *et al.* have investigated the use of Neural Networks in controlling dual-spin projectiles [169]. The design in question uses one set of canards to de-spin the front section while a second pair of control canards provides a control force which is continuous across a range. The NN is used in an adaptive controller in an attempt to decouple the coupling dynamics of the two sections. Results showed that the NN was able to reduce the coupling of the two sections to a point where control authority of the projectile was possible.

2.5.3 General applications

Yang *et al.* [170] investigated the effect of different reward terms in a deep-RL animation of an agent based box manipulation task. The reward terms investigated were distance, orientation, collision and time. The agent was then trained four separate times, in the same environment for 5×10^5 episodes each. Each case omitted one of the four reward terms from the reward function. Where distance was omitted, the agent completely failed to learn any desirable behaviour, indicating that this was the most significant term. When orientation, collision and time were omitted, the agent learned to perform acceptably after approximately 2×10^5 episodes in each case. When omitting orientation, collision and time terms, the terminal mean rewards were approximately 26, 37 and 44 respectively. This shows that the order of importance for the inclusion of reward term, with the most important being first and least important being last, were: distance to goal, orientation to target, collision with obstacles, then time taken.

Selvi *et al.* [171] used machine learning, amongst genetic algorithms and particle swarm algorithms as a solution for weapon allocation in the multi-layer defence scenario. In this scenario, the aim is to decide which layer of defence is best to expend at a particular time against a series of oncoming missile threats. This paper is objectively concerned with developing an algorithm for resource distribution, as opposed to navigation. The method described in the paper is a Learning Vector Quantisation (LVQ) - Radial Basis Function (RBF), multi agent hybrid architecture. Essentially, the input observations are intelligently quantised to reduce the dimensions Q function, which is approximated by an RBF neural network. The proposed method proved more efficient at allocating resources than conventional solutions to the problem.

Other notable works

Zhang Ruoyu *et al.* have investigated the radar reflection properties of projectiles with high spin rates [172]. It was found that the reflected signal is an AM-FM combination. The AM index indicates the attitude of the projectile while modulation frequency indicates the spin rate. The ability of both Chirp-Z and Fast-Fourier-Transforms to improve the signal precision was investigated. It was found that spin rates of up to 164Hz could be discerned

with good signal to noise ratio. Other work has also taken place developing algorithms to spatially locate projectiles without the use of GPS, as is tradition [173].

Wells describes the considerations of the GPS and receiver vulnerabilities in the projectile guidance modules [174]. The GPS receiver application module (GRAM) which GPS equipped projectiles use to navigate, must also be fitted with a selective availability/anti-spoof module (SAASM) to prevent electronic tampering in the battlefield. This is the GPS technology currently used in the XM982, or Excalibur, 155mm artillery round.

Liu *et al.* have proposed a MEMS based IMU design, to measure spin-stabilised projectiles with high spin rates [175]. A test platform was built, utilising off-centre accelerometers in conjunction with three single axis roll gyros. It was found that as projectile speed increased, as well as flight time, the MEMS configuration was susceptible to a drift error during the measurement. A flight test showed that the MEMS accelerometer gave readings of 5deg/s what the gyroscopes measured, with an absolute error under 6deg. The authors suggested that this configuration was thus more suited to projectiles with short flight times, which in turn suggests smaller calibre projectiles. In addition, it was noted that the vibrations present in the projectile during the launch phase and throughout the flight led to errors in the accelerometer output, which were then compounded when calculating the roll angle. If a projectile with a high spin rate relied on the accurate measurements of the roll angle, then this MEMS configuration would be advantageous due to its simplicity and low volumetric requirements. A ballistic projectile with no propulsion mechanism would also have less vibrations and therefore benefit more from this design.

Barrett *et al.* [28] have conducted a review of flight control mechanisms pertaining to bullets. The Barrel-launched adaptive munition (BLAM) uses piezoelectric actuators to articulate a 10^o, 37mm pivoting nose section of a projectile. The nose section was showed to achieve a response rate of up to 200Hz at a speed of Mach 3.3.

Fresconi has proposed a flight control methodology for a 40mm projectile with a front mounted camera with input from a roll angle sensor [77]. The projectile is adorned with a singular control surface protruding from the aft section of the body. The control method generates controller commands directly from the imager feedback using gain-scheduled proportional control. The primary problem with this guidance method as a design is that it relies on a relatively low, spin rate or at least some mechanism for slowing the roll

rate to an acceptable level. Of course, while the methodology behind the mechanism has no feasible limitations except for computer processing speed, the limiting factor of the design is the response rate and resilience of the actuator and subsystems; any externally mounted control surface or mechanism is subject to more extreme conditions. Monte Carlo simulations showed that the completed architecture was able to reduce the circular error probability (CEP) from 8.6m to 2.7m.

Low cost MEMS gave been proposed for orientation estimators in guided projectiles [176]. Thermopile sensors and magnetometers are used in conjunction with *a priori* trajectory information to account for the effects of weather disturbances. Monte Carlo simulations were used to evaluate estimator performance when the thermopile was rendered useless by weather conditions as well as when realistic sensor errors and environmental disturbances were introduced.

2.6 Summary

Upon consideration of the above literature, there are certain key points which should be highlighted for their importance to this project. A 6-DoF dynamic model, using q-LPV linearisation [54], can be used in conjunction with aerodynamic coefficients of a projectile to provide a true likeness of the projectile and target dynamics [91, 92], including for small calibre projectiles [177], at least to the degree of uncertainty of the parameters and coefficients [129, 76]. This is also true for dual-spin projectile utilising a 7-DoF model [53]. Effectiveness of the GL and resulting trajectories can then be quantified using dispersion metrics such as CEP [74, 77, 78, 79]. This process has been used in its entirety for understanding the feasibility of novel projectile concepts [178, 179]. CFD analysis has been used to determine aerodynamic coefficients to calculate the stability factors of projectiles with small geometry changes [180].

The ballistic stability factors are a primary criteria for projectile designers before [81], and it is insufficient to rely on the actuation mechanism to provide stability; the passivated projectile geometry itself must satisfy the gyroscopic stability criteria [5]. It is imperative then that the ballistic stability of framework of dual-spin projectiles is thoroughly understood and shown to be reconcilable with single-spin projectiles, to adequately describe

any design. This framework can be used to bound the design and ensure early problems are identified, however reliable trajectories necessitate that aerodynamic coefficients are obtained. It has been shown that CFD programs such as ANSYS [181, 182], or semi empirical programs like PRODAS [95], can be used to generate coefficients over chosen flight envelope for novel [84, 85] and traditional [91, 90] geometries. CFD methods have been shown to be in good agreement with experimental data [96].

The actual projectile actuation mechanism response can be modelled by a mathematical functions [129, 131], of course provided treatment of the function can be mapped for the whole function scope. These arbitrary functions often give rise to opportunities for bespoke GLs which are better suited to guide a particular system given intrinsic knowledge of the projectile dynamics. When proposing a bespoke GL for the projectile, certain aspects must be considered. GLs are often described from the perspective of the XZ plane also known as the 'picture plane' [120, 133, 134]. Some of the aforementioned sources use kinematic models for the derivation and validation of the control law [121, 141, 124, 119, 122], but dynamic models provide a better likeness of the system response and as such, a dynamic model should be used during testing. The performance of GLs can be greatly improved by modifying the GL with arbitrary terms to characterise imperfections in the modelling of the system [126]. It is common to test the GL using arbitrary model parameters to facilitate more efficient and reliable interpretation of the results [133, 134]. Any bespoke GL parameters are shown to perform well when optimised using optimisation algorithms [145].

Proportional Navigation (PN) is a very common and widespread GL due to the simplicity of its fundamental operating principle. Almost all guided weapons system could function using PN, but almost all guided weapons system could function more optimally if they utilised other GLs which specifically characterise and address the nuances of the engagement situations, such as impact angles and actuator capabilities. All literature reviewed at the time of writing shows that while PN does provide an effective guidance solution, there is always a modification, adaptation or entirely different GL which delivers better performance when considering a specific projectile/target situation. For the simplicity of its implementation and elegance of operation however, PN should be considered as a baseline or reference GL to which any novel law or modification can be compared. ZEM

is also a very strong candidate for direct fire projectiles due to the strength of simplifying the flight to a flat fire trajectory [83] and as such, ZEM methods will likely form the basis of a bespoke GL solution.

The implementation of SMC depends entirely on the existence of a well-defined sliding surface, the creation of which is non-trivial. PN and ZEM can provide satisfactory control with significantly easier implementation. This project is primarily focussed with demonstrating whether the concept is a feasible alternative to current methods and as such, there is no benefit in evaluating the performance of the projectile under every GL. The use of SMC to guide this system should be investigated in future work, along with other GLs. Finally, AI technologies including reinforcement learning are a rapidly growing sector with many applications to guided weapons including: path planning [166, 164] for kinematic and dynamic systems; GLs using two common types of RL architectures DDPG [162] and DQN [167]. Due to the abstraction of RL agents, they are an ideal candidate for application to such a novel actuation mechanism. The blind operation requires little detailed knowledge of the domain which is in the case of ballistic projectiles, highly non-linear and coupled. As such, the viability of RL agents to control both the actuation mechanism itself and as a GL will be investigated.

Chapter 3

Theory

In this chapter, a coordinate system is established in order to build a non-linear, dynamic model of the form $\dot{\vec{x}} = f(\vec{x}(t), \vec{u}(t), t)$, with system motion $\dot{\vec{x}}$ in terms of system states $\vec{x}(t)$ and measurable inputs $\vec{u}(t)$. This model consists of a set of equations describing the kinematic and dynamic motion of the body. It will include various aerodynamic coefficients corresponding to the external forces acting upon the projectile in flight (these forces and moments are discussed in Appendix A.1), which are in turn discussed. These coefficients can either be used from existing databases or simulated using Computational fluid dynamics (CFD) analysis. A linearisation process can be applied to simplify the system into a format conducive with control theory design. The aim of the simplification is to achieve a dynamic model framework of the form $\dot{\vec{x}} = (A - B\vec{K})\vec{x}(t)$ with dynamics matrix A and input matrix B, where $\vec{K}$ is the control system gain. The resulting dynamic model is validated against available literature.

The pitching and yawing motions of projectiles is then shown, along with how the stability factors arise from the framework. The stability factors change depending on whether they represent dual-spin or single spin projectiles in addition to them having passivated control surfaces. The evolution of the factors is shown from literature and an example is given to analyse the stability over the flight envelope. The stability theory forms the basis of publication [40], in appendix C. A novel method of analysing stability across the flight envelope is then shown in a technical note, in appendix C.

3.1 Dynamic model of a dual-spin projectile

In 2008, Gkritzapis et al [183] constructed a 'Physicomathematical' model of projectiles, specifically small calibre bullets, with the purpose of estimating and analysing trajectories. Their paper demonstrates a high agreement between their model and "other technical data and recognised exterior atmospheric projectile flight computational models". A 4^{th} order Runge-Kutta method is used to numerically solve, simultaneously, twelve first-order ordinary differential equations. In 2013, L. Baranowski released a paper detailing the equations of motion for a spin-stabilized projectile [184]. Its purpose is to define the system and present a derivation in its entirety according to ISO (1151) standards. Both papers use Tait-Bryan (as opposed to 'Proper' Euler) angles to convert between stationary and projectile axis, supplemented by quaternions where applicable. In 2017, Séve, Theodoulis & Wernert *et al.* proposed a full non-linear, parameter-dependent dynamic model for a dual-spin canard guided projectile [60], shown in fig. 3.1.1. Since the dual-spin projectile is considered later, the model is included here. The paper builds on work by Costello *et al.* [185] in 2000 and continues the joint contribution of Theodoulis & Wernert [57, 59], in 2010 and 2013 respectively. This project uses a coordinate system, reference frame and interaction consideration shared by all of the above texts as well as many industry standard reference texts [93], though the nomenclature is altered for consistency within this project.

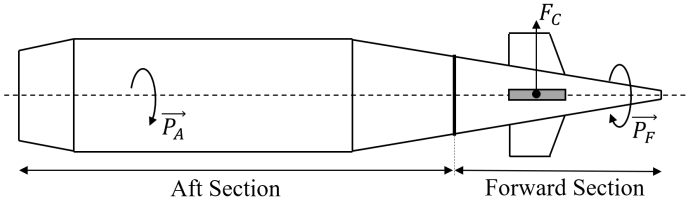

FIGURE 3.1.1 Projectile design with fixed F_c

3.1.1 Coordinate axis and frames of reference

There are twelve state variables needed to describe the projectile throughout its entire fight: the linear distances x, y & z, the translational speeds u, v & w, the angular positions ϕ, θ & ψ and the angular velocities p, q, & r. A dynamic model then uses two coordinate systems, a stationary reference frame (usually an Earth frame) and another centred about

the projectile. While the state variables are almost always consistent throughout different models, the choice of coordinate systems and frames of reference change. Tricks are often employed to reduce the mathematical complexity of conversions, which helps reduce the burden on processing units which may need to calculate the system evolution and course corrections. Most often employed is to align an axis, *e.g.* the $\hat{y}$ axis, with either the pitch (θ) or yaw (ψ) components of the total yaw; that way only one contribution need be considered, since the other will be zero. Another example is to employ a no-roll frame rotating axis, whereby $\phi = p = 0$, since the axis rotates with the projectile. Figure 3.1.2

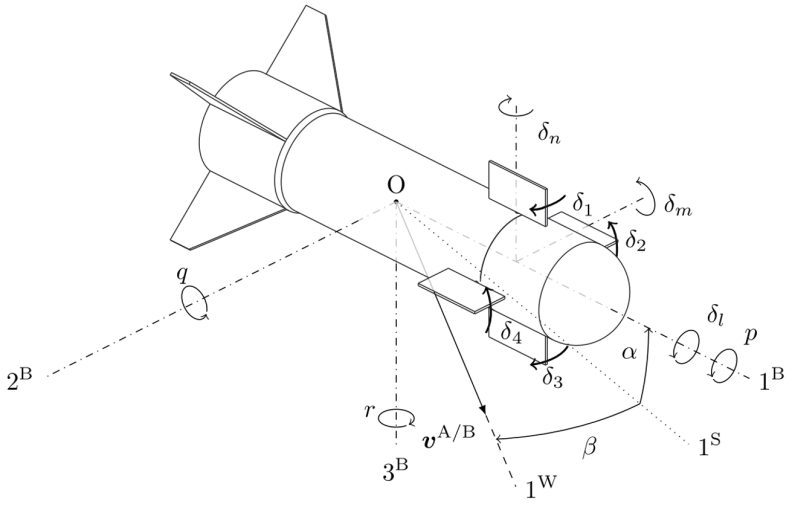

FIGURE 3.1.2 Axis convention from the projectile reference frame [186]

shows the conventional axis definitions used in the field of ballistics, it is used in popular textbooks by both McCoy [93] and Carlucci & Jacobson [83]. Motion of a projectile is traditionally presented by the wind axis coordinates (V,α,β), which describe the angular displacement of the velocity vector with respect to the longitudinal axis of the projectile. The axis $\hat{x}$, $\hat{y}$, $\hat{z}$ correlate to the translational distances x, y, z and translational speeds u, v, w respectively. The figure shows how the wind $[]^W$ axis coordinates are determined from the Cartesian body $[]^B$ axis coordinates for a present side-slip β and angle of attack α. To clarify, $[1^B\ 2^B\ 3^B]^{\mathrm{T}} = [x\ y\ z]^{\mathrm{T}}$ and $[1^W\ 2^W\ 3^W]^{\mathrm{T}} = [V\ \alpha\ \beta]^{\mathrm{T}}$. The projectile velocity relative to the medium $\vec{V}$ also has a scalar magnitude V, hence it is useful to define a unit vector in the direction of motion $\hat{v} = \vec{V}/V$, where

$$V = \sqrt{u^2 + v^2 + w^2} \tag{3.1}$$

Pitch and Yaw deviation are measured by the angle of attack α and angle of side-slip β respectively. They measure the angular displacement of the longitudinal axis (1^{B} or $\hat{x}$) relative to the velocity vector V along the normal and lateral planes. We can write α and β as

$$\alpha = \arctan\left(\frac{w}{u}\right) \tag{3.2a}$$

$$\beta = \arctan\left(\frac{v}{\sqrt{u^2+w^2}}\right) = \arcsin\left(\frac{u}{V}\right) \tag{3.2b}$$

The above parameters, V, α & β are known as the 'wind axis system' variables. They are differentiated here with respect to time for later use.

$$\dot{V} = \frac{u\dot{u}+v\dot{v}+w\dot{w}}{V} \tag{3.3a}$$

$$\dot{\alpha} = \frac{u\dot{w}-w\dot{u}}{u^2+w^2} \tag{3.3b}$$

$$\dot{\beta} = \frac{-uv\dot{u}+(u^2+w^2)\dot{v}-vw\dot{w}}{V^2\sqrt{u^2+w^2}} \tag{3.3c}$$

Equation 3.4a combines the wind axis variables into the total angle of attack α_T, which can be simplified under the small angle approximation ($< 15^o$ is a reliable boundary [93]) shown in equation 3.4b.

$$\alpha_T = \sqrt{\sin\alpha^2\cos\beta^2+\sin\beta^2} \tag{3.4a}$$

$$\alpha_T = \sqrt{\alpha^2+\beta^2} \tag{3.4b}$$

3.1.2 Aerodynamic coefficient inclusion

Section A.1 has described the various forces that affect a projectile in flight and the coefficients corresponding to them. Because the coefficients are representation of an instantaneous force being experienced, they change throughout the flight as a function of airframe speed V, as well as α and β. A parametric investigation can be undertaken and the coefficients can be parametrised in terms of any flight variable, but it is predominantly the wind axis coordinates. In addition to this, a non-zero α and β mean some forces no longer act parallel to the projectile axis shown in figure 3.1.2, the axis along which the resultant

forces and moments will be resolved in to determine airframe accelerations. As such, a new set of coefficients are introduced, listed in full in the nomenclature (pg. xxii) , which represent the total aerodynamic component acting in each projectile axis. It also shows the constituent flight variables of each of the total aerodynamic coefficients where applicable. All coefficients are dependent on the Mach number. The coefficients are directionally orientated with the projectile axis, *e.g.* a positive C_{A0} produces a force acting in $\vec{x}^+$. Likewise, for moments, a positive C_{n0} produces a turning force about the $\vec{y}^+$ axis in the positive mathematical direction.

Note that forces of a different kind, while they may act in along the same axis, must be considered as separate contributions due to additional factors in their respective formulae. For example, while a component of the Magnus force can act in the same axis as the normal force, the Magnus force equation has an extra pd/V term; it is thus considered in its own body coefficient, C_{Np}, instead of C_{N0}. Figure 3.1.3 shows a side view (X-Z plane) of a projectile in flight for a zero and non-zero value α. From figure 3.1.3B, the body

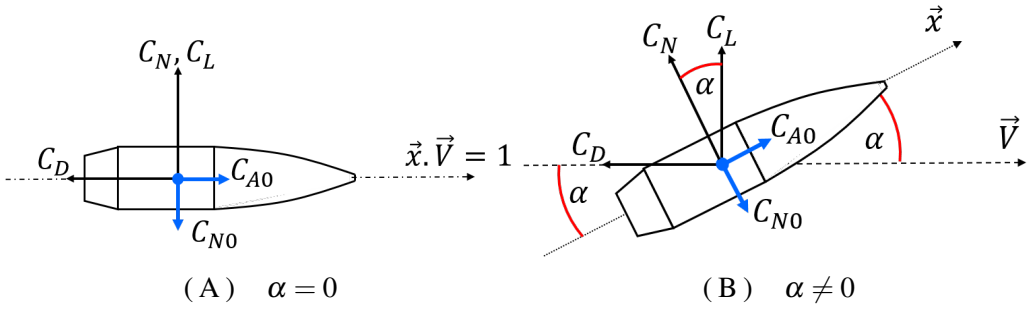

FIGURE 3.1.3 Variation projectile frame coefficients due to non-zero α

coefficient C_{N0} corresponding to the projectile z$^+$-axis, is given by

$$C_{N0}(\alpha) = -C_N - C_L\cos(\alpha) - C_D\sin(\alpha) \tag{3.5}$$

The resultant force in this direction is given by

$$F_{N0} = F_z = \bar{q}SC_{N0} \tag{3.6}$$

Of course, the coefficients will need to be resolved in 3 dimensions, since β could also be non-zero. The resultant decomposition for C_{X0}, with only the effects considered in figure

3.1.3, is given by

$$C_{X0}(\alpha,\beta) = -C_L\sin(\alpha) - C_D\cos(\alpha)\cos(\beta) \tag{3.7}$$

3.1.3 Equations of motion

The equations necessary for describing the system dynamics are derived from Newton's equations of motion:

$$\vec{F} = m\left(\frac{\mathrm{d}\vec{V}}{\mathrm{d}t}\right) \tag{3.8}$$

$$\vec{M} = \left(\frac{\mathrm{d}\vec{H}}{\mathrm{d}t}\right) \tag{3.9}$$

Here $\vec{H}$ is the angular momentum and $\vec{M}$ is the sum of externally applied moments. Subscript F denotes the forward section and subscript A denotes the aft section. The assumption is made that the total CoM coincides with the aft CoM (the mass of the forward part is small with respect to that of the aft part) and the nose moment of inertia $I_{xx,F}$ is small compared to the aft one $I_{xx,A}$. In general, $I_{jj,(A/F/T)}$ is the Aft/Forward/Total moment of inertia with respect to the j^{th} axis of the body as a whole. Equations 3.10 & 3.11 are the non-linear Kinematic translational and rotational equations, they describe the position of the projectile with respect to the inertial Earth frame (subscript e). Equations 3.12 & 3.13 are the Dynamic translational and rotational equations of motion for the dual-spin projectile, they describe the motion and rotation of the CoM respectively*.

Kinematic translational:

$$\begin{bmatrix}\dot{x}_e\\ \dot{y}_e\\ \dot{z}_e\end{bmatrix} = \begin{bmatrix}\cos(\theta)\cos(\psi) & -\sin(\psi) & \sin(\theta)\cos(\psi)\\ \cos(\theta)\sin(\psi) & \cos(\psi) & \sin(\theta)\sin(\psi)\\ -\sin(\theta) & 0 & \cos(\theta)\end{bmatrix}\begin{bmatrix}u\\ v\\ w\end{bmatrix} \tag{3.10}$$

*the kinematic equations describe the location of the CoM

Kinematic rotational:

$$\begin{bmatrix} \dot{\phi}_F \\ \dot{\phi}_A \\ \dot{\theta} \\ \dot{\psi} \end{bmatrix} = \begin{bmatrix} 1 & 0 & 0 & \tan(\theta) \\ 0 & 1 & 0 & \tan(\theta) \\ 0 & 0 & 1 & 0 \\ 0 & 0 & 0 & \sec(\theta) \end{bmatrix} \begin{bmatrix} p_F \\ p_A \\ q \\ r \end{bmatrix} \tag{3.11}$$

Dynamic translational:

$$\begin{bmatrix} \dot{u} \\ \dot{v} \\ \dot{w} \end{bmatrix} = \frac{1}{m} \begin{bmatrix} F_X \\ F_Y \\ F_Z \end{bmatrix} - \begin{bmatrix} 0 & -r & q \\ r & 0 & r\tan(\theta) \\ -q & -r\tan(\theta) & 0 \end{bmatrix} \begin{bmatrix} u \\ v \\ w \end{bmatrix} \tag{3.12}$$

Dynamic rotational:

$$\begin{bmatrix} \dot{p}_F \\ \dot{p}_A \\ \dot{q} \\ \dot{r} \end{bmatrix} = \begin{bmatrix} 0 \\ 0 \\ -\left(\frac{I_{xx,A}}{I_{yy}}\right) p_A r - r^2 \tan(\theta) \\ \left(\frac{I_{xx,A}}{I_{yy}}\right) p_A q + qr\tan(\theta) \end{bmatrix} + \begin{bmatrix} \frac{1}{I_{xx,F}} & 0 & 0 & 0 \\ 0 & \frac{1}{I_{xx,A}} & 0 & 0 \\ 0 & 0 & \frac{1}{I_{yy}} & 0 \\ 0 & 0 & 0 & \frac{1}{I_{yy}} \end{bmatrix} \begin{bmatrix} m_{1,F} \\ m_{1,A} \\ m_m \\ m_n \end{bmatrix} \tag{3.13}$$

The force matrix $[F_X\ F_Y\ F_Z]^{\mathrm{T}}$ in equation 3.12 and the moment matrix $[m_{1,F}\ m_{1,A}\ m_m\ m_n]^{\mathrm{T}}$ in equation 3.13 are actually comprised of the forces and moments listed in §A.1. Both matrices are shown in equations 3.14 & 3.15 respectively.

$$\begin{bmatrix} F_X \\ F_Y \\ F_Z \end{bmatrix} = \bar{q}S \left\{ \begin{bmatrix} -C_{A0} \\ C_{Y0} \\ -C_{N0} \end{bmatrix} + \frac{p_A d}{V} \begin{bmatrix} 0 \\ C_{Yp} \\ -C_{Np} \end{bmatrix} + \begin{bmatrix} 0 \\ C_{Y\delta}\delta_y \\ -C_{N\delta}\delta_z \end{bmatrix} \right\} + mg \begin{bmatrix} -\sin(\theta) \\ 0 \\ \cos(\theta) \end{bmatrix} \tag{3.14}$$

$$\begin{bmatrix} m_{1,F} \\ m_{1,A} \\ m_m \\ m_n \end{bmatrix} = \bar{q}Sd \left\{ \begin{bmatrix} 0 \\ 0 \\ C_{m0} \\ -C_{n0} \end{bmatrix} + \frac{d}{V} \begin{bmatrix} 0 \\ C_{lp} \\ C_{mq} \\ C_{nr} \end{bmatrix} + \frac{p_A d}{V} \begin{bmatrix} 0 \\ 0 \\ C_{mp} \\ C_{np} \end{bmatrix} + \begin{bmatrix} 0 \\ 0 \\ C_{m\delta}\delta_z \\ C_{n\delta}\delta_y \end{bmatrix} \right\} + \begin{bmatrix} \tau_M + \tau_{F,A} \\ -\tau_{F,A} \\ 0 \\ 0 \end{bmatrix} \tag{3.15}$$

Here, $\mathscr{M}$ is the Mach number, τ_M is the motor torque which controls the roll angle of the forward guidance section (ϕ_F) and $\tau_{F,A}$ is the frictional torque which counteracts this. The frictional torque can be modelled as a hydrodynamic and roller bearing in combination, shown below, where k_s and k_v are the static and viscous friction coefficients respectively

$$\tau_{F,A} = \frac{1}{2}\rho S d\, C_{A0}(\mathscr{M}, \alpha, \beta)\, \mathrm{sgn}(p_A - p_F)(k_s + k_v|p_A - p_F|) \tag{3.16}$$

The coefficients[†] of C_D in equation A.1b are $-\bar{q}S$ which can be seen outside the brackets of the first term in equation 3.14. By matching the coefficients of the respective force and moment equations from §A.1, respective contributions can be easily substituted into equations 3.14 & 3.15. This presentation of coefficient terms in the order of body-static, Magnus effects and canard induced is present in many other literature sources [186],[59], [57] [185].

Additionally, there are the 'virtual signal' normal and lateral controls from the canards, δ_z and δ_y respectively, which depend on the forward section roll angle ϕ_F and the individual canard roll angles. For clarity, δ_z is the contribution of all canards resulting in projectile yaw in the xz plane, congruent with $\vec{q}$ (or the xy plane congruent with $\vec{r}$ for δ_y). Figure 3.1.2 shows the axis and deflection angle conventions, relative to the model.

Canards 1 and 3 (originally aligned with the y-axis) are a pair, their joint contribution will be written as

$$\delta_m = (\delta_1 + \delta_3)/2 \tag{3.17}$$

like wise the contribution from canards 2 and 4 shall be expressed as

$$\delta_n = (\delta_2 + \delta_4)/2 \tag{3.18}$$

This notation makes the assumption that opposing canards are 'locked' in rotation about the contribution axis. In other words, the canard pairs' leading edge deflects in the direction the body is to rotate in, this is shown with directional arrows in figure 3.1.2. Thus, we can

[†]coefficient in the mathematical sense, which C_D is multiplied by

write the control vector in terms of the standard rotation matrix $R(\phi_F)$ as

$$\begin{bmatrix} \delta_z \\ \delta_y \end{bmatrix} = \frac{1}{2} \begin{bmatrix} \cos(\phi_F) & -\sin(\phi_F) \\ \sin(\phi_F) & \cos(\phi_F) \end{bmatrix} \begin{bmatrix} \delta_1 + \delta_3 \\ \delta_2 + \delta_4 \end{bmatrix} = R(\phi_F) \begin{bmatrix} \delta_m \\ \delta_n \end{bmatrix} \tag{3.19}$$

For convenience during the trimming procedure later, the rotation matrix and its inverse are explicitly written as

$$R(\phi_F) = \begin{bmatrix} \cos(\phi_F) & -\sin(\phi_F) \\ \sin(\phi_F) & \cos(\phi_F) \end{bmatrix} \qquad R^{-1}(\phi_F) = \begin{bmatrix} \cos(\phi_F) & \sin(\phi_F) \\ -\sin(\phi_F) & \cos(\phi_F) \end{bmatrix} \tag{3.20}$$

Strub & Basset [186] investigated the design of a skid-to-turn autopilot, implemented in an 80mm canard guided (fin stabilised) projectile body. Though their design was single spin as opposed to dual-spin, many aspects of the dynamic model they developed are in agreement with the presented framework. One notable inclusion is to account for the rotational displacement of the canards due to pitch and yaw, as opposed to just roll. This is represented by the δ_l term in the equation below, an extension of equation 3.19.

$$\begin{bmatrix} \delta_l \\ \delta_m \\ \delta_n \end{bmatrix} = \begin{bmatrix} -\frac{1}{4} & -\frac{1}{4} & -\frac{1}{4} & -\frac{1}{4} \\ \frac{1}{2} & 0 & -\frac{1}{2} & 0 \\ 0 & -\frac{1}{2} & 0 & -\frac{1}{2} \end{bmatrix} \cdot \begin{bmatrix} \delta_1 \\ \delta_2 \\ \delta_3 \\ \delta_4 \end{bmatrix} \tag{3.21}$$

The dynamic and kinematic equations 3.12-3.11 also take into account any external forces affecting the projectile during flight, the frame load factors at the CoM, a. However, the frame load factors actually detected by the accelerometers, a^S, will be different due to the sensor location (assumed to be CoM_F) ahead of the CoM $\vec{r}_{Fx} > 0$.

$$a^S = \begin{bmatrix} a_x^S \\ a_y^S \\ a_z^S \end{bmatrix} = \begin{bmatrix} 1 & 0 & 0 \\ 0 & \cos(\phi_F) & -\sin(\phi_F) \\ 0 & \sin(\phi_F) & \cos(\phi_F) \end{bmatrix} \left\{ \begin{bmatrix} a_x \\ a_y \\ a_z \end{bmatrix} + \frac{\vec{r}_{Fx}}{g} \begin{bmatrix} -q^2 - r^2 \\ p_F q + \dot{r} \\ p_F r - \dot{q} \end{bmatrix} \right\} \tag{3.22}$$

$$a = \begin{bmatrix} a_x \\ a_y \\ a_z \end{bmatrix} = \frac{\bar{q}S}{mg} \left\{ \begin{bmatrix} -C_{A0} \\ C_{Y0} \\ -C_{N0} \end{bmatrix} + \frac{p_A d}{V} \begin{bmatrix} 0 \\ C_{Yp} \\ -C_{Np} \end{bmatrix} + \begin{bmatrix} 0 \\ C_{Y\delta} \\ -C_{N\delta}.\delta_z \end{bmatrix} \right\} \tag{3.23}$$

The rotational measurements from sensors ω^S can be written as

$$\omega^S = \begin{bmatrix} p_F^S \\ q^S \\ r^S \end{bmatrix} = \begin{bmatrix} 1 & 0 & 0 \\ 0 & \cos(\phi_F) & -\sin(\phi_F) \\ 0 & \sin(\phi_F) & \cos(\phi_F) \end{bmatrix} \begin{bmatrix} p_F \\ q \\ r \end{bmatrix} \tag{3.24}$$

There is a better representation for these coordinates which is more suited to autopilot design, following the procedure of ref. [60], they are rewritten in the wind coordinate system (V, α, β). First, the translational speeds $(u,\ v,\ w)$ are written in terms of wind axis variables from equations 3.1-3.2b

$$u = V\cos(\alpha)\cos(\beta) \tag{3.25a}$$

$$v = V\sin(\beta) \tag{3.25b}$$

$$w = V\sin(\alpha)\cos(\beta) \tag{3.25c}$$

These translational speeds $(u,\ v,\ w)$, along with their derivatives $(\dot{u},\ \dot{v},\ \dot{w})$ from equation 3.12, are substituted into the derivative wind axis variables (equations 3.3a), yielding

$$\begin{bmatrix} \dot{V} \\ \dot{\alpha} \\ \dot{\beta} \end{bmatrix} = \begin{bmatrix} 0 \\ q + r\tan(\beta)\left(\cos(\alpha)\tan(\theta) - \sin(\alpha)\right) \\ -r\left(\sin(\alpha)\tan(\theta) + \cos(\alpha)\right) \end{bmatrix} + \frac{1}{mV} \begin{bmatrix} u & v & w \\ -\frac{\sin(\alpha)}{\cos(\beta)} & 0 & \frac{\cos(\alpha)}{\cos(\beta)} \\ -\cos(\alpha)\sin(\beta) & \cos(\beta) & -\sin(\alpha)\sin(\beta) \end{bmatrix} \times \begin{bmatrix} F_X \\ F_Y \\ F_Z \end{bmatrix} \tag{3.26}$$

3.1.4 State-space non-linear system

The equations of motion from §3.1 shows how all different aspects and parameters of the system are related, however the model is highly non-linear and coupled which is the case

with most complex, real systems. To better define the system in a manner more conducive to the application of a control and guidance architecture, the state and outputs dynamics are defined and written in the generic form of a non-linear, parameter dependent system in state-space. State-space representation is a powerful method of equation manipulation, as it restructures many differential equations in a form more conducive for computer methods to solve, in addition to being in a popular form to which established analytical control methods can be applied. A system can be described in state-space as follows:

$$\left.\begin{aligned} \dot{x}(t) &= f_x(x(t), u(t), \sigma(t)) \\ y(t) &= f_y(x(t), u(t), \sigma(t)) \\ \dot{\sigma}(t) &= f_\sigma(x(t), \sigma(t)) \end{aligned}\right\} \qquad t \in \mathbb{R}^+ \tag{3.27}$$

and the definitions of the state-space matrices are shown in table 3.1. The functions listed

Matrix	Expression
System states	$x = [\alpha, q, \beta, r]^{\mathrm{T}}$
Outputs (system)	$y = [a_z^S, a_y^S, q^S, r^S]^{\mathrm{T}}$
Outputs (from sensor)	$y_m = [a_{z,m}^S, a_{y,m}^S, q_m^S, r_m^S]^{\mathrm{T}}$
Parameters†	$\sigma = [V, p_F, p_A, h, \phi_F, \theta]^{\mathrm{T}}$
Controls (actual)	$u = [\delta_m, \delta_n]^{\mathrm{T}}$
Controls (desired)	$u_c = [\delta_{m,c}, \delta_{n,c}]^{\mathrm{T}}$
Functions of x	$f_x = [f_\alpha, f_q, f_\beta, f_r]^{\mathrm{T}}$
Functions of y	$f_y = [f_{a_z^S}, f_{a_y^S}, f_{q^S}, f_{r^S}]^{\mathrm{T}}$
Functions of σ	$f_\sigma = [f_V, f_{p_F}, f_{p_A}, f_h, f_{\phi_F}, f_\theta]^{\mathrm{T}}$

TABLE 3.1 Choice of state-space matrices
† - Though $\sigma = \sigma(x)$, it is assumed to be a system input which varies slowly wrt. system dynamics

are the right-hand sides of the relevant equation of the i^{th} element in §3.1. The components of the parameter matrix σ_i are all assigned some operational range ensuring they are bound within the flight envelope, $\Gamma_\sigma \subset \mathbb{R}^6$. The inclusion of y_m and u_c matrices represent the imperfect performance of the installed hardware. Though we will demand a deflection u_c of the canards they will in practice output some different deflection u which will be the

actual input for calculating system evolution. Likewise, the actual load factors the sensors should read y will have some systematic or random error, causing an observed y_m. The sensor and canard actuators can be modelled as second order filters [60].

For a chosen parameter matrix $\bar{\sigma} = [\bar{V}, \bar{p}_F, \bar{p}_A, \bar{h}, \bar{\phi}_F, \bar{\theta}]^{\mathrm{T}}$ defining the system operation, finding the equilibrium point consists of obtaining the corresponding input matrix $\bar{u}$ at which the system state derivative is zero, i.e.

$$\left.\frac{\mathrm{d}x(t)}{\mathrm{d}t}\right|_{\bar{\sigma}} := 0 \tag{3.28}$$

An equilibrium manifold is obtained by calculating $\bar{u} \; \forall \; (\bar{\sigma} \in \Gamma_\sigma)$, computing the manifold is also known as 'airframe trimming'. From equation 3.27, we can write a set of four equations:

$$f_x(\bar{x}(t), \bar{u}(t), \bar{\sigma}(t)) := 0 \tag{3.29}$$

with equilibrium state $\bar{x} = [\bar{\alpha}, \bar{q}, \bar{\beta}, \bar{r}]^{\mathrm{T}}$ and equilibrium input $\bar{u} = [\bar{\delta}_m, \bar{\delta}_n]^{\mathrm{T}}$ matrices, both of which are unknown. The equilibrium states $\bar{x}$ need to be calculated first, then used in conjunction with the chosen $\bar{\sigma}$ to obtain $\bar{y}$. Conventionally, this would be achieved using Newton-Raphson-like numerical methods, but the highly coupled system requires the use of alternative methods to distinguish the meaningful equilibrium points [60]. Since there are a total of six unknowns in $\bar{x}$ & $\bar{u}$ with only four equations describing the system, two of the unknown parameters must be set, α and β are chosen here. We then define the trimming vector $\bar{\rho}(x, \sigma)$, again with each parameter assigned some operational value which defines the trimming envelope $\Gamma_\rho \subset \mathbb{R}^8$. Equation 3.29 can then be solved for the remaining unknowns, $\bar{q}, \bar{r}, \bar{\delta}_m, \bar{\delta}_n$ which will result in the state trim map X and input trim map U fulfilling the conditions

$$\left.\begin{aligned} X(\bar{\rho}) &= \bar{x} \\ U(\bar{\rho}) &= \bar{u} \\ \therefore f_x(X(\bar{\rho}), U(\bar{\rho}), \bar{\sigma}(t)) &\triangleq 0 \end{aligned}\right\} \qquad \forall \; (\rho \in \; \Gamma_\rho) \tag{3.30}$$

A map for the measured outputs Y can then be computed by substituting X and U into

equation 3.27

$$\left.\begin{aligned} Y(\bar{\rho}) &= f_y(X(\bar{\rho}), U(\bar{\rho}), \sigma(t)) \\ Y(\bar{\rho}) &= \bar{y} \end{aligned}\right\} \quad \forall\ (\rho \in \Gamma_\rho) \tag{3.31}$$

Table 3.2 surmises the equilibrium matrices and vectors used in the trimming process. The

Matrix	Expression
Equilibrium system states	$\bar{x} = [\bar{\alpha}, \bar{q}, \bar{\beta}, \bar{r}]^{\mathrm{T}}$
Chosen parameters	$\bar{\sigma} = [\bar{V}, \bar{p}_F, \bar{p}_A, \bar{h}, \bar{\phi}_F, \bar{\theta}]^{\mathrm{T}}$
Trimming vector	$\bar{\rho} = [\alpha, \beta, \sigma]^{\mathrm{T}} = [\alpha, \beta, \bar{V}, \bar{p}_F, \bar{p}_A, \bar{h}, \bar{\phi}_F, \bar{\theta}]^{\mathrm{T}}$
Controls (actual)	$\bar{u} = [\bar{\delta}_m, \bar{\delta}_n]^{\mathrm{T}}$

TABLE 3.2 Choice of state-space matrices and maps for manifold mapping

objective of the trimming algorithm in general is to compute the control input (δ_n, δ_m) required to maintain equilibrium for a given trim vector $\rho(x, \sigma) = [\alpha, \beta, V, p_F, p_A, h, \phi_F, \theta]^{\mathrm{T}}$. At equilibrium, the dynamic rotational and wind axis translational equations (3.13 & 3.26) can be arranged to give 4 simultaneous equations which only have q, r, δ_y and δ_z as unknowns, since we assume a known $\rho(x, \sigma)$. The simultaneous equations are:

$$k_{\alpha 0} = q + k_{\alpha r} r + k_{\alpha \delta_z} \tag{3.32a}$$

$$k_{q0} = k_{qq} q + k_{qr} r + k_{qr^2} r^2 + k_{q\delta_z} \delta_z \tag{3.32b}$$

$$k_{\beta 0} = k_{\beta r} r + k_{\beta \delta_y} \delta_y + k_{\beta \delta_z} \delta_z \tag{3.32c}$$

$$k_{r0} = k_{rq} q + k_{rr} r + k_{rqr} qr + k_{r\delta_y} \delta_y \tag{3.32d}$$

The various terms included above are of the form k_{ij}, where i indicates the dynamic equation they are derived from and j indicates the variable they are the coefficient of. *e.g.* within $\dot{\alpha} = 0$ (equilibrium assumption), after all like terms are grouped then $k_{\alpha r}$ is the coefficient of the r term. These terms are explained fully in appendix A.2. To solve these simultaneous equations, they are first written terms of q and r. Rearranging equations 3.32a-3.32d, we can write

$$\delta_z = \frac{k_{q0} - q - k_{\alpha r} r}{k_{\alpha \delta_z}} \tag{3.33}$$

which can then be substituted into 3.32c to give an expression for δ_y:

$$\delta_y = \frac{k_{\beta\delta_z} q + (k_{\alpha r} k_{\beta\delta_z} - k_{\alpha\delta_z} k_{\beta r}) r + (k_{\alpha\delta_z} k_{\beta 0} - k_{\alpha 0} k_{\beta\delta_z})}{k_{\alpha\delta_z} k_{\beta\delta_y}} \tag{3.34}$$

Substituting these expressions for δ_y and δ_z into equations 3.32b and 3.32d produces

$$k'_{q0} = k'_{qq} q + k'_{qr} r + k'_{qr^2} r^2 \tag{3.35a}$$

$$k'_{r0} = k'_{rq} q + k'_{rr} r + k'_{rqr} qr \tag{3.35b}$$

The k' terms follow the same convention as the non-prime k's, they are also shown in full in A.2. Solving equation 3.35b for q yields

$$q = \frac{k'_{r0} - k'_{rr} r}{k'_{rq} + k'_{rqr} r} \tag{3.36}$$

This is substituted back into equation 3.35a yields a cubic equation in r:

$$C_3 r^3 + C_2 r^2 + C_1 r + C_0 = 0 \tag{3.37}$$

where C_i represents the coefficient of the term with r^i. These are functions of the k' terms, and are as follows:

$$C_3 = k'_{qr^2} k'_{rqr} \tag{3.38a}$$

$$C_2 = k'_{qr} k'_{rqr} + k'_{qr^2} k'_{rq} \tag{3.38b}$$

$$C_1 = -k'_{rr} k'_{qq} + k'_{qr} k'_{rq} - k'_{q0} k'_{rqr} \tag{3.38c}$$

$$C_0 = k'_{qq} k'_{r0} - k'_{q0} k'_{rq} \tag{3.38d}$$

Thus, we now have a singular cubic equation with the only unknown variable being r. This can be solved by a computer, which will only consider the real solution. This value for r can be substituted into equation 3.36 to obtain a value for q. These values are then used to obtain δ_y and δ_z from equations 3.34 and 3.34 respectively. Finally, δ_n and δ_m can be

obtained by using the inverse rotation matrix

$$\begin{bmatrix} \delta_m \\ \delta_n \end{bmatrix} = \begin{bmatrix} \cos(\phi_F) & \sin(\phi_F) \\ -\sin(\phi_F) & \cos(\phi_F) \end{bmatrix} \begin{bmatrix} \delta_z \\ \delta_y \end{bmatrix} \tag{3.39}$$

3.1.5 Quasi-LPV modelling of the non-linear system

State-space representation of the differential equations of motion is a powerful technique, but the equations are still non-linear. Linearisation is a powerful systematic process in which the state-space system is re-expressed in a specifc model form, each with their own parametric dependencies. Figure 3.1.4 shows some examples using the notation from table 3.1, namely Linear Parameter Varying (LPV), Linear Time Invariant (LTI) and Linear Time Varying (LTV) models. A quasi-LPV (q-LPV) methodology is chosen here due to its robustness and prevalence in the field of guided projectile control [57, 60].

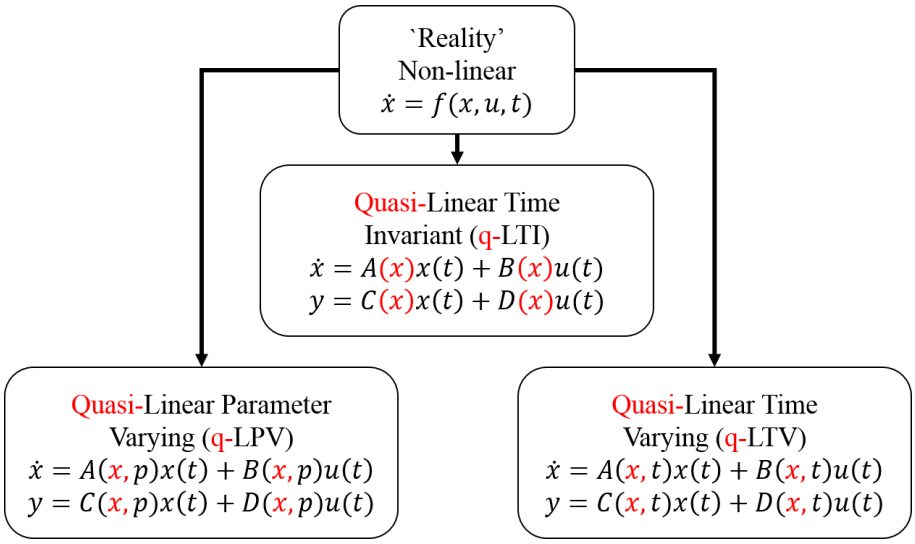

FIGURE 3.1.4 Partial classification of state-space forms (adapted from [187])

These LPV, LTI or LTV models can be good approximations of the non-linear system, under rigorously justified assumptions, when evaluated in proximity to the equilibrium manifold [187]. During the manifold computation the trimming vector $\rho(x,\sigma)$ was used, which has a dependency on both system parameters and states, thus the resulting linear model $\mathscr{S}(\rho)$ is of the q-LPV variety. If the state-space model $\mathscr{S}(\rho)$ exists for all $\rho \in \Gamma_\rho$ given the trim maps $Y(\rho)$, $X(\rho)$ and $U(\rho)$, then there exists a family of q-LPV models $\mathscr{S}(\bar{\rho})$ where the values of ρ are fixed close to the equilibrium manifold. The non-linear

parameter-dependent model written in equation 3.27 can now be fully re-written as a q-LPV model

$$\mathscr{S}(\rho): \begin{bmatrix} \dot{x}_\delta(t) \\ y_\delta(t) \end{bmatrix} = \begin{bmatrix} A(\rho) & B(\rho) \\ C(\rho) & D(\rho) \end{bmatrix} \begin{bmatrix} x_\delta(t) \\ u_\delta(t) \end{bmatrix} \Bigg\}, \qquad \forall\, (\rho \in \Gamma_\rho),\ t \in \mathbb{R}^+ \tag{3.40}$$

Or rather,

$$\dot{x}_\delta(t) = A(\rho)x_\delta(t) + B(\rho)u_\delta(t) \tag{3.41a}$$

$$y_\delta(t) = C(\rho)x_\delta(t) + D(\rho)u_\delta(t) \tag{3.41b}$$

With the state deviation $x_\delta(t) = x - x(\rho)$, input deviation $u_\delta(t) = u - u(\rho)$ and output deviation $y_\delta(t) = y - y(\rho)$; these are known as the deviation variables. The state-space matrices $A(\rho)$, $B(\rho)$, $C(\rho)$ and $D(\rho)$ are obtained from a Jacobian linearisation (Appendix A.3) of ($\dot{\alpha}$, $\dot{q}$, $\dot{\beta}$, $\dot{r}$, a_y^S, a_z^S) in terms of states (α, q, β, r) and virtual control inputs (δ_z, δ_y). The parameters $\dot{q}$ & $\dot{r}$, $\dot{\alpha}$ & $\dot{\beta}$ and a_y^S & a_z^S are given by the airframe dynamics equations in 3.13, 3.26 and 3.22 respectively. They are written in full as

$$\begin{aligned} \dot{\alpha} = {} & q + r\tan(\beta)\Big(\cos(\alpha)\tan(\theta) - \sin(\alpha)\Big) + \frac{1}{mV}\left[\frac{\sin(\alpha)}{\cos(\beta)}\Big(\bar{q}SC_{A0} + mg\sin(\theta)\Big)\right. \\ & \left. - \frac{\cos(\alpha)}{\cos(\beta)}\left(\bar{q}S\Big(C_{N0} + \frac{p_A d}{V}C_{Np} + C_{N\delta}\delta_z\Big) - mg\cos(\theta)\right)\right] \end{aligned} \tag{3.42a}$$

$$\dot{q} = \left(\frac{I_{xx,a}}{I_{yy}}\right)p_A r - r^2\tan(\theta) + \frac{1}{I_{yy}}\left[\bar{q}Sd\left(C_{m0} + \frac{d}{V}C_{mq}q + \frac{p_A d}{V}C_{mp} + C_{m\delta}\delta_z\right)\right] \tag{3.42b}$$

$$\begin{aligned} \dot{\beta} = {} & -r\Big(\sin(\alpha)\tan(\theta) + \cos(\alpha)\Big) + \frac{1}{mV}\left[\cos(\alpha)\sin(\beta)\Big(\bar{q}SC_{xBody} + mg\sin(\theta)\Big)\right. \\ & + \cos(\beta)\Big(\bar{q}S(C_{Y0} + \frac{p_A d}{V}C_{Yp} + C_{N\delta}\delta_y)\Big) \\ & \left. + \sin(\alpha)\sin(\beta)\Big(\bar{q}S\Big(C_{N0} + \frac{p_A d}{V}C_{Np} + C_{N\delta}\delta_z\Big) - mg\cos(\theta)\Big)\right] \end{aligned} \tag{3.42c}$$

$$\dot{r} = \left(\frac{I_{xx,y}}{I_{yy}}\right)p_A q + qr\tan(\theta) + \frac{1}{I_{yy}}\left[\bar{q}Sd\left(C_{n0} + \frac{d}{V}C_{nr}r + \frac{p_A d}{V}C_{np} + C_{n\delta}\delta_y\right)\right] \tag{3.42d}$$

$$
\begin{aligned}
a_z^S = & -\sin(\phi_F)\left(\frac{\bar{q}S}{mg}\left(C_{Y0}+\frac{p_A d}{V}C_{Yp}+C_{Y\delta}\delta_y\right)+\frac{x_s}{g}(p_F q+\dot{r})\right) \\
& -\cos(\phi_F)\left(\frac{\bar{q}S}{mg}\left(-C_{N0}-\frac{p_A d}{V}C_{Np}-C_{N\delta}\delta_z\right)+\frac{x_s}{g}(p_F r+\dot{q})\right)
\end{aligned} \tag{3.42e}
$$

$$
\begin{aligned}
a_y^S = & -\cos(\phi_F)\left(\frac{\bar{q}S}{mg}\left(C_{Y0}+\frac{p_A d}{V}C_{Yp}+C_{Y\delta}\delta_y\right)+\frac{x_s}{g}(p_F q+\dot{r})\right) \\
& -\sin(\phi_F)\left(\frac{\bar{q}S}{mg}\left(-C_{N0}-\frac{p_A d}{V}C_{Np}-C_{N\delta}\delta_z\right)+\frac{x_s}{g}(p_F r+\dot{q})\right)
\end{aligned} \tag{3.42f}
$$

Where the right hand side of equations 3.42 are the Jacobian functions $f_J = [f_\alpha,\, f_q,\, f_\beta,\, f_r,\, f_{a_z},\, f_{a_y}]^{\mathrm{T}}$. The only variables in these equations are the states (α, q, β, r) and virtual control inputs (δ_z, δ_y), since the value of the parameter matrix $\sigma = [V, p_F, p_A, h, \phi_F, \theta]^{\mathrm{T}}$ was fixed and the values $\bar{q}$, S, m, x_s, g, $I_{ij,k}$ and C_{aero} are assumed to be all known, computable or at least an estimate can be made. In the linearisation process, the state-space matrices of equations 3.41a are calculated using the matrix of partial derivatives for the full system, where the summing iterator k_i include both the states (α, q, β, r)=(k_1, k_2, k_3, k_4) and controls (δ_z, δ_y)=(k_5, k_6).

$$
\sum_{i=1}^{6}\frac{\partial f}{\partial k_i} = \left[\begin{array}{cc}
\begin{bmatrix} f_{\alpha,\alpha} & f_{\alpha,q} & f_{\alpha,\beta} & f_{\alpha,r} \\ f_{q,\alpha} & f_{q,q} & f_{q,\beta} & f_{q,r} \\ f_{\beta,\alpha} & f_{\beta,q} & f_{\beta,\beta} & f_{\beta,r} \\ f_{r,\alpha} & f_{r,q} & f_{r,\beta} & f_{r,r} \end{bmatrix} & \begin{bmatrix} f_{\alpha,\delta_z} & f_{\alpha,\delta_y} \\ f_{q,\delta_z} & f_{q,\delta_y} \\ f_{\beta,\delta_z} & f_{\beta,\delta_y} \\ f_{r,\delta_z} & f_{r,\delta_y} \end{bmatrix} \\
\begin{bmatrix} f_{a_z,\alpha} & f_{a_z,q} & f_{a_z,\beta} & f_{a_z,r} \\ f_{a_y,\alpha} & f_{a_y,q} & f_{a_y,\beta} & f_{a_y,r} \end{bmatrix} & \begin{bmatrix} f_{a_z,\delta_z} & 0 \\ 0 & f_{a_y,\delta_y} \end{bmatrix}
\end{array}\right] = \begin{bmatrix} A'(\rho) & B'(\rho) \\ C'(\rho) & D'(\rho) \end{bmatrix} \tag{3.43}
$$

where $f_{i,P} = \frac{\partial f_i}{\partial P}$. Note by construction, $f_{a_z,\delta_y} = f_{a_y,\delta_z} = 0$. The full list of matrix terms are computed in appendix A.3; the derivative of coefficient x with respect to y is left in the form $C_{x,y}$. Since the linearisation was computed using virtual controls (δ_y, δ_z), the rotation matrix from equation 3.19 is used to obtain the actual control inputs (δ_n, δ_m). This leads to the matrices below which are actually used in equation 3.40, $\bar{R}(\phi_F)$ is the conjugate of the transformation matrix $R(\phi_F)$.

$$A(\rho) = A'(\rho) \tag{3.44a}$$

$$B(\rho) = B'(\rho)R(\phi_F) \tag{3.44b}$$

$$C(\rho) = \bar{R}(\phi_F)C'(\rho) \tag{3.44c}$$

$$D(\rho) = \bar{R}(\phi_F)D'(\rho)R(\phi_F) \tag{3.44d}$$

Further inspection of the stability matrix $A(\rho)$ better shows the coupling of pitch-yaw dynamics. Firstly, $A(\rho)$ is split into four regular 2×2 matrices, given by

$$A(\rho) = \begin{bmatrix} A_{NN}(\rho) & A_{NL}(\rho) \\ A_{LN}(\rho) & A_{LL}(\rho) \end{bmatrix} \tag{3.45}$$

The diagonal submatrix $A_{NN}(\rho)$ represents the influence of the normal axis states on the normal axis dynamics, $A_{LL}(\rho)$ represents the influence of the lateral axis states on the lateral axis dynamics. The off-diagonal $A_{NL}(\rho)$ represents the influence of the lateral axis states on the normal axis dynamics, $A_{LN}(\rho)$ represents the influence of the normal axis states on the lateral axis dynamics. For clarity, the normal and lateral states are α, q and β, r respectively. For clarity, the normal and lateral dynamics are $\dot{\alpha}$, $\dot{q}$ and $\dot{\beta}$, $\dot{r}$ respectively.

3.2 Validating 7-DoF dynamic model

The equations of motion above were expressed in state-space representation, linearised, and expressed in wind axis coordinates (V, α, β). The resulting EOM (eq. 3.42) are now implemented into a MATLAB/Simulink environment. The Simulink environment has been changed to use absolute tolerances for the solver error, to stop precision drift with a varying state value. Since the simulations are not real-time, a Simulink environment can be used opposed to Matlab, to utilise the more user friendly interfaces.

This 7-DoF dynamic model is capable of capturing all forces and moments along and about the three principle projectile axis: normal, lateral and longitudinal. Each particular aerodynamic interaction that causes a force or moment is characterised in magnitude by its associated aerodynamic coefficient. As was shown in figure 3.1.3, individual aerodynamic

effects acting along the same direction are amalgamated into the total aero coefficients, C_A, C_Y, and C_N, normalising the individual coefficients with static pressure as needed. Either individual or summated coefficients can be used in the simulations, but knowing the individual coefficients is preferable since it will allow behaviour to be more accurately modelled over a wider trajectory envelope. The accuracy of the dynamic models is thus entirely dependent on the accuracy of these aerodynamic coefficients. If any are missing, the contribution of the force they represent would be entirely absent or based on speculation and educated predictions.

Aside from possessing true coefficients, the model must be also be shown to be performing correctly. To this aim, coefficients published in articles or sources can be used in the present MATLAB environment, along with the respective projectile parameters and initial conditions to produce trajectories. If these trajectories are in good agreement with those presented by the source from which they were obtained, then it is a positive indicator that the dynamic model and system is working as expected, or at least similarly to the comparisons. The viable trajectories which can be used to validate the model are few in number, since aerodynamic coefficients are difficult to obtain, many authors and companies are reluctant to publish them. In addition, even if more information is known *a posteriori* about the coefficients than was available to the authors at the time their simulations were conducted, this new information obviously cannot be used in the validation experiment, else it would be an unfair comparison.

This section will use suitable works identified in the literature review which present aerodynamic coefficients, projectile data, simulation parameters and trajectory data. It will use that data in the present dynamic model and compare the resulting trajectories against the material in whichever format it was presented, to ensure a fair comparison. It is nonsensical to quantitatively compare the trajectory similarities if the results are in different formats, such as only range data or angles of attack. Precisely what these results are is of no relevance provided they are derived from the data output of the dynamic model and can be faithfully replicated and compared; *i.e.* the results could be spatial path plots, velocity profiles, angle of attack data or modal yawing analysis *etc*. The validation runs may use any projectile, provided the accompanying data is included in the manuscript or an exact model is given for which the information can be readily obtained. Due to the

relative novelty of dual-spin projectiles there currently exists no relevant literature looking at dual-spin projectiles, as a result the 7-DoF model will be simplified to 6-DoF. Where coefficients are omitted, they are set to 0 so there is no contribution from the respective force or moment that particular coefficients represents.

In cases where numerical data was unavailable and only graphical results were presented, the numerical data is extracted from the figure using a custom MATLAB script. The script determines a datum value based on its geometric location with respect to the axis. More data points are shown where the figure uses plain lines instead of line markers, as the algorithm samples more of the line to increase reliability of the method. All associated errors in this transcription process are shown in the relevant figures.

BAE range data

In this section, velocity data is intentionally redacted from the figures. Figure 3.2.1 shows the velocity profile of four different models of 7.62x51mm NATO bullets: Ball, tracer, HP and EP. The tracer and ball rounds both weight 9.3g, the HP weighs 10g and the EP weighs 8.8g. Multiple rounds were fired for each of the different models. Each of the bullets were fired at the same operating muzzle velocity from the same mounted barrels and were measured by a radar chronograph. There is minimal discrepancy in the firings of the different models, aside from the divergences which are present for ranges above 600m, where instability leads to varying drag forces. EP rounds have a noticeably larger range of velocities between bullets. The rate of deceleration between rounds is very similar, indicating there was unlikely to be significant perturbation differences. There is a noticeable difference in muzzle velocity in the EP rounds which, in combination of the consistent decelerations, indicate that the muzzle velocity discrepancy is the cause of the variations observed.

Figure 3.2.2 shows the average velocity profile for each of the four bullet models compared on the same axis. Of particular note is the significantly high loss of velocity of the tracer rounds. Tracer rounds are significantly longer than conventional ammunition so that incandescent material can be packed into the aft section. The burning of material in the base actually leads to a lower base drag. This is visible in the fig whereby the tracer rounds maintain a higher velocity than the other rounds at larger ranges.

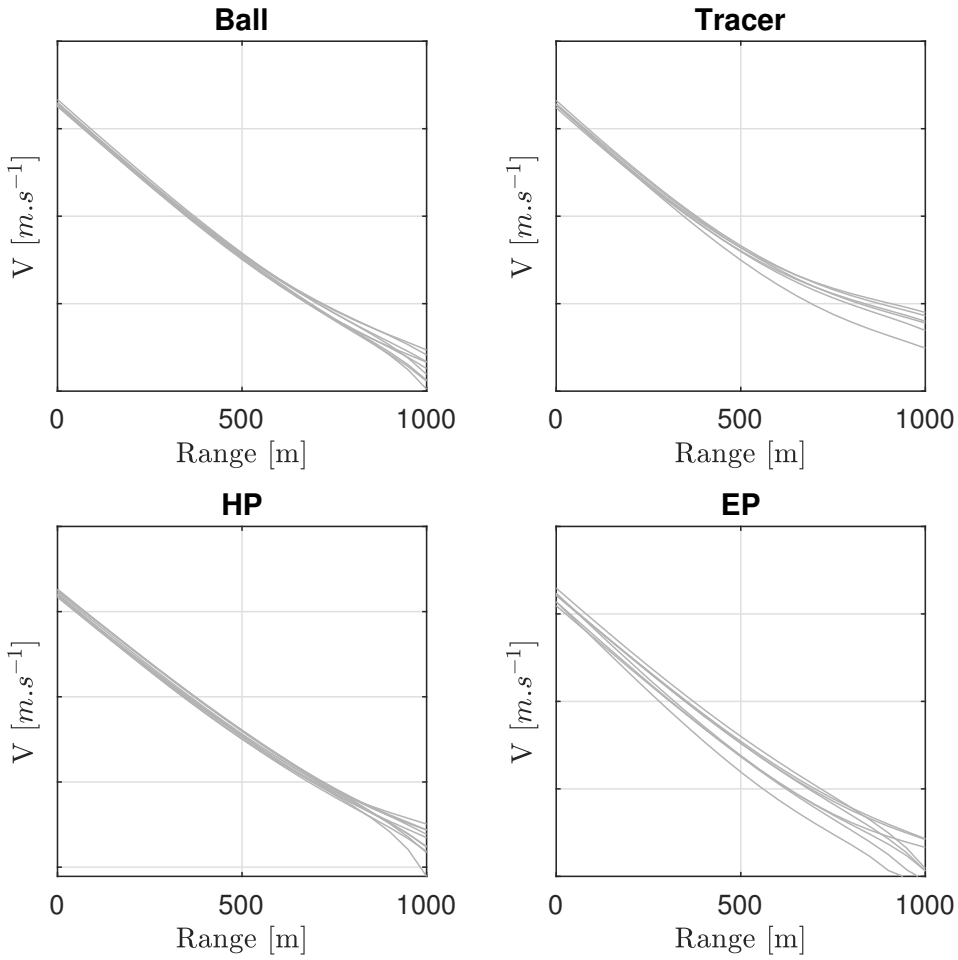

FIGURE 3.2.1 Individual firings of various 7.62x51mm bullets

Figure A.1.2 shows the drag coefficient for a 7.62x51mm NATO ball bullet measured by radar from a firing range (from BAE). This provides a variable drag coefficient as a function of bullet velocity, however there is no consideration of the variable angle of attack and as such, the dynamic model is effectively operating under a flat fire assumption. Figure 3.2.3 shows the results of the dynamic model, overlaid onto the individual radar measurements. The trajectory from the dynamic model is in good agreement with all the individual firings from the range. Up to a trajectory range of around 600m, all the instances lay very closely to the same velocities. Past 600m, variations in the angle of attack cause an increase in the drag force on the bullets at different rates. The dynamic model trajectory also varies in the same way, but remains within the stochastic variations seen from the individual range firings.

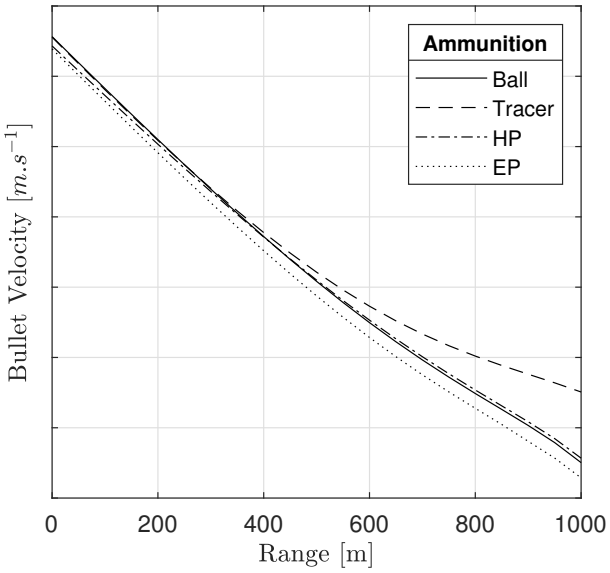

FIGURE 3.2.2 Average velocity profiles of different ammunitions

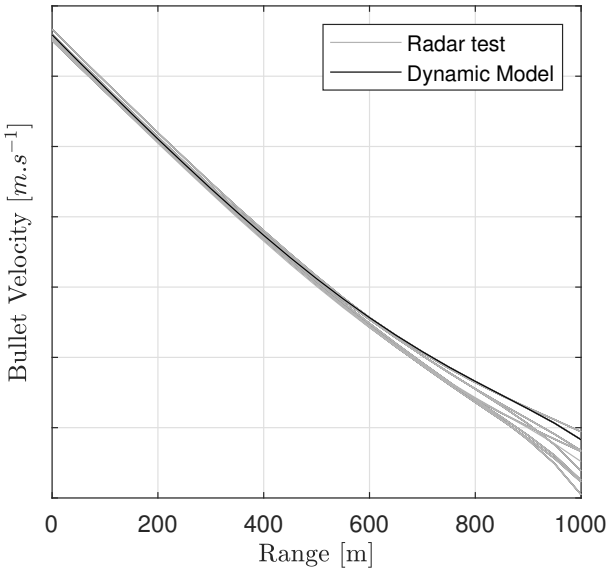

FIGURE 3.2.3 Velocity profile for dynamic Model against radar measurements for 7.62x51mm NATO ball ammunition

Range and Endgame Performance Assessment of a Smart Projectile Using Hingeless Flight Control (Patel *et al.*)

Patel *et al.* have investigated the trajectory predictions from simulation for a novel 105mm smart projectile which uses miniature deployable spoilers [32]. The investigated coefficients were then combined axial drag C_A, pitching moment C_m and yawing moment C_n.

These coefficients were measured in a wind tunnel using a physical prototype of the projectile, measured over a Mach range of 0.1, 0.56, 0.61, 0.76, 0.9, 0.95, 1.05, 1.15, 2.4, and 3.0. These empirical coefficients have been supplemented with computations from DATCOM. Selected from the paper is the trajectory (fig. 3.2.4A) and velocity profile (fig. 3.2.4B) for the novel projectile in uncontrolled ballistic flight. Muzzle velocity of 600m.s^{-1} and 30° elevation. The results of the dynamic model are in good agreement with predictions from the paper, with all points lying within the margin of error of the data. This is to be expected since the trajectory shown is only two dimensions, which is predominantly governed by the drag data, with coefficients determining spin damping *etc.* having little effect. The path predicted by the dynamic model has a slightly longer range than that from the authors, but the velocity profile is in complete agreement. In addition to this, the angle of attack has no effect on the coefficients being used, so there is little deviation.

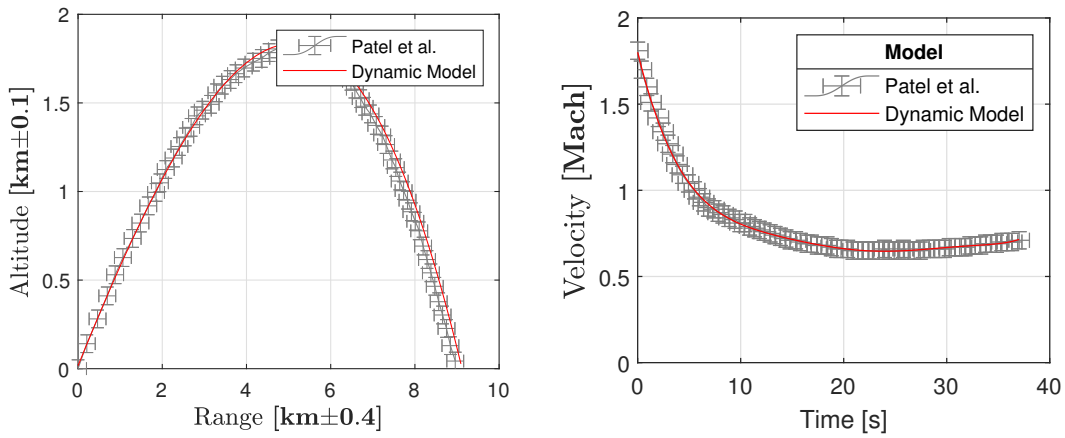

(A) Trajectory estimation (B) Velocity profile

FIGURE 3.2.4 Dynamic model predictions against results by Patel *et al.* [32] for unguided novel 105mm projectile

Dispersion Analysis for Spinning Artillery Projectile (Khalil *et al.*)

Khalil *et al.* conducted a parametric investigation to understand how projectile parameters affect the terminal impact error [95]. The simulations were varied form an initial launch angle of $\theta = 44°$ and a muzzle velocity of 684.3m.s^{-1}. From here the projectile mass, inertia, velocity, spin rate and elevation/elevation-angle were all varied along a small

given range; *e.g.* $\theta = 44 \pm 0.4°$. The simulations were then run again throughout this range, taking values at regular intervals and evaluating the terminal miss distance. These values were the collated to produce a plot of miss distance against initial launch parameter variation from the norm. In addition to these results, the authors also produced a trajectory and velocity profile plot for the nominal case, which is used to compare against the output of the dynamic model. Figure 3.2.5 shows the results for both the trajectory (fig. 3.2.5A) and velocity profile (fig. 3.2.5B). In both cases, the output of the dynamic model agrees very closely with that of the authors, lying within the error bounds of all extracted data points.

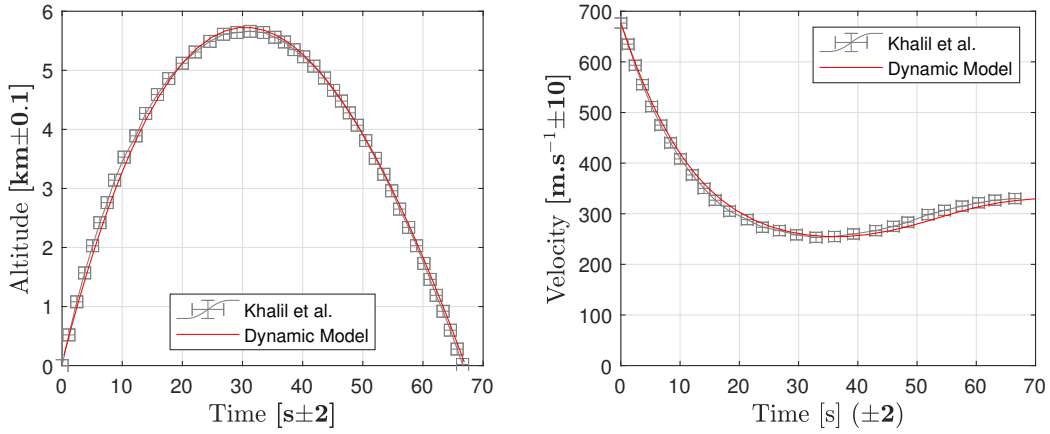

(A) Trajectory estimation (B) Velocity profile

FIGURE 3.2.5 Dynamic model predictions against results by Khalil *et al.* [95] for M107 155mm projectile

Physicomathematical simulation analysis for small bullets (Gkritzapis *et al.*)

Gkritzapis *et al.* have investigated the modelling of ballistic trajectories for a 7.62x51mm NATO bullet [183, 177]. The simulations were run for incident angles of 1°, 7° and 15°, but only 15° is used for the comparison here, with initial velocity of 793m.s^{-1}, as the 15° trajectories have the largest data set and thus will better represent the data. The trajectories and velocity profiles were investigated for both static and dynamic coefficients. The dynamic coefficients were found through a linear interpolation of static coefficients stated in McCoy [93], the average of these is used as the static coefficients.

Figure 3.2.6 shows the comparison of results from the dynamic model. Both simula-

tions are in good agreement with the data from the article. Figure 3.2.6A uses the static coefficients while fig. 3.2.6B uses the dynamic coefficients. The highest discrepancy is shown on fig. 3.2.6B, after 300m.s^{-1} in the transonic region. Data from the article shows a definite heel in the data where the deceleration suddenly changes. This is characteristic of the projectiles slowing across the sonic boundary, where the drag coefficient increases suddenly. The change is present in the dynamic model results, but to a lesser extent than that from the article. However, the dynamic model is within the margin of error across all points in both figures.

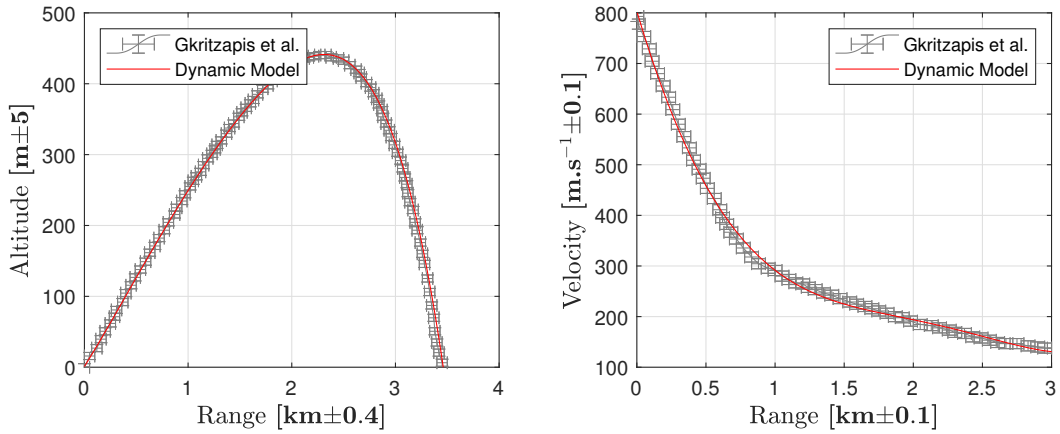

(A) Trajectory estimation (B) Velocity profile

FIGURE 3.2.6 Dynamic model predictions against results by Gkris *et al.* [183] for a 7.62x51mm NATO bullet

Aerodynamic and trajectory characteristics of a typical mortar projectile with a deflectable nose (Ren *et al.*)

Ren *et al.* have investigated the aerodynamic coefficients of a novel 120mm mortar shell with interchangeable nose angles. The investigated coefficients were drag C_D, lift C_L and pitching moment coefficient C_{M_α}. The coefficients were investigated for nose angles of 0°, 3°, 6° and 9°, each investigated at angles of attack ranging from $\alpha \in [-10°, +10°]$ in 0.5° increments and also Mach speeds $V \in [0.3, 0.9]$ in 0.1 increments. A physical prototype of the projectile was built, and the coefficients were measured empirically by means of a wind tunnel. Because of this, the article provides a comparison between both the results of the live experiments and those from a simulation. This means that the results

from the dynamic model presented from this work can be compared against both. The results are shown in fig. 3.2.7 for both the trajectory (fig. 3.2.7A) and velocity profile (fig. 3.2.7B). In both cases, the results of the dynamic model are in good agreement with both the simulation and flight test data from the article. The terminal region of the trajectory in fig. 3.2.7A shows that the simulations for both the dynamic model here and of Ren *et al.* overestimate the range, however both simulations are in good agreement with each other.

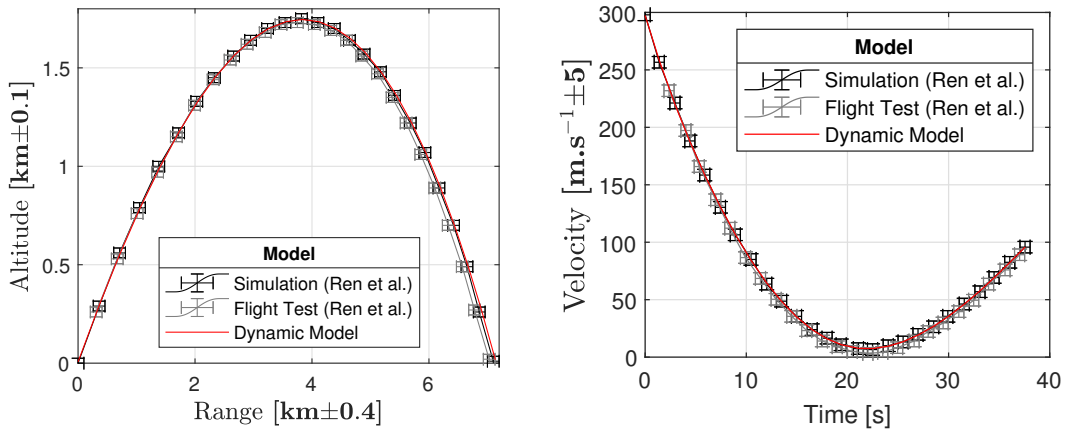

(A) Trajectory estimation (B) Velocity profile

FIGURE 3.2.7 Dynamic model predictions against results by Ren *et al.* [85] for novel 120mm mortar

Conclusions

This section has shown that the dynamic model presented thus far is capable of recreating the results of several academic sources, to the extent of the information provided within them regarding simulation parameters and aerodynamic coefficients. This indicates that the results from the dynamic model represent a true likeness of a realistic scenario, provided the parameters aerodynamic coefficients used in the simulation accurately reflect said scenario.

3.3 Stability factor origins from projectile pitching and yawing motion

In this section, the aerodynamic effectiveness of a projectile is quantified via 'stability'. Before discussing this it is necessary to define the principle axis of inertia. If the rotation of a body can be encoded into a 3x3 matrix $\mathbf{M}_{ij}$ then the set of principal axis are the set of eigenvectors $\vec{\mathbf{v}}_\lambda$ such that $\mathbf{M}_{ij}$ is diagonal ($m_{ij} = 0 \; \forall \; i,j \in \{1,2,3\}, i \neq j$). I.e. the product of all moments of inertia about that axis are zero. Any inertial moment considered in a cylinder about its longitudinal axis ($\hat{x}$) will be perfectly counteracted by a circularly symmetric moment, thus $\hat{x}$ is a principal axis in this instance. Another useful concept is to define is the distance from the CoM to the CoP as X_{CMCP}, with the positive direction taken to be from the aft to the ogive.

3.3.1 Static stability

If the CoP is regarded as the point through which the aerodynamic force acts, then the CoM can be thought of as the fulcrum about which the projectile pivots in response to the force. For non-spinning projectiles, if the CoP is ahead of the CoM ($X_{CMCP} > 0$) then it is statically unstable. A small deviation in airflow will cause projectile yaw, increasing the susceptible moment arm, causing a cascade effect and the projectile will tumble during flight. If the CoP is behind the CoM ($X_{CMCP} < 0$) when a deviation occurs, the forces that act are now aligning, bringing the principal axis back into alignment with $\vec{V}$. This is static stability; when an object disturbed from an equilibrium position experiences a restorative force acting to return the object to the equilibrium position. It can be either linear or rotational static stability, depending on the action of the restorative force. McCoy defines a parameter M as the static stability parameter, but it is relabelled here as S_S to remain consistent with other nomenclature.

$$S_S = \frac{1}{2\vec{I}_y}\rho S D^3 m C_{M_\alpha} \tag{3.46}$$

where $C_{M\alpha}$ is the overturning moment coefficient as a function of angle of attack α, or $C_{M\alpha} \equiv \partial C_M / \partial \alpha$ [188]. A body has 'positive' static stability (i.e. is statically stable) if

$S_S < 0$; $S_S = 0$ and $S_S > 0$ correlate to neutral and negative static stability respectively. Depending on whether the static stability is positive, neutral or negative, the body's alignment after a disturbance will respectively: return to its original position, maintain its new alignment or continue moving in the direction of the disturbance. Apart from $C_{M\alpha}$, all parameters in equation 3.46 are positive, hence to achieve $S_S < 0$ we necessitate that $C_{M\alpha} < 0$; for a non-spin stabilised body this means practically that the CoM is located ahead of the centre of pressure (CoP). To optimise S_S based on the coefficients of $C_{M\alpha}$, a heavy projectile with a large cross section and small transverse moment of inertia is preferable, though this contradicts conventional ballistic design.

3.3.2 Simplified un-spun pitching & yawing motion

The linear equation of motion (EOM) for a statically stable, un-spun and symmetric projectile is given by

$$\vec{I}_y \ddot{\zeta} - M_q \dot{\zeta} - M_\alpha \zeta = 0 \tag{3.47}$$

With complex yaw $\zeta = \alpha + i\beta$. $\vec{I}_j$ is the moment of inertia about axis j, e.g. $\vec{I}_y$ is the transverse moment of inertia. By making the substitutions $\mathscr{J}_\alpha = M_\alpha / v^2$, $\mathscr{J}_q = M_q / v$ and $v = \mathrm{d}s/\mathrm{d}t$ we can write

$$\vec{I}_y \zeta'' - \mathscr{J}_q \zeta' - \mathscr{J}_\alpha \zeta = 0 \tag{3.48}$$

where ζ' denotes the derivative of ζ with respect to the arc length of projectile trajectory, $\zeta' = \mathrm{d}\zeta/\mathrm{d}s$. The standard solution for second order differential equation of this form is

$$\zeta = k_1 e^{a_1 s} + k_2 e^{a_2 s} + i\sigma \tag{3.49}$$

with k_1, k_2, a_1 & a_2 being generic constants and the $i\sigma$ term being the steady state solution. Figure 3.3.1 shows a graphical representation of this equation and one can see the rudimentary origins of actual flight behaviour. Again, from standard solutions, we can write

$$a_1 + a_2 = \frac{\mathscr{J}_q}{\vec{I}_y} \tag{3.50a}$$

$$a_1 a_2 = -\frac{\mathscr{J}_\alpha}{\vec{I}_y} \tag{3.50b}$$

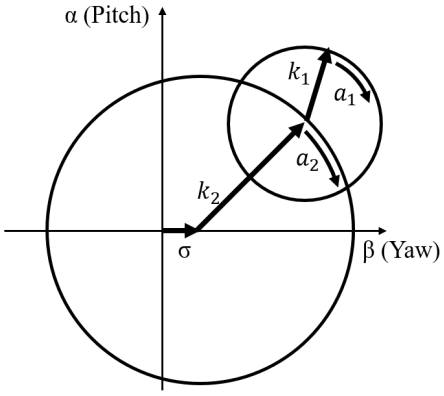

FIGURE 3.3.1 Pictorial representation of equation 3.49, with slow arm subscript 2 and fast arm subscript 1

Let us then 'arbitrarily' redefine the generic constants, $a_k = \lambda_k + i\omega_k$ such that

$$\lambda_1 + \lambda_2 = \frac{\mathscr{J}_q}{\vec{I}_y} \tag{3.51a}$$

$$\lambda_1\lambda_2 - \omega_1\omega_2 = -\frac{\mathscr{J}_q}{2\vec{I}_y} \tag{3.51b}$$

and rotation rate $\omega \approx \sqrt{-\mathscr{J}_\alpha/\vec{I}_y}$. Now we can approximate the complex yaw angle as

$$\zeta \approx \exp\left(\frac{s\mathscr{J}_q}{2\vec{I}_y}\right)([k_1+k_2]cos(\omega_1 s) + i[k_1-k_2]\sin(\omega_2 s)) + i\sigma \tag{3.52}$$

This is a reoccurring mathematical form describing an elliptical, damped oscillatory motion. The exponential term is an envelope function, creating boundaries the oscillations will stay within, while the rest of the equation forms the underlying oscillations. By comparing our values to the known elliptical equation, we see the values ω_1 & ω_2 are the *nutational* and *precessional* rates of the projectile and λ_1 & λ_2 are the associated damping rates (note by definition $\omega_1 > \omega_2$). Henceforth, we shall call the nutation rate $\lambda_1 = \lambda_n$ and the precession rate $\lambda_2 = \lambda_p$. These quantities describe the motion of a *yaw rosette*, see figure 3.3.2. Mathematically, in order for the exponential term to converge as distance s increases and velocity v decreases, the exponent $\mathscr{J}_q/2\vec{I}_y$ must be negative; therefore both λ_n and λ_p must be negative. Note that for a generic damping coefficient the more negative it is the more heavily the system it damps.

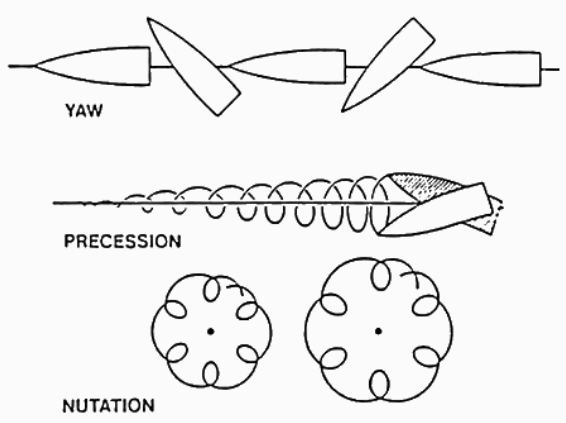

FIGURE 3.3.2 Nutation creating the characteristic 'yaw rosette' [189]

This oscillatory motion while in flight is highly unfavourable as it will lead to a large increase in drag, thus the projectile must be stabilised. There are two main ways to achieve this, fin stabilisation and gyroscopic stabilisation. Rear mounted fins stabilise the projectile by increasing the restorative force when the projectile pitches. However, it is difficult to adorn a SCP with flight hardened fins, which is the motivation behind imparting spin onto bullets. Projectile spin is effective because the resulting moment of a spinning projectile following a disturbance, is always at right angles to both the spin axis and the disturbance force; the resulting precession helps mitigate the effects of the disturbance force. Too little spin and the projectile will insufficient gyroscopic inertia to resist the disturbance force and the precession will be too large. In bullets, a spin rate which is too low is audible as a loud whirring noise [189]. Too much spin and the gyroscopic inertia will resist the aligning aerodynamic forces creating too large an angle of attack; this is known as *superstability*. Both of these states are illustrated in figure 3.3.3.

As reference, a 5.56x45mm NATO cartridge weighs 4g and has a muzzle velocity of 960 ± 11m/s from a 31cal./rev, 508mm match grade barrel. A spin rate of 86,400 rpm is necessary to stabilize this bullet, though this is in the upper range of spin stabilisation rates. There are two notable instances of amplified instability. Spin-yaw resonance occurs when the spin rate approaches the yaw rate, the projectile may begin to undergo a large amplitude yawing motion called 'lunar' yawing. The other is catastrophic yaw, where a large yawing motion is amplified by non-linear Magnus effects creating further dynamic instability which leads to a cascade effect.

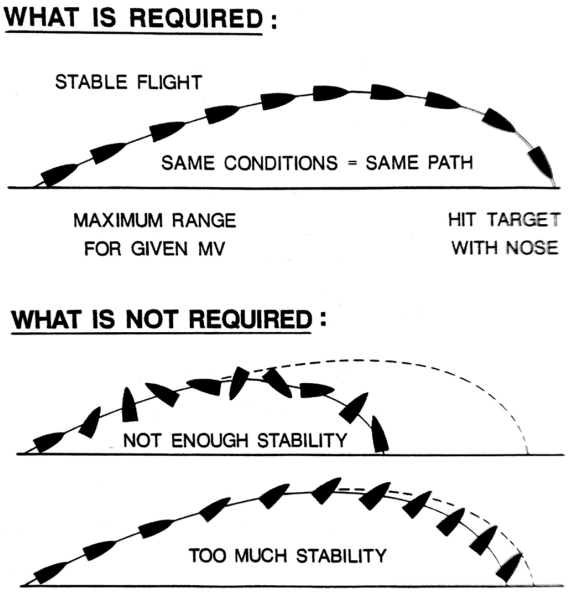

FIGURE 3.3.3 Ideal effects of imparting spin [189]

3.3.3 Complete linearised pitching & yawing

We can use this same procedure to determine the effects of variable spin stabilisation and variable velocity due to drag and gravity; this is called the 'Complete linearised Pitching & Yawing motion of projectiles'. The following assumptions are made:

1. The projectile is a rigid, Newtonian symmetric body. Small asymmetries can be accounted for but are usually negligible [94]

2. Small yaw angles, $\sin(\alpha) \approx 1$ and $\cos(\alpha) \approx \alpha$. This model is void for large yaw or buff nosed projectiles (hollow points)

3. Medium & projectile densities as well as mass are constant

All vectors are in the fixed plane basis unless explicitly stated. The derivation, following ref. [94], is largely the same as before; first we write the EOM in terms of the complex yaw ζ as

$$\zeta'' + (H - iP)\zeta' - (M + iPT)\zeta = -iPG \tag{3.53}$$

The substitution parameters are given by

$$H = C^*_{L_\alpha} - C^*_D - k_y^{-2}(C_{M_q} + C_{M_{\dot{\alpha}}})^* + \frac{k_x^{-2}}{2} C^*_{L_p} - \left(\frac{8mg\sin(\theta_T)}{\pi\rho d^2 V^2}\right) \tag{3.54}$$

$$P = \left(\frac{|\vec{I}_x|}{|\vec{I}_y|}\right)\frac{|\vec{p}|d}{V} \tag{3.55}$$

$$M = k_y^{-2} C^*_{M_\alpha} \tag{3.56}$$

$$T = C^*_{L_\alpha} + k_x^{-2} C^*_{M_{P\alpha}} \tag{3.57}$$

$$k_j^{-2} = \frac{md^2}{|\vec{I}_j|} \tag{3.58}$$

$$G = \frac{gd\cos\theta_T}{V^2} \tag{3.59}$$

$$()^* = () \cdot \frac{\rho SD}{2m} \tag{3.60}$$

g is the gravitational constant. H is sometimes modified further in different texts [93][94] to account for spin damping and velocity variation with gravity & drag, where g is the acceleration due to gravity and θ_T is the trajectory angle subtended by $\vec{V}\cdot\vec{x}$. Note equation 3.56 is the same as the previously defined equation 3.46, with the new notation. Secondly, the solutions to this equation can be written in the form

$$\zeta = \left[A_0\, e^{\lambda_n s}\right] e^{i(\omega_{n0}+\omega'_n s)} + \left[B_0\, e^{\lambda_p s}\right] e^{i(\omega_{p0}+\omega'_p s)} + \zeta_R \tag{3.61}$$

with new generic constants A_0 & B_0 and steady state solution

$$\zeta_R = \frac{iPG}{M + iPT} \tag{3.62}$$

From this we can write the complex rotation rates $\omega_{n/p}$ and the complex damping terms $\lambda_{n/p}$ as

$$\omega_{n/p} = \frac{1}{2}\left[P \pm \sqrt{P^2 - 4M}\right] \tag{3.63a}$$

$$\lambda_{n/p} = -\frac{1}{2}\left[H \pm \frac{P(2T-H)}{\sqrt{P^2-4M}}\right] \tag{3.63b}$$

In order for this mathematical framework to predict a stable flight of real and damped oscillations, we necessitate that the

1. Rotation rates $\omega_{n/p}$ must be real

2. Damping exponents $\lambda_{n/p}$ must be real and negative

Thus from equations 3.63a & 3.63b we have

$$\frac{P^2}{4M} \geq 1 \tag{3.64}$$

and

$$\frac{2T}{H} < \left(1 - \frac{4M}{P^2}\right)^2 + 1 \tag{3.65}$$

3.3.4 Ballistic stability and the gyroscopic & dynamic stability factors

From inequalities 3.64 and 3.65 we can define, for a single spin projectile with no control surfaces (SSNC), the gyroscopic and dynamic stability factors

$$S_g(\text{SSNC}) = \frac{P^2}{4M} \tag{3.66a}$$

$$S_d(\text{SSNC}) = \frac{2T}{H} \tag{3.66b}$$

Future iterations of the stability factors are written in this compact form and all substitution parameters are shown in Appendix A. The mathematical condition for gyroscopic stability is

$$S_g \geq 1 \tag{3.67}$$

though it has been shown that the ballistic coefficient of a bullet is adversely affected from tumbling as S_g is lowered past a threshold of 1.3 [190]. The ratio p/V decreases along the trajectory of an uncontrolled projectile (assuming flat-fire), and so it is apparent that since $P \propto p/V$, S_g will decrease down range. A projectile is dynamically stable if

$$S_g > \frac{1}{S_d(2 - S_d)} \tag{3.68}$$

If we substitute 3.66a into 3.67, we can define the axial spin limit S_{lim} to be

$$S_{\text{lim}} = \frac{2\rho S D^3 C_{M_\alpha}}{S_d(2 - S_d)} \tag{3.69}$$

which shows the critical spin value for which inequality 3.68 is no longer satisfied. Figure 3.3.4 shows a plot of the corresponding *equality* of 3.68, with a label indicating where the *inequality* is fulfilled.

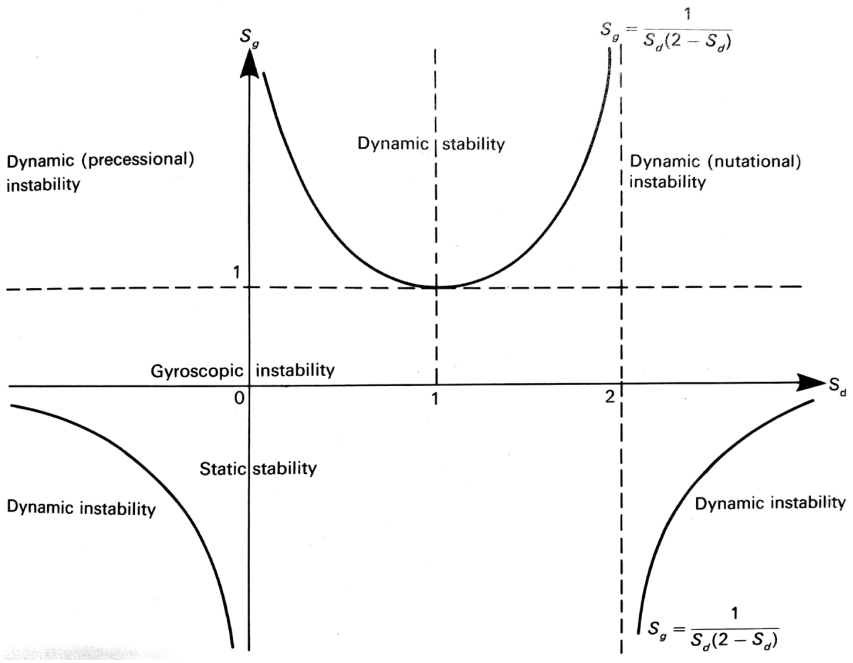

FIGURE 3.3.4 Stability regimes [94]

Dynamic stability is concerned with the oscillations induced in a moving body after a disturbance is applied and as with static stability, it can be positive, neutral or negative. With positive dynamic stability the oscillations eventually damp towards the original alignment, neutral dynamic stability causes oscillations to reside indefinitely with constant amplitude, while negative dynamic stability has oscillations which amplify chaotically. When $S_d = 1$ the body has positive dynamic stability or is perfectly dynamically stable. If $S_d < 1$ the precession is unstable and if $S_d > 1$ the nutation is unstable, both catastrophically so at the asymptotes ($S_d = 0$ or $S_d = 2$ respectively). The transition from positive to neutral to negative dynamic stability for a projectile is dependent on the magnitude of the deviation from $S_d = 1$ The magnitude at which the transitions occur is dependent on the projectile and trajectory parameters, but is not well characterised. Provided $0 < S_d < 2$ in practice, the projectile can be spun sufficiently to ensure ballistic stability. Table 3.3 summarises the ballistic stability which results from occupying different static and dynamic regimes.

Note that the projectile geometry required to maximise aerodynamic efficiency and

Static regime	Dynamic Regime	Ballistic result
Stable, $S_S < 0$	$0 < S_d < 2$	Ballistically stable
	$S_d < 0$ or $0 > S_d$	Ballistically stable if $p < S_{\text{lim}}$
Unstable, $S_S > 0$	$0 < S_d < 2$	Ballistically stable if $p > S_{\text{lim}}$
	$S_d < 0$ or $0 > S_d$	Never ballistically stable

TABLE 3.3 Summary of ballistic stability criteria

terminal effectiveness, almost always results in negative static stability. From table 3.3 we can see that in the unstable static regime, a dynamically stable projectile can still be ballistically stabilised if the spin rate is sufficiently high. Thus, projectile designers can effectively disregard the static stability of a projectile, solely focusing on the relation between S_d and S_g; i.e. it is sufficient, to ensure a prototype projectile lies in the stable region (as central as possible) of figure 3.3.5 for the anticipated flight envelope. Figure

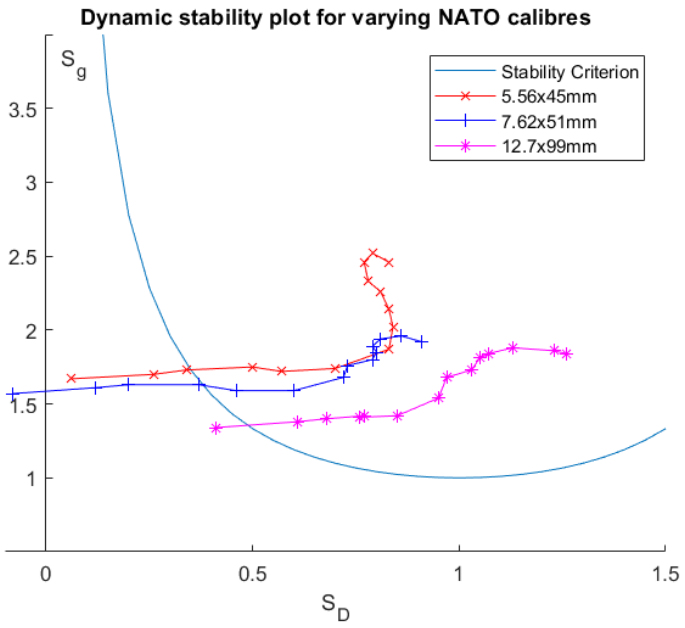

FIGURE 3.3.5 Stability of different calibres for $V = \text{Mach}(1.5 + 0.5m) \mid m \in \{0, 1, ..., 5\}$

3.3.5 shows a dynamic stability plot for three conventional NATO calibres: 5.56x45mm, 7.62x51mm and 12.7x99mm. The bullet geometry is loaded into PRODAS ballistic software and calculated for flat-fire trajectories. Each line represents one calibre, each point on the line represents a pair of stability factors calculated at a given bullet velocity. The velocity range is Mach 1.5 - 4 in increments of 0.5, the lowest speed corresponds to the

lowest/left most point of each line, increasing progressively.

Single-Spin Projectile with passivated Control surfaces (SSC)

A simple method to account for the addition of control surfaces is to introduce an aerodynamic moment generated by the canards, directly into the EOM for the complete linearised system, shown below

$$\zeta'' + (H - iP)\zeta' - (M + iPT)\zeta = -iPG + \mathfrak{m} \tag{3.70}$$

where $\mathfrak{m}$ is given by [58]

$$\mathfrak{m} = \frac{d^2}{I_{yy}}(-i\delta_c e^{i\Phi_N} + \zeta)\frac{\mathrm{d}C_{N\delta}}{\mathrm{d}t} \tag{3.71}$$

$\delta_c = i\delta_z - \delta_y = i\delta_{13} - \delta_{24}$ is the complex deflection of both pairs of canards. Φ_N is the roll angle of the canard adorned forward section. $C_{N\delta}$ is the normal force coefficient for a canard pair. Thus, we can write

$$\zeta'' + (H - iP)\zeta' - (M_c + iPT)\zeta = -i(PG + K) \tag{3.72}$$

and define

$$M_c = M + \frac{d^2}{I_{yy}}\frac{\mathrm{d}C_{N\delta}}{\mathrm{d}t} \tag{3.73}$$

$$K = \frac{d^2}{I_{yy}}\delta_c e^{i\Phi_N}\frac{\mathrm{d}C_{N\delta}}{\mathrm{d}t} \tag{3.74}$$

In this simple case then we see from equations 3.66a & 3.66b that the only affected variable is M. Thus only S_g will change under the implementation of canards, at least in this simple model. The SSC stability factors are given by

$$S_g(SSC) = \frac{P^2}{4M_c} \tag{3.75a}$$

$$S_d(SSC) = S_d(SSNC) \tag{3.75b}$$

It is possible therefore, to alter S_g by adjusting the canard shape to affect the normal force coefficient $C_{N\delta}$.

Dual-Spin projectile with No Control surfaces (DSNC)

A comprehensive paper by Costello *et al.* [185], provides a stability framework for a dual-spin projectile. It takes into account a non-diagonal inertia matrix, considers all rotational moments about the body connection, all with an arbitrarily located centre of mass. Figure 3.3.6 shows an illustration of the dual-spin design, though there is assumed to be no contribution from the canards until §3.3.4. The total projectile of mass m is separated into an aft (rearward) and forward section with respective masses $m_{A/F}$. The distance between the cumulative CoM and a section CoM is $\vec{r}_{(A/F)x}$. $\vec{p}_A$ & $\vec{p}_F$ are the spin vectors of the aft and forward sections respectively. The procedure for deriving the

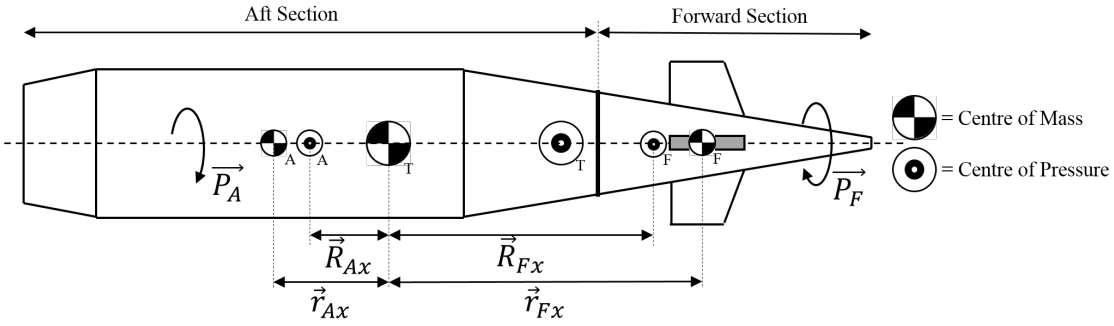

FIGURE 3.3.6 Dual-spin projectile with passivated control surfaces

resulting stability factors is the same as both iterations of single spin: generate the system EOM and solve the inequalities resulting from constraining the standard solutions. The substitution parameters are defined in 3.76a-3.76e.

$$A = C^*_{N\alpha} = \left(C_{N\alpha} + \frac{S_c}{S} C_{N\delta} \right)^* \tag{3.76a}$$

$$T \Rightarrow B = \frac{1}{V} k_y^{T\,-2} \left(\frac{C^F_{NP\alpha} p_F}{2} \left(R m_{fx} + r_{fx} \right) + \frac{C^A_{NP\alpha} p_A}{2} \left(R m_{ax} + r_{ax} \right) \right)^* \tag{3.76b}$$

$$M \Rightarrow C = \frac{1}{V} k_y^{T\,-2} \left(C^F_{N\alpha} \left(R_{fx} + r_{fx} \right) + C^A_{N\alpha} \left(R_{ax} + r_{ax} \right) \right)^* \tag{3.76c}$$

$$H \Rightarrow E = k_y^{T\,-2} \frac{\left(C_{M_q} + C_{M_{\dot{\alpha}}} \right)^*}{2} \tag{3.76d}$$

$$P \Rightarrow F = \frac{d}{V} \frac{\left(I^A_x |\vec{p}_A| + I^F_x |\vec{p}_F| \right)}{I^T_y} \tag{3.76e}$$

$$k_j^{T\,-2} = \frac{m d^2}{|\vec{I}^T_j|} \tag{3.76f}$$

Here, $\vec{R}_{(A/F)x}$ is the vector distance between the aft/forward section CoM and the aft/forward section Magnus CoP, S_c is the reference area of the canards and x_c is the reference length. All other parameters are as previously defined. Using these substitutions parameters and the corresponding EOM, the DSNC stability factors can then be written as

$$S_g(DSNC) = \frac{F^2}{4C} \tag{3.77a}$$

$$S_d(DSNC) = \frac{2((A+C^*_{D0})F+B)}{F((A-2C^*_{D0})-E)} \tag{3.77b}$$

Dual-Spin projectile with passivated Control surfaces (DSC)

Wernert [58] has considered the dual-spin design and the contribution from the canards. The model assumes an ideal centre of mass with only rolling moments about the connection and diagonal inertia matrices. The result is the modification to the following substitution parameters:

$$A \Rightarrow A' = \left(C_{N\alpha} + \frac{S_c}{S}C_{N\delta}\right)^* \tag{3.78a}$$

$$C \Rightarrow C' = k_y^{T-2}\left(C^F_{N\alpha}\left(R_{fx}+r_{fx}\right) + C^A_{N\alpha}\left(R_{ax}+r_{ax}\right) + \frac{S_c x_c}{S}C_{N\delta}\right)^* \tag{3.78b}$$

Using these new stability factors, Wernert writes the DSC stability factors as

$$S_g(DSC) = \frac{F^2}{4C'} \tag{3.79a}$$

$$S_d(DSC) = \frac{2((A'+C^*_{D0})F+B)}{F((A'-2C^*_{D0})-E)} \tag{3.79b}$$

Zhu *et al.* [191] developed this framework further, to account for the effects of gravity and Euler pitch angle (θ_E), as well as coupling between the two; yielding the modified stability factors:

$$S_g(DSC) = \frac{P^2}{4\tilde{M}} \tag{3.80a}$$

$$S_d(DSC) = \frac{2T}{\tilde{H}} \tag{3.80b}$$

The substitution parameters here are given by

$$\tilde{M} = \frac{M}{1-\varepsilon\alpha_e} + \frac{\varepsilon\beta_E PT}{(1-\varepsilon\alpha_e)^2} + \frac{\varepsilon\beta_E PM}{(1-\varepsilon\alpha_e)\tilde{H}} + \frac{(\varepsilon\beta_e PT + \varepsilon\beta_e M)^2 - 2\varepsilon\beta_e PTM}{(2-\varepsilon\alpha_e)\tilde{H}^2} \tag{3.81a}$$

$$\tilde{H} = (1-\varepsilon\alpha_e)(H - 2g_*) \tag{3.81b}$$

$$g_* = \frac{gl\sin(\theta_T)}{V^2} \tag{3.81c}$$

$$\varepsilon = \frac{1}{2}\tan(\theta_E) \tag{3.81d}$$

where α_e and β_e are the trim angles of attack and side-slip respectively.

3.3.5 Summary of projectile stability

Analysing equation 3.77a we can see that S_g^{DS} depends on: the spin vectors $\vec{p}_A$ & $\vec{p}_F$ of the aft and forward sections; the moments of inertia I_{yy}^T and I_{xx}^F; projectile geometry S, D and $C_{M\alpha}$; canard geometry S_c, x_c and $C_{N\delta}$; flight conditions ρ and V. Interestingly canard cant angles $\delta_{y/z}$ and roll angle ϕ have no influence on S_g^{DS}. On the other hand, S_d^{DS} depends on the whole range of aerodynamic coefficients explored. If $I_{xx}^A = 0$, $I_{xx}^F = I_{xx}^T$ and we disregard any input from the canards, then we are modelling the conventional spin stabilised projectile and as expected S_g^{DS} reduces to S_g. Note that by design, $S > 0$, $S_c > 0$ & $d > 0$. From this we can draw several very important implications for the design of a GSCP. If the lifting surfaces are in fact canards ($x_c > 0$) instead of fins ($x_c < 0$) then gyroscopic stability is reduced. If canard size S_c or normal force coefficient $C_{N\delta}$ increases, then gyroscopic stability is reduced. If the forward section has very little spin ($\Delta p \cong \bar{p}$) with a small guidance fuse ($0 < \tilde{I}_{xx} << 1$) then gyroscopic stability is preserved. Additionally, gyroscopic stability can be increased by spinning the forward section faster than the aft ($p_F > p_A$), or by imparting a high spin rate on the forward section opposing the aft section ($p_F < -p_A$). However, both of these modifications increase the difficulty of guidance due to the high forward spin (assuming canards) opposing the rationale behind installing canards.

Chapter 4

Novel Design

THIS chapter will explore the novel actuation mechanism which was shown in the introduction, including a full description of the operating principle and the required subsystems. As was shown in the preceding chapter, a projectile in flight undergoes many different oscillatory and spinning motions. Projectile imperfections cause precession and nutation in addition to imparted spin. Any such projectile motions, or combinations of such, have been shown to interact with the flight medium causing aerodynamic effects, *e.g.* a non-zero angle of attack induces an overturning moment. Such effects, while predominantly detrimental, could be used to intentionally control the projectile; in the same way that some aircraft are made intentionally unstable to allow them to perform acrobatic feats that would be otherwise impossible.

Firstly, a mathematical description is given of how a control force is used to create a controllable variable, which can be expressed either as an acceleration or as a change in velocity. The acceleration of the projectile is shown from first principles and a set of axioms is proclaimed which must be satisfied if the system is to be controlled. Certain simplifications are made to test the fundamental operation of the mechanism. These simplifications are explained in detail and then slowly relaxed, investigating the effect each of them plays on the system response, primarily the rate of switching between the two operating states. A process is then described whereby a designer can model the actuator step response by an arbitrary mathematical function and obtain a conversion between desired control vector and actuator instructions.

For the initial conceptualisation of the problem, it is pertinent to neglect some of

the forces acting on the system, to understand the reasons behind any behaviour that is observed. As complexity is added, system traits can be specifically attributed to certain changes which can be noted as the analysis progresses. Table 4.1 shows a comparison between the idealised parameters which are used during analysis of the idealised system, and values that can be expected for real systems.

Parameter	Projectile system		
	Nominal	105mm	155mm
ω_B [rad.s^{-1}]	$\pi/2$	N/A	N/A
ω_0 [rad.s^{-1}]	2π	1050 [49]	1668 [69]
m [kg]	1	15 [49]	42.798 [72]
F_c [N]	1	$[-35.48, 58.33]$ [49]	20 [69]

TABLE 4.1 Comparison of simulation parameters used against real-world projectiles

4.1 Simulation Design

This section describes how the dynamic model is implemented in Simulink/MATLAB to test and explain the actuation mechanisms and any GLs which may be applied. Figure 4.1.1 shows a block diagram of the Simulink model. ODE4 Runge−Kutta (RK4) was used throughout these simulations, which is widely accepted due to it being an accurate numerical method while not being resource intensive [192]. RK4 was shown to be 84% more accurate than Euler in some applications, while still executing computations at 100× larger time steps and running 100× quicker [193].

The left most Guidance Law block includes any GLs which will be used. It includes the primary equations as well as any supplementary information required. In proportional navigation for example, the navigation constant N will be included in the block, but it may also be passed to the block by a secondary outside controller which might be responsible for optimisation procedures, such as gain scheduling N. Multiple GLs can be programmed and computed in parallel but only one set of controller demands be passed onwards. The GL takes feedback from the dynamics about the current system state, including position

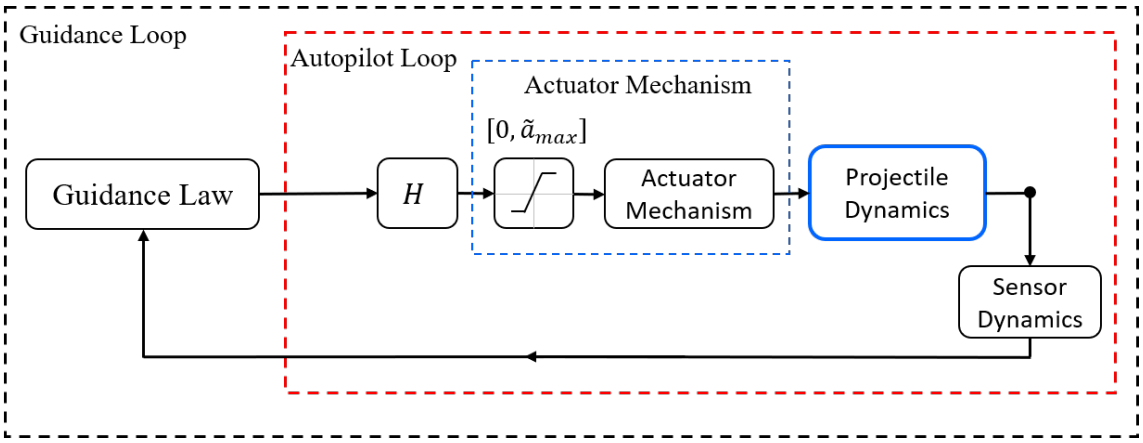

FIGURE 4.1.1 Simulink block diagram for the velocity-based actuation mechanism and GL

and target velocities. In practical applications of this circuit, any value used by the GL would have to be physically measured by a sensor, which introduces errors and uncertainties with the data used. To emulate this, a `Sensor dynamics` box is included between the projectile dynamics and GL block. At this point, noise or systematic bias can be added to replicate the imperfect measurements, as well as being able to add post measurement corrective measures to clean the measurement signals.

The controller demand from the GL block is then passed into the `Controller` loop, which contains a controller H and the actuation mechanism. For the implementation used in this project H only contains a PID controller, but it could contain any standardised controller. The demands from the GL which will feed into the actuator mechanism are split into two separate channels, a normal and lateral channel, whereby individual PID controller gains can be separately applied. This allows separate tuning if certain effects are more prominent in either of the two channels, as well as facilitating the application of gain scheduling or other such optimisation methods.

The actuator mechanism is a separate script responsible for converting the GL demand into the actual bias angles throughout which the actuator torque is applied, using whichever actuation mechanism is to be considered. Both the actuation mechanism demand variable (latax or δV) and the state switching model will be discussed in this chapter. Once the bias coordinates have been computed, this block is also responsible to changing the actuator torque which affects the spin rate of the forward section. This change is enacted by directly modifying ω (or $\dot{\phi}$) to reflect the performance delivered by the hardware. The output of the

actuation mechanism into the projectile dynamics box is just the computed front section roll rate, ω.

If at any instant during the roll, the inequality $\phi_i < \phi_{i-1}$ is true, then the projectile has just completed one revolution and the angle has wrapped. At this point, the GL is polled for the updated controller command, which is then converted into bias ranges. These bias ranges are held in a loop constantly, until such a time when the projectile has completed another rotation, whereby it is updated from the GL again. Until this time, the current angle ϕ is compared against the range through which biases are required. Importantly, the actuator mechanism block also keeps track of when the projectile has wrapped to $\phi = 0$. This allows analysis to consider only the wrapping points, when the GL is polled for an update, to better understand and characterise the system behaviour as a whole continuous system, without the data being obscured by the oscillatory nature of the system. Figure 4.1.2 shows how the angular region of the bias can overlap the zero-point of rotation. The bias starts at ϕ_{ON} and ends at ϕ_{OFF}. If the bias range overlaps the wrapping point, the magnitude of ϕ_{ON} is higher than ϕ_{OFF}, which while trivial to fix must be considered by the actuation code block.

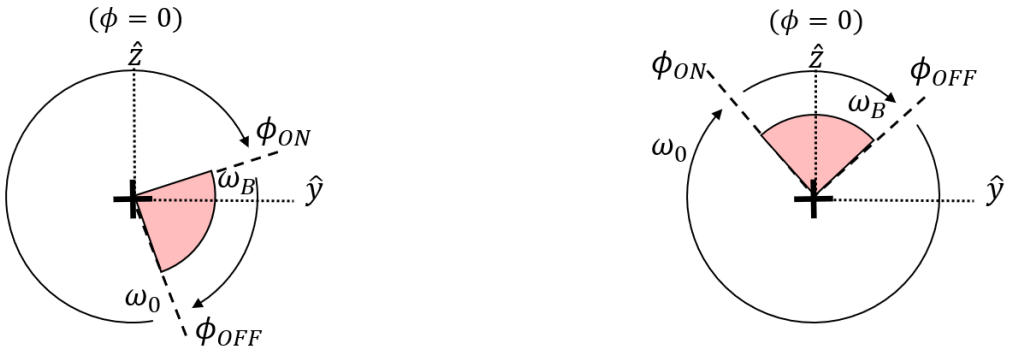

(A) Unwrapped, $|\phi_{ON}| < |\phi_{OFF}|$ (B) Wrapped, $|\phi_{OFF}| < |\phi_{ON}|$

FIGURE 4.1.2 Wrapping of bias angles, bias starts at $\phi_{ON} = \phi_B - \phi_a$ and ends at $\phi_{OFF} = \phi_B + \phi_a$

Within fig. 4.1.1 is the projectile dynamics, or `Dynamics` box, which contains the q-LPV linearised state-space equations of motion. Initially, they are simplified from the full model shown in chapter 3, by only considering lateral and normal motion in the described picture plane. It is assumed for the initial purposes of controller validation

that the only force acting within the system is the oscillatory control force, which was shown to be common practice by many sources in chapter 2. Any optimisation using the 7-DoF model would be very resource intensive, by only implementing it once the optimisation procedure is ready a lot of time will be saved. Within the dynamics box in the simulation code is a separate script, `Integrate/Export`, which is responsible for integrating the model parameters for the next time step as well as exporting them to the simulation workspace. The integrator blocks also import any initial conditions from the external file `initialConditions.m` so the parameters can be tuned by the user or a stochastic initialisation algorithm as needed. Algorithm 1 shows a step by step process of the code used for the simulations and .

Algorithm 1 Dynamic model execution order

Require: initialConditions.m
Ensure:
while $t < T \,||\, z > 0$ **do**
  if $\phi_i < \phi_{i-1}$ **then**
    Poll GL for $a_{x,\mathrm{Dem}}$, $a_{y,\mathrm{Dem}}$, then convert to ϕ_B, ϕ_a.
  else
    Use existing ϕ_B, ϕ_a.
  end if
  if $\phi \in \phi_B \pm \phi_a$ **then**
    Bias, change to unlocked state ω_B
  else
    Set locked state ω_0
  end if
  Evaluate equation of motion for current time step.
  Integrate and export the parameters to the workspace
end while

4.2 Actuation mechanism, velocity based ΔV

The integral of Newton's second law relates the impulse of a system to the change in velocity:

$$F = \frac{dp}{dt} \tag{4.1}$$

$$\int_{t_0}^{t_1} F.dt = m \int_{t_0}^{t_1} a dt \tag{4.2}$$

$$\int_{t_0}^{t_1} F.dt = m\Delta V \tag{4.3}$$

Here the mass can be taken as constant since there are no onboard resources being consumed. The contribution to F_x from F_c as it rotates through an angle ϕ relative to $\hat{x}$ is given by

$$F_x = F_c \sin(\phi) \tag{4.4}$$

where ϕ is the roll angle of the projectile and force vector. However, this decomposition can be generalised to a force along any orthogonal axis system i, j which would have the corresponding forces F_i, F_j. Let the desired decomposition axis i be a bearing ϕ_B from the normal axis $\hat{z}$ (where $\phi = 0$). Let ϕ_i be a particular angle between F_c and the arbitrary decomposition axis i. Let ϕ_a be the angle through which F_c sweeps at a given rate ω such that the sweep begins at the bearing $(\phi_B - \phi_a)$ and ends at ϕ_B. This is scenario which will be considered and is shown in fig. 4.2.1. The decomposition of F_c onto F_i at an angle ϕ_B

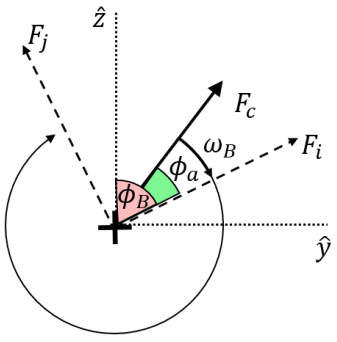

FIGURE 4.2.1 Bias centre point ϕ_B with force sweep angle of size ϕ_a

is given by

$$F_i = F_c \cos(\phi_B) \tag{4.5}$$

Equation 4.1 can be combined with 4.5, to show the total impulse as F_c sweeps through the full range of ϕ_a.

$$\int_{t_0}^{t_1} F_c \cos(\phi).dt = m\Delta v \tag{4.6}$$

The integration variable of time can be substituted in terms of the angle and angular rate, since $t = \phi_a/\omega$, giving:

$$\int_0^{\phi_a/\omega_B} F_c \cos(\phi)\frac{1}{\omega_B}.\mathrm{d}\phi = m\Delta v \tag{4.7}$$

The foundation of the control method is that the rotation of F_c is slowed or biased when sweeping through a range of angles. We define the range of angles during which F_c is slowed as being the bias angle. Let the mid-point of the bias angle coincide with decomposition axis i, such that the symmetrical angle on either side of the midpoint is ϕ_a. The bias angle thus starts at $(\phi_B - \phi_a)$ and ends at $(\phi_B + \phi_a)$ with a midpoint of ϕ_B. This is shown in fig. 4.2.2. The total impulse on axis i from F_c throughout the bias angle on the

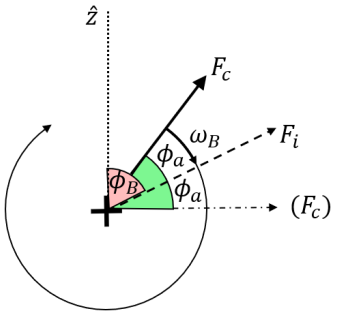

FIGURE 4.2.2 Bias range with centre point ϕ_B and symmetric ϕ_a on either side.

full range $[(\phi_B - \phi_a), (\phi_B + \phi_a)]$ is twice that of the impulse from the start to the midpoint, on the range $[(\phi_B - \phi_a), \phi_B]$ or range $[\phi_B, (\phi_B + \phi_a)]$. The total impulse through $2\phi_a$ shown in fig. 4.2.2 from F_c toward F_i, is therefore twice equation 4.7:

$$\frac{2F_c}{\omega_B}\int_0^{\phi_a/\omega_B} \cos(\phi_i).\mathrm{d}\phi_i = m\Delta v \tag{4.8}$$

assuming F_c, m and ω are constant. Calculating the integral gives

$$-\frac{2F_c}{\omega_B}\sin(\phi)\Big|_{\phi=0}^{\phi=\phi_a} = m\Delta v$$
$$-\frac{2F_c}{\omega_B}[\sin(\phi_a) - \sin(0)] = m\Delta v$$

$$-\frac{2F_c}{\omega_B}\sin(\phi_a) = m\Delta v$$

Thus we can write a conversion between Δv and half the angle swept during the bias ϕ_a as

$$\Delta v = -\frac{2F_c}{m\omega_B}\sin(\phi_a) \tag{4.9}$$

Equation 4.9 shows the change in velocity along the i^{th} axis, as a result of F_c sweeping through an angle ϕ_a either side of the i^{th} axis, at a rate of ω_B. However, F_c will continue to rotate through the rest of the bearing ϕ eventually sweeping another angular range $(\phi_B + \pi) \pm \phi_a$ (wrapped so $\phi \in [0, 2\pi]$). During this time the resulting change in velocity is directed along the negative i^{th} axis. This destructive angular range, $(\phi_B + \pi) \pm \phi_a$, is shown in figure 4.2.3. We define ΔV as the total change in velocity of one whole rotation

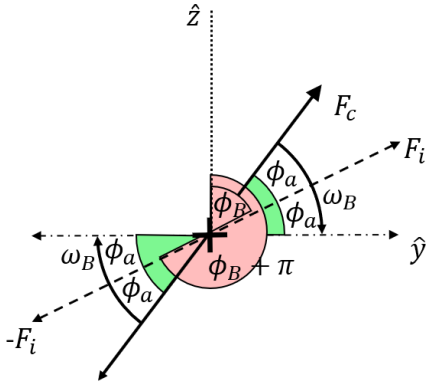

FIGURE 4.2.3 Bias angle at ϕ_B corresponds to a counter bias angle of $\phi_B + \pi$

in sweeping through equal but opposing angles at different rates ω_0 and ω_B. This is calculated by

$$\Delta V = -\frac{2F_c}{m\omega_B}\sin(\phi_a) - -\frac{2F_c}{m\omega_0}\sin(\phi_a) \tag{4.10}$$

giving

$$\Delta V = \frac{2F_c}{m}\sin(\phi_a)\left(\frac{\omega_0 - \omega_B}{\omega_0\omega_B}\right) \tag{4.11}$$

Thus the bias angle required to produce a desired ΔV is given by

$$\phi_a = \frac{\omega_0\omega_B}{\omega_0 - \omega_B}\sin^{-1}\left(\frac{m\Delta V}{2F_c}\right) \tag{4.12}$$

Under the assumption that the bias axis coincides with the reference axis, then $\phi_B = 0$

and the two equations agree. The maximum of equation 4.11 is found when $\phi_a = \pi/2$. Using the ideal system parameters from table 4.1, equation 4.11 is used to calculate the maximum ΔV per rotation as

$$\Delta V_{\max} = \Delta V|_{\phi_a=\pi/2} = \frac{2F_c}{m}\left(\frac{\omega_0 - \omega_B}{\omega_0\omega_B}\right) \tag{4.13}$$

$$\frac{2\times 1}{1}\left(\frac{2\pi - (\pi/2)}{2\pi(\pi/2)}\right) = 0.9549\text{ms}^{-1} \tag{4.14}$$

4.2.1 System Axioms (After nominal simulation)

The Simulink environment is now used to prove certain aspects of the system in order to create repeatable and predictable movement. Each of the following points must be satisfied to guarantee robust foundation on which to formulate a complete guidance architecture. In order of importance:

1. The integral of the contribution of F_c to F_x at all points through a set angle of rotation will correlate to an acceleration of the projectile and thus a change in velocity ΔV.

2. The net acceleration of the system will be zero if a full rotation is completed at the same ω. The cyclic motion of the projectile in this case will vary depending on the initial velocities of the projectile at the start of the rotation.

3. Asymmetrical biasing of the spin through certain angles of one rotation, by switching from the fast rate ω_0 to the biased rate ω_0, produces a net acceleration of the system.

4. After an acceleration has been imparted, the system will continue to move under this new velocity in a new cyclic pattern.

5. Symmetrical biasing of the spin through opposing angles of one rotation, causes no net acceleration of the system.

6. By biasing one rotation and imparting a net acceleration, the projectile will move in a new cyclic fashion. If after some amount of unbiased rotations, a bias is applied which opposes the initial bias, the system should be 'decelerated' and continue a motion identical to that if the system experience no net acceleration at all.

Using the above discussion, the six axioms written above can be proven analytically then corroborated experimentally, using the parameters from table 4.1 in the Simulink model. The projectile is initialised at $[x_0, y_0, u_0, v_0] = [0,0,0,0]$ with $\omega_B = \pi/2$ and $\omega_0 = 2\pi$. In the diagrams illustrating a manoeuvre, green indicates the resting rotation rate ω_0 and red indicates the actively slowed bias rate ω_B.

1. *The integral of the contribution of F_c to F_x at all points through a set angle of rotation ϕ will correlate to an acceleration of the projectile and thus a change in velocity ΔV.*

   From equation 4.11, both the horizontal and vertical ΔV can be calculated from the impulse through an angle of $\pi/2$ as

$$\Delta V = \frac{2 \times 1}{1 \times 2\pi} \sin(\pi/2) = 0.1592 \tag{4.15}$$

   Figure 4.2.4A shows a pictorial representation of what happens in the simulation and figure 4.2.4B shows the experimental results. Since the contribution to u and v as F_c sweeps through the first angle of $\pi/2$, the resulting magnitude of both is equal, which is visible from the figure. The y-coordinate shown on the figure represents both the u and v value, which agrees with the analytical prediction in equation 4.15.

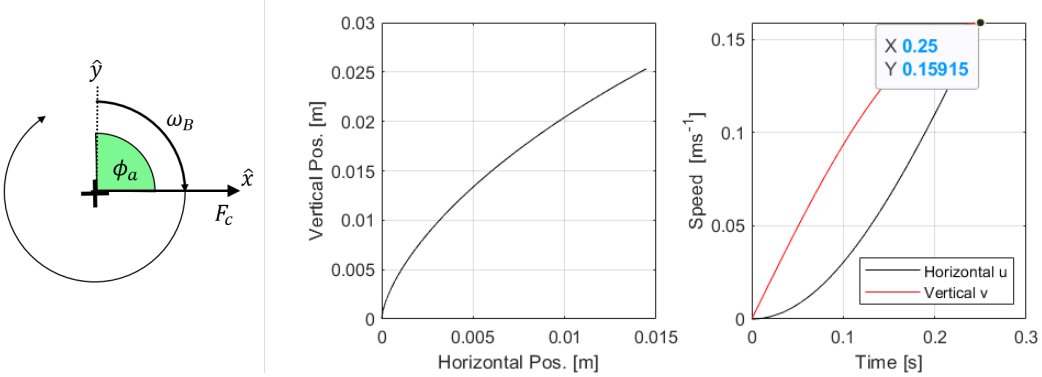

(A) $\omega_B = \pi/2$[rad.s^{-1}] through $\pi/2$

(B) Position and speed profile

FIGURE 4.2.4 Axiom 1

2. *The net acceleration of the system will be zero if a full rotation is completed at the same ω. The cyclic motion of the projectile in this case will vary depending on the initial velocities of the projectile at the start of the rotation.*

Equation 4.13 can be used to calculate the ΔV of the system when the bias angle is the same, for both horizontal and vertical velocities:

$$\Delta V_{\max}|_{\omega_B=\omega_0} = \frac{2\times 1}{1}\left(\frac{0}{\omega_0^2}\right) = 0 \tag{4.16}$$

Figure 4.2.5A shows a pictorial representation of what happens in the simulation and figure 4.2.5B shows the experimental results. Since one complete rotation has elapsed, there is no net impulse on the system and thus it should return to its initial speeds. The coordinates on figure 4.2.5B show that for both u and v, the speed has reduced to 1.63×10^{-13} compared to the analytical estimation of 0 from equation 4.16. This discrepancy is due to numerical integration errors, but is negligible.

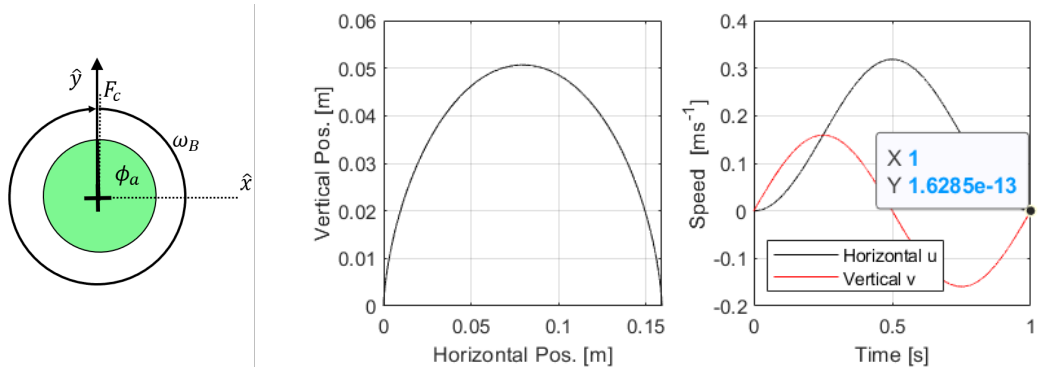

(A) $\omega_B = \pi/2$ through 2π

(B) Position and speed profile

FIGURE 4.2.5 Axiom 2

3. *Asymmetrical biasing of the spin through certain angles of one rotation, by switching from the fast rate ω_0 to the biased rate ω_B, produces a net acceleration of the system.*

From equation 4.11 the change in velocity of the system can be calculated for a bias of certain angle. An angular segment of $\pi/2$ will be used, centred about the bias angle $\phi_B = \pi/2$. This equates to a $\phi_a = \pi/4$, one either side of ϕ_B.

$$\Delta V = \frac{2 \times 1}{1} \sin(\pi/4) \left(\frac{2\pi - \pi/2}{(\pi/2)2\pi} \right) = 0.67524 \tag{4.17}$$

Figure 4.2.6A shows a pictorial representation of what happens in the simulation and figure 4.2.6B shows the experimental results. Figure 4.2.6A shows the opposing $\pi/2$ angles for the bias at $\phi_B = \pi/2$ and the corresponding opposing angle at $\phi_B + \pi$, where F_c rotates at ω_B and ω_0 respectively. However, the rotation rate still continues at ω_0 when outside of this range, but since that motion is symmetrical it has no net effect on the system, which was proven in axiom 2. Equation 4.17 predicts that Δu (ΔV decomposed in the x direction) will be 0.67524, which agrees with the results of the simulation shown on figure 4.2.6B. On the figure, the Y-value data point indicates the speed of the horizontal velocity.

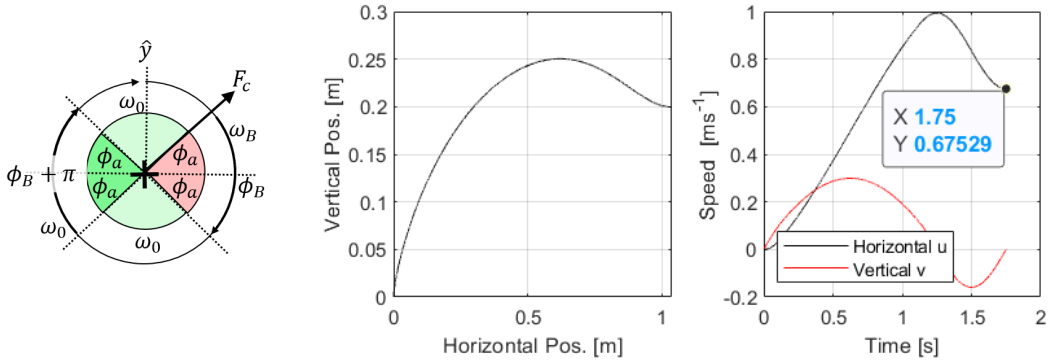

(A) Bias of ω_B through $\phi_B \pm \phi_a$, ω_0 otherwise

(B) Position and speed profile

FIGURE 4.2.6 Axiom 3 $[\phi_B, \phi_a] = [\pi/2, \pi/4]$

4. *After an acceleration has been imparted, the system will continue to move under this new velocity in a new cyclic pattern.*

Proof of this follows from axiom 3 which showed that a bias causes a change in velocity. The same simulation is run twice more for 5 complete rotations each, once where the first rotation is unbiased and second where the first rotation is biased. The illustration of axiom 4 shown in figure 4.2.7A is the same as that for axiom 3, shown in figure 4.2.6A. Equation 4.17 predicts the ΔV of the system after biasing which should remain unchanged after subsequent unbiased rotations. The terminal speeds of the simulation shown in figure 4.2.7B are identical to the speeds predicted by equation 4.17.

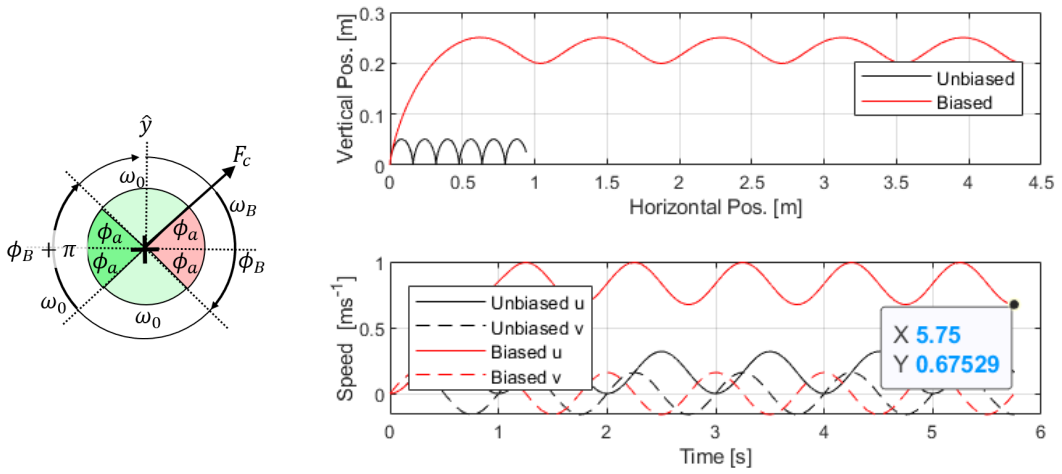

(A) Bias of ω_B through $\phi_B \pm \phi_a$, ω_0 otherwise

(B) Trajectory and speed profile

FIGURE 4.2.7 Axiom 4: $[\phi_B, \phi_a] = [\pi/2, \pi/4]$

5. *Symmetrical biasing of the spin through opposing angles of one rotation, causes no net acceleration of the system.*

Equation 4.11 is again used to calculate ΔV, which gives:

$$\Delta V = \frac{2\times 1}{1}\sin(\pi/4)\left(\frac{\pi/2-\pi/2}{(\pi/2)(\pi/2)}\right) = 0 \tag{4.18}$$

Figure 4.2.8A shows a pictorial representation of what happens in the simulation, which is similar to figure 4.2.6A except the destructive counter bias is now also a bias with rate ω_B. Again, the rotation rate still continues at the natural ω_0 when outside of this range having no net effect on the system. Equation 4.18 predicts $\Delta u = 0$, which again agrees with the results of the simulation in figure 4.2.8B. The terminal value of u shown on the fig. is 0.

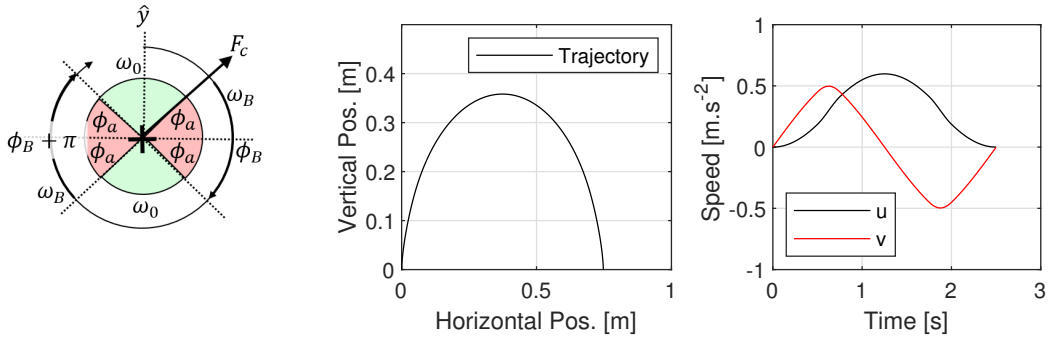

(A) Bias of ω_B through $\phi_B \pm \phi_a$ and $(\phi_B + \pi) \pm \phi_a$, ω_0 otherwise

(B)

FIGURE 4.2.8 Axiom 5: $[\phi_B, \phi_a]_1 = [\pi/2, \pi/4]$, $[\phi_B, \phi_a]_2 = [3\pi/2, \pi/4]$

6. *By biasing one rotation and imparting a net acceleration, the projectile will move in a new cyclic fashion. If after some amount of unbiased rotations, a bias is applied which opposes the initial bias, the system should be 'decelerated' and continue a motion identical to that if the system experience no net acceleration at all.*

This combines both axiom 4 and 5. The initial bias to the system causes an acceleration to a new speed, which the system then maintains until the final counter-bias, bringing it back to the initial state. The bias from axiom 5 is used, with 3 unbiased rotations between the acceleration and deceleration phases. An additional 2 unbiased rotations are included before and after the manoeuvre for reference. Figure 4.2.9 shows the results of the simulation. The coordinates included in the figure show u after the bias manoeuvre and u after the deceleration manoeuvre. The figures from the simulation, 0.67524ms^{-1} and $1.14 \times 10^{-12}\text{ms}^{-1}$ agree with the analytical predictions from equations 4.17 and equation 4.18 respectively.

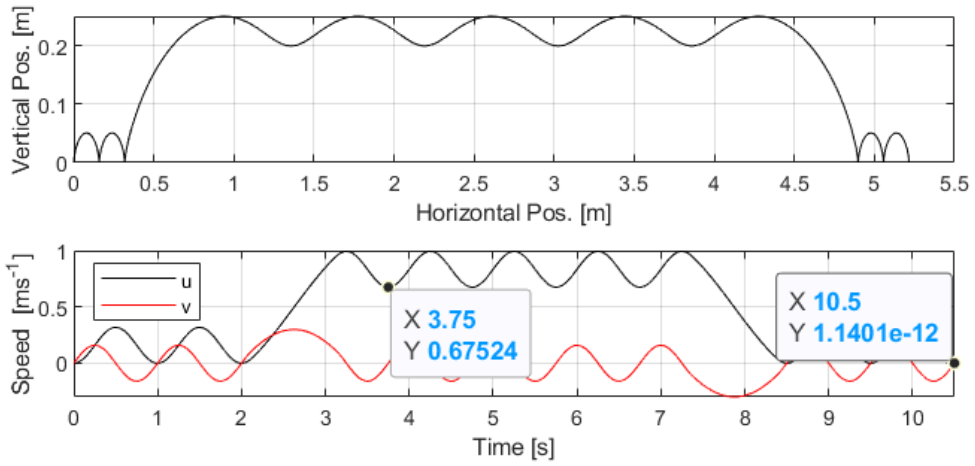

FIGURE 4.2.9 Axiom 6: $[\phi_B, \phi_a]_1 = [\pi/2, \pi/4]$, $[\phi_B, \phi_a]_2 = [3\pi/2, \pi/4]$

4.2.2 Initial conditions for circular resting state

For proof of the axioms, the initial conditions were set to be $[u_0, v_0] = [0,0]$, which creates the paths shown in figure 4.2.6B and 4.2.9. If the initial conditions are set to be equivalent to what would be expected from circular motion, then the resulting path will be circular due to the circular nature of the system dynamics. The initial velocities necessary for this are equal in magnitude but opposite in direction to what can be expected from a quarter rotation worth of acceleration, which is exactly what was calculate in equation 4.15 for axiom 1. The initial conditions for circular motion are thus $[u_0, v_0] = [-0.1592, 0]$. Figure 4.2.10 shows a repeat of the axiom 6 manoeuvre with the initial conditions $[x_0, y_0, u_0, v_0] = [0,0,-0.1592,0]$. It is visible on the graph that the projectile begins with circular oscillations as expected form the initial conditions, it moves in a sinusoidal pattern due to the unequal right bias as predicted from axiom 4, then a deceleration of the system resuming the circular motion as expected from axiom 6. This

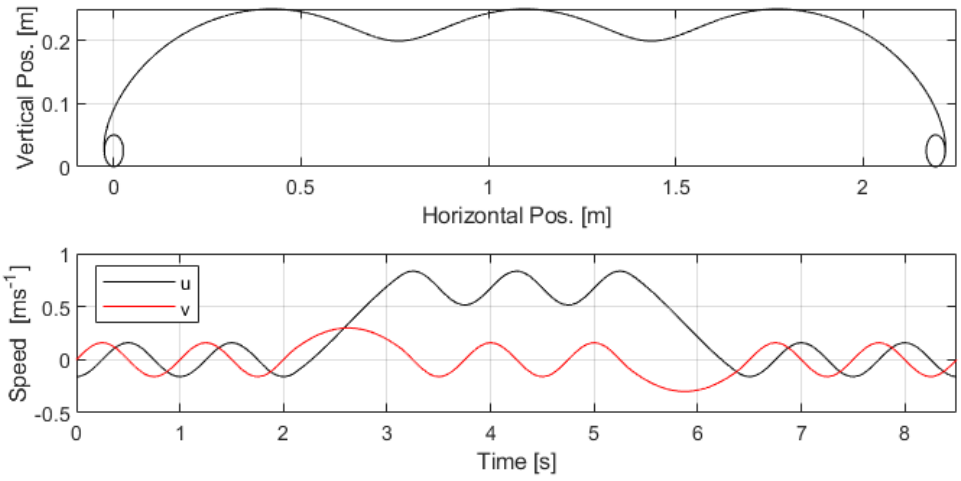

FIGURE 4.2.10 Circular initial conditions ($[u_0, v_0] = [-0.1592, 0]$) with a bias, progression then counter bias, showing the continuation of circular motion

circular motion is useful for the purposes of designing a control system as the circular motion represents an equilibrium state of the system where there is no net motion of the system. The radius of the circular oscillation will either be within the levels of accuracy required of the projectile, which would require less control effort, or the projectile would need terminal correction to account for its position in the circular path a particular time.

Bias manoeuvres

The current relative velocity of projectile to target is the difference between the projectile and target velocity, $V_R = V - V_T$, again noting that these velocities are in the YZ picture plane. In full, this is given by

$$V_R = \begin{bmatrix} u_R \\ v_R \end{bmatrix} = \begin{bmatrix} u - u_T \\ v - v_T \end{bmatrix} \tag{4.19}$$

As stated, the projectile must initiate the trajectory with some motion to ensure the resulting trajectory is circular. Thus, V_{DR0} is defined as the ΔV correction necessary to bring the projectile to a stable circular orbit relative to the target which explicitly, may be written as

$$V_{DR0} = \begin{bmatrix} u_R + \Delta V|_{\phi=\pi/4} \\ v_R \end{bmatrix} \tag{4.20}$$

For the idealised system of table 4.1, this becomes

$$V_{DR0} = \begin{bmatrix} u_R + 0.159 \\ v_R \end{bmatrix} \tag{4.21}$$

To test the functionality of the above equations, they alone can be used as the desired target speed. Since this is the only speed being demanded of the projectile, the motion will act to bring the projectile to rest, relative to the target. In this case, the target can be assumed to be a stationary point at any coordinate, since the residual velocity is obviously only a function of target velocity, as opposed to including position. The implementation is shown in algorithm 2. This algorithm is tested for effectiveness using initial residual velocities directed into all four quadrants of the 2D plane. This approach helps to probe the algorithm for any errors caused by wrapping calculations. Figure 4.2.11 shows the results for initial velocities. A close up of the end trajectory of the $[u_+, v_+]$ quadrant is shown in figure 4.2.12. The figure shows that the residual velocity of the system is successfully eliminated, leaving the projectile to rotate with the desired circular motion. Again, the centre of this orbit is not yet directed towards any location in particular, the purpose of this algorithm check is to ensure that any relative velocity between the two can be eliminated.

Algorithm 2 Pseudo-code for bringing projectile to relative rest

1: **if** $\phi_i < \phi_{i-1}$ **then**
2: Set demanded speed to current residual speed:
3: `[phi_B, phi_a] = bias([u_R, v_R])`
4: Calculate bias angles
5: `[phi_B, phi_a] = bias([u_R, v_R])`
6: **end if**
7: **if** $((\phi_B - \phi_a) < \phi \leq (\phi_B + \phi_a))$ **then**
8: Bias, $\omega = \omega_B$
9: **else**
10: Natural, $\omega = \omega_0$
11: **end if**

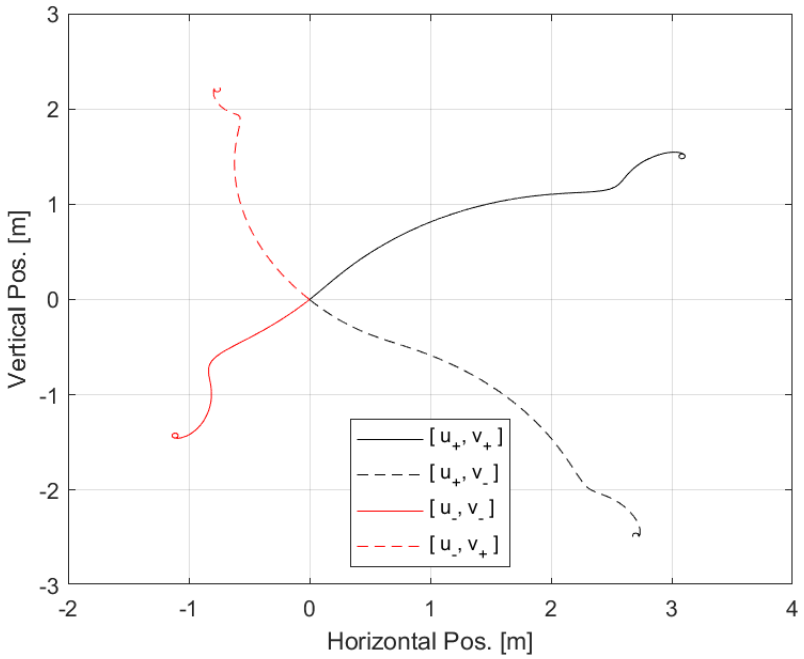

FIGURE 4.2.11 Stop algorithm check for residual velocities in all four quadrants

The figure also shows the spin rate demanded by the controller to bring the system to circular motion. Figure 4.2.12A shows the terminal phase of the stop manoeuvre where the projectile should enter a circular orbit. The figure shows a thick line indicating a path overlap where the orbit is near-circular, but imperfect. This is due to numerical errors in the simulation as well as tolerances in the velocity check, to determine the bias points. If there is an external force acting on the system, as is the case in figure 4.2.13, the drift problem is exacerbated. The bias points are calculated when $\phi = 0$ and the rotation will continue with the bias being executed to eliminate the ΔV_R which was present at $\phi = 0$. This means an external force can constantly accelerate the system during the rotation,

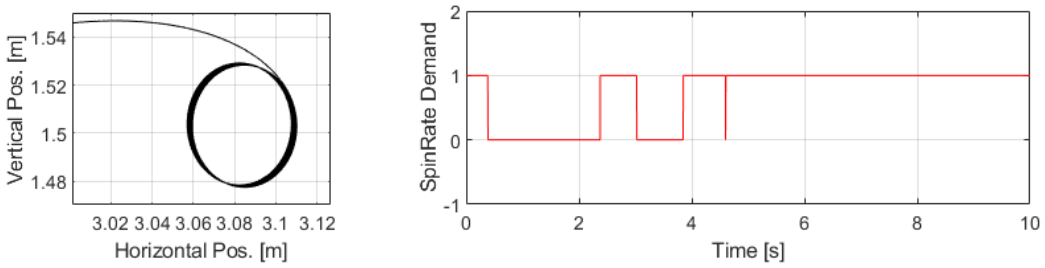

(A) Terminal phase during stop manoeuvre

(B) Spin rate demand from controller

FIGURE 4.2.12 Terminal phase of stop algorithm check

introducing a ΔV which was unaccounted for. This would then have been accounted for on the following rotation but the same process will happen again. If the forces which cause the drift errors are constant and known, their effect through one rotation can be accounted for during the bias point calculation. For example, in the current test system one rotation takes 1s for $\omega_0 = 2\pi$. If an arbitrary continuous external force of 0.01N acts on the system in the $-\hat{z}$ direction an acceleration of $0.01/1 = 0.01\text{ms}^{-2}$ is produced which equates to a Δv per rotation of $0.01 \times 1 = 0.01\text{ms}^{-1}$. This ΔV can then be accounted for in the bias manoeuvre, to produce a constant bias which accounts for its affect. Figure 4.2.13 shows the effect of both introducing the 0.01N force and accounting for the constant effects in the bias manoeuvre. However, the fig. shows that the resting orbit is still imperfectly circular, due to numerical inaccuracies during the computation. This shows that modelling external forces acting on the projectile, using this velocity-based actuation mechanism is viable.

If the forces acting on the projectile are high compared to the control force, the system will be unable to enact any significant change in trajectory. The effects of gravity are traditionally accounted for in conventional projectiles prior to launch, such that the vertical change in position coincides with the target position at range. A similar approach should be taken with this prototype. As there are no on-board resources which can extend the range of the projectile, any correction made throughout the duration of the trajectory is at the expense of range, since the aerodynamic surface providing the lift/control force increases the drag. Since effects such as gravity, wind and Coriolis forces *etc.* are already well understood for launching conventional projectiles, the same practices can be used when firing this novel design, leaving the control system free to account for the small disturbances and perturbation present during flight. It is also pertinent to consider the

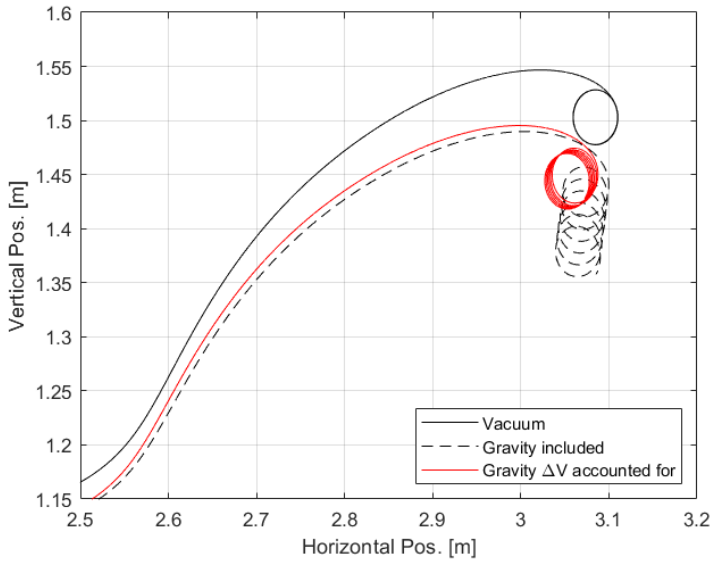

FIGURE 4.2.13 Drift effect in system

motion of the projectile in terminal approach to the target. In the current implementation, the projectile will orbit a point close to the target. It may be advantageous to a designer to implement such a terminal correction system that the projectile is able to coincide with the target location precisely as the flight terminates. For example, a 'virtual target' point can be set with respect to the actual target position. This could allow the projectile to orbit such that the target is located precisely at the centre of the orbit, or it could be designed such that the two intersect at a particular time in the orbit. While the design possibility is acknowledged here the investigation is left as the topic of future work. This work focuses mainly on the general guiding concept, the optimisation of which will allow more high-fidelity movements and corrections such as the terminal interception manoeuvre described here.

4.3 Actuation mechanism, latax based $\tilde{a}$

A traditional missile operates by deflecting control surfaces, which produce a deflection force, by some angle δ. If a GL demands a latax from the missile, the actuation mechanism describes how the missile changes and orientates the control surface to deliver that latax. The missile deflects the fins which produces a control force, roughly following $F_c \alpha \sin(\delta_c)$. The missile often has two pairs of fins which are capable of control motion

along orthogonal axis and thus the correction is continuous, in the sense that it is limited only to the extent of the physical actuation hardware. The prototype described cannot simply provide a latax demanded by the GL and sustain it, as the control force is always rotating. This section discusses the conceptual actuation mechanism from a latax perspective, describing the limitations and the parameters which affect it. This uses the same picture plane consideration as the preceding section which considered the ΔV perspective of the actuation mechanism.

By definition, acceleration is the infinitesimal change of velocity per infinitesimal unit time.

$$a = \frac{\mathrm{d}V}{\mathrm{d}t} \tag{4.22}$$

Extrapolating this to the time taken for one complete revolution, the latax of the projectile experienced over one complete revolution is

$$\tilde{a} = \frac{\delta V}{\tau} \tag{4.23}$$

where δV is the picture plane net change in velocity for one full rotation and τ is the time taken for one complete rotation. From the definition of angular rotation, we can write the time taken for one rotation τ in terms of the instantaneous angular velocity as

$$\frac{\mathrm{d}\phi}{\mathrm{d}t} = \omega(\phi) \tag{4.24}$$

$$\frac{1}{\omega(\phi)}\mathrm{d}\phi = \mathrm{d}t \tag{4.25}$$

$$\therefore\ \tau = \int \omega(\phi)^{-1}\mathrm{d}\phi \tag{4.26}$$

where $\omega(\phi)$ is the angular speed of the projectile as a function of ϕ, while assumed not to be a function of time. Integrating Newton's second law, we can write the net change in speed over one complete rotation as

$$F = ma \tag{4.27}$$

$$\int_0^\tau \mathbf{F}\mathrm{d}t = m\int_0^\tau a\mathrm{d}t \tag{4.28}$$

$$\therefore\ \delta V = \frac{1}{m}\int \mathbf{F}\mathrm{d}t \tag{4.29}$$

Where **F** is the vector sum of forces acting on the projectile which for the purposes of derivation, we define as only comprising of the control force F_c. In addition, δV is the change in velocity along the bias axis. Substituting the above into the definition of acceleration yields the acceleration per rotation in the direction of bias

$$\tilde{a} = \frac{\int_0^\tau \mathbf{F} \mathrm{d}t}{m \int_0^{2\pi} \omega(\phi)^{-1} \mathrm{d}\phi} \tag{4.30}$$

Herein lies a problem, as $\omega(\phi)$ is the result of complex dynamics involving motor bearing and couplings. The function $\omega(\phi)$ is the roll rate ω after evolving for some time according to given bearing dynamics. The bearing dynamics could be modelled as a highly trivial instantaneous switching, where the spin rate assumes ω_0 or ω_B on demand. Or, the function $\omega(\phi)$ may be non-trivial, switching speeds according to a sigmoid function with decay rates emulating the variable dynamics of the system, such as a fast acceleration (lock) but a slow deceleration (unlock, caused by spin damping moment). Finally, the function could be highly complicated, such as an interpolation from empirical measurements of a real dynamic system, or non-linear a model with full aerodynamic coefficients and material parameters. In any case, the system acceleration over one rotation $\tilde{a}$ from equation 4.30 can then be decomposed along the desired correction axis via the bias angle. Since the force biasing which produces the acceleration is by design, directed along ϕ_B, the decomposition is given by

$$\begin{bmatrix} a_x \\ a_y \end{bmatrix} = \tilde{a} \begin{bmatrix} \cos(\phi_B) \\ \sin(\phi_B) \end{bmatrix} \tag{4.31}$$

This equation equates the projectile latax over one rotation to the bias angle ϕ_B and size ϕ_a. To implement these equations, it is necessary to encapsulate the roll rate function $\omega(\phi)$.

$$\begin{bmatrix} a_x \\ a_y \end{bmatrix} = \frac{\frac{1}{m}\int_0^\tau \mathbf{F} \mathrm{d}t}{\int_0^{2\pi} \omega(\phi)^{-1} \mathrm{d}\phi} \begin{bmatrix} \cos(\phi_B) \\ \sin(\phi_B) \end{bmatrix} \tag{4.32}$$

This method of describing the radial impulse distribution is a more generic and complete representation than other considered works [131], which have only considered fixed roll rates and fixed impulse shapes. These works also assumed that impulse thrusters are

used as the correction method, which are of course a limited correction resource. The following subsections will consider the system behaviour in the most simplistic case, instantaneous switching between states. These simplifications will then be relaxed, up until the function is purely abstract, and the behavioural change in the system response will be investigated.

4.3.1 Instantaneous switching

The most simple case that can be imagined is to assume instantaneous and binary switching of the roll rate between a high speed ω_0 and a low speed ω_B during the bias. Figure 4.3.1 shows the evolution of spin speeds throughout flight under the simplified model. The phases of flight are as follows*:

1. During the launch phase, the projectile is ballistically accelerated while the brake mechanism is locked. Both the forward and aft sections accelerate to the natural launch spin rate of the system ω_0.

2. During free flight of the projectile, with the brake mechanism engaged, the spin rate of the two sections are assumed to remain constant throughout the flight with no decay.

3. At the point the lock mechanism is disengaged, the spin rate of the front section will begin to decelerate quicker since, by design it has a higher spin damping instantaneously drops to a new equilibrium speed, ω_B.

4. The de-coupled steady state speed ω_B is maintained indefinitely for the duration of the bias manoeuvre, in addition to the aft section maintaining the natural speed of ω_0

5. When the lock mechanism is re-engaged, the simplification used is that front section instantaneously increases back to the natural roll rate ω_0. There is assumed to be no loss of spin rate of the aft section as a result of the front section being accelerated in this manner

*referring to fig. 1.1.1 on pg. 13

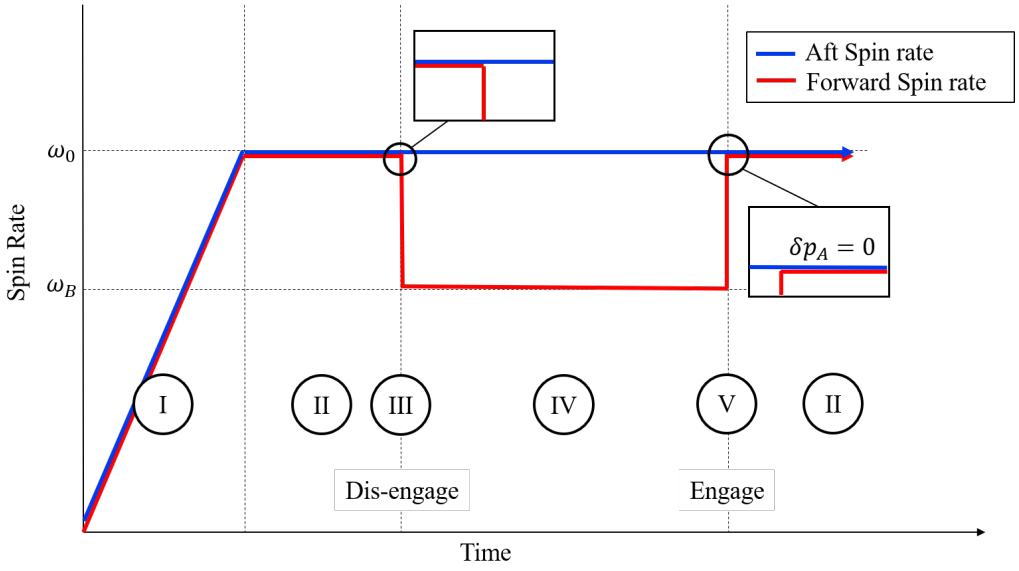

FIGURE 4.3.1 Simplifications to spin rate for control architecture
† - Phase II is repeated because both instances represent free flight

The function $\omega(\phi)$ can thus be expressed as

$$\omega(\phi) = \begin{cases} \omega_B, & \forall\ \phi \in [\phi_B \pm \phi_a] \\ \omega_0, & \text{otherwise} \end{cases} \tag{4.33}$$

The sum of forces $\mathbf{F}$ acting on the projectile is written as

$$\mathbf{F} = F_c \cos(\phi_B) \tag{4.34}$$

The projectile parameters and spin rates are again shown in table 4.1. Considering a bias of size ϕ_a located at angle ϕ_B as was shown in fig. 4.2.2 (pg. 121) it is now possible to compute the change in velocity and time taken per rotation as a function of these bias coordinates.

δV - Change in speed from one rotation along bias axis

Under the prior assumptions from Newton's second law, it can be shown that the impulse of the system reduces as

$$\delta V_{xy} = \frac{1}{m} \int_0^{\tau} \mathbf{F} \mathrm{d}t \tag{4.35}$$

$$\delta V_{xy} = \frac{1}{m}\int_0^{\tau} F_c \cos(\phi_B)\mathrm{d}t \tag{4.36}$$

where δV_{xy} is the change in velocity from one rotation, along non-rotating projectile axis. Since the control force is assumed to be constant, a variable substitution results in

$$\delta V_{xy} = \frac{F_c}{m}\int_0^{2\pi} \frac{\cos(\phi_B)}{\omega(\phi)}\mathrm{d}\phi \tag{4.37}$$

Due to the instantaneous switching shown in equation 4.33, this integrand can be written as a linear sum of the integrands representing the motion in and outside of a bias.

$$\delta V_{xy}\frac{m}{F_c} = \underbrace{\int_0^{\phi_B-\phi_a} \frac{\cos(\phi)}{\omega(\phi)}\mathrm{d}\phi + \int_{\phi_B+\phi_a}^{2\pi} \frac{\cos(\phi)}{\omega(\phi)}\mathrm{d}\phi}_{\text{Unbiased, } \omega(\phi)=\omega_0} + \underbrace{\int_{\phi_B-\phi_a}^{\phi_B+\phi_a} \frac{\cos(\phi)}{\omega(\phi)}\mathrm{d}\phi}_{\text{Biased, } \omega(\phi)=\omega_B} \tag{4.38}$$

Computing this integral yields

$$\delta V_{xy}\frac{m}{F_c} = \frac{1}{\omega_0}\left([\sin(\phi)]_0^{\phi_B-\phi_a} + [\sin(\phi)]_{\phi_B+\phi_a}^{2\pi}\right) + \frac{1}{\omega_0}\left([\sin(\phi)]_{\phi_B-\phi_a}^{\phi_B+\phi_a}\right) \tag{4.39}$$

$$\delta V_{xy}\frac{m}{F_c} = \left(\frac{1}{\omega_B} - \frac{1}{\omega_0}\right)(\sin(\phi_B+\phi_a) - \sin(\phi_B-\phi_a)) \tag{4.40}$$

Using the identity $\sin(A\pm B) = \sin(A)\cos(B) \pm \cos(A)\sin(B)$ and substituting the respective values of ω_0 and ω_B, this can be written as

$$\delta V_{xy} = \frac{2F_c}{m}\sin(\phi_a)\cos(\phi_B)\left(\frac{\omega_0-\omega_B}{\omega_0\omega_B}\right) \tag{4.41}$$

The factor of $\cos(\phi_B)$ indicates the directionality of δV_{xy} is along the vertical axis. By now defining $\delta V_{xy} = \delta V$ the change in velocity resulting from a singular biased rotation along the decomposition axis now coincides with the bias axis, and this factor tends to 1. By also substituting the respective values of ω_0 and ω_B, this reduces to.

$$\delta V = \left[\frac{2F_c}{m}\sin(\phi_a)\left(\frac{\omega_0-\omega_B}{\omega_0\omega_B}\right)\right]_{\omega_B=\pi/2,\omega_0=2\pi} \tag{4.42}$$

$$\delta V = \frac{3}{\pi}\sin(\phi_a) \tag{4.43}$$

Under the same simplifications, we have arrived at the equation used to describe the ΔV, shown in eq. 4.11 (pg. 122).

τ - Time taken for one revolution

From the definition of angular speed, we can relate τ to the angular speed function $\omega(\phi)$ by

$$\phi = \omega(\phi)t$$
$$\int_0^{\tau} \mathrm{d}t = \int_0^{2\pi} \omega(\phi)^{-1}\mathrm{d}\phi$$

Again, the time taken to complete the rotation can be split into bias and non-biased motion, which yields

$$\tau = \underbrace{\int_0^{\phi_B-\phi_a} \omega(\phi)^{-1}\mathrm{d}\phi + \int_{\phi_B+\phi_a}^{2\pi} \omega(\phi)^{-1}\mathrm{d}\phi}_{\text{Unbiased, } \omega(\phi)=\omega_0} + \underbrace{\int_{\phi_B-\phi_a}^{\phi_B+\phi_a} \omega(\phi)^{-1}\mathrm{d}\phi}_{\text{Biased, } \omega(\phi)=\omega_B} \tag{4.44}$$

Computing this integral yields

$$\tau = \frac{1}{\omega_0}\left([\phi]_0^{\phi_B-\phi_a} + [\phi]_{\phi_B+\phi_a}^{2\pi}\right) + \frac{1}{\omega_B}\left([\phi]_{\phi_B-\phi_a}^{\phi_B+\phi_a}\right) \tag{4.45}$$
$$\tau = \frac{1}{\omega_0}2\left(\pi-\phi_a\right) + \frac{1}{\omega_B}\phi_a \tag{4.46}$$
$$\tau = \left[\frac{2(\pi-\phi_a)}{\omega_0} + \frac{2\phi_a}{\omega_B}\right]_{\omega_B=\pi/2,\omega_0=2\pi} \tag{4.47}$$

Upon substituting the values of ω_0 and ω_B, the time taken is thus

$$\tau = 1 + \frac{3}{\pi}\phi_a \tag{4.48}$$

$\tilde{a}$ - Latax for one revolution

Following these reductions, the acceleration per rotation is given by substituting the value of δV from eq. 4.43 and τ from eq. 4.48:

$$\tilde{a} = \frac{\delta V}{\tau} = \frac{\frac{3}{\pi}\sin(\phi_a)}{1+\frac{3}{\pi}\phi_a} = \frac{3\sin(\phi_a)}{3\phi_a+\pi} \tag{4.49}$$

and so,

$$\tilde{a} = \frac{\sin(\phi_a)}{\phi_a + \frac{\pi}{3}} \tag{4.50}$$

which can be substituted into the latax equation (eq. 4.32) yielding

$$\begin{bmatrix} a_x \\ a_y \end{bmatrix} = \frac{\sin(\phi_a)}{\phi_a + \frac{\pi}{3}} \begin{bmatrix} \cos(\phi_B) \\ \sin(\phi_B) \end{bmatrix} \tag{4.51}$$

We can consider that equation 4.50 is of the form

$$f(x) = \frac{\sin(x)}{x+k} \tag{4.52}$$

where k is a generic constant. By setting the derivative of this function with respect to x equal to zero

$$f'(x) = \frac{(x+k)\cos(x) - \sin(x)}{(x+k)^2} = 0 \tag{4.53}$$

the periodic inflection points are found when the equation

$$\tan(x) - x = k \tag{4.54}$$

is satisfied. Using this, the value of ϕ_a which produces the maximum acceleration is found to be 65.32°, and the corresponding maximum acceleration is 0.42ms^{-2}. Figure 4.3.2A shows a plot of equation 4.50, the function $\tilde{a}(\phi_a)$, for $\phi_a \in [0, \pi/2]$.

The maximum latax $\tilde{a}_{\max}$ is not located at $\phi_a = \pi/2$ as one would expect, though indeed $\phi_a = \pi/2$ does produce the largest overall force along ϕ_B. However, when F_c is towards the limits of the bias range, $\phi \to (\phi_B - \phi_a)^+$ or $\phi \to (\phi_B + \phi_a)^-$, the contribution of motion towards the bias axis $\hat{\phi}_B$ is small compared to the time spend biasing through those angles. *i.e.* There is a region of diminishing returns, henceforth referred to as the *deadzones*, in which the time spend 'accruing' force in the desired direction of motion is no longer worth the time it takes to do so. Figure 4.3.2B depicts the dead zones of the bias angles. For the system speeds $\omega_0 = 2\pi$ and $\omega_B = \pi/2\text{rad.s}^{-1}$ ($\omega_B = \omega_0/4\text{rad.s}^{-1}$), it was found that $\tilde{a}_{\max}$ is at $\phi_a \approx 65^o$. If ω_B is closer to ω_0 such that $\omega_B/\omega_0 \to 1^-$ then the time spent in the outer limits of the bias range to increase $\tilde{a}$ is no longer substantially slower than if the system was rotating at the natural frequency. It is thus worth while staying

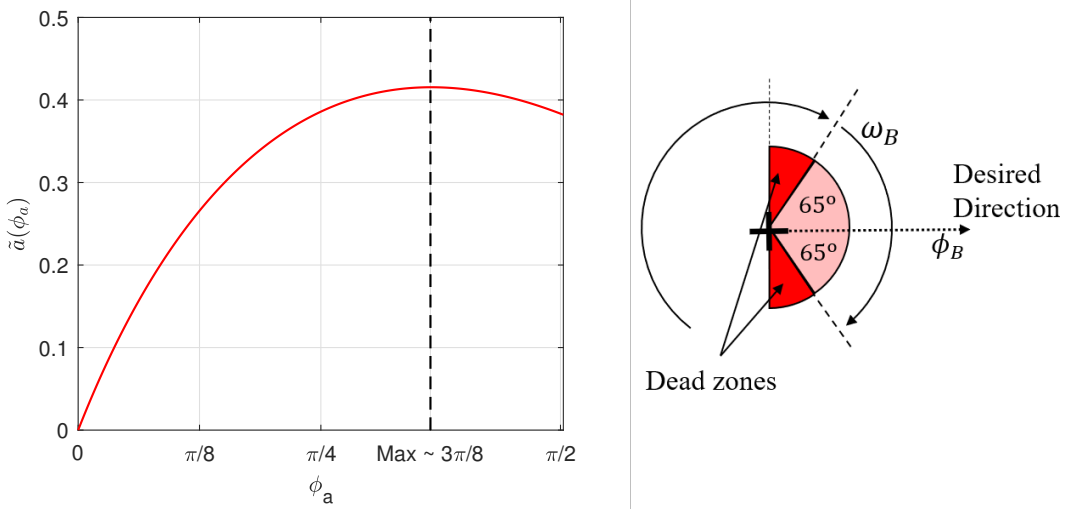

(A) Latax of simplified system against bias angle size ($\tilde{a}(\phi_a)$ in eq. 4.50)

(B) Illustration of deadzone

FIGURE 4.3.2 'Deadzones' for bias manoeuvres with: $\omega_B = \pi/2$ [rad.s^{-1}], $\omega_0 = 2\pi$ [rad.s^{-1}]

at the more extreme bias angles (higher values of ϕ_a) and the resulting dead zones are smaller.

From equations 4.41 and 4.46, it can be shown that $\tilde{a}$ can be written in terms of ϕ_a, ω_0 and ω_B for the simplified system as

$$\tilde{a}(\phi_a, \omega_0, \omega_B) = \frac{\frac{F_c}{m}\sin(\phi_a)}{\frac{\pi\omega_B}{\omega_0 - \omega_B} + \phi_a} \tag{4.55}$$

Under the assumption that $F_c/m = 1$ and $\pi\omega_B/(\omega_0 - \omega_B) = k$, this equation then reduces following the abstraction in equations 4.52-4.53. The dependency of both $\tilde{a}$ and $\tilde{a}_{\max}$ on ω_0 and ω_B is displayed entirely through the k term. It can also be inferred that it is not the magnitude of the two rotational speeds which affects the acceleration of the system, but the ratio of the two, ω_B/ω_0. It should also be noted that under the substitution of $\omega_0 = 2\pi$ and $\omega_B = \pi/2$ that eq. 4.55 reduces to eq. 4.50.

Figure 4.3.3 shows how changing the ratio of the bias to unbiased rotational speeds, ω_B/ω_0, affects the maximum latax of the system as well as the ϕ_a at which it occurs and therefore the boundary of the dead zone. As expected, when ω_B/ω_0 is close to 1, $\tilde{a}_{\max}$ occurs at values of ϕ_a close to $\pi/2$, meaning the dead zones are very small. Conversely, when ω_B/ω_0 approaches 0, $\tilde{a}_{\max}$ occurs at very low values of ϕ_a and thus the dead zones

are very large. In addition, as was predicted above from the k term in eq. 4.52, the magnitude of $\tilde{a}_{\max}$ only depends on the ratio ω_B/ω_0, not the magnitude of the values.

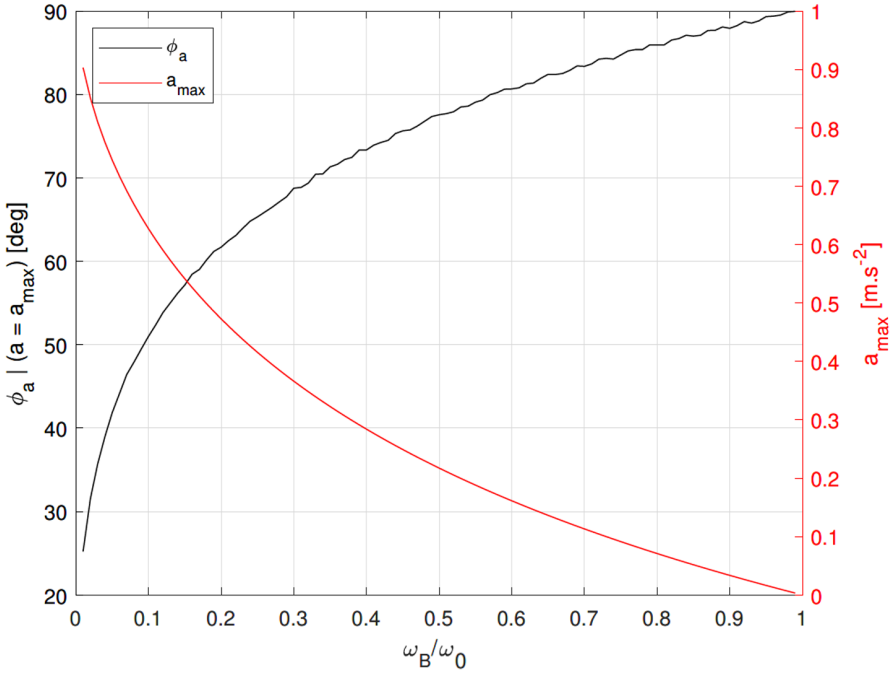

FIGURE 4.3.3 The effect of ω_B/ω_0 on the size of ϕ_a which produces the maximum acceleration, $\tilde{a}_{max}$

The latax $\tilde{a}$ demanded of the projectile by the GL can be expressed in either Cartesian or polar coordinates, given the transforms

$$\begin{bmatrix} |a| \\ a_\phi \end{bmatrix} = \begin{bmatrix} \sqrt{a_x^2 + a_y^2} \\ \tan^{-1}(a_x/a_y) \end{bmatrix} \tag{4.56}$$

$$\begin{bmatrix} a_x \\ a_y \end{bmatrix} = |a| \begin{bmatrix} \sin(a_\phi) \\ \cos(a_\phi) \end{bmatrix} \tag{4.57}$$

N.B. the acceleration is a result of the bias which is assumed to be both symmetrical and centred about ϕ_B in this instantaneous switching case, thus the bias angle and latax angle are equivocal: $a_\phi = \phi_B$.

4.3.2 Non-instantaneous switching

The front and aft section behave as one body whilst the brake mechanism is engaged and the spin rate of the two sections are identical and will reach an equilibrium. Throughout the flight, the spin section of both sections will constantly decay due to the spin-damping moment, of which each section will contribute a different amount. When the brake disengages the two sections are no longer radially coupled and will, due to the discrepancy of the spin-damping moments of each section, continue until they reach a new equilibrium. Figure 4.3.4 depicts the spin rates of the front and aft sections throughout the initial section flight. Each phase of flight is as follows:

1. During the launch phase, the projectile is ballistically accelerated while the brake mechanism is locked. Both the forward and aft sections accelerate to the natural launch spin rate of the system ω_0.

2. During free flight of the projectile, with the brake mechanism engaged, the spin rate of the two sections will decay at a rate proportional to the combined spin-damping moment of the two sections.

3. At the point the lock mechanism is disengaged, the spin rate of the front section will begin to decelerate quicker since, by design it has a higher spin damping moment and a lower mass than the aft section. The behaviour of the front section spin rate in the moments immediately following the de-coupling is referred to as the `BiasON` function, which can also be a generic mathematical function chosen to model that behaviour.

4. The de-coupled steady state is achieved when the two halves reach a new equilibrium. During this phase, the spin rate of the two sections decays individually, according to the spin-damping moment of the two sections, as well as any friction from the bearing attaching the two sections.

5. When the lock mechanism is re-engaged, the front section will rapidly accelerate due to the sudden increase in 'friction' through the bearing. The sudden acceleration of the front section also accompanies a sudden deceleration of the aft section. The spin speeds of both sections will converge again as equilibrium is achieved. The new

whole body ω will be closer to the ω of the aft section before the locking, rather than the forward section before the locking, because the aft section is more massive and thus has a higher inertia.

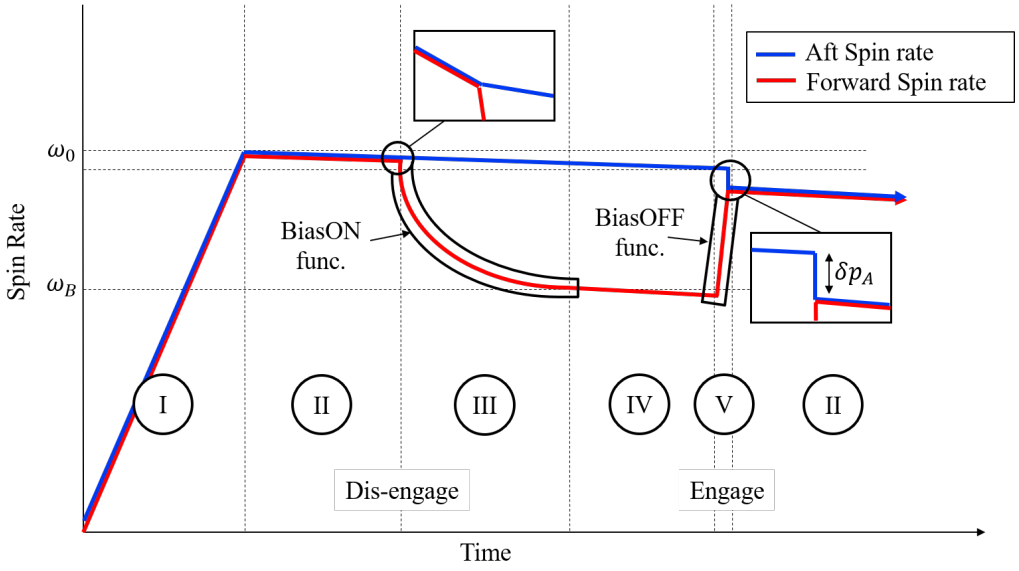

FIGURE 4.3.4 Spin rates of dual-spin sections throughout various flight phases
† - Phase II is repeated because both instances represent free flight

4.3.3 Procedure for deriving latax

The behaviour and spin rate of the two sections evolves according to the dynamics of the system, which is itself a function of many different factors such as bearing torque and spin damping moment. To gain a practical understanding of the system's capabilities, it is prudent to approximate the behaviour with a function. In this sense, the performance and capabilities can be measured against any system metric and extreme cases can be analysed. A procedure is therefore defined whereby the two functions `BiasON` and `BiasOFF` defined above, are used to generate the latax response. *i.e.* for a given system behaviour, modelled by the functions `BiasON` and `BiasOFF`, the resulting latax $\tilde{a}$ can be numerically mapped for varying bias coordinates, $[\phi_{ON}, \phi_{OFF}]$. The bias manoeuvre can be defined by ϕ_{ON} and ϕ_{OFF}, which are the values of phi at which the `BiasON` and `BiasOFF` functions begin respectively. While the bias is no longer symmetrical, the use of ϕ_B and ϕ_a is still useful.

Now, ϕ_B defines the mid-point between ϕ_{ON} and ϕ_{OFF} while ϕ_a is the half distance.

$$\phi_a = \frac{\phi_{\text{OFF}} - \phi_{\text{ON}}}{2} \tag{4.58}$$

$$\phi_B = \phi_{\text{ON}} + \phi_a \tag{4.59}$$

The procedure for identifying the latax is exactly as described in §4.3, except the values of δV and τ are found by numerical methods instead of analytically solving them, due to the arbitrary complexity of the `BiasON` and `BiasOFF` functions. In this instance, it is still assumed that there is no global decay of ω_0 or ω_B caused by spin damping. The key change here is that the switching between the two speeds is now governed by a function instead of being instantaneous. Figure 4.3.5 shows the resulting $\omega(\phi)$ function when `BiasON` and `BiasOFF` connect two spin states, at the chosen points $[\phi_{ON}, \phi_{OFF}]$. Since $\tau = \int_0^{2\pi} \omega^{-1}(\phi).\mathrm{d}\phi$, τ can be found by numerically integrating the inverse of the function $\omega(\phi)$.

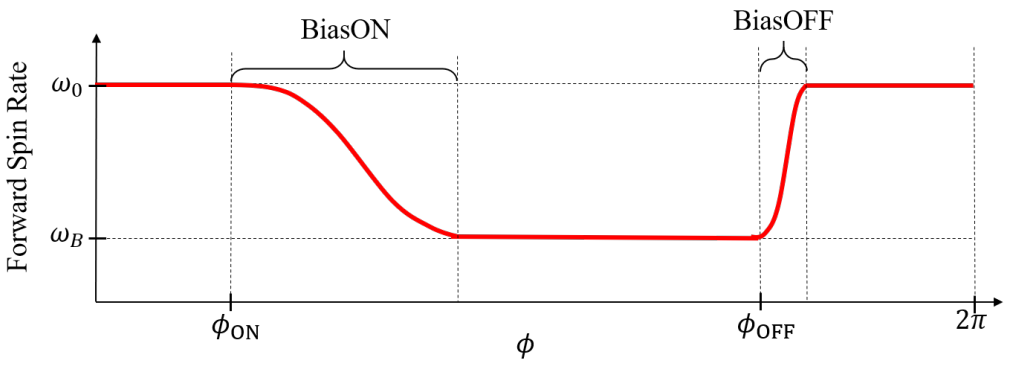

FIGURE 4.3.5 Example $\omega(\phi)$ created by inserting the chosen BiasON and BiasOFF functions at ϕ_{ON} and ϕ_{OFF} respectively

Figure 4.3.6 shows an instance in which the `BiasON` and `BiasOFF` functions overlap. In this case, ω will evolve according to the `BiasOFF` function, since at this point the locking mechanism would be engaged. In addition, when the `BiasOFF` function is triggered at ϕ_{OFF}, the evolution of ω should be properly defined by the `BiasOFF` function as being proportional to the speed difference, as opposed to the current spin rate. This ensures that if ϕ_{OFF} is triggered at a later time, then ω is prevented from assuming the value it would have at this point, had the `BiasOFF` function been incorrectly defined from some arbitrary fixed point. Lastly, both `BiasON` and `BiasOFF` can be considered functions of the current

spin rate and the target spin rate. This again, reflects the behaviour of a dynamic system, *e.g.* where the force returning a displaced spring is proportional to the magnitude of the displacement, as opposed to the distance location.

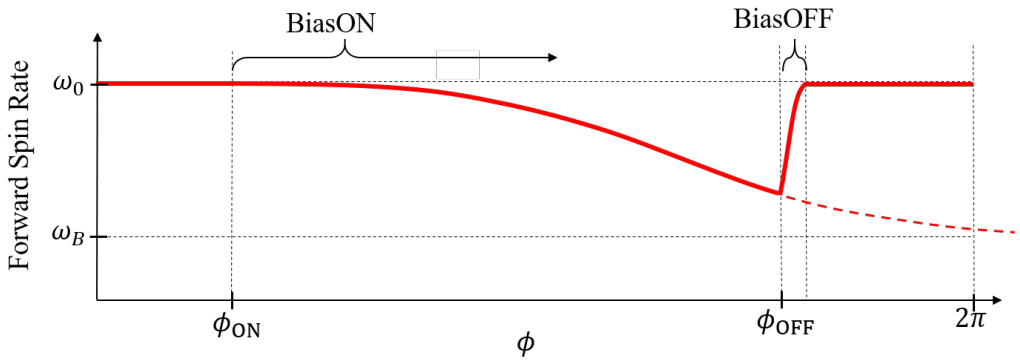

FIGURE 4.3.6 Example $\omega(\phi)$ when BiasON and BiasOFF functions overlap

Next, the net impulse of one rotation must be found, which requires knowing both the magnitude and direction of the force at every point in time. Since $\omega(\phi)$ is the known function, one cannot simply integrate this analytically to find $\phi(t)$, since $\omega(\phi)$ is not a function of time. However by definition, ω is the gradient at every point on $\phi(t)$ and thus numerical integration methods will work. Figure 4.3.7 illustrates a plot of $\phi(t)$ one can expect to find from integrating a plot resembling fig. 4.3.5. Initially, the gradient $\phi(t)$ is high, since the system begins the unbiased speed ω_0. At ϕ_{ON}, the `BiasON` function is initiated and the gradient decreases until it reaches the bias value ω_B, where it remains for the duration of the bias. At ϕ_{OFF} the bias is instructed to end and the gradient increases again throughout the duration of `BiasOFF`, back up to ω_0.

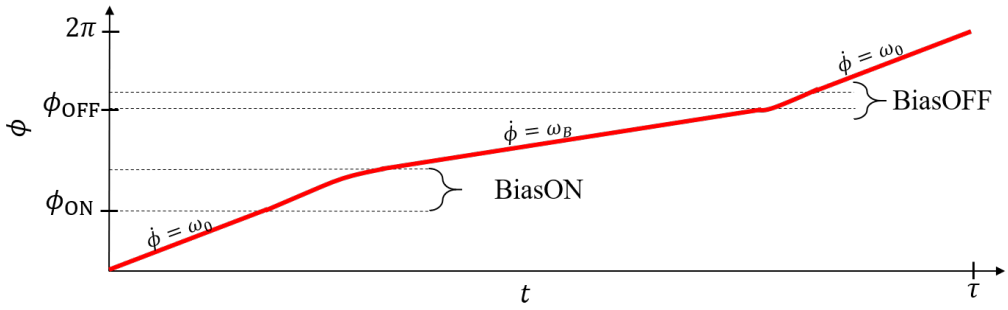

FIGURE 4.3.7 Example $\phi(t)$ produced by numerically integrating $\omega(\phi)$ with chosen BiasON and BiasOFF functions

Since $\phi(t)$ is the direction component of the force vector, it can be used to numerically

solve for the resulting impulse, since τ has been computed. Since both δV and τ are now know, $\tilde{a}$ can be computed. Figure 4.3.8 shows the flow of information and order of operations for computing $\tilde{a}$ from $\omega(\phi, \phi_{\text{ON}}, \phi_{\text{OFF}})$. In summary, the bias functions and coordinates are used to create $\omega(\phi)$. The inverse of $\omega(\phi)$ is integrated numerically to calculate τ, which is used in conjunction with the instantaneous integrations of $\omega(\phi)$ to produce $\phi(t)$. From this, δV can be computed and finally $\tilde{a}$ can be computed for the given inputs. This process can be repeated as necessary to map the latax response over the bias range, highlighting any dead zones that may be present for the system configuration.

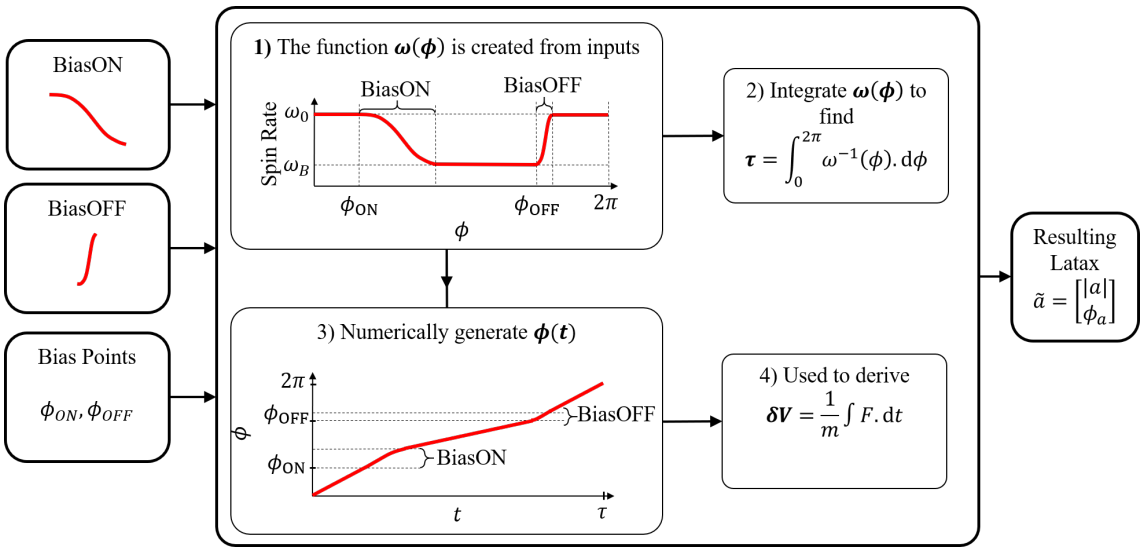

FIGURE 4.3.8 How BiasON/BiasOFF functions are used to generate $\tilde{a}$ for a system

Non-instantaneous method reduces to instantaneous results

To ensure this numerical method is in agreement with the instantaneous switching calculations, the `BiasON` and `BiasOFF` functions are modelled to be instantaneous switches. While this entirely defeats the point of introducing the functions, with this simplification, the system is now behaving as it does in the simplified model from §4.3.1. Firstly, the analytic predictions from equation 4.50 predict the a_{mag} which results from a given ϕ_a in the simplified model; this equation was plotted in fig. 4.3.2A. Secondly, the numerical methodology described in §4.3.3 is executed for $\phi_a \in [0, \pi/2]$, with the `BiasON` and `BiasOFF` functions being instantaneous switching. Lastly, the dynamic model is run multiple times, manually triggering the biases for each point in the analytic and numerical sweeps, for

$\phi_a \in [0, \pi/2]$. The results are shown in fig. 4.3.9.

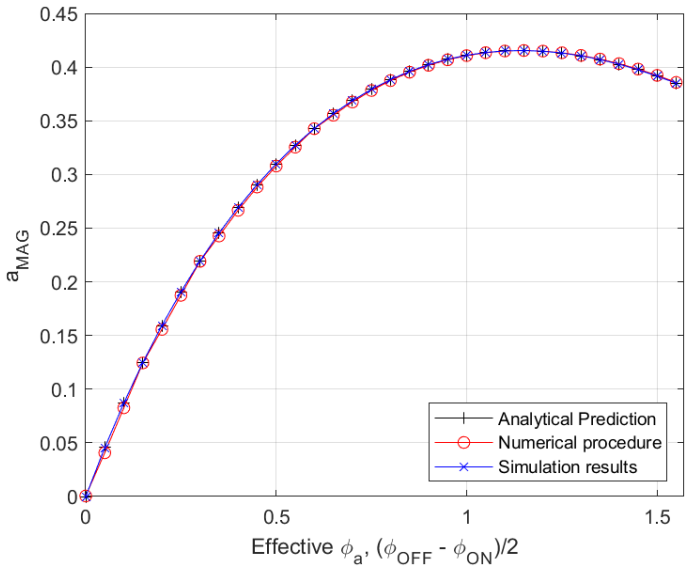

FIGURE 4.3.9 Analytic and Numeric predictions of simple latax response for varying ϕ_a

Note that because the bias is no longer symmetric, ϕ_a has been replaced with the effective ϕ_a, which is computed from the bias points as $(\phi_{OFF} - \phi_{ON})/2$, instead of when the spin rate actually assumes the biased and unbiased spin rates. Both the analytic predictions and the numerical method are in good agreement with the results of the simulations. Importantly, the simulations and numerical methods support the discussion of §4.3.1 about the deadzones, where extreme values of ϕ_a do not translate to an increases latax, due to the increased time spent accruing the impulse. Figure 4.3.10A shows the error of each prediction against the simulation results

Figure 4.3.10B shows the effects of modifying the sample interval on the accuracy of the numeric predictions. That is, the step size in the ϕ array used to calculate $\omega(\phi)$ and therefore, $\phi(t)$. It can be observed that as the sample frequency of the numerical method increased, there was no change in the magnitude of the error, indicating that the error is unlikely to be caused by reproduction and interpolation errors, rather it is a present and real error likely caused by machine rounding errors, especially since the error is inversely proportional to the numerical value of ϕ_a for the analytic, numeric and simulation results.

The important conclusion to draw from these results is that the numerical method of computing latax response is valid, when analytical solutions are unfeasible, such as for arbitrarily complex bias transition functions. In addition, the resolution with which

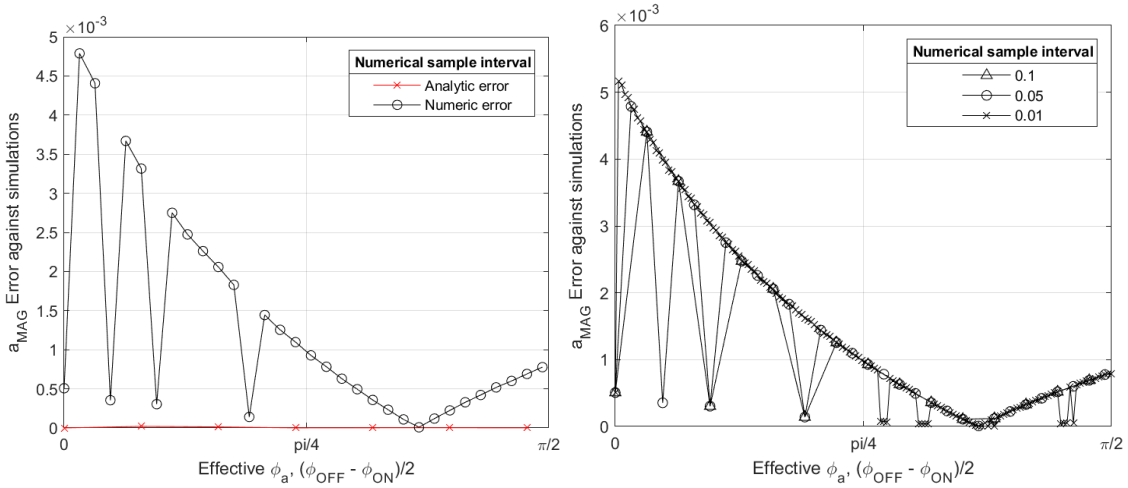

(A) Error (B) Varying sample intervals

FIGURE 4.3.10 Error of Analytic and Numeric predictions against simulation results

the function $\omega(\phi)$ is defined has no effect on the accuracy of the numerical analysis in predicting the latax of the system (behaving according to the specified $\omega(\phi)$). As such, $\omega(\phi)$ need only be defined to a resolution which is capable of producing a sufficiently smooth latax range, to then be used by the GL. *i.e.* if the GL requires the latax to be distinguishable at 0.1ms^{-2} intervals, then the step size of the ϕ array used in the numerical domain must be sufficiently small that the step size of the latax output in the numerical range can accommodate a 0.1ms^{-2} demand. It is also possible that the function could be generated roughly to conserve resources during the analysis period, then interpolated after the fact in regions of interest.

Numerical procedure example, introducing ϕ_a offset from ϕ_B

Let the `BiasON` and `BiasOFF` functions be defined by the following:

$$f_{\text{ON}} = k_{ON}\left(\frac{\omega-\omega_B}{\omega_0-\omega_B}\right), \quad k_{ON}=0.2 \tag{4.60}$$

$$f_{\text{OFF}} = k_{OFF}\left(1-\frac{\omega-\omega_B}{\omega_0-\omega_B}\right), \quad k_{OFF}=1 \tag{4.61}$$

where k_{ON} and k_{OFF} are the decay and growth rates of the ON/OFF switching functions respectively. A higher switching rate produces a function which transitions faster from

one state to another. The bias coordinates are chosen as

$$\begin{bmatrix} \phi_{\text{ON}} \\ \phi_{\text{OFF}} \end{bmatrix} = \begin{bmatrix} \pi/2 \\ 3\pi/2 \end{bmatrix} \tag{4.62}$$

Using this information, the function $\omega(\phi)$ is constructed, which is shown in fig. 4.3.11. This function is numerically integrated to produce both value of τ, as well as the function $\phi(t)$, which is shown in fig. 4.3.12. Both latax response $\tilde{a}$ and the rotation time τ are shown in table 4.2

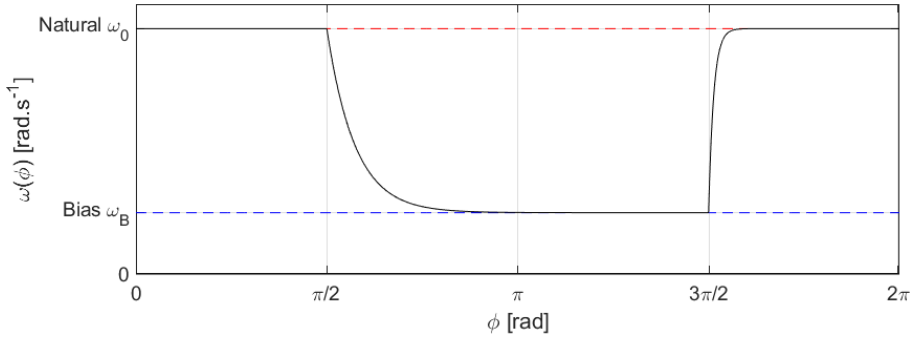

FIGURE 4.3.11 $\omega(\phi)$ for equation 4.60 with $[\phi_{\text{ON}},\ \phi_{\text{OFF}}] = [\pi/2,\ 3\pi/2]$

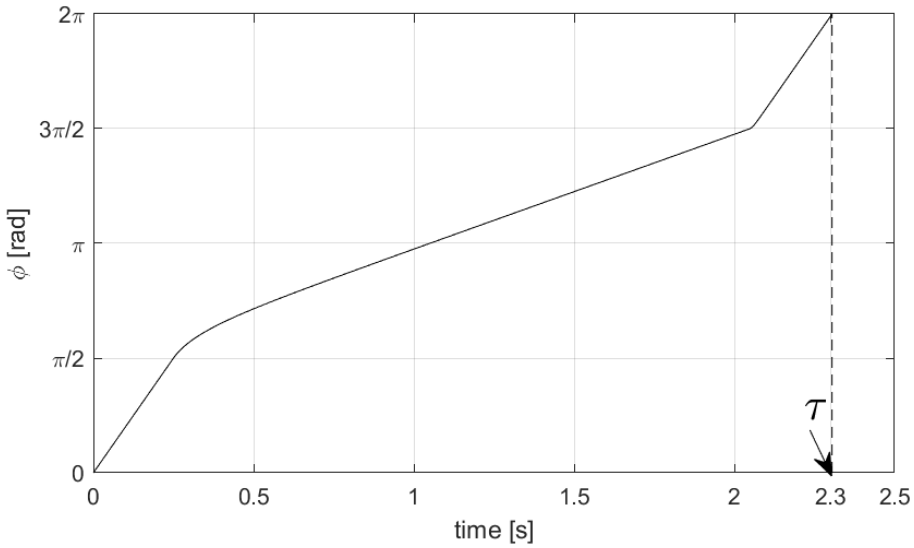

FIGURE 4.3.12 Resulting $\phi(t)$ from $\omega(\phi)$ generated in fig. 4.3.11

With that function generation demonstrated, the latax response can be evaluated by varying ϕ_{OFF} and ϕ_{ON}, for $\phi_{\text{OFF}} - \phi_{\text{ON}} \in [0, \pi]$. Figure 4.3.13 shows the a_{Mag} which is generated for every value of ϕ_a, for both the instantaneous switching simplified model

Parameter	Value
$\lvert\tilde{a}\rvert$	$0.3970[\mathrm{ms}^{-2}]2$
ϕ_a	$3.3507[\mathrm{rad}]$
τ	$2.3048[s]$

TABLE 4.2 Numerical method results for equation 4.60 with $[\phi_{\mathrm{ON}},\ \phi_{\mathrm{OFF}}] = [\pi/2,\ 3\pi/2]$

and the non-instantaneous model from eq. 4.60. It is noted that the value of ϕ_a at which $\tilde{a} = \tilde{a}_{\max}$ increases as the switching functions become less instantaneous. In addition, the rate at which $\tilde{a}_{\max}$ increases depending on ϕ_a decreases as the switching functions become less instantaneous. At low values of ϕ_a, the situation in fig. 4.3.6 is observed, where there is insufficient time for the system to transition into the biased state and therefore cannot 'accrue' acceleration before the bias ends.

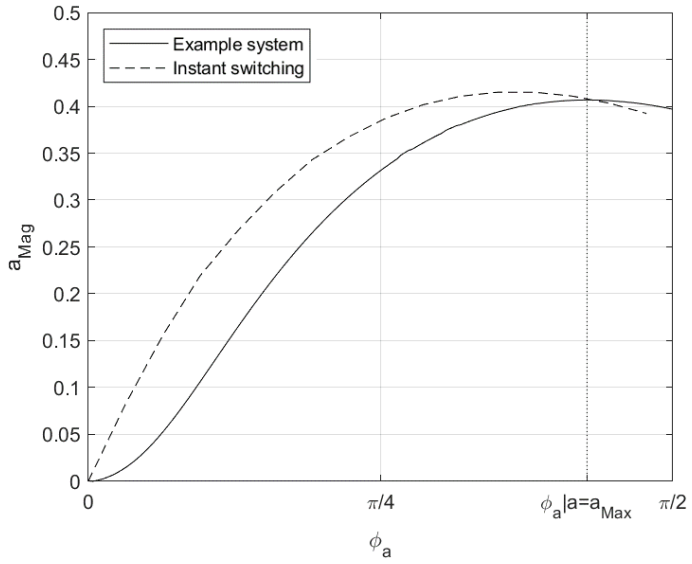

FIGURE 4.3.13 Latax generated across for every bias size for bias functions in eq. 4.60

While fig. 4.3.13 shows the magnitude of the latax response across a range of bias sizes it is also important to observe how the direction of latax changes for non-instantaneous switching. Firstly, it must be noted how much the latax direction a_ϕ is offset from the centre of the bias coordinates, ϕ_B. Secondly, it should be understood whether this offset is then itself scaled proportional to the magnitude of the bias ϕ_a. For a given ϕ_{ON} and ϕ_{OFF}, the value of ϕ_a and ϕ_B are calculated from equation 4.58. It is of no importance what the absolute values of ϕ_{ON} and ϕ_{OFF} are, only the distance between them, since it

is the offset of a_ϕ from ϕ_B that is being observed, rather than the angles themselves. The numerical analysis procedure is then conducted as above, to compute τ, a_{Mag} and a_ϕ. Each increasing value of ϕ_a produces a specific a_ϕ, which is compared against ϕ_B. Figure 4.3.14 shows the offset of the system described in eq. 4.60 for varying ϕ_a.

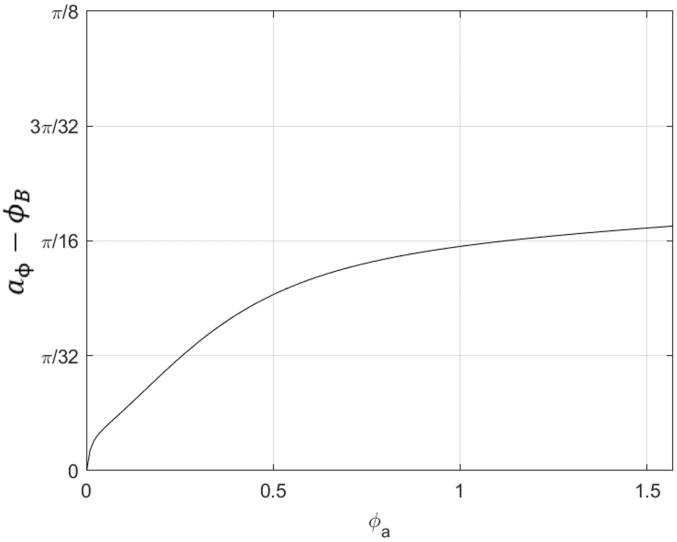

FIGURE 4.3.14 Offset of a_ϕ from ϕ_B as a result of non-instantaneous switching

A slow bias activation means the force vector is not travelling as slowly as it could in the bias window, if there is an instantaneous de-activation then the actual acceleration a_ϕ will be ahead of the intended bias centre ϕ_B. A slow bias deactivation means the force vector keeps acting for longer than it should after the bias window which, if there is an instantaneous activation, also results in the actual acceleration a_ϕ being ahead of the intended bias centre ϕ_B. This means that any non-instantaneous switching function results in an actual acceleration a_ϕ being ahead of the intended bias centre ϕ_B. Thus, $a_\phi > \phi_B$ and following from this it can be seen that $a_\phi - \phi_B$ will always be positive [†], which is shown on figure 4.3.15. Next, the effect of varying the ratio of switching function rates k_{ON}/k_{OFF} will be investigated. The bias coordinates are fixed at $\phi_{ON} = \pi/2$ and $\phi_{OFF} = 3\pi/2$, resulting in a fixed value of $\phi_a = \pi/2$. Then, a value of k_{OFF} is chosen, varying from 0.5 to 2.5 in increments of 0.5. The numerical procedure is conducted for values of k_{ON} as a fraction of these chosen k_{OFF} values, such that k_{ON}/k_{OFF} ranges from 0 to 1. This range is chosen because the bias activation function is always longer than the deactivation function, hence the rates follow the inequality $k_{ON} < k_{OFF}$ and so it is

[†]Assuming there is wrapping

necessitated that $(kON/kOFF) < 1$. The results of this are shown in fig. 4.3.15. Figure 4.3.15A shows a broad sweep for $kON/kOFF \in [0,1]$, while fig. 4.3.15B shows a higher resolution sweep on values of $k_{ON}/k_{OFF} \in [0, 10e-3]$.

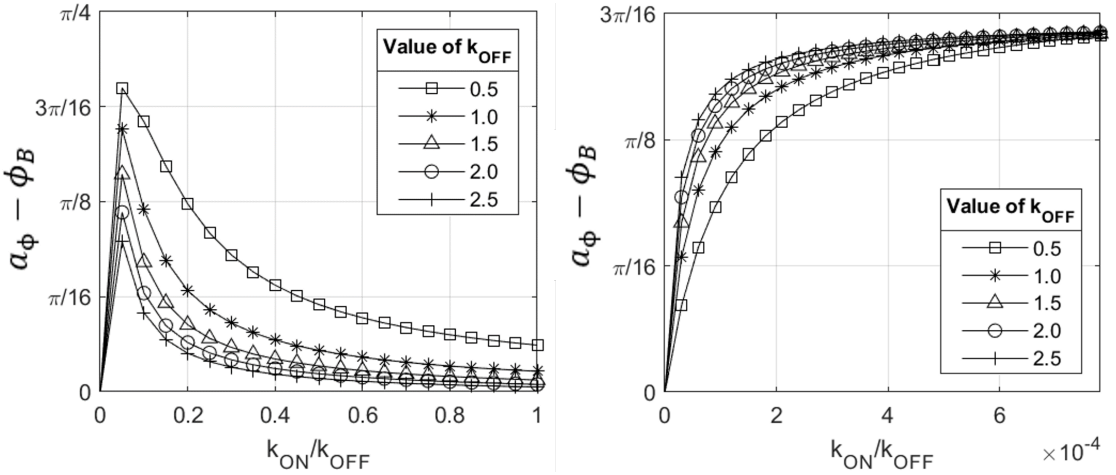

(A) Full range (B) Close up

FIGURE 4.3.15 Effect of modifying k_{ON}/k_{OFF} on offset for various k_{OFF}

As the switching rates get larger, the switching becomes more instantaneous and the offset decreases. This is shown on figure 4.3.15A, as lines representing higher values of k_{OFF} give lower values of $a_\phi - \phi_B$ across all ratios. As $k_{ON}/k_{OFF} \to 1$, the rates assume their maximum values for the fixed k_{OFF}. Higher rates equate to faster switching and so the offset is lower. This is also seen on the figure, as $k_{ON}/k_{OFF} \to 1$ for all values of k_{OFF} give a lower offset. As expected for the opposite of this, lower values of k_{ON}/k_{OFF} increase the offset. In the limit that $k_{ON}/k_{OFF} \to 0$ (and thus $k_{ON}zrightarrow0$) the bias activation is so slow that there is effectively no bias manoeuvre at all. There is no change in ω induced by the function over the duration of the bias and hence there can be no overshoot. The resulting latax reduces to $\tilde{a} = [a_{\text{Mag}}\ a_\phi] = [0\ \phi_B]$. This is also supported by the figure, as $k_{ON}/k_{OFF} \to 0$ yields an offset of 0 for all values of k_{OFF}.

As is shown in fig. 4.3.15A, there is a point of inflection around $k_{ON}/k_{OFF} = 9 \times 10^{-4}$, at which the higher values of k_{OFF} begin to produce the highest overshoot errors. This is an artefact of this particular investigation. While each data point is equally spaced on the figure, the values it represents are not. The values comprising the line representing $k_{OFF} = 0.5$ are all 5 times smaller than those data points in the line representing $k_{OFF} =$ 2.5. In the extreme region of $k_{ON}/k_{OFF} \to 0$, this results in k_{ON} approaching zero 5 times

quicker. This phenomenon is present in the region of $k_{ON}/k_{OFF} \to 0$ because the rates are too small to cause a significant offset.

For small values of k_{ON} the transition becomes less instantaneous. Figure 4.3.16A is a modified version of fig. 4.3.5, highlighting how a_ϕ can be defined in terms of the area. Since the integral of ω dictates the magnitude of the resulting latax, the centre point of the integral denotes the angle. The latax direction a_ϕ can thus be defined as

$$a_\phi := \qquad A_{ON} = A_{OFF} \tag{4.63}$$

or

$$a_\phi := \qquad \int_{\phi_{\mathrm{ON}}}^{a_\phi} (\omega_0 - \omega(\phi)).\mathrm{d}\phi = \int_{\mathrm{a}_\phi}^{\phi_{\omega_0}} (\omega_0 - \omega(\phi)).\mathrm{d}\phi \tag{4.64}$$

where

$$\phi_{\omega_0} \mid f_{\mathrm{OFF}}(\phi_{\omega_0}) = \omega_0 \tag{4.65}$$

While this does not simplify the procedure for arbitrarily complex switching functions, this representation of a_ϕ is useful for explaining the inflection phenomena for small values of k_{ON} shown in figure 4.3.15. For normal values of k_{ON} shown in fig. 4.3.16A there will be some offset between a_ϕ and ϕ_B. As k_{OFF} decreases, the bias on function gets slower and a_ϕ increases so that the areas on either side remains balanced. There eventually comes a critical point, represented in fig. 4.3.16B where any further decrease of k_{ON} requires that a_ϕ *decreases* in order to keep equal areas either side.

Transition functions longer than rotation period τ

While the previous sections have all considered the latax of the system from one revolution, there might be an instance in which the duration of the switching functions is significantly longer than τ. In this case, the system must be left under the influence of the switching functions for multiple revolutions and the latax sampled over as many revolutions as it takes to activate and deactivate the bias. To consider the offset of the biases over multiple rotations, ϕ_B will still be used, but the location of ϕ_{ON} and ϕ_{OFF} will be superimposed onto a singular τ window. Figure 4.3.17 shows an example system where the switching functions are significantly longer than the duration of one rotation, meaning the system un-

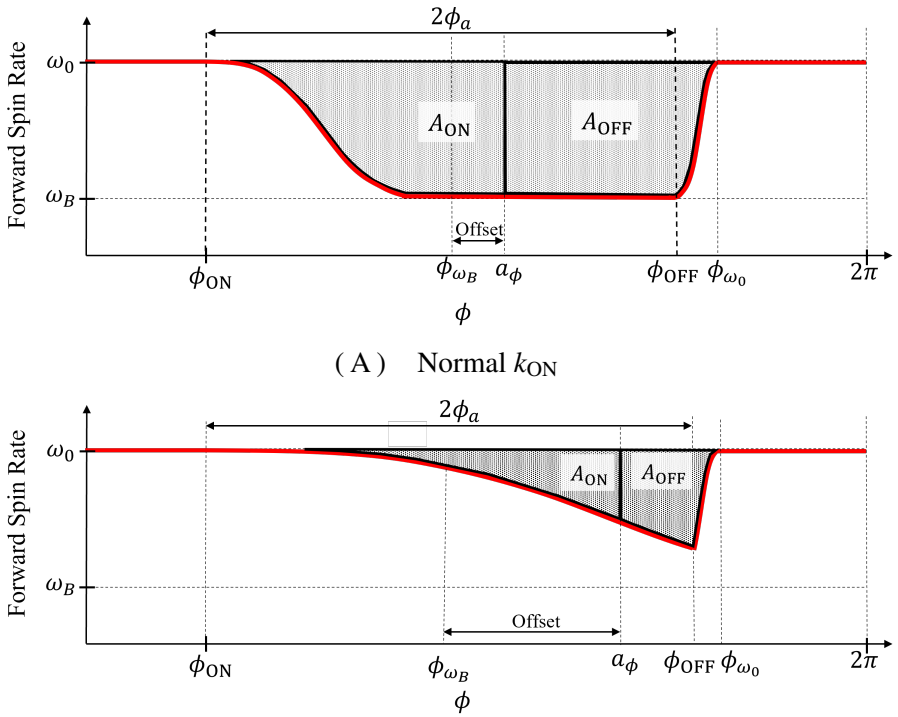

FIGURE 4.3.16 How offset of a_ϕ from ϕ_B can be interpreted from integrals of $\omega(\phi)$

dergoes 4 full rotations before the bias is fully engaged then fully disengaged. Computing the resulting latax from this system using the numerical method is functionally identical to the previous cases except that the integrals are evaluated over all of the rotations. Due to the commutative nature of integrals, the rotations can either be considered individually and then compiled at the end or considered as one full episode. The main difference for a bias over multiple rotations is that the magnitude of the latax is considerably lower, since the system spends longer in the slower, bias spin state ω_B.

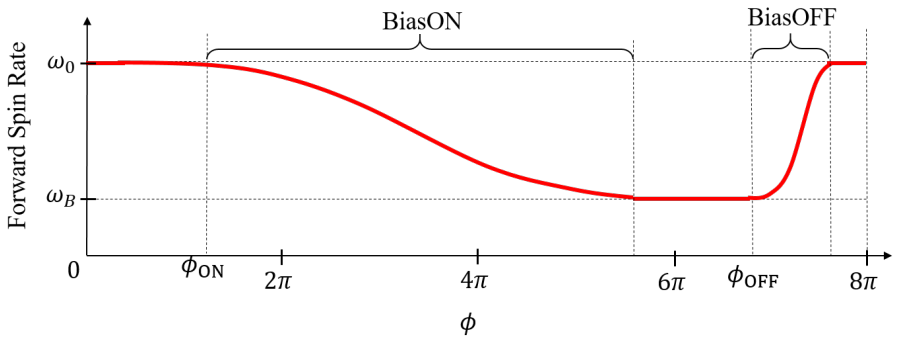

FIGURE 4.3.17 Example $\omega(\phi)$ when the switching duration is longer than τ

Any fully symmetric rotations can be completely neglected from the perspective of analysing latax, as symmetrical rotations have no contribution to the net impulse. Figure 4.3.18A shows an $\omega(\phi)$ signal which has been constructed with one entirely redundant bias rotation during the bias, highlighted in red. In this figure, when $\phi \in [4\pi, 6\pi]$, $\omega(\phi) = \omega_B$ which results in no net contribution to the impulse. The only purpose this section serves is to increase the time taken for all rotations in the bias, $\Sigma\tau$. The spin signal $\omega(\phi)$ should be designed without this detriment, and a suitable alternative such as that shown in fig. 4.3.18B, should be used instead. The result of eliminating this redundant section is evident from the latax results in the captions of figure 4.3.18: eliminating the redundant rotation reduces the total time from $\Sigma\tau = 14.46$ to $\Sigma\tau = 10.46$ and the total acceleration is therefore increased from $\tilde{a} = 0.028$ to $\tilde{a} = 0.039$. This change in time of 4s also agrees with theory, since $\omega_B = \pi/2[\text{rad.s}^{-1}]$ over one complete revolution takes 4s.

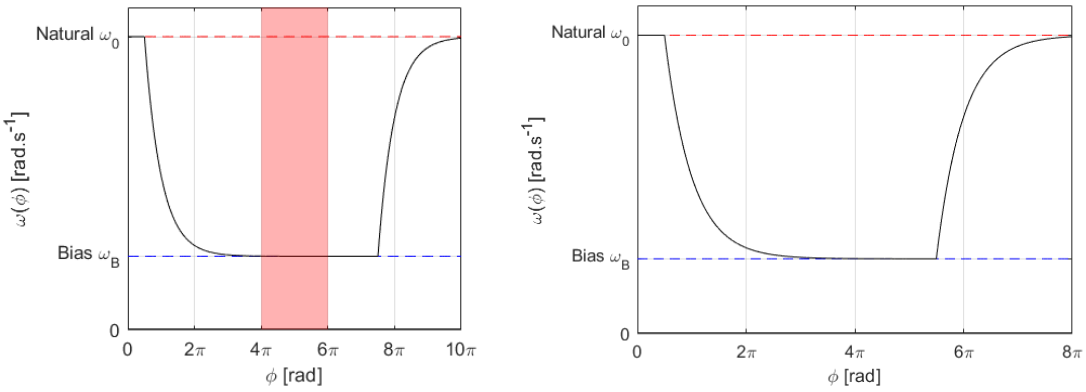

(A) $\Sigma\tau = 14.46$, $\tilde{a} = 0.028$ $a_\phi = 3.91$ (B) $\Sigma\tau = 10.46$, $\tilde{a} = 0.039$ $a_\phi = 3.91$

FIGURE 4.3.18 Unnecessary rotations during bias increase τ reduce effective latax

4.3.4 Design parameters affecting bias manoeuvre

This section discusses the design parameters available to the designer, which can be modified to affect different aspects of the bias manoeuvre. The main aspects of the bias manoeuvre which a designer would desire to control are the switching time to the biased speed T_{ON} and switching time to the unbiased spin speed T_{OFF}, as well as the biased roll rate ω_B itself. It is desirable to have the shortest T_{ON} and T_{OFF} possible as this allows the highest fidelity control and therefore more bias manoeuvres for the whole flight. Both

switching speeds and ω_B depend upon the relation between the torques acting on the front section. The acceleration from friction in the bearing $\tau_{F,A}$ and deceleration from the roll damping moment. The net torque from resolving these contributions about the bearing will cause the front section to accelerate, which affects T_{ON} and T_{OFF}, but also a variation between them causes equilibrium to be reached at a different roll rate, which affects ω_B. From chapter 3, the friction torque from the bearing is given by

$$\tau_{F,A} = \frac{1}{2}\rho SD\, C_{A0}\, \text{sgn}(p_A - p_F)(k_s + k_v|p_A - p_F|) \tag{4.66}$$

and the spin damping moment, assuming the entire contribution comes from the forward section with the asymmetric aerodynamic features, is given by

$$M_{l_P} = \left(\frac{\bar{q}SD^2 p_F}{V}\right) C_{l_P} \tag{4.67}$$

From these equations is can be seen that the friction in the bearing $\tau_{F,A}$ is a function of the the total body longitudinal coefficient C_{A0}, the static friction coefficient k_s, viscous friction coefficient k_v and the spin section discrepancy $p_A - p_F$. The spin damping moment M_{l_P} is a function of the spin damping coefficient C_{l_P} and forward spin rate p_F.

Figure 4.3.19 shows the relation between $\tau_{F,A}(C_{A0}, k_s, k_v, (p_A - p_F))$ and the negative $M_{l_P}(C_{l_P}, p_F)$ as a function of front spin rate p_F. The spin damping moment will always produce a torque opposing the spin direction of the front section, hence it will always be negative. However on the figure, it is plotted as a positive, so that its absolute value can be more easily compared with the bearing friction. In addition, one would conventionally think of friction as an adverse and so negative force, however in this system it is the driving force keeping the front section spinning in the desired direction and is hence, positive. Another behaviour of note from fig. 4.3.19 is the magnitude of the bearing friction. When the front and aft section spin rates are equal, there is no friction in the bearing because there is no spin discrepancy; this is evident on the figure where $\tau_{F,A} = 0$ where $p_F = p_A$. If $p_F < p_A$, then the bearing friction will be positive, since it is acting to accelerate the front section. Conversely if somehow $p_F > p_A$, then the bearing friction would act to slow the spin rate of the front section. As one would logically expect for the spin damping moment, the figure shows $M_{lp} > 0 \; \forall \; p_F > 0$

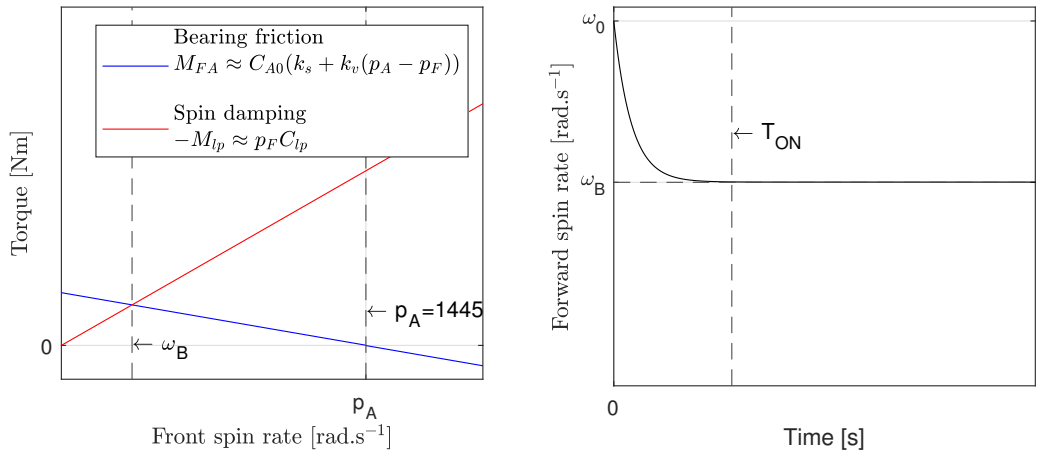

(A) Torque equilibrium (B) Spin rate response

FIGURE 4.3.19 Relationship between torques which affect bias manoeuvre

When the spin damping and bearing friction torques are in equilibrium ($\tau_{F,A}(p_F) = M_{l_P}$) it is possible to solve for the equilibrium forward spin rate; which is by definition the bias speed ω_B. So $p_F = \omega_B$ when the equation

$$\frac{1}{p_F} sgn(p_A - p_F)\,(k_s + k_v|p_A - p_F|) = -VD\frac{C_{lp}}{C_{A0}} \tag{4.68}$$

is satisfied. This coincides with the value of p_F on fig. 4.3.19 where the lines intersect. The result of the system evolving under these forces is shown in fig. 4.3.19B, which is a MATLAB output representing the depiction of fig. 4.3.5 (pg. 147). Here it is apparent that the time it takes after the bias manoeuvre has begun, until the system reaches the new equilibrium speed ω_B is the time, T_{ON}.

As stated however, the torques $\tau_{F,A}(C_{A0}, k_s, k_v, (p_A - p_F))$ and $M_{l_P}(C_{lp}, p_F)$ are both functions of variables which are available to the designer to alter to effect a change in the behaviour of the bias manoeuvre. The adjustable parameters from the torque equilibrium are C_{A0}, k_s, k_v and C_{lp}. Since the net torque causes the acceleration it is obvious that the acceleration can be changed by altering the mass and thus m_F is also a design variable. It is now possible to vary these parameters and observe how the response changes, such that designers know how the parameters should be tuned in relation to one another to achieve the desired effect.

Firstly, by varying C_{lp} we can observe the change in behaviour shown by fig. 4.3.20.

We can see from fig. 4.3.20A that varying C_{lp} only alters the spin damping moment, as expected. In addition, as C_{lp} increases, the equilibrium point is reached at a lower frontal spin rate. This is because an increasing C_{lp} means the spin-damping moment is greater by a proportional increase, thus it can counteract a larger bearing friction before being opposed completely. The spin rate response can be seen in fig. 4.3.20B, whereby and increasing C_{lp} causes the spin rate to tend towards incrementally lower equilibrium ω_B values. However, the increase in C_{lp} causes no significant decrease in response time T_{ON} beyond what one would expect the system to achieve from simply tending towards a lower target speed. This is because the force and therefore acceleration increases proportional to the variation of C_{lp}.

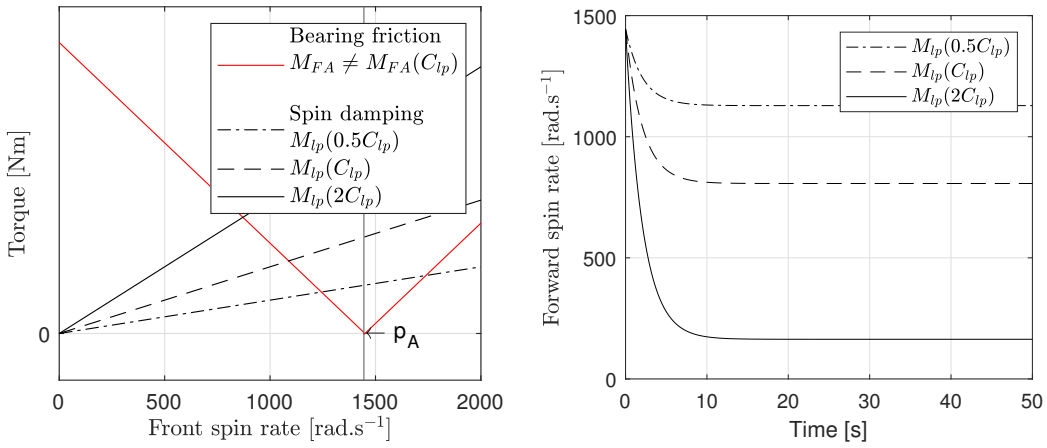

(A) Torque equilibrium (B) Spin rate response

FIGURE 4.3.20 Effect of varying C_{lp} on torque equilibrium and spin response

Next, fig. 4.3.21 shows the effect of varying the bearing friction coefficients. The friction is varied here simply by doubling the respective static (k_s) and viscous (k_v) coefficients. Only the bearing friction moment varies, as can be seen in fig. 4.3.21A. Logically, an increase in friction coefficients induces a greater restorative torque for a greater roll rate disparity. Similar to the variation of fig. 4.3.20A, it can be seen that increasing the friction coefficients leads to a higher equilibrium roll rate ω_B. However, from fig. 4.3.21B we can see that decreasing the friction coefficients results in a lower magnitude equilibrium spin rate ω_B, but also increases the time taken (T_{ON}) to reach it when compared to the response rates of fig. 4.3.20. This is because increasing the coefficients affects the equilibrium state as well as the motion of the spin speed moving towards the equilibrium state.

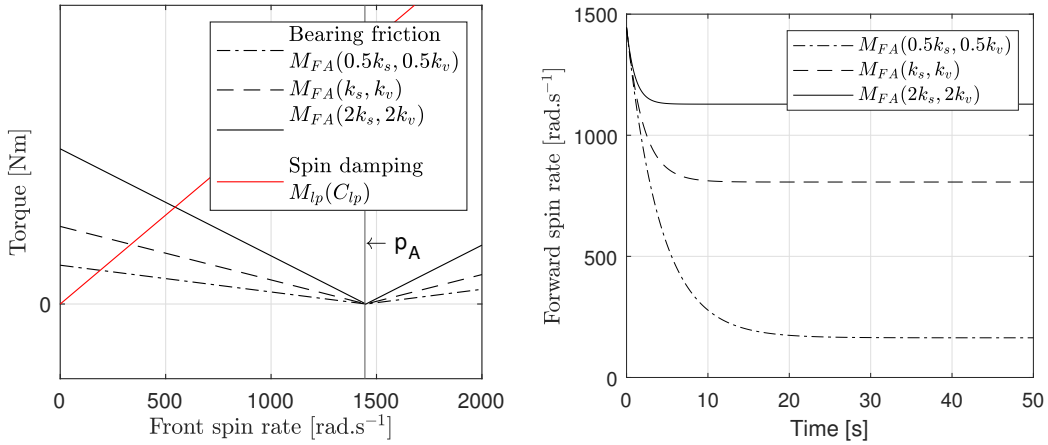

(A) Torque equilibrium (B) Spin rate response

FIGURE 4.3.21 Effect of varying bearing friction coefficients k_s & k_v on torque equilibrium and spin response

Finally, we can investigate the effect of modifying the front section mass, m_F. Because neither $\tau_{F,A}(C_{A0}, k_s, k_v, (p_A - p_F))$ or $M_{l_P}(C_{lp})$ depend on the mass, there is no effect on the torque equilibrium and as such, they are omitted. However, the resulting acceleration from resolving torques is affected and this is shown in fig. 4.3.22. As expected, the equilibrium spin speed ω_B is unaltered, however the switching time T_{ON} is altered. As m_F increases it is apparent that T_{ON} increases, which is logical following the decrease in acceleration caused by the $F = ma$ relation.

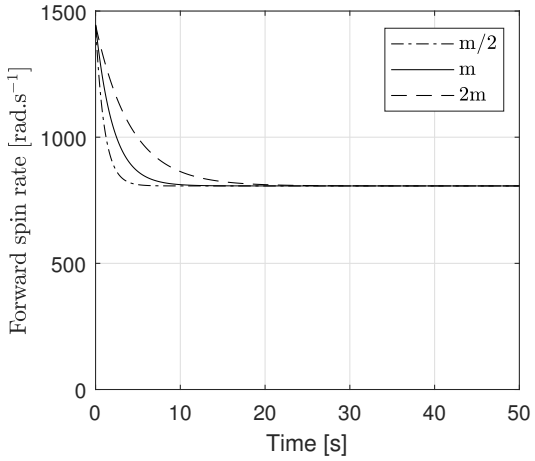

FIGURE 4.3.22 Effect of varying front section mass m_F on spin response

In summary, it is apparent that it is highly desirable from a control fidelity perspective to keep m_F as low as possible, to shorten the switching time in the bias manoeuvres. If the

designer needs to lower the bias speed ω_B, then it is advantageous to do this by increasing C_{lp}, rather than by decreasing the bearing friction as there is no associated increase in switching time. It is likely that the bearing friction will be fixed out of necessity, using which ever bearing technology is suitable for this use, and then achieving the maximum possible C_{lp} permitted by the geometry restrictions. This of course assumes that C_{lp} is not a function of p_F. However, C_{lp} is a function of V, and since both V and p_F are intrinsically linked, C_{lp} will likely be a function of p_F in much the same way C_D is a function of V.

Chapter 5

Guidance Laws

A traditional control architecture includes the projectile, with the accompanying actuator and body dynamics. The dynamic equations of motion governing the projectile and target are shown in chapter 3, which are implemented in simulations to emulate the real-world and test any proposed solutions. The actuator dynamics describe the operation of the physical hardware which enacts the controlling manoeuvres, and any simplifications which are made to the models. The actuator dynamics describe the transform between the controller input, for example an applied voltage, and the output, such as the missile latax. In §4.3 it was shown how the actuator dynamics are in this instance, combined into an overarching actuation mechanism. This additional step describes how the discrete, instantaneous latax can be viewed as continuous across consecutive roll rotations. The GL is responsible for deciding what latax is actually demanded of the projectile to successfully hit a target. The GL will consider things such as minimising controller effort, actuator saturations, target movements, impact angles *etc.* which were discussed in depth in §2.4.

Firstly, a Methodology is described whereby a Monte Carlo simulation is used to characterise aspects of the trajectory for a meaningful comparison of the GLs against desirable flight behaviour. The description of the velocity-based actuation mechanism in the preceding chapter naturally leads to a bespoke GL, whereby the bias points are kinematically linked to a velocity change of the system. This bespoke GL is discussed in detail, the parameters it contains and their effect on the system response are investigated in a parametric study and finally, these parameters are optimised using a genetic algorithm. The bespoke ΔV based GL can be modified to include the time taken for a rotation and thus demand a

latax instead of a ΔV. This can then be used in conjunction with the acceleration-based actuation mechanism considerations to provide more options for future implementations. A brief description of artificial intelligence and machine learning algorithms is then given. The most applicable and promising ideas are then proposed with a scenario for implementation. The reward function used to train the RL agents is then explored in depth and the reward space is explored. The agents are trained according to this reward function and their performance is analysed using the Monte Carlo methods described at the beginning of the chapter.

5.1 Monte Carlo batch analysis

To verify a GL is producing a satisfactory level of correction and also compare the performance of different GLs against each other, a Monte Carlo Simulation (MCS) procedure is defined here. This procedure runs a MCS with the projectile and target each being initialised with different speeds and positions in the picture plane. The projectile will then approach the target in the picture plane as dictated by a given GL. The approach behaviour and terminal miss distance after time has elapsed can then be quantified numerically and, under the assumption of large numbers, be compared meaningfully.

Table 5.1 shows the range in which the parameters can be randomised upon initialisation, unless otherwise explicitly stated. Once the projectile and target are initialised with randomised speeds and positions the simulation runs for a fixed time of 50s, unless otherwise specified. This time is completely arbitrary, but was specifically chosen to be sufficient to allow the projectile to close on the target given the maximum initial distances and also to hold a sufficient duration to observe the approach behaviour dictated by the chosen GL.

Each simulation produces a system response, a plot of radial miss distance against time, which is then normalised against the random initial distance. Multiple MCSs are run in a 'batch'. The average system response for a batch is formed by averaging the system responses for each individual simulation in the batch. Increasing the batch size results in an average system response which is sampled over a larger number of simulations and is thus more representative of the true system performance. If the average system response is

Parameter	Value (stationary)	Value (Moving)
(x_0, y_0)	$[-100, 100]$	$[-100, 100]$
(u_0, v_0)	$(0, 0)$	$[-1, 1]$
(ϕ_0)	$[0, 2\pi]$	$[0, 2\pi]$
(xT_0, y_{T0})	$[-10, 10]$	$[-10, 10]$
(u_{T0}, v_{T0})	$(0, 0)$	$[-1, 1]$

TABLE 5.1 MC initialisation values

compared for multiple batches of the same size, the maximum discrepancy between them is inversely proportional to the batch size; *i.e.* if a batch size is larger, there should be less variation in batch mean if the same batch size is run repeatedly. The demonstrate this, the projectile GL is set to move at 1m.s^{-1} radially towards the target, then at 0m.s^{-1} once it is within 1×10^{-3}m. Figure 5.1.1 shows the maximum discrepancy in average system response against time, for multiple batch sizes. For each batch size: 10^2, 10^3 simulations per batch *etc.*, five batches are run. The Normalised error at each point in time is compared across all five batches of the given batch size and the maximum difference is plotted on the figure.

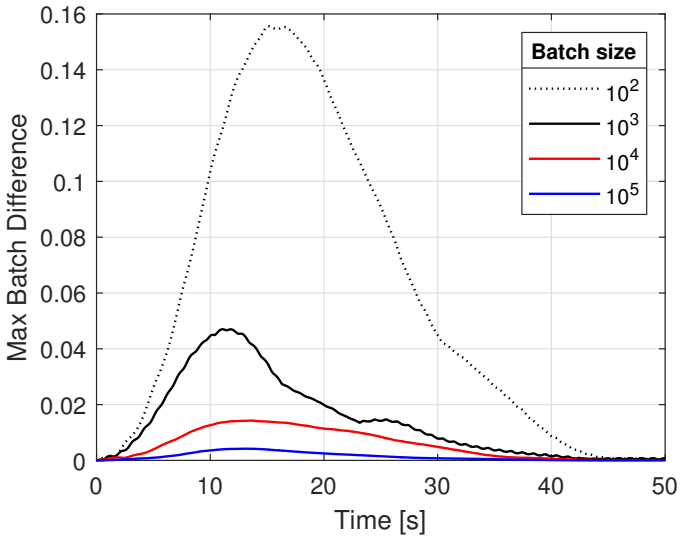

FIGURE 5.1.1 Instantaneous miss distance discrepancy between five batches of varying batch size

All batch sizes on the figure start with the same zero error, since the error curves which are being averaged are normalised, they each begin at their respective maximum error. In

addition, the same GL parameters are used in every simulation across all batch sizes, so the terminal error reduction capabilities produce the same steady state error in all cases; assuming of course the GL is in fact stable and that there is sufficient time in the simulation to allow a convergence. This results in the maximum error difference being small at the beginning and end of every batch. Table 5.2 shows the peak error difference, total integral error and computation time for each batch size. A batch size of 10^4 was chosen as the optimal trade-off between peak difference and computation time. While a batch size of 10^3 produced an integral error of the same magnitude as 10^4, the peak difference was unacceptably high.

Batch	Peak Difference	Integral Error	Time
10^2	15.56%	2.95×10^4	13 mins
10^3	4.70%	7.16×10^3	2 hrs
10^4	1.43%	2.90×10^3	22 hrs
10^5	0.42%	6.88×10^2	9 Days

TABLE 5.2 Maximum error against computation time

The system response of each individual simulation is normalised against the initial distance error, which was in turn randomised at the beginning of each simulation. The instantaneous normalised error for and individual simulation, ε_t is given by

$$\varepsilon_t = \frac{d_t}{d_0} \tag{5.1}$$

The integral error of the normalised system response is thus given by

$$\varepsilon = \int_0^\tau \varepsilon_t . \mathrm{dt} \tag{5.2}$$

By integrating the whole system response in this way, the system response for different GL configurations can be numerically compared. The size of the steady state error amplitude is small compared to the initial and transient error amplitudes. Thus, ε_m is representative only of the initial convergence and transient errors. However, the error amplitude of overshoots are significant compared to transient error amplitudes, thus overshoots will be detected by the integration. Likewise, the 'batch average integral' error, $\hat{\varepsilon}$, can be computed for a

batch size M as

$$\hat{\varepsilon} = \sum_{m=1}^{M} \frac{\varepsilon_m}{M} \tag{5.3}$$

where ε_m is the normalised integral system response (ε) of MCS m. This value allows a direct and meaningful numerical comparison of batches with different GL parameter configurations.

5.2 Bespoke ZEM-based GL for ΔV actuation mechanism

As was shown in §4.2.2, V_{DR0} is the change in velocity needed to bring the projectile to a stable, circular orbit relative to the target motion in the picture plane. However, with this speed alone the projectile will never actually approach the target. We thus define the term $V_{PT}(d)$, which is the closing speed of the projectile to the target as a function of its current distance. This is analogous to the latax which would be demanded by a traditional GL, *i.e.* it is the speed at which the guidance method dictates the projectile should approach the target. Again, analogous to a traditional system, the velocity demand of the autopilot will be a linear combination of the term required for equilibrium and the term demanded for projectile closing:

$$V_{Dem} = V_{DR0} + V_{PT}(d) \tag{5.4}$$

The bias points for $V_{PT}(d)$ are calculated at a distance d_i when the force vector is located at $\phi = 0$. Since the system can only change velocity during a roll rotation, the system won't reach the target speed until one full rotation has elapsed after it was calculated. The system will thus reach $V_{PT}(d)$ not at d_i, but at d_{i+1}. The function $V_{PT}(d)$ will need to account for this lag in the system. Importantly, the function must demand speeds which remain within the capabilities of what the system can correct, instead of being a further source of overshoot or error. The projectile will constantly adjust its speed to match the $V_{PT}(d)$ function. While there may initially be a high-speed discrepancy between the current and demanded speeds, over time the current speed will converge to the demand. In addition, the bias manoeuvres could be turned off entirely at very large distances when a certain speed cap has been reached. This is so there is no unnecessary demand on the actuator, as well as avoiding causing the system to reach very high speeds which it is

unable to recover from the event of suddenly changing system dynamics.

From §4.3, the maximum permitted ΔV of the most simplistic system from one bias manoeuvre is 0.955ms^{-1} and the time it takes to complete this is 2.5s, both theoretically and experimentally. This leads to an acceleration of 0.382ms^{-2}. By assuming the maximum correction that can be made at each step, the maximum permitted relative speed for a given distance can be calculated as

$$V_{lim}(d) = \sqrt{2d\frac{\Delta V_{Max}}{t_{\Delta V_{Max}}}} \tag{5.5}$$

As mentioned above, this speed is what the projectile should have at the current distance d_i. However, the system only reaches this speed one full rotation after it has been designated as the goal, at which point it will actually need to have assumed some lower velocity $V_{PT}(d_{i+1})$ at this new closer distance d_{i+1}. This is shown in figure 5.2.1. The dashed black line shows $V_{lim}(d)$ at every d as described by equation 5.5. Every check mark on the figure indicates a specific coordinate when $\phi = 0$ and the bias angles were calculated. Fig. 5.2.1 shows the system response when $V_{PT}(d) = V_{lim}(d)$ if the projectile is initialised with $[x_0\ y_0\ V_{R0}] = [200\ 200\ 11]$. These initial values are arbitrary but show the system response over a significantly large distance. The solid blue line shows what the controller demands the speed to be at that given value of d, which matches the speed limit by design. The result of this lag is that the system constantly exceeds the speed limit and is thus unable to bring itself to an orbit in time, overshooting the target. Note that by definition, if the projectile overshoots $V_{lim}(d)$, the intrinsic speed limit, at *any* point in the trajectory there will be an overshoot error.

Figure 5.2.2 shows how the resulting closing speeds change if the goal speed is modified by a multiplicative factor k, such that the final function is of the form $V_{PT}(d) = V_{max}(kd)$. The value used in the figure is $k = 0.7$, but this is arbitrary for demonstration purposes. The same initial conditions are used as in fig 5.2.1. The system still exceeds the goal speed, as it still achieves the speed it was supposed to on the prior rotation. However, $V_{lim}(d)$ is never exceeded meaning there will be no overshoot of the system. The optimal closing velocity function will be designed such that the overshoot of the system perfectly follows $V_{lim}(d)$. In other words, this means that the actual system response following the

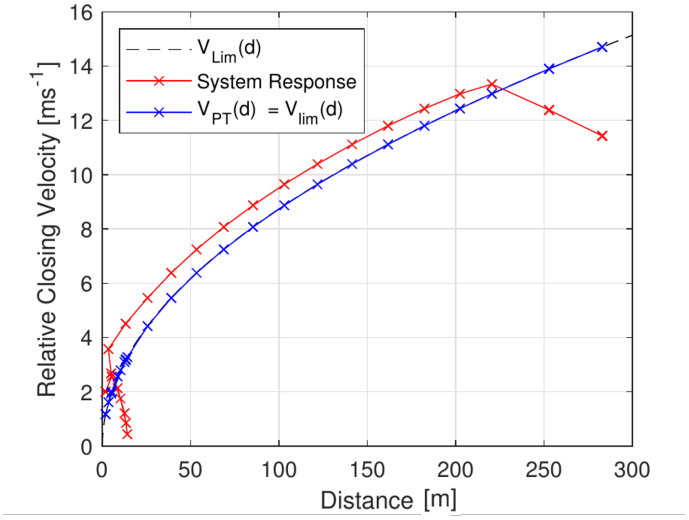

FIGURE 5.2.1 System response when $V_{PT}(d) = V_{lim}(d)$

lag caused by the roll rotation, is always at a point where it can be corrected in time so that there is no overshoot.

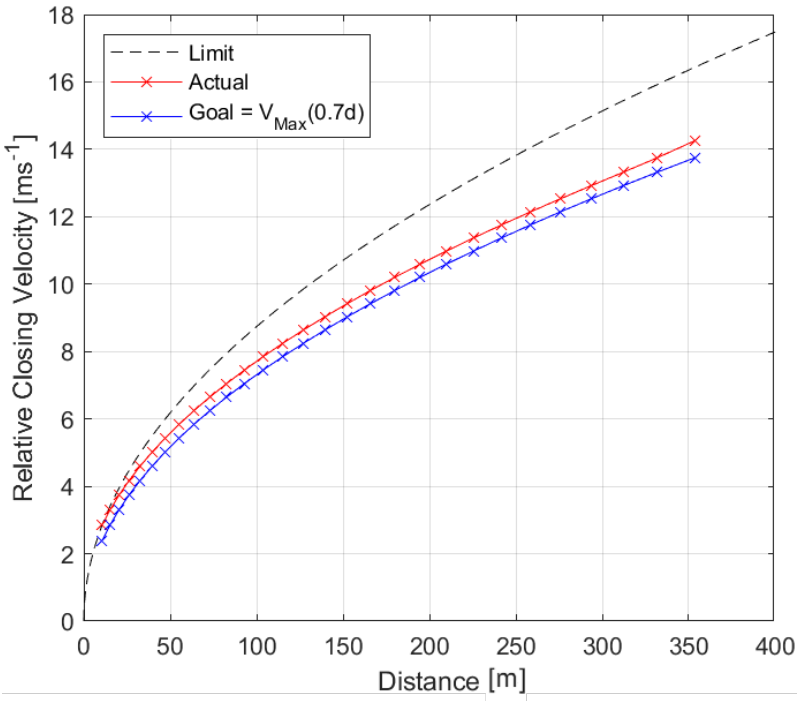

FIGURE 5.2.2 $V_{PT}(d)$ when the target speed is set to $V_{max}(kd)$, for $k = 0.7$

Figure 5.2.2 uses a scale factor to adjust $V_{PT}(d)$, but a translation is required for optimum performance since the lag which causes the overshoot is directly proportional to the function (velocity) itself, rather than have a quadratic, cubic or other dependence. Figure 5.2.3 illustrates this modification to $V_{PT}(d)$, adding an external vertical displacement term,

instead of the internal multiplicative factor that was shown in fig. 5.2.2. Since the error is proportional to the function itself, or the speed of the projectile, it is logical to append the linear term externally rather than internally in the function. Translating the function in this way is analogous to DC Gain correction. Importantly, the figure now shows a consistent change in the system response along the whole path, rather than just the initial distance *i.e.*, the system response is more uniformly close to V_{Lim}, as opposed to the large discrepancy shown in fig. 5.2.2. Again, this modification is made with the intention that the system response at no point exceeds the system limit, which would have resulted in an overshoot. The linear translation constant ξ is incorporated into the closing speed term as

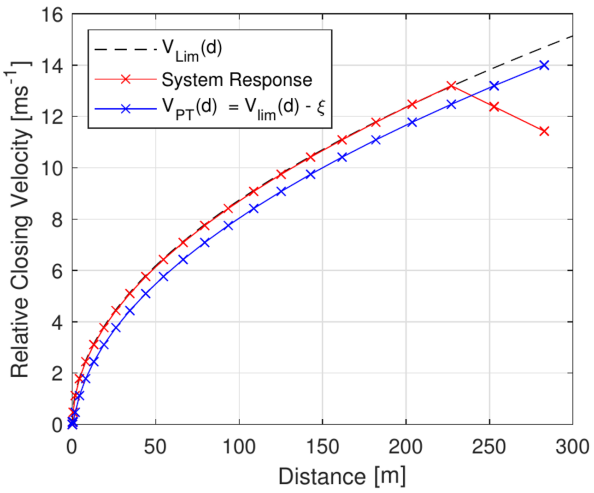

FIGURE 5.2.3 Idyllic system response for chosen $V_{PT}(d)$

$$V_{PT}(d) = V_{lim}(d) - \xi, \qquad \xi \in \mathbb{R} \geq 0 \tag{5.6}$$

where ξ is a constant such that $V_{PT}(d) = V_{lim}(d) - \xi \mid V_R(d) \not> V_{lim}(d)$. In translating the function in this way, the closing speed is undefined when $d \leq d_1$ where $d_1 | \, (V_{lim}(d_1) - \xi = 0)$. As such, the function $V_{lim}(d) - \xi$ is only valid for $d \in (d_1, \infty]$ and must be defined by other means for $d \in [0, d_1]$. Using the value of $V_{lim}(d)$ from eq. 5.5 we can write

$$V_{lim}(d_1) - \xi = 0$$
$$\therefore \sqrt{2d_1 \frac{\Delta V_{Max}}{t_{\Delta V_{Max}}}} - \xi = 0$$

which, using the value of V_{Max} for the simplistic system from eq. 4.13, becomes

$$\sqrt{\frac{4d_1F_c}{m.t_{\Delta V_{Max}}}\left(\frac{\omega_0-\omega_B}{\omega_0\omega_B}\right)}-\xi=0$$

Solving this equation for d_1 yields

$$d_1=\frac{m}{4F_c}t_{\Delta V_{Max}}\xi^2\left(\frac{\omega_0-\omega_B}{\omega_0\omega_B}\right)^{-1} \tag{5.7}$$

The motion of the projectile within this region ($d \leq d_1$) is split into different regimes, to enforce desired behaviours of the projectile. Firstly, the projectile must remain relatively stationary when it is on course to hit the target. The distance d_2 is arbitrary, but is chosen to represent the desired level of precision for the projectile; so $V_{PT}(d)=0 \; \forall \; d \; \in \; [0,d_2]$. Secondly, a region is defined where the projectile takes small steps toward the target in anticipation of either stopping or accelerating by a larger amount. This is represented by $V_{PT}(d)=V_k \; \forall \; d \; \in [d_2,d_1]$ where $d_2<d_1$ and V_k is a constant speed. Actuator and resource preservation is the priority in this region, where it is likely the projectile will remain for the majority of the flight, correcting small drift errors. In its entirety the function $V_{PT}(d)$, and thus the GL, in the range $[0,\infty]$ is given by

$$V_{PT}(d)=\begin{bmatrix} V_{lim}(d)-\xi \\ V_k \\ 0 \end{bmatrix} \forall \; d \in \begin{cases} d_1 \leq d \\ d_2 \leq d < d_1 \\ 0 \leq d < d_2 \end{cases} \tag{5.8}$$

Figure 5.2.4 shows an example system response with annotations showing the different regimes governed by equation 5.8. $V_{PT}(d)=V_{lim}(d)-\xi$ is the closing regime, $V_{PT}(d)=V_k$ is the linear regime and $V_{PT}(d)=0$ is the stationary regime. In addition, the aspects of the steady state error are the transient, the steady state amplitude and the oscillation amplitude. The transient is also the motion of the projectile in the linear regime; a faster V_k provides a faster transient speed. The steady state amplitude can be thought of as the distance d of the 'orbital centre' from the target. The oscillation amplitude and oscillation frequency is governed by F_c, ω_0 and ω_B; neither can be affected by modifying V_k or ξ.

These oscillations are caused by the orbit described above, if the orbit locus coincides with the target then there will be no oscillations. However, any small perturbation offsets the orbit loci and thus increases the amplitude of the steady state error. If the steady state oscillation continues then the orbit is stable, and the projectile is remaining in the stationary regime. If the steady state has another, lower frequency oscillation, the orbit is unstable. This is caused by the linear regime velocity V_k being too great for the current d_2, causing the projectile to pass straight through the stationary regime. *N.B.* the regimes are governed by d and so the vertical lines representing them on figure 5.2.4 should be horizontal; this was done to aid interpretation.

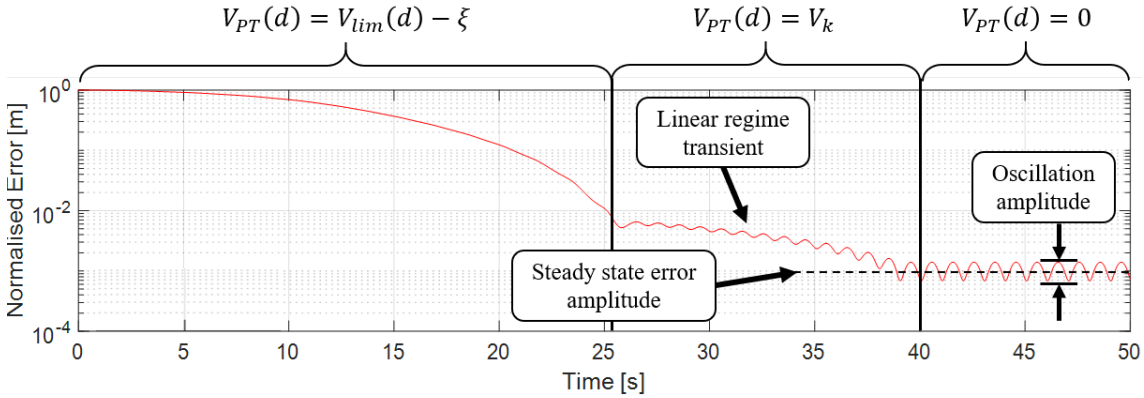

FIGURE 5.2.4 System response to GL eq. 5.8

Figure 5.2.5 shows a diagram of how V_{lim} is modified in the GL to account for the system response lag. V_{lim} acts as the reference signal which the GL then modifies using ξ, according to the parameters of a given system. The closing speed function $V_{PT}(d)$ is then passed to the autopilot, which calculates the change in speed per revolution demanded from the projectile's actuator mechanism V_{Dem}. The V_{Dem} can then be passed through a chosen controller H, such as a PID. The V_{Dem} which has been modified by the controller H is then passed to the actuator mechanism which saturates the signal such that $V_{Dem} \in [0, \Delta V_{max}]$. *N.B.* V_{max} is an absolute limit of the system resulting from the maximum bias angle half of one roll revolution, rather than the characteristics of a physical hardware actuator. If $V_{Dem} > V_{Max}$ the system will saturate and will only be able to deliver V_{Max}. As such, any $H > 1$ when the autopilot is already demanding $V_{PT} = V_{max}$ will have no effect on the system whatsoever.

The sensor block shown in fig. 5.2.5 represents the sensor dynamics of the system

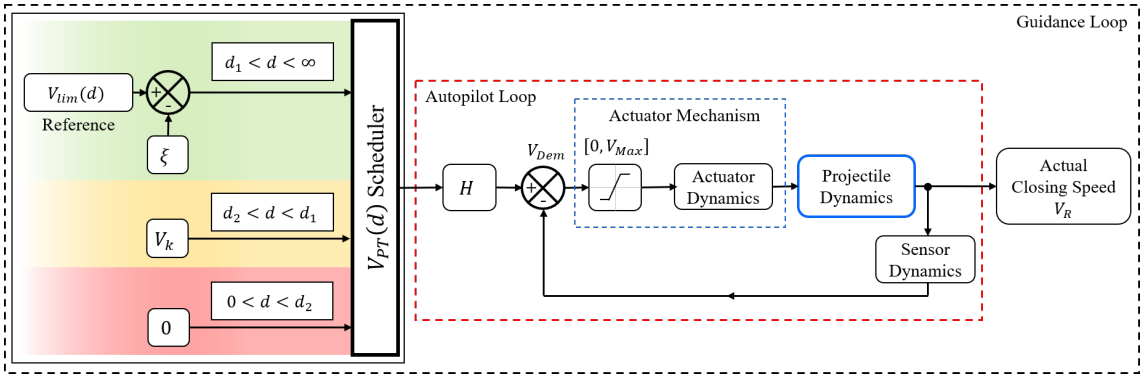

FIGURE 5.2.5 Modification of V_{lim} for speed controller with velocity feedback

which are assumed in the idyllic system to be perfect and instantaneous. For practical implementation, conventional onboard sensors or an external detection system could be used to measure the roll angle, similar to that described in [194]. If space restrictions permit, onboard image sensing hardware could be used [77]. Linear ballistic theory could also be used to estimate the change in roll rate of the projectile along the trajectory beyond what is known from projectile launch and then used to supplement the information from the sensors.

5.2.1 Parametric studies and investigations

The above discussion has shown how the velocity-based mechanism and controller closing speed rely on the parameters V_k, ξ, d_1 and d_2. This section explores the effect of these parameters and conducts a parametric study and optimisation on them where applicable. It is emphasised again that d_2 is a completely arbitrary value, chosen by the designer to represent the desired degree of accuracy for the system, below which the velocity controller demands a stationary hold to ensure the projectile hits the target. The parameter d_1 is the distance at which the closing velocity function becomes ill-defined at the boundary of the closing regime, $d_1 \mid (V_{lim}(d_1) - \xi = 0)$. As a result, the values d_1 and d_2 are omitted from the optimisation process. The study uses the most simplistic system with instantaneous switching.

Parametric investigation

Figure 5.2.6A shows how modifying ξ to extreme values affects the system response. The projectile and target are initialised at rest with $[x_0\ y_0\ x_{T0}\ y_{T0}] = [0\ 0\ 8\ 8]$ and the simulation is run for 50s. When $\xi = 0$, the system response exceeds V_{lim} which was the case in fig. 5.2.1; leading to a large overshoot and oscillatory motion where the projectile closes with a speed which is too high. The purpose of ξ is to translate the speed limit down. Any negative value of ξ would increase the demanded speed above the limit, which is counter-intuitive and is therefore omitted from the figure. For low values, $0 < \xi < 1$, the error is reduced quickly with a low amplitude steady state error and no higher order oscillations. High values, $\xi \geq 1$, produces a large amplitude steady state error.

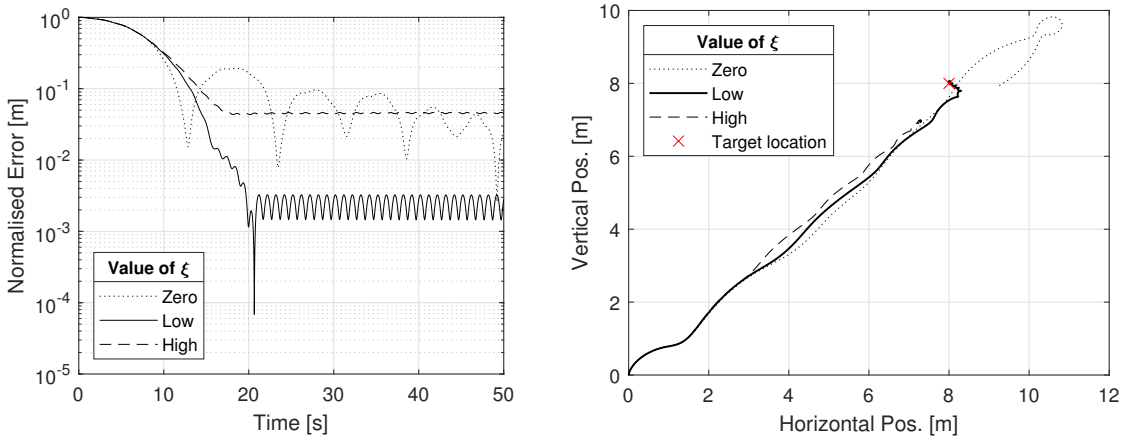

(A) Normalise errors (B) Picture plane trajectories

FIGURE 5.2.6 How extreme values of ξ affect the system response

Figure 5.2.6B shows three example trajectories which correspond to the extreme values of ξ from fig. 5.2.6A. The high steady state error for large ξ is represented by the projectile being brought to rest too far from the target. The high amplitude decaying oscillations in normal error for $\xi = 0$ are visible as the projectile overshoots the target by a large margin. This is caused by too high a speed being demanded and the projectile is unable to reduce its speed in time due to the system lag. For low values of ξ the projectile is brought sufficiently close to the target to initiate a regime change.

Figure 5.2.7 shows the effect of modifying the linear regime constant velocity V_k. All speeds initially follow the same error reduction path, from $t = 0$ to $t = 12$. This is the range governed by $V_{PT}(d) = V_{lim}(d) - \xi$ and thus modifying V_k has no effect. If V_k is

sufficiently small, as the projectile transitions from the linear velocity to the stationary regime, the orbital centre is brought to rest very close to the boundary of the stationary regime, d_2. This results in a higher amplitude steady state error than if the velocity was high enough to reduce the distance to $d \to 0$ before it was brought to rest. This is apparent from the figure, as an increasing value of V_k results in a lower amplitude of steady state error, up to the point that V_k is too high resulting in an overshoot. The optimal V_k is a trade off with d_2 to deliver the orbital centre sufficiently close to the target before switching to the stationary regime.

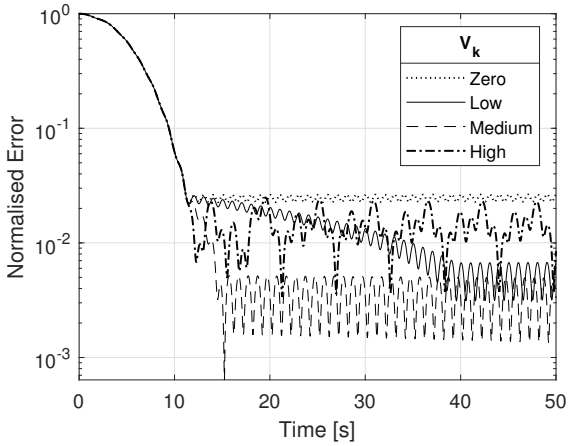

FIGURE 5.2.7 How varying V_k affects transient and steady state error

In this case for $V_k = 0$ the linear regime vanishes, merging with the stationary regime *i.e.* $V_{PT}(d|d \in [0, d_2]) = V_{PT}(d|d \in [d_2, d_1]) = 0$. The result of this is that the projectile enters the stationary regime at a distance d_1 and this is apparent from the figure, with a steady but large magnitude steady state error. For low values of V_k the transient is very slow, but the amplitude of the steady state error is small. For medium values of V_k, the most desirable system behaviour can be observed. There is a very quick transient period followed by a low steady state error amplitude. For high values of V_k there is an unstable switch between the linear and stationary regimes, caused by a sufficiently high overshoot to exceed d_2.

Figure 5.2.8 shows the effect of modifying the boundaries of the linear regime, d_1 and d_2. While d_1 is determined after a value of ξ has been selected, since $d_1 | \, (V_{PT}(d_1) - \xi = 0)$, it is varied manually here to illustrate the impact. Likewise, d_2 is selected based on the chosen level of accuracy of the system. If the boundaries are set to be equal, $d_1 = d_2$, then

there is no linear regime, it is bypassed completely, and the velocity is brought to relative rest immediately. This leads to a large steady error, as was the case for low values of ξ and V_k. The steady state oscillation amplitude is the same as for any other case, since F_c, ω_0 and ω_1 remain unmodified. If d_2 is small, then the projectile gets closer to the target before switching to the stationary regime. When d_2 is sufficiently small it becomes significant compared to the distance that can be travelled by the projectile travelling at speed V_k during the time for one complete roll rotation. This results in an unstable steady state oscillation from overshooting, where the projectile continuously switches between the linear and stationary regime, which is indicated by the late regime termination on the figure. Desirable system behaviour is observed from the ideal duration on the figure, with a steady transient from the dynamic to the stationary regime followed by a stable steady state oscillation. With an early regime activation, the speed demanded of the projectile is significantly lower than $V_{lim}(d)$, resulting in a transient period significantly longer than in the other cases.

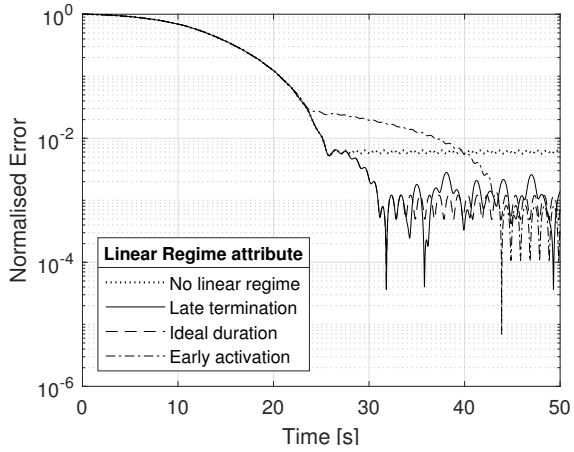

FIGURE 5.2.8 How varying linear regime boundaries affects transient and steady state error

The steady state amplitude for early regime activation is lower than the ideal scenario, which is not expected since the lower bound of the linear regime is the same for both simulations. The stationary regime governs all $d < d_2$, which describes a circular area around the target of radius d_2. Since the projectile only calculates the bias points when $\phi = 0$, the projectile will switch regimes at a different point depending on where the first bias calculation takes place within d_2. Small deviations in trajectory can thus cause a discrepancy in steady state amplitude, though the oscillation amplitude will remain the

same in all cases. This discrepancy must be mitigated by averaging a large number of simulations.

Heuristic variation

Before conducting any optimisation process, it is advantageous to conduct a preliminary manual sweep of the candidate parameters. For the variation of the parameters, the accuracy level of the system is chosen to be $d_2 = 0.1$. The value of d_1, can be computed after the values of ξ and V_k are found.

Figure 5.2.9 shows the effect of varying ξ on the normalised error. In all cases, any value of ξ provides the same initial error reduction rate up to approximately 25s. In this region the projectile is constantly accelerating at V_{max} in order to reach the target speed designated by $V_{PT}(d) - \xi$. When $\xi = 0.9$ the steady state error is too large to provide a convergence to the stationary regime. For $\xi = 0.8$ the transient is slow but is does converge to the stationary regime. A small overshoot is present for $\xi = 0.6$ and a large overshoot is present for $\xi = 0.5$. The quickest transient and lowest steady state error is found for $\xi = 0.7$.

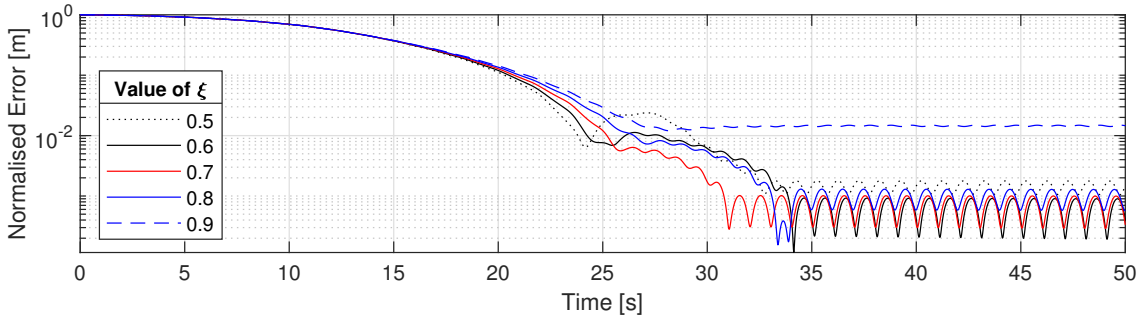

FIGURE 5.2.9 Variation of ξ on normalised error

Figure 5.2.10 shows a close-up of the linear and steady state regimes for varying values of V_k. A value of $V_k = 0.06$ provides the slowest transient but the lowest steady state amplitude. When $V_k = 0.14$ the transient is fastest but there is also a small overshoot, increasing the steady state amplitude slightly. All other values of V_k provide a consistent transient with no overshoot and similar steady state errors. This indicates that $V_k = 0.14$ is the maximum closing speed for the current system where there is no significant induced overshoot.

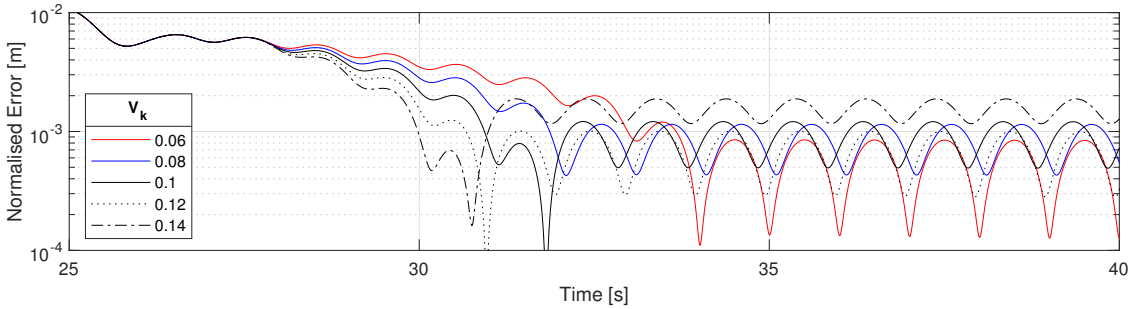

FIGURE 5.2.10 Variation of V_k on normalised error

From the above analysis, the modification parameter and closing speed are $\xi = 0.7$ and $V_k = 0.1$ respectively. This value of ξ is then used as above to calculate d_1 from its definition in eq. 5.7. This becomes

$$d_1 = \frac{1}{4} \times 2.5 \times (0.7)^2 \left(\frac{2\pi - (\pi/2)}{2\pi(\pi/2)} \right)^{-1} \approx 0.64$$

Using the values $[\xi \; V_k \; d_1 \; d_2] = [0.7 \;\; 0.1 \;\; 0.64 \;\; 0.05]$, the heuristic closing function can be written as

$$V_{PT}(d) = \begin{bmatrix} V_{lim}(d) - 0.7 \\ 0.1 \\ 0 \end{bmatrix} \forall \, d \in \begin{cases} 0.64 \leq d \\ 0.1 \leq d < 0.64 \\ 0 \leq d < 0.1 \end{cases} \tag{5.9}$$

Implementing PID controller

Figure 5.2.5 included a block H which represents the chosen controller for V_{Dem}. A PID controller is used to investigate the effect of controlling V_{Dem} with conventional methods, as it may reveal system behaviour that was otherwise unobvious from the previously discussed framework. The MATLAB algorithm for executing the GL first calculates the $V_{PT}(d)$, then V_{Dem} given information from the simulated sensors. The bearing of the target from the projectile in the YZ plane is then calculated using the same information and V_{Dem} is then decomposed into the YZ axis giving $[u_{Dem} \; v_{Dem}]^{\mathrm{T}}$. This vector is then modified by the chosen controller and exported to the actuator block which calculates the bias angles using the ΔV method discussed in chapter 4. This means that one controller can act on both channels simultaneously or two controllers could act separately on each channel. Since

the environment is simplified to a point of planar symmetry, one controller is chosen to act on both channels simultaneously. If external forces are introduced into the environment then two controllers would be better suited to account for forces which are biased to one direction, such as gravity. Using two controllers requires re-normalising the signal so any gain applied to one channel isn't lost during saturation by the actuation mechanism. Figures 5.2.11, 5.2.12 and 5.2.13 show the effect of individually altering the proportional k_P, integral k_I and differential k_D gains for the PID controller. For each gain value, a batch size of 10^4 MC simulations are run against static targets.

In fig. 5.2.11, $k_I = k_D = 0$ while the value of k_P is varied for the values shown on the figure. This value directly scales the V_{Dem} that is sent to the actuator. Any $k_P < 1$ results in a V_{Dem} which is lower than what the system is capable of delivering without overshoot. This is visible on the figure for the gains of 0.8, 0.6 and 0.4, with each successively lower gain taking increasingly more time for the projectile to close the distance sufficiently to being an orbit. For $k_P > 1$ the value of V_{Dem} will regularly be scaled beyond V_{lim}. As a result, the projectile will have too high a velocity and while it will reduce the error quicker, it will also over shoot and never be able to reach steady state. This is visible for gains of 1.2, 1.4 and 1.6 on the figure. There is little difference between the gains for $k_P > 1$ since V_{Dem} saturates and there is no difference between the effective demand of each gain. The proportional constant is effectively scaling V_{lim}. As was previously discussed, V_{lim} requires a translation transformation which is provided by ξ, instead of the linear scaling provided by k_P. A linear scalar cannot evenly map the system response to V_{lim} and thus varying k_P is only detrimental.

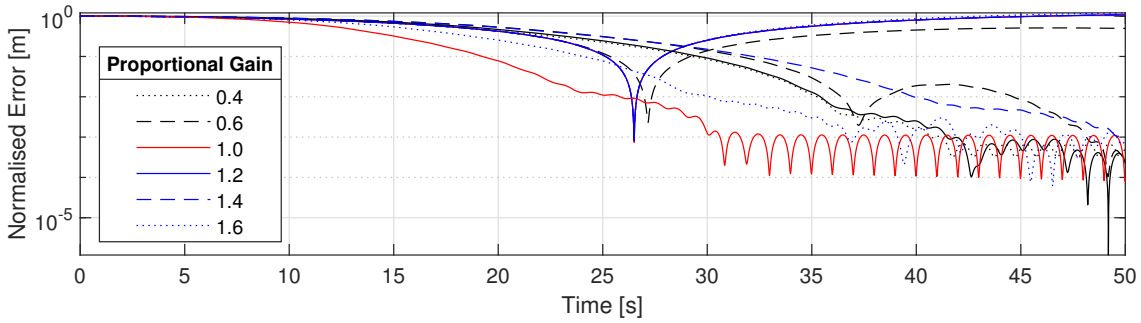

FIGURE 5.2.11 Effect on normal error for different Proportional Gain k_P

To observe the effect of varying the integral error, the MC simulations are run with

$k_P = 1,\ k_D = 0$; the results are shown in fig. 5.2.12. The integral error term keeps a history of error from the beginning of the simulation. As the integral term increases so does the factor by which V_{Dem} is multiplied with the factor itself being multiplied by k_I. Since the error of this system to begin with is initially large, the integral term quickly grows too large and saturates V_{Dem}. This is visible on fig. 5.2.12 as any value of k_I shows a projectile overshoot where there is a consistent $V_{Dem} = V_{lim}$.

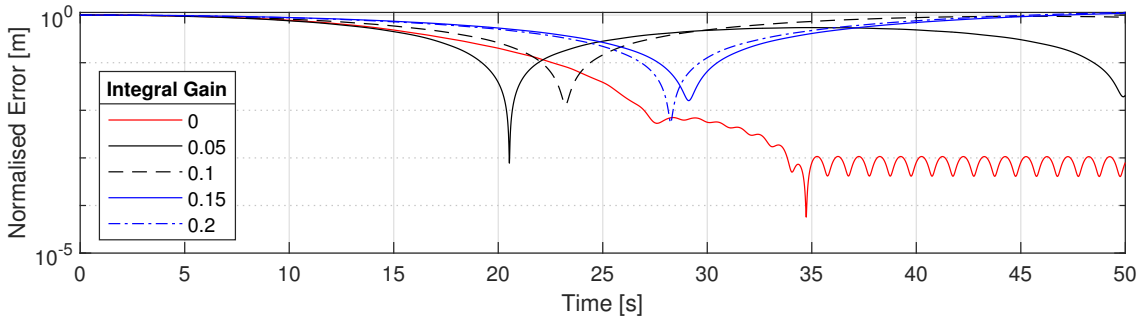

FIGURE 5.2.12 Effect on normal error for different Integral Gain k_I

In fig. 5.2.13, the simulation is run with $k_P = 1,\ k_I = 0$ for all values of k_D shown on the figure. The differential term takes the rate of change of error at each step in the simulation, multiplied by k_D. The differential term will initially be low as the relative speeds are low. As the projectile reduces error and closes the distance, the differential term will increase and has the effect of increasing the time it takes for the projectile to begin decelerating. As a result, the projectile will overshoot the target, by a smaller margin than was present when modifying k_I. A value of $k_D = 0.05$ on fig. 5.2.13 shows the projectile reduces error quicker than the unmodified $k_D = 0$. As predicted however the projectile does overshoot causing a large initial steady state error. To investigate the effect of small k_D further, the simulation is run again for a smaller and narrower range of k_D, shown in fig. 5.2.14.

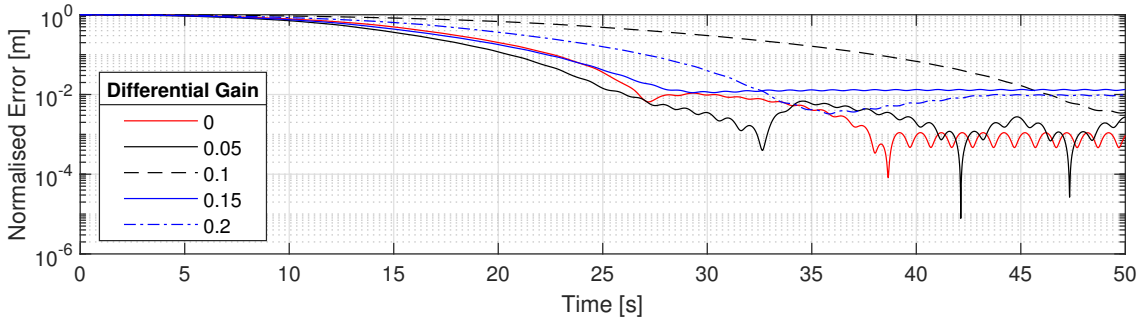

FIGURE 5.2.13 Effect on normal error for different Differential Gain k_D

All values of k_D provide a slower response in the regime governed by $V_{lim}(d) - \xi$. In the linear regime transient, all values of k_D correct this error discrepancy to a point where all values reconverge to the same error at the same time. In the stationary regime, all values of k_D induce an unstable steady state error, indicating the constant switching between V_k and 0 as the projectile oscillates about the boundary point d_2. This is caused by $V_k + k_D.\dot{V}_k$ being too great and preventing a convergence. However, while $k_D = 0.01$ still has an unstable steady state error, it is on average a lower error than using $k_D = 0$, though this could be an inconsistency from averaging MC simulations. It is apparent

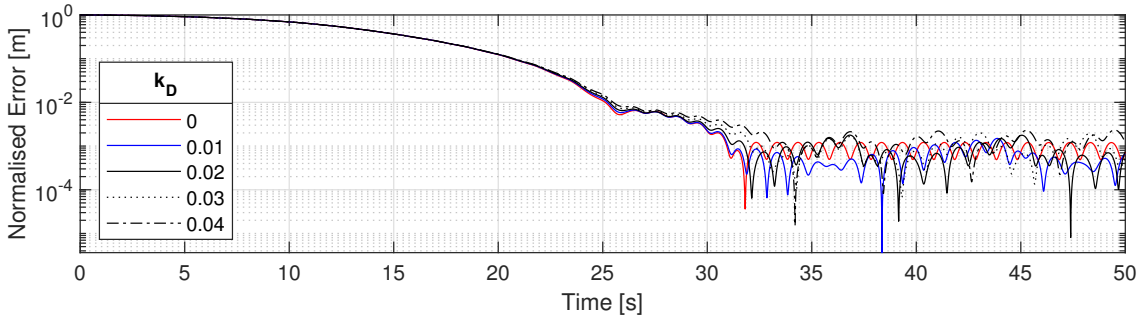

FIGURE 5.2.14 Effect on normal error for different Differential Gain k_D over a small range

from fig 5.2.14 that while k_D is applied to $V_{PT}(d)$ for the whole trajectory, there is only a benefit in the linear and steady state regimes. The supports the evidence in fig. 5.2.11 and 5.2.12 which indicated any scalar modification to $V_{lim}(d) - \xi$ causes the system response to either exceed $V_{lim}(d)$ causing an overshoot or be sufficiently below it to slow the system response. This suggests the application of a PID or PD controller is an alternative method of controlling system convergence characteristics beyond directly modifying ξ, V_k and d_2.

Figure 5.2.15 shows the effect of modifying the PID gains, as was shown in section 5.2.1, but instead of using 10^4 MC simulations per dataset, this figure compares a specific set of initial conditions to observe the difference in one trajectory. The case shown here follows the trend seen in section 5.2.1. If $k_P > 1$ the system overshoots and $k_P < 1$ causes an extended transient. Any value of k_I saturates the controller causing a divergence. This figure shows that any value of k_D produces a less satisfactory system response, but section 5.2.1 showed that over a large number of simulations, a small value of k_D can be used in the linear and steady state regimes instead of modifying the GL parameters ξ and V_k.

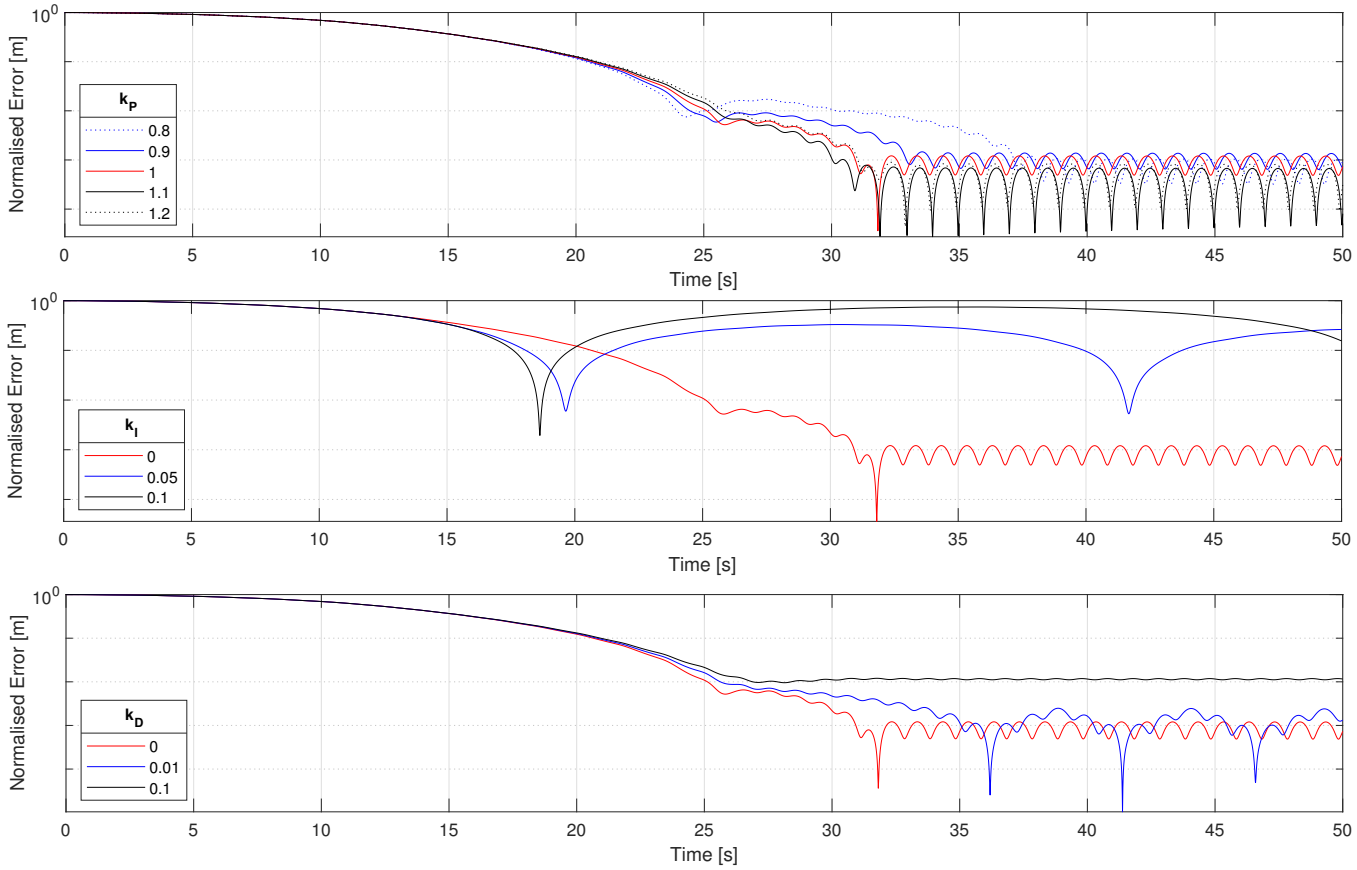

FIGURE 5.2.15 Effect on system response by varying PID controller gains

Fuzzy logic PID controller

To further investigate the effect of k_D on the transient and steady state error, a fuzzy logic scheduler is used to apply k_D only in the linear and stationary regimes. The fuzzy rules are:

- Rule 1: IF d is LOW (d<0.7) THEN k_D is ON ($k_D = 0.03$)
- Rule 2: IF d is HIGH (d>0.7) THEN k_D is OFF ($k_D = 0$)

The ON membership function is governed by the sigmoid function

$$S(d) = \frac{1}{1 + e^{\kappa(d-\lambda)}} \tag{5.10}$$

and the OFF membership function is governed by the zigmoid function

$$Z(d) = \frac{-1}{1+e^{-\kappa(d-\lambda)}} \tag{5.11}$$

where κ is the steepness of the function and λ is the value of d where $S(d)$, $Z(d) = 0.5$. Figure 5.2.16 shows the $S(d)$ and $Z(d)$ with the values $\kappa = 10$ and $\lambda = 0.07$.

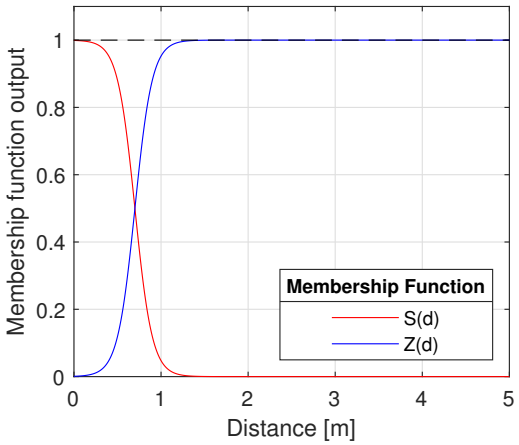

FIGURE 5.2.16 Output Membership functions

The differential gain value at the output of the fuzzy scheduler, $k_{D,OUT}$ is thus

$$k_D = k_{D,\text{ON}}.S(d) + k_{D,\text{OFF}}.Z(d) \tag{5.12}$$

where $k_{D,\text{OFF}} = 0$ and $k_{D,\text{ON}} = 0.03$. Figure 5.2.17 shows how the fuzzy logic scheduler is incorporated with the $V_{PT}(d)$ scheduler and implemented in the Simulink code. When $\phi_{i+1} < \phi_i$, which triggers the calculation of $V_{PT}(d)$ and the bias angles according to the GL, the current d is fed into the fuzzy logic controller. *N.B.* the fuzzy logic scheduler acts concurrently with the $V_{PT}(d)$ scheduler. The fuzzy logic controller calculates a differential gain k_D, which the controller H then applies to the demand of the $V_{PT}(d)$ scheduler. In this sense, all the intricacies of the $V_{PT}(d)$ scheduler (such as response lag) are still captured with the fuzzy logic implementation. When the fuzzy controller is implemented the computation time for one simulation increased by a factor of 300.

Figure 5.2.18 shows the results of using a fuzzy gain scheduler to selectively modify k_D throughout the trajectory. Similar to fig. 5.2.14, the trajectory is unaltered through the closing regime. Figure 5.2.19 shows a close up of the transition between the closing

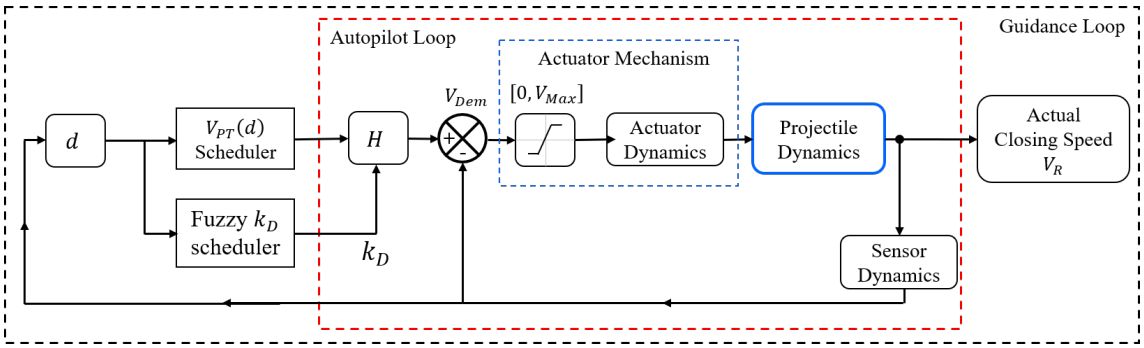

FIGURE 5.2.17 Illustration of fuzzy k_D scheduler implementation

and linear regime. At this boundary, $k_D.\dot{d}$ provides a more significant contribution to V_{Dem}. Since $\dot{d}$ is effectively constant in this regime, from the perspective of the bias calculation points, the effect of k_D is consistent. Importantly, it can be seen the application of $k_D = 0.03$ using the fuzzy scheduler provides a faster system response in the linear regime. While the steady state error amplitude is lower, it is not significantly lower than the variation present from the MC batch size variation The linear regime response being faster shows that using a fuzzy equipped PID controller to alter $V_{PT}(d)$ is a viable alternative to modifying V_k, though it was over 300 times slower to compute when using the fuzzy controller.

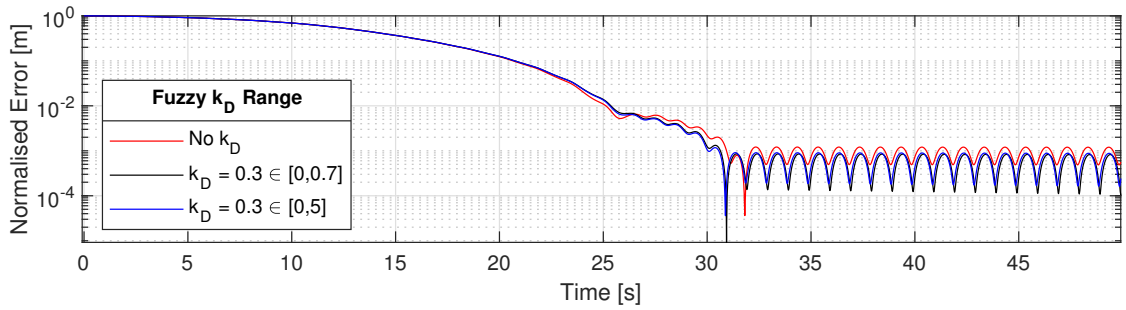

FIGURE 5.2.18 Impact of fuzzy k_D scheduler on normal error

Genetic Algorithm Optimisation

Genetic algorithms (GAs) are a well understood and proven method of optimising system parameters and PID controller gains [195, 196, 197, 198]. A GA is chosen as the optimisation method here due to this N-dimensional reliability as well as the low number of test candidates, which is an important factor in this instance because one specific configuration

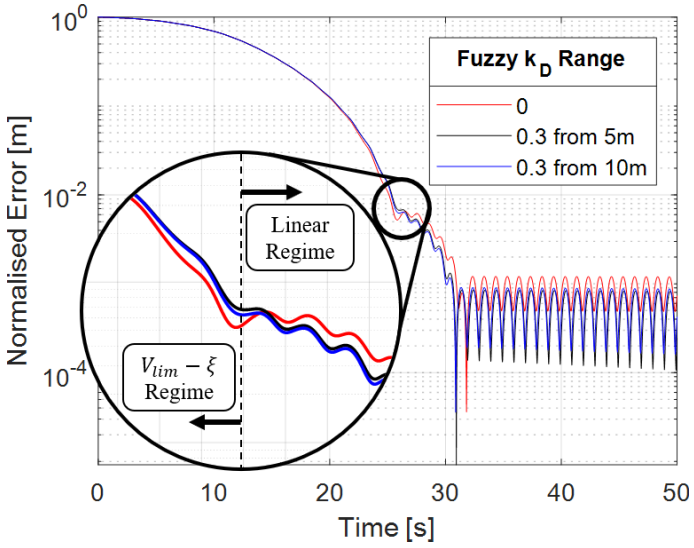

FIGURE 5.2.19 Annotated effects of fuzzy k_D scheduler

is evaluated as a batch (shown in §5.1, pg. 166). GAs emulate the process of natural selection, to optimise an N-dimensional system. A candidate is comprised of N values for each of the problem dimensions, which have a value within a predefined range. A population of candidates are evaluated against some function which produces a numeric output. The candidates that perform well will score highly and the top performers are selected to enter the next generation. They are then used to re-populate the population back up to the starting number, and the values which scored highly undergo an artificial cell division mitosis and mutation stage. The mutation rate is then lowered throughout the subsequent generations. This evaluation, selection, reproduction and mutation cycle is continued for all chosen generations until eventually the mutation rate decays sufficiently that the population is comprised solely of optimum or near-optimum solutions; the performance of which can be seen by the user and thus the optimum solution identified. A basic genetic algorithm is implemented using the parameters shown in table 5.3.

The algorithm chosen uses a fitness-proportional roulette-wheel-like selection method. When the population is evaluated, each candidate will have a fitness score or value, *e.g.* f. The total fitness of all candidates is given by $F = \sum_i f$. A 'fitness space' is constructed by defining regions in the range $[0, F]$ such that each region corresponds to a particular candidate, by linearly appending and summating the fitness of each subsequent candidate to that preceding it. For example, if $f_1 = 4$, $f_2 = 5$ and $f_3 = 8$ then $F = 4+5+8 = 17$. The fitness space is defined by the range $[0, 17]$; where $[0, 4]$, $(4, 9)$ and $(9, 17]$ correspond

to f_1, f_2 and f_3 respectively. A random number r is generated following $r \in [0, F]$, such that the probability of r being in the region of the 'fitness space' pertaining to specimen i is given by f_i/F. The larger the fitness function of a specimen, the higher the probability the random number will land in the corresponding region. Because of this, if a specimen is chosen in this way it is deemed 'successful' in this generational stage and it will be chosen as a seed for the next generation. If a specimen is chosen, its fitness is removed from the fitness space so that no duplicate selections can be made.

Parameter	Value
Generations G	200
Population size N	100
Mutation chance η	50%
Mutation decay η_λ	0.02
MC Batch size M	10^4

TABLE 5.3 Range of values for initialisation of MCS

To verify the algorithm is operating as expected, the GA is first tested on a drop-wave function of the form

$$f(x_1, x_2) = -\frac{1 + \cos\left(12\sqrt{x_1^2 + x_2^2}\right)}{0.5(x_1^2 + x_2^2) + 2} \tag{5.13}$$

which is a non-convex, multi-modal, continuous function with

$$min\,[f(\mathbf{x})] = -1 \text{ when } \mathbf{x} = (0, 0) \tag{5.14}$$

The drop-wave function is shown in fig. 5.2.20. As can be seen from the figure this is an ideal function to use to test the GA functionality as there are many local minima in the function, which could easily be mistaken as the global minima to a poorly tuned GA. While the figure only shows $x, y \in [-4, 4]$, the GA is tested on the function with $x, y \in [-10, 10]$ and a step size of 10^{-3}. The GA converged to the same optimum value for 10 individual trial runs, to within 3 s.f., verifying the GA can repeatedly converge to a known optimum solution in the given configuration.

Using this MCS batch procedure, each specimen of each generation within the GA

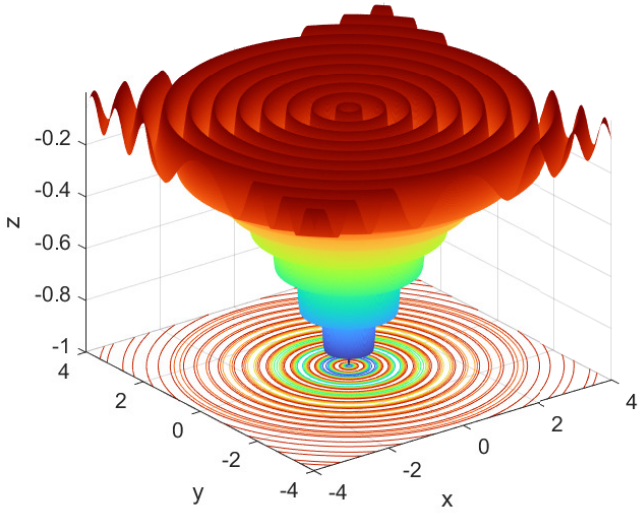

FIGURE 5.2.20 Drop-wave function for $x, y \in [-4, 4]$

can now be meaningfully compared such that an optimal solution may evolve. Algorithm 3 shows the order of operations for the GA. The fitness function, FIT, of the GA to be minimised is simply $\hat{\varepsilon}$, since this represents the average error over time for many instances for a particular GL parameter candidate.

$$\text{FIT} = \hat{\varepsilon} \tag{5.15}$$

The normalised integral error of the system response for the m^{th} MCS follows from eq. 5.2 as

$$\varepsilon_m = \int_0^\tau \varepsilon_t . \mathrm{dt} \tag{5.16}$$

Likewise, the mean normalised integral error of system response for a MC batch of size M for specimen n follows from eq. 5.3 as

$$\hat{\varepsilon} = \sum_m^M \frac{\varepsilon_m}{M} \tag{5.17}$$

The MC batch size for the proceeding is $M = 10^4$, the justification for which was discussed in section 5.1.

Optimising the $V_{PT}(d)$ parameters: ξ and V_k

To reduce computation time, a preliminary search is conducted to inform the scope of the GA. Figure 5.2.21 shows a $\hat{\varepsilon}$ surface for the joint variation of $\xi \in [0.2, 1]$ and $V_k \in [0, 1.5]$. Low regions on the figure correspond to a low $\hat{\varepsilon}$ and the lowest point is with certainty, bounded by $\xi \in [0.3, 0.8]$ and $V_k \in [0, 0.5]$. High values of ξ or V_K lead to a large $\hat{\varepsilon}$. Large values of ξ produce a saturated response regardless of the value of V_k. In either case, $V_{PT}(d) > V_{lim}(d)$ and there is a substantial overshoot, confirming what was seen in fig. 5.2.6A & 5.2.7. In addition, low values of V_k have a small rise in $\hat{\varepsilon}$. Rather than being caused by an overshoot, it is instead due to a slow transient, which produces a residual error which is not present for higher values of V_k which reduces the error quicker. In addition, this surface is less complex than the drop-wave function on which the GA was evaluated during the preliminary tests, indicating the GA will with high probability, converge to the true solution.

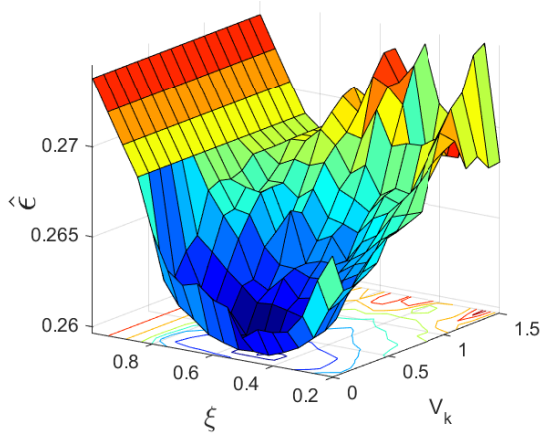

FIGURE 5.2.21 System response error $\hat{\varepsilon}$ as function of GL parameters ξ and V_k

Algorithm 3 shows the steps involved with executing the GA to optimise the GL parameters. To increase the computation time the results for a specific pairing of (ξ, V_k) are saved at the end of each batch. This way, if there are numerous duplicates of the same candidate there is no substantial amount of time lost re-doing the same computations which will lead to very little deviation, as was shown by the very small discrepancy between batches when the MC procedure was described (§5.1).

Figures 5.2.22 and 5.2.22B show the convergence rate for the GA operating under the boundary conditions for ξ and V_k. The optimal GL parameters from the GA were found

Algorithm 3 Execution of GA optimisation using MCS procedure

```
Randomly initialise N specimens, (ξ, v_K)_n
for Each generation g ∈ [1 : G] do
    for Every Specimen in the population n ∈ [1 : N] do
        Set GL parameters equal to specimen (ξ, v_K) = (ξ, v_K)_n
        for For MCS m ∈ [1 : M] do
            Run MCS m with random initial conditions
            Compute ε_m
        end for
        Compute specimen Fitness: FIT_n = ε̂_n
    end for
    Rank specimens in order of fitness and select candidates for reproduction
    Create offspring from candidates and cull resulting population to size
    Mutate population, then reduce mutation factor
end for
```

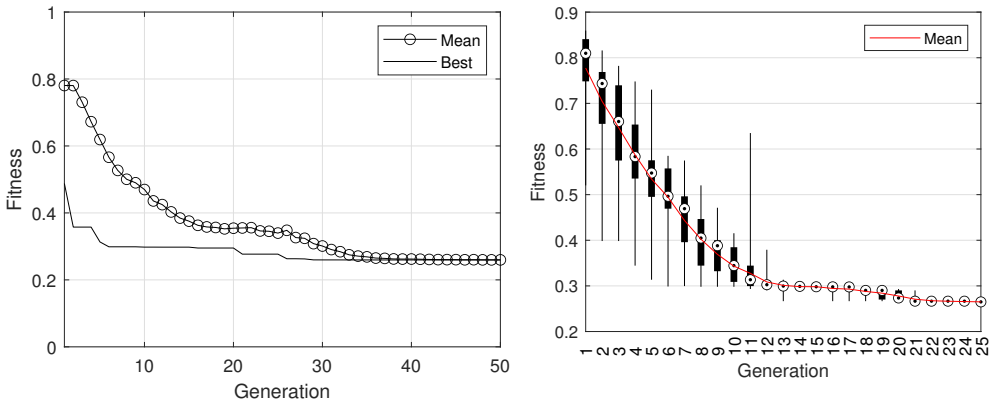

(A) Convergence (B) Convergence distribution

FIGURE 5.2.22 2D GA to optimise GL parameters

to be $\xi = 0.54$ and $V_k = 0.18$.

Optimising PID controller gain

Figure 5.2.23 shows a preliminary search of independently varying the PID controller gains, corollary to figure 5.2.21. The gains are initially held at $[k_P \; k_I \; k_D]^{\mathrm{T}} = [1 \; 0 \; 0]^{\mathrm{T}}$, which emulates the absence of a PID controller. Each gain is individually swept over the given range while the other gains remain fixed, and a MCS batch is run to determine the corresponding $\hat{\varepsilon}$ for each specific gain configuration. As with the optimisation of the GL parameters, the intention is to reduce the scope of the GA optimisation and therefore computation time. The ranges bounding the optimum solution were found to be $k_P \in$

$[0.6, 1.4]$, $k_I \in [0, 0.1]$ and $k_D \in [0, 0.5]$. The GA is then modified from algorithm 3, such that each specimen is now $(k_P\ k_I\ k_D)_n\ \forall\ n \in N$.

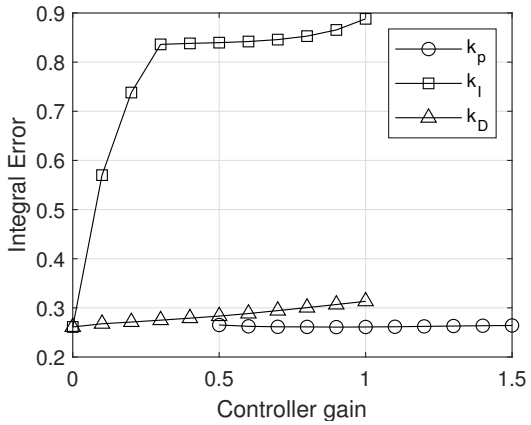

FIGURE 5.2.23 Contribution of independent k_P, k_I and k_D to system error

Figures 5.2.24 and 5.2.24B show the convergence rate of the 3D-adapted GA. The optimal configuration of PID gains was found to be $[k_P\ k_I\ k_D]^{\mathrm{T}} = [1\ 0\ 0]^{\mathrm{T}}$, indicating that tuning the GL parameters is a sufficient and complete optimisation, without the need of an external controller. It is of note that the GA converged to a local minimum much quicker than when optimising for ξ and V_k. This is likely due to the adverse effect any $k_I,\ k_D > 0$ has on the system response, which quickly coerces the evolution, effectively reducing the search to a 1D GA. The minimum $\hat{\varepsilon}$ achieved during the optimisation of the PID controller gains was equal to the minimum $\hat{\varepsilon}$ during the optimisation of the GL, to 3sf. This is within the expected MCS batch error.

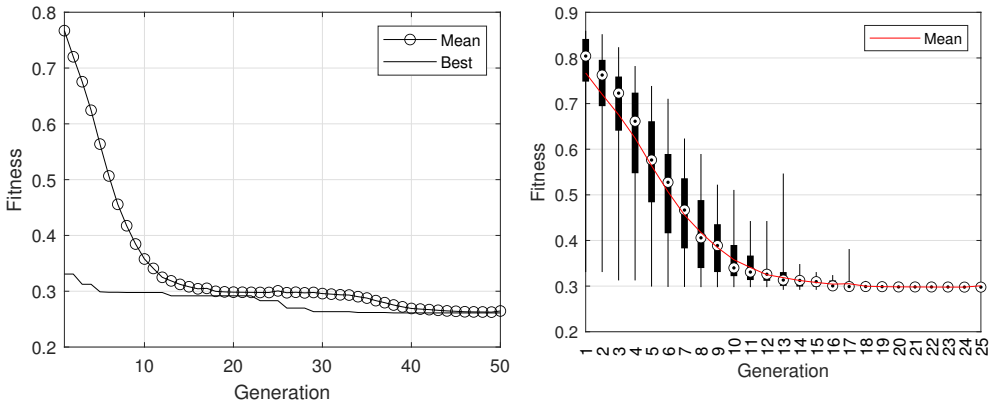

(A) Convergence (B) Convergence distribution

FIGURE 5.2.24 3D GA to optimise PID controller gains

Testing and Disturbance rejection

With the relative methods shown for optimising the GL parameters and PID controller gains, the resulting architectures can be compared for efficiency. Figures 5.2.25A and 5.2.25B show example trajectories for both stationary and moving targets respectively. The black/red cross and line shows the starting point and trajectory of the projectile/target. One trajectory corresponds to one MC simulation. An average system response from a batch size of 10^4, discussed in section 5.2.1, is an average of 10^4 of these trajectories.

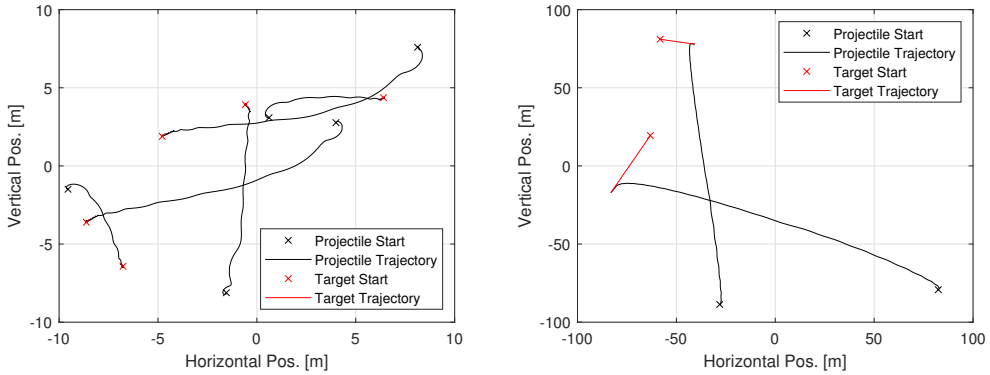

(A) Five example trajectories against a stationary target

(B) Two example trajectories against a moving target

FIGURE 5.2.25 Example trajectories for bespoke GL and ΔV actuation method

The optimised GL is now tested for disturbance rejection capabilities and performance against different target profiles. Figures 5.2.26 and 5.2.27 show how the projectile responds to different disturbances. In each case, the projectile and target are initialised at a specified distance, the target closes the distance under normal operation and is then allowed to remain in steady state for a sufficient time until the chosen disturbance is applied, synchronised at 50s.

Figure 5.2.26 shows disturbance displacements, where at 50s the target coordinates are set to be a magnitude of 0.5x, 1x and 2x that of the initial displacement, as indicated by the figure. For all magnitudes of displacement, the error change is discontinuous. The initial correction response is similar for all, due to the demand of the velocity autopilot saturating the control mechanism. Once the projectile has slowed sufficiently it enters the linear regime at the same point in each case, $d \approx 10^{-2}$, since the regime switching is governed by a certain distance. There is a small discrepancy between linear regime

switching for the disturbances and the initial reference signal. The reference signal enters slightly later at a lower distance. This is likely caused by the projectile crossing the regime threshold d_2 with more of the roll rotation left to complete, meaning it will travel longer before the speed is corrected again. The similarity in response is because in all cases, the initial relative velocity between the projectile and target is zero and thus the system will respond as if the simulation has just been initialised at different distances.

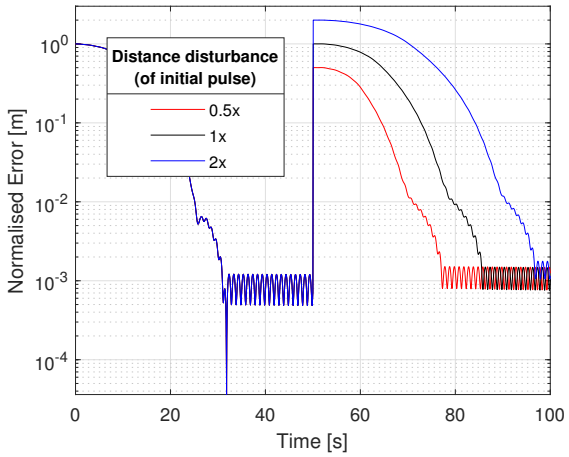

FIGURE 5.2.26 System response to various target distance disturbances

Figure 5.2.27 shows velocity displacements, where at 50s the relative velocity of the target is instantaneously changed to a low, medium and high respective speed, radially away from the projectile. The positions of the projectile and target are initialised at the same positions, whereby they are then free to dynamically evolve. When the velocity disturbance is low, within what the actuator mechanism is capable of correcting in one roll rotation, the disturbance is corrected quickly. With a medium disturbance, beyond the correction of one bias manoeuvre, the system takes longer to recover. Since this is a velocity disturbance the maximum error increase is non-instantaneous, rather it coincides with the instant where the target is no longer moving away from the projectile and the relative speed is zero. From this point, the closing of the projectile is similar to the distance disturbances. This is the same for the high velocity disturbance, except rate of reduction of error divergence takes longer to correct.

Figure 5.2.28 shows the normalised error for 10^4 MC simulations against both stationary and moving targets using the values shown in table 5.1. The distance over time is normalised with the initial distance of each episode and then averaged over all 10^4

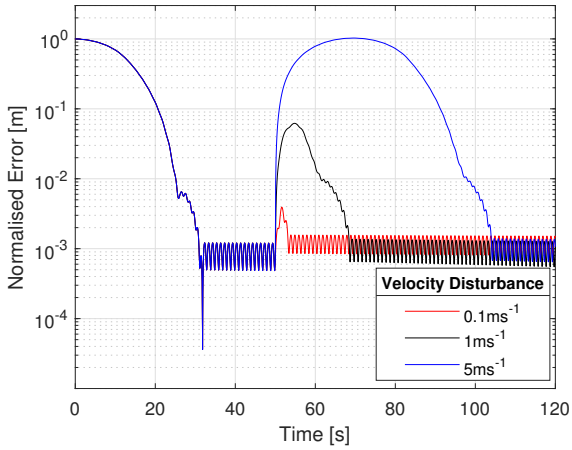

FIGURE 5.2.27 System response to various target velocity disturbances

simulations. Against stationary targets the error reduces exponentially which is expected from the described GL. Against moving targets however, the error initially increases a small amount before decreasing in a manner similar to the response against static targets. This initial increase is due to the random chance of the projectile being initialised with speeds directed away from the target, then having to correct this dispersive motion before beginning the correction procedure. They system takes less than 3 seconds to mitigate this separation and begin closing the distance.

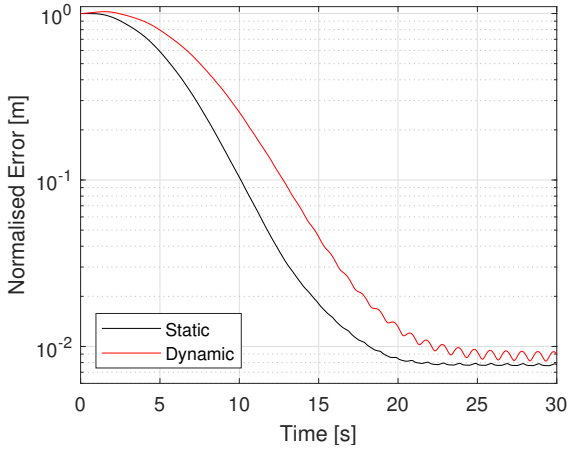

FIGURE 5.2.28 Performance of GL against target profiles

5.2.2 Conclusions

The most important aspect of this GL is that it operates by first determining the maximum velocity the projectile can be going at any point in the 2D plane, relative to the target

such that it has sufficient time and distance to bring itself to rest. The target and projectile positions are overlaid, then the projectile is given maximum acceleration, radially away from the target, while the velocity of the projectile is measured at any given point. The next consideration must be the lag between demanding a velocity of the projectile and what it can deliver. The parameters ξ and V_k were used to account for this lag and the above procedure has detailed a variety of optimisation and control methods. In the procedure shown, the projectile was assumed to have instantaneous switching and the velocity profile (fig. 5.2.1) was determined under kinematic assumptions from this. However, using the process described, it is completely feasible to model the actuator using the described bias functions, to increase the domain knowledge of the GL if the response of the actuator is known.

In addition to increasing the complexity of the actuator model, external forces and effects can be considered here. The velocity profile of fig. 5.2.1 for example is effectively *in vacuo*, thus the profile is completely symmetric radially about the target reference frame. If one considers an asymmetric external force, such as gravity, the acceleration of the projectile is dependent on its orientation. Figure 5.2.29 shows how the effect of gravity on the projectile closing speed is biased. Depending on whether the projectile is above or below the target in the picture plane, gravity is aligned with or against the desired direction of motion respectively. Below the target, part of the actuator effort is spent counteracting the acceleration due to gravity, leaving only a subset of the available actuator effort to actually enact the demand. This means the velocity limit is lower, directly below the target, since the projectile has less acceleration available to it. The opposite is true directly above the projectile, where gravity works to assist the deceleration of the projectile. The implication of this may seem to be that the projectile can close with a higher speed when above the target, however the speed must still be eliminated to bring the projectile and target in alignment. The projectile will have less deceleration available to it above the target because of gravity, and so it will need to start decelerating sooner. The result of the external force asymmetry is that the closing speed velocity can no longer be determined purely as a function of radial distance d, but must be computed depending on the spatial orientation with respect to the target, *i.e.* $V_{PT} = V_{PT}(\delta x, \delta y) \neq V_{PT}(d)$

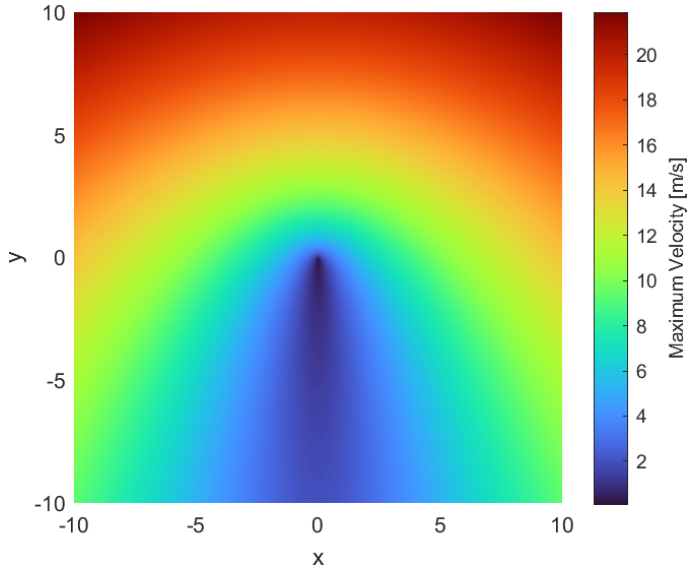

FIGURE 5.2.29 Maximum picture plane closing velocity variation due to gravity

5.3 Reinforcement Learning AI control

This section will discuss the implementation of machine learning algorithms into different aspects of the novel control mechanism. Two different reinforcement learning algorithms are used, DQN and DDPG. Firstly, there is a discussion on the reward function which will be used during the agent training. It must be designed in such a way as to mitigate and prevent undesired actions. A DQN agent is then used to directly control the brake between the front and aft section, or rather it controls when the roll rate switches between ω_0 and ω_B. Then a DDPG agent is used to generate a target latax, which takes the place of a traditional GL. This DDPG GL is then modified to account for lag in the system response.

5.3.1 The reward function

The concept of reinforcement learning is that and agent will, for a given system state, use a policy to determine which action it should take to maximise a 'reward'. This reward is calculated from the reward function R. The reward function does not have to contain any of the observations the agent makes of the environment or be any states of the system. Since the reward is computed externally it can be completely arbitrary, the purpose of the reward function is to characterise the behaviour we require of the agent. It can use a *reward* to reinforce good behaviour or a *penalty* to penalise undesirable behaviour. In

general, rewards incentivise the agent to keep doing what it's doing to accumulate reward, while penalties cause the agent to attempt to reach a terminal state as quickly as possible to minimise loss.

By design, the policy used by the agent should maximise the expected reward by any means necessary. Quite characteristic of machine learning is the concept of a local minima, where the agent has learnt to exploit a particular aspect of the environment to increase its short-term reward. It is possible for the agent to continue exploration and navigate out of this local minimum, but the agent may continue the exploitation if the training doesn't contain sufficient episodes. Alternatively, the gradient between the local minima and the global maxima may be so great that the chances of the agent exploring through it is very low, even with sufficient episodes. As such, the reward function should be chosen very carefully and may even require different iterations after observing the results of agent training.

If rewards are only given for achieving a goal, the agent may never fully explore the environment to attain the reward and even if it does, it may happen very slowly. To rectify this, additional reward can be given for behaviour which tends towards the final goal but even this must be carefully chosen. If the reward is given in discrete chunks then the same problem will arise as with only rewarding success, the agent will learn much slower. As such, the given reward for good behaviour should be continuous where possible, with a bonus given for success. This is the same for penalties*, where bad behaviour should be penalised continuously with a substantial negative reward accompanying a failure. A common idea is to reduce the scope of the search by prematurely terminating an episode if the parameters stray outside a certain range, where a large penalty will accompany the termination. This should be tested during implementation, as a successfully trained agent should still achieve its goal when operating outside of the given range.

Take for example a simplified robot golf, where an agent must move a ball around a field with the aim of dropping it into a target hole. Initially, a reward will be given for achieving the goal of getting the ball in the hole, which is a success. Equally there is no point exploring millions of miles away from the hole. If for example, the ball strays further

*A 'penalty' is simply a negative reward, *e.g.* a penalty of 5 equates to a 'reward' of -5, with the associated negative connotations.

than 10m away then the episode can then be terminated along with a substantial penalty.

One could provide a reward directly proportional to the distance from the hole in addition to a lump sum reward for achieving the goal. This incentivises the ball to move closer toward the hole. Unfortunately, the agent is able to exploit this system in two ways. Firstly, the ball can orbit the hole, to indefinitely accumulate a mediocre reward as shown in figure 5.3.1A. Alternatively it could move straight past the hole, to maximise the reward in one quick burst but never actually achieve success, as shown in figure 5.3.1B. A

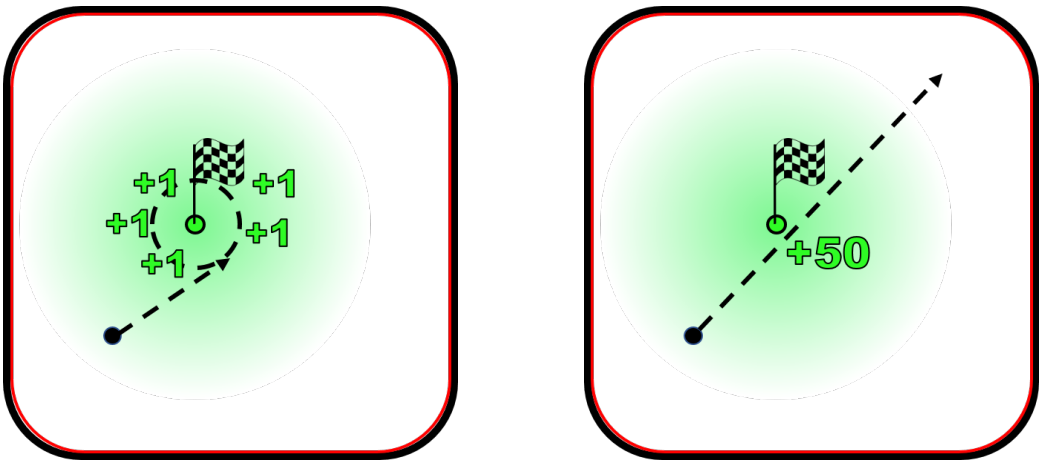

(A) Accumulate reward by 'orbiting' the goal indefinitely

(B) Maximise reward by moving past the goal

FIGURE 5.3.1 Effects of adding a reward proportional to distance

temporal aspect can be added to the reward by penalising the agent for the time it takes to complete the episode. If the ball continues to orbit the hole as in figure 5.3.2A, it will continue to be penalised. There is a larger probability the agent will explore alternative options and find a more ideal path toward the hole. If the goal of an agent is to avoid failure as opposed to achieving a goal, as in the inverted pendulum system, then a reward might be given for each consecutive time-step the system doesn't fail.

A notable case of exploitation is where the penalty for terminating an episode early is small compared to the reward for moving straight past hole. This, combined with a penalty for taking a long time to achieve the objective causes the agent to move the ball past the hole and fly outside the search range as fast as possible. This is referred to as a 'dive-bomb', shown in figure 5.3.2B. This maximises the reward, terminates the episode early to stop the agent being penalised. From this, it can be deduced that the reward magnitude for moving towards success should be significantly smaller that the magnitude

of the penalty for premature termination, which should in turn be significantly smaller than the reward for achieving the goal.

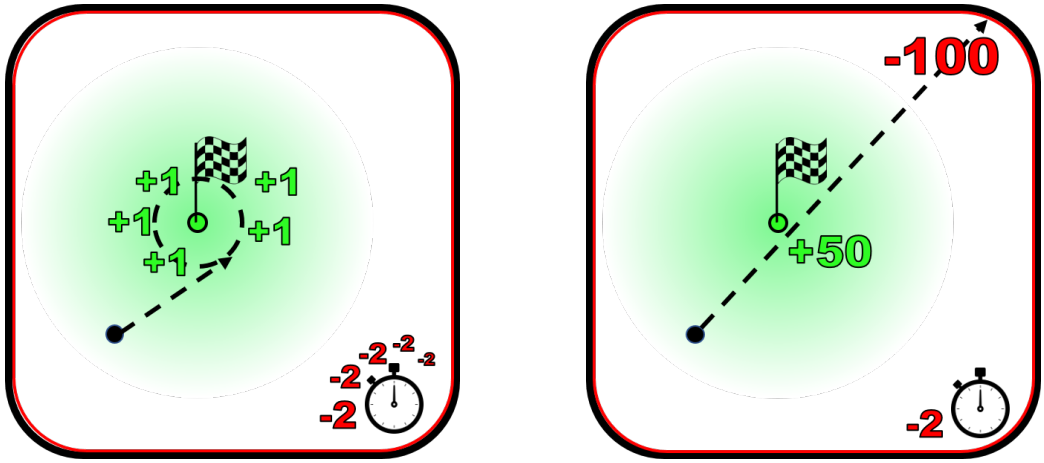

(A) A time penalty can fix the orbiting issue

(B) Adding time can cause a 'dive-bomb' issue

FIGURE 5.3.2 Effect of adding a time penalty

Following the justification in §5.3.1, the reward function is chosen to be:

$$R(d,\dot{d},t) = \left\{ \begin{array}{lll} k_t t & \text{for} & d < d_L \\ -d & \text{for} & d_L \leq d < d_T \\ k_T & \text{for} & d_T \leq d \end{array} \right\} + -\dot{d}d \tag{5.18}$$

where $k_t = 10$ is the time dependent reward coefficient, $k_T = -1000$ is the early termination penalty, $d_T = 12$ is the early termination distance and d_L is the lower accuracy threshold. This reward function is shown graphically in figure 5.3.3. The first term of equation 5.18 provides the associated reward for the distance around the target. If the projectile is more than d_T away from the target at any point in time, the episode is immediately terminated and a 1000-point penalty is incurred. For $d_L < d < d_T$ the penalty is directly proportional to distance. Lastly, a reward of k_t is given for a any value of $d < d_L$. Note that d cannot be negative, since it is a radial distance. This reward is then scaled by the time duration of the episode, if $d < d_L$ at the end of the episode it will receive a much higher reward than travelling through the target initially. While this may cause the agent to attempt to arrive at the target right at the end of the episode, it will achieve substantially more reward by hovering over the target throughout the episode. This is shown in fig.

5.3.4A.

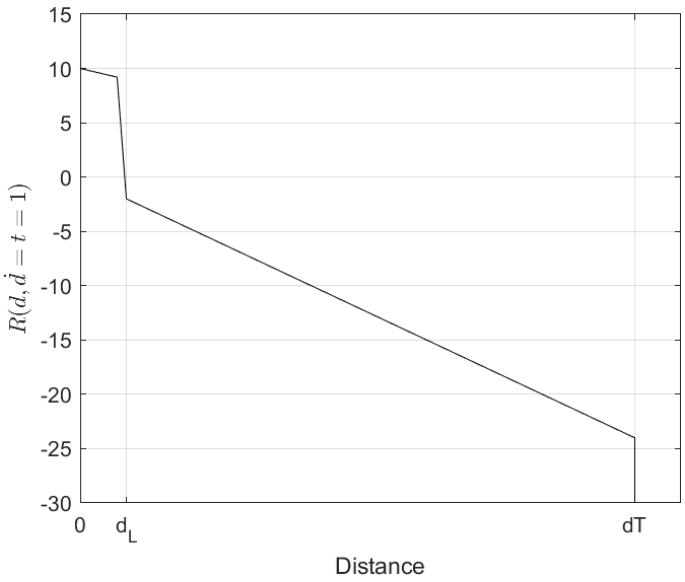

FIGURE 5.3.3 Graphical representation of Reward function (eq. 5.18) for the preliminary test

The second term includes the error rate, $\dot{d}$. This dynamic system has a constant force vector. It is a reasonable assumption that to guide the projectile to the target, the agent will keep the force vector pointed in direction of the target for as long as possible to achieve the goal. However, since the episode doesn't terminate when the target is reached the projectile will likely fly straight past the target in a scenario similar to the 'sling-shot' shown in figure 5.3.1B. By observing $\dot{d}$, the agent will be able to deduce when both $\dot{d}$ and d are small, the reward is maximised. *i.e.* if the projectile moves slower when in close proximity to the target it will maximise the reward over time. Note that a negative $\dot{d}$ indicates the projectile is moving towards the target. The $-\dot{d}d$ term in equation 5.18 punishes the agent for moving away from the target and is scaled proportional to d. This is still consistent with the goal of being less than d_L away; a perfectly circular orbit with a radius of less than d_L will have $\dot{d} = 0$, which results in no punishment for the agent, while still rewarding it for the close proximity. This is shown in fig. 5.3.4B.

The boundary of d_L used during training is arbitrary, but the reasoning is justified. For the creation of a direct-fire guided-projectile to be worthwhile it must deliver dispersion characteristics that are at least the same or better than the equivalent unguided projectile. As such, this d_L boundary, in a more complete training environment, will represent the accuracy level required by the round at that range. This also leads onto the justification

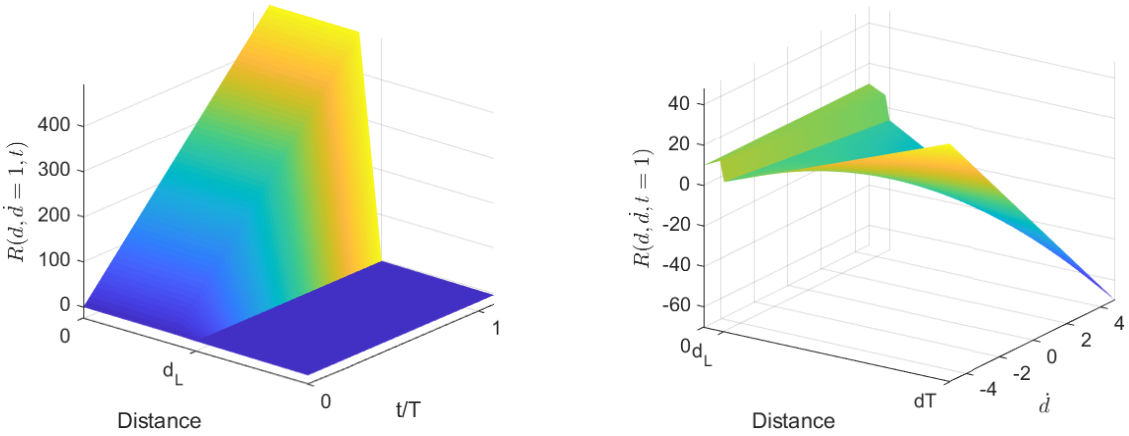

(A) Effect of time, $\partial R/\partial \dot{d} = 0$ (B) Effect of $\dot{d}$, $\partial R/\partial t = 0$

FIGURE 5.3.4 Reward function dependency on t and $\dot{d}$

for continuing to run the episode when the projectile arrives at the target. The purpose of the guided weapon is to account to for variation in target location caused by factors only introduced during the projectile's flight. This includes range, which would affect the time of impact, even if that is accounted for at launch. Since the prototype is designed to be a beam rider, this logic for the agent is used to keep the projectile on the beam.

5.3.2 Implementing RL agents into Simulink dynamic model

MATLAB has a Reinforcement Learning toolbox which can be used to create a variety of RL agents, as well as a Deep Learning Toolbox which can be used for the implementation of neural networks [199]. The Simulink model for the AI controller is the same implementation as in fig. 4.1.1. Where applicable, the AI agent will either replace the actuator autopilot or the GL block. Instead of having a MATLAB function responsible for executing the controller logic, the MATLAB function takes parameters from the system and uses them to compute the inputs for the RL agent training: observation assignment, the reward function and the criteria for determining the end of an episode. The output of the MATLAB function is then forwarded to a pre-made Simulink box which is responsible for feeding the observations, reward and completion check to an RL agent which has been created in the workspace.

The environment is set to be the Simulink model described in §4.1. The number of observations with their upper and lower bounds are set. The number of actions is defined

by the allowed values, which are taken from the output of the dynamics box. A reset function is also defined, which sets initial conditions of the observations for the simulation; these can either be randomised or fixed. Before the training begins, the parameters of the actor and critic neural networks are defined, with the number of hidden and active layers, their types (*e.g.* ReLU Layer), and the paths between them. DQN agent parameters are configured, including the discount factor γ. In any implementation described in the coming analysis, a full description of the neural network parameters will be given.

The agent training options are configured, such as maximum number of episodes, steps per episode and the reward threshold at which the training is terminated. The agent is trained in the defined environment using the set parameters and the resulting trained agent is saved to by implemented by a controller in any environment.

In more detail, algorithm 4 shows how MATLAB updates the neural networks for each episode.

Algorithm 4 Step algorithm for actor/critic update

Ensure: Critic $Q(s,a)$ is initialised with parameter values θ_Q, then the target critic is initialised with the same parameter values: $\theta_{Q'} = \theta_Q$
At each time step:
if RAND $> \varepsilon$ **then**
  Given the current observation S, select a random action A with probability ε
else
  Select and action for which the critic value function is greatest *e.g.* $A = \max_A |Q(S,A|\theta_Q)|$
end if
Execute action A and observe the reward R and next observation S'
Store the combined experience S,A,R,S' in the buffer
Sample a random batch of M experiences, S_i,A_i,R_i,S'_i
if S'_i is a terminal state **then**
  Set the value function target to be the current reward $y_i = R_i$.
else
  Set the value function target to be: $y_i = R_i + \gamma \max_{A'} \left| Q(S'_i,A'|\theta'_Q) \right|$
end if
Update the critic parameters by minimising the loss L across the M sampled experiences:
$L = \frac{1}{M}\sum_{i=1}^{M}(y_i - Q(S_i,A_i|\theta_Q))^2$
Update the target critic periodically: $\theta_{Q'} = \theta_Q$
Update ε for selecting a random action.

5.3.3 DQN direct control

This section will investigate the direct application of a DQN agent to control every aspect of the system in one instance. The actuation mechanisms described above, responsible for converting the bias points ϕ_{ON}, ϕ_{OFF} to either a latax or ΔV, will be combined with the GL. The DQN agent will have direct control over whether the projectile is in the biased or natural state and will be responsible for taking all simulation parameters into account to produce a desirable approach to the target. In essence, the DQN agent will be controlling a fixed magnitude force vector rotating clockwise at the two selectable speeds, ω_0 and ω_B. This is the most complex application of AI to the considered system.

A full list of the training parameters for the neural network, simulation and training are shown in appendix A.4. Both the target and projectile have no initial velocity and they are initialised at the same point every episode. The positions can then be randomised to continue the training if the agent shows improvement. The observations are distance d, closing velocity $\dot{d}$, target bearing from projectile ϕ_T and current roll angle of control force ϕ. Figure 5.3.5 shows the training results for the first batch of training episodes. A segment of the raw training data is shown in fig. A.4.1 in appendix A.4. The agent did show a

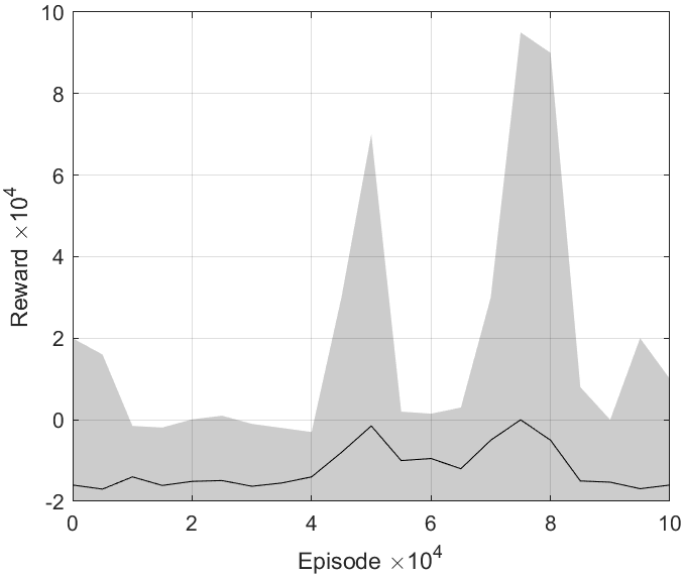

FIGURE 5.3.5 Training for the first 10^5 episodes of the implementation test

very small development in controlling both the actuator mechanism and the GL as a whole. Figures A.4.2 & A.4.3 in appendix A.4 show the small performance increase of the DQN agent. There was a significant improvement in reward at episodes 5×10^4 and 8×10^4, but

the agent was unable to retain significant knowledge of the gained experience to capitalise on this reward increase. The fact that the increase in reward was only temporary, and that there was no subsequent permanent increase in performance, indicates the surge was likely caused by the agent exploring the action space. In addition, it is a characteristic trait of under-training, where there is an insufficient action space to map all possible system states which in the environment considered above, is very large due to it being near-continuous. Since the initial conditions for this simulation were held constant, it is likely that in this configuration, the agent was unable to learn the system to a degree that it could effectively enact control. Due to time constraints, it was not possible to train the agent any longer. Future work should allow the agent to train for longer, using a neural network with more nodes and layers. This will allow the agent to explore a larger action space, mapping the actions to desirable outcomes. The larger number of nodes and layer in the neural network also means the agent will avoid being under-trained.

Another possible change that could be made to improve training success and times is to discretise the observation space. Consider that the current target bearing ϕ_T is continuous $\in [0, 2\pi]$ at least to within the bounds of machine and rounding errors in MATLAB. Instead of feeding this raw data to the agent it could be categorised such that ϕ_T is binned in 10° increments. This reduces the observation space from being effectively continuous to having 36 discrete possibilities, making it much more efficient to map every possible system state to an action. While this will reduce the precision and fidelity of the action system it will return *some* performance by the agent to ascertain whether this method of complete control is viable. There could be either some secondary architecture which allows further control fidelity within these bins, or the agent could be retrained with a more continuous or less discretised environment.

5.3.4 DDPG Guidance Law

While the DQN agent described in the previous sections is capable only of discrete actions, a Deep Deterministic Policy Gradient (DDPG) has a continuous action space. Different implementation methods must be used to accommodate the continuous action space of the DDPG agent. Whereas the DQN agent used in 5.3.3 was responsible for both the actuation mechanism and the GL, the DDPG implementation will be constructed so it is responsible for only one or the other. In this implementation, a DDPG agent is used to create a GL which dictates the trajectory of the projectile on approach to the target, by demanding a latax.

A key difference must be made to the neural network when using a DDPG agent as opposed to a DQN. The output of action layer in the DQN network was a binary 0 or 1, depending on what the weighting activation of the layer decided. The output of a DDPG action layer is continuous in the range $A \in [-\infty, \infty]$, but this is well outside the range of the latax which can be demanded of the projectile, due to saturation of the actuation mechanism. To account for this, a tanh layer is used to map the action range to $A \in [-1, 1]$. This is then also passed through a scaling layer, so that the action which is actually fed to the actuation mechanism is $A \in [-\tilde{a}_{max}, \tilde{a}_{max}]$.

Guidance laws usually demand latax both horizontal and normal to the projectile travel, though sometimes they may demand purely a lateral acceleration. In this sense, they are dual-channel, where each channel represents the acceleration normal and lateral to the longitudinal velocity of the direct fire projectile. While the implementation of the DQN agent in §5.3.3 encompassed actuator control and dual-channel latax, the operation and output of the agent doesn't necessarily have to cover both channels. Much like conventional Cartesian control, the agent can have full control over a single channel and two of them can be used in combination, to generate the final signal sent to the projectile. In this sense the agent can be trained in a 1D environment, which is shown in fig. 5.3.6. Two point masses of $m = 1$, the projectile and target are free to move along a generic 1D axis with distances from the origin being x_P and x_T respectively. Both have respective speeds of v_P and v_T directed solely along this axis. The DDPG agent is responsible for issuing an acceleration command to the point mass projectile.

Table A.2 in appendix A.4 shows the model parameters for the training. The agent

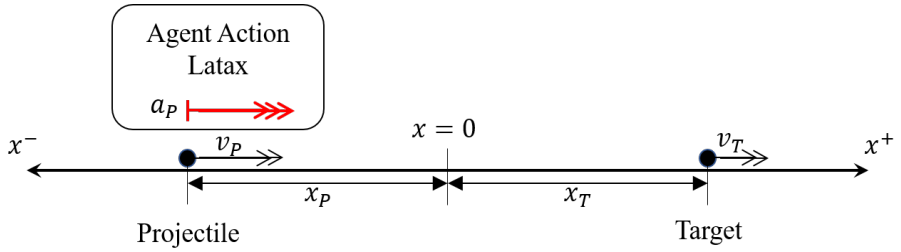

FIGURE 5.3.6 Illustration of 1D latax problem

is trained using the reward function described in §5.3.1. Notable differences are that the episode will be prematurely terminated depending on the single axis distance $x_T - x$, as opposed to the 2D radial distance d. This means the termination distance in the reward function becomes $d_T = x_T = 50$. Likewise the observations have been reduced to simply the 1D equivalents, $(d, \dot{d}) \rightarrow (x, \dot{x})$. As mentioned, the agent action is no longer controlling the bias points, but the acceleration demand of the projectile. The action space is a single latax demand $A = a_x \in [-\tilde{a}_{max}, \tilde{a}_{max}]$, mapped into this range from $[-\infty, \infty]$ using the tanh layer.

Figure 5.3.7 shows the training data for the DDPG agent in the 1D latax control system. There is an obvious disparity between episodes which were terminated early due to too great a miss distance, and the episodes which had a poor performance. Around the 3000^{th} episode, the agent was capable of preventing the early termination of the episodes. A reward of between -300 and 0 indicates an episode wasn't a failure, but also the agent was insufficiently reducing the error to increase the reward. By episode 7000, the agent could reliably reduce the error to within the accuracy bound demanded. In the last 3000 episodes, the agent steadily improved performance to a mean reward of 3×10^4

Since the agent was able to control the 1D dynamic system with the neural network configuration additional complications can be made. The primary difference the novel actuation mechanism faces in comparison to a traditional point mass model is the lag of the system in achieving the desired control variable. As such, an actuator lag is added to emulate the delay in system response caused by the projectile needing to complete one full rotation before enacting the command of the GL. The delay is modelled by a simple time-based signal delay block in Simulink, which holds a given signal by a predetermined amount of time, before passing it along. In this way, the agent is still receiving valid

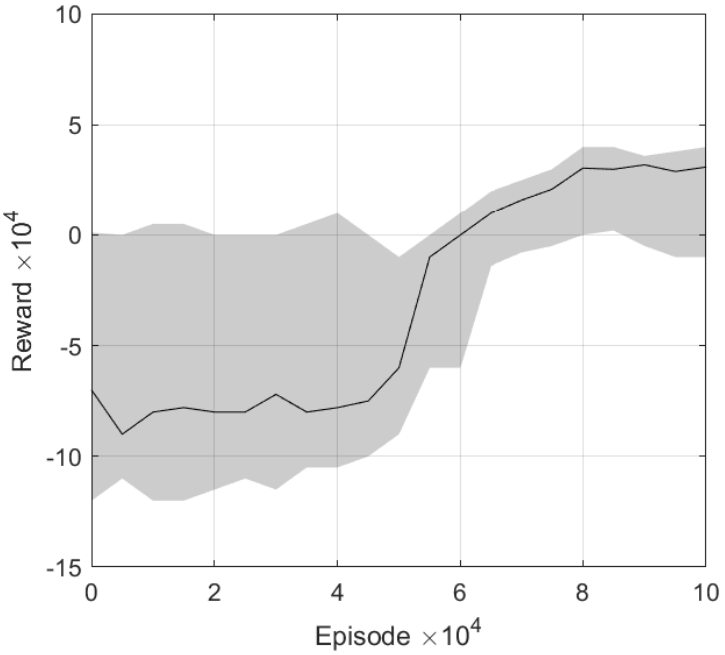

FIGURE 5.3.7 Training data for basic 1D control model (MATLAB 2020a)

information about the state of the system, it merely must learn that there is a delay present before the actions are executed. There is also no dynamic noise which goes unobserved, causing perturbations which would go unnoticed by the agent. The signal delay, or actuator lag, is set to 0.1, 0.02 and 0.01 seconds; since the agent sample time T_A is 0.1s these actuator lags correlate to T_A, $T_A/5$ and $T_A/10$ respectively. Figure 5.3.8 shows the training data for agents with different levels of actuator lag.

The figure shows that for both delay times of 0.01s and 0.02s, the agent is capable of learning actions which substantially increase the episode reward. For a 0.1s delay, the agent was unable to learn desirable actions as defined by the reward function. It should be noted that the agent may eventually have been able to learn the environment given sufficiently more episodes with the current network configuration. However, project constraints must be imposed somewhere and the results presented in the figure show that the capability is present within a suitable training time. Such neural-network optimisations should be considered during any higher TRL implementation but are outside the scope of this project.

Figure 5.3.9 shows the performance of the agent with a 0.02s actuator lag after the 10^5 episodes of training from fig. 5.3.8. The DDPG based GL visibly reduces the miss

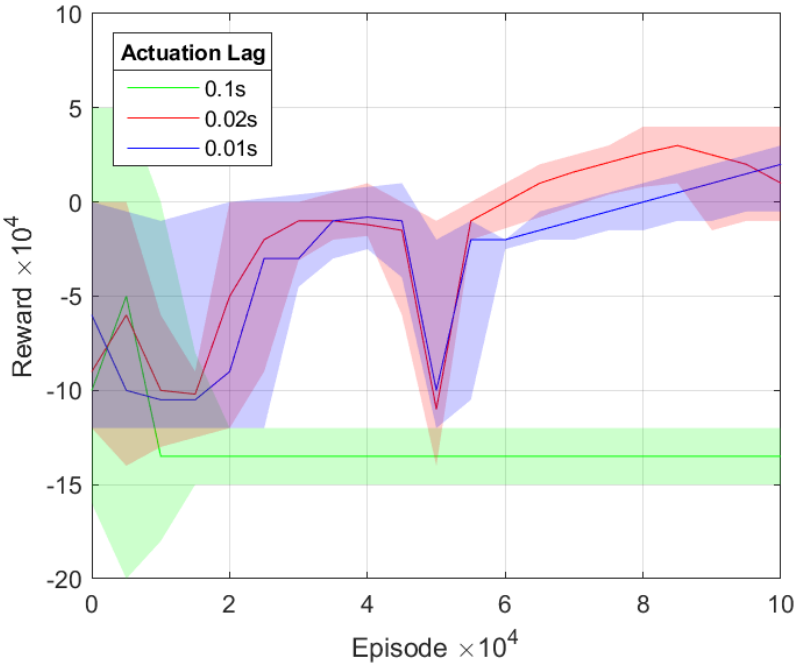

FIGURE 5.3.8 Training data for single channel environment and actuator lags

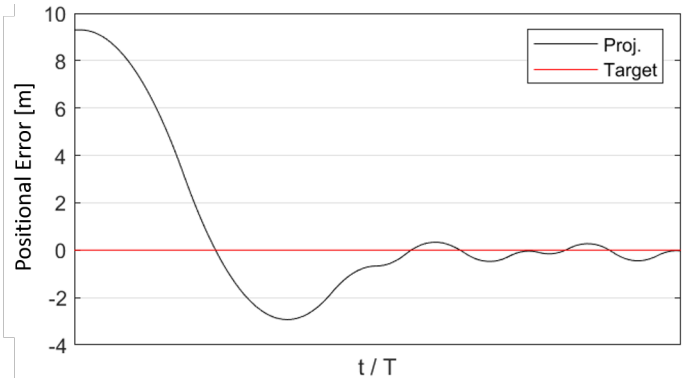

FIGURE 5.3.9 Performance trajectory for trained agent with 0.02s actuator lag

distance of the projectile and is able to hold in an effort to reduce the steady state error.

Summary

This section has discussed different RL AI agents, their implementations and has shown two ways in which they can be used to control different aspects a novel projectile with relative ease. A DQN agent was utilised to control both the actuation mechanism and GL of the system. This implementation was unsuccessful, but did show behaviour improvements, indicating the success is likely limited by time and resources. A larger and more complex NN capable of capturing more macroscopic system behaviours is necessary for further

improvements, as well as the time to run significantly more training episodes. Next, a DDPG agent has been used to create a single channel GL capable of reducing the miss distance along a single dimension and holding it there with an actuator delay modelled. This single channel GL can then be implemented along both vertical and lateral controls of the picture plane simplistic system to allow the agent to control the projectile flight completely.

The field of AI and reinforcement learning is still a relatively new one. While this section does demonstrate the feasibility of the technology and its applications to guided projectiles, the approach will be able to be refined significantly as the field progresses more. The performance of the agent is heavily dependent on the reward function used to train it and the reward function is entirely subjective. One approach to reduce the prejudice and inaccuracy of the reward function might be to create one which is linearly parametrised in terms of the model dependencies, such as distance, with different coefficients. The coefficients could then be optimised using a chosen algorithm, for example the GA discussed here. However, whereas the GA discussed here runs a batch of MC simulations for each candidate, optimising an AI agent would require a full training session. Multiple thousands of episode per training session each for multiple thousands of generations and candidates may make this method computationally unfeasible with current hardware, but the procedure itself would likely eliminate much of the perceived bias creators have when assigning importance to different aspects of the reward function.

Chapter 6

Simulations and Discussion

In this chapter, the various combinations of actuation method and GLs are then compared against each other and the free ballistic case. Firstly, in the picture plane, the nominal case, shows which configuration is able to reduce the miss distance under the most simplistic conditions. While this is more mathematically abstract and quite removed from a 7-DoF implementation, the results will help identify intricacies and nuances in the system behaviours which may otherwise be imperceivable in a realistic simulation. The initial conditions are varied from random to normal to isolate different characteristics of the correction trajectory. An optimal GL and actuation mechanism candidate can then be selected for further analysis.

A novel projectile design is then proposed. This is an illustration of how the actuation mechanism can be implemented into a traditional projectile form factor. The designs are created in CAD, then undergo CFD analysis to determine the corresponding aerodynamic coefficients. The output of the CFD process is compared against the results of other similar publications to verify it is producing satisfactory coefficients. Because CFD simulations are time consuming and resource intensive, only a few illustrative designs will undergo the analysis. The coefficients are then used to conduct ballistic stability analysis, described in chapter 3. At this point, the optimal GL from the preceding analysis is incorporated in the full 7-DoF model from chapter 3, along with the aerodynamic coefficients for different projectile types, to understand what level of correction can be expected when this control method is used with traditional projectiles.

6.1 Nominal Guidance Law comparison

With the descriptions of the guidance laws, actuation mechanisms, Monte Carlo procedures and system responses now given, an experiment can now be undertaken to compare the effectiveness of different combinations to reduce the miss distance. Figure 6.1.1 illustrates the flow of information, order of operations and a general overview of how the enclosed concepts and methodologies come together in the simulations. The GL will be chosen from those listed in Chapter 5, and as described it will either demand a ΔV or $\tilde{a}$ depending on the model of actuation mechanism. This demand passes through a generic controller **H** of the autopilot loop and then enters the actuation mechanism. The first process is to saturate the demand according to which regime the GL assumes; velocity will either be bound as $\Delta V \in [0, \Delta V_{Max}]$ or latax will be bound as $\tilde{a} \in [0, \tilde{a}_{Max}]$. The bias computer is then responsible for computing which values of ϕ_{ON} and ϕ_{OFF} are necessary to produce the saturated a_{Dem}. In the event a GL has perfect knowledge of the system it would never demand a value in excess of what the mechanism is capable of delivering and as such the demand would not need to be saturated. In a more practical implementation, the saturation block need only be present as a fail-safe, to ensure the algorithms present in the Bias computer need only work within a designated range.

Alongside this the actuator model function $\omega(\phi)$ is chosen, which represents the behaviour of the actuator and the resulting front section spin rate ω_F, or $\dot{\phi}_F$. This is a description of the `BiasON` and `BiasOFF` functions which can be used to re-create the actuator response for any combination of ϕ_{ON} and ϕ_{OFF}. Any complications to this model can be made, representing real world imperfect knowledge. For the implantation in the coming analysis, such complications are omitted and perfect knowledge is assumed. Before the simulation begins, for the given actuator model function, the numerical procedure from §4.3.3 (fig. 4.3.8) is used to produce a connection between ϕ_a and $\tilde{a}$. This is then fed into the Bias Computer block which uses the procedure to determine which ϕ_a is needed to produce a $\tilde{a}$, to meet the controller demand a_{Dem}. Additionally the procedure also determines the lag of the latax direction $\tilde{a}_\phi$ behind the intended bias centre ϕ_B, caused by non-instantaneous switching functions. Taking this lag into account, ϕ_B is adjusted so that the actual latax direction is in the direction required by the controller, $\tilde{a}_\phi \cdot a_\phi = 1$. In the following nominal

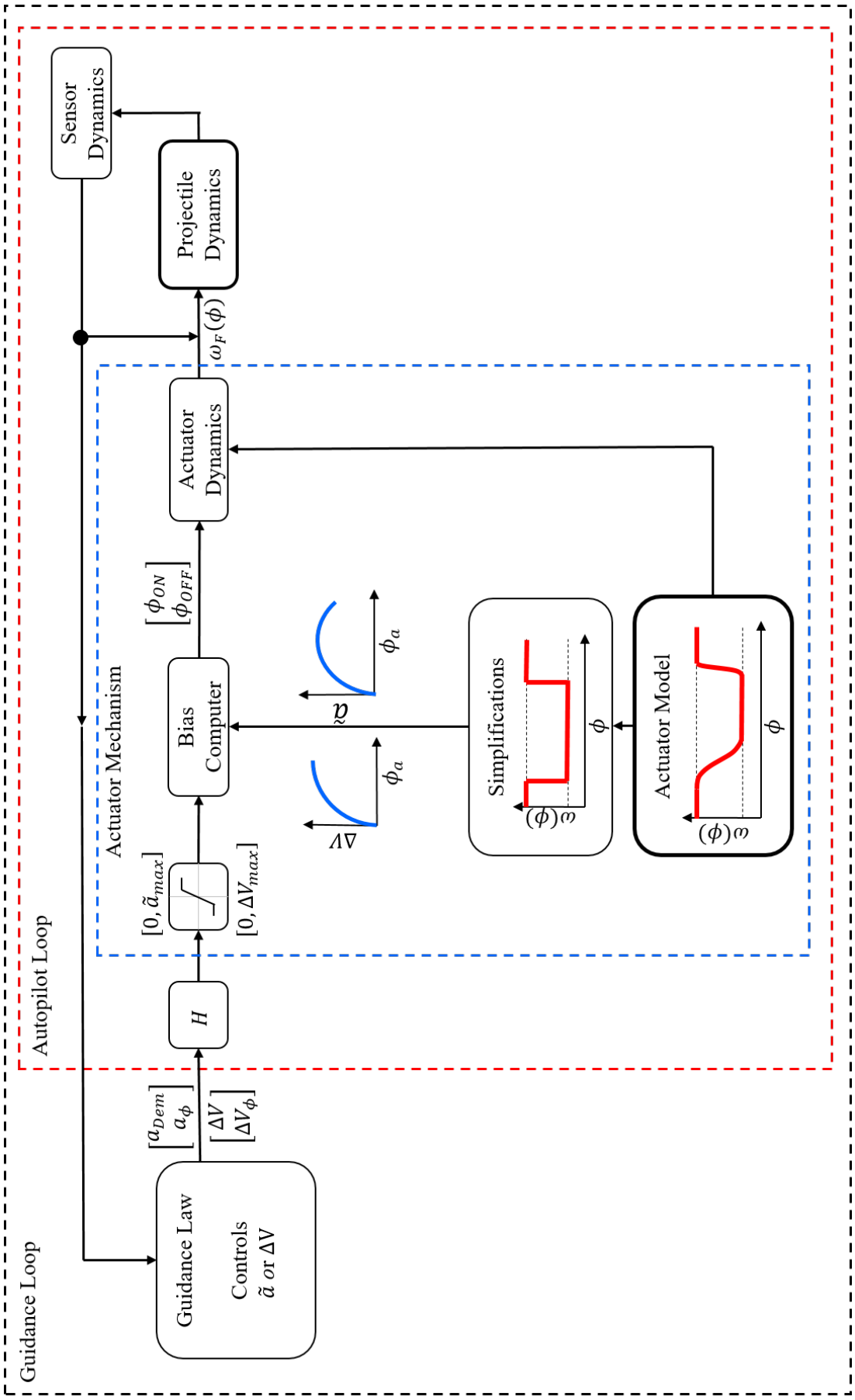

FIGURE 6.1.1 Block diagram showing information flow in nominal GL comparison

analysis the instantaneous switching model of $\omega(\phi)$ is used,

In addition to this, the actuator model is fed into the actuator dynamics box, which in its entirety acts as a simplification of the 7-DoF equations of motion responsible for the ogive section behaviour. The ϕ_{ON} and ϕ_{OFF} coordinates generated by the Bias Computer are used by the actuator dynamics box, in conjunction with the actuator model to create the actuator response function to this particular rotation. The projectile dynamics box then evolves according to the equations of motion, where the front section roll rate is dictated by the function supplied by the actuator dynamics box. The projectile dynamics compute one step, integrate the outputs using RK4 and then proceed to the sensor dynamics box, which again is capable of emulating any noise or bias in the measurement equipment or methodology. This information is fed back into the guidance law to compute the next set of instructions, when the roll rate next wraps to $\phi = 0$. The system state information is also fed back directly into the projectile dynamics box for constant iteration.

The simulation is run for $T = 50$s, and the update rate of the dynamics is set to 10^{-3}s, while the GL is polled every time the roll angle wraps to zero. This way the Bias points are only calculated when needed in order to avoid slowing the computation unnecessarily. In §5.3.4, it was found that in the current configuration, the DDPG agent could only accommodate the delay if the actuator lag T_L was at most $1/5$ of the agent poll rate T_A. The actuator lag time in the nominal system is $T_L \in [1, 2.5]^*$, and so the agent is polled every $5 \times \max[T_L] = 5$s. The lower bound is chosen here so there is never a period where the agent could go without instruction. The observations of the agent are x and $\dot{x}$, so the actual measurements d and $\dot{d}$ are first decomposed into x, y, $\dot{x}$ and $\dot{y}$. The agent is then polled twice, once for (x,$\dot{x}$) then again for (y, $\dot{y}$). The axial latax demands of the agent are then recombined to give a $[\tilde{a}\ a_\phi]^T$.

For the implementation of the PN GL, the navigation constant is set to $N = 1$. It can be shown that the traditional GL structure of eq. 2.5 (pg. 45) can be written in the form

$$\vec{a} = N\vec{V}_R \times \vec{\Omega} \tag{6.1}$$

*Using the values from table 4.1

where the LoS rotation vector $\vec{\Omega}$ is given by

$$\vec{\Omega} = \frac{\vec{R} \times \vec{V_R}}{\vec{R} \cdot \vec{R}} \tag{6.2}$$

This allows the LoS to be computed directly from the relative range $\vec{R}$ and relative velocities $\vec{V_R}$. While the simulation runs for 50s, the PN GL requires information on the relative speeds and distance, as such a representative downrange speed is fixed at $w = 10\text{m.s}^{-1}$. The relative values can easily be computed using $V_R = (u^2 + v^2 + w^2)^{1/2}$ and $R = (x^2 + y^2 + (w(T-t))^2)^{1/2}$.

Because the simplified switching model is assumed for the coming analysis, the values of ξ and V_k found from the GA optimisation can be used. When the actuator dynamics are modelled using the ΔV framework, the demands of the GL can be converted directly to bias coordinates. When the actuator dynamics are modelled using the $\tilde{a}$ framework, the ΔV which the GL demands must first be converted into a latax. This can be done with relative ease, since the roll time taken for the bias manoeuvre τ can be calculated, and used in combination with the ΔV to produce the equivalent $\tilde{a}$.

The procedure for evaluating the performance of the guidance laws against each other is as follows. MATLAB will be programmed to cycle through each configuration of the actuation mechanism, and then through each GL which operates using it. In each configuration, a Monte Carlo batch will be executed according the procedure in §5.1. Each batch must contain a sufficiently high number of simulations such that any difference between the performance of candidates is due to the configuration, as opposed to the random initial conditions; this batch size was determined to be 10^4. The data from each individual run is then saved for access later.

Dispersion

The control architecture presented thus far has of course been designed for a direct fire projectile. The best metric for comparing the corrective capabilities of such a system is to compare the terminal dispersion at the target. To emulate variation in trajectories, the launch conditions are no longer initialised randomly within a given bounds, but generated

according to the Gaussian probability density function; given by

$$f(x) = \frac{1}{\sigma\sqrt{2\pi}} e^{-\frac{1}{2}\left(\frac{x-\mu}{\sigma}\right)^2} \tag{6.3}$$

where σ is the standard deviation and μ is the mean of the parameter. It is assumed that using direct fire projectiles, before launch the operator would try and ensure the projectile will ballistically intercept the target: the control system more fulfils a disturbance rejection role than being solely relied upon to impact the target. Because of this, both the target and projectile have the same initial position in the picture plane and there is taken to be no relative velocity between the two. To emulate deviations in the firing conditions, perturbations are generated following the normal function, such that the majority of firings lie as close as possible to nominal conditions, with few outliers as would be expected with conventional ammunition. Thus, positional perturbations are generated with $\mu = 0$, $\sigma = 3$, while velocity perturbations are generated using $\mu = 0$, $\sigma = 0.3$. The `MATLAB` function `normrnd(mu,sigma)` is used to generate the normal numbers. Figure 6.1.2 shows a test of the function, using $\mu = 0$ and $\sigma = 3$, to ensure the function is generating numbers over the correct function. It is visible from the figure that the generation distribution is satisfactory, in addition the returned mean of the data was 0.000 with a standard deviation of 3.000 to 4 significant figures.

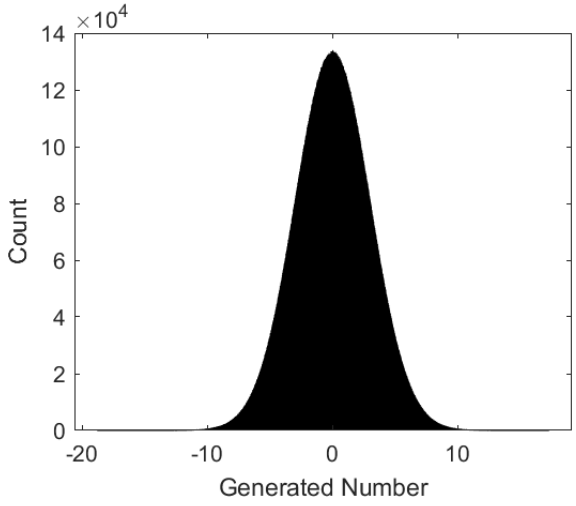

FIGURE 6.1.2 Test of MATLAB 'normrnd(mu,sigma)' function for 10^8 generated numbers ($\mu = 0$, $\sigma = 3$)

There are many different ways to evaluate or compare the planar dispersion of projectile

impact points. The majority of them involve placing a circle with a centre which coincides with the mean point of all the considered impacts. The radius of this circle is then increased until a certain threshold of projectile lie within the resulting circle. The most widely used dispersion metric counts 50% of the impacts within this circle, known as Circular error probability (CEP); other metrics include Distance Root Mean Squared (DRMS) which includes 63.21% (or 2σ) and R95 which includes 95%. CEP is the most commonly used metric across both the academic and industrial fields of ballistics, and the validity of using it has been critiqued by a variety of sources including the US Army Laboratory [32, 200]. A parametric investigation has been undertaken to understand the effect of varying projectile parameters on terminal miss distance by measuring CEP [95]. CEP is predominantly the metric for artillery dispersion, but not small calibre projectiles. As such, CEP will be used when referring to the impact dispersion of artillery shells, while R95 will be used when to compare the dispersion of small calibre direct fire projectiles, where accuracy is paramount.

10^3 simulations are run for each guidance law, with initial conditions generated according to the normal distribution in eq. 6.3. For each simulation, the terminal impact points are recorded as (x, y) coordinates, which can then be used to record the radial miss distance d. The mean impact points (μ_x, μ_y) can then be computed using the number of impacts $N_I = 10^3$ as

$$\mu_x = \frac{1}{N_I}\sum_{i=1}^{N_I} x_i \ , \qquad \mu_y = \frac{1}{N_I}\sum_{i=1}^{N_I} y_i \tag{6.4}$$

Once the mean impact point has been calculated, the radial distance from the mean impact point for the i^{th} impact $\bar{d_i}$, is calculated with

$$\bar{d_i} = \left((\mu_x - x_i)^2 + (\mu_y - y_i)^2\right)^{1/2} \tag{6.5}$$

The impacts are then ordered according to this mean miss. The radius of the circle containing P percentile of impacts $R_{P\%}$, where $P = 0.5$ for CEP *etc.*, can then be computed by accessing the index of the ordered impacts

$$R_{P\%} = \text{Impact}[\text{n}], \qquad \text{where} \qquad \text{n} = \lceil \text{P} \cdot \text{N}_\text{I} \rceil \tag{6.6}$$

Note that the ceiling function is used here instead of the floor to represent a worst-case scenario of this frequentist approach, instead of the more continuous, Bayesian methods which have been considered in other literature [200].

Table 6.1 shows the results of the described simulations, with a range of dispersion metrics corresponding to each guidance law. In the ballistic case the controller effort is switched off and the projectile trajectory evolves according to the initial conditions. It is apparent that the novel guidance law provided the highest level of error correction, with the lowest value of CEP, DRMS and R95 against all other guidance laws. This was the case for both the ΔV based and acceleration-based controller demands.

Actuation Mechanism	GL	CEP [mm]	DRMS [mm]	R95 [mm]
Ballistic		1.94×10^4	2.21×10^4	4.05×10^4
$\tilde{a}$	PN	83	90	160
	DDPG AI	404	457	874
	Novel $\tilde{a}$	50	61	101
ΔV	Novel ΔV	48	58	105
DQN AI			N/A	

TABLE 6.1 Dispersion measurements for nominal system

Fig. 6.1.3 shows 100 impacts from each of the guidance laws, selected at random from the 10^3 runs. *N.B.* no impact points are covered by the legend. Because the ΔV based and acceleration-based controller demand GLs had some similar performance dispersion, the acceleration-based novel GL dispersions are shown. It is apparent that all guided cases have fairly even distribution of rounds, with a small deviation of outliers. All 100 impacts that were selected from the set are shown on the figures, there were no impact points extreme enough to warrant exclusion from the plots. There is a high density region of impact points which would indicate a bias in the GLs towards specific locations in space. AI does show a circular dense region of impacts centred directly over the target at (0,0), in addition to a semi-circular cluster along the right side of the CEP and DRMS circumferences. Further statistical data analysis will confirm whether the dispersion bias

is significant. All guidance laws implemented under these nominal simulation conditions provided satisfactory levels of dispersion correction.

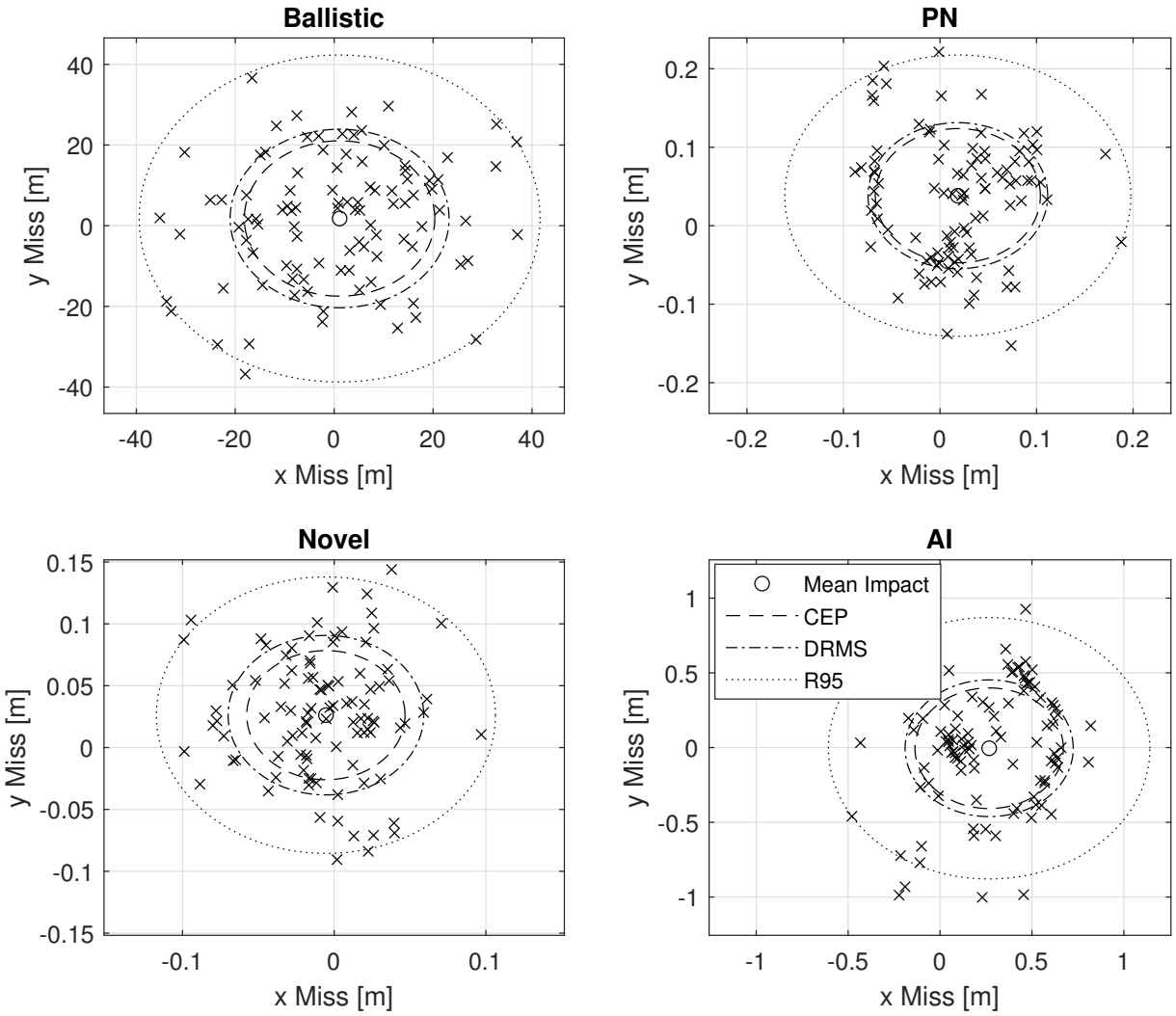

FIGURE 6.1.3 Terminal dispersion of various guidance laws controlling $\tilde{a}$, with target at $(0,0)$
*The legend present for AI represents all sub-figures and no data points are obscured

Statistical data analysis

In addition to the dispersion circles shown in table 6.1, more rigorous statistical analysis, following ref. [201] is shown in table 6.2. The impact location means were calculated in eq 6.4. The standard deviations are of course calculated using

$$\sigma_x = \sqrt{\frac{\sum_{i=1}^{N_I}(x_i - \mu_x)^2}{N_I}} \qquad \text{and} \qquad \sigma_{\mathrm{y}} = \sqrt{\frac{\sum_{\mathrm{i}=1}^{\mathrm{N_I}}(\mathrm{y_i} - \mu_{\mathrm{y}})^2}{\mathrm{N_I}}} \tag{6.7}$$

and the correlation coefficient $\rho(x,y)$ is given by

$$\rho(x,y) = \frac{1}{N_I - 1}\sum_{i=1}^{N_I}\left(\frac{x_i - \mu_x}{\sigma_x}\right)\left(\frac{y_i - \mu_y}{\sigma_y}\right) \tag{6.8}$$

Whilst there is no Hypothesis **H** to imply any causative correlation between a spatial x and y impact coordinate, it is useful to suggest that any significant correlation between the impact points is indicative of a bias in the guidance laws. As such, we define the null hypothesis H_0 (eq. 6.9) and alternative hypothesis H_A (eq. 6.10) as:

There **is no** significant correlation or bias in the impact point dispersions

$$H_0 := \lim_{N_I \to \infty} \rho \approx 0 \tag{6.9}$$

There **is** significant correlation or bias in the impact point dispersions

$$H_A := \lim_{N_I \to \infty} \rho >> 0 \tag{6.10}$$

To determine if a significant bias is present it is necessary to calculate the p-value, which illustrates the probability, under assumption of **H**, of observing data with equal or lesser compatibility with **H** relative to the current data [†]. In Bayesian statistics, the p-value, under the assumption of a hypothesis **H** can be defined in terms of a test statistic t, from a t-distribution, as

$$p_H = \int_{-\infty}^{t} f(t'|\mathbf{H})\mathrm{dt}' \tag{6.11}$$

where $f(t'|H)$ is the probability density function of a counted test statistic t under the assumption of **H**. This assumes a left-tailed test which evaluates the integral between $[-\infty, t]$, but a right tailed test can also be used which evaluates on the range $[t, \infty]$. The

[†]As opposed to the probability that the hypothesis is true, $P(\mathbf{H})$

t-distribution can be defined in terms of the gamma function $\Gamma(n)$, or the beta function $B(x,y)$. Following ref. [201] it shall be defined in terms of the beta function, given by

$$B(x,y) = \int_0^1 t^{x-1}(1-t)^{y-1}.\mathrm{dt} \tag{6.12}$$

The t-distribution probability distribution function (PDF) can be written as

$$f(t,\nu) = \frac{1}{\sqrt{\nu}\, B(\frac{1}{2},\frac{\nu}{2})}\left(1+\frac{t^2}{\nu}\right)^{-\frac{\nu+1}{2}} \tag{6.13}$$

where the number of degrees of freedom is $\nu = N_I - 2$ and t is the test statistic. Where one has knowledge of the Pearson correlation coefficient, which is the case from eq. 6.8, then following can be used to generate the test statistic t:

$$t = \frac{\rho\sqrt{\nu}}{\sqrt{1-\rho^2}} \tag{6.14}$$

Finally, the p-value is computed by integrating the t-distribution PDF up to this computed t-statistic

$$p = \int_{-\infty}^{t} f(t,\nu)\mathrm{d}.t' \tag{6.15}$$

using t from eq. 6.14 and $\nu = N_I - 2$. If $p \leq \alpha$ the null hypothesis H_0 is rejected and the alternative hypothesis H_A is accepted. If $p > \alpha$ the null hypothesis H_0 is accepted. This analysis is computed for each of the GLs using all $N_I = 10^3$ impact points in the set, using a significance level of $\alpha = 0.05$. The results are shown in table 6.2.

Guidance Law	μ_x	μ_y	σ_x	σ_y	ρ	p-Value
Ballistic	1.095	1.786	16.893	15.312	0.165	0.102
PN	0.019	0.038	0.056	0.085	-0.045	0.65
AI	0.267	-0.005	0.277	0.389	0.264	0.008
Novel $\tilde{a}$	0.0013	-0.008	0.044	0.050	0.038	0.229
Novel ΔV	-0.006	0.026	0.042	0.049	-0.004	0.971

TABLE 6.2 Statistical Analysis of GL dispersions with $\alpha = 0.05$

From table 6.2 it is apparent that only the AI had a p-value less than the significance

level. This means that the correlation of impact dispersion observed when the nominal system projectile controlled by the described AI based GL, is statistically significant, indicating there is a significant bias. The correlation present for AI is weak, appearing to be more clustered than following a traditional linear relation. However, the significance of the results indicate that this pattern is unlikely to be due to chance. The clusters that are present are centred about the target location, (0,0). The 'off-target' cluster, along the right side of the CEP and DRMS circumferences, is the cause of the correlation. This overcorrection to the right is indicative of a skew-trained agent with non-optimal actions. It is unclear at present whether this is due to insufficient training, training in a non-representative environment, or implementing a single-channel agent in a dual-channel configuration. Due to the stochastic initialisation of the simulations these clusters are unlikely to be an artefact of identical agent actions, it is more likely that it may be a result of the dual-channel implementation or biased agent experience.

For no other guidance laws are the p-values lower than the significance level α, indicating that any correlation present in the impact dispersion are likely due to chance and that there is no significant indication of bias in the correction performance of the GL.

Correction characteristics

Figure 6.3 shows the integral errors for each implementation, with the batch average system responses are shown in fig. 6.1.4. Figure 6.1.4 shows a comparison of the Monte Carlo batch averages for the considered guidance laws, or the zero-effort miss along the trajectory. Note that the ballistic case is omitted from the following analysis since there is no controlled error reduction to be compared.

The integral error for the averaged system response indicates how much of the trajectory was spent with high error, thus a lower integral error is desirable as this shows a fast convergence and stable steady state. It is apparent that PN had by far the largest integral error compared with the other guidance laws. This is highly likely due to the nature of the PN GL itself, which is to ensure a collision between the projectile and target upon impact, as opposed to mitigating disturbances during the flight. This is an undesirable behaviour for the projectile, due to the saturation of the actuation mechanism. Figure 6.1.4 shows that the error correction rate of PN is very similar to that of the novel GL, but

Actuator Method	Guidance Law	Integral Error ($\times 10^4$)
	PN	4.115
$\tilde{a}$	DDPG AI	1.435
	Novel	1.287
ΔV	Novel	1.264
	DQN AI	N/A

TABLE 6.3 Comparison of actuation mechanisms and guidance laws for instantaneous switching

the correction of PN only significantly begins when the projectile is already significantly closer to the target. If any present error remains uncorrected in the early phases of the flight, any subsequent perturbation may induce a scenario where the available latax is insufficient to reduce the error to a satisfactory level. As such, one cannot recommend PN for this implementation and configuration of the described dual-spin, direct fire projectile. It is possible that PN can be modified in some way as has been done in the majority of the considered literature. One possibility is to set a 'virtual target', closer to the projectile than the main target actually is, such that PN begins correcting the error sooner. Once the ZEM has been reduced, the virtual target can be removed and replaced with the real target for usual guidance. In addition to this, the steady state error of PN is higher than that of the novel GLs. This is caused by N being too great and scaling up any small demand in the governing equation, *i.e.* there is a minimum, non-zero acceleration demand which can be issued by the GL. Finally, there is a sharp rise in error at the termination of the trajectories. As the projectile is on terminal approach to the target the LoS rate increases rapidly. This inflates the acceleration demand of the system to near maximum causing an overshoot from actuator saturation. However, both artefacts can likely be fixed by implementing a gain scheduling procedure to ensure a high-fidelity acceleration command can be issued when precision guidance is required. The scheduling would need to be a function of both longitudinal distance R, as well as radial distance d, which would result in a PN-like guidance law effectively operating in different regimes like that of the novel GLs.

Initially, AI converged at the same rate as both novel GLs, but the error reduction rate slowed for $t/T \gtrsim 0.3$, due to the agent slowing the projectile sooner than was necessary. For $t/T \gtrsim 0.3$ The AI agent is trained in a single-channel environment but implemented in a dual-channel configuration. The coupling between the channels will lead to differences in operation which the agent cannot perceive and therefore act to mitigate. In addition to this, the single channel environment only contained an actuator lag which emulated the lag which the agent would experience in the actual implementation. Since the lag is variable, an artefact of the time taken to enact a bias, an optimisation of the training lag would be non-trivial. The lag would have to be modelled after the actuator response function $\omega(\phi)$. This eliminates the simplicity of the point mass training system and would require a more complex neural network and AI agent to learn in the environment. In such a case, resources would be better spent training a dual-channel GL agent directly on the system.

Both novel guidance laws considering ΔV and acceleration begin to converge at the same rate and unlike the AI or PN GLs, there is no overshoot. This is the expected outcome, seeing as the GL parameters ξ and V_k were optimised to minimise the overshoot of the system entirely. For values of $0 \leq t/T \lessapprox 0.4$ the both novel approaches converge at nearly identical rates. For values of $t/T \gtrapprox 0.4$ the acceleration-based method provides a quicker convergence than the ΔV. In this region, the projectile is close enough that the controller is no longer demanded maximum acceleration and discrepancies in the methodologies will show. Because the acceleration-based model includes the time when considering the approach velocities, the velocity changes are enacted quicker, primarily due to the ΔV method demanding velocity changes located in a dead-zone which of course it has no knowledge of. The acceleration-based GL begins switching to the transient regime at $t/T \approx 0.6$, whereby it approaches at the designated approach speed V_k.

The ΔV based GL continues to reduce error throughout the transient regime until it reaches the steady state regime at $t/T \gtrapprox 0.85$. At this point, the optimisation of V_k ensure that any residual or relative velocity is completely eliminated at the time the projectile reaches the desired level of accuracy. The steady state error for the ΔV based system is lower than the acceleration-based novel GL, but by a small margin. As was shown in table 6.1, this discrepancy in steady state error led to no significant or in fact discernible difference between the impact point accuracy, at least with the considered metrics.

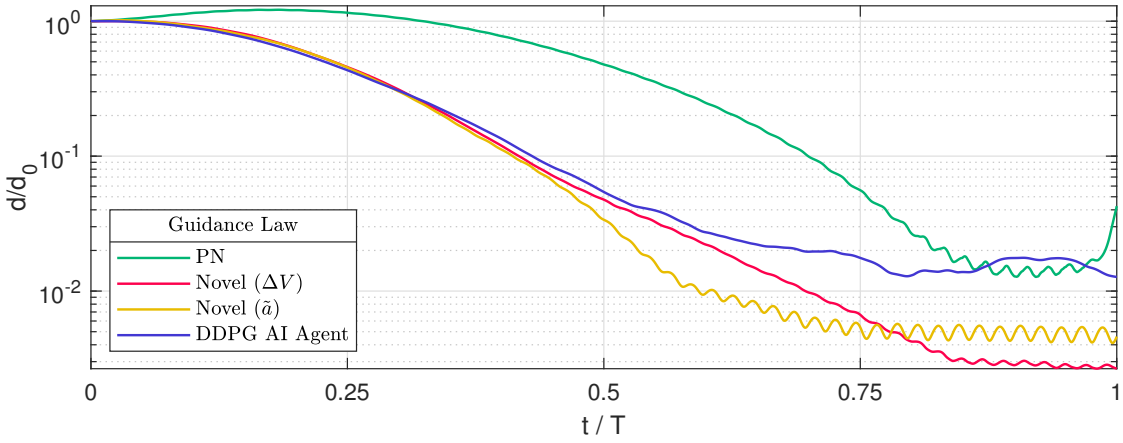

FIGURE 6.1.4 Error reduction capability of GLs

6.2 Novel geometry analysis

In this section, two examples of projectiles are created to demonstrate how the novel actuation mechanism can be implemented. The first is a direct fire 7.62x51mm NATO, the second is a 155mm M107, which is traditionally an indirect fire artillery shell. The designs are created in the CAD software Space Claim. These CAD files are then used in CFD simulations to determine aerodynamic coefficients which are in turn used in combination with the stability framework outlined in the previous chapters to map the ballistic stability of the projectiles over the expected flight envelope. In both instances, the novel projectile model is made to resemble the original as closely as possible in terms of physical properties. In particular, the mass is kept the same in both projectiles; while the physical volume of the ogive is reduced, it is assumed that the mass distribution and density is modified in such a way as to preserve the centre of gravity and moments of inertia. Table 6.4 shows the parameters for both of the projectiles.

6.2.1 CAD models

The actual geometry of the projectile will require a considerable amount of further research and optimisation. The boattail angle alone of projectile has undergone decades of research before the optimal geometries used by modern projectiles were found and this is traditionally something which is found through trial and error. Guided projectiles are obviously significantly more expensive to manufacture per-round than traditional projectiles, as such

Parameter	Artillery Shell (M107)	Bullet (L54)	Units
D	155	7.83	mm
L	698	29.93	mm
m	43	9.33×10^{-3}	kg
x_{CoM}	459	12	mm
I_{xx}	0.144	7.228×10^{-8}	kg.m^2
$I_{yy} = I_{zz}$	1.216	5.379×10^{-7}	kg.m^2

TABLE 6.4 Projectile parameters

it is impractical to use a large volume of test rounds when optimising the designs empirically. It is likely that as with traditional guided projectiles, a large amount of theoretical research will need to be conducted using simulations. What follows are two illustrations of projectile designs which utilise the novel actuation method.

7.62x51mm NATO

Figure 6.2.1 and fig. 6.2.2 show different perspectives of a modified 7.62x51mm, with the blunted face or facet highlighted to distinguish it. Due to the length of the ogive, the curvature of the hybrid ogive (Appendix B.2.2, fig. B.2.4) is visually quite subtle and thus facet is difficult to distinguish in the profile view of fig. 6.2.1B. The blunted surface is the upper side of the ogive on fig. 6.2.1B, the lower is the regular hybrid curvature. Since the curvature of the surface frontally exposed to the oncoming free stream velocity has been partially reduced, the drag force will increase. Since the surface area of the ogive has reduced, the skin friction will reduce which would in turn lead to a reduction in the spin damping moment. However, the reduction in surface area also causes the surface area of the projectile to be perpendicular to the surrounding air, as the projectile rotates, which causes the spin-damping moment to increase more than it decreases from the surface area reduction. It is this mechanism which provides the roll damping moment necessary for the actuation mechanism to function, but any method of achieving the increase is acceptable.

Figure 6.2.2 shows the front (fig. 6.2.2A) and rear (fig. 6.2.2B) trimetric views of the design. The blunted ogive can be described by a plane which intersects with the

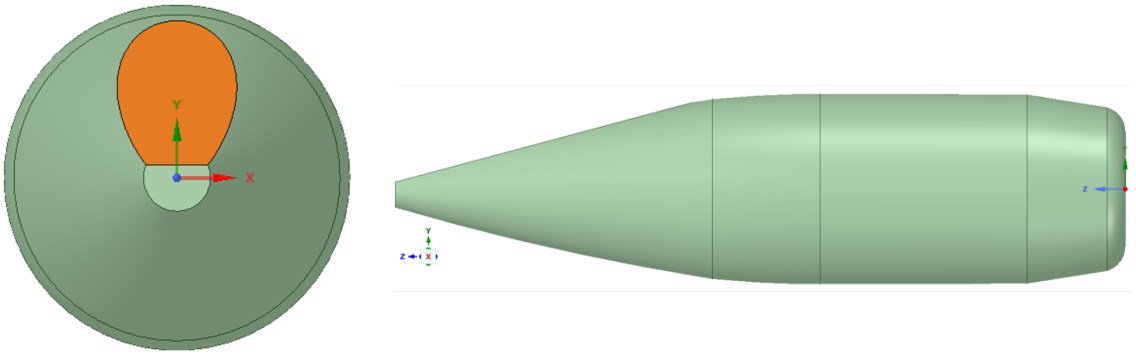

(A) Front (B) Side

FIGURE 6.2.1 Plan views of 7.62mm projectile design with blunted face

traditional geometry. A point p_1 is identified on the projectile meplat, centred laterally but raised in the normal axis. This point can be on the outer edge of the meplat, such that it coincides with the meplat-ogive vertex, or it can be closer to the longitudinal axis of the projectile. Another point p_2 is located on the ogive, at the tangent-secant boundary. The line connecting p_1 and p_2 is then used as the limit at which all material above is removed, to create the blunted surface. Simply, these points can be moved to reduce or increase the surface area of the blunted face. However, it is more likely that a more optimal design will consider a complex topology to achieve the desired increase in roll damping moment and lift force, while keeping the drag force low. In this case, p_2 is chosen to be the tangent-secant boundary and p_1 is chosen to be $\frac{1}{2}$ the distance from the centre to the outer edge of the meplat.

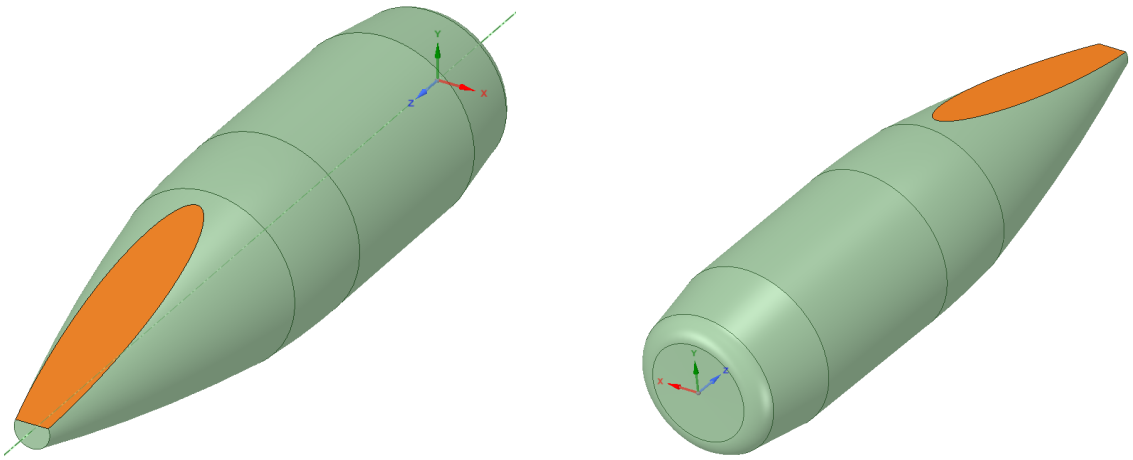

(A) Front (B) Back

FIGURE 6.2.2 Trimetric view of 7.62mm projectile design with blunted face

155mm M107

Figure 6.2.3 and fig. 6.2.4 show different perspectives of a modified M107 shell. A frontal view is shown in figure 6.2.3A, where the blunted face visibly occupies a considerably smaller proportion of the projectile cross section than the 7.62mm projectile in fig. 6.2.1A. The blunted face is created using the same two-point placement system as in the 7.62mm design. However, the boundary of the hybrid ogive in the M107 projectile is defined by the projectile fuse, which carried across in this design. Physically, the blunted section of the M107 is considerably larger than the 7.62mm, but obviously accounts for a significantly smaller amount of the M107. The resulting effect on the trajectory, for the spin damping, lateral control force and drag will be considerably smaller. Figure 6.2.4 shows a side view of the 155mm projectile. The front section has the blunted face on the top side of the image, while the regular ogive profile is on the bottom.

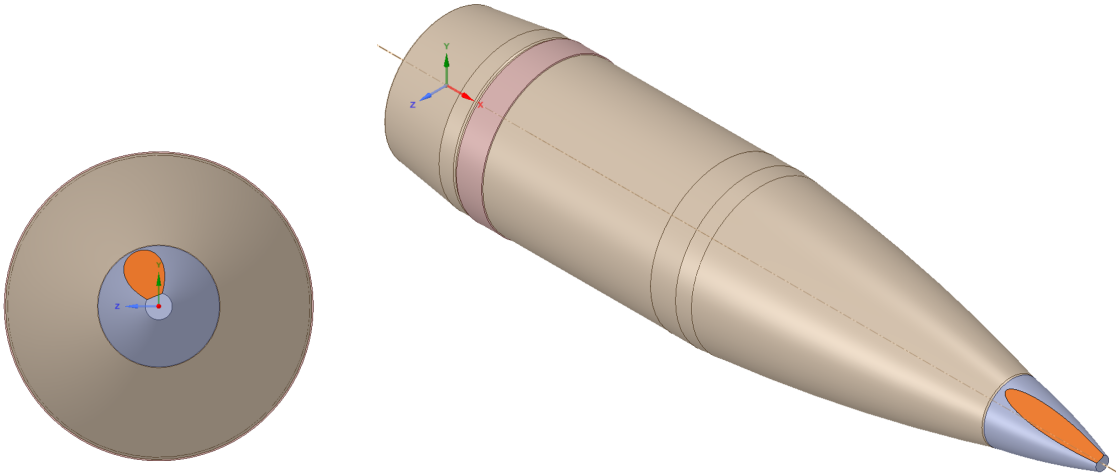

(A) Front (B) Isometric

FIGURE 6.2.3 Views of novel M107 155mm projectile design

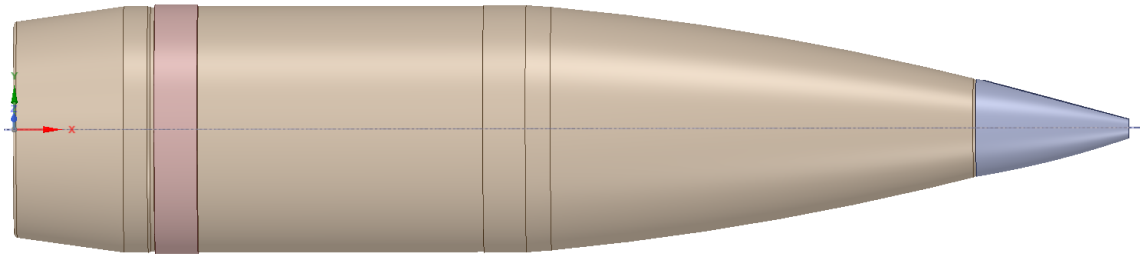

FIGURE 6.2.4 Side view of novel M107 155mm projectile design

6.2.2 Aerodynamic coefficients using CFD analysis

This section describes the CFD process used to determine the aerodynamic coefficients of the novel projectile, which are necessary to determine the efficiency of the novel control mechanism. In addition, it will allow the trajectory changes which have resulted from the geometric differences to be differentiated. While semi-empirical code architectures such as PRODAS, can be used to determine the coefficients, Navier-stokes based CFD approaches have shown to provide significantly more accurate coefficient data when compared to available experimental flight data [84]. The process of using CFD simulations to determine projectile aerodynamic coefficients over a range of flight conditions has been well documented, predominantly ANSYS-Fluent [90, 97, 96] but other CFD packages have also been used [88, 202].

The process for obtaining the coefficients is as follows. Firstly, the projectile is designed in CAD software, which has already been shown in the preceding section. Next, the mesh and cell type are defined such that they can sufficiently capture the behaviour of the fluid flow around the projectile. Then, the boundary conditions are set and the solver type chosen. Finally, the simulations are run and the resulting coefficients are calculated from the corresponding force and moment outputs.

Validation of methodology

Before the novel geometry is evaluated, the coefficients obtained from the CFD procedure are validated against available literature using a traditional geometry. In ref. [92] the coefficients for an M107 projectile are computed, on the same M107 design on which the novel design described here is based. Importantly, the drag, lift and spin damping coefficients are explicitly stated. Following Wessam and Chen, the M107 CAD geometry is imported into ANSYS-FLUENT and the mesh is created using quadrilateral cells for the fluid domain and hexahedral cells for the projectile. The domain was defined by a 3.5 calibre cylinder centred about the projectile centroid, extending 1 calibre in front of the tip and 7 calibres below the base. In total, 3.5×10^5 cells were used compared to 346352 in the reference. A coarser mesh could be used, but it has been shown that coefficients vary around 2% on average between fine, medium and coarse meshes [203]. The far field

boundary condition is `pressure far field density-based`, with free stream values of $T = 300K$ and $P = 1$atm. Figure 6.2.5 shows the results of the CFD analysis against those obtained from the literature for the drag force C_D (fig. 6.2.5A) and spin damping moment C_{lp} (fig. 6.2.5B).

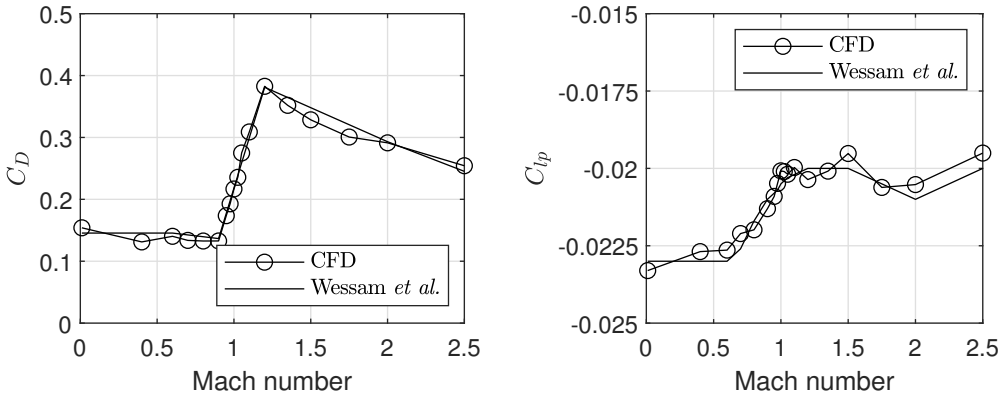

(A) Drag force (B) Spin damping moment

FIGURE 6.2.5 CFD results against those from ref. [92]

It is apparent that all of the coefficients obtained are in good agreement with respective source they are being compared to. There is no bias or consistent discrepancy across the two comparisons, which would indicate a systematic error in the procedure in a certain Mach region. There appears to be a larger discrepancy in C_{lp} than in C_D, but this is likely due to the very low resolution for that coefficient. The spin damping moment often varies by only 10^{-2} across the investigated Mach range and so the parametric variance is often only a few multiples of the machine computation resolution. This is partly why C_{lp} have the lowest uncertainty in many literature sources [64, 56], because there is so little variation across the Mach range.

Because the traditional design is completely radially symmetric, there is no difference between the normal and lateral force coefficients. When the geometry has radial symmetry, a non-zero values of α and β induces the normal and lateral forces via the angle of attack/side-slip dependant force terms, $C_{N\alpha}$ and $C_{Y\beta}$ respectively. A radially symmetric projectile will have no lift at $\alpha = 0$, as it is by definition an aerofoil asymmetry which causes lift. As such, the normal and lateral force coefficients are omitted from the investigation.

Results for novel geometry

The value of the novel coefficients has been intentionally redacted, but they are shown without a scale to illustrate the relative variance. Figure 6.2.6 shows the aerodynamic coefficients for the drag force (fig. 6.2.6A) and spin-damping moment (fig. 6.2.6B) for novel geometry modifications made to the 155mm M107 projectile. The Mach range used for the investigations is the same, concentrating the data points around Mach 1 to capture behaviour in the transonic regime. Because the total area of the 155mm projectile effected by the modification was so small, even from the frontal free stream perspective, the change to the drag coefficient is nearly negligible. Because the lift coefficient is at the expense of drag, it is apparent that the control force available for the projectile to use during the correction manoeuvres is also low.

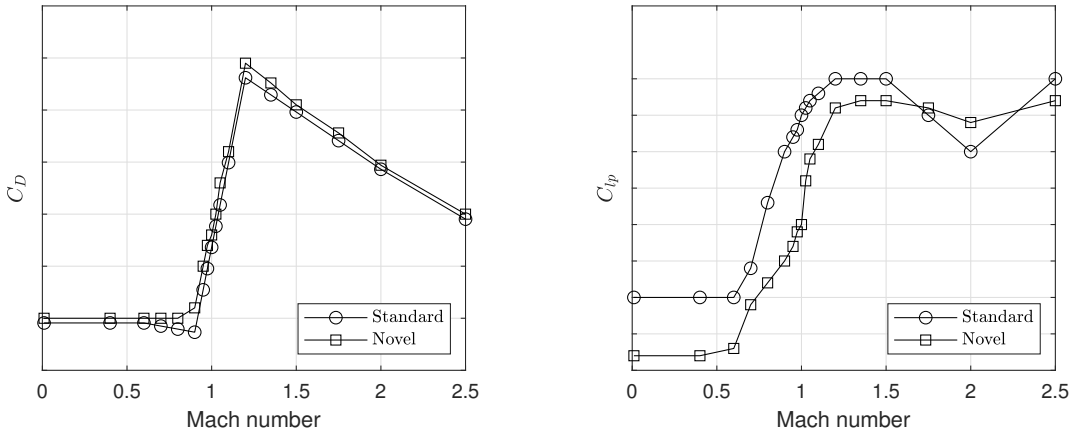

(A) Drag (B) Spin Damping

FIGURE 6.2.6 Aerodynamic coefficients of novel geometry against traditional 155mm M107

The change of the roll damping moment is more significant for the novel case. Because symmetric projectiles have very little roll damping moment, the only contribution being skin friction drag, any asymmetric modification to the projectile will cause an increase. Note that the novel projectile actually has more negative values than the traditional projectile. This is due to the sign convention, a more negative spin-damping moment means the moment causes a larger deceleration of the roll rate. Because the magnitude of the traditional spin damping moment is so low, the presence of any induced C_{lp} is visually more significant.

Figure 6.2.7A shows the drag coefficient change across a Mach range resulting from

the novel geometry changes on a 7.62x51mm NATO round. It is apparent that the drag coefficient for the novel geometry is significantly higher for all observed Mach numbers. The drag coefficient for the traditional 7.62mm round is significantly higher than the traditional 155mm M107 is, without modifications. This is due to the ogive profile of the 7.62x51mm being substantially less aerodynamic than the 155mm; it is shorter proportional to the body and the cross section subjected to the frontal free stream velocity has a lower radius of curvature. The increase in C_D in fig. 6.2.7A after the geometry modification is more significant because the blunted section of ogive contributes a much larger proportion of the frontal area presented to the oncoming free stream. The drag also increases by a larger amount in the transonic regime than towards the higher Mach numbers, which is in part due to the formation of bow shocks at the higher Mach speeds, preventing flow separation around the blunted face. This variation in C_D as a result of the geometry modification is similar to the results seen in Appendix B.2.2, during modification of the meplat tip diameter in the PRODAS parametric investigation.

The increase in drag coefficient leads to a decrease in effective range of up to 10% of what can be expected by a traditional round. It is a rule of thumb that 80J is required of ballistic projectiles to achieve the desired terminal effects. Because kinetic energy is proportional to V^2 and the velocity drop is directly proportional to the drag coefficient increase, the geometry modifications will cause the projectile to drop below this energy threshold approximately 10% sooner than it would do otherwise. The associated lift coefficient is only computed at $V = 2.4$ Mach for the 7.62mm and $V = 1.6$ Mach for the 155mm. This is because the lift coefficient is assumed to be constant throughout the flight to more closely represent the discussions of the control mechanisms.

Figure 6.2.7B shows the spin damping moment coefficient for the modified 7.62mm round. It is apparent that the novel design has a significantly lower spin damping moment than the traditional design over all evaluated speeds, especially in the expected operating region of $V >$Mach 1.5. Of interest is that the novel C_{lp} was not significantly lower than the traditional round in the transonic region, where one would expect asymmetric shock formation

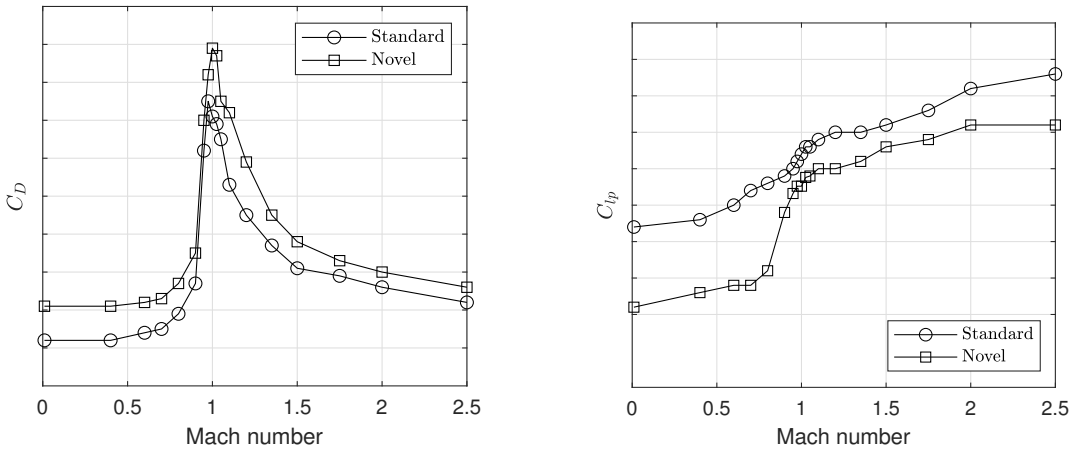

(A) Drag (B) Spin Damping

FIGURE 6.2.7 Aerodynamic coefficients of novel geometry against traditional 7.62x51mm NATO

6.2.3 Stability analysis

With the projectile geometries established, using the blunted ogive modification to a standardised projectile design, stability analysis can now be conducted using the framework outlined in chapter 3. Coefficients are only non-zero if they were derived from the preceding analysis. Figure 6.2.8 shows the stability plots for various projectile velocities expected for the flight envelope of the 7.62x51mm NATO and 155mm M107 projectiles. Figure 6.2.8A shows the 7.62x51mm NATO and fig. 6.2.8B shows the 155mm M107. The dual-spin projectile with passivated control surfaces is used and the effect of the blunted face is modelled as canard contribution: the surface area and angle are calculated from the CAD software. The traditional 7.62mm remains ballistically stable for all projectile velocities above $V = 1.8$ Mach, below which there is insufficient gyroscopic stability. Removing a significant portion of the ogive during the blunting process lowers the moments of inertia and also shifts the CoM towards the rear. This increases the moment arm, increases the overturning moment and decreases the dynamic stability by decreasing the stability factor. This leads to the novel projectile being significantly less stable than the traditional, becoming ballistically unstable below velocities of $V = 2.2$ Mach. This indicates the novel actuation method will be able to provide satisfactory control at least above these velocities, for the considered simulation parameters. However, the control force is achieved at the expense of an increase in drag which will ultimately decelerate the

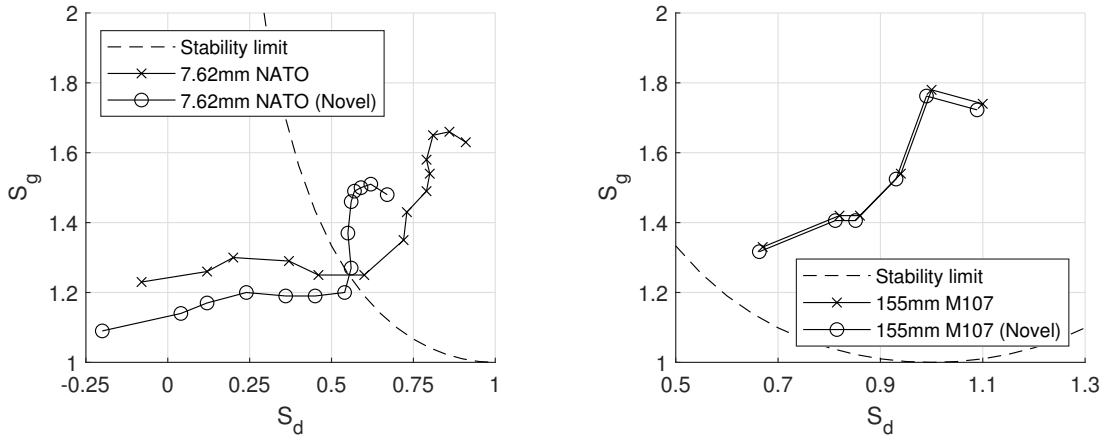

(A) 7.62x51mm NATO for $V = \text{Mach}(0.6 + 0.2m) \mid m \in \{0,1,...,14\}$

(B) 155mm M107 for $V = \text{Mach}(1+0.2m) \mid m \in \{0,1,...,6\}$

FIGURE 6.2.8 Projectile stability change from geometry alteration

projectile quicker, meaning the controllable range is significantly shorter than it would be otherwise.

The M107 projectile remains stable for all velocities covered by the calculations, indicating the unstable region is below Mach 1. The material removed from the ogive is very small compared to the whole projectile, a significantly smaller fraction than that from the 7.62mm. The reduction in moment of inertia, both longitudinal and transverse, is therefore nowhere near as significant. Figure 6.2.8B shows that the change in ballistic stability of the 155mm projectile across the considered flight envelope, as a result of the novel geometry changes, is near-negligible. This indicates that the guidance method can be implemented on the M107 with little effect. However, the ballistic instability is caused by the increased drag and reduced inertias which is a trade off with the increased lateral control force. The fact that ballistic stability remains relatively unchanged, indicates that the magnitude of terminal correction which can be provided by the novel control mechanism may be small. This will become apparent once the aerodynamic coefficients derived in the coming sections are used in the dynamic model to produce example trajectories.

From fig. 1.1.1 (pg. 13) it can be seen that there is a fairly even distribution of internal material which is assumed to be removed from the projectile and replaced with components and subsystem necessary for the prototype operation. The heaviest component which will be introduced is the power supply. This means, from a design perspective, the CoM and

therefore the stability can be fine tuned by shifting the power supply towards either the front or back of the aft section.

6.3 7-DoF dynamic model example trajectories

This section will use the 7-DoF dynamic model in combination with the novel aerodynamic coefficients and the control architectures compared in the previous section, to produce a comparison between the free ballistic flight and the novel guidance method. A step response graph is shown using an estimation of the bearing dynamics following academic literature to establish equilibrium. Using this model of bias response, a trajectory is generated for both ballistic and controlled flight. Dispersion analysis is then conducted, identical to §6.1, to show the magnitude of dispersion changes.

Bias manoeuvre step response

The preceding aerodynamic analysis characterised the spin damping moment coefficient C_{lp} of the projectile, and therefore the ogive. However, it is not possible to faithfully create a step response function to model a bias manoeuvre of the projectile, because the roll rate decay modelled by the `BiasON` and `BiasOFF` functions is caused by an equilibrium being reached between both the roll damping moment and the torque of the bearing. Both Wang *et al.* [72] and Guan *et al.* [204] have included values of the static and viscous friction coefficients, k_s and k_v respectively, which are used to model the bearing dynamics. Wang *et al.* use the values $k_s = 2 \times 10^{-3}$ and $k_v = 4 \times 10^{-5}$, while Guan *et al.* use $k_s = 1 \times 10^{-3}$ and $k_v = 1 \times 10^{-5}$. While the actual estimates may vary, importantly both authors agree on the order of magnitude of the variables, though neither cite the sources for their respective values. Guan *et al.* investigated the spin rate as part of their work and so their respective values of the friction coefficients are used here, so that the results here might be given some context.

Figure 6.3.1 shows the spin rate of the front section p_F of the 155mm and 7.62mm from the 7-DoF model. The brake is engaged up until the front section has attained the initial spin rate of 1200rad.s^{-1}, whereby it is immediately disengaged at $t = 0$s to decelerate under the effect of the spin damping moment. The spin rate takes approximately 1s to

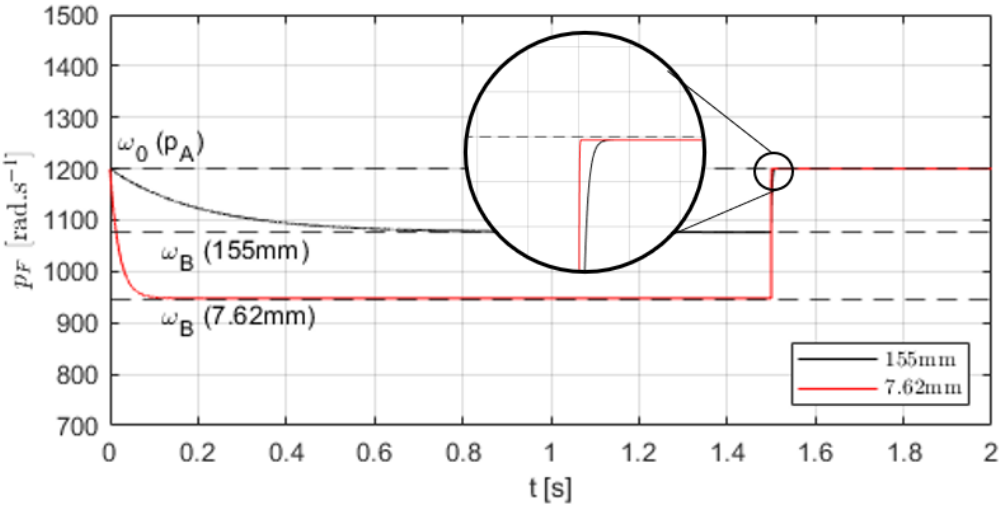

FIGURE 6.3.1 Forward spin rates during bias switching

reach the equilibrium roll rate of ω_B, dropping from 1200rad.s^{-1} to 1076rad.s^{-1}. In the results shown by Guan [204], the canards activating, therefore increasing the spin damping moment[‡], causes p_F to drop from 1300rad.s^{-1} to 450rad.s^{-1} in 10 seconds. While the drop time it took for the deceleration was longer, the forward mass used by Guan was not shown, only the composite whole-body mass. This would indicate the discrepancy is caused by some combination of a more massive forward section and varying spin damping and bearing friction moments. Small calibre direct fire projectiles often have flight times of only a few seconds, which would indicate that the time it takes for the bias to passively engage is too long with the current configuration. However, from chapter 4 it was shown that it is unnecessary for the front section to fully reach the equilibrium roll rate. The bias can be cut short and still have sufficient asymmetric roll rate to produce a control impulse, it is only of importance that the spin speed is significantly different to produce an impulse of usable magnitude. In the present system however, the deceleration of the front end was comparable to that demonstrated by Guan.

The front section of the 7.62mm projectile de-spins significantly quicker than the M107, taking approximately 0.1s to reach the bias spin state. Furthermore, the natural roll rate is achieved almost instantaneously. This increase in switching rate by a factor of ~ 10, correlates with the mass discrepancy between the two sections, which are also different by a factor of ~ 10. The reason for this significantly faster switching speed is that

[‡]though it should be noted this was not their primary purpose

the geometry blunting constituted a significantly larger portion of the ogive. In addition, the mass of the ogive is significantly less than for the M107, so the larger de-spinning moment acts on a less massive section which creates a larger acceleration. The initial spin rates of the projectile are set to be the same, even though the traditional implementations of these projectile would not have the same spin rates. This is done to compare how the geometry and mass changes affect the transition. It can be seen that ω_B for the 7.62mm projectile is lower than for the M107. While the same bearing torque profile was used for both projectiles, the spin damping moment was higher. As was shown in §4.3.4, increasing M_{lp} without altering the bearing torque results in the bias rate being lower. The results observed from the 7-DoF model thus agree with the theoretical predictions of §4.3.4.

The data shown on the figure is used to create the BiasON and BiasOFF functions. These functions are then used as part of the inputs for the numerical procedure described in §4.3.3, whereby the latax is computed for the corresponding sizes of ϕ_a and offset distance.

Error reduction capabilities

Now that the bias manoeuvre has been characterised for this system, it is possible to investigate the dispersion and correction capabilities of the novel design. To achieve this, relevant sources will be identified which detail the dispersion characteristics of the traditional projectile geometries which were used as the base for the novel modifications. The sources will include a description of the scenario which produced the described dispersion, target distance, muzzle velocity *etc.* A Monte Carlo simulation will then be conducted with the 7-DoF model, using the initial conditions described by the real-world source material. The variance of the MC initialisation parameters will then be tuned such that the dispersions achieved from the dynamic model, using the traditional geometry models, match the dispersions of the real projectiles from the literature. The projectile can then be swapped to the novel geometry equivalent with the MC run again, but with a passivated control scheme. In this way, the effect of purely altering the geometry can be observed. Finally, the control system can be activated, and the resulting CEP compared against the passivated novel and traditional geometries from the model, and the real-world geometries. From the above analysis it was concluded that the $\tilde{a}$ based actuation mechanism using the novel GL provided the best correction capabilities in the nominal comparison and so that

configuration will be used for the actively controlled novel projectile below.

While it is possible to vary a plethora of environmental factors, such as air density, temperature and humidity *etc.*, the variation was restricted to only factors directly accounted for in the 7-DoF model, which are shown in table 6.5. One issue that arises from this is how to arrange the distribution of the MC initialisation conditions to replicate the CEP shown in the literature, as different configurations may produce the same dispersion, but be unrepresentative of a real environment. For example, a greater lateral dispersion can be achieved by increasing crosswind, or azimuth angle. The distributions are chosen to follow those shown in ref. [90], which follow experimental observations. As before, the values are varied by generating perturbations following a normal distribution with mean μ and standard deviation σ shown in the table. The mean is taken to be the noted values in the accompanying experimental reports, while σ is adjusted until the model CEP reflects the experimental CEP.

Parameter		7.62mm†		155mm‡	
		μ	σ	μ	σ
V	$\mathrm{m.s^{-1}}$	834	5	550	2
Elevation	$^\circ$	0.2	5×10^{-4}	45	0.1
Azimuth	$^\circ$	0	5×10^{-3}	0	0.1
Crosswind	$\mathrm{m.s^{-1}}$	0	2	0	2
Headwind	$\mathrm{m.s^{-1}}$	0	2	0	2

TABLE 6.5 Mean and standard deviation of variables in 7-DoF MC dispersion tests
† - From BAE quality control tests, ‡ - Ref. [90]

The 7.62mm is fired directly at a target located 500m away as per test data, while the 155mm is fired for maximum range, at 45°, landing at a distance of 30km over flat ground. When either projectile meets the respective impact criteria, the simulation is terminated, and the miss distance is recorded. As for the nominal analysis, the mean impact point is computed using eq. 6.4 & 6.5, then the CEP or R95 is computed using eq. 6.6. For both projectiles, 10^4 rounds are fired in both the test data and MC simulations. This is significantly more rounds than would be used in a real experimental test, but computer-based simulations can afford the luxury of large sample sizes. There is assumed to be no

variance in the mass or calibre of the projectiles.

The actuation mechanism and GL in chapters 4 & 5 are described from the picture plane. For implementation in the 7-DoF model, the target resolution plan is defined such that the normal axis of the plane $\hat{n}$ is the longitudinal axis of the projectile. In addition, the angle of attack is fixed at 0° such that $\hat{n} = \vec{V} = \hat{x}_{proj}$. The guidance system is enabled for the 7.62mm round at $t = 0.5$s and for the 155mm at $t = 30$s. These values are heuristically chosen as the points where the respective projectiles are on a relatively straight trajectory at terminal approach.

Source	Projectile variant	7.62mm R95 [mm]	155mm CEP [m]
Experimental	Traditional	70†	270 ‡
7-DoF Dynamic model	Traditional	70	267
	Novel passivated	71	268
	Novel guided	33	264

TABLE 6.6 Dispersion comparison for range of projectiles
† - From BAE quality control tests, ‡ - From ref. [205, 206]

Table 6.6 shows the final comparison of dispersions between each iteration of the novel projectiles. *N.B.* that R95 is the dispersion metric for the 7.62mm, while CEP is used for the 155mm. In addition, the dispersions of the 155mm are in the ground plane (lateral-longitudinal), while the 7.62mm uses a target plane (lateral-normal). This is because CEP is traditionally used when discussing larger artillery calibres, whereas R95 captures variations which would affect the consistent high precision demanded by the lower calibres. Changing the traditional 155mm projectile for the novel variant causes the CEP to increase by an insignificant amount, within the variation to be expected from using a Monte Carlo simulation. This is reassuring that the blunted ogive was unable to significantly affect the trajectory when no control system was present, as would be the case in the event of a software malfunction. However, when the guidance system was activated, the CEP was reduced from 268m to 264m, a reduction of less than 2%. While the is a significant change caused by the guidance system being in operation, it is very small and thus unlikely to be useful when considering the financial cost increase compared to the traditional ballistic

rounds. This very small reduction is primarily due to the very small lateral control force being generated by the blunted ogive, which in turn causes a very small acceleration of the projectile due to the large mass.

The dynamic model provided an estimate for the traditional ballistic 7.62mm identical to that found in experiments. This projectile being direct fire and considerably shorter range than the artillery shell results in the perturbations having less of an effect on the trajectory, *i.e.* the dispersion is less sensitive to a change in initialisation standard deviations. Replacing the traditional geometry with the novel geometry did not cause a significant increase in the R95 value. However, the guidance system activation reduced the R95 from 70mm to 33mm, a reduction of 53%. This is a significantly larger reduction in dispersion, which is due to the significantly higher latax available because of the significantly lower projectile mass. Because a larger proportion of the projectile was altered during the blunting process, a higher C_{lp} resulted which generated a larger latax when acting on the less massive 7.62mm projectile. In scenarios where accuracy is paramount and a dispersion of 70mm offered by the traditional rounds is unacceptable, this guidance method may be an attractive alternative considering the reduction in dispersion it provides. In the event the guidance system fails, the natural stability guaranteed by the being designed to be ballistically stable has been demonstrated to perform at least as well as the traditional round.

Figure 6.3.2 shows trajectories from the Monte Carlo simulations for the 7.62mm projectile. Only 50 trajectories were selected, at random, from the full sample size to be displayed on the figure. The guided paths observably tend towards the target region and impact closer than the unguided case. The correction capability of the novel 155mm geometry was too small to be distinguished in a similar graph and is hence, omitted. The scale on the figure makes it difficult to distinguish any significance in the trajectory difference when the control and guidance architecture is enabled.

Figure 6.3.3 show the terminal dispersion for the 7.62mm projectile for the unguided traditional (fig. 6.3.3A) and novel guided (fig. 6.3.3B) cases. The origin has been zeroed on the impact point for the unperturbed impact point and the axis distances and scales are the same on both figures to aid interpretation. The same randomly selected 50 samples from fig. 6.3.2 are shown here, to represent the full Monte Carlo batch.

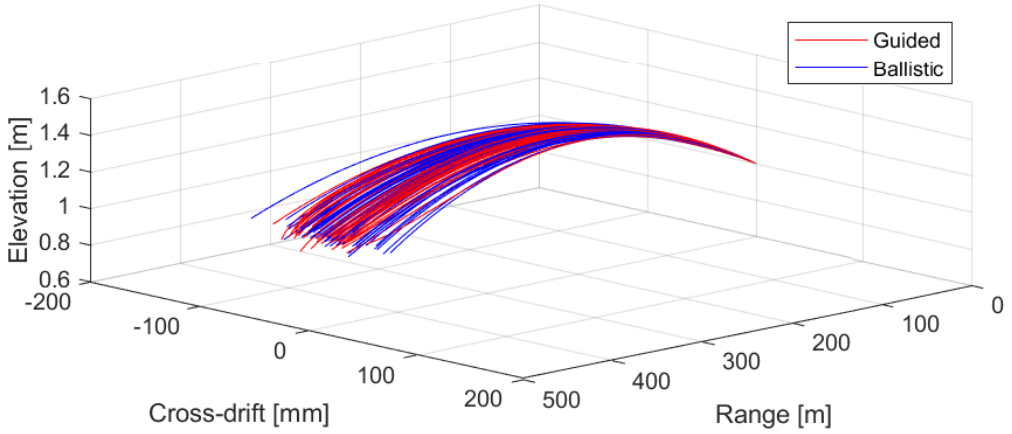

FIGURE 6.3.2 Monte Carlo trajectories of traditional ballistic and novel guided 7.62mm projectiles

The dispersion for the ballistic case is evenly distributed with no bias in impact location. There are insufficient impacts shown to appear normally distributed about the mean, as would be expected from the normally distributed launch variables. This is caused by the low number of displayed impacts, as opposed to being a characteristic of the behaviour. The guided impacts are significantly more clustered with what appears to be a vertical bias. There is a centrally located, vertical line of impacts. This indicates the guidance system is able to reduce the lateral error more than the vertical error. Because the preceding section showed that there was no significant bias present for GLs operating in the nominal system, any bias present here is an artefact of the specific implementation and system dynamics.

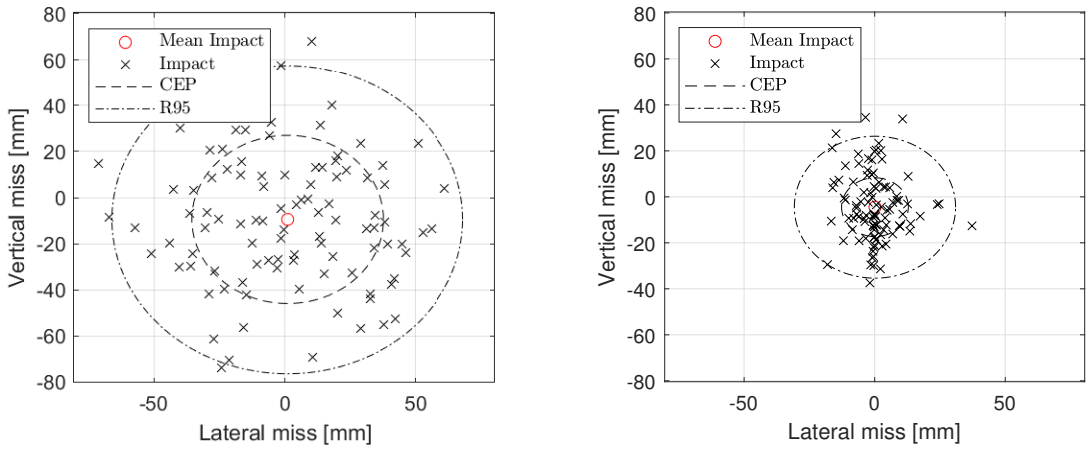

(A) Traditional round, ballistic (B) Novel round, guided

FIGURE 6.3.3 Dispersion patterns of traditional ballistic and novel guided 7.62mm projectiles; origin centred on unperturbed impact point

The same statistical data analysis conducted for the nominal GL comparison is repeated here. Because the dispersion of the 155mm projectile was reduced only by a very small amount, only the 7.62mm is evaluated. The mean impact points μ and standard deviations σ are calculated from the impact points, which are used to compute the correlation coefficient from eq. 6.8. This is used to compute the t-statistic using eq. 6.14 which is used in conjunction with the t-distribution PDF (eq. 6.13) to compute to the p-value from eq. 6.15. The null hypothesis H_0 and alternative hypothesis H_A (pg. 220) are also reused here. The results of this procedure is shown in table 6.7.

Projectile	μ_x	μ_y	σ_x	σ_y	ρ	p-Value
Traditional	-8.600	-18.901	28.553	33.581	0.014	0.460
Novel	0.2165	-7.2989	7.384	17.310	0.129	0.187

TABLE 6.7 Statistical Analysis of 7-DoF MC dispersions with $\alpha = 0.05$

In both the traditional and guided implementations, the mean impact points were beneath the unperturbed impact point $\mu_y < 0$, while the guidance system was able to correct the $\mu_x < 0$. The standard deviation of both the lateral and normal axis were close to equal in the ballistic case, which is what one would expect from an unbiased and normally distributed initial conditions. However, σ_y was more than double σ_x in the guided case, further supporting the fact that the lateral error is being reduced more than the vertical error. While the dispersion correlation was significantly non-zero in the guided case, indicates the presence of a positive correlation, neither of the p-values were less than the significance level α. This shows that while there is a non-zero correlation present, it is insignificant given the number of rounds fired; that H_0 should be accepted and that there is no significant dispersion pattern in the impact points.

Chapter 7

Conclusions

THIS chapter will present the key findings of the project. The primary focus of the project is to prove the feasibility of operating principle underlying the actuation mechanism; can a rotating control force be used to control a projectile by only slowing the rate of rotation? However, other supporting material has been investigated in depth, such as AI reinforcement learning and ballistic stability. Firstly, a detailed narrative overview of the enclosed works is given. Secondly, the main conclusions, results and findings from the enclosed chapters are presented, specifically addressing the aims and objectives described in the introduction. Thirdly, an explicit list is given which highlights the novel contributions of the project, as well as any areas where existing knowledge has been applied in novel ways. Finally, there is a discussion on future work to improve understanding of the enclosed discussions, from improvements in the actuation mechanism and design to auxiliary works such as the GL and AI implementation.

7.1 Project summary

In chapter 3, the coordinate axis and reference frames are established for a projectile adorned with lifting surfaces. The aerodynamic interactions are described along with the importance of accurately characterising the aerodynamic coefficients which describe them. The non-linear equations of motion, expressed in state space notation, are linearised using q-LPV method and a Jacobian linearisation method is applied to trim the model at certain operating conditions. The equations are then implemented in a MATLAB/Simulink

environment to form the 7-DoF dynamic model. It was shown to reduce to the conventional 6-DoF model under the assumption that the ogive (or aft section) is negligible in every way. The model was validated by comparing the predictions with relative literature.

The pitching and yawing motion of projectiles is explored, leading to the fast and slow yawing modes, whereby analysis of the boundary conditions leads to the gyroscopic and dynamic stability factors, S_g and S_D respectively. The relationship between these two factors is imperative early in the design process as it indicates whether the projectile, under free ballistic flight, will remain stable without further consideration of the guidance system activity. Literature pertaining to these stability factors has been reconciled to show the evolution from simple ballistic single-spin projectiles through to guided dual-spin projectiles. This resulted in a publication [40]. The stability of various bullet calibres is computed over a predicted flight envelope. Lastly, a rudimentary parametric and sensitivity study is conducted, investigating the effect of projectile geometry on the stability factors, which is shown in appendix B.

Chapter 4 explored the novel design focused on the fundamental operating principle. A control force and roll damping moment are constantly present. The control force is constantly rotating and is slowed by disengaging the brake, causing the front section to spin-down under the influence of the roll damping moment. During favourable angles, the roll rate is slowed, which results in a biased distribution of the force through a roll rotation. This results in a net impulse, the magnitude and direction of which can be controlled by intelligently choosing the bias start ϕ_{ON} and bias stop points ϕ_{OFF}.

Two different approaches for describing the impulse as a function of bias coordinates were investigated. The change in motion from the bias can be characterised as a change in velocity ΔV, which can then be combined with the time it takes for a singular rotation τ to produce an acceleration $\tilde{a}$ (latax). The actuation mechanism is implemented into the 7-DoF model. While ΔV and $\tilde{a}$ both describe the motion of a singular discrete rotation, it has been shown by verifying a set of axioms that the motion can be extrapolated across multiple rotations to control the lateral motion of the projectile on a continuous, macro scale. This means that the projectile bias manoeuvres can be governed in the classical way by a GL which either controls ΔV or $\tilde{a}$. In either case, an instruction set is created which converts the value demanded by the GL into bias coordinates.

Simplifications are first made to the system, primarily the switching between the natural roll rate ω_0 and the biased roll rate ω_B is assumed to be instantaneous. The switching simplification is relaxed, and the motor/bearing dynamics are modelled by an arbitrary mathematical function $\omega(\phi)$, which emulates the real actuator response reacting to engaging and dis-engaging the bearing brake at certain roll orientations. Because this function is arbitrary, the enclosed treatment is independent of modelling method, meaning the same treatment can be applied to a real system when the complex and non-linear behaviour of the actuator dynamics can be modelled or obtained. This function $\omega(\phi)$ is generated using ω_0, ω_B and the arbitrary functions `BiasON` and `BiasOFF` . `BiasON` represents the spin deceleration resulting from the spin damping moment when the brake is disengaged; `BiasOFF` represents the spin acceleration from the increase in bearing torque when the two sections a re-coupled after the brake is re-engaged. In summary, for a given system dynamic model, the function $\omega(\phi)$ and the accompanying numerical treatment act to directly link a desired magnitude and direction of ΔV or $\tilde{a}$ with the ϕ_{ON} and ϕ_{OFF} which produces it. The magnitude of the latax which can be achieved during bias manoeuvres with arbitrary switching functions are investigated in addition to how the magnitude changes as the ratio of spin speeds ω_B/ω_0 changes. Lastly, the switching profile is explored as a function of the bearing torque, spin damping moment and front section mass.

In chapter 5, various GLs are explored for their applicability in guiding the novel system. A Monte Carlo procedure is defined, which runs a batch of simulations with randomised initial conditions to characterise the performance of a specific GL/AM configuration. This allows different configurations can be meaningfully compared against one another.

During the formulation of the actuation mechanism from a ΔV perspective, an opportunity presented itself to formulate a ZEM-based GL derived from the maximum kinematic motion permitted by the mechanism. This novel GL uses a function $V_{PT}(d)$ to determine the closing velocity as a function of the instantaneous miss distance d. It has two tunable parameters; the global scaling factor ξ and the terminal closing speed V_k which are used to increase response rate and prevent an overshoot. The GL is comprised of three independent regimes to allow higher fidelity control over the projectile in close proximity

to the target, since accuracy is paramount in small calibre. A parametric investigation and sensitivity study is conducted to observe the effect of modifying ξ and V_k, on the trajectory. A PID controller is applied, along with a fuzzy logic controller. The GL parameters and PID controller gains were then optimised using a genetic algorithm for a GL controlling a nominal, instantaneously switching projectile. The genetic algorithm search was bounded using heuristic variation. It yielded optimum values of $[\xi\ V_k] = [0.54\ 0.18]^{\mathrm{T}}$ and $[k_P\ k_I\ k_D] = [1\ 0\ 0]^{\mathrm{T}}$ which indicates that the PID controller provides no significant benefit over just the GL parameters with the analysed configuration.

Two different implementations of RL AI agents investigated. Firstly, the reward function is constructed based on a discussion of possible agent behaviours, attempting to mitigate undesirable performances and exploitations. In the first implementation, a DQN agent was given direct control over both the actuation mechanism and GL. The agent acted continuously to activate or release the bearing brake; the action space is $A = [\omega_0\ \omega_B]^{\mathrm{T}}$. The chosen observations were the relative kinematic differences of both the projectile and target. The relatively simple neural network (NN) used here was unable to learn the environment sufficiently to deliver desirable correction performance, using the discussed reward function. However, the agent did show signs of improving and it is speculated that the agent will be able to learn the environment significantly given a larger NN with more layers and training time. In the second implementation, a DDPG agent is used in a single axis (channel) model to reduce the distance error of a point mass to a target. The action space is chosen to be $A = [-\tilde{a}\ \tilde{a}]^{\mathrm{T}}$. This model is modified to include an action lag, which emulates the delay in command caused by the one full roll rotation being required to enact a change. The single channel agent was successfully trained on using values from the instantaneous switching model and then implemented in a dual-channel configuration, operating as a GL.

The performance of traditional PN, novel ZEM-based, and the AI GLs are compared against each other in a nominal case for instantaneous switching. This directly compares the miss-distance reduction capabilities of the GLs without the actuation mechanism complexities. The dispersion characteristics are then measured using CEP, DRMS and R95 metrics by running a Monte Carlo simulation with normally distributed initial conditions. All GLs provided significant levels of error correction compared to the free ballistic case,

with the bespoke ZEM based GL providing the best capabilities of all. Statistical tests indicated that only the AI GL generated any significant correlation, which is suspected to be caused by incomplete training and dual-channel implementation of a single-channel agent. The correction characteristics were investigated which showed that the PN GL corrected the error very late, towards the terminal stages of the trajectory which is undesirable. Due to the intrinsic saturation of the actuation mechanism, early error correction is paramount to avoid actuator saturation ending in an avoidable miss distance. This can likely be corrected easily in future iterations using gain scheduling, to correct this error sooner.

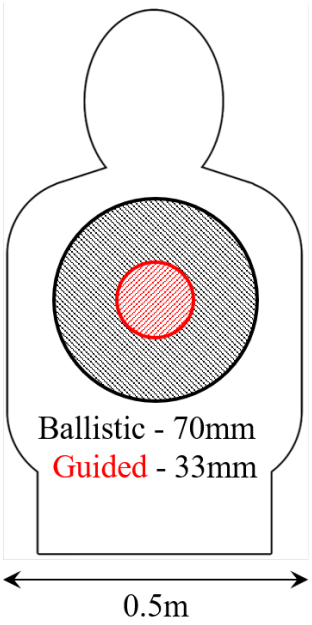

FIGURE 7.1.1 Correction capabilities of 7.62mm using novel control method against humanoid target at 500m; in proportion.

To provide the main findings of the project with context, a design process is shown. Two illustrative CAD models are created, which modify existing traditional projectile geometries to include the dual-spin, blunted ogive design. A rudimentary CFD analysis is conducted to obtain aerodynamic coefficients, which are used to compute the ballistic stability and investigate the front roll rate response during a bias manoeuvre. Finally, the projectile models, actuation model and GL are combined using the full 7-DoF model in a Monte Carlo simulation to generate dispersion patterns. The current implementation was unable to significantly reduce the CEP for a 155mm projectile. However, the 7.62mm

design R95 was reduced from 70mm to 33mm, which is shown in fig. 7.1.1. There was a correlation present in the guided impacts, however statistical data analysis showed this to be insignificant, meaning there is no indication of bias. The lift coefficient was assumed to be constant throughout the flight, which is more reconcilable with the shorter ranges of the small calibre projectile. This assumption would not necessarily hold for the larger calibre indirect fire artillery shells, but it has been shown regardless that the presented control mechanism is sub-optimal for larger calibres.

7.2 Key findings

This section will highlight the most important aspects of the enclosed work. It is split into two section. Firstly from a manufacturers perspective, the 'Design variables and discussion' heading encompasses aspects of the architecture which are key to controlling and manipulating elements of the system. These design variables and limitations can be discussed from the perspective of what purpose this system has. Finally the 'Aims and Objectives' heading specifically addresses each of the respective goals from the introduction, clearly indicating where and how these requirements have been fulfilled.

Design variables and discussion

This project has demonstrated to a satisfactory standard, that the proposed control mechanism is a viable method of controlling a projectile and provides certain key benefits over conventional control methods to warrant further investigation. Namely:

1. The design is volumetrically small. The only components required to guide the projectile according to the enclosed discussions are the power supply, bearing/motor, brake mechanism, receiver and supplementary IMU. Because direct fire projectiles traditionally don't carry a payload, they rely entirely on kinetic energy to achieve a desired target effect, the whole body of the projectile can be used, unlike the CCFs used in artillery shells. The tracking method, either passive or active would be adorned on the outside of the projectile, the stability effects of which can be modelled fully and considered by the framework in §3.3, and is thus excluded from

the volumetric budget inside the projectile.

2. The design is power efficient. This is primarily due to the absence of conventionally power intensive components, such as active laser homing equipment or indeed any onboard optical tracking equipment. Additionally, if the tracking method is passive, *e.g.* a reflective panel, then no or very little power will be consumed.

3. The design is robust, to withstand the hostile launch conditions. There are no protruding aerodynamic surfaces which could be damaged during launch through contact with the weapon barrel. Furthermore, there is no delicate deployment mechanism which is susceptible to failure or shock damage. Due to the fact that imaging equipment is optional and possible only requiring passive base tracking methods, the number of electronic systems susceptible to launch damage or failures is generally reduced. The main mechanism susceptible to damage during launch is the bearing, the functionality and frictionless operation of which is paramount to the control strategy. Projectile bearings have already beginning to see use in artillery shells with CCFs, which is an assuring statement as to the state of the bearing technology, since the launch conditions in artillery systems are more extreme than in small calibre-projectiles. The reliability and repeatability of the design can be ensured in the sense that, even if the mechanism fails and seizes completely, the projectile geometry will still have been designed to be stable, along the trajectory, meaning the path is predictable.

4. The design is effective and can deliver control as long as the projectile has sufficient velocity to remain in flight. Since the control mechanism doesn't need to be deployed, a lift force will be imparted from the blunted ogive as long as there is a free stream being deflected by it. This means control can be initiated as soon as the projectile leaves the barrel, turbulent conditions permitting, so that significant correction can be enacted in the short flight duration

5. The frequency of the control and guidance architecture is significant compared to the spin rate of the projectile. The frequency response of the system is limited by the actuation hardware used in the braking mechanism. Piezoelectric actuators have an effective mechanical frequency response approaching the MHz range, which is significant compared to the roll rate of the fastest spinning projectiles in the KHz range. Note that from §3.3 it is detrimental for a projectile to have too high a spin rate, thus the MHz response frequency of the piezoelectric actuators is likely to be sufficient for almost all spin-stabilised atmospheric projectiles in the foreseeable future. For an actuator response frequency f_A and a projectile spin rate f_P, the control mechanism is capable of making f_A/f_P corrections per revolution. Assuming $f_A/f_P = 10^6/10^3$, this equates to 10^3 possible corrections per revolution, or a fidelity of 0.36deg.

The control fidelity and magnitude can be improved by increasing the difference between the natural and biased roll rates. The natural rate is fixed by the rifling of the weapons system, but the bias rate is a result of the equilibrium between the bearing friction and roll damping. The friction of the bearing is also likely to be fixed by whatever hardware is suitable to be used in a prototype (unless intentionally variable as an additional method of control), leaving only the roll damping moment as a critical design parameter. It should be noted that if the spin damping moment is too high, then rotational energy will be lost during flight to a point where the roll rate of the aft section be drop to a point where the projectile is at risk of becoming gyroscopic unstable. This is unlikely to be realised however as the drag would become an issue before this point. In summary, the geometry should be designed so as to achieve the following:

- Increase lift force as much as much as possible while keeping the geometry stable as dictated by the stability factors.
- Increase drag as little as possible, so the projectile range is remains as close to the unaltered design as possible. This means designing a geometry with a high C_L/C_D ratio.
- Remove as little weight as possible from aft for gyroscopic stability.

- Remove more weight from the ogive section to enable quicker bias switching

- Spin rate discrepancy between the two should be as large as possible for more correction distance and control fidelity, which requires a low bearing friction and high spin damping moment.

The blunted ogive utilised in this project is not essential to the operating mechanism. It is suggested here as a possibility due to the simplicity, robustness and relatively low manufacturing costs compared to electromechanical or novel actuation mechanisms. The investigations of §4.3.4 showed that the mass of the front section should be as low as possible to increase the control fidelity. As such the front section needn't be a complete section at all, but it may comprise some aerodynamic shell, still attached via a bearing, which envelops the ogive and being comprised of a light weight composite material. This would drastically reduce the weight while still allowing the structural strength on which to build an aerodynamic structure capable of both producing a lift force and spin damping moment. It could take the form of an end cap, or heavily contorted asymmetric fin-like structures extending down the sides of the ogive. This would also free up room for critical subsystem inside the projectile.

While the mass of the front section should ideally be reduced for a more responsive control system, mass reduction is intrinsically constrained by the desired terminal effectiveness of the round. Small calibre projectiles are mostly used as anti-infantry rounds either in a suppressive role or direct engagement. As such they are not expected to defeat significant quantities of reinforced armour, but should still be able to penetrate relatively lighter body armour. Predominantly, it is hardness, mass and shape of the penetrator combined with mass which is the effector mechanism for small calibre projectiles. The mass required to maintain this capability must be considered when designing the control system, let alone before the adoption of a payload system.

If a definitive and immediate effect on target is required, the tendency in modern warfare is to employ guided missiles rather than higher risk small calibre fire; be it high volume or high accuracy. Or it may simply be that the engagement profile does not permit use of direct fire small calibre, and that only guided missiles can make any effect on target. The results of this project show a scenario whereby a 7.62x52mm round has the CEP

reduced from 70mm to 33mm. The main use cases which would benefit from such an improvement are scenarios in which small arms are necessitated and accuracy is paramount. A predominant example of this would be snipers or designated marksmen, small calibre equipped drones or unmanned aerial vehicles, and light infantry fighting vehicles. As technology improves and this design becomes cheaper, it can also be used to augment the effectiveness of any small calibre direct fire systems.

Aims and objectives

The aims and objectives outlined in §1 have been completed in the following:

1. Objective 1: *Can a mathematical framework be formulated which robustly describes the motion of the system as a response to the controller instructions?*

    - *Can the motion of the projectile be characterised in terms of a controllable parameter?*
      It was shown that the net impulse from a biased rotation induces motion which can be described by both a change in velocity ΔV (§4.2) and a lateral acceleration $\tilde{a}$ (§4.3).
    - *Can this parameter be expressed linearly in terms of control variable?*
      Both the magnitude and direction of $\tilde{a}$ (and therefore also ΔV) have been characterised in terms of the bias coordinates ϕ_{ON} and ϕ_{OFF} for arbitrarily complex switching dynamics (§4.3.2).

2. *Objective 2: Does a projectile geometry exist which can fulfil the requirements of the control mechanism?*

    - *Does the geometry provide sufficient lift at expected operational conditions?*
      An illustrative design was shown to create a sufficient lift (control) force and roll damping moment, without generating an unacceptably high level of drag, to achieve sufficient control authority to reduce the dispersion by a satisfactory amount 6.3
    - *Does the geometry fulfilling the above do so without detriment to the stability of the ballistic trajectory, in the event no control authority is exerted?*

The example design was shown to maintain ballistic stability across the expected flight envelope (§6.2.3) according to a well-defined framework of ballistic stability (§3.3.4)

7.3 Summary of objective novelty

Many subjects were covered in this project to realise the aim and objectives. Some of the work has been novel and some of the work has applied existing methodologies in new ways. What follows is a brief summary, highlighting the most important original contributions which have arisen.

1. First and foremost, the novel actuation mechanism described utilising the dual-spin design with biased rotation rates. During the patent submission process with the project co-sponsor BAE, prior art [207, 41] was highlighted featuring similar designs to that presented here. In all cases, the designs relied on active de-spinning of the front section via a motor, as well as relying on the front section being rotationally stationary with respect to the earth frame. The design enclosed herein passively de-spins the front section using the roll damping moment and does not require the front section to be significantly de-spun. Lastly since patents are intentionally quite vague, no mathematical description as to the fundamental operation is given, which this project shows in its entirety. Formulating two approaches, both $\tilde{a}$ and ΔV, to describe the inherently discrete behaviour of the actuation mechanism as a variable which can be continuously controlled by autopilots.

2. The bespoke ZEM-based GL with tunable parameters optimised a genetic algorithm and fuzzy-gain scheduled PID signal control.

3. Using a DQN RL agent to control the novel projectile design with binary action space, effectively representing a complete control and guidance loop, by acting as the actuator controller, autopilot and GL.

4. Use of a DDPG RL agent trained in a single channel environment with artificial action lag, emulating real actuation mechanism delay. The agent is cloned and

used in a dual-channel configuration to represent a GL, dictating the motion of the projectile to reduce the ZEM distance.

5. Numerically quantifying the performance of a GL to guide a projectile in a 7-DoF non-linear model. This forms the basis of a Monte Carlo simulation to generate a metric capable of assessing different GL configurations, implementations as well as directly comparing different GLs. Finally using this Genetic Algorithm as a function emulator to define the fitness of specimens used in GA optimisation.

6. The conference paper in appendix C, uses the stability coefficients from chapter 3 to investigate the ballistic stability continuously through the full flight trajectory, rather than trimming the simulation at certain operational points.

7.4 Future work

This section shall briefly describe any opportunities which have arisen from this project and should be pursued in more detail.

As discussed in the conclusions, the blunted ogive is just one possible candidate to robustly provide a lift force and roll damping moment, but other solutions can be used. If the blunt face is to be selected, then its implementation should be investigated in more depth, primarily characterising how the geometry of the blunt face affects the factors dictating controllability and stability: C_{lp}, F_C, C_D, S_g and S_D *etc.* The lift to drag ratio should be increased as much as possible, while still keeping the lateral force below that which can cause instability. In addition, what effect if any does the asymmetric ogive have for internal ballistics?

Traditional control and guidance solutions such as the M982 Excalibur, can cost as much as 3000% more than an unguided 155mm ($\sim$£110,000 compared to £500) while reducing the CEP by more than 95% [208]. While the results from §6.3 showed that this specific design was unable to significantly reduce the CEP of a 155mm projectile, the geometry was only illustrative. Optimising the geometry could lead to significant reductions in CEP using hardware at a fraction of the cost of the traditional means. This would be an attractive alternative to operators.

Suitable candidate technologies for the brake actuator should be identified; piezoelectric actuators are suggested here for their robustness and high operating bandwidth. A frequency response study should be undertaken for the candidates. Is the necessary hardware robust enough to survive the launch conditions? What force must the actuators exert to brake the two halves of the projectile at operation spin rates? What are the power requirements to exert this force over the flight envelope? An upper bound can be found be anticipating constant actuator effort along the whole flight. Importantly, the magnitude of the braking force and resulting torque will determine the acceleration of the ogive roll rate and thus the bias off function. What is the longevity of the brake pad in flight and can it be expected to operate throughout the entire flight? This is primarily considering friction or other resulting contact interaction between the two sections when the brake is applied.

The magnitude of coupling interactions and gyroscopic drift during actuation should be investigated. Is gyroscopic stability enough to keep the projectile stable during the brake operation?

The bias coordinates are currently computed, for any GL and either $\tilde{a}$ or ΔV perspective, when $\phi = 0$. The projectile then executes the bias and computes a new one. Further work should investigate whether there is a system improvement having the bias coordinates continuously being computed online and allowing multiple switches mid-rotation. Further, work should investigate whether any improvement is worth the increased computational burden.

Lastly for the control method, the projectile could theoretically be guided by inverting the control mechanism, such that the ogive remains in the biased state for the majority of flight, locking and switching to the natural state through unfavourable roll angles. This would be less efficient in terms of overall acceleration but may be more conducive to the use of high speed actuators which could 'pulse' the brake at a fixed force instead of requiring a slow and controlled application.

Aside from the direct improvements to the actuation mechanism and physical implementation of it in a working prototype, there are two notable points of interest which have been highlighted from the auxiliary work conducted using AI.

There are two notable aspects for the use of AI in this project. Firstly, using an RL AI agent as a function generator to control ϕ_{ON} and ϕ_{OFF} to produce a desired ΔV or $\tilde{a}$ for

both instantaneous and function governed bias switching. This paper investigated using an agent purely for the GL and as direct control over the GL and actuation mechanism, but function generation is achievable by AI methods and as such this may be another useful approach. Secondly, RL agent scheduling along different points of the trajectory could be used, similar to conventional gain scheduling. In this sense an agent can be trained to control the projectile during the initial, intermediate and terminal flight phases for the optimum and most efficient control over all which may otherwise not be possible. This may prove a more resource effective method than simply adding range as an observation, which would increase the observation space by orders of magnitude.

Gain scheduling is an approach used in control theory where a non-linear system is controlled using linear controllers [209]. Multiple linear controllers are optimised at different operating points of the system. Parameters are then chosen to identify when the operating points of the system switch and this, when the linear controllers should be substituted with another. RL agents have already been used to learning scheduling algorithms for data processing jobs [210]. Work could investigate the feasibility of scheduling different agents which have been trained at different operating points of a system. For example, updating controllers during different phases of a missile flight. Conventionally, the guidance phase of a missile prioritises resource management and stability with slower sweeping motions to correct a course. During the homing phase, the missile uses more resources and updates the trajectory at a much higher rate to ensure the highest accuracy possible. Analogous to this, two different agents could be trained against two different reward functions. One reward function could prioritise resource management and a low actuator demand while the other could prioritise a low distance to target. The finished missile could then switch between the two depending on the proximity to the target. The time required to fully train an agent is substantial and is as such, outside the scope of this project.

References

[1] R. M. and Defence. Excalibur Projectile. URL https://www.raytheonmissilesanddefense.com/capabilities/products/excalibur-projectile.

[2] D. C. Kopp. Artillery for the Army - precision fire with mobility. *Defecnce today magazine*. URL http://www.ausairpower.net/SP/DT-SPH-0705.pdf.

[3] Saab Bofors Dynamics. THOR: A new era of mortar warfare. URL https://saab.com/land/weapon-systems/warheads/thor/.

[4] S. Haughton. *THE BRITISH SNIPER : A CENTURY OF EVOLUTION*. Swift and Bold Publishing, 2018. ISBN 1527223833.

[5] J. W. C. Robinson and F. Berefelt. On Guidance and Control for Guided Artillery Projectiles, Part 1: General Considerations. (October), 2011. URL http://foi.se/ReportFiles/foir{_}3291.pdf.

[6] Global Security. XM1156 Precision Guidance Kit (PGK). URL https://www.globalsecurity.org/military/systems/munitions/m1156.htm.

[7] BAE. Silver Bullet - Precision Guidance Kit, 2015. URL https://www.baesystems.com/en/product/silver-bullet--precision-guidance-kit.

[8] TechTime. IAI has Developed a Course Correction Fuze for Standard Artillery, 2017. URL https://techtime.news/2017/10/15/topgun/.

[9] B. Opall-Rome. Israeli Army Taps IAI's Topgun for Precision Artillery Project. *Defense News*, 2016. URL https://www.defensenews.com/breaking-

news/2016/07/20/israeli-army-taps-iais-topgun-for-precision-artillery-project/.

[10] G. Security. Guidance Integrated Fuze (GIF). 2011. URL https://www.globalsecurity.org/military/systems/munitions/gif.htm.

[11] Christopher F. Foss. Smart ammo: precision-guided munitions for field artillery. URL https://www.janes.com/images/assets/423/54423/precision-guided{_}munitions{_}for{_}field{_}artillery.pdf.

[12] DARPA. EXACTO Guided Bullet Demonstrates Repeatable Performance against Moving Targets. URL https://www.darpa.mil/news-events/2015-04-27.

[13] DARPA. EXtreme ACcuracy Tasked Ordnance (EXACTO) (Archived). URL https://www.darpa.mil/program/extreme-accuracy-tasked-ordnance.

[14] M. Minnicino. BANDSLIP Advancements. (September), 2009.

[15] Sandia National Laboratories. Guided Bullet Technology. URL https://www.sandia.gov/research/robotics/high{_}consequence{_}automation/guided{_}bullet.html.

[16] Sandia National Laboratories. Sandia's self-guided bullet prototype can hit target a mile away, 2012. URL https://share-ng.sandia.gov/news/resources/news{_}releases/bullet/.

[17] C. Zhang, H. Wang, P. Zhang, S. Gao, and H. Xiong. CFD Simulation of a Finned Smart Bullet with Microactuator. *Journal of Physics: Conference Series 2018 / 07 Vol. 1064*, vol. 1064(1), 2018. doi:10.1088/1742-6596/1064/1/012021.

[18] SmartRounds. SAVAGE, 2017. URL http://smartrounds.com/savage.

[19] G. Dynamics. 81mm Roll Controlled Guided Mortar (RCGM). URL gd-ots.com/munitions/mortars-and-mortar-components/81mm-rcgm/.

[20] Thales. STARSTREAK High Velocity Missile (HVM). URL https://web.archive.org/web/20061124093927/http://www.thales-airdefence.com/medias/Starstreak{_}HVM.pdf.

[21] Thales. STARSTREAK, 2019. URL https://www.thalesgroup.com/en/countries/europe/united-kingdom/markets-we-operate/defence/advanced-weapons-systems-uk/effectors.

[22] N. Tiliakos. MEMS for harsh environment sensors in aerospace applications: Selected case studies. In *Mems for Automotive and Aerospace Applications*, pages 245–282. 2013. ISBN 9780857091185. doi:10.1533/9780857096487.2.245.

[23] S. Mani, S. N. Singh, S. K. Parmi, W. Yim, and M. Trabia. Adaptive rotation of a smart projectile fin using a piezoelectric flexible beam actuator. *JVC/Journal of Vibration and Control*, vol. 11(8):1085–1102, 2005. doi:10.1177/1077546305055774.

[24] S. Mani, S. N. Singh, S. K. Parimi, and W. Yim. Adaptive Servoregulation of a Projectile Fin Using Piezoelectric Actuator. *Journal of Dynamic Systems, Measurement, and Control*, vol. 129(1):100, 2007. doi:10.1115/1.2397159. URL http://link.aip.org/link/JDSMAA/v129/i1/p100/s1{&}Agg=doi.

[25] C. G. Kang, J. S. Lee, and J. H. Han. Development of bi-stable and millimeter-scale displacement actuator using snap-through effect for reciprocating control fins. *Aerospace Science and Technology*, vol. 32(1):131–141, 2014. doi:10.1016/j.ast.2013.11.007.

[26] V. Mudupu, M. B. Trabia, W. Yim, and P. Weinacht. Design and validation of a fuzzy logic controller for a smart projectile fin with a piezoelectric macro-fiber composite bimorph actuator. *Smart Materials and Structures*, vol. 17(3), 2008. doi:10.1088/0964-1726/17/3/035034.

[27] M. B. Trabia, W. Yim, and M. Saadeh. Modeling of hysteresis and backlash for a smart fin with a piezoelectric actuator. *Journal of Intelligent Material Systems and Structures*, vol. 22(11):1161–1176, 2011. doi:10.1177/1045389X11414223.

[28] R. Barrett-Gonzalez, R. Barnhart, and R. Bramlette. Steerable Adaptive Bullet Flight Control Mechanism Design. In *53rd AIAA/ASME/ASCE/AHS/ASC Structures, Structural Dynamics and Materials Conference
20th AIAA/ASME/AHS*

*Adaptive Structures Conference
14th AIAA*. 2012. ISBN 978-1-60086-937-2. doi:10.2514/6.2012-1511. URL http://arc.aiaa.org/doi/abs/10.2514/6.2012-1511.

[29] K. C. Massey and S. I. Silton. Combining experimental data, computational fluid dynamics, and six-degree of freedom simulation to develop a guidance actuator for a supersonic projectile. *Proceedings of the Institution of Mechanical Engineers, Part G: Journal of Aerospace Engineering*, vol. 223(4):341–355, 2009. doi:10.1243/09544100JAERO399.

[30] J. McMichael, P. Plostins, J. Sahu, A. Glezer, A. Lovas, G. Brown, and C. Rinehart. Microadaptive Flow Control Applied to a Spinning Projectile. *2nd AIAA Flow Control Conference*, (July), 2004. doi:10.2514/6.2004-2512. URL http://arc.aiaa.org/doi/10.2514/6.2004-2512.

[31] F. Fresconi, G. Cooper, I. Celmins, J. DeSpirito, and M. Costello. Flight mechanics of a novel guided spin-stabilized projectile concept. In *Proceedings of the Institution of Mechanical Engineers, Part G: Journal of Aerospace Engineering*, vol. 226, pages 327–340. 2012. ISBN 9781624101519. doi:10.1177/0954410011408385.

[32] M. Patel, Z. Sowle, T. Ng, and W. Toledo. Range and Endgame Performance Assessment of a Smart Projectile Using Hingeless Flight Control. *44th AIAA Aerospace Sciences Meeting and Exhibit*, (January), 2006. doi:10.2514/6.2006-671. URL http://arc.aiaa.org/doi/abs/10.2514/6.2006-671.

[33] J. Ma, Z.-h. Chen, Z.-g. Huang, J.-g. Gao, and Q. Zhao. Investigation on the flow control of micro-vanes on a supersonic spinning projectile. *Defence Technology*, vol. 12(3):227–233, 2016. doi:10.1016/j.dt.2016.01.008. URL http://dx.doi.org/10.1016/j.dt.2016.01.008.

[34] E. H. Epperson Jr. Gyroscopically Steerable Bullet, 1984.

[35] W. S. Lawhorn and I. L. Clinkenbeard. Small Calibre Guided Projectile, 1985.

[36] A. B. Minick, S. A. Hobart, F. Widman, T. S. Kokan, and F. H. Massey. Guided Projectile, 2011.

[37] P. Mallon. Steerable Projectile, 2011.

[38] C. E. Geswender, R. Dryer, and P. Vesty. Steerable Spin-stabilized Projectile, 2014.

[39] G. Kidd and Thales. Wstc0129: Aerodynamic analysis of gun launched airframes. 2018.

[40] J. Norris, A. Hameed, J. Economou, and S. Parker. A review of dual-spin projectile stability. *Defence Technology*, (xxxx), 2019. doi:10.1016/j.dt.2019.06.003. URL `https://doi.org/10.1016/j.dt.2019.06.003https://linkinghub.elsevier.com/retrieve/pii/S2214914719302430`.

[41] J. Morris and D. Smith. Projectile Trajectory Control System, 2007.

[42] D. Blog. General Dynamics unveils next-gen precision-guided mortar systems during exhibition in Canada, 2019. URL `https://defence-blog.com/news/army/general-dynamics-unveils-next-gen-precision-guided-mortar-systems-during-exhibition-in-canada.html`.

[43] I. Michael Minnicino. Steerable Munitions Projectile, 2016.

[44] D. H. Jenkins, J. Byrne, J. Christiana, P. Franz, and T. Kelly. Spin Stabilized Projectile Trajectory Control, 2008.

[45] W. Flood, P. O'Brien, and E. Carlson. Roll Isolation Bearing, 2010.

[46] K. Lloyd and D. Brown. Instability of Spinning Projectiles During Terminal Guidance. *Journal of Guidance and Control*, vol. 2(1):65–70, 1979. doi:10.2514/3.55833.

[47] G. Cooper, F. Fresconi, and M. Costello. Flight stability of asymmetric projectiles with control mechanisms. *AIAA Atmospheric Flight Mechanics Conference 2010*, (August):1–14, 2010. doi:10.2514/6.2010-7636.

[48] F. E. Fresconi, I. Celmins, and B. E. Howell. Obtaining the aerodynamic and flight dynamic characteristics of an asymmetric projectile through experimental spark range firings. *AIAA Atmospheric Flight Mechanics Conference 2011*, (August):1–8, 2011. doi:10.2514/6.2011-6334.

[49] R. Li, D. Li, and J. Fan. Research on Instability Boundaries of Control Force for Trajectory Correction Projectiles. *Mathematical Problems in Engineering*, vol. 2019, 2019. doi:10.1155/2019/6362835.

[50] B. Litz. *Applied Ballistics For Long-Range Shooting 3rd Edition: Understanding the Elements and Application of External Ballistics for Successful Long-Range Target Shooting and Hunting*. Applied Ballistics, LLC, 3rd ed., 2015. ISBN 978-0990920618.

[51] M. W. Courtney, U. S. A. F. Academy, and D. G. Miller. A Stability Formula for Plastic-Tipped Bullets. pages 1–4, 2009.

[52] E. R. COURTNEY and M. W. COURTNEY. Gyroscopic Stability of Open Tipped Match Style Rifle Bullets. Tech. rep., BTG Research, 2012.

[53] P. Wernert and S. Theodoulis. Modelling and stability snalysis for a class of 155 mm spin-stabilized projectiles with Course Correction Fuse (CCF). *AIAA Atmospheric Flight Mechanics Conference 2011*, (August):1–14, 2011. doi:10.2514/6.2011-6269.

[54] S. Theodoulis and P. Wernert. Flight control for a class of 155 mm spin-stabilized projectiles with course correction fuse (CCF). *AIAA Guidance, Navigation, and Control Conference 2011*, (August):1–10, 2011. doi:10.2514/6.2011-6247.

[55] J. Spagni, S. Theodoulis, and P. Wernert. Flight control for a class of 155 mm spin-stabilized projectile with reciprocating canards. *AIAA Guidance, Navigation, and Control Conference 2012*, (August):1–8, 2012. doi:10.2514/6.2012-4685.

[56] E. Altitude-dependent. Nonlinear Dynamic Inversion Flight Control Design for Guided Projectiles. vol. 47(4):8–11, 2020. doi:10.2514/1.47339.

[57] S. Theodoulis, V. Gassmann, P. Wernert, L. Dritsas, I. Kitsios, and A. Tzes. Guidance and Control Design for a Class of Spin-Stabilized Fin-Controlled Projectiles. *Journal of Guidance, Control, and Dynamics*, vol. 36(2), 2013. doi:10.2514/1.56520.

[58] P. Wernert. Stability analysis for canard guided dual-spin stabilized projectiles. *AIAA Atmospheric Flight Mechanics Conference*, (August):1–24, 2009. doi:10.2514/6.2009-5843.

[59] S. Theodoulis, Y. Morel, P. Wernert, and A. Tzes. LPV modeling of guided projectiles for terminal guidance. *18th Mediterranean Conference on Control and Automation, MED'10 - Conference Proceedings*, pages 1455–1460, 2010. doi:10.1109/MED.2010.5547843.

[60] S. Theodoulis and P. Wernert. Flight Dynamics & Control for Smart Munition: The ISL Contribution. *IFAC-PapersOnLine*, vol. 50(1):15,512–15,517, 2017. doi:10.1016/j.ifacol.2017.08.2127. URL https://doi.org/10.1016/j.ifacol.2017.08.2127.

[61] G. Strub, V. Gassmann, S. Theodoulis, S. Dobre, and M. Basset. Hardware-in-the-loop experimental setup development for a guided projectile in a wind tunnel. *IEEE/ASME International Conference on Advanced Intelligent Mechatronics, AIM*, pages 458–463, 2014. doi:10.1109/AIM.2014.6878120.

[62] F. Seve, S. Theodoulis, P. Wernert, M. Zasadzinski, and M. Boutayeb. Flight dynamics modeling of dual-spin guided projectiles. *IEEE Transactions on Aerospace and Electronic Systems*, vol. 53(4):1625–1641, 2017. doi:10.1109/TAES.2017.2667820.

[63] J. Lahti, T. Sailaranta, M. Harju, and K. Virtanen. Control of exterior ballistic properties of spin-stabilized bullet by optimizing internal mass distribution. *Defence Technology*, vol. 15(1):38–50, 2019. doi:10.1016/j.dt.2018.10.003. URL https://doi.org/10.1016/j.dt.2018.10.003.

[64] R. L. McCoy. Modern Exterior Ballistics, 2012. URL http://www.worldcat.org/oclc/806367850.

[65] J. Nielsen. *Missile Aerodynamics*. American Institute of Aeronautics and Astronautics, Inc., 1988. ISBN 978-0-9620629-0-2. doi:doi:10.2514/4.062902. URL https://doi.org/10.2514/4.062902.

[66] F. Moore. *Approximate Methods for Weapon Aerodynamics*. American Institute of Aeronautics and Astronautics, Inc., 2000. ISBN 978-1-56347-399-9. doi: doi:10.2514/4.473999. URL https://doi.org/10.2514/4.473999.

[67] T. Xu, J. Rong, D. Xiang, C. Pan, and X. Yin. Dynamic modeling and stability analysis of a flexible spinning missile under thrust. *International Journal of Mechanical Sciences*, vol. 119(September):144–154, 2016. doi:10.1016/j.ijmecsci.2016.09.027. URL http://dx.doi.org/10.1016/j.ijmecsci.2016.09.027.

[68] S. Chang, Z. Wang, and T. Liu. Analysis of Spin-Rate Property for Dual-Spin-Stabilized Projectiles with Canards. *Journal of Spacecraft and Rockets*, vol. 51(3):958–966, 2014. doi:10.2514/1.A32830. URL http://arc.aiaa.org/doi/10.2514/1.A32830.

[69] Y. Wang, J. Cheng, J. yan Yu, and X. ming Wang. Influence of yawing force frequency on angular motion and ballistic characteristics of a dual-spin projectile. *Defence Technology*, vol. 12(2):124–128, 2016. doi:10.1016/j.dt.2015.12.007. URL http://dx.doi.org/10.1016/j.dt.2015.12.007.

[70] G. Cooper, F. Fresconi, and M. Costello. Flight Stability of an Asymmetric Projectile with Activating Canards. *Journal of Spacecraft and Rockets*, vol. 49(1):130–135, 2012. doi:10.2514/1.A32022. URL http://arc.aiaa.org/doi/10.2514/1.A32022.

[71] S. Chang. Dynamic Response to Canard Control and Gravity for a Dual-Spin Projectile. vol. 53(3), 2016. doi:10.1128/JVI.79.24.15165.

[72] Y. Wang, X. ming Wang, and J. yan Yu. Influence of control strategy on stability of dual-spin projectiles with fixed canards. *Defence Technology*, vol. 14(6):1–11, 2018. doi:10.1016/j.dt.2018.04.014.

[73] D. Ollerenshaw and M. Costello. Simplified projectile swerve solution for general control inputs. *Journal of Guidance, Control, and Dynamics*, vol. 31(5):1259–1265, 2008. doi:10.2514/1.34252.

[74] J. Cheng, Q. Shen, Z. Z. Deng, and Z. Z. Deng. Novel aiming method for spin-stabilized projectiles with a course correction fuze actuated by fixed canards. *Electronics (Switzerland)*, vol. 8(10), 2019. doi:10.3390/electronics8101135.

[75] J. M. Maley. Efficient Attitude Estimation for a Spin-Stabilized Projectile. *Journal of Guidance, Control, and Dynamics*, vol. 39(2):339–350, 2016. doi:10.2514/1.G001104.

[76] D. Ollerenshaw and M. Costello. Model predictive control of a direct fire projectile equipped with canards. *Collection of Technical Papers - AIAA Atmospheric Flight Mechanics Conference*, vol. 1(March):203–214, 2005. doi:10.2514/6.2005-5818.

[77] F. Fresconi and J. Rogers. Flight Control of a Small-Diameter Spin-Stabilized Projectile Using Imager Feedback. *Journal of Guidance, Control, and Dynamics*, vol. 38(2):181–191, 2015. doi:10.2514/1.g000815.

[78] F. Fresconi. Guidance and control of a fin-stabilized projectile based on flight dynamics with reduced sensor and actuator requirements. *AIAA Guidance, Navigation, and Control Conference 2011*, (February), 2011.

[79] Y. Wang, W. D. Song, D. Fang, and Q. W. Guo. Guidance and Control Design for a Class of Spin-Stabilized Projectiles with a Two-Dimensional Trajectory Correction Fuze. *International Journal of Aerospace Engineering*, vol. 2015, 2015. doi:10.1155/2015/908304.

[80] X. D. Liu, D. G. Li, and Q. Shen. Swerving orientation of spin-stabilized projectile for fixed-cant canard control input. *Mathematical Problems in Engineering*, vol. 2015, 2015. doi:10.1155/2015/173571.

[81] B. Tang, Y. tao Xu, G. Wan, J. Yue, Y. Jin, and H. yuan Li. Method of ballistic control and projectile rotation in a novel railgun. *Defence Technology*, vol. 14(5):628–634, 2018. doi:10.1016/j.dt.2018.07.022. URL `https://doi.org/10.1016/j.dt.2018.07.022`.

[82] Z.-p. Han. External Ballistics of Missiles and Arrows [M]. *Beijing Institute of Technology Press, Beijing*, 2014.

[83] D. and J. S. Carlucci. *Theory and design of guns and ammunition*. CRC Press, 2nd ed., 2008. ISBN 9781420066180.

[84] F. Fresconi and T. Harkins. Aerodynamic characterizations of asymmetric and maneuvering 105mm, 120mm, and 155mm fin-stabilized projectiles derived from telemetry experiments. *AIAA Atmospheric Flight Mechanics Conference 2011*, (August):1–30, 2011. doi:10.2514/6.2011-6268.

[85] Y. ming Ren, S. shan Wang, J. wei Li, X. cheng Guo, and Y. song Mei. Aerodynamic and trajectory characteristics of a typical mortar projectile with a deflectable nose. *Defence Technology*, vol. 15(5):758–767, 2019. doi:10.1016/j.dt.2019.05.019. URL https://doi.org/10.1016/j.dt.2019.05.019.

[86] W. Jiajan, R. S. Chue, T. Nguyen, Y. Y. Pey, and S. C. Yu. Aerodynamic characteristics of high performance rounds at Mach 1.8 to 4. *Aerospace Science and Technology*, vol. 40:62–74, 2015. doi:10.1016/j.ast.2014.10.013. URL http://dx.doi.org/10.1016/j.ast.2014.10.013.

[87] X. Liu, X. Wu, and J. Yin. Aerodynamic characteristics of a dual-spin projectile with canards. *Proceedings of the Institution of Mechanical Engineers, Part G: Journal of Aerospace Engineering*, vol. 0(5):1–13, 2019. doi:10.1177/0954410019827458.

[88] J. Yin, J. Lei, X. Wu, and T. Lu. Aerodynamic characteristics of a spinning projectile with elastic deformation. *School of Aerospace Engineering, Beijing Institute of Technology*, (51):181–191, 2016. doi:10.1016/j.ast.2016.02.010. URL http://dx.doi.org/10.1016/j.ast.2016.02.010.

[89] K. Liang, Z. Huang, and J. min Zhang. Optimal design of the aerodynamic parameters for a supersonic two-dimensional guided artillery projectile. *Defence Technology*, 2017. doi:10.1016/j.dt.2017.05.003.

[90] N. Hamel and E. Gagnon. CFD and parametric study on a 155 mm artillery shell equipped with a roll-decoupled course correction fuze. *29th AIAA Applied Aerodynamics Conference 2011*, (June):1–10, 2011. doi:10.2514/6.2011-3027.

[91] M. E. Wessam and Z. H. Chen. Aerodynamic characteristics of unguided artillery projectile. *Advanced Materials Research*, vol. 1014(August):165–168, 2014. doi:10.4028/www.scientific.net/AMR.1014.165.

[92] M. Wessam and Z. Chen. Firing Precision Evaluation For Unguided Artillery Projectile. (Aiie):584–587, 2015. doi:10.2991/aiie-15.2015.156.

[93] R. L. McCoy. *Modern Exterior Ballistics: The Launch and Flight Dynamics of Symmetric Projectiles*. Schiffer Publishing, 1999.

[94] *Textbook of Ballistics and Gunnery*. 1987.

[95] M. Khalil, H. Abdalla, and O. Kamal. Dispersion Analysis for Spinning Artillery Projectile. *International Conference on Aerospace Sciences and Aviation Technology*, vol. 13(AEROSPACE SCIENCES):1–12, 2009. doi:10.21608/asat.2009.23740.

[96] A. Ko, K. Chang, D. J. Sheen, C. H. Lee, Y. Park, and S. W. Park. Prediction and Analysis of the Aerodynamic Characteristics of a Spinning Projectile Based on Computational Fluid Dynamics. *International Journal of Aerospace Engineering*, vol. 2020, 2020. doi:10.1155/2020/6043721.

[97] S. I. Silton. Navier-stokes predictions of aerodynamic coefficients and dynamic derivatives of a 0.50-cal projectile. *29th AIAA Applied Aerodynamics Conference 2011*, (June):1–17, 2011. doi:10.2514/6.2011-3030.

[98] R. L. Mccoy. The Aerodynamic Characteristics of Caliber .50 Ball, M33, API, M8, and APIT, M20 Ammunition. page 75, 1989.

[99] G. M. Siouris. *Missile Guidance and Control Systems*. Springer, 2004. ISBN 0-387-00726-1.

[100] D. Chwa. Robust Nonlinear Disturbance Observer Based Adaptive Guidance Law Against Uncertainties in Missile Dynamics and Target Maneuver. *IEEE Transactions on Aerospace and Electronic Systems*, vol. 54(4):1739–1749, 2018. doi:10.1109/TAES.2018.2801392.

[101] X. Yan and S. Lyu. Robust intercept guidance law with predesigned zero-effort miss distance convergence for capturing maneuvering targets. *Journal of the Franklin Institute*, vol. 357(2):1118–1136, 2020. doi:10.1016/j.jfranklin.2019.10.021. URL https://doi.org/10.1016/j.jfranklin.2019.10.021.

[102] A. Ratnoo and D. Ghose. Collision-geometry-based pulsed guidance law for exoatmospheric interception. *Journal of Guidance, Control, and Dynamics*, vol. 32(2):669–674, 2009. doi:10.2514/1.37863.

[103] P. Zarchan. *Tactical and Strategic Missile Guidance*. American Institute of Aeronautics and Astronautics, Inc., 6th ed., 2012. ISBN 978-1-60086-894-8.

[104] D. R. Taur and J. S. Chern. Passive ranging for dog-fight air-to-air IR missiles. *1999 Guidance, Navigation, and Control Conference and Exhibit*, (c):1737–1751, 1999. doi:10.2514/6.1999-4289.

[105] T. L. Song and U. M. Tae Yoon. Practical guidance for homing missiles with bearings-only measurements. *IEEE Transactions on Aerospace and Electronic Systems*, vol. 32(1):434–443, 1996. doi:10.1109/7.481284.

[106] X. Zhang, M. Liu, and Y. Li. Sliding mode control and Lyapunov based guidance law with impact time constraints. *Journal of Systems Engineering and Electronics*, vol. 28(6):1186–1192, 2017. doi:10.21629/JSEE.2017.06.16.

[107] J. H. Blakelock. *Automatic Control of Aircraft and Missiles, 2nd Edition*. WILEY Inter-science, 2nd ed., 1991. ISBN 978-0-471-50651-5.

[108] S. He, J. Wang, and W. Wang. A novel sliding mode guidance law without line-of-sight angular rate information accounting for autopilot lag. *International Journal of Systems Science*, vol. 48(16):3363–3373, 2017. doi:10.1080/00207721.2017.1382607. URL https://doi.org/10.1080/00207721.2017.1382607.

[109] I. Yang, D. Lee, and D. S. Han. Designing a robust nonlinear dynamic inversion controller for spacecraft formation flying. *Mathematical Problems in Engineering*, vol. 2014, 2014. doi:10.1155/2014/471352.

[110] . Raymong A et al. Variable structure control of nonlinear multivariable systems: a tutorial. vol. 76(3):1–21, 2009. URL papers3://publication/uuid/020DBA87-2D0E-42D4-AA42-9D54629744EB.

[111] Y. Shtessel, C. Edwards, and L. Fridman. *Sliding Mode Control and Observation, Series: Control Engineering*, vol. 10. 2016. ISBN 978-0-81764-8923. doi:10.1007/978-0-8176-4893-0. URL http://www.springer.com/gp/book/9780817648923{#}reviews.

[112] B. Bandyopadhyay, F. Deepak, and K. S. Kim. *Sliding mode control using novel sliding surfaces*, vol. 392. 2009. ISBN 9783642034473. doi:10.1007/978-3-642-03448-0_1.

[113] J.-J. Slotine and W. Li. *Applied NoLinear Optimal Control*. 1991. ISBN 0-13-040890-5.

[114] VADIM I. UTKIN. Variable Structure Systems with Sliding Modes. *IEEE Transactions on Automatic Control*, vol. 22(2):212–222, 1977.

[115] S. D. Brierley and R. Longchamp. Application of Sliding-Mode Control to Air-Air Interception Problem. *IEEE Transactions on Aerospace and Electronic Systems*, vol. 26(2):306–325, 1990. doi:10.1109/7.53460.

[116] J. C. Wu, J. N. Yang, and A. K. Agrawal. *Applications of Sliding Mode Control*, vol. 1265. 1998. ISBN 9789811023736. doi:10.1007/978-981-10-2374-3.

[117] G. Li, Z. Yu, and Z. Wang. Three-dimensional Adaptive Sliding Mode Guidance Law for Missile with Autopilot Lag and Actuator Fault. *International Journal of Control, Automation and Systems*, vol. 17(6):1369–1377, 2019. doi:10.1007/s12555-017-0731-9.

[118] S. T. Geng, J. Zhang, and J. G. Sun. Adaptive back-stepping sliding mode guidance laws with autopilot dynamics and acceleration saturation consideration. *Proceedings of the Institution of Mechanical Engineers, Part G: Journal of Aerospace Engineering*, vol. 233(13):4853–4863, 2019. doi:10.1177/0954410019835728.

[119] X. Tan. A Novel Sliding Mode Guidance Law with Impact Angle and Time Constraints. pages 5896–5901, 2019.

[120] Z. Li, H. Ye, H. Cui, Z. Guo, and Y. Cai. Sliding mode control-based guidance law with damping term and angle constraint. *Chinese Control Conference, CCC*, vol. 2019-July(61374160):4083–4088, 2019. doi:10.23919/ChiCC.2019.8865893.

[121] A. A. A. Alrawi, S. Graovac, R. B. Ahmad, and M. M. Rahman. Modified guidance law based on a sliding mode controller for a missile guidance system. *Tehnicki Vjesnik*, vol. 23(3):639–646, 2016. doi:10.17559/TV-20130625173047.

[122] A. Ratnoo and T. Shima. Line-of-sight interceptor guidance for defending an aircraft. *Journal of Guidance, Control, and Dynamics*, vol. 34(2):522–532, 2011. doi:10.2514/1.50572.

[123] T. Yamasaki, S. N. Balakrishnan, and H. Takano. Engineering notes: Modified command to Line-of-Sight intercept guidance for aircraft defense. *Journal of Guidance, Control, and Dynamics*, vol. 36(3):901–905, 2013. doi:10.2514/1.58566.

[124] Q. Li, J. Li, Y. Wang, X. Zhang, and X. Qin. The research of terminal optimal guidance law of MANEUVERING vehicle with multiple constrains. *2019 IEEE 10th International Conference on Mechanical and Aerospace Engineering, ICMAE 2019*, pages 74–78, 2019. doi:10.1109/ICMAE.2019.8880990.

[125] C. H. Lee, H. S. Shin, J. I. Lee, and M. J. Tahk. Zero-Effort-Miss Shaping Guidance Laws. *IEEE Transactions on Aerospace and Electronic Systems*, vol. 54(2):693–705, 2018. doi:10.1109/TAES.2017.2764258.

[126] V. C. Lam. Acceleration-compensated zero-effort-miss guidance law. *Journal of Guidance, Control, and Dynamics*, vol. 30(4):1159–1163, 2007. doi:10.2514/1.26948.

[127] Y. Guo, M. Hawkins, and B. Wie. Applications of generalized zero-effort-miss/zero-effort-velocity feedback guidance algorithm. *Journal of Guidance, Control, and Dynamics*, vol. 36(3):810–820, 2013. doi:10.2514/1.58099.

[128] M. D. Mohammad-Abadi and S. H. Jalali-Naini. Evaluation of conceptual midcourse guidance laws for long-range exoatmospheric interceptors. *Journal of Aerospace Technology and Management*, vol. 9(1):101–115, 2017. doi: 10.5028/jatm.v9i1.718.

[129] A. J. Calise, H. A. El-Shirbiny, N. Kim, and A. T. Kutay. An adaptive guidance approach for spinning projectiles. *Collection of Technical Papers - AIAA Guidance, Navigation, and Control Conference*, vol. 5(August):3226–3238, 2004. doi:10.2514/6.2004-5359.

[130] A. J. Calise, B. J. Yang, and J. I. Craig. Augmentation of an existing linear controller with an adaptive element. *Proceedings of the American Control Conference*, vol. 2:1549–1554, 2002. doi:10.1109/ACC.2002.1023242.

[131] M. Gao, Y. Zhang, S. Yang, D. Fang, and D. F. Min Gao, Yongwei Zhang, Suochang. Trajectory Correction Capability Modeling of the Guided Projectiles with Impulse Thrusters. *Engineering Letters*, 2016.

[132] L. D. Fairfax and F. E. Fresconi. Position Estimation for Projectiles Using Low-Cost Sensors and Flight Dynamics. *Journal of Aerospace Engineering*, vol. 27(3):611–620, 2012. doi:10.1061/(asce)as.1943-5525.0000284.

[133] V. N. Khruslov, S. V. Feofilov, O. V. Goryachev, I. M. Lavit, and A. F. Indyukhin. Missile control in the polar coordinate system using a scalar radius. *Gyroscopy and Navigation*, vol. 6(1):66–72, 2015. doi:10.1134/S207510871501006X.

[134] B. G. Penev. An Expanded Two-Dimensional Proportional–Derivative Command to Line-of-Sight Guidance Law. *Gyroscopy and Navigation*, vol. 9(4):344–351, 2018. doi:10.1134/S2075108718040132.

[135] K. B. Pamadi and E. J. Ohlmeyer. Evaluation of two guidance laws for controlling the impact flight path angle of a naval gun launched spinning projectile. *Collection of Technical Papers - AIAA Guidance, Navigation, and Control Conference 2006*, vol. 1(August):642–652, 2006. doi:10.2514/6.2006-6081.

[136] B. C. Gruenwald and J. Bryson. Adaptive Control for a Guided Projectile using an Expanded Reference Model. (January):1–12, 2020. doi:10.2514/6.2020-1822.

[137] W. Park, C. K. Ryoo, B. S. Kim, Y. Kim, and J. Kim. A new practical guidance law for a guided projectile. *AIAA Guidance, Navigation, and Control Conference 2011*, (August):1–9, 2011. doi:10.2514/6.2011-6249.

[138] A. J. Calise and H. A. El-Shirbiny. An analysis of aerodynamic control for direct fire spinning projectiles. *AIAA Guidance, Navigation, and Control Conference and Exhibit*, (August), 2001. doi:10.2514/6.2001-4217.

[139] A. Catovic, B. Zecevic, and J. Terzic. ANALYSIS OF TERMINAL EFFECTIVENESS FOR SEVERAL TYPES OF HE PROJECTILES AND IMPACT ANGLES USING COUPLED NUMERICAL -CAD NUMERICAL - CAD TECHNIQUE. (May 2014), 2009.

[140] R. Decker, M. Duca, and S. Spickert-Fulton. Measurement of bullet impact conditions using automated in-flight photography system. *Defence Technology*, vol. 13(4):288–294, 2017. doi:10.1016/j.dt.2017.04.004. URL `http://dx.doi.org/10.1016/j.dt.2017.04.004`.

[141] Y. Zhe, W. Zhengjie, F. Ningjun, Z. Yang, Z. Wang, and N. Fan. Virtual target based optimal guidance law with impact angle and burst height constrains. *Proceedings of 2015 7th International Conference on Modelling, Identification and Control, ICMIC 2015*, (Icmic):1–6, 2016. doi:10.1109/ICMIC.2015.7409437.

[142] C. Wang, W. Dong, J. Wang, S. Member, and J. Shan. Nonlinear Suboptimal Guidance Law with Impact Angle Constraint : an SDRE-Based Approach. vol. XX(X):1–10, 2020. doi:10.1109/TAES.2020.3003105.

[143] Y. R. Sharma and A. Ratnoo. A Bearings-Only Trajectory Shaping Guidance Law with Look-Angle Constraint. *IEEE Transactions on Aerospace and Electronic Systems*, vol. 55(6):3303–3315, 2019. doi:10.1109/TAES.2019.2906090.

[144] S. Lee and Y. Kim. Capturability of Impact-Angle Control Composite Guidance Law Considering Field-of-View Limit. *IEEE Transactions on Aerospace and Electronic Systems*, vol. 56(2):1077–1093, 2020. doi:10.1109/TAES.2019.2925485.

[145] A. Banerjee, M. un Nabi, and T. Kumbasar. Big Bang Big Crunch based Near-Optimal Guidance Law for Interceptor Problem. pages 790–794, 2020. doi:10.23919/eleco47770.2019.8990571.

[146] X. ZHANG, X. YAO, and Q. ZHENG. Impact point prediction guidance based on iterative process for dual-spin projectile with fixed canards. *Chinese Journal of Aeronautics*, vol. 32(8):1967–1981, 2019. doi:10.1016/j.cja.2019.06.002. URL `https://doi.org/10.1016/j.cja.2019.06.002`.

[147] Q. W. Guo, W. D. Song, Y. Wang, and Z. C. Lu. Guidance Law Design for a Class of Dual-Spin Mortars. *International Journal of Aerospace Engineering*, vol. 2015, 2015. doi:10.1155/2015/952076.

[148] OpenAI. Kinds of RL Algorithms. URL `https://spinningup.openai.com/en/latest/spinningup/rl{_}intro2.html`.

[149] D. Silver, T. Hubert, J. Schrittwieser, I. Antonoglou, M. Lai, A. Guez, M. Lanctot, L. Sifre, D. Kumaran, T. Graepel, T. Lillicrap, K. Simonyan, and D. Hassabis. Mastering Chess and Shogi by Self-Play with a General Reinforcement Learning Algorithm. pages 1–19, 2017. `1712.01815`, URL `http://arxiv.org/abs/1712.01815`.

[150] V. Mnih, D. Silver, and M. Riedmiller. Playing Atari with Deep Reinforcement Learning. pages 1–9.

[151] V. Mnih, K. Kavukcuoglu, D. Silver, A. A. Rusu, J. Veness, M. G. Bellemare, A. Graves, M. Riedmiller, A. K. Fidjeland, G. Ostrovski, S. Petersen, C. Beattie, A. Sadik, I. Antonoglou, H. King, D. Kumaran, D. Wierstra, S. Legg, and D. Hassabis. Human-level control through deep reinforcement learning. *Nature*, vol. 518(7540):529–533, 2015. doi:10.1038/nature14236. URL `http://dx.doi.org/10.1038/nature14236`.

[152] P. Yves Glorennec. Fuzzy Q-learning and dynamical fuzzy Q-learning. *IEEE International Conference on Fuzzy Systems*, vol. 1:474–479, 1994. doi:10.1109/fuzzy.1994.343739.

[153] V. Mnih, M. Mirza, A. Graves, T. Harley, T. P. Lillicrap, and D. Silver. Asynchronous Methods for Deep Reinforcement Learning. vol. 48, 2016. arXiv:1602.01783v2.

[154] E. Robustness, O. F. Deep, F. Learning, and W. Continuous. EVALUATING ROBUSTNESS OF DEEP REIN -. pages 1–11, 2020.

[155] C. Tessler, Y. Efroni, and S. Mannor. Action Robust Reinforcement Learning and Applications in Continuous Control. 2019. 1901.09184, URL http://arxiv.org/abs/1901.09184.

[156] L. Pinto, J. Davidson, R. Sukthankar, and A. Gupta. Robust adversarial reinforcement learning. *34th International Conference on Machine Learning, ICML 2017*, vol. 6:4310–4319, 2017.

[157] S. Devi Mahalakshmi and V. Geethanjali. Plant classification using deep learning. *Journal of International Pharmaceutical Research*, vol. 46(3):745–749, 2019. doi:10.14419/ijet.v7i2.7.10892.

[158] T. Haarnoja, S. Ha, A. Zhou, J. Tan, G. Tucker, and S. Levine. Learning to Walk via Deep Reinforcement Learning. 2018. 1812.11103, URL http://arxiv.org/abs/1812.11103.

[159] B. Gaudet and R. Furfaro. Missile homing-phase guidance law design using reinforcement learning. *AIAA Guidance, Navigation, and Control Conference 2012*, (October 2016), 2012. doi:10.2514/6.2012-4470.

[160] B. Gaudet, R. Furfaro, and R. Linares. Reinforcement Learning for Angle-Only Intercept Guidance of Maneuvering Targets. *Aerospace Science and Technology*, vol. 99:1–16, 2019. doi:10.1016/j.ast.2020.105746. 1906.02113, URL http://arxiv.org/abs/1906.02113.

[161] C. Liang, W. Wang, Z. Liu, C. Lai, and B. Zhou. Learning to Guide: Guidance Law Based on Deep Meta-Learning and Model Predictive Path Integral Control. *IEEE Access*, vol. 7:47,353–47,365, 2019. doi:10.1109/ACCESS.2019.2909579.

[162] X. Yan, J. Zhu, M. Kuang, and X. Wang. Missile aerodynamic design using reinforcement learning and transfer learning. *Science China Information Sciences*, vol. 61(11):1–3, 2018. doi:10.1007/s11432-018-9463-x.

[163] H. Shao, Y. Han, C. Wei, and R. Wang. A novel recurrent convolutional neural network-based estimation method for switching guidance law. *IEEE Access*, vol. 8:10,159–10,168, 2020. doi:10.1109/ACCESS.2020.2964285.

[164] Y. Zhao, Z. Zheng, X. Zhang, and Y. Liu. Q learning algorithm based UAV path learning and obstacle avoidence approach. *Chinese Control Conference, CCC*, pages 3397–3402, 2017. doi:10.23919/ChiCC.2017.8027884.

[165] K. Zheng, J. Gao, and L. Shen. UCAV Path Planning Algorithm Based on Deep Reinforcement Learning. In Y. Zhao, N. Barnes, B. Chen, R. Westermann, X. Kong, and C. Lin, editors, *Image and Graphics*, pages 702–714. Springer International Publishing, Cham, 2019. ISBN 978-3-030-34110-7.

[166] Y. Zhang, W. Zu, Y. Gao, and H. Chang. Research on autonomous maneuvering decision of UCAV based on deep reinforcement learning. *Proceedings of the 30th Chinese Control and Decision Conference, CCDC 2018*, pages 230–235, 2018. doi:10.1109/CCDC.2018.8407136.

[167] B. Gaudet, R. Linares, and R. Furfaro. Deep Reinforcement Learning for Six Degree-of-Freedom Planetary Powered Descent and Landing. *Advances in Space Research*, 2018. doi:10.1016/j.asr.2019.12.030. `1810.08719`, URL `http://arxiv.org/abs/1810.08719`.

[168] Z. Wang, H. Li, H. Wu, F. Shen, and R. Lu. Design of Agent Training Environment for Aircraft Landing Guidance Based on Deep Reinforcement Learning. *Proceedings - 2018 11th International Symposium on Computational Intelligence and Design, ISCID 2018*, vol. 2:76–79, 2018. doi:10.1109/ISCID.2018.10118.

[169] J. Sung, B. S. Kim, and M. S. Song. Neural Network-Based Adaptive Control Design of Dual-Spin Projectile with Rotating Canards. *International Journal of Aeronautical and Space Sciences*, vol. 20(3):806–814, 2019. doi:10.1007/s42405-019-00162-9. URL https://doi.org/10.1007/s42405-019-00162-9.

[170] H.-y. Yang. Effects of Reward Terms in Agent-Based Box-Manipulation Animation Using Deep Reinforcement Learning.

[171] S. SELVI, R.MALMATHANRAJ, and S. RAJ. Solving Missile Defense and Interceptor allocation problem using Reinforcement learning and optimization techniques. *Int. J. of Recent Trends in Engineering and Technology*, vol. 2(3):117–119, 2009.

[172] R. Zhang, Y. Wang, Wutao, and W. Geng. Radar reflected signal process of high spinning rate projectiles. *2007 8th International Conference on Electronic Measurement and Instruments, ICEMI*, pages 3982–3985, 2007. doi: 10.1109/ICEMI.2007.4351084.

[173] B. L. Allik, C. Miller, and J. Maley. Target learning, acquisition, and tracking on a guided projectile. *AIAA Information Systems-AIAA Infotech at Aerospace, 2018*, (209989), 2018. doi:10.2514/6.2018-1630.

[174] L. L. L. Wells. Projectile GRAM SAASM for ERGM and Excalibur. *Record - IEEE PLANS, Position Location and Navigation Symposium*, pages 106–111, 2000. doi:10.1109/plans.2000.838290.

[175] F. Liu, Z. Su, H. Zhao, Q. Li, and C. Li. Attitude measurement for high-spinning projectile with a hollow MEMS IMU consisting of multiple accelerometers and gyros. *Sensors (Switzerland)*, vol. 19(8), 2019. doi:10.3390/s19081799.

[176] J. Rogers and M. Costello. A low-cost orientation estimator for smart projectiles using magnetometers and thermopiles. *Navigation, Journal of the Institute of Navigation*, vol. 59(1):9–24, 2012. doi:10.1002/navi.5.

[177] D. N. Gkritzapis, E. E. Panagiotopoulos, D. E. Margaris, and D. G. Papanikas. Computational atmospheric trajectory simulation analysis of spin-stabilised

projectiles and small bullets. *International Journal of Computing Science and Mathematics*, vol. 2(1-2):53–72, 2008. doi:10.1504/IJCSM.2008.019723.

[178] J. T. Bryson, J. D. Vasile, I. Celmins, and F. E. Fresconi. Approach for understanding range extension of gliding indirect fire munitions. *2018 Atmospheric Flight Mechanics Conference*, 2018. doi:10.2514/6.2018-3158.

[179] D. Machala, S. Dobre, M. Albisser, M. Gilson, and F. Collin. The analysis of vehicle's in-flight behaviour using quasi-lpv and nonlinear models. *AIAA Scitech 2019 Forum*, (January):1–12, 2019. doi:10.2514/6.2019-1321.

[180] P. Weinacht. Validation and prediction of the effect of rifling grooves on small-caliber ammunition performance. *Collection of Technical Papers - 2006 Atmospheric Flight Mechanics Conference*, vol. 1:128–139, 2006. doi:10.2514/6.2006-6010.

[181] A. Materials, O. Rabinovitch, and J. R. Vinson. Smart fins: Analytical modeling and basic design concepts. *Mechanics of Advanced Materials and Structures*, vol. 10(3):249–269, 2003. doi:10.1080/15376490306742.

[182] B. Feng and C. Ming. Numerical Prediction of Magnus Effect for Dual-Spin Projectile. *2018 6th International Conference on Mechanical, Automotive and Materials Engineering (CMAME)*, pages 51–55, 2018.

[183] D. N. Gkritzapis, N. E. Tsiatis, E. E. Panagiotopoulos, and D. P. Margaris. Physicomathematical simulation analysis for small bullets. *Journal of Engineering Science and Technology Review*, vol. 1(1):70–74, 2008.

[184] J. C. Williams, P. B. O'Donovan, R. A. Vandenberg, R. E. Sturm, and E. H. Wood. EQUATIONS OF MOTION OF A SPIN-STABILIZED PROJECTILE FOR FLIGHT STABILITY TESTING. *JOURNAL OF THEORETICAL AND APPLIED MECHANICS*, vol. 51(1):235–246, 2013.

[185] M. Costello and A. Peterson. Linear Theory of a Dual-Spin Projectile in Atmospheric Flight. *Journal of Guidance, Control, and Dynamics*, vol. 23(5, September-October), 2000. doi:10.2514/2.4639.

[186] G. Strub, S. Theodoulis, V. Gassmann, S. Dobre, and M. Basset. Gain-Scheduled Autopilot Design and Validation for an Experimental Guided Projectile Prototype. *Journal of Guidance, Control, and Dynamics*, pages 1–15, 2017. doi:10.2514/1.G002916. URL https://arc.aiaa.org/doi/10.2514/1.G002916.

[187] J. T. Economou, A. Tsourdos, and B. A. White. Takagi-Sugeno model synthesis of a quasi-linear parameter varying mobile robot. (October), 2002. URL http://www.scopus.com/inward/record.url?eid=2-s2.0-0036452424{&}partnerID=MN8TOARS.

[188] MIT. Aircraft stability and control Lecture 2, 2004. URL https://ocw.mit.edu/courses/aeronautics-and-astronautics/16-333-aircraft-stability-and-control-fall-2004/lecture-notes/lecture{_}2.pdf.

[189] G. M. Moss, D. W. Leeming, and C. L. Farrar. *Military Ballistics*. Brassey's, 1st ed., 1995.

[190] E. R. COURTNEY and M. W. COURTNEY. Aerodynamic Drag and Gyroscopic Stability. Tech. rep., BTG Research.

[191] D. Zhu, S. Tang, J. Guo, and R. Chen. Flight stability of a dual-spin projectile with canards. *Proceedings of the Institution of Mechanical Engineers, Part G: Journal of Aerospace Engineering*, vol. 229(4):703–716, 2015. doi:10.1177/0954410014539293.

[192] G. L. Penny and John. Numerical Methods Using MATLAB. Academic Press, 2019. ISBN 978-0-12-812256-3. doi:https://doi.org/10.1016/B978-0-12-812256-3.00006-3. URL http://www.sciencedirect.com/science/article/pii/B9780128122563000063.

[193] John W. Harris and H. Stöcker. *Handbook of mathematics and computational science*. Springer-Verlag New York, 1st ed., 1998. ISBN 9780387947464.

[194] V. N. Khruslov, S. V. Feofilov, O. V. Goryachev, I. M. Lavit, and A. F. Indyukhin. Missile control in the polar coordinate system using a scalar radius. *Gyroscopy and Navigation*, vol. 6(1):66–72, 2015. doi:10.1134/S207510871501006X.

[195] C. F. Lin, P. A. Bao, S. J. Braasch, and M. S. Whorton. Genetic algorithm based parameter optimization of a fuzzy logic controller. *1999 Guidance, Navigation, and Control Conference and Exhibit*, (c):1117–1122, 1999. doi:10.2514/6.1999-4152.

[196] Y. Eun and H. Bang. Cooperative task assignment and path planning of multiple UAVs using genetic algorithm. *Collection of Technical Papers - 2007 AIAA InfoTech at Aerospace Conference*, vol. 3(May):2680–2697, 2007. doi: 10.2514/6.2007-2982.

[197] B. Hong, L.-p. Pey, and T.-y. Soh. STRUCTURAL PARAMETER IDENTIFICATION USING ROBUST GENETIC ALGORITHM OPTOMIZATION METHOD. (April 2004):1–9, 2015. doi:10.2514/6.2004-2015.

[198] O. Kramer. *Studies in Computational Intelligence 679 Genetic Algorithm Essentials*. 2017. ISBN 9783319521558. URL `https://www.mendeley.com/research-papers/studies-computational-intelligence-679-genetic-algorithm-essentials/?utm{_}source=desktop{&}utm{_}medium=1.17.13{&}utm{_}campaign=open{_}catalog{&}userDocumentId={%}7B7a663108-07c0-4ee8-bd54-f1a7009fb46e{%}7D`.

[199] M. P. Thomas and Stephanie. *MATLAB Machine Learning*. 2016. ISBN 9781484222492.

[200] D. W. Webb. Circular Probable Error for Circular and Noncircular Gaussian Impacts. *US Army Research Laboratory*, (September), 2012.

[201] G. Cowan. *Statistical Data Analysis*. Oxford University Press, 1st ed., 1998. ISBN O-19-850156-O.

[202] J. DeSpirito. CFD aerodynamic characterization of 155-mm projectile at high angles-of-attack. *35th AIAA Applied Aerodynamics Conference, 2017*, (June):1–20, 2017. doi:10.2514/6.2017-3397.

[203] J. Despirito and K. R. Heavey. CFD Computation of Magnus Moment and Roll Damping Moment of a Spinning Projectile. 2006.

[204] J. Guan and W. Yi. Modeling of dual-spinning projectile with canard and trajectory filtering. *International Journal of Aerospace Engineering*, vol. 2018, 2018. doi: 10.1155/2018/1795158.

[205] C. O. Knudson. Cannon Artillery and Mortar Precision Effects. URL `https://ndiastorage.blob.core.usgovcloudapi.net/ndia/2008/psa{_}peo/Knudson.pdf`.

[206] The Evolution of Artillery for Increased Effectiveness, 2008. URL `https://ndiastorage.blob.core.usgovcloudapi.net/ndia/2008/psa{_}peo/Demella.pdf`.

[207] Steerable projectile with a rotatable nose cone having a flat formation extending off-axis from the tip of the nose.

[208] M. R. Brady and P. Goethals. A comparative analysis of contemporary 155 mm artillery projectiles. *Journal of Defense Analytics and Logistics*, vol. 3(2):171 – 192, 2019. doi:10.1108/jdal-05-2019-0011.

[209] D. Rotondo. *Advances in Gain-Scheduling and Fault Tolerant Control Techniques*. Springer, Cham, 2018. ISBN 978-3-319-62901-8. doi:https://doi.org/10.1007/978-3-319-62902-5.

[210] H. Mao, M. Schwarzkopf, S. B. Venkatakrishnan, Z. Meng, and M. Alizadeh. Learning scheduling algorithms for data processing clusters. *SIGCOMM 2019 - Proceedings of the 2019 Conference of the ACM Special Interest Group on Data Communication*, pages 270 – 288, 2019. doi:10.1145/3341302.3342080. `1810.01963`.

[211] B. Litz. Aerodynamic Drag Modeling for Ballistics Part 1: Aerodynamic Drag 101. pages 1 – 13, 2016.

[212] B. Feng and C. Ming. Numerical Prediction of Magnus Effect for Dual-Spin Projectile. *2018 6th International Conference on Mechanical, Automotive and Materials Engineering (CMAME)*, pages 51 – 55, 2018.

[213] B. Litz. Tangent, Secant, Hybrid Ogive Bullets. URL http://www.accurateshooter.com/ballistics/tangent-vs-secant-vs-hybrid-ogive-bullets/.

All references were confirmed operational and last accessed at the time this thesis was submitted for publication, on 05/01/2022

Appendix A

Explicit calculations

This appendix shows in full, any important equations, derivations or terms which are used throughout the manuscript.

A.1 Aerodynamic forces & moments

This section describes the main interactions between a body in motion, and the medium through which it travels. In general, any 'x' aerodynamic attribute has a corresponding coefficient C_x, force F_x and moment M_x, though not all interactions have both a force and a moment. An important concept in aerodynamics is the Centre of pressure (CoP), defined as the point where the total sum of a pressure field acts towards and is considered the point through which a resulting force vector will act. Importantly, a body can have one CoP for each field it is subjected to, *e.g.* the Magnus force CoP may be different to the lift force CoP. The discussions in the section can be found in many aerodynamics text, but ref. [93] is used here.

A.1.1 The drag force

The main opposition to motion a projectile will experience during flight is the resistance of the ambient fluid medium, known as drag. This causes the drag force F_D. It is comprised of pressure drag normal to the surface area, skin friction parallel to the surface area and wave drag caused by the shock wave of local surface speeds in excess of Mach 1. F_D is a

function of the density of host medium ρ, $\vec{V}$ and the reference area S. The reference area is generally arbitrary, it can either be the total surface area, the area of frontal projection or a cross section. For projectiles it usually taken as the largest permissible planar cross section, perpendicular to the longitudinal axis $\vec{x}$. We define the dynamic pressure as $\bar{q} = \frac{1}{2}\rho\ V^2$, a term often used in fluid mechanics which represents the effective pressure of the oncoming airflow. In ballistics the reference area is therefore $S = \pi D^2/4$*,with projectile diameter D being the projectile calibre. Note that S and D must be considered with regards to each individual application of the dynamic pressure, e.g. S & D will be different when considering the lift force acting on a set of fins and the body they are attached to. The magnitude of drag force is defined in full vector or simplified scalar notation as

$$\vec{F_D} = -\frac{1}{2}\rho\ V.\vec{V}S\ C_D \tag{A.1a}$$

$$F_D = -\bar{q}S\ C_D \tag{A.1b}$$

We see F_D is quantified by the non-linear drag coefficient,

$$C_D = C_{D_0} + C_{D_2}\sin^2(\alpha_T) \tag{A.2}$$

expressed as the sum of the yaw-independent, linear C_{D_0} and the yaw-dependent, cubic C_{D_2} terms; the latter term taking into consideration any rotational displacement caused by yaw, pitch or roll movements. The linear/cubic terms are named as such since their dependency on the yaw angle is $\sin(\alpha_T)$ and $\sin^3(\alpha_T)$ respectively. This non-linear coefficient representation is a common model and will be used throughout section A.1. C_D is introduced to scale $F_D(V)$ according to the projectile shape. Neither F_D nor C_D can be calculated theoretically, the force must be measured empirically or found through computer simulations, then the coefficient is calculated from it. The coefficients are purely proportional constants which represent the forces and moments that are actually observed in real life. Figure A.1.1 shows a stereotypical 'drag curve', a plot of C_D against Mach number, for two different bullet geometries. While there is a wide range of industry standard bullet shapes, for our purposes now it is sufficient to know that they are used as a benchmark

*In ballistics, the reference diameter is usually the diameter immediately following the ogive [93]

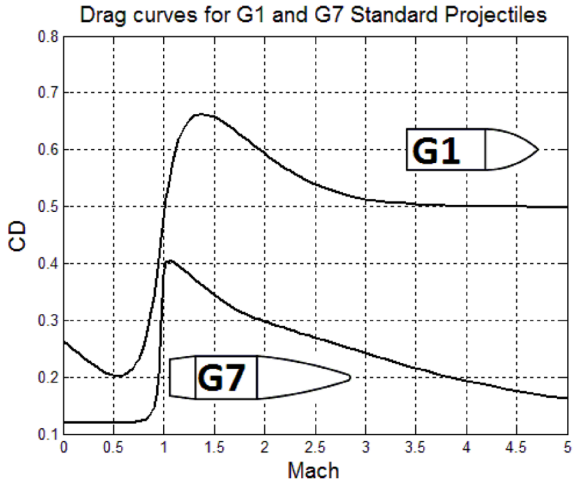

FIGURE A.1.1 Drag curves against Mach number [211]

that any design can be compared to. We can see that the more streamlined G7 projectile has a lower drag coefficient across all Mach ranges than the more blunt G1 projectile. At the critical Mach number $M*$ ($\approx$ Mach 0.8) parts of the body will have a local airflow in excess of Mach 1, creating local shock waves which impart a considerable amount of drag. In the supersonic regime, when all airflow around the body exceeds Mach 1, these local shocks coalesce into a singular shock front, lowering the experienced drag. This is the cause of the characteristic peak of C_D about Mach 1.

Figure A.1.2 shows a comparison of the drag coefficient for a 7.62x51mm NATO bullet from both live fire range data, conducted by BAE, and C_D obtained using the ballistic modelling software PRODAS and DATCOM. To compute the coefficients experimentally, radar is used to measure the speed, which is in turn used to compute the deceleration. Knowing the dynamic pressure and projectile properties, the deceleration can be used to compute the slowing force which is assumed to be entirely because of drag, meaning the drag coefficient can be computed at every instant. Appendix B shows a brief study of projectile geometry using PRODAS, to illustrate simply how one might obtain various coefficients using computer programs instead of needing to conduct live fire experiments. Coefficients obtained from the semi-empirical methods used in PRODAS or DATCOM are slightly less accurate than one would get from refined CFD analysis [96], but even semi-empirical methods produce coefficients in good agreement with that which can be obtained from live fire experiments; especially considering the large source of measurement error from measuring the projectile speeds used to calculate C_D from eq. A.1b. For the

preliminary projectile design phase, using such methods are highly attractive due to the vast improvement of computation time compared to CFD methods, while still delivering dependable coefficients for analysis.

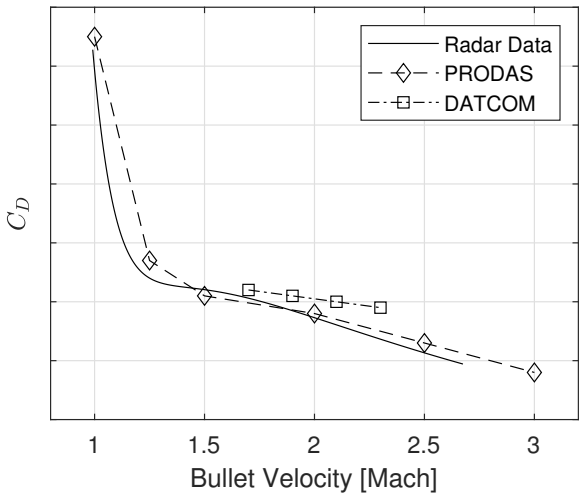

FIGURE A.1.2 BAE Radar range data against PRODAS and DATCOM C_D coefficients for a 7.62x51mm NATO round

A.1.2 Spin interaction

Gyroscopic stabilisation provides an inherent degree of resistance to external trajectory-altering effects, hence it is useful to impart spin on projectiles in order to increase weapon accuracy. It is therefore useful to define a spin vector $\vec{p}$, which has encoded the axis of rotation and rotational speed p (the magnitude), and is conventionally a right handed spin. Ideally the projectile would have $\vec{p}\cdot\vec{x} = \vec{x}\cdot\vec{v} = 0$ but in practice there is usually $\vec{p}\cdot\vec{x} \neq 0$ and some precession of $\vec{p}$ about $\vec{x}$. This will be discussed in greater detail in §3.3.2.

When a projectile spins in a medium there is a viscous interaction between the two causing the projectile roll rate to slow, the magnitude of which can be quantified in the spin-dampening (or spin damping) moment M_{l_P}, given by

$$M_{l_P} = \bar{q}SD\left(\frac{pD}{V}\right)C_{l_P} \tag{A.3}$$

Note the additional reference length D included here, since a moment is the product of a force over a distance. In addition, the term $\frac{pD}{V}$ is known as the spin per calibre of

projectile travel; or the ratio of axial spin rate to forward velocity. If the projectile has control surfaces such as canards or fins, a roll torque M_{l_δ} causes spin up; this torque vector is orientated in the same direction as $\vec{p}$, written as

$$M_{l_\delta} = \bar{q} S \, D \, \delta_F \, C_{l_\delta} \tag{A.4}$$

Here δ_F is the cant angle applied to the fins to achieve lift.

A.1.3 Lift

In general lift is the aerodynamic force orthogonal to the velocity vector, not necessarily $\vec{p}$ or $\vec{x}$. As with the drag force, lift can be represented in vector or scalar notation as

$$F_L = \frac{1}{2}\rho \; SC_{L_\alpha}[\vec{V} \times (\vec{x} \times \vec{V})] \tag{A.5a}$$

$$F_L = \bar{q} S C_{L_\alpha} \sin^2(\alpha_T) \tag{A.5b}$$

where the non-linear lift coefficient C_{L_α} is

$$C_{L_\alpha} = C_{L_{\alpha 0}} + C_{L_{\alpha 2}} \sin^2(\alpha_T) \tag{A.6}$$

From equation A.5b it is obvious that if there is no zero-yaw lift, $C_{L_{\alpha 0}} = 0$, then no total yaw ($\alpha_T = 0$) results in no lift force, since $\delta = 0$. Having no zero-yaw lift is common for symmetric airframes such as projectiles.

A.1.4 The Magnus force

The Magnus force is a spin-medium interaction where the effects are amplified by any flow of the host medium, such as wind. The Magnus force arises when a circular cross-sectioned rotating objecting is immersed in a flow field. Referring to figure A.1.3, the free stream velocity on the lower side of the object is additive with the surface velocity (red, dense mesh), but subtractive on the upper side (blue, sparse mesh). This creates a high pressure area on the lower half, which induces movement toward the relatively low pressure area above. Bernoulli's relation for two laminar flow points of equal density ρ

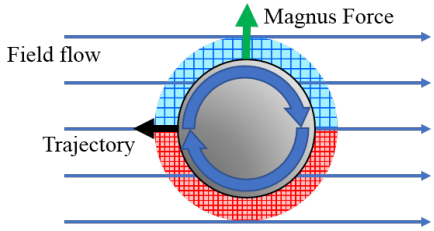

FIGURE A.1.3 The Magnus effect

and height h under gravity g is shown in equation A.7.

$$P_1 + \frac{1}{2}\rho V_1^2 + \rho g h = P_2 + \frac{1}{2}\rho V_2^2 + \rho g h \tag{A.7}$$

The turbulent high pressure area of our object will have the lower relative velocity, which agrees with Bernoulli's equation. The Magnus force $F_{N_{P_\alpha}}$ is described by

$$\vec{F}_{N_{P_\alpha}} = \bar{q}S\left(\frac{pD}{V}\right)C_{N_{P_\alpha}}(\hat{i}\times\vec{x}) \tag{A.8a}$$

$$F_{N_{P_\alpha}} = \bar{q}S\left(\frac{pD}{V}\right)C_{N_{P_\alpha}}\delta \tag{A.8b}$$

with non-linear Magnus force coefficient

$$C_{N_{P_\alpha}} = C_{N_{P_{\alpha_0}}} + C_{N_{P_{\alpha_2}}}\delta^2 \tag{A.9}$$

Note the Magnus force disappears entirely for spinning projectiles with zero yaw value. The Magnus moment $M_{M_{P_\alpha}}$ arising from this force however is given by

$$M_{M_{P_\alpha}} = \bar{q}SD\left(\frac{pD}{V}\right)C_{M_{P_\alpha}}(\hat{i}\times\vec{x}) \tag{A.10a}$$

$$M_{M_{P_\alpha}} = \bar{q}SD\left(\frac{pD}{V}\right)C_{M_{P_\alpha}}\delta \tag{A.10b}$$

with non-linear Magnus moment coefficient

$$C_{M_{P_\alpha}} = C_{M_{P_{\alpha_0}}} + C_{M_{P_{\alpha_2}}}\delta^2 \tag{A.11}$$

Equation A.10 shows how the Magnus moment acts perpendicular to both the Magnus force and the $\vec{V}$. *N.B.* the Magnus force is sufficiently small to be neglected in most scenarios, however, the Magnus moment must be considered since it is a major contributor to projectile instability, making other aerodynamic forces such as drag have a greater effect [203, 212].

A.1.5 Overturning moment

Given a small rotational perturbation to the free stream velocity causes the drag to be asymmetrically distributed. This creates a moment arm which can either create further rotation or act to realign. This is known as the overturning moment M_α, which is given by

$$M_\alpha = \bar{q}SDC_{M_\alpha}(\hat{i} \times \vec{x}) \tag{A.12}$$

Again the non-linear form of C_{M_α} can be written as

$$C_{M_\alpha} = C_{M_{\alpha 0}} + C_{M_{\alpha 2}}\delta^2 \tag{A.13}$$

From equation A.12 we can deduce the sign implications of the overturning moment coefficient. $C_{M_\alpha} > 0$ produces a positive M_α, meaning the projectile will act to pitch about the CoM. If $C_{M_\alpha} = 0$ then we have the trivial $M_\alpha = 0$ and there is no moment. $C_{M_\alpha} < 0$ produces a negative M_α, this implies the resultant moment counteracts the displacement that caused it. Thus, the condition $C_{M_\alpha} < 0$ is required for static stability (see §3.3.1).

A.1.6 Pitch damping

Consider a right circular cylinder immersed in a flow field parallel to $\vec{x}$. If the cylinder rotates about $\vec{x}$ then it will experience a small drag force from the fluid. However, if the rotational axis is changed to be perpendicular to $\vec{x}$, then the retarding effect of viscous action will be substantially larger. This is known as pitch damping; the pitching motion of a projectile being reduced due to air resistance. The pitch damping force is given by $\mathscr{N}_q + \mathscr{N}_{\dot{\alpha}}$. The reason for this long naming convention will become be clear momentarily, for now however it is abbreviated to $F_{\mathscr{N}}$. For projectiles, the pitch damping force is given

by

$$F_{\mathscr{N}} = \frac{1}{2}\rho VSDC_{N_q}\left(\frac{\mathrm{d}\vec{x}}{\mathrm{d}t}\right) + \frac{1}{2}\rho VSDC_{N_\alpha}\left(\frac{\mathrm{d}\vec{x}}{\mathrm{d}t} - \frac{\mathrm{d}\vec{l}}{\mathrm{d}t}\right) \tag{A.14}$$

When reduced to a scalar, this becomes

$$F_{\mathscr{N}} = \bar{q}S\frac{d}{V}\left(q_t\, C_{N_q} + \dot{\alpha}\, C_{N_\alpha}\right) \tag{A.15}$$

where we have defined the total pitching motion q_t and the total rate of change of angle of attack $\dot{\alpha}$ as

$$q_t = \sqrt{q^2 + t^2} \qquad \dot{\alpha} = \frac{\mathrm{d}\alpha_T}{\mathrm{d}t} \tag{A.16}$$

Figure A.1.4 illustrates of the difference with arrows showing the orientation of the projectile at increasing time intervals. In other words, q_t is the projectile pitch relative to a reference axis and $\dot{\alpha}_t$ is the change of angle of attack relative to the velocity vector of the projectile itself. These are the two distinct contributions which give rise to the multi-term definition of the Pitch damping force. The Pitch damping moment, likewise known by

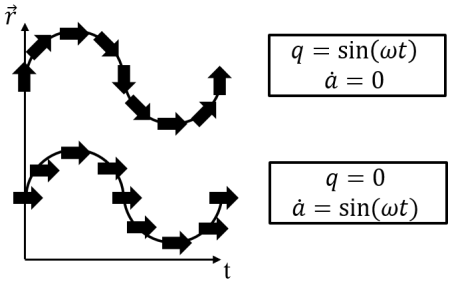

FIGURE A.1.4 Illustrating the difference between q_t and $\dot{\alpha}_t$. The angular frequency $\omega = p$

$M_q + M_{\dot{\alpha}}$ and here abbreviated to $M_{\mathscr{N}}$, is given by

$$\frac{1}{2}\rho VSD^2C_{M_q}\left(\vec{x}\times\frac{\mathrm{d}\vec{x}}{\mathrm{d}t}\right) + \frac{1}{2}\rho VSD^2C_{M_\alpha}\left[\left(\vec{x}\times\frac{\mathrm{d}\vec{x}}{\mathrm{d}t}\right) - \left(\vec{x}\times\frac{\mathrm{d}\vec{l}}{\mathrm{d}t}\right)\right] \tag{A.17}$$

For clarity, M_q & $M_{\dot{\alpha}}$ are the pitch damping moments caused by projectile pitch and angle of attack respectively. This can be reduced into a somewhat more manageable scalar form

$$M_{\mathscr{N}} = \bar{q}SD\left(\frac{q_t d}{V}\right)\left[C_{M_q} + C_{M_\alpha}\right] \tag{A.18}$$

The pitch damping force can usually be disregarded however the moment must always be considered due to its effect on the dynamic stability (§3.3.3). A positive $M_{\mathscr{N}}$ usually increases the transverse angular velocity which has a destabilising effect. The condition for dynamic stability is $C_{M_q} + C_{M_{\dot{\alpha}}} < 0$.

A.1.7 Summary

This section has shown the fundamental interactions between a spinning projectile and the medium (fluid) it is travelling through. Assuming that there is no yaw the spin-interaction forces can be entirely neglected, apart from the Drag force. When there is yaw present, the forces are still considered negligible compared to the increase in drag force their corresponding moments contribute to.

A.2 Airframe trimming coefficients

Below are the terms which result by rearranging the dynamic rotational and wind axis translational equations (3.13 & 3.26) in equilibrium. As mentioned in the text, the terms are of the form k_{ij}, where i indicates the dynamic equation they are derived from and j indicates the variable they are the coefficient of.

$$k_{\alpha 0} = -\frac{1}{mV}\left(\frac{\cos(\alpha)\cos(\theta)+\sin(\alpha)\sin(\theta)}{\cos(\beta)}\right)mg + \ldots \left(\frac{\bar{q}S}{mV}\right)\left[\frac{\cos(\alpha)}{\cos(\beta)}\left(C_{N0}+\frac{d}{V}C_{Np}p_a\right)-\frac{\sin(\alpha)}{\cos(\beta)}C_{A0})\right] \tag{A.19a}$$

$$k_{\alpha r} = \tan(\beta)\left(\cos(\alpha)\tan(\theta)-\sin(\alpha)\right) \tag{A.19b}$$

$$k_{\alpha\delta_z} = -\left(\frac{\bar{q}S}{mV}\right)\left(\frac{\cos(\alpha)}{\cos(\beta)}\right)C_{N\delta} \tag{A.19c}$$

$$k_{q0} = -\left(\frac{\bar{q}Sd}{I_{yy}}\right)\left(C_{m0}+\left(\frac{d}{V}\right)C_{mp}p_A\right) \tag{A.19d}$$

$$k_{qq} = \left(\frac{\bar{q}Sd}{I_{yy}}\right)\left(\frac{d}{V}\right)C_{mq} \tag{A.19e}$$

$$k_{qr} = -\frac{I_x^A}{I_y}p_A \tag{A.19f}$$

$$k_{qr^2} = -\tan(\theta) \tag{A.19g}$$

$$k_{q\delta_z} = \left(\frac{\bar{q}Sd}{I_{yy}}\right) C_{m\delta} \tag{A.19h}$$

$$k_{\beta 0} = \frac{1}{mV}\sin(\beta)\left(\cos(\alpha)\sin(\theta) - \sin(\alpha)\cos(\theta)\right) mg + \left(\frac{\bar{q}S}{mV}\right)\Big[... \\ \cos(\alpha)\sin(\beta)C_{A0} + \cos(\beta)\left(C_{Y0} + \frac{d}{V}C_{Yp}p_A\right) + \sin(\alpha)\sin(\beta)\left(C_{N0} + \frac{d}{V}C_{Np}p_A\right)\Big] \tag{A.19i}$$

$$k_{\beta r} = \sin(\alpha)\tan(\theta) + \cos(\alpha) \tag{A.19j}$$

$$k_{\beta\delta_y} = -\left(\frac{\bar{q}S}{mV}\right)\cos(\beta)C_{Y\delta} \tag{A.19k}$$

$$k_{\beta\delta_z} = -\left(\frac{\bar{q}S}{mV}\right)\sin(\alpha)\sin(\beta)C_{N\delta} \tag{A.19l}$$

$$k_{r0} = -\left(\frac{\bar{q}Sd}{I_{yy}}\right)\left[C_{n0} + \frac{d}{V}C_{np}p_A\right] \tag{A.19m}$$

$$k_{rq} = \frac{I_x^A}{I_y}p_A \tag{A.19n}$$

$$k_{rr} = \left(\frac{\bar{q}Sd}{I_{yy}}\right)\frac{d}{V}C_{nr} \tag{A.19o}$$

$$k_{rqr} = \tan(\theta) \tag{A.19p}$$

$$k_{r\delta_y} = \left(\frac{\bar{q}Sd}{I_{yy}}\right)C_{n\delta} \tag{A.19q}$$

(A.19r)

The above k_{ij} values are used to reduce four, linear simultaneous equations to two. The resulting coefficients of those equations are shown below, denoted by k'_{ij}, and are functions of the above k_{ij}.

$$k'_{qq} = k_{qq} - \frac{k_{q\delta_z}}{k_{\alpha\delta_z}} \tag{A.20a}$$

$$k'_{qr} = k_{qr} - \frac{k_{\alpha r}k_{q\delta_z}}{k_{\alpha\delta_z}} \tag{A.20b}$$

$$k'_{qr^2} = k_{qr^2} \tag{A.20c}$$

$$k'_{q0} = k_{q0} - \frac{k_{\alpha 0}k_{q\delta_z}}{k_{\alpha\delta_z}} \tag{A.20d}$$

$$k'_{rq} = k_{rq} + \frac{k_{\beta\delta_z}k_{r\delta_y}}{k_{\alpha\delta_z}k_{\beta\delta_y}} \tag{A.20e}$$

$$k'_{rr} = k_{rr} - \frac{k_{\beta r} k_{r\delta_y}}{k_{\beta\delta_y}} + \frac{k_{\alpha r} k_{\beta\delta_z} k_{r\delta_y}}{k_{\alpha\delta_z} k_{\beta\delta_y}} \tag{A.20f}$$

$$k'_{rqr} = k_{rqr} \tag{A.20g}$$

$$k'_{r0} = k_{r0} - \frac{k_{\beta 0} k_{r\delta_y}}{k_{\beta\delta_y}} + \frac{k_{\alpha 0} k_{\beta\delta_z} k_{r\delta_y}}{k_{\alpha\delta_z} k_{\beta\delta_y}} \tag{A.20h}$$

(A.20i)

A.3 Jacobian partial derivatives matrix coefficients

Given the non-linear differential equation

$$\dot{x}(t) = f(x(t), u(t)) \tag{A.21}$$

with states $x(t)$, inputs $u(t)$ and functions f mapping $R^n \times R^m \to R^m$, a point is called an equilibrium point $\bar{x}(t)$ if the following condition is satisfied:

$$\bar{x} \in R^n \iff \{\bar{u} \in R^m \mid f(\bar{x}(t), \bar{u}(t)) = 0\}$$

where $\bar{u}(t)$ is the equilibrium input. Given the system in equation A.21 is initialised at a starting point $x(t_0) = \bar{x}$ and has an input $u(t) = \bar{u},\ \forall\ (t \geq t_0)$ applied, then we can also say that $x(t) = \bar{x},\ \forall\ (t \geq t_0)$ due to the nature of equilibrium points. Let us then define the deviation variables $x_\delta(t) = x(t) - \bar{x}$ and $u_\delta(t) = u(t) - \bar{u}$, for point and input deviation respectively. Substituting these into equation A.21 we have the exact solution

$$\dot{\delta}_x(t) = f(\bar{x} + \delta_x(t), \bar{u} + \delta_u(t))$$

Computing a Taylor expansion, neglecting second order terms and above, we have

$$\dot{\delta}_x(t) \approxeq f(x,u)|_{\substack{x=\bar{x}\\u=\bar{u}}} + \left.\frac{\partial f}{\partial x}\right|_{\substack{x=\bar{x}\\u=\bar{u}}} \delta_x(t) + \left.\frac{\partial f}{\partial u}\right|_{\substack{x=\bar{x}\\u=\bar{u}}} \delta_u(t)$$

though $f(\bar{x}, \bar{u}) = 0$. Thus we have a linear, time-invariant, differential equation describing the variation of the variables $\delta_x(t)$ and $\delta_u(t)$ providing they are small. We can then write the Jacobian linearisation of system A.21 about the equilibrium point $(\bar{x}, \bar{u})$ as

$$\dot{\delta}_x(t) = A \cdot \delta_x(t) + B \cdot \delta_u(t) \tag{A.22}$$

where

$$A := \left.\frac{\partial f}{\partial x}\right|_{\substack{x=\bar{x}\\u=\bar{u}}} \in R^{n \times n} \tag{A.23a}$$

$$B := \left.\frac{\partial f}{\partial u}\right|_{\substack{x=\bar{x}\\u=\bar{u}}} \in R^{n\times m} \tag{A.23b}$$

Note here that A and B are partial differential matrices, e.g. if $f \in R^i$ and $x \in R^j$, then A has the form

$$A := \frac{\partial f}{\partial x} = \begin{bmatrix} \frac{\partial f_1}{\partial x_1} & \frac{\partial f_1}{\partial x_2} & \cdots & \frac{\partial f_1}{\partial x_j} \\ \frac{\partial f_2}{\partial x_1} & \frac{\partial f_1}{\partial x_1} & \cdots & \vdots \\ \vdots & \vdots & \ddots & \vdots \\ \frac{\partial f_i}{\partial x_1} & \cdots & \cdots & \frac{\partial f_i}{\partial x_j} \end{bmatrix}_{i\times j} \tag{A.24}$$

Equation 3.14 is the Force vector which carries the aerodynamic coefficient dependency in the stated dynamic translational EOM. The terms are non-zero when differentiated with respect to α, β, δ_z and δ_y. The derivatives with respect to α and β are written here for the sake of formatting in later equations. Throughout this appendix, the notation $F_{G,H} = \frac{\partial F_G}{\partial H}$ and $f_{i,P} = \frac{\partial f_i}{\partial P}$ is used.

$$\begin{bmatrix} F_{X,\alpha} \\ F_{Y,\alpha} \\ F_{Z,\alpha} \end{bmatrix} = -\bar{q}S \begin{bmatrix} C_{A0,\alpha} \\ -\left(\frac{p_A d}{V}\right) C_{Yp,\alpha} \\ C_{N0,\alpha} + \left(\frac{p_A d}{V}\right) C_{Np,\alpha} \end{bmatrix} \tag{A.25a}$$

$$\begin{bmatrix} F_{X,\beta} \\ F_{Y,\beta} \\ F_{Z,\beta} \end{bmatrix} = \bar{q}S \begin{bmatrix} -C_{A0,\beta} \\ C_{Y0,\beta} + \left(\frac{p_A d}{V}\right) C_{Yp,\beta} \\ -\left(\frac{p_A d}{V}\right) C_{Np,\beta} \end{bmatrix} \tag{A.25b}$$

The following is a list of partial derivatives of the airframe dynamics with respect to the state and control vectors. Normal force faa pitch moment fqa pitch damping moment fqq magnus moment fqb gyroscopic moment fqr

$$\begin{aligned} f_{\alpha,\alpha} = & -r\tan(\beta)\big(\sin(\alpha)\tan(\theta)+\cos(\alpha)\big) + \left(\frac{1}{mV}\right)\left[-\left(\frac{\cos(\alpha)}{\cos(\beta)}\right)F_X\right. \\ & \left. -\left(\frac{\sin(\alpha)}{\cos(\beta)}\right)F_{X,\alpha} - \left(\frac{\sin(\alpha)}{\cos(\beta)}\right)F_Y + \left(\frac{\cos(\alpha)}{\cos(\beta)}\right)F_{Y,\alpha}\right] \end{aligned} \tag{A.26}$$

$$f_{\alpha,q} = 1 \tag{A.27}$$

$$f_{\alpha,\beta} = \left(\frac{r}{\cos^2(\beta)}\right)\left(\cos(\alpha)\tan(\theta) - \sin(\alpha)\right) + \left(\frac{1}{mV}\right)\left[-\left(\frac{\sin(\alpha)\sin(\beta)}{\cos^2(\beta)}\right)F_X - \left(\frac{\sin(\alpha)}{\cos(\beta)}\right)F_{X,\beta} - \left(\frac{\cos(\alpha)\sin\beta}{\cos^2(\beta)}\right)F_Y + \left(\frac{\cos(\alpha)}{\cos(\beta)}\right)F_{Y,\beta}\right] \tag{A.28}$$

$$f_{\alpha,r} = \tan(\beta)\left(\cos(\alpha)\tan(\theta) - \sin(\alpha)\right) \tag{A.29}$$

$$f_{\alpha,\delta_z} = -\left(\frac{1}{mV}\right)\left(\frac{\cos(\alpha)}{\cos(\beta)}\right)\bar{q}SC_{N\delta} \tag{A.30}$$

$$f_{\alpha,\delta_y} = 0 \tag{A.31}$$

$$f_{q,\alpha} = \frac{1}{I_{yy}}\left[\bar{q}SdC_{m0,\alpha} + \bar{q}Sd\left(\frac{p_A d}{V}\right)C_{mP,\alpha}\right] \tag{A.32}$$

$$f_{q,q} = \frac{1}{I_{yy}}\bar{q}Sd\left(\frac{d}{V}\right)C_{mq} \tag{A.33}$$

$$f_{q,\beta} = \frac{1}{I_{yy}}\bar{q}Sd\left(\frac{p_A d}{V}\right)C_{mp,\beta} \tag{A.34}$$

$$f_{q,r} = -\left(\frac{I_{xx,a}}{I_{yy}}\right)p_A - 2r\tan(\theta) \tag{A.35}$$

$$f_{q,\delta_z} = \left(\frac{1}{I_{yy}}\right)\bar{q}SdC_{m\delta} \tag{A.36}$$

$$f_{q,\delta_y} = 0 \tag{A.37}$$

$$f_{\beta,\alpha} = -r\left(\cos(\alpha)\tan(\theta) - \sin(\alpha)\right) + \left(\frac{1}{mV}\right) + \left[\sin(\alpha)\sin(\beta)F_X - \cos(\alpha)\sin(\beta)F_{X,\alpha} + \cos(\beta)F_{Y,\alpha} - \cos(\alpha)\sin(\beta)F_Z - \sin(\alpha)\sin(\beta)F_{Z,\alpha}\right] \tag{A.38}$$

$$f_{\beta,q} = 0 \tag{A.39}$$

$$f_{\beta,\beta} = \left(\frac{1}{mV}\right) + \left[\cos(\alpha)\cos(\beta)F_X - \cos(\alpha)\sin(\beta)F_{X,\alpha} - \sin(\beta)F_Y + \cos(\beta)F_{Y,\alpha} - \sin(\alpha)\cos(\beta)F_Z - \sin(\alpha)\sin(\beta)F_{Z,\alpha}\right] \tag{A.40}$$

$$f_{\beta,r} = -\left(\sin(\alpha)\tan(\theta) + \cos(\alpha)\right) \tag{A.41}$$

$$f_{\beta,\delta_z} = \left(\frac{1}{mV}\right)\bar{q}S\sin(\alpha)\sin(\beta)C_{N\delta} \tag{A.42}$$

$$f_{\beta,\delta_y} = \left(\frac{1}{mV}\right)\bar{q}S\cos(\beta)C_{Y\delta} \tag{A.43}$$

$$f_{r,\alpha} = \frac{1}{I_{yy}}\bar{q}Sd\left(\frac{p_A d}{V}\right)C_{np,\alpha} \tag{A.44}$$

$$f_{r,q} = \left(\frac{I_{xx,a}}{I_{yy}}\right)p_A + r\tan(\theta) \tag{A.45}$$

$$f_{r,\beta} = \frac{1}{I_{yy}}\left[\bar{q}SdC_{n0,\beta} + \bar{q}Sd\left(\frac{p_A d}{V}\right)C_{nP,\beta}\right] \tag{A.46}$$

$$f_{r,r} = q\tan(\theta) + \left(\frac{1}{I_{yy}}\right)\bar{q}Sd\left(\frac{d}{V}\right)C_{nr} \tag{A.47}$$

$$f_{r,\delta_z} = 0 \tag{A.48}$$

$$f_{r,\delta_y} = \left(\frac{1}{I_{yy}}\right)\bar{q}SdC_{n\delta} \tag{A.49}$$

$$f_{a_z,\alpha} = \left(\frac{1}{mg}\right)\left[-\bar{q}SC_{N0,\alpha} - \bar{q}S\left(\frac{p_A d}{V}\right)C_{Np,\alpha}\right] - \left(\frac{x^s}{g}\right)f_{q,\alpha} \tag{A.50}$$

$$f_{a_z,q} = -\left(\frac{x^s}{g}\right)f_{q,q} \tag{A.51}$$

$$f_{a_z,\beta} = -\left(\frac{1}{mg}\right)\bar{q}S\left(\frac{p_A d}{V}\right)C_{Np,\beta} - \left(\frac{x^s}{g}\right)f_{q,\beta} \tag{A.52}$$

$$f_{a_z,r} = \left(\frac{x^s}{g}\right)(p_F - fq,r) \tag{A.53}$$

$$f_{a_z,\delta_z} = -\left(\frac{1}{mg}\right)\bar{q}SC_{N\delta} - \left(\frac{x^s}{g}\right)f_{q,\delta_z} \tag{A.54}$$

$$f_{a_z,\delta_y} = 0 \tag{A.55}$$

$$f_{a_y,\alpha} = \left(\frac{1}{mg}\right)\bar{q}S\left(\frac{p_A d}{V}\right)C_{Yp,\alpha} + \left(\frac{x^s}{g}\right)f_{r,\alpha} \tag{A.56}$$

$$f_{a_y,q} = \left(\frac{x^s}{g}\right)(p_F + fr,q) \tag{A.57}$$

$$f_{a_y,\beta} = \left(\frac{1}{mg}\right)\left[\bar{q}SC_{Y0,\beta} + \bar{q}S\left(\frac{p_A d}{V}\right)C_{Yp,\beta}\right] + \left(\frac{x^s}{g}\right)f_{r,\beta} \tag{A.58}$$

$$f_{a_y,r} = \left(\frac{x^s}{g}\right)f_{r,r} \tag{A.59}$$

$$f_{a_y,\delta_z} = 0 \tag{A.60}$$

$$f_{a_y,\delta_y} = \left(\frac{1}{mg}\right)\bar{q}SC_{N\delta} + \left(\frac{x^s}{g}\right)f_{r,\delta_y} \tag{A.61}$$

A.4 AI Agent training parameters

This section contains list the auxiliary information for any of the AI material in the project.

DQN

Table A.1 shows values of the parameters used during the training of the DQN agent.

Training parameters	
Maximum Episodes	200,000
Max Steps per Episode	1000
Episode termination	$t > 100$ or $d > 12$
Reward value to terminate	20,000
Observations	$[d, \dot{d}, \psi]$
Actions	$\omega = \omega_0$ or ω_B
Neural Network configuration	
Discount factor γ	0.99
MiniBatchSize	256
ExperienceBufferLength	10^5
TargetUpdateFrequency	4
Episode Initial conditions	
ω_0	2π
ω_B	$\pi/2$
x_0, y_0	$(2,2)$
u_0, v_0	$(0,0)$
ϕ_0	0
xT_0, yT_0	$(0,0)$
uT_0, vT_0	$(0,0)$

TABLE A.1 Full parameters for DQN implementation

Figure A.4.1 shows the reward progression for the first 5×10^3 episodes of the 2×10^5 training set. It is visible that the agent does make significant learning progress compared to no improvement at all.

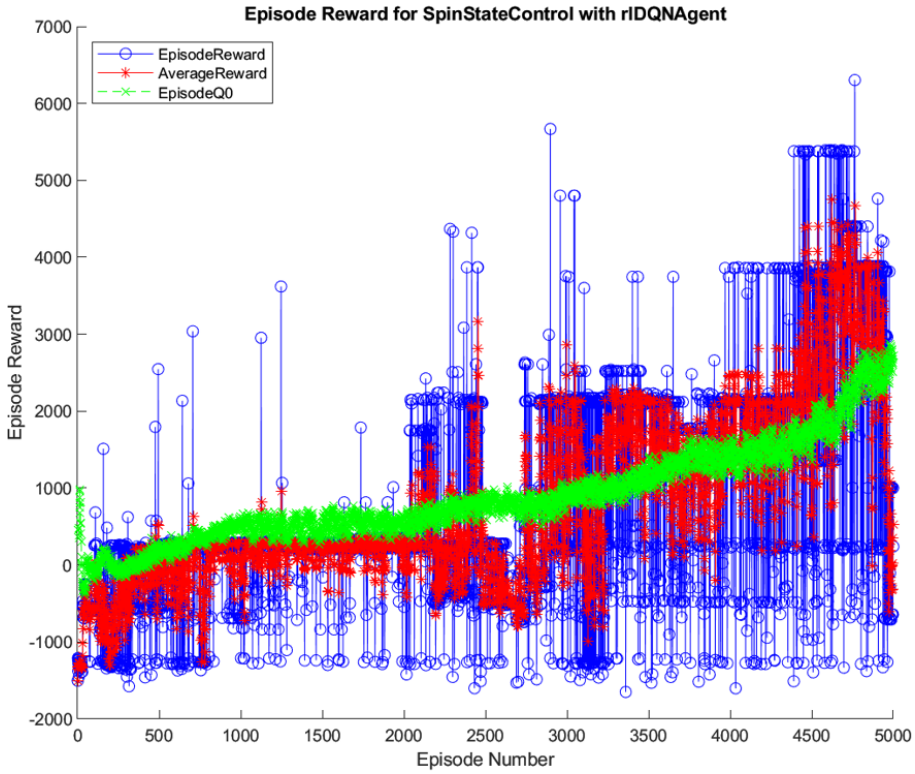

FIGURE A.4.1 Reward data for the first 5000 episodes of DQN agent training

Figures A.4.2 and A.4.3 shows the performance of the DQN agent at different stages of the training procedure. While the training process is conducted using randomised positions and orientations, for a fair comparison both of these figures utilise fixed projectile and target parameters at the beginning of the simulation. It can be seen that the agent does improve in its ability to stay near the target, but still has too large of a steady state error, as well as a divergence at the end of the simulation.

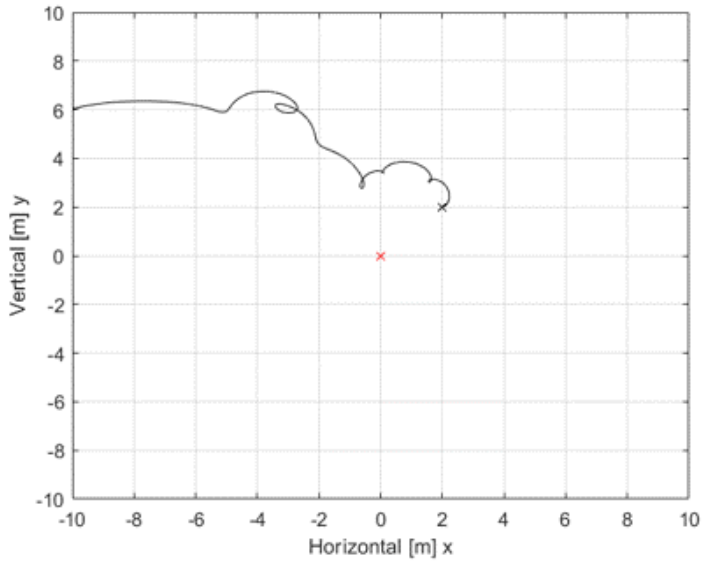

FIGURE A.4.2 Performance of DQN agent after 10^4 episodes

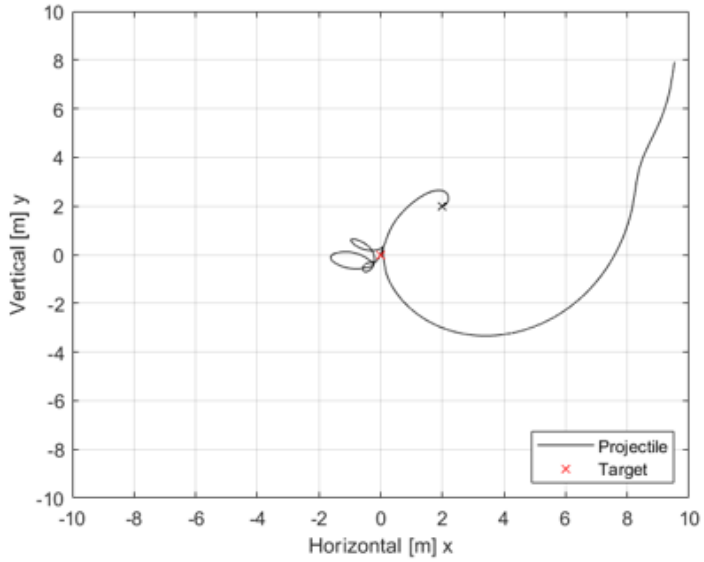

FIGURE A.4.3 Performance of DQN agent after 2×10^5 episodes

DDPG

Table A.2 shows values of the parameters used during the training of the DDPG agent.

Training parameters	
Maximum Episodes	200,000
Max Steps per Episode	1000
Episode termination	$t > 50$ or $x > 50$
Reward value to terminate	20,000
Observations	x and $\dot{x} = u_x$ both $\in [-\infty, \infty]$
Actions	$a_x \in [-\tilde{a}_{max}, \tilde{a}_{max}]$
Neural Network configuration	
Discount factor γ	0.99
MiniBatchSize	256
ExperienceBufferLength	10^5
TargetUpdateFrequency	4
Episode Initial conditions	
x_0	$[-10, 10]$
u_0	$[-10, 10]$
xT_0	$[-10, 10]$
uT_0	$[-10, 10]$

TABLE A.2 Full parameters for single channel DDPG implementation

Appendix B

Geometry modelling in PRODAS and Ballistic stability analysis

In this appendix, a cursory procedure is shown as to how the design of a small calibre-direct fire projectile can be tested for ballistic stability along the flight trajectory. being ballistically stable across the range of velocities present in the flight envelope ensure that a projectile will remain on a predictable trajectory even in the event a mounted control system fails; this assumes that the failure state (*e.g.* seized deflection angle of canards) can be captured and also ensured by the factors. One can calculate the stability factors using the framework discussed in §3.3.4 or use a ballistic package like PRODAS, which is used here.

B.1 PRODAS modelling

This section shall detail the methods for constructing and then analysing a model using PRODAS. Since flight stability is largely dependent on a higher projectile weight, one should remove the relatively less dense steel to maximise available volume for guidance hardware. As such, the primary aim of this model is to remove or drastically reduce the weight of the steel penetrator and observe the change in stability. Other aspects of the bullet geometry will then be changed. The projectile stability of these changes will be measured, to determine whether it is feasible to install guidance systems on the selected range of calibres.

A model in PRODAS is called an 'assembly'. To construct it, one adds various 'components' which in turn contain 'elements'. The components are the fundamental constituents of the the projectile: the lead core, steel penetrator and protective jacket. The elements within these are rudimentary shapes which are superimposed in order to give the component dimensions. They are rotationally symmetric by default though this can be changed for structures such as fins. Figure B.1.1 shows the finished design of a 5.56x45mm ball projectile, both the view from PRODAS (B.1.1A) and a coloured version (B.1.1B) to represent how the design is interpreted by the computer. In figure B.1.1B we see the full metal

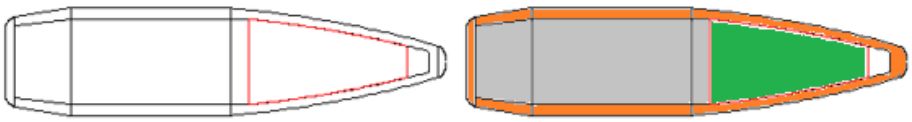

(A) Raw design as seen in PRODAS (B) Coloured to represent computer interpretation

FIGURE B.1.1 Design of 5.56mm Ball projectile constructed in PRODAS

jacket in orange, the lead core in grey, the steel tip (to be modified) in green and an air cavity at the front of the ogive in white. This air cavity is a remnant of the manufacturing process after the steel tip is set inside the jacket. When constructing a component, the metal jacket for example, elements are constructed from left to right. The user can change the left/right diameters and the curvature of the top/bottom connecting lines. By default, the end (right side) of previous element defines the start (left side) of the next however, this can be changed. This is continued until the perimeter of these elements describes the *exterior* surface geometry of the jacket component. If the component is hollow, this process is then repeated, but the perimeter of the next string of elements should describe the *interior* surface geometry. The property type `Void` is set to `Yes` which tells the interpreter that this region is empty space. Note while the bullet is in itself, not hollow, the jacket alone can be considered as a hollow shell which is what we are representing; the final model raster will superimpose all the components and evaluate the projectile as a whole.

Figure B.1.2 shows the model with penetrator material set as steel (note the characteristic density of 7.87 g/cm^3) and a brief glimpse of the `Assembly->Component->Element` hierarchy. Once the desired values have been entered we initiate the `Calc Mass` command, which determines the centres of mass & pressure and the transverse & longitudinal

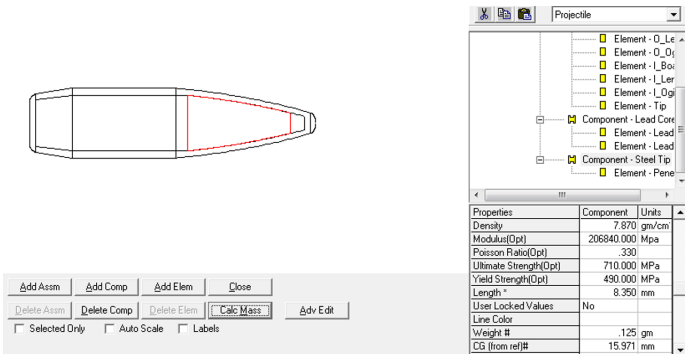

FIGURE B.1.2 Design of 5.56mm Ball projectile constructed in PRODAS

axial moments of inertia, results shown in figure B.1.3. PRODAS uses a semi-empirical method for calculating the aerodynamic coefficients which have been shown to be inferior to CFD based approaches [96]. For the demonstration purposes used here, the methods are sufficient to demonstrate proceedings. These results are then used in the aerodynamic

{LANDSCAPE}

Custom.pr3 - 0
10/30/2017 14:31
Mass2000 Version 3.5.1

	Mass	Transverse Inertia	Axial Inertia	CG from Nose	Diameter
	gm	gm-cm^2	gm-cm^2	mm	mm
Total Projectile:					
Baseline	3.971102	1.286672	0.1425144	14.05266	
Calculated	3.971102	1.286672	0.1425144	14.05266	
Launch Vehicle:					
Baseline	3.971102	1.286672	0.1425144	14.05266	
Calculated	3.971102	1.286672	0.1425144	14.05266	
Flight Vehicle:					
Baseline	3.971102	1.286672	0.1425144	14.05266	5.660000
Calculated	3.971102	1.286672	0.1425144	14.05266	5.660000

Calculated Aerodynamic Features of the Flight Vehicle (calculated values are used unless locked)

FIGURE B.1.3 Results of Calc Mass analysis

analysis to determine the drag coefficient C_D as a function of Mach number, figure B.1.4. A combination of the mass and aerodynamic analysis can be viewed pictorially as in figure B.1.5. All of this data can be combined to produce a graph gyroscopic stability factor S_g against Mach number, shown in figure B.1.6. Note that the C_D data will not change between substitution of the penetrator materials, since C_D is based solely on the surface geometry of the projectile. In order to change the material type of a component, one need only select the component followed by the `Retrieve Data` function of the built-in material library. Since in practice the volume will not be empty space, a generic miscellaneous plastic with reference density of 1.66 g/cm^3 is used, slightly less dense than the plastic composite used in circuit boards.

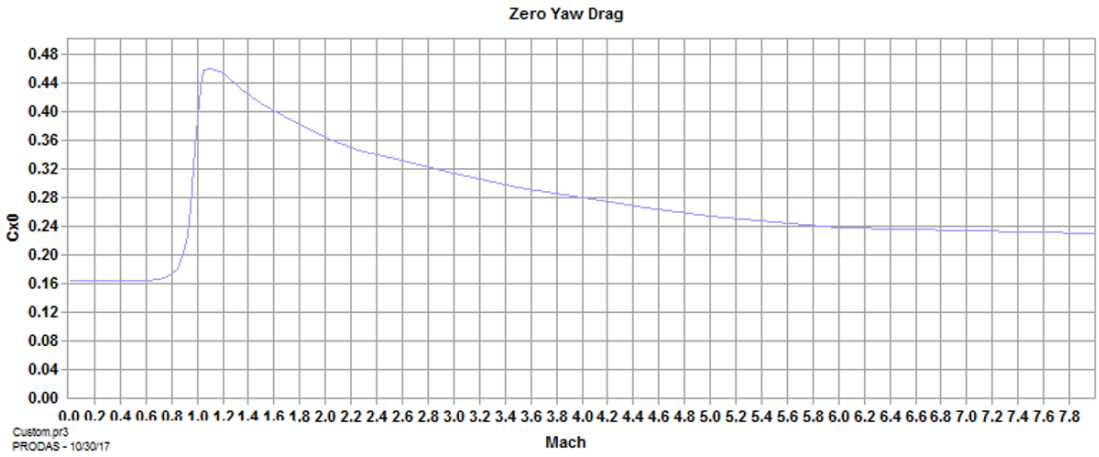

FIGURE B.1.4 Zero yaw drag as a functions of Mach number

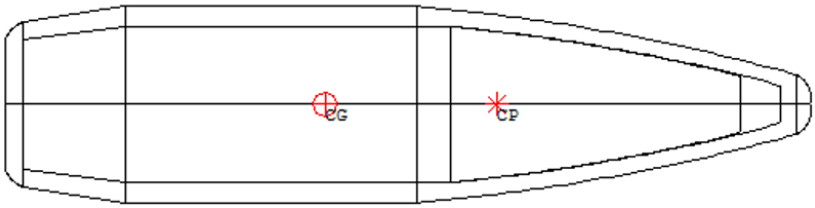

Muzzle Velocity	903.0 m/sec	Aircraft Velocity	0.0 m/sec
Air Density	1.22500 kg/m^3	Air Temperature	15.0 C
Muzzle Spin Rate	7725. CPS	Muzzle Exit Twist	21.0 cal/rev
CP from Nose	9.09 mm	CP from Nose	1.61 Calibers
CG from Nose	14.05 mm	CG from Nose	2.48 Calibers
Mach Number	2.65	Gyro Stab Factor	5.17
Ballistic Coeff.	0.285	Cd at Muzzle	0.329
Deceleration	1154.59 m/s/1000m	Muzzle Jump Factor	0.006 mils/rad/sec

FIGURE B.1.5 Pictorial representation of Calc Mass

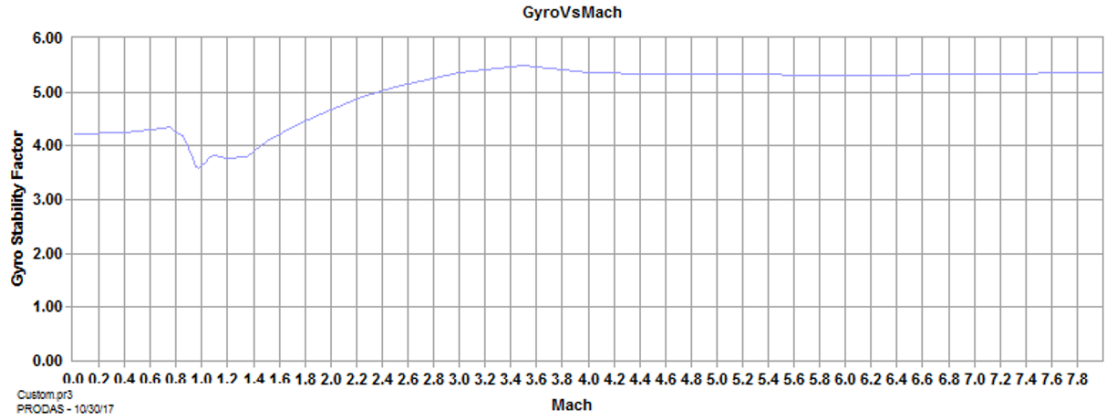

FIGURE B.1.6 Gyroscopic stabilisation coefficient as a function of Mach number

B.2 Parametric investigation of projectile geometry affecting ballistic stability factors

This section briefly investigates how the parameters of projectile geometry affect the ballistic stability. While a more detailed optimisation and approach would need to be considered for any serious designs, this informs the reader of the effect of extreme modifications to major parameters including: penetrator density, ogive radius, meplat (tip) diameter, body length and boattail angle.

B.2.1 Calibre Comparison

Figure B.2.1A shows the design of the 7.62mm L51A1 projectile, note that it has a proportionately larger penetrator size in comparison to the 5.56mm. Great care was taken to reproduce the curvature of the jacket near the boattail, though the displacement of lead immediately inside caused by this was not replicated. This discrepancy caused a total projectile mass of 10.4g, a 4% increase compared to the actual stated mass of 10.0±0.1g. The mass imperfection is likely not solely caused by this however, as the curvature profile of the jacket at the ogive is difficult to perfectly replicate and some thickness deviations are almost certainly prevalent. Figure B.2.1B shows the 12.7x99mm NATO design, with even larger steel penetrator size, this time located towards the aft of the projectile with the lead load in the ogive. For both 5.56mm and 7.62mm, the penetrator material is changed

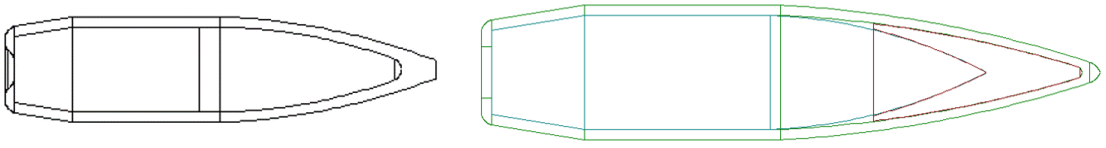

(A) 7.62mm L51A1 (B) 12.7x99mm NATO

FIGURE B.2.1 PRODAS geometry of the 7.62mm L51A1 and 12.7mm NATO projectile projectiles

and all of the analysis steps above are re-run to generate new values. 12.7mm is omitted since we are trying to implement guidance systems in the smallest feasible calibre.

The data is extracted and imported into MATLAB as previously mentioned. Figure B.2.2 show a comparison of S_g for the two calibres with different penetrator materials.

Here we can see that at higher Mach levels the heavier steel core provides better gyroscopic

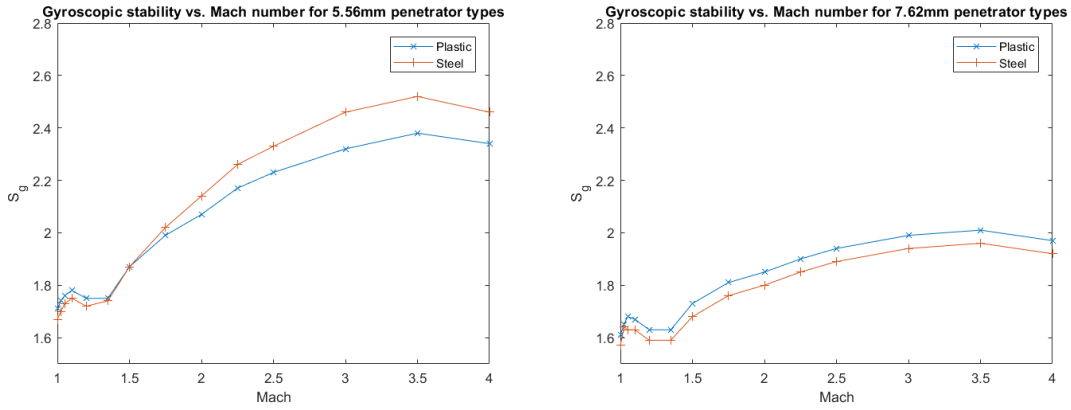

(A) 5.56x45mm (B) 7.62x51mm

FIGURE B.2.2 S_g against Mach number for different penetrator materials

stability, which is to be expected due to the higher moments of inertia. Interestingly at lower levels, the 5.56mm plastic penetrator has a higher S_g. This is likely due to the very low weight of the projectile. Though unlikely it could also be an artefact of the model design. The steel penetrator of the 7.62mm provides a higher S_g than plastic at every calculated Mach number. This is likely due to the increase in mass of this round compared to the 5.56mm, thus we should see even more consistent S_g increases at projectiles with even more mass. Even at this stage of analysis, we can see that using a larger calibre is going to be advantageous, due to the additional weight stabilization and the volume available to accommodate guidance components.

Now we will extract the dynamic stability coefficient S_D data, which will illustrate how stable the projectiles are. The condition for dynamic stability is

$$S_g > \frac{1}{S_D(2 - S_D)} \tag{B.1}$$

The Textbook of Ballistics and Gunnery [94] gives an excellent treatment of this. Figure B.2.3A shows a comparison of all 3 standard calibres while figure B.2.3B shows the stability diagram for both 5.56mm & 7.62mm calibres with both penetrator types. A projectile is dynamically stable if it satisfies equation B.1 i.e. it lies above the parabola. Each line is a data set of S_g vs S_D coordinates for increasing Mach numbers. Mach numbers range from 1 to 4, with Mach 1 being the left most data point of each line; this is logical

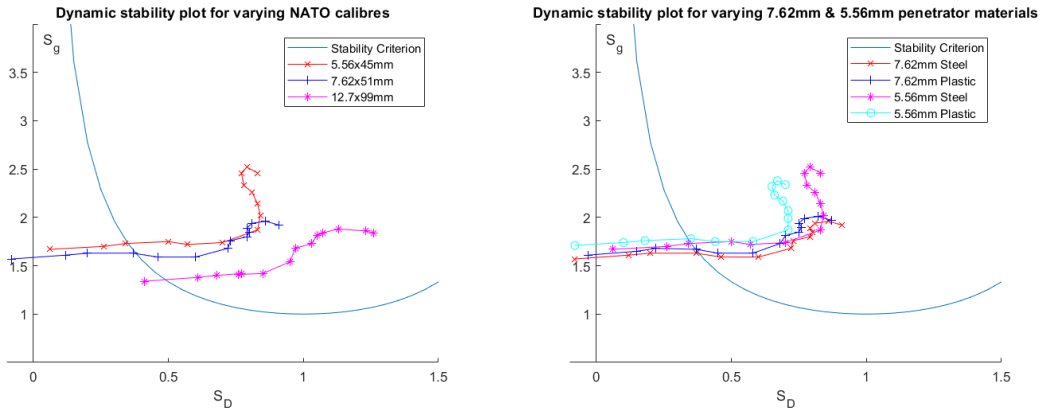

(A) Calibre comparison (B) 5.56mm & 7.62mm calibres with plastic and steel penetrators

FIGURE B.2.3 Dynamic stability plots with the criteria for dynamic stability

since S_D correlates highly with projectile velocity. In figure B.2.3A, we can see that the smaller calibres have a lower S_d but a much higher S_g in general over all speeds. This is due to the much higher spin speed and lower mass. Figure B.2.3B shows, as expected, that a reduction of mass, moving the CoM towards the aft, causes a reduction in S_d with a small reduction in S_g. Since the reduction in mass was similar for both calibres, the effect is more apparent for the lighter 5.56mm calibre.

B.2.2 Surface geometry

Let us, before adding any canards, confirm how modification of the existing surface geometry will alter the drag and stability characteristics.

Ogive Radius

There are three classifications of ogive curvature: tangent, secant and hybrid, which are shown in figure B.2.4. This section describes modification of a tangent ogive, which is the default configuration for the selected model bullet. The ogive properties define how much of the body surface is normal to the flow field (assuming no yaw) and this is where the biggest difference will be made. Figure B.2.5A shows varying ogive curvatures, keeping projectile & ogive length the same. No parameters have been held fixed during these alterations, as such the weight is free to fluctuate as material is added/lost. This is of no concern unless otherwise stated as we are looking at C_D. As would be expected, there is

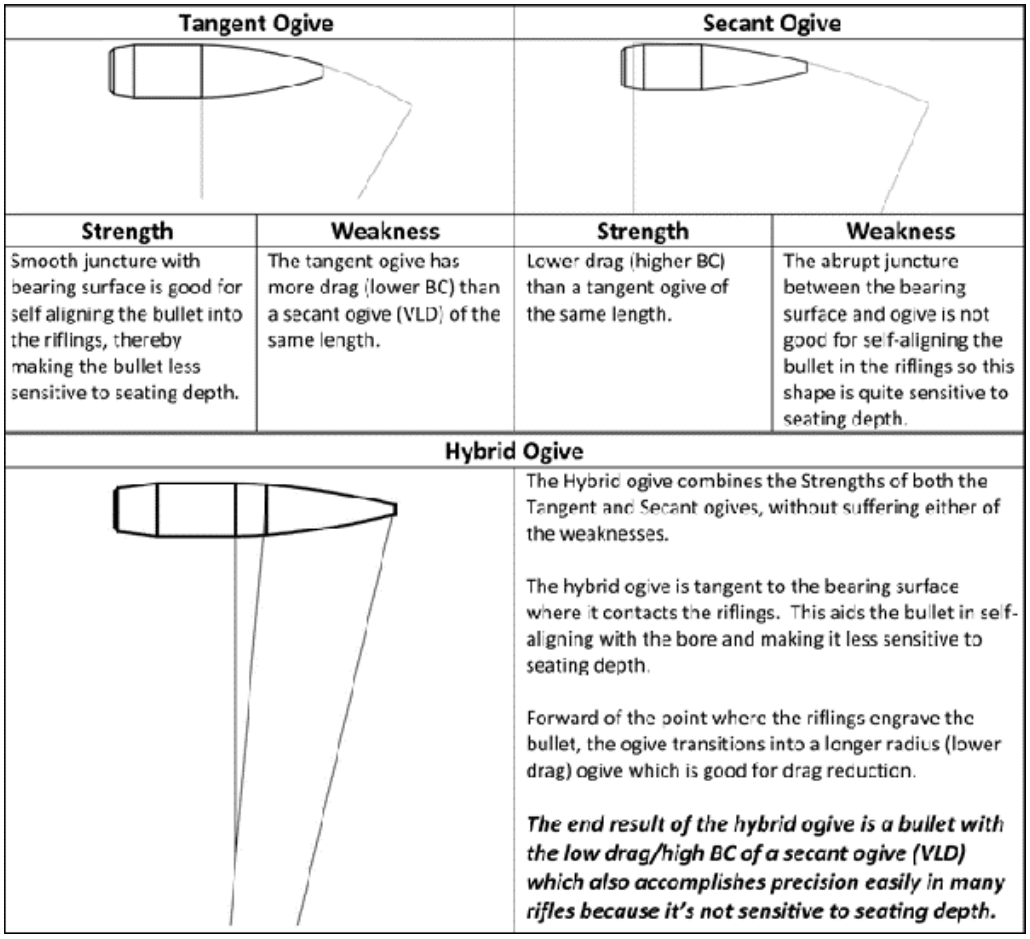

FIGURE B.2.4 Different Ogive profiles [213]

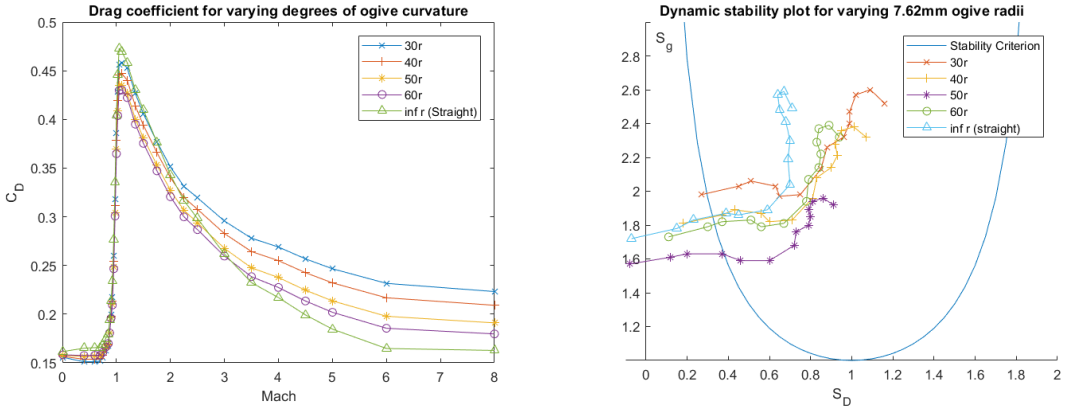

(A) Drag coefficient against ogive curvature (B) Plastic penetrator

FIGURE B.2.5 Dynamic stability plots for various body lengths and penetrator materials

a correlation between a lower ogive radius and a lower C_D. This is because there is less surface area normal to the fluid flow able to produce drag. The exception to this is the zero-curvature ogive, which produces a much higher C_D immediately after Mach 1 which

then provides the lowest C_D after Mach 4. This is due to the sharp angle of the ogive joining the main body causing an oblique shock wave at lower Mach numbers.

Tip Diameter

Next, the tip diameter of the projectile can be varied, again keeping all other parameters the same, which is shown in figure B.2.6A. Here again we see what is expected, a correlation

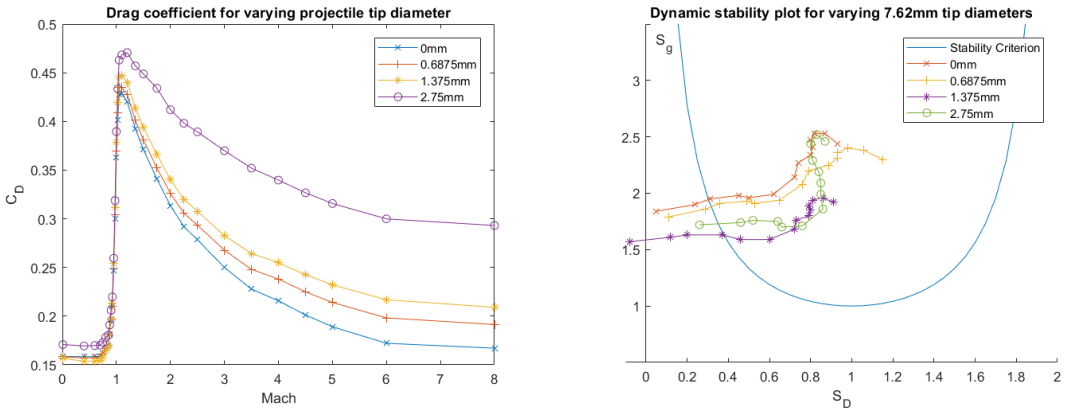

(A) Drag coefficient against projectile tip diameter

(B) Plastic penetrator

FIGURE B.2.6 Dynamic stability plots for various body lengths and penetrator materials

between a lower tip diameter and a lower C_D, again due to a lower normal surface area.

Body Length

Now we can change the projectile body, such that the ogive and boattail lengths remain the same. Varying the projectile length will have two major impacts on drag and dynamic stability. Firstly, a longer projectile means there is additional mass to improve gyroscopic stability. Secondly, the distance between the CoM and CoP is increased, meaning the overturning moment will be higher and dynamic stability will be reduced. The initial body length is 11mm. For the following comparisons this length is increased and reduced by $\approx 36\%$ (4mm), giving lengths of 7mm and 15mm respectively. These lengths are arbitrary but have sufficient differences to show any correlations. Figure B.2.7A shows a comparison of C_D for the three body lengths. There is a direct correlation between a shorter projectile length and a lower C_D. However, for the 36% change in body length there is a minuscule change in C_D, especially compared to the ogive changes made above.

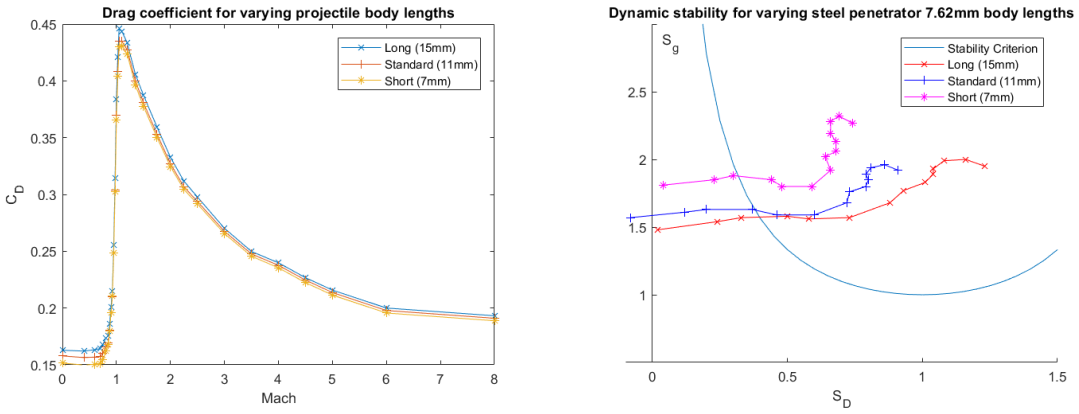

(A) Drag coefficient against projectile length (B) Plastic penetrator

FIGURE B.2.7 Dynamic stability plots for various body lengths and penetrator materials

Figure B.2.7 show drag coefficients and the dynamic stability plots for the different body lengths.

Boattail

The boattail, though located at the rear of the projectile, still contributes a very large amount to the drag forces acting on a projectile. When flow separates at the front of the projectile it must then re-join at the aft section. If the flow re-joins too quickly, this can create relatively low pressure turbulent flow, which imparts a very large pressure drag on the projectile. The projectile must be shaped like a wing aerofoil to ensure the flow is reunited with minimum disturbance. This is what the boattail design achieves, by gradually bringing the separated flow back together.

Figure B.2.8A and B.2.8B show the drag coefficient and dynamic stability plots respectively, for different angles of boattails. Only 3 variations were used, though this is sufficient to observe the effects of positive boattail curvature, *i.e.* curving inwards towards the back of the bullet as opposed to flaring outwards: No angle, standard angle and double angle. Here we can see the slightly counter intuitive effect, that while a larger boattail angle improves the drag performance to a degree it actively hinders the stability of the projectile.

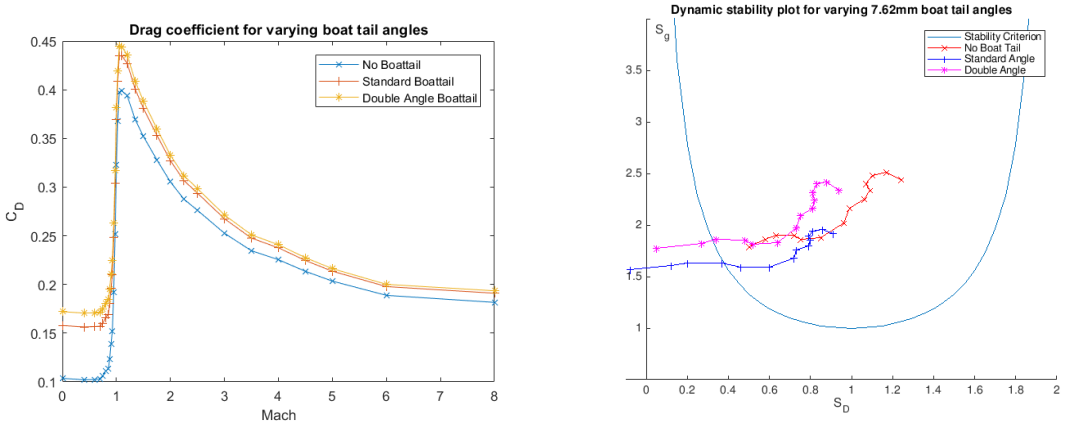

(A) Drag coefficient (B) Dynamic Stability

FIGURE B.2.8 Aerodynamic characteristics against boattail angle

Geometry Summary

Modern Exterior Ballistics by McCoy [93] is a very comprehensive review of the subject and is used here for validation of findings. In addition to what was explored here, McCoy also details the results of varying ogive length. He notes that by varying ogive length from 1.5cal to 3.5cal in 0.5cal increments at Mach 1.8, "short nose lengths dramatically increase the drag at this speed". The effect of ogive radius is then described however, the parametrisation is slightly different. McCoy characterises the radius with the 'headshape' parameter R_T/R, where R is the arc radius responsible for the ogive curvature (as used in this report) and R_T is the radius of the necessary tangent ogive (§B.2.2) for the given nose length. A tangent ogive has $R_T = R$ and a headshape parameter of 1, while a conical ogive has a headshape parameter $R_T/\infty = 0$. As such this parameter can characterise all permutations of tangent/secant ogive shapes by plotting a ratio range between 0 and 1. Figure B.2.9 shows the data presented by McCoy. Comparing this to B.2.5A we can see both graphs show characteristic improvement of the $R_T/R = 0$ straight ogive at lower Mach levels. At least in this instance of ogive curvature, this data supports that produced by PRODAS.

Next the change in tip diameter, or the blunting of a sharp nose to produce a 'meplat'. It is noted that a meplat less than 0.1cal is insignificant, though, just above Mach 1, a meplat between 0.10cal and 0.15cal is generally advantageous, providing a lower drag coefficient than can be expected from a sharp nose projectile. While this cannot be directly seen

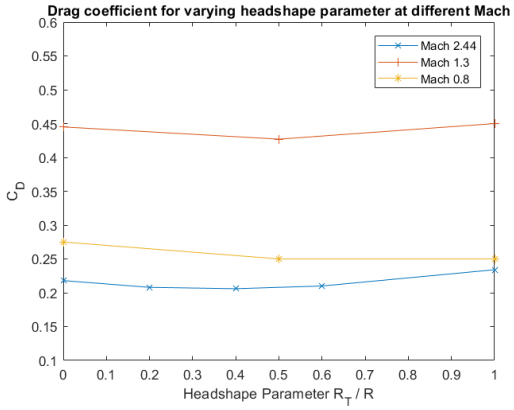

FIGURE B.2.9 Drag performance of various ogive curvatures

from figure B.2.6A its presence is apparent, since the order of the lowest 3 tip diameters changes either side of the Mach 1 transition peak; again, the two are in agreement.

Boattail length is a highly discussed topic, with many more factors taken into account than are discussed in this report. In summary the longer a boattail is, the lower the associated C_D, although this will make the projectile dynamically unstable very quickly. Ideally, a boattail should be between 0.5cal and 1cal. A boattail angle of approximately 7 degrees provides the lowest C_D for all lengths, C_D increases with any deviation from this low point. Figure B.2.8A shows only two boattail angles and neither accurately represent what would be expected from the deviation, this is worthy of further exploration at a later date.

Data validation was conducted simply, by comparing the results with those produced by the manufactures (BAE Systems) engineering department. Figure A.1.2 shows the results. It was found in all analysed cases of modifying bullet geometry, that S_g was a factor of 2 higher in the results presented here than it has been found to be experimentally; $S_g \approx 4$ compared to the experimental $S_g \approx 2$. Upon closer inspection of the equations used to generate this data, the discrepancy was found to be caused by an inaccurate twist rate in the rifling profile used in the initial conditions. As a guideline the 7.62x51mm NATO calibre, a projectile should have one full revolution imparted on it per travel distance of 30 calibres. That is, a rifling profile of approximately 30cal/rev should have been used, not the default 20cal/rev. This mistake was caused by assuming the parameters initialised by PRODAS were representative of our baseline conditions. Upon correcting this value S_D analysis was conducted again using the new rifling profile and all the figures included

within this report show this updated data.

B.3 Conclusions

In general, geometry modifications which reduce drag also lower the static stability. The main result of increasing the ogive radius is that there is less material and thus less mass in the ogive; this shifts the CoM backwards. In addition, the surface geometry change makes the projectile more aerodynamic and thus reduces the drag. Together this means that as the ogive radius increases, S_D decreases and at first, S_g also decreases. As the mass and thus inertia increase sufficiently with the radii, this will dominate the increase in drag which results in S_g increasing again. S_g thus has an inflection point with a minimum. Similar to the ogive radius, as the tip diameter increases there is more mass in the ogive which results in a forward shifted CoM, as well as leading to a higher drag. An increasing tip diameter causes S_g to increase, while S_D increases at first but then decreases. Increasing the projectile length greatly increases the mass and also the moments of inertia, while having a minimal effect on the drag, since neither the forward or rear cross sections change with respect to the free stream velocity. The result is a direct correlation; increasing the projectile body length decreases S_g but increases S_D. Finally, as the boattail angle increases, there is less mass in the aft section and the CoM will shift forwards. In addition, the drag will increase slightly, and a sharper (higher) boattail angle will result in vortex shedding. Increasing the boattail angle causes S_D to decrease linearly, while S_g will increase at first due to the inertia increase, but then begins to decrease as the CoP moves forward with respect to the CoM.

Geometric change	Main implications	S_g Action	S_D Action
Ogive Radii increase	- Less mass in ogive - CoM shifted backwards - Less drag	Inflection w/ *minima*	Decreases
Tip diameter increase	- More mass in ogive - CoM shifted forwards - More drag	Decreases	Inflection w/ *maxima*
Projectile body length increase	- More mass - Longer projectile - Larger distance between CoM & CoP	Decreases	Increases
Boattail angle increase	-Less mass -CoM shifted forwards	Inflection w/ *maxima*	Decreases

TABLE B.1 Summary of parametric investigations on the effect of projectile geometry on ballistic stability

B.4 Example analysis of Tungsten Tipped 7.62x51mm NATO using ballistic stability framework

This section briefly shows how the ballistic stability framework and the associated factors S_g and S_D can be used to guide the design of novel ammunition. While further refinement of the design must always be undertaken, for example optimising ogive profiles and boattail angles to minimise drag, this process guarantees at least satisfactory and repeatable firings. Traditional guidance system in projectiles, even in the relatively more technologically advanced dual-spin projectiles, contain all of the control and guidance hardware on the ogive. From the discussion on projectile stability it was observed that small calibre projectiles are spin stabilised to ensure they remain stable throughout the flight. A key factor to this stability is that the CoM be located as far forward as possible. This however, is in direct contraction to the first point, since the control and guidance hardware is substantially light than the lead traditionally found at the front of small calibre projectiles.

A proposed solution is suggested here, and evaluated using the stability framework as

a guide, is to utilize a much harder and more dense material for the ogive. Figure B.4.1A shows the US Army's M855A1 5.56x45mm cartridge. It features an exposed steel core in the ogive which the Guilding metal wraps around, as well as a non-toxic bismuth-tin alloy core. Guilding metal is a brass (copper alloy) comprised of 95% Copper and 5% Zinc. In military applications Guilding metal comprises the full metal jacket of most ball ammunition, the driving band of artillery shells as well as the jacket of some of the shells themselves. It can be annealed between 427-788°C. Here we propose the use of the even harder and more dense Tungsten as a tip, shown in figure B.4.1B. More dense materials have already been used in some ammunition, such as depleted Uranium, but that is not considered here due to the ethical and health issues surrounding its usage. The Guilding

(A) US Army M855A1 5.56x45mm cartridge

(B) Dynamic stability

FIGURE B.4.1 Design of a custom Tungsten tipped 7.62mm projectile

metal jacket is cut a certain degree along the ogive in order to accommodate the Tungsten. Tungsten is strong enough to withstand the launch and so there is no need to cover the tip with the jacket. The tip is then hollowed to create room for the guidance system, but still extends a small way under the jacket to allow the two surfaces to be crimped together. A portion of the lead core can then be removed to create even more space. Additionally, the lead could be substituted for a different material which would also adhere to new 'green' policies.

Figure B.4.2A shows C_D analysis and figure B.4.2B shows S_D analysis. Since there is no change in the geometry of the projectile, there is no significant change in the drag profile. Above Mach 4 there is a slight increase which is likely due to the joining of

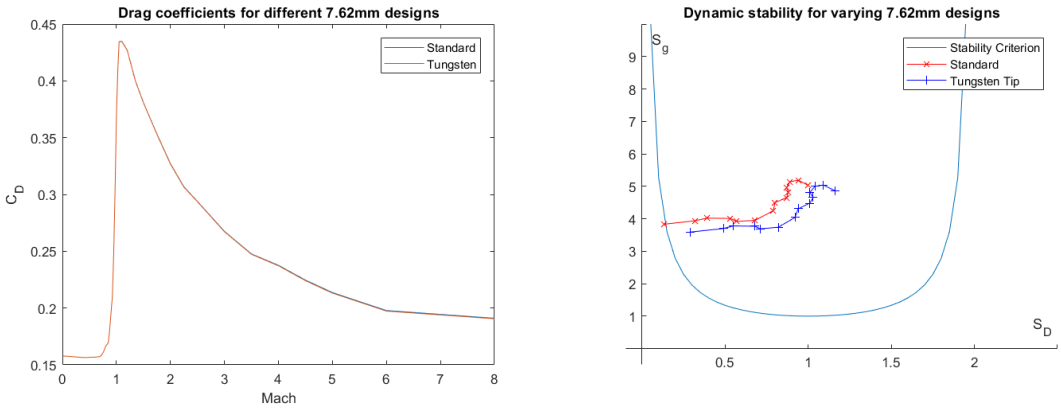

(A) Drag coefficients (B) Dynamic stability

FIGURE B.4.2 Characteristics of Tungsten design against standard 7.62mm

the two jacket materials. The dynamic stability is improved across all Mach numbers. This is a novel idea that maybe worth consideration in the future, at present however the manufacturing techniques are not refined enough to produce titanium parts of the desired thickness. Additionally, it would be infeasible to put exposed titanium rounds into production due to the direct damage to the barrel during launch.

Appendix C

Academic Publications

Review of Dual-spin projectile stability

This manuscript is a review of the stability factor frameworks used to describe different configurations of projectile. It also reviews any auxiliary material pertaining to projectile stability which doesn't necessarily consider the stability factors. At the time of writing, this paper has been published in Defence Technology journal [40].

Technical Note: Stability analysis of a dual-spin 155mm artillery projectile

This note shows a methodology for evaluating the stability of projectiles across a flight envelope. Instead of evaluating the stability at discrete trim points offline, this paper continuously evaluates the stability factors online as a method of determining the control inputs necessary to re-establish stability. At the time of writing, this paper has been submitted to the Defence Technology journal.

A novel quasi-dynamic guidance law for a dynamic dual-spin projectile with non-conventional, asymmetric roll constraints

This paper describes the novel actuation mechanism and accompanying ZEM based GL enclosed in the paper. It shows how the GLs can be used to successfully control the mechanism in a nominal comparison with traditional GLs, similar to the analysis conducted in chapter 6. At the time of writing, this paper has been submitted to the Proceedings of the iMeche, Part G: Journal of Aerospace Engineering.

Defence Technology 16 (2020) 1–9

Contents lists available at ScienceDirect

Defence Technology

journal homepage: www.keaipublishing.com/en/journals/defence-technology

A review of dual-spin projectile stability

James Norris [a, *], Amer Hameed [a], John Economou [a], Simon Parker [b]

[a] Centre for Defence Engineering, Cranfield University, Defence Academy of the United Kingdom, Shrivenham, SN6 8LA United Kingdom
[b] BAE Systems, United Kingdom

ARTICLE INFO

Article history:
Received 13 March 2019
Received in revised form
16 May 2019
Accepted 5 June 2019
Available online 6 June 2019

Keywords:
Guided projectiles
Dual-spin
Gyroscopic
Dynamic
Stability
Canards

ABSTRACT

This paper gives a succinct review of dual-spinprojectile stability and some technologies relating to them. It describes how the traditional stability factors from linear projectile theory are modified to better describe a controlled dual-spin projectile. Finally, it reviews works which have investigated how different aspects of a controlled dual-spin design can affect flight stability, primarily airframe structure and canard properties. A conclusion is given, highlighting important guidelines from the enclosed discussions.

1. Introduction

Generic airframe stability has three distinct forms: static, dynamic and gyroscopic, quantified by the stability factors S_S, S_d & S_g respectively. At a specific instance, a projectile is 'stable' in one of these ways if the associated stability factor fulfils its respective inequality. If a body is statically stable then, under the influence of a small disturbing force, the body will act towards its original alignment. If a body is dynamically stable, the disturbance induces an oscillatory motion, which will damp until the body attains its initial alignment. Gyroscopic stability is the resistance of a rotating body to changing its axis of rotation. Stability factors are advantageous for projectile designers, as they allow a good estimate of ballistic stability without having to analyse a large flight envelope with numerical analysis, which can be time consuming and resource intensive.

Projectiles are spun to mitigate aerodynamic disturbances which may detrimentally affect the flight of the projectile. Guided projectiles are far more effective, albeit more expensive per unit, at achieving a desired effect on target; however they are primarily designed to be non-spinning. A Dual-spin projectile design is one possible solution to imparting the benefits of controlled flight onto spin-stabilised projectiles. This paper consolidates the major works to date, which describe the stability factors for single spin (un) guided and dual-spin (un)guided projectiles. Additional literature describing any aspect of dual-spin flight stability is enclosed and discussed. Any meaningful conclusions about projectile design which can be drawn from the enclosed analysis or discussions are listed.

Section 2 presents the origin and justification for the use of dual-spin projectiles, some useful technologies and novel guidance methods for generic guided projectiles. Section 3 provides a brief origin of the static, dynamic and gyroscopic stability factors from linear projectile theory, followed by a review of the major works to date which have built upon these factors to account for the addition of control surfaces, a dual-spin design and a combination of both. Section 4 gives a review of works which have investigated how stability can be analysed from other perspectives, as well as how it is affected by both projectile and control mechanism parameters. Section 5 gives a summary of the paper and important elements of the enclosed discussions.

2. Dual-spin projectiles and related technologies

This section explains why spin stabilisation is useful for projectiles along with some of the problems which can arise after implementing it. Guided projectiles are introduced along with the

* Corresponding author.
E-mail address: james.norris@cranfield.ac.uk (J. Norris).
Peer review under responsibility of China Ordnance Society

https://doi.org/10.1016/j.dt.2019.06.003

Nomenclature

$\alpha_{(e)}$	(Trim) Angle of attack
$\beta_{(e)}$	(Trim) Angle of sideslip
$C_{D(0)}$	(Zero yaw) Drag coefficient
C_{La}	Lift (slope) coefficient
C_{Lp}	Spin damping moment coefficient
$C_{M\alpha}$	Overturning (Static) moment coefficient
$C_{M\delta}$	Overturning moment coefficient of canards
$C_{MP\alpha}$	Magnus moment coefficient
$C_{Mq} + C_{M\dot{\alpha}}$	Pitch damping moment coefficient
$C_{Na}^{(A,F)}$	Normal force coefficient (of the Aft/Forward section)
$C_{N\delta}$	Normal force coefficient of canards
$C_{NP\alpha}^{(A,F)}$	Magnus force coefficient (of the Aft/Forward section)
d	Projectile reference diameter
δ_c, $\delta_{y,z}$	Canard deflection, in the y/z plane
g	Gravitational constant
$I_x^{(A,F)}$	Axial moment of inertia (of the Aft/Forward section)
$I_y^{(A,F)}$	Transverse moment of inertia (of the Aft/Forward section)
l	Projectile length
$\lambda_{n,p}$	Damping frequency of nutation/precession
$m_{(A,F)}$	Projectile mass (of the Aft/Forward section)
$p_{(A,F)}$	Spin rate (of the Aft/Forward section)
Φ_T	Roll angle of de-spun front section
$R_{(A,F)x}$	Distance between section COM and section COP
$Rm_{(A,F)x}$	Distance between section COM to section Magnus COP
$r_{(A,F)x}$	Distance from composite COM to section COM
ρ	Density of medium
S	Projectile reference area
S_c	Reference area of canards
S_d	Dynamic stability factor
S_g	Gyroscopic stability factor
S_{lim}	Axial spin limit
S_S	Static stability factor
θ_E	Euler pitch angle
θ_T	Trajectory angle subtended by $\vec{V}.\vec{x}_e$
V	Projectile air-relative velocity
V_M	Projectile velocity [Mach]
$\omega_{p,n}$	Frequency of nutation/precession
$\vec{x}$	Longitudinal axis of projectile
x_c	Distance of canard root chord from total COM
ξ	Complex yaw, $\alpha + i\beta$
$()^*$	$() \times \rho Sd/2m$

Abbreviations

SSNC	Single-spin, no control
SSC	Single-spin, with control
DSNC	Dual-spin, no control
DSC	Dual-spin, with control
COM	Centre of Mass
COP	Centre of Pressure
DOF	Degree of freedom

rationale behind the dual-spin configuration. Finally, relevant technology such as MEMS, piezoelectric actuators and novel methods of imparting a control moment are presented.

The projectile, as an effector, has been used in warfare for almost as long as warfare has existed. It has long been known that spinning a projectile improves stability and since Greenhill's formula [1], that there is an optimal spin rate. Too little spin and the projectile will not have the gyroscopic inertia to resist the disturbing force experienced during flight and the precession will be too large. Too much spin and the gyroscopic inertia will resist the aligning aerodynamic forces from the aerodynamic design creating too large an angle of attack; known as super-stability [2]. Ballistic stability, as it is understood today, is defined as the ability of a projectile to maintain its trajectory, ensuring the desired range and designated level of accuracy is achieved. A ballistically unstable projectile will tumble during flight, adversely affecting the aerodynamics and thus the range and accuracy. Hence, spinning a projectile intends to alleviate the inconsistency and inaccuracy caused by these disturbances.

However, there are two notable instances of amplified instability when projectiles are spun. Spin-yaw resonance occurs when the spin rate approaches the yaw rate, the projectile may begin to undergo a large amplitude yawing motion called 'lunar' yawing [2]. Catastrophic yaw occurs when a large yawing motion is amplified by non-linear Magnus effects, which creates further dynamic instability, leading to a cascade effect. Indeed, Magnus force interactions affect a projectile's flight in many ways, Seifert [3] has provided a comprehensive review of the Magnus effect and its implications in aeronautics. In another relevant study [4] CFD simulations were used to predict the aerodynamic coefficients and flow fields for a 25 mm spin-stabilised projectile. The goal being to deduce which parameters are necessary for an accurate computation of the Magnus moment and roll damping moment. While spun projectiles are subject to Magnus forces in flight, these can be reliably accounted for prior to projectile launch [5].

The accuracy demanded by today's weaponry has led to the development of guided weapons, where control and guidance hardware is incorporated directly into the projectile. Guided weapons provide substantial benefits over conventional ammunition, namely reduced collateral damage, improved lethality and effectiveness per unit. Conventional, non-spun, guided munitions are already well established in modern arsenals (e.g. M982 Excalibur [6], M712 Copperhead [7]), primarily using control surfaces such as canards for control. However, the high RPM inherent with spin stabilisation is not conducive to the use of tracking sensors or guidance hardware. A relatively recent solution to this problem is to use a 'dual-spin' configuration, shown in Fig. 1. The aft section of the projectile retains its high spin rate and innate gyroscopic stability while the foreword section, adorned with the guidance and control hardware, has a much lower spin rate. This design allows spun projectiles to be controlled in instances where reducing the spin is

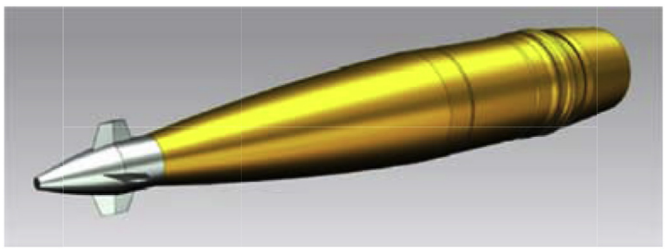

Fig. 1. Depiction of dual-spin projectile (Liang et al. [57]).

detrimental or otherwise undesired, an example of this would be smaller calibres which are more susceptible to aerodynamic disturbances. If stockpiles of unguided, spin-stabilised munitions exist, they can be upgraded by replacing the existing fuse with a course-correcting fuse (CCF) which contains the control and guidance hardware [8].

Restricting the control and guidance hardware to such a small volume is driving the miniaturisation of sub-systems. As a result, technology is being adopted from other fields. Micro-electromechanical Systems (MEMS) for example, are already being made more resilient due to use in aerospace [9]. MEMS describe any system with moving parts on the micro-scale; relevant examples used in guided projectiles would be gyroscopes and accelerometers. Additionally, experiments are being conducted to adapt newer technologies, such as piezoelectric actuators, which are robust, have very high operational frequencies and no moving parts (aside from the physical deformation of the actuator). Different designs of piezoelectric actuators, such bi-morph actuators [10,11] and snap-through actuators [12], have been incorporated into projectile fins and control methodologies have been considered [13,14]. Smaller designs usually equate to higher projectile speeds [15]. It has been shown both numerically and experimentally, that conventional fin designs are able to produce significant deflections when subjected to supersonic speeds in excess of Mach 4 [16] (a 25 mm projectile achieved 1.4 m of deflection over a range of 160 m).

Much research has been conducted into unconventional control methodologies. While fins are still the primary source of control moments for projectiles, developments in these novel methods may prove useful in future guided weapon design, dual-spin or not. Project SCORPION, a collaboration between DARPA, U.S. Army Research Labs (USARL) and Georgia Institute of Technology, investigated the feasibility of mircoadaptive flow control (MAFC) as a means to control spin stabilised projectiles [17]. It utilised the Coandă effect interaction with the projectile boattail, in combination with a high frequency piezoelectric actuator which distorts the boattail. The USARL have also proposed and analysed an asymmetric, spin stabilised projectile controlled by a singular fin or 'paddle' [18]. 'Tail-spoilers' have been proven able to manoeuvre a 105 mm projectile at speeds up to Mach 3 [19], with a range enhancement of 7% or a controllable deflection of 1.5 km, over a 10 km range. Tests have been conducted with an articulable nose/ogive, achieving bandwidths of up to 200 Hz at Mach 3.3 [15]. Microvanes have been investigated as a method for flow control on a supersonic spinning projectile [20]. It was found that the vanes inhibit flow separation on the surface of the projectile, the normal force coefficient and pitching moment stabilised, which led to greater projectile stability via reduced oscillations. In addition, there exist a plethora of patents [21–25] describing novel guidance methods such as air jets, gyroscopes and asymmetric ogives. Since fin control methods are so predominant, they are assumed to be the source of all control moments throughout this paper.

3. Stability factors

Many popular textbooks and literature [2,26–30] can provide a detailed derivation of the stability factors from linear projectile theory, this section gives a brief description following McCoy [26]. It then elaborates on the relation between these factors and their importance in determining the effect projectile dimensions have on ballistic stability. Then it is shown how different works to date have modified these factors to account for different iterations of projectile models. The DOF models form which the stability factors are derived from have been shown able to replicate technical data and atmospheric flight models, when applied to small calibre munitions [31]. The NATO Armaments Ballistic Kernel (NABK) also utilises a 6-DOF model, which has also been shown to predict the behaviour of small calibre munitions (7.62 mm × 51 mm) [32]. Additionally, the statistical methodology used to evaluate projectile dispersion during that study characteristics is sufficient [33].

3.1. Classical aeroballistic stability factors

The static stability factor S_s, for a projectile of mass m, is given by

$$S_S = \frac{1}{2I_y}\rho S d^3 m C_{M\alpha} \tag{1}$$

where $C_{M\alpha}$ is the overturning moment coefficient as a function of angle of attack α, or $C_{M\alpha} \equiv \partial C_M/\partial\alpha$ [34]. A body has 'positive' static stability (i.e. is statically stable) if $S_S < 0$; $S_S = 0$ and $S_S > 0$ correlate to neutral and negative static stability respectively. Depending on whether the static stability is positive, neutral or negative, the body's alignment after a disturbance will respectively: return to its original position, maintain its new alignment or continue moving in the direction of the disturbance. Apart from $C_{M\alpha}$, all parameters in Eq. (1) are positive, hence to achieve $S_S < 0$ we necessitate that $C_{M\alpha} < 0$; for a non-spin stabilised body this means practically that the COM is located ahead of the centre of pressure (COP). Fig. 2 shows a plot of the relation between C_M and α, static stability is present when the line pertaining to a given body has negative gradient. To optimise S_S based on the coefficients of $C_{M\alpha}$, a heavy projectile with a large cross section and small transverse moment of inertia is preferable, though this contradicts conventional ballistic design.

The procedure for deriving the gyroscopic and dynamic stability factors involves solving, under a series of assumptions, the equations of motion (EOM) for a projectile model and imparting boundary conditions on the solutions. In the most basic case presented, we assume a spin stabilised, uncontrolled projectile which is aerodynamically symmetric, has a rigid body, a uniform density and the centre of mass (COM) located on the longitudinal axis. Euler angles and angles of attack are assumed to be small and the effects of gravity are neglected. The solutions to a projectile's EOM describe damped oscillatory motion with two modes; a large amplitude slow frequency 'precession' (ω_p) and a low amplitude fast frequency 'nutation' (ω_n) with damping frequencies λ_p and λ_n respectively. For the solutions to represent real and damped

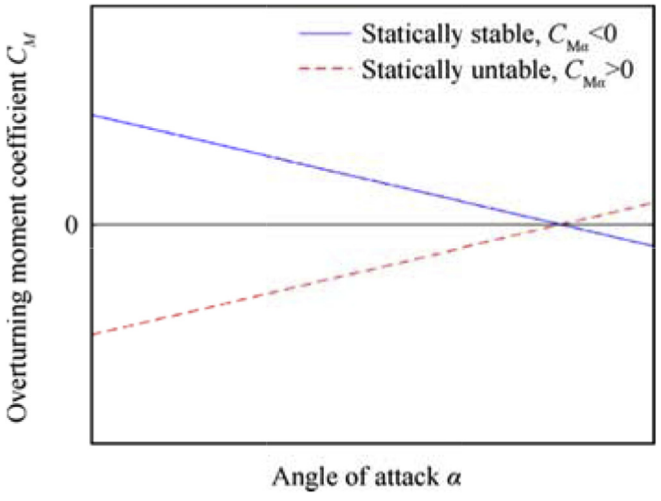

Fig. 2. Example of overturning moment coefficient $C_{M\alpha}$ against angle of attack α for two abstract bodies.

oscillations, we impose boundaries on the oscillation and damping rates. From the resulting inequalities, the gyroscopic stability factor is defined as

$$S_g = \frac{p^2 I_x^2}{4 I_y V^2 C^*_{M\alpha}} \tag{2}$$

The dynamic stability factor is defined as

$$S_d = \frac{2\left(C^*_{L\alpha} + \frac{md^2}{I_x} C^*_{M_{p\alpha}}\right)}{C^*_{L\alpha} - C^*_D - \frac{md^2}{2I_y}\left(C_{Mq} + C_{M\dot{\alpha}}\right)^* + \frac{1}{2} k_x^{-2} C^*_{Lp} - \frac{8mg\cos(\theta_T)}{\pi\rho d^2 V^2}} \tag{3}$$

N.B. the last two terms in the denominator of Eq. (3) are only included by some texts [26,29] to account for variable velocity due to drag and gravity. These equations are cumbersome so they are written in a more compact notation using substitution parameters, the gyroscopic stability factor is written as

$$S_g(\text{SSNC}) = \frac{P^2}{4M} \tag{4}$$

and the dynamic stability factor is represented as

$$S_d(\text{SSNC}) = \frac{2T}{H}. \tag{5}$$

Future iterations of the stability factors are written in this compact form and all substitution parameters are shown in Appendix A. The mathematical condition for gyroscopic stability is $S_g \geq 1$, though it has been shown that the ballistic coefficient of a bullet is adversely affected by tumbling as S_g is lowered past a threshold of 1.3 [35]. The ratio p/V decreases along the trajectory of an uncontrolled projectile (assuming flat-fire), thus it is apparent S_g will decrease down range. A projectile is dynamically stable if

$$S_g > \frac{1}{S_d(2 - S_d)} \tag{6}$$

By substituting S_g from Eq. (4) into Eq. (6) we can define the axial spin limit S_{lim} from the resulting inequality,

$$P^2 < \frac{4M}{S_d(2 - S_d)} \triangleq S_{lim} \tag{7}$$

which shows the critical value of P^2 for which the inequality in Eq. (6) is no longer satisfied. Fig. 3 shows a plot of the corresponding equality of Eq. (6), with the shaded region indicating where the inequality is fulfilled.

Dynamic stability is concerned with the oscillations induced in a moving body after a disturbance is applied and as with static stability, it can be positive, neutral or negative. With positive dynamic stability the oscillations eventually damp towards the original alignment, neutral dynamic stability causes oscillations to reside indefinitely with constant amplitude, while negative dynamic stability has oscillations which amplify chaotically. When $S_d = 1$ the body has positive dynamic stability, or is perfectly dynamically stable. If $S_d < 1$ the precession is unstable and if $S_d > 1$ the nutation is unstable, both catastrophically so at the asymptotes ($S_d = 0$ or $S_d = 2$ respectively). The transition from positive to neutral to negative dynamic stability for a projectile is dependent on the magnitude of the deviation from $S_d = 1$. The magnitude at which the transitions occur is dependent on the projectile and trajectory parameters, but is not well characterised. Provided $0 < S_d < 2$ in practice, the projectile can be spun sufficiently to ensure ballistic stability. Table 1 shows the effect on ballistic stability of occupying

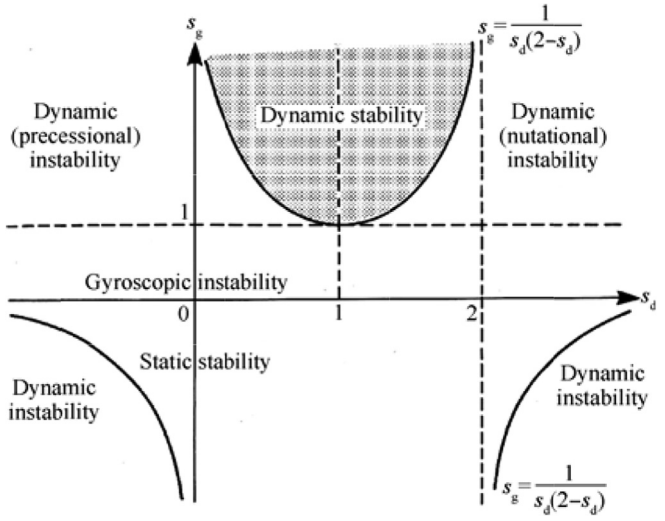

Fig. 3. Stability relations [29].

Table 1
Criteria for stability regimes.

Static regime	Dynamic Regime	Ballistic result
Stable $S_S < 0$	$0 < S_d < 2$	Always ballistically stable
	$S_d < 0$ or $S_d > 2$	Ballistically stable if $P^2 < S_{lim}$
Unstable $S_S > 0$	$0 < S_d < 2$	Ballistically stable if $P^2 > S_{lim}$
	$S_d < 0$ or $S_d > 2$	Never Ballistically stable

different static and dynamic regimes.

Note that the projectile geometry required to maximise aerodynamic efficiency and terminal effectiveness, almost always results in negative static stability. From Table 1 we can see that in the unstable static regime, a dynamically stable projectile can still be ballistically stabilised if the spin rate is sufficiently high. Thus, projectile designers can effectively disregard the static stability of a projectile, solely focusing on the relation between S_d and S_g; *i.e.* it is sufficient, to ensure a prototype projectile lies in the stable region (as central as possible) of Fig. 3 for the anticipated flight envelope.

Fig. 4 shows a dynamic stability plot for three conventional

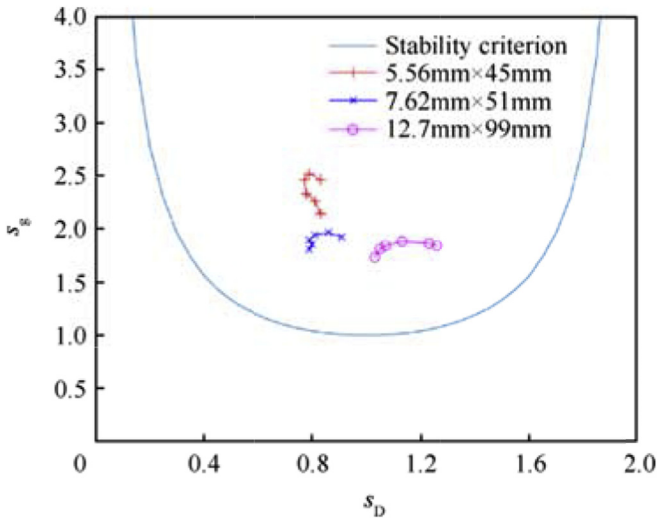

Fig. 4. Dynamic stability plot of various NATO calibres for different projectile velocities.

NATO calibres: 5.56 mm × 45 mm, 7.62 mm × 51 mm and 12.7 mm × 99 mm. The bullet geometry is loaded into PRODAS ballistic software and calculated for flat-fire trajectories. Each line represents one calibre, each point on the line represents a pair of stability factors calculated at a given bullet velocity. The velocity range is Mach 1.5–4 in increments of 0.5, the lowest speed corresponds to the lowest/left most point of each line, increasing progressively.

3.2. Stability factor development

To account for the contribution of passivated control surfaces (canards or fins), a term $\mathfrak{n}$ can be appended to the EOM [30,36], where

$$\mathfrak{n} = \frac{1}{I_y} d^2 \left(-i\delta_c \, e^{i\Phi_T} + \xi \right) \frac{dC_{N\delta}}{dt} \tag{8}$$

Note that the $\mathfrak{n}$ term could be modified to account for any of the novel control methodologies described at the end of Section 2, provided the control moment can be characterised and integrated into the EOM. If the same mathematical treatment as above is applied to this modified EOM, the result is that S_d is unaffected, while S_g becomes:

$$S_g(\mathrm{SSC}) = \frac{P^2}{4\left(M + \frac{d^2}{I_y}\frac{dC_{N\delta}}{dt}\right)} = \frac{P^2}{4M_c} \tag{9}$$

$$S_d(\mathrm{SSC}) = S_d(\mathrm{SSNC}) \tag{10}$$

At least for the assumptions of this model, the canard parameters considered only affect S_g, not S_d. In a comprehensive paper by Costello et al. (2000) [37] a dynamic model was produced for a dual-spin projectile with no control surfaces, which utilised a 7-DOF model. The stability factors derived from this are shown below in Eq. (11) and Eq. (12).

$$S_g(\mathrm{DSNC}) = \frac{F^2}{4C} \tag{11}$$

$$S_d(\mathrm{DSNC}) = \frac{2\left((A + C^*_{D0})F + B\right)}{F\left(A - 2C^*_{D0} - E\right)} \tag{12}$$

Burchett et al. [38] developed this model further to analyse the effect that lateral pulse jets, as a method of control, have on the swerving motion of a projectile; though they did not derive any stability factors for their model. Costello uses the same assumptions as the classical case with the addition that V, ϕ_A & ϕ_F are large compared to the dynamic model coordinates θ, ψ, q, r, v, & w, so a product of any of these small quantities and any of their derivatives is negligible.

Wernert (2009) [39] expanded this dual-spin model to include the contribution of passivated canards, leading to the following stability factors

$$S_g(\mathrm{DSC})_1 = \frac{F^2}{4C'} \tag{13}$$

$$S_d(\mathrm{DSC})_1 = \frac{2\left((A' + C^*_{D0})F + B\right)}{F\left(A' - 2C^*_{D0} - E\right)} \tag{14}$$

Comparing Eq. (11) and Eq. (13), we can see the method for including canard effects for the dual-spin design is analogous to the single-spin design between Eq. (4) and Eq. (9), the addition of a term in the denominator. However, Wernert remarks that the S_d he arrived at is not satisfactory since the contribution of the canards to the Magnus forces/moments was not considered.

Zhu et al. [40] further developed this model by including terms to account for the effects of gravity and Euler pitch angle (θ_E), which led them to the following stability factors.

$$S_g(\mathrm{DSC})_2 = \frac{P^2}{4\tilde{M}} \tag{15}$$

$$S_d(\mathrm{DSC})_2 = \frac{2T}{\tilde{H}} \tag{16}$$

Using the assumption of a flat fire trajectory, $\theta_E = 0$, the stability factors were then shown to reduce and remain consistent with the previously established theory. Fig. 5 illustrates the model and various parameters used by both Wernert and Zhu et al. The value of S_g in Eq. (4) for a single spin, uncontrolled projectile has been validated for conventional small scale projectiles [35], though the dual-spin modifications to S_g made by Costello, Wernert and Zhu et al. are yet to be validated for small scale, due to the absence of such small scale dual-spin prototypes.

Fig. 6 shows a comparison of each iteration of the stability factors, equations (4), (5), (9)–(14), for a 155 mm projectile. There is an inherent difficulty in directly comparing these equations, since they model fundamentally different projectiles. We can assume the total mass of a single spin projectile is the sum of masses of the forward and aft sections. Canards are assumed to have negligible mass, yet still provide an aerodynamic moment. The aft spin rate is chosen to be equal to the single-spin (1445 rad/s) while the forward section is chosen be sufficiently low to allow the operation of control and sensing hardware (30 rad/s). The aerodynamic coefficients, moments of inertia and balancing distances ($R_{(A,F)x}$, $Rm_{(A,F)x}$ $r_{(A,F)x}$) were calculated using a projectile model in PRODAS, once the single spin projectile was divided into two distinct sections. It is worthwhile to note which modifications to a dual-spin projectile are necessary to achieve the stability of a single-spin projectile. However, this optimisation task is very complex and beyond the scope of this paper, since all aerodynamic coefficients are functions of projectile geometry.

4. Works pertaining to dual-spin stability

This section reviews publications which consider different elements affecting projectile stability from a perspective other than stability factors. The chapters categorise a number of publications which have a similar focal point.

An alternative method of stability analysis, conducted by Theodoulis et al. [41], created a linear-parameter-varying (LPV) model for a canard guided, single spin projectile. The aerodynamic information is encoded into certain state space matrices, the eigenvalues of which correspond to the precession and nutation frequencies of the projectile at any given instance. Additionally, root locus analysis of the system can identify stable operating regions, the parameters of which can be obtained and substituted into the stability criteria, depending on how the system is modelled. Indeed, ISL have conducted a significant amount of research into the modelling and control of dual-spin projectiles [39,41–45].

The ‘Miller twist rule’ is an imperial unit formula which can be used to calculate the optimal twist rate of a barrel as a function of bullet attributes and S_g [5], thus it can also be used to determine S_g if the twist rate is known. Courtney et al. has shown empirically, that the Miller rule can be modified for use with plastic tipped bullets with non-homogenous densities [46], as well as for open tip style bullets [47].

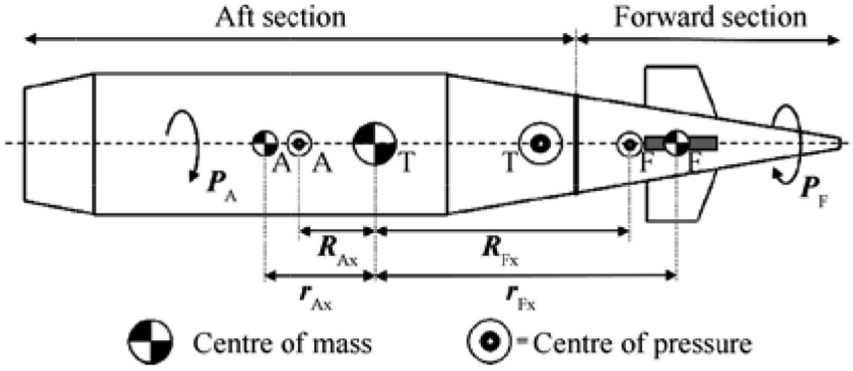

Fig. 5. Depiction of dual-spin projectile model (modified from Ref. [40]).

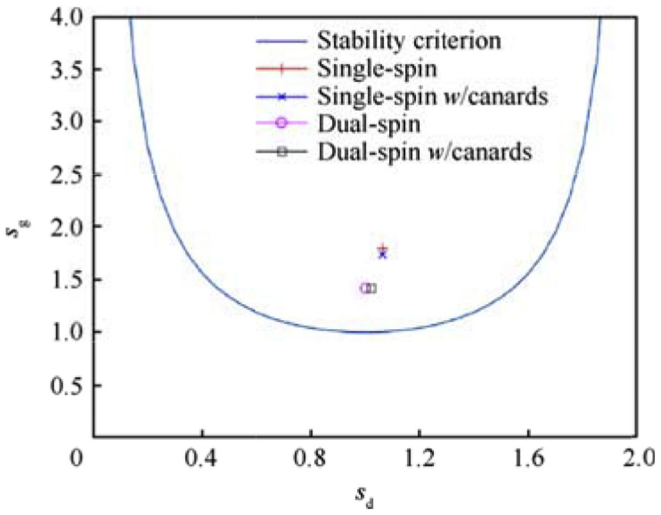

Fig. 6. Dynamic stability comparison for each iteration of stability formula.

4.1. Airframe

Lahti et al. [48] designed a methodology to control the exterior ballistic properties of a spinning projectile by re-distributing the centre of mass around the inside of the bullet. The stability factors used in the paper follow McCoy [26], an appropriate usage since bullets are single-spin stabilised projectiles with no control method. The aerodynamic coefficients used in the analysis are calculated from a modified version of Slender Body Theory [49], where a correction term $\sqrt{M_v}$ is appended to account for flow compressibility. While it is stated the coefficients are not well estimated near the transonic boundary, they are assumed to be representative based on experimental data [50]. A bullet model was created with a large number of cells populating the interior, each may possess a specific density. A global optimisation algorithm was then used to find the mass distribution which can provide ballistic stability at the lowest velocity, by satisfying the stability factors. Since velocity decreases with projectile range, this method will find the mass distribution which enables the longest range (a training round with limited range was also investigated, but this review is mainly concerned with results from the long range specimen). Fig. 7 shows the result from their paper.

It is stated the Magnus effect is the main method by which the mass distribution affects stability, especially toward the aft of the projectile [26]. From Fig. 7, it is apparent the algorithm selected the largest available density to populate mostly the aft of the projectile, which has the effect of minimising the resulting Magnus moment. These results indicate that mounting control and guidance hardware in the forward section of a projectile is beneficial for projectile stability, since electronic components generally have a lower density than the conventional core material, lead.

Jintao et al. [51] have investigated the effects to flight stability and manoeuvrability caused by the elastic deformation of a spinning projectile by conducting numerical simulations. It was shown that aerodynamic coefficients increase with movement frequency, that an elastic deformation induces two aerodynamic components opposite and perpendicular to the deformation, and that the induced angle of attack from deformation decreases as Mach number increases.

Xu et al. [52] have modelled the stability factors for a missile under thrust, assuming a flexible chassis. It was shown that thrust has a 'critical value' where dynamic stability is maximised; if thrust is higher or lower than the critical value, then dynamic instability is induced by elastic or rigid vibrational frequencies respectively. Additionally, structural stiffness is lowered as thrust increases, which leads to reduced static stability.

4.2. Canard modification and general control

Chang et al. [53] have investigated the spin-rate of dual-spin projectiles as a function of canard properties, by characterising the ratio of aft to forward axial moment of inertia, I_x^A/I_x^F. The canards were modelled with zero deflection angle, so any contribution comes purely from the roll damping moment. It was found that for an initial spin rate of 420 rev/s (muzzle velocity 980 m/s with elevation angle of 45°), the dual-spin configuration itself causes a spin-rate discrepancy of 25 rev/s between the aft and forward sections, while deploying the canards led to a difference of 250 rev/s. The spin attenuation of the aft section was greater for values of $I_x^A/I_x^F < 1$, while the spin attenuation of the forward section was greater for values of $I_x^A/I_x^F > 1$. For very large values of I_x^A/I_x^F, the aft section spin-rate was found to drastically reduce at first, then increase for a short period and finally attenuate as prior. Impact point drift was caused by any deviation from $I_x^A/I_x^F = 1$. The maximum angle of attack was found to increase drastically to 16° for $I_x^A/I_x^F < 0.3$, but remain around 1.7° for all $I_x^A/I_x^F > 0.3$. The ratio of inertial moments has significant effects on both spin rate and angle of attack and must therefore be considered carefully during the design of a dual-spin projectile.

Wang et al. [54] have conducted numerical simulations investigating the effect of yawing force frequency on the angular motion and ballistic characteristics of dual-spin projectiles. The precession and nutation rates (λ_p and λ_n) were calculated following the linear theory described in Ref. [26]. It was found λ_p and λ_n for the system

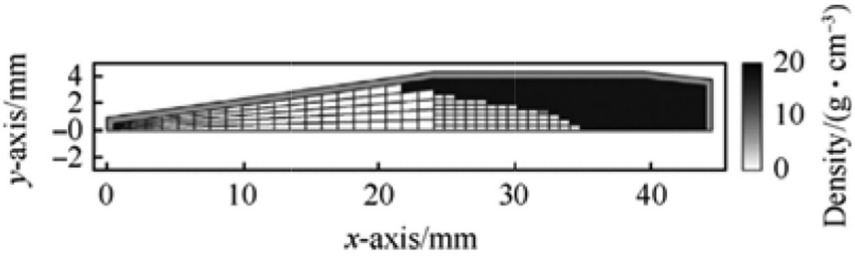

Fig. 7. The optimal mass distribution of a long range bullet, Lahti et al. [48].

decrease over the projectile trajectory. As a result, the spin-rate of the aft or forward section could coincide with these intrinsic frequencies at certain intervals, which are dependent on the chosen projectile parameters. At resonance, there is an increase in angle of attack (~0.2°) and decrease in projectile range (~0.4 km decrease over ~33.5 km). A Monte Carlo simulation was then conducted, which showed a 10 Hz control force applied to the projectile reduces projectile dispersion, but not significantly.

Cooper et al. have investigated the implications on flight stability caused by projectile asymmetry from the addition of canards [55]. Linear projectile theory was extended to account for radial mass asymmetries, which was shown to reduce back to standard theory when the asymmetry was zero. The dynamic stability of the projectile was found by root locus analysis of the system eigenvalues in state space, in the same way as Theodoulis et al. [41,42,44]. The canards were modelled with sinusoidal actuation, when the frequency of this driving wave is close to λ_p or λ_n, dynamic instability results; this is in agreement with the investigation of [54]. When the actuation moment of the canards was sufficiently large, it was shown to adversely affect the oscillatory motion of the projectile, leading to ballistic instability.

Chang [56] has studied the dynamic response of a dual-spin, canard-stabilised projectile, when the coupling between canard control and gravity are considered. A new analytical solution was proposed to predict the maximum angle of attack induced by canard actuation, the yaw of repose due to canard control and the phase shift of the swerve response. It was found if the moment imparted on the projectile by the canards, or 'control moment', is large then it will more drastically alter the trajectory, but lead to airframe instability.

Wang et al. [36] investigated the effects of different control strategies on the flight stability criterion derived in Ref. [40], by assuming all parameters other than those associated with the rolling motion of the body to be invariant. It was found that canards should be designed so the produced roll moment is as small as possible. During the period in which the roll angle is adjusted, it was found that control strategy has no impact on flight stability; it was suggested that the target spin rate of the forward section should be as low as possible for practical purposes (as discussed in Section 1). The behaviour of the motor torque was also characterised in terms of both trajectory and projectile parameters.

Liang et al. [57] have proposed a methodology for optimising the aerodynamic parameters of control canards. A 3D model is created with chosen canard parameters, then the aerodynamic coefficients for this are generated through the CFD program FLUENT and the efficiency is analysed by mapping how the normal force coefficient ($C_{N\alpha}$) changes with respect to canard deflection angle, over different angles of attack and Mach numbers. It would be interesting to see how this methodology could improve if used in conjunction with all the works listed above, where the canards' performance is quantified for each mechanism of affecting projectile stability, for varying control strategies, and having the optimum configuration selected based upon this.

5. Conclusions

This paper has shown the origin of stability factors, their use and interpretation for projectile design and how they should be modified to describe a dual-spin, controlled projectile. When more dual-spin prototypes are available, further work should involve validating the 7-DOF models used in numerical analysis. What follows is a summary of the publications reviewed here, aiming to provide guidelines to maximise the ballistic stability of a prototype projectile; full detail being found in the accompanying reference.

Lahti et al. [48] have shown that mass should be concentrated at the back of the projectile as much as possible, to increase the range. Jintao et al. [51] have shown that an increasing airframe vibrational frequency, or increasing elastic deformation amplitude, will increase aerodynamic coefficients through an increasing angle of attack, at a rate proportional to Mach number. Xu et al. [52] showed that projectile thrust has an optimal value to maximise dynamic stability, which is dependent on airframe parameters. This is not so applicable to gun-launched projectiles but is an important consideration nonetheless. Chang et al. [53] showed that spin attenuation of the aft/forward section increased for $I_x^A/I_x^F < 1$ and $I_x^A/I_x^F > 1$ respectively, and that maximum angle of attack increases drastically (~16°) for all $I_x^A/I_x^F < 0.3$, remaining almost constant (~1.7°) otherwise. The intrinsic nutation and precession frequency, which are dependent on airframe parameters, decrease over a trajectory. It has been sown that the control force frequency (Wang et al. [54]) and canard actuation frequency (Cooper et al. [55]) should be chosen to avoid these modes if possible. Chang [56] has shown that if the control moment of the canards is too large then ballistic stability is affected. Finally, Wang et al. [36] have shown that the roll moment of the canards should be as small as possible.

Conflicts of interest

None to declare.

Funding

This paper was sponsored by EPSRC ICASE Grant reference 1700064 and BAE Systems.

APPENDIX

A. Substitution parameters

Single-spin no canards (Classic)

The last two terms of H are added by certain authors [26,29] to represent variable velocity due to gravity and drag.

$$P = \frac{I_x}{I_y}\frac{pd}{V}$$

$$M = k_y^{-2} C^*_{M\alpha}$$

$$T = C^*_{L\alpha} + k_x^{-2} C^*_{MP_\alpha}$$

$$H = C^*_{L\alpha} - C^*_D - k_y^{-2}\left(C_{Mq} + C_{M\dot{\alpha}}\right)^* + \frac{1}{2}k_x^{-2} C^*_{Lp} - \frac{8mg\cos(\theta_T)}{\pi\rho d^2 V^2}$$

where

$$k_{x,y}^{-2} = \frac{md^2}{I_{x,y}}$$

Canard Guided

$$M_c = M + \frac{d^2}{I_y}\frac{dC^*_{N\delta}}{dt}$$

Dual-spin without canards

Any symbol with an *A* or *F* subscript or superscript indicates the usual meaning of the symbol, but with respect to the Aft or forward section of the projectile respectively.

$$F = \frac{d}{V}\frac{\left(I_x^F p_F + I_x^A p_A\right)}{I_y^T}$$

$$C = \frac{md}{I_y^T}\left(\left(R_{fx} + r_{fx}\right)C_{N\alpha}^{F\ *} + (R_{ax} + r_{ax})C_{N\alpha}^{A\ *}\right)$$

$$A = C^*_{N\alpha}$$

$$B = \frac{md^2}{I_y^T}\frac{1}{V}\left(\left(Rm_{fx} + r_{fx}\right)\frac{C^F_{NP\alpha}\, p_F}{2} + (Rm_{ax} + r_{ax})\frac{C^A_{NP\alpha}\, p_A}{2}\right)^*$$

$$E = \frac{md^2}{2I_y^T}\left(C_{Mq} + C_{M\dot{\alpha}}\right)^*$$

where

$$I_y^T = I_y^F + m_f r_{fx}^2 + I_y^A + m_a r_{ax}^2$$

Dual-spin with canards

$$A' = \left(C_{N\alpha} + \frac{S_c}{S}C_{N\delta}\right)^*$$

$$C' = \frac{md}{I_y^T}\left(\left(R_{fx} + r_{fx}\right)C_{N\alpha}^F + (R_{ax} + r_{ax})C_{N\alpha}^A + \frac{S_c x_c}{S}C_{N\delta}\right)^*$$

Then by Zhu

$$\tilde{M} = \frac{M}{1 - \varepsilon\alpha_e} + \frac{\varepsilon\beta_e PT}{(1 - \varepsilon\alpha_e)^2} + \frac{\varepsilon\beta_e PM}{(1 - \varepsilon\alpha_e)\tilde{H}} + \frac{(\varepsilon\beta_e PT + \varepsilon\beta_e M)^2 - 2\varepsilon\beta_e PTM}{(1 - 2\varepsilon\alpha_e)\tilde{H}^2}$$

$$\tilde{H} = (1 - \varepsilon\alpha_e)(H - 2g_*)$$

Where $g_* = gl\sin(\theta_T)/V^2$ and $\varepsilon = 0.5\tan(\theta_E)$.

References

[1] Miller D. How good are simple rules for estimating refiling twist?, vols. 48–52; 2009. http://www.jbmballistics.com/ballistics/bibliography/articles/miller_stability_2.pdf. [Accessed 5 February 2019].
[2] Moss GM, Leeming DW, Farrar CL. Military ballistics. first ed. Brassey's; 1995.
[3] Seifert J. A review of the Magnus effect in aeronautics. Prog Aerosp Sci 2012;55:17–45. https://doi.org/10.1016/j.paerosci.2012.07.001.
[4] Despirito J, Heavey KR. CFD computation of Magnus moment and roll damping moment of a spinning projectile. 2006.
[5] Litz B. Applied ballistics for long-range shooting 3rd edition: understanding the elements and application of external ballistics for successful long-range target shooting and hunting. third ed. Applied Ballistics, LLC; 2015.
[6] Raytheon. Excalibur Projectile. n.d. https://www.raytheon.com/capabilities/products/excalibur.
[7] Kopp DC. Artillery for the Army - precision fire with mobility. Def Today Magn.[d].
[8] 360 J. Full production for PGK [ES18D3]. Eurostatory 2018 2018. https://www.janes.com/article/80920/full-production-for-pgk-es18d3.
[9] Tiliakos N. MEMS for harsh environment sensors in aerospace applications: selected case studies. Mems Automot Aerosp Appl 2013:245–82. https://doi.org/10.1533/9780857096487.2.245.
[10] Mani S, Singh SN, Parmi SK, Yim W, Trabia M. Adaptive rotation of a smart projectile fin using a piezoelectric flexible beam actuator. JVC/J Vib Control 2005;11:1085–102. https://doi.org/10.1177/1077546305055774.
[11] Mani S, Singh SN, Parimi SK, Yim W. Adaptive servoregulation of a projectile fin using piezoelectric actuator. J Dyn Syst Meas Control 2007;129:100. https://doi.org/10.1115/1.2397159.
[12] Kang CG, Lee JS, Han JH. Development of bi-stable and millimeter-scale displacement actuator using snap-through effect for reciprocating control fins. Aerosp Sci Technol 2014;32:131–41. https://doi.org/10.1016/j.ast.2013.11.007.
[13] Mudupu V, Trabia MB, Yim W, Weinacht P. Design and validation of a fuzzy logic controller for a smart projectile fin with a piezoelectric macro-fiber composite bimorph actuator. Smart Mater Struct 2008;17. https://doi.org/10.1088/0964-1726/17/3/035034.
[14] Trabia MB, Yim W, Saadeh M. Modeling of hysteresis and backlash for a smart fin with a piezoelectric actuator. J Intell Mater Syst Struct 2011;22:1161–76. https://doi.org/10.1177/1045389X11414223.
[15] Barrett-Gonzalez R, Barnhart R, Bramlette R. Steerable adaptive bullet flight control mechanism design. In: 53rd AIAA/ASME/ASCE/AHS/ASC Struct. struct. dyn. mater. conf. AIAA/ASME/AHS adapt. struct. conf. AIAA; 2012. https://doi.org/10.2514/6.2012-1511.
[16] Massey KC, Silton SI. Combining experimental data, computational fluid dynamics, and six-degree of freedom simulation to develop a guidance actuator for a supersonic projectile. In: Proc inst mech eng Part G J aerosp eng, vol. 223; 2009. p. 341–55. https://doi.org/10.1243/09544100JAERO399.
[17] McMichael J, Plostins P, Sahu J, Glezer A, Lovas A, Brown G, et al. Micro-adaptive flow control applied to a spinning projectile. In: 2nd AIAA flow control conf; 2004. https://doi.org/10.2514/6.2004-2512.
[18] Fresconi F, Cooper G, Celmins I, DeSpirito J, Costello M. Flight mechanics of a novel guided spin-stabilized projectile concept. In: Proc inst mech eng Part G J aerosp eng, vol. 226; 2012. p. 327–40. https://doi.org/10.1177/0954410011408385.
[19] Patel M, Sowle Z, Ng T, Toledo W. Range and endgame performance assessment of a smart projectile using hingeless flight control. In: 44th AIAA aerosp Sci meet exhib; 2006. https://doi.org/10.2514/6.2006-671.
[20] Ma J, Chen Z, Huang Z, Gao J, Zhao Q. Investigation on the flow control of micro-vanes on a supersonic spinning projectile. Def Technol 2016;12:227–33. https://doi.org/10.1016/j.dt.2016.01.008.
[21] Epperson Jr EH. Gyroscopically steerable bullet 1984;4(431):150.

[22] Lawhorn WS, Clinkenbeard IL. Small calibre guided projectile 1985;4(537):371.
[23] Minick AB, Hobart SA, Widman F, Kokan TS, Massey FH. Guided projectile. US 7,891,298 B2, 2011.
[24] Mallon P. Steerable projectile. 2011/0270617 A1. 2011.
[25] Geswender CE, Dryer R, Vesty P. Steerable spin-stabilized projectile. US 8,916,810 B2, 2014.
[26] McCoy RL. Modern exterior ballistics: the launch and flight dynamics of symmetric projectiles. Schiffer Publishing; 1999.
[27] Carlucci DJS. Theory and design of guns and ammunition. 2008.
[28] Cook MV. Flight dynamics principles: a linear systems approach to aircraft stability and control. Third. Elsevier; 2013.
[29] Textbook of ballistics and gunnery. 1987.
[30] U.S. Army Materiel Command. Engineering design handbook design for control of projectile flight characteristics. 1966.
[31] Gkritzapis DN, Tsiatis NE, Panagiotopoulos EE, Margaris DP. Physicomathematical simulation analysis for small bullets. J Eng Sci Technol Rev 2008;1:70–4.
[32] Corriveau D. Validation of the NATO Armaments Ballistic Kernel for use in small-arms fire control systems. Def Technol 2017. https://doi.org/10.1016/j.dt.2017.04.006.
[33] Rabbath CA, Corriveau D. A statistical method for the evaluation of projectile dispersion. Def Technol 2017. https://doi.org/10.1016/j.dt.2017.04.008.
[34] MIT. Aircraft stability and control Lecture 2. 2004. https://ocw.mit.edu/courses/aeronautics-and-astronautics/16-333-aircraft-stability-and-control-fall-2004/lecture-notes/lecture_2.pdf.
[35] COURTNEY ER, COURTNEY MW. Aerodynamic drag and gyroscopic stability. [n.d].
[36] Wang Y, Wang X ming, yan Yu J. Influence of control strategy on stability of dual-spin projectiles with fixed canards. Def Technol 2018:1–11. https://doi.org/10.1016/j.dt.2018.04.014.
[37] Costello M, Peterson A. Linear theory of a dual-spin projectile in atmospheric flight. J Guid Control Dyn 2000;23. https://doi.org/10.2514/2.4639.
[38] Burchett B, Peterson A, Costello M. Prediction of swerving motion of a dual-spin projectile with lateral pulse jets in atmospheric flight. Math Comput Model 2002;35:821–34. https://doi.org/10.1016/S0895-7177(02)00053-5.
[39] Wernert P. Stability analysis for canard guided dual-spin stabilized projectiles. In: Proc AIAA atmos flight mech conf exhib; 2009. p. 1–24. https://doi.org/10.2514/6.2009-5843.
[40] Zhu D, Tang S, Guo J, Chen R. Flight stability of a dual-spin projectile with canards. Proc Inst Mech Eng Part G J Aerosp Eng 2015;229:703–16. https://doi.org/10.1177/0954410014539293.
[41] Theodoulis S, Gassmann V, Wernert P, Dritsas L, Kitsios I, Tzes A. Guidance and control design for a class of spin-stabilized fin-controlled projectiles. J Guid Control Dyn 2013;36. https://doi.org/10.2514/1.56520.
[42] Theodoulis S, Morel Y, Wernert P, Tzes A. LPV modeling of guided projectiles for terminal guidance. In: 18th mediterr conf control autom MED'10 - conf proc; 2010. p. 1455–60. https://doi.org/10.1109/MED.2010.5547843.
[43] Strub G, Gassmann V, Theodoulis S, Dobre S, Basset M. Hardware-in-the-loop experimental setup development for a guided projectile in a wind tunnel. In: IEEE/ASME Int conf adv intell mechatronics. AIM; 2014. p. 458–63. https://doi.org/10.1109/AIM.2014.6878120.
[44] Seve F, Theodoulis S, Wernert P, Zasadzinski M, Boutayeb M. Flight dynamics modeling of dual-spin guided projectiles. IEEE Trans Aerosp Electron Syst 2017;53:1625–41. https://doi.org/10.1109/TAES.2017.2667820.
[45] Theodoulis S, Wernert P. Flight dynamics & control for smart munition: the ISL contribution. In: IFAC-PapersOnLine, vol. 50; 2017. p. 15512–7. https://doi.org/10.1016/j.ifacol.2017.08.2127.
[46] Courtney MW, Academy USAF, Miller DG. A stability formula for plastic-tipped bullets. 2009.
[47] Courtney ER, Courtney MW. Gyroscopic stability of open tipped match style rifle bullets. 2012.
[48] Lahti J, Sailaranta T, Harju M, Virtanen K. Control of exterior ballistic properties of spin-stabilized bullet by optimizing internal mass distribution. Def Technol 2019;15:38–50. https://doi.org/10.1016/j.dt.2018.10.003.
[49] Nielsen J. Missile aerodynamics. American Institute of Aeronautics and Astronautics, Inc.; 1988. https://doi.org/10.2514/4.062902.
[50] Moore F. Approximate methods for weapon aerodynamics. American Institute of Aeronautics and Astronautics, Inc.; 2000. https://doi.org/10.2514/4.473999.
[51] Yin J, Lei J, Wu X, Lu T. Aerodynamic characteristics of a spinning projectile with elastic deformation. Sch Aerosp Eng Beijing Inst Technol 2015:181–91. https://doi.org/10.1016/j.ast.2016.02.010.
[52] Xu T, Rong J, Xiang D, Pan C, Yin X. Dynamic modeling and stability analysis of a flexible spinning missile under thrust. Int J Mech Sci 2016;119:144–54. https://doi.org/10.1016/j.ijmecsci.2016.09.027.
[53] Chang S, Wang Z, Liu T. Analysis of spin-rate property for dual-spin-stabilized projectiles with canards. J Spacecr Rocket 2014;51:958–66. https://doi.org/10.2514/1.A32830.
[54] Wang Y, Cheng J, yan Yu J, X ming Wang. Influence of yawing force frequency on angular motion and ballistic characteristics of a dual-spin projectile. Def Technol 2016;12:124–8. https://doi.org/10.1016/j.dt.2015.12.007.
[55] Cooper G, Fresconi F, Costello M. Flight stability of an asymmetric projectile with activating canards. J Spacecr Rocket 2012;49:130–5. https://doi.org/10.2514/1.A32022.
[56] Chang S. Dynamic response to canard control and gravity for a dual-spin projectile, vol. 53; 2016. https://doi.org/10.1128/JVI.79.24.15165.
[57] Liang K, Huang Z, Zhang J min. Optimal design of the aerodynamic parameters for a supersonic two-dimensional guided artillery projectile. Def Technol 2017. https://doi.org/10.1016/j.dt.2017.05.003.

Technical Note: Stability analysis of a dual-spin 155mm artillery projectile

James Norris, Prof. Amer Hameed, Dr. John Economou

***Abstract*—The gyroscopic and dynamic stability factors are used to investigate the ballistic stability of a dual-spin 155mm projectile. A dynamic model is used to generate trajectory profiles. The ballistic stability is investigated over the flight envelope as a function of various projectile parameters and aerodynamic coefficients.**

***Index Terms*—Dual-spin, Guided, Projectile, Stability**

I. Introduction

THE dual-spin projectile (DSP) design is one solution to incorporating guidance hardware into projectiles where the preservation of high spin is important. Figure 1 illustrates the design, where the forward and aft section can both roll independently through a bearing connecting the two sections. Control hardware is mounted on the forward section, while the guidance computer and auxiliary systems are not relegated to the forward section, but are assumed to be located there as well.

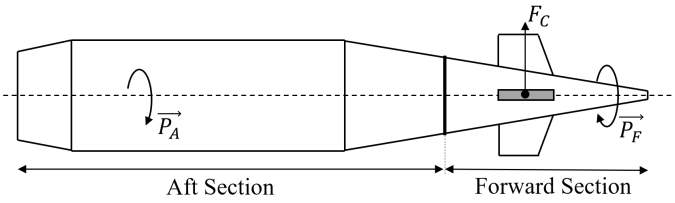

Fig. 1. DSP with fixed control force F_c

The stability factor framework determines whether a projectile is ballistically stable under certain trim conditions by calculating gyroscopic and dynamic stability factors. A review of dual-spin projectile stability [1] has shown how the gyroscopic and dynamic stability factors, S_g and S_d respectively, are used to determine whether a projectile will remain ballistically stable throughout the flight envelope. The validity of these factors to predict ballistic stability is supported experimentally [2], [3]. If instability occurs at any point in flight, drag and other aerodynamic effects become sufficiently large to adversely affect the range and the ability of the guidance system to exert control. This paper investigates how certain parameters and coefficients, which can be modified during the design process, affect the stability of the projectile in flight.

J.Norris (Corresponding Author) - PhD Researcher in Defence & Security, Cranfield University, Defence Academy of the United Kingdom, Shrivenham
A.Hameed - Professor in Defence Engineering, Cranfield University and Saudi Arabian Military Industries, Riyadh, KSA
J.Economou - Deputy Head of Centre for Defence Engineering, Cranfield University

Section II describes the 7 degree-of-freedom (DoF) model used to describe the DSP. Section III discuss the procedure used to evaluate the stability after modifying parameters and coefficients. Section IV presents and discuss the results of the proceeding analysis. Section V summarises the findings of the paper.

II. Projectile dynamics

This section describes the 7 DoF dynamic model of the DSP, which has previously been used to investigate DSPs [4], [5], [6] and is a derivative of the well-established conventional projectile model used by McCoy [7]. Subscript F denotes the forward section and subscript A denotes the aft section. The assumption is made that the total centre of mass (COM) coincides with the aft COM, *i.e.* the mass of the forward part is small with respect to that of the aft part and the nose moment of inertia $I_{xx,F}$ is small compared to the aft one $I_{xx,A}$. The forces and moments the projectile is subject to are represented by an aerodynamic coefficient. The whole body longitudinal C_{A0}, transverse C_{Y0} and normal C_{N0} coefficients represent the combined effect of these individual forces, and are shown in figure 2 for non-zero angle of attack α. Aerodynamic coefficients for projectile were computed from projectile models in DATCOM, PRODAS and ANSYS Fluent.

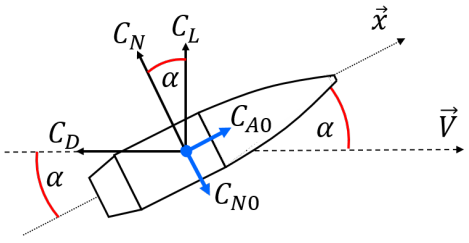

Fig. 2. Projectile coefficients when $\alpha \neq 0$

The non-linear kinematic translational and rotational equations are given by equations 1 and 2 respectively.

$$\dot{\mathbf{x}}_e = \mathbf{T}_x \cdot \mathbf{v}_e \tag{1}$$

$$\dot{\mathbf{\Theta}}_e = \mathbf{T}_\Theta \cdot \mathbf{\Omega}_e \tag{2}$$

where $\dot{\mathbf{x}}_e = [\dot{x}_e\ \dot{y}_e\ \dot{z}_e]^{\mathrm{T}}$ is rate of change of earth axis position coordinates, $\mathbf{T}_x$ is the earth axis positional transformation matrix, $\mathbf{v}_e = [u\ v\ w]^{\mathrm{T}}$ are the current earth axis positional speeds, $\dot{\mathbf{\Theta}}_e = [\dot{\phi}_F\ \dot{\phi}_A\ \dot{\theta}\ \dot{\psi}]^{\mathrm{T}}$ is the rate of change of earth axis rotational coordinates, $\mathbf{T}_\Theta$ is the earth axis rotational transformation matrix, and $\mathbf{\Omega}_e = [p_F\ p_A\ q\ r]^{\mathrm{T}}$ are the current earth axis rotational speeds.

Accordingly, the dynamic translational and dynamic rotational equations are shown in eq. 3 and 4 respectively.

$$\dot{\mathbf{v}}_e = \frac{1}{m}\mathbf{F} - \mathbf{T}_\Omega \cdot \mathbf{v}_e \tag{3}$$

$$\dot{\mathbf{\Omega}}_e = \mathbf{T}_v + \mathbf{I} \cdot \mathbf{m} \tag{4}$$

where $\mathbf{T}_v$ is the body velocity transformation matrix, $\mathbf{T}_\Omega$ is the body rotational-velocity transformation matrix and I is the inertia matrix. In addition, the body axis forces $\mathbf{F} = [F_X \ F_Y \ F_Z]^\mathrm{T}$ and body axis moments $\mathbf{m} = [m_{1,F} \ m_{1,A} \ m_m \ m_n]^\mathrm{T}$ are given by equations 5 and 6 respectively

$$\mathbf{F} = \bar{q}S\left(\mathbf{C}_X + \frac{p_A d}{V}\mathbf{C}_{Xp} + \mathbf{C}_{X\delta} \cdot \boldsymbol{\delta}_X\right) + mg\mathbf{T}_g \tag{5}$$

$$\mathbf{m} = \bar{q}Sd\left(\mathbf{C}_{X0} + \frac{d}{V}\mathbf{C}_{l\theta} + \frac{p_A d}{V}\mathbf{C}_{lp} + \mathbf{C}_{l\delta} \cdot \boldsymbol{\delta}\right) + \boldsymbol{\tau} \tag{6}$$

The coefficient matrices are the body axis $\mathbf{C}_X$, the Magnus force $\mathbf{C}_{Xp}$, canard forces $\mathbf{C}_{X\delta}$, body moments $\mathbf{C}_{X0}$, spin coupling $\mathbf{C}_{l\theta}$, Magnus moment $\mathbf{C}_{l\theta}$, and canard moments $\mathbf{C}_{l\delta}$.

III. Procedure

A comprehensive review of the stability framework and terms can be found in reference [1], which includes a review of relevant works [8], [9]. The gyroscopic and dynamic stability factors are shown in equations 7 and 8 respectively.

$$S_g = \frac{P^2}{4\tilde{M}} \tag{7}$$

$$S_d = \frac{2T}{\tilde{H}} \tag{8}$$

The substitution parameters are shown in appendix B. The projectile is ballistically stable if

$$S_g > \left(S_d(2 - S_d)\right)^{-1} \tag{9}$$

Henceforth, let $f(S_d) = \left(S_d(2 - S_d)\right)^{-1}$. Aerodynamic coefficients and thus the stability factors, are a function of many terms included in the dynamic model. We define the parameter vector as

$$\boldsymbol{\zeta} = [V_t \ \alpha_t \ \beta_t]^\mathrm{T} \tag{10}$$

At any instant in the trajectory, the parameter vector is determined from the current simulation parameters. The instantaneous stability factors are then computed under this trim condition such that $S_g|_{\boldsymbol{\zeta}}$ and $S_d|_{\boldsymbol{\zeta}}$. This allows the stability of the projectile to be evaluated over the whole trajectory, taking time t_τ. Figure 3 shows an example trajectory illustrating the points where the projectile becomes unstable, by no longer fulfilling equality 9. The projectile becomes unstable at time t_1 and becomes stable again at time t_2 (if at all).

Figure 4 shows the value of the terms in equality 9 over the entire trajectory. When $S_g < f(S_d)$ the projectile becomes unstable, indicated by the highlighted region on the figure, which corresponds to the unstable section of the path on fig. 3. It is obvious that equality 9 has a singularity when $S_d = 2$, such that

$$\lim_{S_d \to 2^\pm} [f(S_d)] = \infty^\mp \tag{11}$$

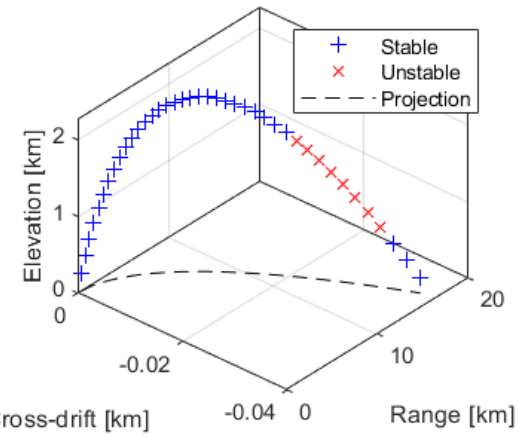

Fig. 3. Stability of 155mm shell during flight

which presents as the asymptote in fig. 4. Of note is the intersection of the two inequality terms:

$$\nabla S_g \cdot \nabla f(S_d)\Big|_{t_1} \approx 1 \tag{12}$$

$$\nabla S_g \cdot \nabla f(S_d)\Big|_{t_2} \to 0 \tag{13}$$

While the behaviour of $f(S_d)$ is extreme, the change in the dependent parameters and coefficients are not as volatile. *i.e.* the smoothness of the physical transition from stable to unstable (at t_1) is the same as unstable to stable (at t_2), even though the rate at which the inequality terms converge to each other in either case is not similar.

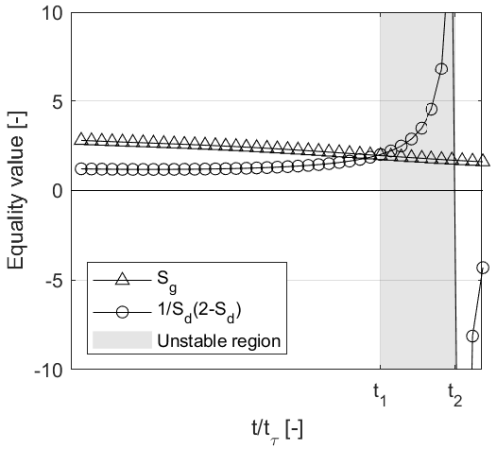

Fig. 4. Equality terms over entire trajectory

Figure 5 show the value of stability factors themselves when evaluated at the parameter vector at intervals along the trajectory. S_g decreases along the trajectory primarily due to the reduction in rotational velocity caused by spin damping. S_d increases primarily due to the fluctuation of V along the trajectory.

To demonstrate the importance of majority flight stability, the overturning moment of the projectile is varied for multiple

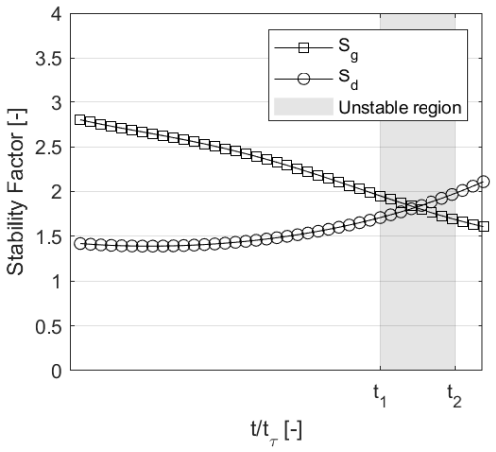

Fig. 5. Equality terms over entire trajectory

simulations. Figure 6 shows the percentage of trajectory over which the projectile remained stable, against the loss in range. *N.B.* these preliminary simulations only account for inertial and coupling losses, they neglect aerodynamic interactions such as a massively increased drag which would result from the tumbling. Since the inertial and coupling losses are the least significant contributions, the losses in the figure indicate the effective minimum losses which one could expect from the flight instability percentages.

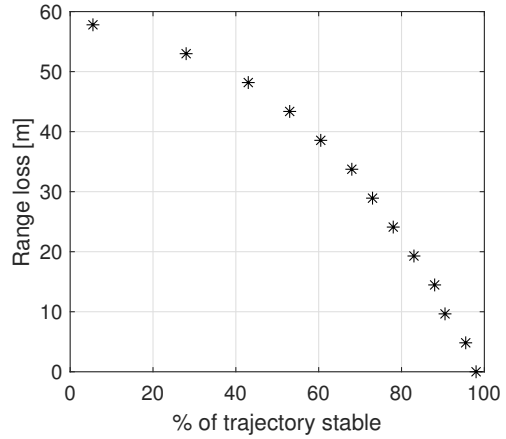

Fig. 6. Range loss caused by flight instability of uncontrolled projectile at 16.5km

IV. Results

The effect on flight stability of modifying various design parameters and coefficients is now investigated. All simulations are initialised with the same initial conditions, shown in table I. Each coefficient is scaled, from 0x to 2x, a multiple of its original value. By independently varying the coefficients and parameters in this way, the magnitude of their contribution to the stability can be directly observed. However, during the design phase of a projectile, any modification of the geometry to enact a change in one coefficient will inevitably lead to others unintentionally changing, due to the intrinsically coupled nature of the coefficients.

TABLE I
Simulation initial conditions

Parameter	Value
θ	30 [deg]
p	1445 [rad.s^{-1}]
V_0	452 [m.s^{-1}]

Figure 7 shows the percentage of the flight over which the projectile remains stable, as various aerodynamic coefficients are swept as a function of their initial value. This shows which coefficients are the predominant cause for instability. It is apparent that the Magnus moment coefficient C_{lp} has the greatest proportional effect on the flight stability.

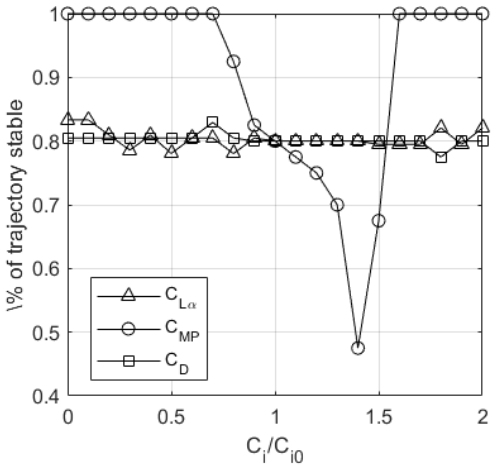

Fig. 7. Flight stability for various coefficient scaling

Figure 8 shows the effect of modifying canard deflection angles for the side canards δ_Y, vertical canards δ_N and both simultaneously δ_Y, δ_N. Note that any modification of the side mounted canards δ_Y produces a deflection in the normal axis and *vice versa*.

Figure 9 shows the effect of modifying the normal force coefficient for the side canards $C_{Y\delta}$, vertical canards $C_{N\delta}$ and both simultaneously $C_{Y\delta}, C_{N\delta}$. Both lateral and normal canard pairs are held at $0.5\delta_{max}$ for the duration of the simulation.

V. Conclusions

The dynamic model of a dual-spin projectile is shown and various simulations are run for an indirect-fire, 155mm artillery shell. The stability factors and thus the projectile stability is evaluated at trim conditions along the trajectory, whereby the percentage of the trajectory the projectile remains stable for is deduced. Projectile parameters and aerodynamic coefficients are then varied

Appendix A
Dynamic Model Terms

The following terms are used in the dynamic model for the dual-spin projectile.

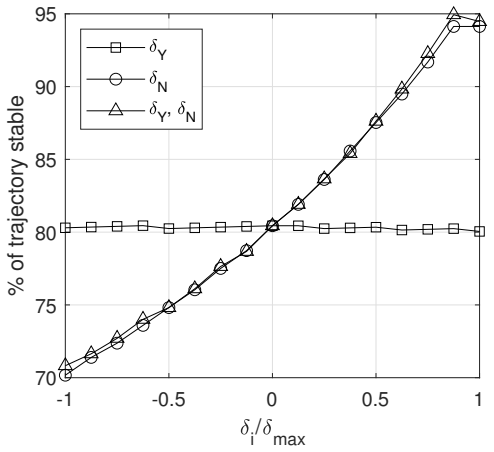

Fig. 8. Flight stability for varying canard deflections

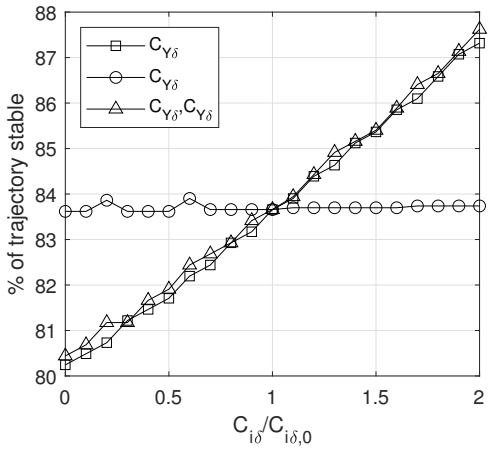

Fig. 9. Flight stability for canard lift coefficients

A. Transformation Matrices

$$\mathbf{T}_x = \begin{bmatrix} \cos(\theta)\cos(\psi) & -\sin(\psi) & \sin(\theta)\cos(\psi) \\ \cos(\theta)\sin(\psi) & \cos(\psi) & \sin(\theta)\sin(\psi) \\ -\sin(\theta) & 0 & \cos(\theta) \end{bmatrix} \tag{14}$$

$$\mathbf{T}_\Theta = \begin{bmatrix} 1 & 0 & 0 & \tan(\theta) \\ 0 & 1 & 0 & \tan(\theta) \\ 0 & 0 & 1 & 0 \\ 0 & 0 & 0 & \sec(\theta) \end{bmatrix} \tag{15}$$

$$\mathbf{T}_v = \begin{bmatrix} 0 & -r & q \\ r & 0 & r\tan(\theta) \\ -q & -r\tan(\theta) & 0 \end{bmatrix} \tag{16}$$

$$\mathbf{T}_\Omega = \begin{bmatrix} 0 \\ 0 \\ -\left(\frac{I_{xx,A}}{I_{yy}}\right) p_A r - r^2\tan(\theta) \\ \left(\frac{I_{xx,A}}{I_{yy}}\right) p_A q + qr\tan(\theta) \end{bmatrix} \tag{17}$$

$$\mathbf{T}_g = \begin{bmatrix} -\sin(\theta) \\ 0 \\ \cos(\theta) \end{bmatrix} \tag{18}$$

B. Other

$$\mathbf{I} = \begin{bmatrix} I_{xx,F}^{-1} & 0 & 0 & 0 \\ 0 & I_{xx,A}^{-1} & 0 & 0 \\ 0 & 0 & I_{yy}^{-1} & 0 \\ 0 & 0 & 0 & I_{yy}^{-1} \end{bmatrix} \tag{19}$$

$$\boldsymbol{\delta}_X = \begin{bmatrix} \delta_x \\ \delta_y \\ \delta_z \end{bmatrix} \tag{20}$$

$$\boldsymbol{\tau} = \begin{bmatrix} \tau_M + \tau_{F,A} \\ -\tau_{F,A} \\ 0 \\ 0 \end{bmatrix} \tag{21}$$

Here, τ_M is the motor torque which controls the roll angle of the forward guidance section (ϕ_F) and $\tau_{F,A}$ is the frictional torque which counteracts this:

$$\tau_{F,A} = \frac{1}{2}\rho S d\ C_{A0}\text{sgn}(p_A - p_F)(k_s + k_v|p_A - p_F|) \tag{22}$$

where k_s and k_v are the static and viscous friction coefficients respectively

APPENDIX B
SUBSTITUTION PARAMETERS

Substitution parameters for the gyroscopic and dynamic stability factors are given by. A full description of the terms can be found in reference [1].

$$\tilde{M} = \frac{M}{1-\epsilon\alpha_e} + \frac{\epsilon\beta_e PT}{(1-\epsilon\alpha_e)^2} + \frac{\epsilon\beta_e PM}{(1-\epsilon\alpha_e)\tilde{H}} + \\ + \frac{(\epsilon\beta_e PT + \epsilon\beta_e M)^2 - 2\epsilon\beta_e PTM}{(1-2\epsilon\alpha_e)\tilde{H}^2} \tag{23}$$

$$\tilde{H} = (1-\epsilon\alpha_e)(H - 2g_*) \tag{24}$$

and

$$M = I_y V^2 C^*_{M\alpha} \tag{25}$$

$$P = \frac{I_x}{I_y}\frac{|p|d}{V} \tag{26}$$

$$T = C^*_{L\alpha} + \frac{md^2}{I_y} C^*_{MP\alpha} \tag{27}$$

$$H = C^*_{L\alpha} - C^*_D - k_y^{-2}\left(C_{Mq} + C_{M\dot{\alpha}}\right)^* + \\ + \frac{1}{2}k_x^{-2} C^*_{Lp} - \frac{8mg\cos(\theta_T)}{\pi\rho d^2 V^2} \tag{28}$$

FUNDING SOURCES

The authors have no conflict of interest to declare. This paper was sponsored by EPSRC ICASE Grant reference 1700064 and BAE Systems

REFERENCES

[1] J. Norris, A. Hameed, J. Economou, and S. Parker, "A review of dual-spin projectile stability," *Defence Technology*, no. xxxx, 2019. [Online]. Available: https://doi.org/10.1016/j.dt.2019.06.003

[2] M. W. Courtney, U. S. A. F. Academy, and D. G. Miller, "A Stability Formula for Plastic-Tipped Bullets," US Air Force, Tech. Rep., 2009.

[3] D. Miller and M. Courtney, "Gyroscopic Stability of Open Tipped Match Style Rifle Bullets Gyroscopic Stability of Open Tipped Match Style Rifle Bullets," pp. 1–8, 2012.

[4] Q. W. Guo, W. D. Song, Y. Wang, and Z. C. Lu, "Guidance Law Design for a Class of Dual-Spin Mortars," *International Journal of Aerospace Engineering*, vol. 2015, 2015.

[5] F. Seve, S. Theodoulis, P. Wernert, M. Zasadzinski, and M. Boutayeb, "Flight dynamics modeling of dual-spin guided projectiles," *IEEE Transactions on Aerospace and Electronic Systems*, vol. 53, no. 4, pp. 1625–1641, 2017.

[6] R. Li, D. Li, and J. Fan, "Research on Instability Boundaries of Control Force for Trajectory Correction Projectiles," *Mathematical Problems in Engineering*, vol. 2019, 2019.

[7] R. L. McCoy, *Modern Exterior Ballistics: The Launch and Flight Dynamics of Symmetric Projectiles*. Schiffer Publishing, 1999.

[8] P. Wernert, "Stability analysis for canard guided dual-spin stabilized projectiles," *Proceedings of the AIAA Atmospheric Flight Mechanics Conference and Exhibit*, no. August, pp. 1–24, 2009.

[9] D. Zhu, S. Tang, J. Guo, and R. Chen, "Flight stability of a dual-spin projectile with canards," *Proceedings of the Institution of Mechanical Engineers, Part G: Journal of Aerospace Engineering*, vol. 229, no. 4, pp. 703–716, 2015.

Journal Title
XX(X):1–13

DOI: 10.1177/ToBeAssigned
www.sagepub.com/
SAGE

A novel quasi-dynamic guidance law for a dynamic dual-spin projectile with non-conventional, asymmetric roll constraints

James Norris[1], Dr. John Economou [2] and Dr. Amer Hameed[3]

Abstract

A novel quasi-dynamic guidance law (QDGL) is presented for a dual-spin projectile (DSP) with unconventional constraints on roll direction. A 7 Degree-of-freedom (DoF) dynamic model is established and the projectile operational mechanism is presented with a description of how it is used to enact control. The QDGL is presented and a parametric study is conducted to show how the QDGL parameters affect the system response. A procedure of using batches of Monte Carlo simulations is described, to numerically compare the system response with different QDGL configuration. A Genetic Algorithm is then used to optimise both the innate system parameters and PID controller gains. The disturbance rejection capabilities of the optimal QDGL is then evaluated along with the performance against different target profiles. It was found that the GA optimised QDGL is able to provide satisfactory control capabilities against static and dynamic targets.

Keywords

Guidance Law, Dual-spin, Projectile, Genetic-Algorithm

Introduction

The calibre of guided weapons is getting ever smaller to meet the evolving needs of modern engagement scenarios. This is in turn driving a reduction of critical subsystem volumes of guidance and control hardware. It is thus pertinent to develop a novel method of control so as to either minimise the necessary subsystems occupying a volume or reduce the demand on subsystems / materials which are included in the projectile. This would allow a reduction in calibre with currently available technology without having to advance the capabilities of any specific subsystem / material.

Dual-spin projectiles (DSPs), such as STARSTREAK[1], are becoming more prevalent in today's military arsenals as they enable a wide scope of target engagement profiles. The dual spin configuration slows the roll rate of the forward section to a point where the response rate of the actuators is sufficiently high compared to their roll rate such that effective control can be enacted. The aft section stays at the high roll rate and the projectile thus maintains gyroscopic stability. Guidance modules in the form of course corrected fuses are also being retrofitted onto conventional munitions, such as the Orbital ATK Armament Systems' M1156 Precision Guidance Kit[2] and BAE's Silver Bullet[3]. In these larger weapon systems (155mm), the roll rate of the projectiles is relatively low compared to smaller calibres. For smaller projectile calibres with high roll rates, it may not prove feasible to mitigate the high roll rates to apply conventional control methods.

Some prevalent examples of conventional guidance laws (GLs) used in projectiles include Proportional Navigation (PN), Proportional Derivative (PD) and Sliding Mode Control (SMC)[4]. Conventional SMC or variations thereof have already considered constraints such as autopilot lag and actuator fault[5], accelerator saturation[6], and modelling uncertainty in missile/target dynamics. Impact angle is often the considered aspect for control in a GL. In addition to purely controlling the impact angle[7], secondary constraints have also been placed on trajectory time[8], field-of-view[9–11], and manoeuvrability[12]. External uncertainties and missile jerk have also been considered[13]

A modified SMC GL was used to improve the chattering, miss-distance and finite time over conventional SMC and PN methods[14]. The validity of the PN-like LOS GL has been investigated for three body (two aircraft, one missile) system where the launch platform is also moving[15]. A novel variation, called 'airborne-CLOS' utilises two separate LOS rates with one gain to control the three body problem[16].

A novel GL has been created utilising virtual targets for impact angle and burst height constraints[17]. A polar GL has been investigated which controls a missile based on the polar radius and angle of the target from the missile[18]. An Expanded 2D PD GL was created for a skid-to-turn command to LOS anti-tank guided missile, which builds upon classic PD, with the objective of eliminating a spiral trajectory which is an artefact of PD GLs[19]. A proposed

[1] PhD Researcher in Defence & Security, Cranfield University, Defence Academy of the United Kingdom, Shrivenham
[2]Deputy Head of Centre for Defence Engineering, Cranfield University
[3]Professor in Defence Engineering, Cranfield University AND Saudi Arabian Military Industries, Riyadh, KSA

Corresponding author:
Defence Academy of the United Kingdom, Faringdon Rd, Shrivenham, Swindon SN6 8LA, UK.
Email: james.norris@cranfield.ac.uk

method uses a weighted zero-effort-miss (ZEM) to shape the actual ZEM, presenting as a PN GL with an extra time varying gain.

A few publications specifically pertain to the guidance of DSPs. Iterative impact point prediction has been used to create a GL for a DSP with control force imparted by fixed canards[20]. A modified form of projectile linear theory is used to predict where the projectile will land and make the necessary corrections to the control system. Proportional navigation has been used in the GL of a dual-spin mortar during the ascent and descent phase[21]. The results of the GL were validated with hardware-in-the-loop testing and Monte Carlo simulations.

It is common practice to neglect gravitational forces when creating a GL[22–25]. Once an idealistic GL has been created, constraints can then be placed on the model which reflect conditions present in chosen real world systems. GLs are often described from the perspective of the YZ plane (shown in fig. 3) also known as the 'picture plane'[7,18,19]. Some of the cited literature use kinematic models for the derivation and validation of the control law[8,12,14,15,17], while this paper uses a dynamic projectile model. It is common to test the GL using arbitrary model parameters to facilitate more efficient and reliable interpretation of the results[18,19].

Conventional projectile control utilises control surfaces which are able to adjust the roll angle of a projectile as well as the magnitude of the control force. The conventional guidance strategy is to roll the projectile to align the controllable pitch axis with the desired direction, then increase the force by actuating the control surfaces which results in lateral movement. Dual spin projectiles use a similar method with the addition of a coaxial motor to assist the correction of the forward section roll angle[26]. This paper proposes a quasi-dynamic GL (QDGL) for a DSP, with a fixed roll direction as well and a fixed magnitude control force; however the phase of the force can change, hence the quasi nature. Control is enacted by adjusting the roll *rate* of the control force, slowing it down through certain roll angles to bias the force in the desired direction. There currently exists no literature which describes a GL for a DSP with roll-direction, roll-rate and control-force magnitude constraints.

Section describes the 7 Degree-of-freedom (DoF) dynamic model of the projectile used in simulations. Section introduces the projectile design and describes how control is enacted with the asymmetric roll constraints. The QDGL and associated parameters are introduced, with a brief parametric investigation showing their effect on the system response. Section presents a Monte Carlo procedure which is used to numerically compare the effect that different QDGL configurations have on the system response. A Genetic algorithm is then run to optimise the QDGL parameters as well as the gains of a PID controller. The system response of the optimised QDGL is evaluated against various disturbances and target profiles. Section gives a summary of the paper and the key findings.

Projectile dynamics

This section describes the 7 DoF dynamic model of the DSP, which has previously been used to investigate DSPs[21,27–29] and is a derivative of the well-established model for a conventional projectile used by McCoy[30]. Subscript F denotes the forward section and subscript A denotes the aft section. The assumption is made that the total centre of mass (COM) coincides with the aft COM, *i.e.* the mass of the forward part is small with respect to that of the aft part and the nose moment of inertia $I_{xx,F}$ is small compared to the aft one $I_{xx,A}$. The forces and moments the projectile is subject to are represented by an aerodynamic coefficient. The whole body longitudinal C_{A0}, transverse C_{Y0} and normal C_{N0} coefficients represent the combined effect of these individual forces, and are shown in figure 1 for non-zero angles of attack α. The non-linear kinematic translational

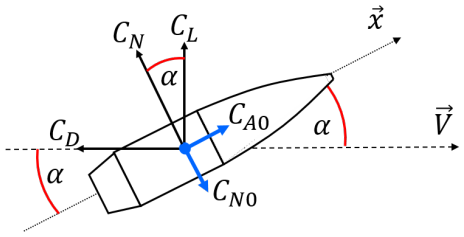

Figure 1. Projectile coefficients when $\alpha \neq 0$

and rotational equations are given by equations 1 and 2 respectively.

$$\begin{bmatrix}\dot{x}_e\\ \dot{y}_e\\ \dot{z}_e\end{bmatrix} = \begin{bmatrix}\cos(\theta)\cos(\psi) & -\sin(\psi) & \sin(\theta)\cos(\psi)\\ \cos(\theta)\sin(\psi) & \cos(\psi) & \sin(\theta)\sin(\psi)\\ -\sin(\theta) & 0 & \cos(\theta)\end{bmatrix}\begin{bmatrix}u\\ v\\ w\end{bmatrix} \tag{1}$$

$$\begin{bmatrix}\dot{\phi}_F\\ \dot{\phi}_A\\ \dot{\theta}\\ \dot{\psi}\end{bmatrix} = \begin{bmatrix}1 & 0 & 0 & \tan(\theta)\\ 0 & 1 & 0 & \tan(\theta)\\ 0 & 0 & 1 & 0\\ 0 & 0 & 0 & \sec(\theta)\end{bmatrix}\begin{bmatrix}p_F\\ p_A\\ q\\ r\end{bmatrix} \tag{2}$$

Accordingly, the dynamic translational is shown in eq. 3

$$\begin{bmatrix}\dot{u}\\ \dot{v}\\ \dot{w}\end{bmatrix} = \frac{1}{m}\begin{bmatrix}F_X\\ F_Y\\ F_Z\end{bmatrix} - \begin{bmatrix}0 & -r & q\\ r & 0 & r\tan(\theta)\\ -q & -r\tan(\theta) & 0\end{bmatrix}\cdot\begin{bmatrix}u\\ v\\ w\end{bmatrix} \tag{3}$$

while the dynamic rotational equation is shown in eq. 4

$$\begin{bmatrix}\dot{p}_F\\ \dot{p}_A\\ \dot{q}\\ \dot{r}\end{bmatrix} = \begin{bmatrix}0\\ 0\\ -\left(\frac{I_{xx,A}}{I_{yy}}\right)p_A r - r^2\tan(\theta)\\ \left(\frac{I_{xx,A}}{I_{yy}}\right)p_A q + qr\tan(\theta)\end{bmatrix} + \begin{bmatrix}I_{xx,F}^{-1} & 0 & 0 & 0\\ 0 & I_{xx,A}^{-1} & 0 & 0\\ 0 & 0 & I_{yy}^{-1} & 0\\ 0 & 0 & 0 & I_{yy}^{-1}\end{bmatrix}\cdot\begin{bmatrix}m_{1,F}\\ m_{1,A}\\ m_m\\ m_n\end{bmatrix} \tag{4}$$

Here, the forces $[F_X \;\; F_Y \;\; F_Z]^{\mathrm{T}}$ and moments $[m_{1,F} \;\; m_{1,A} \;\; m_m \;\; m_n]^{\mathrm{T}}$ are given by equations 5 and 6

respectively

$$\begin{bmatrix} F_X \\ F_Y \\ F_Z \end{bmatrix} = \bar{q}S \left\{ \begin{bmatrix} -C_{A0} \\ C_{Y0} \\ -C_{N0} \end{bmatrix} + \frac{p_A d}{V} \begin{bmatrix} 0 \\ C_{Yp} \\ -C_{Np} \end{bmatrix} + \right. \\ \left. + \begin{bmatrix} 0 \\ C_{Y\delta}\delta_y \\ -C_{N\delta}\delta_z \end{bmatrix} \right\} + mg \begin{bmatrix} -\sin(\theta) \\ 0 \\ \cos(\theta) \end{bmatrix} \quad (5)$$

$$\begin{bmatrix} m_{1,F} \\ m_{1,A} \\ m_m \\ m_n \end{bmatrix} = \bar{q}Sd \left\{ \begin{bmatrix} 0 \\ 0 \\ C_{m0} \\ -C_{n0} \end{bmatrix} + \frac{d}{V} \begin{bmatrix} 0 \\ C_{lp} \\ C_{mq} \\ C_{nr} \end{bmatrix} + \right. \\ \left. + \frac{p_A d}{V} \begin{bmatrix} 0 \\ 0 \\ C_{mp} \\ C_{np} \end{bmatrix} + \begin{bmatrix} 0 \\ 0 \\ C_{m\delta}\delta_z \\ C_{n\delta}\delta_y \end{bmatrix} \right\} + \begin{bmatrix} \tau_M + \tau_{F,A} \\ -\tau_{F,A} \\ 0 \\ 0 \end{bmatrix} \quad (6)$$

Here, $\mathcal{M}$ is the Mach number, τ_M is the motor torque which controls the roll angle of the forward guidance section (ϕ_F) and $\tau_{F,A}$ is the frictional torque which counteracts this. The frictional torque can be modelled as a hydrodynamic and roller bearing in combination where k_s and k_v are the static and viscous friction coefficients respectively

$$\tau_{F,A} = \frac{1}{2}\rho S d\, C_{A0}(\mathcal{M}, \alpha, \beta)\text{sgn}(p_A - p_F)(k_s + k_v|p_A - p_F|) \quad (7)$$

Quasi-dynamic guidance law formulation

This section describes the control method of the DSP design with unconventional roll constraints. The QDGL is formulated and the resulting system response is shown. A brief parametric study is conducted to illustrate how the QDGL parameters affect the system response.

Most guided projectiles have fins which can roll the projectile and induce a variable control force along a pitching axis. If lateral deflection is required, the projectile adjusts its roll angle such that the axis of the control force is parallel to the direction of required travel, whereby it increases the control force and therefore imparts an acceleration. Fig. 2 shows the DSP design, a control force F_c is produced by aerodynamic lifting surfaces on the forward section. At launch, the aft section engages with the rifling which accelerates the roll rate, while the forward section producing F_c remains de-spun. During flight, the two sections will reach an equilibrium through the bearing torque $\tau_{F,A}$ and the forward section will have a relatively slow roll rate, ω_0. If $\tau_{F,A}$ is increased during flight (*e.g.* by means of a brake) then there will be new equilibrium where the forward section has a higher roll rate, ω_1.

Figure 3 shows the key parameters of the control method, as well as the YZ plane, referred to as as the picture plane. The constant magnitude F_c moves through a roll angle ϕ with rate ω_0 or ω_1, where $\omega_0 < \omega_1$. The $\phi \in [0, 2\pi]$ describes the roll orientation of F_c with respect to the normal axis. It sweeps in the negative mathematical direction, since most conventional projectiles have a right hand twist. The novel guidance strategy proposed herein uses a fixed magnitude F_c

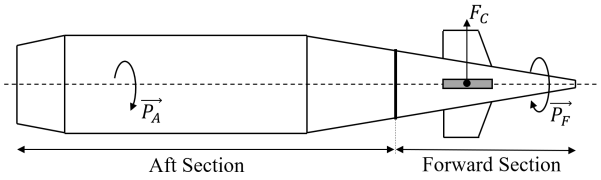

Figure 2. DSP with fixed control force F_c

rolling at speed ω_1. The roll rate is slowed to ω_0 through favourable roll angles when F_c is aligned with the desired correction axis, then accelerated back to ω_1 through the remaining unfavourable roll angles. The act of slowing F_c when sweeping through favourable roll angles is henceforth referred to as a 'bias'. All measurements and symbols henceforth are given in the 'picture plane' reference frame unless explicitly stated.

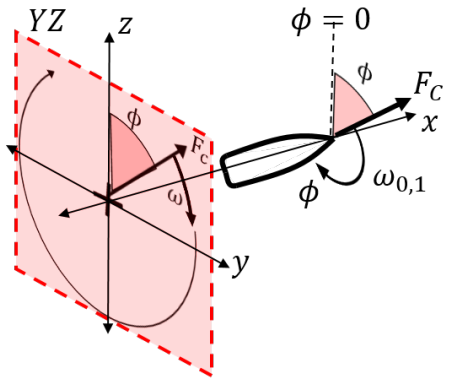

Figure 3. Earth axis perspective of picture plane and control force F_c rotating at rate ω_1 through angle ϕ

The integral of Newton's second law relates the impulse of an object, J, to its change in velocity Δv.

$$J|_{\Delta t} = m\, \Delta v|_{\Delta t} \quad (8)$$

Here the mass is assumed constant since there are no on-board resources being consumed. A generalised decomposition of F_c onto any orthonormal axis i, j in the YZ plane has the corresponding forces F_i, F_j. Let the desired decomposition axis i be an angle ϕ_B from the normal axis $\hat{z}$ (where $\phi = 0$). Let ϕ_i be a particular angle between F_c and the arbitrary decomposition axis i. Let ϕ_a be the angle through which F_c sweeps at a given rate ω such that the sweep begins at the angle $(\phi_B - \phi_a)$ and ends at ϕ_B.

The range of angles during which F_c is slowed is defined as the bias angle. Let the mid-point of the bias angle coincide with decomposition axis i, such that the symmetrical angle on either side of the midpoint is ϕ_a. The bias angle thus starts at $(\phi_B - \phi_a)$ and ends at $(\phi_B + \phi_a)$ with a midpoint of ϕ_B. This is shown in fig. 4. However, F_c will continue to rotate through the rest of the angle ϕ eventually sweeping another angular range $(\phi_B + \pi) \pm \phi_a$ (wrapped so $\phi \in [0, 2\pi]$). During this time the resulting change in velocity is directed along the negative i^{th} axis.

We define ΔV as the total change in velocity of one whole roll rotation in sweeping through equal but opposing angles of size $2\phi_a$, at different rates ω_0 and ω_1. Assuming F_c, m

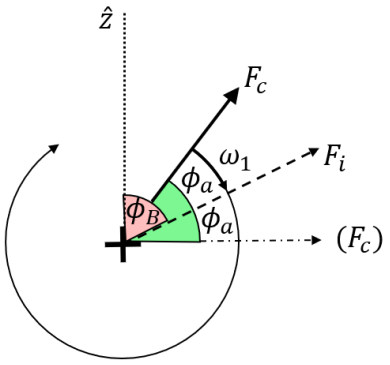

Figure 4. Bias manoeuvre of size ϕ_a centred about ϕ_B

and ω are constant, it can be shown from eq.8 that

$$\Delta V = \frac{2F_c}{m}\sin(\phi_a)\left(\frac{\omega_0 - \omega_1}{\omega_0\omega_1}\right) \tag{9}$$

The maximum bias angle is half of a roll rotation, $\phi_{a,\max} = \pi/2$. The maximum ΔV per rotation is thus given by

$$\Delta V_{\max} = \Delta V|_{\phi_a=\pi/2} \tag{10}$$

which is evaluated for a given system. Table 1 shows a comparison between the idealised parameters which are used during analysis of the QDGL, and values that can be expected for real systems. Lloyd & Brown[31] investigated the maximum lateral control force F_c which can be applied to the nose of a projectile before flight instability occurs. For a 15kg, 105mm projectile, no more than 40N (0.34g) could be applied. Li *et al.*[29] continued this work and concluded that the same projectile would remain stable provided $F_c \in [-35.48, 58.33]$. Provided F_c is within the limits defined by these frameworks, projectile stability is ensured by satisfying the gyroscopic stability criterion[32]. When designing such a projectile, the gyroscopic and dynamic stability framework for DSPs[33] or other methods[34] can be used.

Since the purpose of this paper is to test whether the uni-rotational, fixed magnitude control force can be used to guide a projectile in the 2D plane, all forces and moments except the control force are neglected. Additionally, there is no transient between the fast and slow oscillations, the switching is instantaneous.

By design, the QDGL calculates a desired change in speed when $\phi = 0$, then calculate the bias angles from eq. 9. The projectile will then continue to roll, whereby the actuator will slow the roll down if the current roll angle lies within the bias range previously calculated. In practice, the desired speed change and resulting bias angles are calculated when ϕ lies in a small range, $\phi \in [0, 0.001]$, to account for the machine computation inaccuracy. While this calculation could be conducted and updated continuously, the relative speeds would have to transformed to the $\phi = 0$ reference frame which adds another layer of computational complexity. In addition, this discrete computation of speeds at the beginning of each rotation accommodates the bandwidth of hardware with respect to the roll rate of the projectile.

The current relative velocity of projectile to target is the difference between the projectile and target velocity, $V_R = V - V_T$, or in full

$$\mathbf{V}_R = \begin{bmatrix} u_R \\ v_R \end{bmatrix} = \begin{bmatrix} u - u_T \\ v - v_T \end{bmatrix} \tag{11}$$

N.B. the projectile having $[u_0, v_0] = [0, 0]$ and undergoing consecutive unbiased rotations does not result in a circular trajectory; instead a semi-circular trajectory would result. To achieve a circular trajectory in the resting state, the horizontal velocity at the beginning of the bias calculation must assume the control force has already rotated through one quarter rotation. Taking this into consideration, we define V_{DR0} as the ΔV correction necessary to bring the projectile to a stable circular orbit relative to the target, including the current relative velocity

$$V_{DR0} = \begin{bmatrix} u_R + \Delta V|_{\phi=\pi/4} \\ v_R \end{bmatrix} \tag{12}$$

This only allows the autopilot to bring the projectile to relative rest, the desired closing speed $V_{PT}(d)$ describes the chosen approach speed as a function of d. The total demanded velocity change from the velocity autopilot V_{Dem} is then a linear combination of the necessary relative speed correction to bring the system to an orbit, V_{DR0}, and the closing velocity $V_{PT}(d)$ dictated by the QDGL:

$$V_{Dem} = V_{DR0} + V_{PT}(d) \tag{13}$$

$V_{PT}(d)$ must only demand speeds which can be delivered by the actuation mechanism, given that ΔV can never exceed ΔV_{max}. Let the function $V_{lim}(d)$ be the maximum relative speed the projectile can have at a distance $d \geq 0$, such that it is still able to decelerate in time to be at relative rest when $d = 0$. This function can be calculated by starting with a stationary projectile and applying consecutive ΔV_{max} biases, since the process is reversible. From the rates given by the idealised system parameters in table 1, a $\Delta V_{max} = 0.9549\mathrm{ms}^{-1}$ bias is enacted by the projectile in 2.5s. An effective acceleration value, $\tilde{a}$, is measured from simulations for consecutive ΔV_{max} biases. Using this, it can be shown that

$$V_{Lim}(d) = (2\tilde{a}d)^{\frac{1}{2}} \tag{14}$$

Since the function $V_{PT}(d)$ is calculated when $\phi = 0$ at a particular distance d_1, the desired ΔV will not be achieved until after the bias manoeuvre has been executed, one full rotation later. Hence, the process is discontinuous. By this point the projectile will have moved to some new distance d_2 under its residual velocity. Fig. 5 shows the delay of the system response when the target speed is set to be the limit of the system, *e.g.* $V_{PT}(d) = V_{lim}(d)$. The data points indicate specific positions where $\phi = 0$, triggering the calculation of the bias angles. The fig. illustrates how the value of $V_{lim}(d)$ demanded at a specific point is achieved at the next calculation point, but after the delay caused by the roll rotation. This delay causes the system to exceed $V_{lim}(d)$, resulting in an overshoot. To account for the delay, the demanded speed is modified by a factor ξ which ensures the relative speed never exceeds $V_{lim}(d)$. The delay does not directly scale with distance but rather with $V_{PT}(d)$ as it is the result of dynamic system evolution. Hence the closing speed function is written as

$$V_{PT}(d) = V_{lim}(d) - \xi, \quad \xi \in \mathbb{R} \geq 0 \tag{15}$$

Table 1. Comparison of simulation parameters used against real-world projectiles

Parameter	Idealised System	105mm	155mm Projectile
ω_0 [rad.s^{-1}]	$\pi/2$	N/A	N/A
ω_1 [rad.s^{-1}]	2π	1050[29]	1668[35]
m [kg]	1	15[29]	42.798[36]
F_c [N]	1	$[-35.48, 58.33]$[29]	20[35]

where ξ is a constant to be optimised. The result of this modification is also shown in fig. 5, where the adapted system response never exceeds the limit, *e.g.* $V_{PT}(d) = V_{lim}(d) - \xi \mid V_R(d) \not> V_{lim}(d)$.

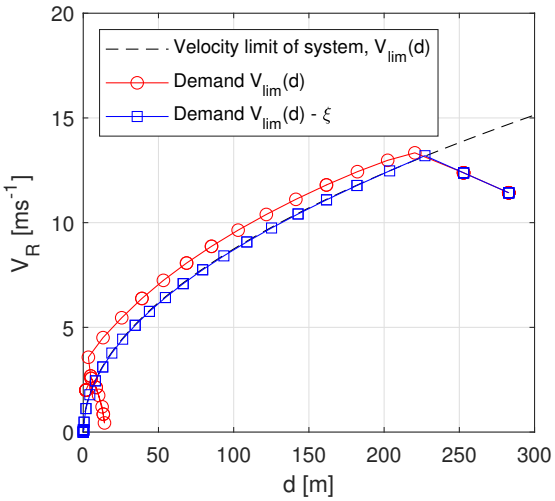

Figure 5. Effect of ξ to prevent system response exceeding $V_{lim}(d)$

By including ξ, $V_{PT}(d)$ is not properly defined when $d \leq d_1$ where $d_1 | (V_{PT}(d_1) - \xi = 0)$. From eq. 14 this boundary is

$$d_1 = \frac{\xi^2}{2\tilde{a}} \tag{16}$$

As such, the function $V_{lim}(d) - \xi$ is only valid for $d \in (d_1, \infty]$ and must be defined by other means for $d \in [0, d_1]$. Firstly, the distance d_2 is chosen to represent the desired level of precision for the projectile. The projectile will remain relatively stationary within this threshold, when it is on course to hit the target, so $V_{PT}(d) = 0 \; \forall \; d \; \in \; [0, d_2]$ where $d_2 \in \mathbb{R} \geq 0$. Secondly, a linear region is defined where the projectile moves at a low constant velocity toward the target in anticipation of either stopping or accelerating by a larger amount. This is represented by $V_{PT}(d) = V_k \; \forall \; d \; \in [d_2, d_1]$ where $d_2 < d_1$ and $V_k \in \mathbb{R} \geq 0$ is a constant speed. In its entirety the function $V_{PT}(d)$, and thus the QDGL, for $d \in [0, \infty]$ is given by

$$V_{PT}(d) = \begin{bmatrix} V_{lim}(d) - \xi \\ V_k \\ 0 \end{bmatrix} \forall \; d \in \begin{cases} d_1 \leq d \\ d_2 \leq d < d_1 \\ 0 \leq d < d_2 \end{cases} \tag{17}$$

Figure 6 shows an example system response with annotations showing the different regimes governed by equation 17. $V_{PT}(d) = V_{lim}(d) - \xi$ is the closing regime, $V_{PT}(d) = V_k$ is the linear regime and $V_{PT}(d) = 0$ is the stationary regime. In addition, the aspects of the steady state error are the transient, the steady state amplitude and the oscillation amplitude. The transient is also the motion of the projectile in the linear regime; a faster V_k provides a faster transient speed. The steady state amplitude can be thought of as the distance d of the 'orbital centre' from the target. The oscillation amplitude, and in addition the oscillation frequency, is governed by F_c and $\omega_{0,1}$, neither can be affected by modifying V_k or ξ. These oscillations are caused by the holding orbit described in eq. 12, if the locus of the assumed circular orbit coincides with the target then there will be no oscillations. However, if any small perturbation offsets the orbit loci or the orbit isn't perfectly circular, the amplitude of the steady state error and steady state oscillations will increase. If the steady state oscillation continues periodically then the orbit is stable, and the projectile is remaining in the stationary regime. If the steady state has another, lower frequency oscillation, the orbit is not stable. This is caused by the linear regime velocity V_k being too great for the current d_2, causing the projectile to pass straight through the stationary regime. *N.B.* the regimes are governed by d and so the vertical lines representing them on fig. 6 should be horizontal; this was intentional, to aid interpretation.

Figure 7 illustrates how V_{lim} is modified in the QDGL to account for the system response lag. V_{lim} acts as the reference signal which the QDGL then modifies using ξ. The closing speed function $V_{PT}(d)$ is then passed to the autopilot, which calculates the change in speed per revolution demanded from the projectile's actuator mechanism V_{Dem}. The V_{Dem} can then be passed through a chosen controller H, such as a PID. The V_{Dem}, modified under the action of controller H, is then passed to the actuator mechanism which saturates the signal such that $V_{Dem} \in [0, \Delta V_{max}]$. *N.B.* V_{max} is an absolute limit of the system resulting from the maximum bias angle of one half roll revolution, it is not a characteristic of any physical actuator hardware. If $V_{Dem} > V_{Max}$ the system will saturate and will only be able to deliver V_{Max}. As such, any $H > 1$ when the autopilot is already demanding $V_{PT} = V_{max}$ will have no effect on the system whatsoever.

The sensor block shown in fig. 7 represents the sensor dynamics of the system which are assumed in the idyllic system to be perfect and instantaneous. For practical implementation, conventional on-board sensors or an external detection system could be used to measure the roll angle, similar to that described in[37]. If volumetric restrictions permit, on-board image sensing hardware could be used[38]. Linear ballistic theory could also be used to estimate the change in roll rate of the projectile along the

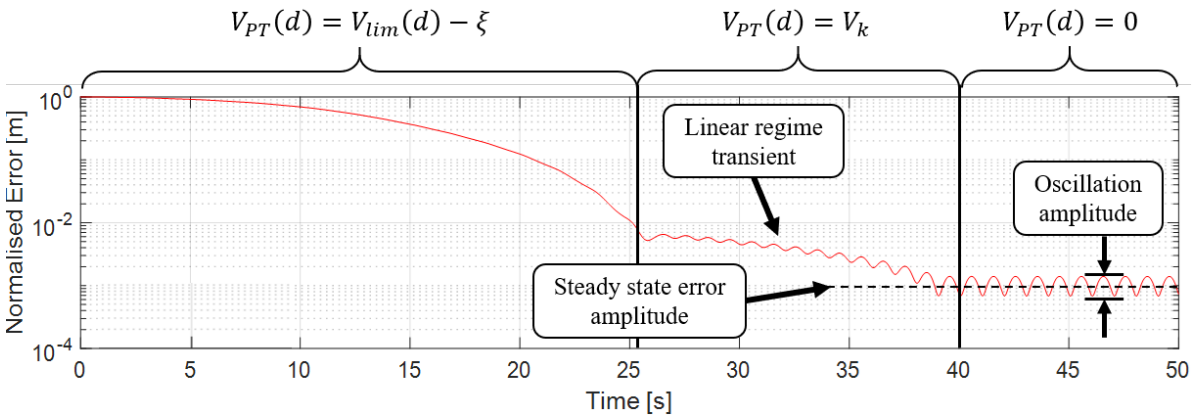

Figure 6. System response showing different QDGL regimes

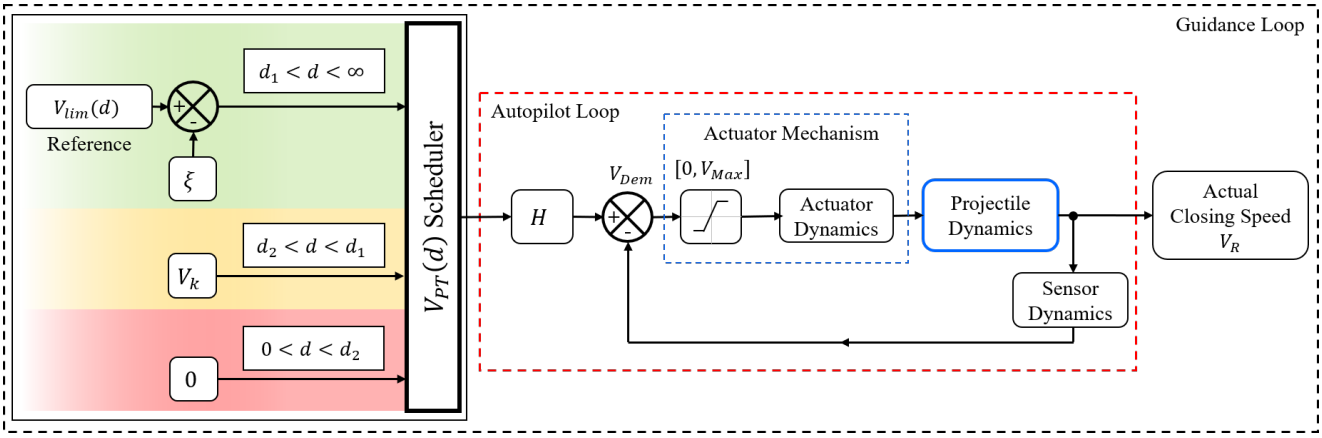

Figure 7. Modification of V_{lim} for speed controller with velocity feedback

trajectory beyond what is known from projectile launch, to supplement information from the sensors.

Parametric investigation

With the QDGL fully presented, the system parameters V_k, ξ, d_1 and d_2 can be investigated, with extreme variation in the parameters being shown to demonstrate their functionality and impact on system response. A more high-fidelity optimisation is conducted in section .

Figure 8 shows how modifying ξ to extreme values affects the system response. When $\xi = 0$, the system response exceeds V_{lim} which was the case in fig. 5; leading to a large overshoot and oscillatory motion where the projectile closes with a speed which is too high. Any negative value of ξ yield a steady state error that is unacceptably high, thus it is not shown on the figure. For low values, $0 < \xi < 1$, the error is reduced quickly with a low amplitude steady state error and no higher order oscillations. High values, $\xi \geq 1$, produces a large amplitude steady state error

Figure 9 shows three example trajectories which correspond to the extreme values of ξ from fig. 8. The high steady state error for large ξ is represented by the projectile being brought to rest too far from the target. The high amplitude decaying oscillations in normal error for $\xi = 0$ is visible as the projectile overshoots the target by a large margin. This is caused by too high a speed being demanded and the projectile is unable to reduce its speed in time due to

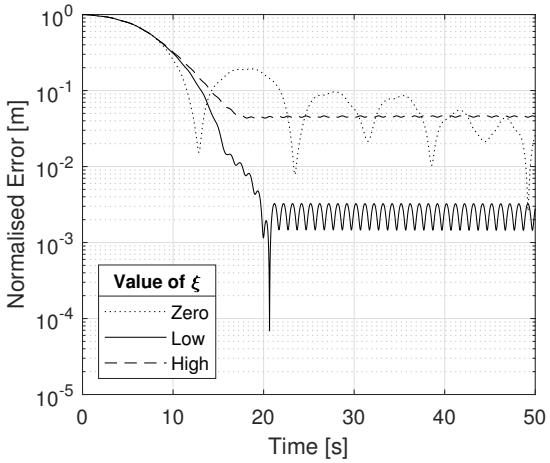

Figure 8. How extreme values of ξ affect the normalised error

the system lag. For low values of ξ the projectile is brought sufficiently close to the target to initiate a regime change.

Figure 10 shows the effect of modifying the linear regime constant velocity V_k. All speeds initially follow the same error reduction path, from $t = 0$ to $t = 12$. This is the range governed by $V_{PT}(d) = V_{lim}(d) - \xi$ and thus modifying V_k has no effect. If V_k is sufficiently small, as the projectile transitions from the linear velocity to the stationary regime, the orbital centre is brought to rest very close to the boundary of the stationary regime, d_2. This results in a higher

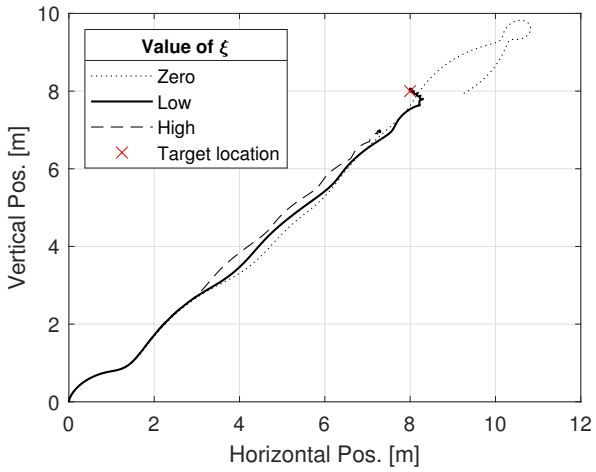

Figure 9. How extreme values of ξ affect picture plane trajectory

amplitude steady state error than if the velocity was high enough to reduce the distance to $d \to 0$ before it was brought to rest. This is apparent from the figure, as an increasing value of V_k results in a lower amplitude of steady state error, up to the point that V_k is too high resulting in an overshoot. The optimal V_k is a trade off with d_2 to deliver the orbital centre sufficiently close to the target before switching to the stationary regime.

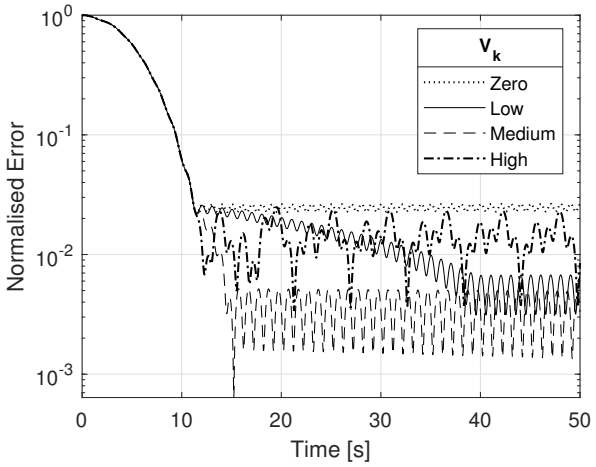

Figure 10. How varying V_k affects transient and steady state error

In this case for $V_k = 0$ the linear regime vanishes, merging with the stationary regime *i.e.* $V_{PT}(d|d \in [0, d_2]) = V_{PT}(d|d \in [d_2, d_1]) = 0$. The result of this is that the projectile enters the stationary regime at a distance d_1 and this is apparent from the figure, with a steady but large magnitude steady state error. For low values of V_k the transient is very slow, but the amplitude of the steady state error is small. For medium values of V_k, the most desirable system behaviour can be observed. There is a very quick transient period followed by a low steady state error amplitude. For high values of V_k there is an unstable switch between the linear and stationary regimes, caused by a sufficiently high overshoot to exceed d_2.

Figure 11 shows the effect of modifying the boundaries of the linear regime, d_1 and d_1. While d_1 is determined after a value of ξ has been selected, since $d_1|\ (V_{PT}(d_1) - \xi = 0)$, it is varied manually here to illustrate the impact. Likewise, d_2 is selected based on the chosen level of accuracy of the system. If the boundaries are set to be equal, $d_1 = d_2$, then there is no linear regime, it is bypassed completely and the velocity is brought to relative rest immediately. This leads to a large steady error, as was the case for low values of ξ and V_k. The steady state oscillation amplitude is the same as for any other case, since F_c, ω_0 ad ω_1 are not being modified. If d_2 is small then the projectile gets closer to the target before switching to the stationary regime. When d_2 is sufficiently small it becomes significant compared to the distance that can be travelled by the projectile travelling at speed V_k during the time for one complete roll rotation. This results in an unstable steady state oscillation from overshooting, where the projectile continuously switches between the linear and stationary regime, which is indicated by the late regime termination on the figure. Desirable system behaviour is observed from the ideal duration on the figure, with a steady transient from the dynamic to the stationary regime followed by a stable steady state oscillation. With an early regime activation, the speed demanded of the projectile is significantly lower than $V_{lim}(d)$, resulting in a transient period significantly longer than in the other cases.

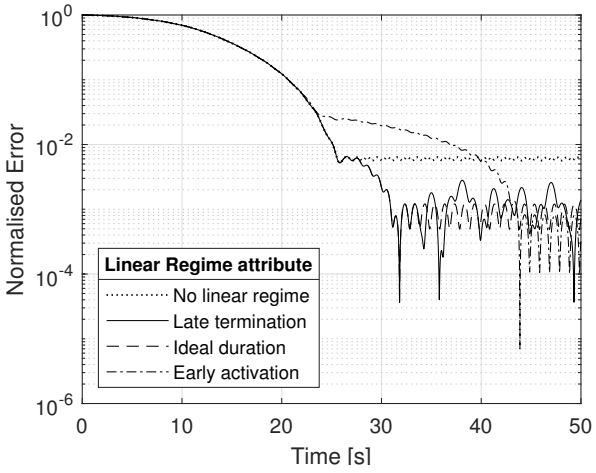

Figure 11. How varying linear regime boundaries affects transient and steady state error

The steady state amplitude for early regime activation is lower than the ideal scenario, which is not expected since the lower bound of the linear regime is the same for both simulations. The stationary regime governs all $d < d_2$, which describes a circular area around the target of radius d_2. Since the projectile only calculates the bias points when $\phi = 0$, the projectile will switch regimes at a different point depending on where the first bias calculation takes place within d_2. Small deviations in trajectory can thus cause a discrepancy in steady state amplitude, though the oscillation amplitude will remain the same in all cases. This discrepancy must be mitigated by averaging a large number of simulations.

Results and discussion

This section discusses a procedure of using a batch of Monte Carlo simulations (MCSs) to compare different QDGL configurations. This procedure is then used in a genetic

algorithm to optimise the QDGL parameters, ξ and V_K, as well as the gains of a PID controller. As discussed in section the values of d_1 and d_2 cannot be optimised and are therefore not included in this section. The performance of the QDGL with the optimised ξ and V_K is then assessed for performance rejection capabilities and evaluated against stationary and moving targets.

Monte Carlo Procedure

MCSs are used to compare the performance of different QDGL parameter configurations. Table 2 shows the range in which the model parameters are randomised upon initialisation. Once the projectile and target are initialised with randomised speeds and positions the simulation runs for a fixed time of 50s, unless otherwise specified.

Table 2. Range of values for initialisation of MCS

Parameter	Initialisation range
x_0, y_0	$[-100, 100]$
(u_0, v_0)	$(0, 0)$
ϕ_0	$[0, 2\pi]$
xT_0, yT_0	$[-10, 10]$
(uT_0, vT_0)	$(0, 0)$

Multiple MCSs are run in a 'batch'. Fig. 12 shows the average system responses for four batches of 10^4 MCSs. The difference in response is caused by the stochastic nature of the MCS initialisation. Increasing the batch size results in an average system response which is sampled over a large number of simulations, providing more consistency between batches as well as being more representative of the true system behaviour. Obviously, the maximum discrepancy between multiple batches is inversely proportional to the batch size.

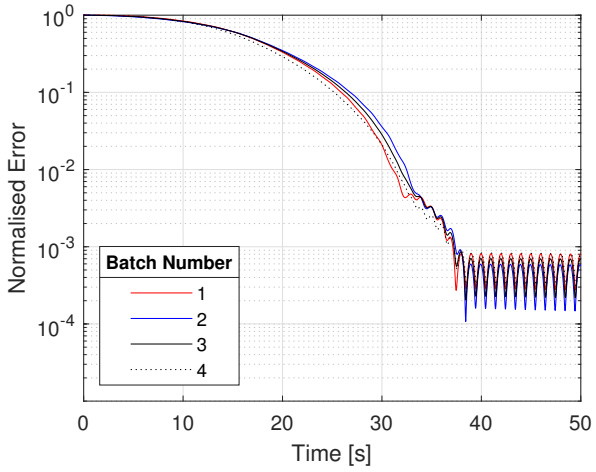

Figure 12. Response discrepancy between multiple batches of 10^4 MCSs

Figure 13 shows the instantaneous maximum error for varying batch sizes over time. For a given batch size, four separate batches are run. The maximum discrepancy between any of the four batches at any specific instances is plotted, for duration of the simulations. This process is repeated for four different batch sizes.

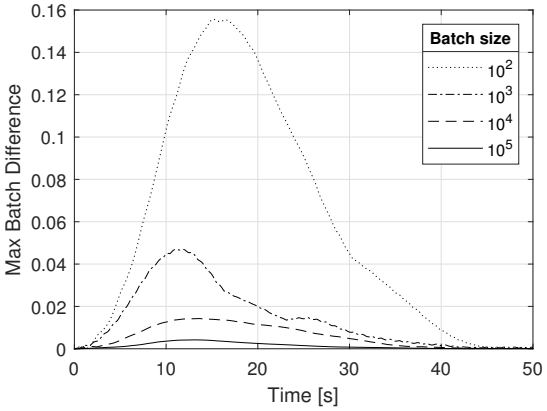

Figure 13. Instantaneous maximum variation of normalised error of different batch sizes

All batch sizes on the fig. start with the same zero error, since the error curves which are being averaged all begin at the maximum error. In addition, the same QDGL parameters are used in every simulation in a given batch, so the identical terminal error reduction capabilities produce the same steady state error in all cases. This results in the maximum error difference being small at the beginning and end of every batch. Table 3 shows the peak error difference, total integral error and computation time for each batch size shown in fig. 13. A batch size of 10^4 was chosen as the optimal trade-off between peak difference and computation time. While a batch size of 10^3 produced an integral error of the same magnitude as 10^4, the peak difference was unacceptably high.

Each MCS produces a system response like that shown in fig. 6. The system response of each MCS is normalised against the initial distance error, which was in turn randomised at the beginning of each simulation. The instantaneous error, ϵ_t is given by

$$\epsilon_t = \frac{d_t}{d_0} \tag{18}$$

The integral of the normalised system response is thus given by

$$\epsilon = \int_0^\tau \frac{\epsilon_t}{\epsilon_0}.\mathrm{dt} \tag{19}$$

where ϵ_0 is the initial error. By integrating the whole system response in this way, the system response for different QDGL configurations can be numerically compared. The size of the steady state error amplitude is small compared to the initial and transient error amplitudes. Thus, ϵ_m is representative only of the initial convergence and transient errors. However, the error amplitude of overshoots are not negligible compared to transient error amplitudes, thus overshoots will be detected by the integration. Likewise, the 'batch average integral' error, $\hat{\epsilon}$, can be computed for a batch size M as

$$\hat{\epsilon} = \sum_{m=1}^{M} \frac{\epsilon_m}{M} \tag{20}$$

where ϵ_m is the normalised integral system response of MCS m. This value allows a direct and meaningful numerical

Table 3. Error characteristics and computation time for varying MCS batch sizes

MCSs per batch	Peak difference	Total envelope error	Computation time
10^2	15.56%	2.95×10^{-1}	13 mins
10^3	4.70%	7.16×10^{-2}	2 hrs
10^4	1.43%	2.90×10^{-2}	22 hrs
10^5	0.42%	6.88×10^{-3}	9 Days

comparison of batches with different QDGL parameter configurations.

System parameter optimisation using Genetic Algorithm

Genetic algorithms (GAs) are a proven method of optimising system parameters and PID controller gains[39–42]. A basic genetic algorithm is implemented using the parameters shown in table 4. The GA was first tested on a drop-wave function of the form

$$f(x_1, x_2) = -\frac{1 + \cos\left(12\sqrt{x_1^2 + x_2^2}\right)}{0.5(x_1^2 + x_2^2) + 2} \tag{21}$$

which is a non-convex, multi-modal, continuous function with

$$min\left[f(\mathbf{x})\right] = -1 \text{ when } \mathbf{x} = (0, 0) \tag{22}$$

The GA converged to the same optimum value for 10 individual trial runs, to within 3sf, verifying the GA can repeatedly converge to a known optimum solution in the given configuration.

Both the initialisation of the GA and the MCS procedure are stochastic in nature, hence the optimum value found is not necessarily the 'true' optimum. However, the MCS procedure consistently represents the system response to within the desired degree of accuracy. In addition, the GA is of low dimensionality and is operating in a relatively low complexity space. This, in conjunction with the consistent performance of the GA when optimising the drop-wave function, reaffirm the optimum values provided by the GA are satisfactory for the scope of this paper.

Table 4. Range of values for initialisation of MCS

Parameter	Value
Generations G	200
Population size N	100
MC Batch size M	10^4

Using this MCS batch procedure, each specimen of each generation within the GA can now be meaningfully compared such that an optimal solution may evolve. Algorithm 1 shows the order of operations for the GA. The fitness function, FIT, of the GA to be minimised is simply $\hat{\epsilon}$, since this represents the average error over time for many instances for a particular QDGL parameter candidate.

$$\text{FIT} = \hat{\epsilon} \tag{23}$$

The normalised integral error of the system response for the m^{th} MCS follows from eq. 19 as

$$\epsilon_m = \int_0^\tau \frac{\epsilon_t}{\epsilon_0}.\text{dt} \tag{24}$$

Likewise, the mean normalised integral error of system response for a Monte Carlo batch of size M for specimen n follows from eq. 20 as

$$\hat{\epsilon} = \sum_m^M \frac{\epsilon_m}{M} \tag{25}$$

The Monte Carlo batch size for the proceeding is $M = 10^4$, the justification for which was discussed in section .

Algorithm 1 Execution of GA optimisation using MCS procedure

```
Randomly initialise N specimens, (ξ, v_K)_n
for Each generation g ∈ [1 : G] do
    for Every Specimen in the population n ∈ [1 : N] do
        Set QDGL parameters equal to specimen (ξ, v_K) = (ξ, v_K)_n
        Set d_1 = ξ^2/2ã (From eq. 16)
        for For MCS m ∈ [1 : M] do
            Run MCS m with random initial conditions
            Compute ε_m
        end for
        Compute specimen Fitness: FIT_n = ε̂_n
    end for
    Rank specimens in order of fitness and select candidates for reproduction
    Create offspring from candidates and cull resulting population to size
    Mutate population, then reduce mutation factor
end for
```

To reduce computation time, a preliminary search is conducted to inform the scope of the GA. Fig. 14 shows a $\hat{\epsilon}$ surface for the joint variation of $\xi \in [0.2, 1]$ and $V_k \in [0, 1.5]$. Low regions on the fig. correspond to a low $\hat{\epsilon}$ and the lowest point is with certainty, bounded by $\xi \in [0.3, 0.8]$ and $V_k \in [0, 0.5]$. High values of ξ or V_K lead to a large $\hat{\epsilon}$. Large values of ξ produce a saturated response regardless of the value of V_k. In either case, $V_{PT}(d) > V_{lim}(d)$ and there is a substantial overshoot, confirming what was seen in fig. 8 & 10. In addition, low values of V_k have a small rise in $\hat{\epsilon}$. This is not due to an overshoot, rather a slow transient results in residual error which is not present for higher values of V_k which reduces the error quicker. In addition, this surface is less complex than the drop-wave function which the GA was evaluated on during the preliminary tests, indicating the GA will with high probability, converge to the true solution.

Figures 15 and 16 show the convergence rate for the GA operating under the boundary conditions for ξ and V_k.

The optimal QDGL parameters from the GA were found to be $\xi = 0.54$ and $V_k = 0.18$.

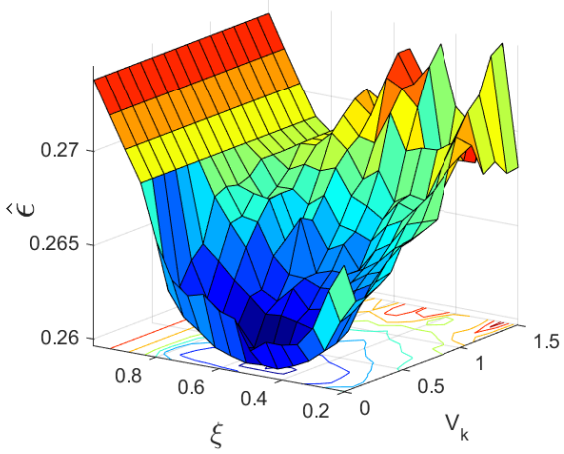

Figure 14. System response error $\hat{\epsilon}$ as function of QDGL parameters ξ and V_k

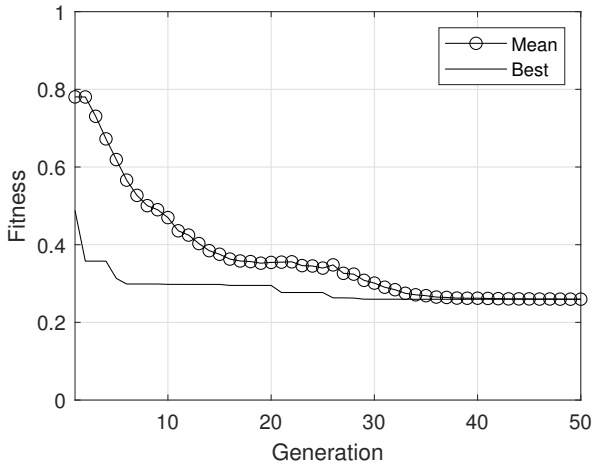

Figure 15. Convergence of 2D GA to optimise QDGL parameters

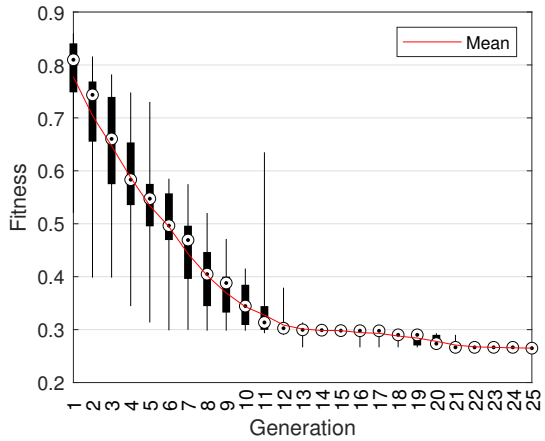

Figure 16. Generation distribution during initial convergence of GA for QDGL parameters

PID controller gain optimisation

Figure 7 included a block H which represents the chosen controller for V_{Dem}. A PID controller is used to investigate the proportional, integral and differential aspects of V_{Dem} during feedback. The use may reveal system behaviour that was not otherwise obvious from the previously discussed framework and highlight any weaknesses of the QDGL approach. During the simulation, V_{Dem} is decomposed in the YZ plane to the YZ earth axis giving $[u_{Dem}\ v_{Dem}]^{\mathrm{T}}$. This vector is then modified by the chosen controller and exported to the actuator block which calculates the bias angles using the method discussed in section . This means that one controller can act on both channels simultaneously or two controllers could act separately on each channel. Since the environment is simplified to a point of planar symmetry, one controller is chosen to act on both channels simultaneously. If external forces are introduced into the environment then two controller would be better suited to account for non-symmetrical forces which are biased to one direction, such as gravity. Using two controllers may require re-normalising the signal so any gain applied to one channel isn't lost during saturation by the actuation mechanism. Figure 17

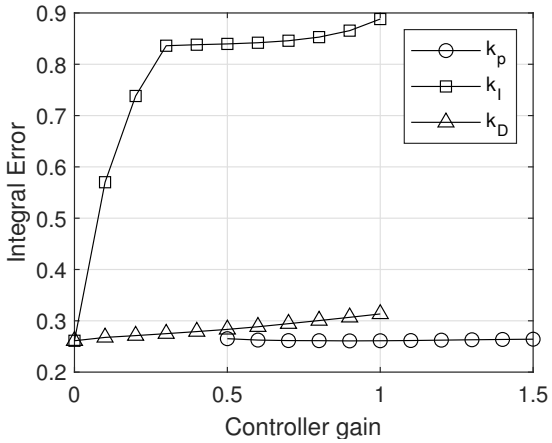

Figure 17. Contribution of independent k_P, k_I and k_D to system error

shows a preliminary search of independently varying the PID controller gains, corollary to fig. 14. The gains are initially held at $[k_P\ k_I\ k_D]^{\mathrm{T}} = [1\ 0\ 0]^{\mathrm{T}}$, which emulates the absence of a PID controller. Each gain is individually swept over the given range while the other gains remain fixed, and a MCS batch is run to determine the corresponding $\hat{\epsilon}$ for each specific gain configuration. As with the optimisation of the QDGL parameters, the intention is to reduce the scope of the GA optimisation and therefore computation time. The ranges bounding the optimum solution were found to be $k_P \in [0.6, 1.4]$, $k_I \in [0, 0.1]$ and $k_D \in [0, 0.5]$. The GA is then modified from algorithm 1, such that each specimen is now $(k_P\ k_I\ k_D)_n\ \forall\ n \in N$. Figures 18 and 19 show the convergence rate of the 3D-adapted GA. The optimal configuration of PID gains was found to be $[k_P\ k_I\ k_D]^{\mathrm{T}} = [1\ 0\ 0]^{\mathrm{T}}$, indicating that tuning the QDGL parameters is a sufficient and complete optimisation, without the need of an external controller. It is of note that the GA converged to a local minima much quicker than when optimising for ξ and V_k. This is likely due to the adverse effect any $k_I,\ k_D > 0$ has on the system response, which quickly coerces the evolution, effectively reducing the search to a 1D GA. The minimum $\hat{\epsilon}$ achieved during the optimisation of the PID controller gains was equal to the minimum $\hat{\epsilon}$ during the

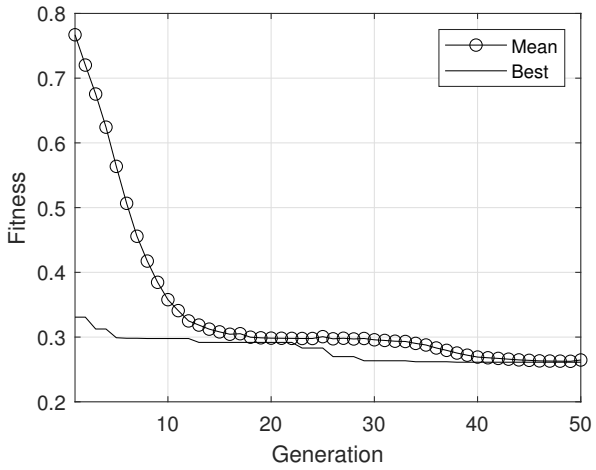

Figure 18. Convergence of 3D GA to optimise PID controller gains

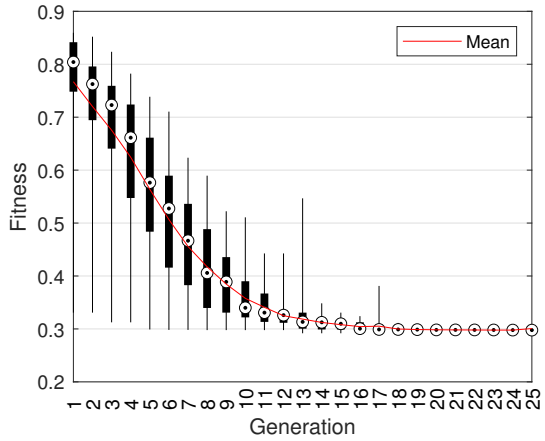

Figure 19. Generation distribution during initial convergence of GA for PID controller gains

optimisation of the QDGL, to 3sf. This is within the expected MCS batch error.

Disturbance rejection and system performance

The optimised QDGL is now tested for disturbance rejection capabilities and performance against different target profiles. Figures 20 and 21 show how the projectile responds to different disturbances. In each case, the projectile and target are initialised at a specified distance, the target closes the distance under normal operation and is then allowed to remain in steady state for a sufficient time until the chosen disturbance is applied, synchronised at 50s.

Figure 20 shows disturbance displacements, where at 50s the target coordinates are set to be a magnitude of 0.5x, 1x and 2x that of the initial displacement, as indicated by the figure. For all magnitudes of displacement, the error change is discontinuous. The initial correction response is similar for all, due to the demand of the velocity autopilot saturating the control mechanism. Once the projectile has slowed sufficiently it enters the linear regime at the same point in each case, $d \approx 10^{-2}$, since the regime switching is governed by a certain distance. There is a small discrepancy between linear regime switching for the disturbances and the initial reference signal. The reference signal enters slightly later at a lower distance. This is likely cause by the projectile crossing the regime threshold d_2 with more of the roll rotation left to complete, meaning it will travel longer before the speed is corrected again. The similarity in response is due to the fact that in all cases, the initial relative velocity between the projectile and target is zero and thus the system will response as if the simulation has just been initialised at different distances.

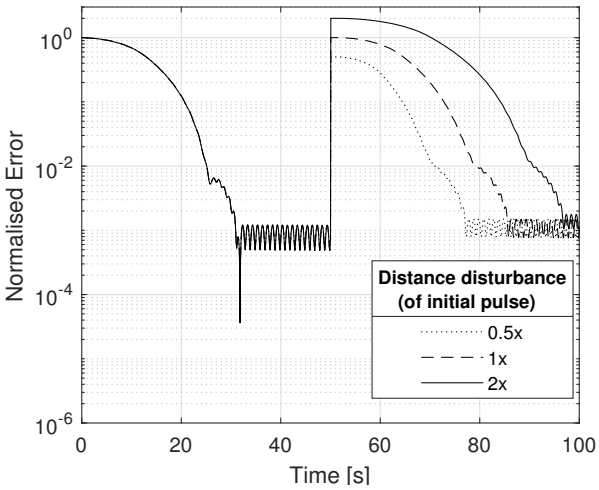

Figure 20. System response to various target distance disturbances

Figure 21 shows velocity displacements, where at 50s the relative velocity of the target is instantaneously changed to a low, medium and high respective speed, radially away from the projectile. The positions of the projectile and target are not changed, they are then free to dynamically evolve. When the velocity disturbance is low, within what the actuator mechanism is capable of correcting in one roll rotation, the disturbance is corrected quickly. With a medium disturbance, beyond the correction of one bias manoeuvre, the system takes longer to recover. Since this is a velocity disturbance the maximum error increase is not instantaneous, rather it coincides with the instant where the target is no longer moving away from the projectile and the relative speed is zero. From this point, the closing of the projectile is similar to the distance disturbances. This is the same for the high velocity disturbance, except rate of reduction of error divergence takes longer to correct.

Figure 22 shows the average normalised error for a 10^4 MCS batch against both stationary and moving targets. The response against stationary targets is the same as previously in this section. Against moving targets however, the error initially increases a small amount before decreasing in a manner similar to the response against static targets. This initial increase is due to the random chance of the projectile being initialised with speeds directed away from the target, then having to correct this dispersive motion before beginning the correction procedure.

Conclusions

A 7DOF dynamic model for a dual-spin projectile (DSP) is presented and implemented in computational simulations.

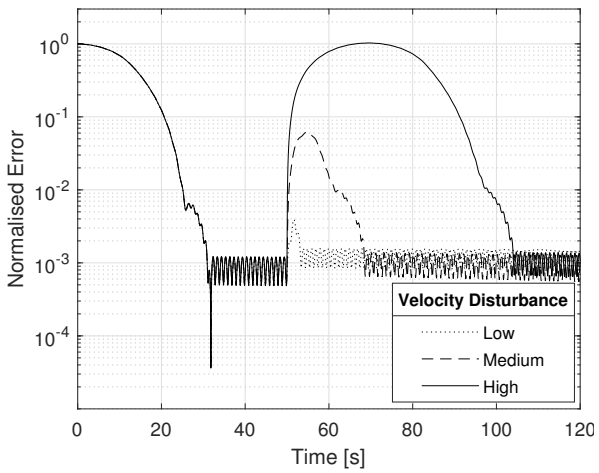

Figure 21. System response to various target velocity disturbances

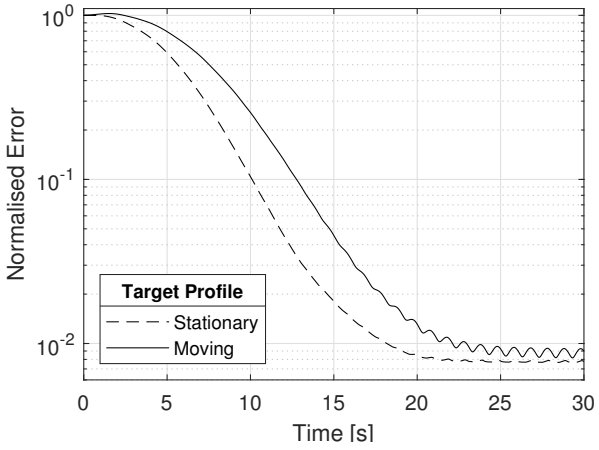

Figure 22. Performance of QDGL against target profiles

A novel projectile design is presented along with the unconventional control method of asymmetric roll-rate biases. The Quasi-Dynamic Guidance Law (QDGL) is developed and a parametric study is conducted which shows how modifying QDGL parameters affect the system response. A Monte Carlo simulation (MCS) procedure is described, which is used to meaningfully compare the system response for different parameter configurations. A Genetic Algorithm which utilises the MCS procedure is then used to optimise the QDGL parameters and PID controller gains. The disturbance rejection capabilities of the optimised QDGL are tested, as well as the effectiveness against both static and dynamic targets. In all cases, the QDGL is able to reduce the distance error to a satisfactory level.

Funding Sources

The authors have no conflict of interest to declare. This paper was sponsored by EPSRC ICASE Grant reference 1700064 and BAE Systems

References

1. Thales. Starstreak high velocity missile (hvm), 2016. URL https://www.thalesgroup.com/sites/default/files/database/document/2018-11/STARStreak_02_16SM.pdf.
2. Global Security. XM1156 Precision Guidance Kit (PGK), 2011. URL https://www.globalsecurity.org/military/systems/munitions/m1156.htm.
3. BAE. Silver Bullet - Precision Guidance Kit, 2015. URL https://www.baesystems.com/en/product/silver-bullet--precision-guidance-kit.
4. Siouris GM. *Missile Guidance and Control Systems*. Springer, 2004. ISBN 0-387-00726-1.
5. Li G, Yu Z and Wang Z. Three-dimensional Adaptive Sliding Mode Guidance Law for Missile with Autopilot Lag and Actuator Fault. *International Journal of Control, Automation and Systems* 2019; 17(6): 1369–1377. DOI:10.1007/s12555-017-0731-9.
6. Geng ST, Zhang J and Sun JG. Adaptive back-stepping sliding mode guidance laws with autopilot dynamics and acceleration saturation consideration. *Proceedings of the Institution of Mechanical Engineers, Part G: Journal of Aerospace Engineering* 2019; 233(13): 4853–4863. DOI:10.1177/0954410019835728.
7. Li Z, Ye H, Cui H et al. Sliding mode control-based guidance law with damping term and angle constraint. *Chinese Control Conference, CCC* 2019; 2019-July(61374160): 4083–4088. DOI:10.23919/ChiCC.2019.8865893.
8. Tan X. A Novel Sliding Mode Guidance Law with Impact Angle and Time Constraints 2019; : 5896–5901.
9. Sharma YR and Ratnoo A. A Bearings-Only Trajectory Shaping Guidance Law with Look-Angle Constraint. *IEEE Transactions on Aerospace and Electronic Systems* 2019; 55(6): 3303–3315. DOI:10.1109/TAES.2019.2906090.
10. Lee S and Kim Y. Capturability of Impact-Angle Control Composite Guidance Law Considering Field-of-View Limit. *IEEE Transactions on Aerospace and Electronic Systems* 2020; 56(2): 1077–1093. DOI:10.1109/TAES.2019.2925485.
11. Wang C, Dong W, Wang J et al. Nonlinear Suboptimal Guidance Law with Impact Angle Constraint : an SDRE-Based Approach 2020; XX(X): 1–10. DOI:10.1109/TAES.2020.3003105.
12. Li Q, Li J, Wang Y et al. The research of terminal optimal guidance law of MANEUVERING vehicle with multiple constrains. *2019 IEEE 10th International Conference on Mechanical and Aerospace Engineering, ICMAE 2019* 2019; : 74–78DOI:10.1109/ICMAE.2019.8880990.
13. Chwa D. Robust Nonlinear Disturbance Observer Based Adaptive Guidance Law Against Uncertainties in Missile Dynamics and Target Maneuver. *IEEE Transactions on Aerospace and Electronic Systems* 2018; 54(4): 1739–1749. DOI:10.1109/TAES.2018.2801392.
14. Alrawi AAA, Graovac S, Ahmad RB et al. Modified guidance law based on a sliding mode controller for a missile guidance system. *Tehnicki Vjesnik* 2016; 23(3): 639–646. DOI:10.17559/TV-20130625173047.
15. Ratnoo A and Shima T. Line-of-sight interceptor guidance for defending an aircraft. *Journal of Guidance, Control, and Dynamics* 2011; 34(2): 522–532. DOI:10.2514/1.50572.
16. Yamasaki T, Balakrishnan SN and Takano H. Engineering notes: Modified command to Line-of-Sight intercept guidance for aircraft defense. *Journal of Guidance, Control, and Dynamics* 2013; 36(3): 901–905. DOI:10.2514/1.58566.

17. Yang Z, Wang Z and Fan N. Virtual target based optimal guidance law with impact angle and burst height constrains. *Proceedings of 2015 7th International Conference on Modelling, Identification and Control, ICMIC 2015* 2016; (Icmic): 1–6. DOI:10.1109/ICMIC.2015.7409437.
18. Khruslov VN, Feofilov SV, Goryachev OV et al. Missile control in the polar coordinate system using a scalar radius. *Gyroscopy and Navigation* 2015; 6(1): 66–72. DOI:10.1134/S207510871501006X.
19. Penev BG. An Expanded Two-Dimensional Proportional–Derivative Command to Line-of-Sight Guidance Law. *Gyroscopy and Navigation* 2018; 9(4): 344–351. DOI:10.1134/S2075108718040132.
20. ZHANG X, YAO X and ZHENG Q. Impact point prediction guidance based on iterative process for dual-spin projectile with fixed canards. *Chinese Journal of Aeronautics* 2019; 32(8): 1967–1981. DOI:10.1016/j.cja.2019.06.002. URL `https://doi.org/10.1016/j.cja.2019.06.002`.
21. Guo QW, Song WD, Wang Y et al. Guidance Law Design for a Class of Dual-Spin Mortars. *International Journal of Aerospace Engineering* 2015; 2015. DOI:10.1155/2015/952076.
22. Ratnoo A and Ghose D. Collision-geometry-based pulsed guidance law for exoatmospheric interception. *Journal of Guidance, Control, and Dynamics* 2009; 32(2): 669–674. DOI:10.2514/1.37863.
23. Zarchan P. *Tactical and Strategic Missile Guidance*. 6th ed. American Institute of Aeronautics and Astronautics, Inc., 2012. ISBN 978-1-60086-894-8.
24. Taur DR and Chern JS. Passive ranging for dog-fight air-to-air IR missiles. *1999 Guidance, Navigation, and Control Conference and Exhibit* 1999; (c): 1737–1751. DOI:10.2514/6.1999-4289.
25. Song TL and Tae Yoon UM. Practical guidance for homing missiles with bearings-only measurements. *IEEE Transactions on Aerospace and Electronic Systems* 1996; 32(1): 434–443. DOI:10.1109/7.481284.
26. Theodoulis S, Gassmann V, Wernert P et al. Guidance and Control Design for a Class of Spin-Stabilized Fin-Controlled Projectiles. *Journal of Guidance, Control, and Dynamics* 2013; 36(2). DOI:10.2514/1.56520.
27. Lee H, Lee CH and Jun BE. Autopilot design for dual-spin projectile based on PI and feedback linearization control. In *2014 IEEE Conference on Control Applications, CCA 2014*. 2, IEEE. ISBN 9781479974092, pp. 2084–2088. DOI:10.1109/CCA.2014.6981610.
28. Seve F, Theodoulis S, Wernert P et al. Flight dynamics modeling of dual-spin guided projectiles. *IEEE Transactions on Aerospace and Electronic Systems* 2017; 53(4): 1625–1641. DOI:10.1109/TAES.2017.2667820.
29. Li R, Li D and Fan J. Research on Instability Boundaries of Control Force for Trajectory Correction Projectiles. *Mathematical Problems in Engineering* 2019; 2019. DOI:10.1155/2019/6362835.
30. McCoy RL. *Modern Exterior Ballistics: The Launch and Flight Dynamics of Symmetric Projectiles*. Schiffer Publishing, 1999.
31. Lloyd K and Brown D. Instability of Spinning Projectiles During Terminal Guidance. *Journal of Guidance and Control* 1979; 2(1): 65–70. DOI:10.2514/3.55833.
32. Robinson JWC and Berefelt F. On Guidance and Control for Guided Artillery Projectiles, Part 1: General Considerations. 2011; (October). URL `http://foi.se/ReportFiles/foir{_}3291.pdf`.
33. Norris J, Hameed A, Economou J et al. A review of dual-spin projectile stability. *Defence Technology* 2019; (xxxx). DOI:10.1016/j.dt.2019.06.003. URL `https://doi.org/10.1016/j.dt.2019.06.003`.
34. Fairfax LD, Vasile JD, Strohm L et al. Trajectory Shaping for Quasi-Equilibrium Glide in Guided Munitions 2020; (January): 1–12. DOI:10.2514/6.2020-0021.
35. Wang Y, Cheng J, yan Yu J et al. Influence of yawing force frequency on angular motion and ballistic characteristics of a dual-spin projectile. *Defence Technology* 2016; 12(2): 124–128. DOI:10.1016/j.dt.2015.12.007. URL `http://dx.doi.org/10.1016/j.dt.2015.12.007`.
36. Wang Y, ming Wang X and yan Yu J. Influence of control strategy on stability of dual-spin projectiles with fixed canards. *Defence Technology* 2018; 14(6): 709–719. DOI:10.1016/j.dt.2018.04.014.
37. Khruslov VN, Feofilov SV, Goryachev OV et al. Missile control in the polar coordinate system using a scalar radius. *Gyroscopy and Navigation* 2015; 6(1): 66–72. DOI:10.1134/S207510871501006X.
38. Fresconi F and Rogers J. Flight Control of a Small-Diameter Spin-Stabilized Projectile Using Imager Feedback 2015; 38(2). DOI:10.2514/1.G000815.
39. Lin CF, Bao PA, Braasch SJ et al. Genetic algorithm based parameter optimization of a fuzzy logic controller. *1999 Guidance, Navigation, and Control Conference and Exhibit* 1999; (c): 1117–1122. DOI:10.2514/6.1999-4152.
40. Eun Y and Bang H. Cooperative task assignment and path planning of multiple UAVs using genetic algorithm. *Collection of Technical Papers - 2007 AIAA InfoTech at Aerospace Conference* 2007; 3(May): 2680–2697. DOI:10.2514/6.2007-2982.
41. Hong B, Pey L and Soh T. *Structural Parameter Identification Using Robust Genetic Algorithm Optomization Method*. 2015. DOI:10.2514/6.2004-2015.
42. Kramer O. *Studies in Computational Intelligence 679 Genetic Algorithm Essentials*. 2017. ISBN 9783319521558.